Non-Covalent Interactions in Supramolecular Hybrid-Polyoxometalates

A thesis submitted to the University of Dublin for the degree of Doctor of Philosophy

Dipl. Chem. Paul Christopher Wix

School of Chemistry

University of Dublin

2020

Declaration

I declare that this thesis has not been submitted as an exercise for a degree at this or any other university and that it is entirely my own work, except where otherwise cited, referenced, acknowledged or accredited.

I agree to deposit this thesis in the University's open access institutional repository or allow the Library to do so on my behalf, subject to Irish Copyright Legislation and Trinity College Library conditions of use and acknowledgement.

I do consent to the examiner retaining a copy of the thesis beyond the examining period, should they so wish (EU GDPR May 2018).

Paul Wix

Summary

The research presented in this thesis revolves around the synthesis and characterisation of novel hybrid organic-inorganic polyoxometalate compounds with focus on the understanding and exploitation of covalent and non-covalent template effects. Cation-π interactions are identified for the first time as an integral part of a hybrid polyoxometalate compounds.

Chapter 1 gives the reader an introduction into the field of polyoxometalate (POM) chemistry to contextualise this work. Key concepts, such as π-π interactions, cation-π interactions and their cooperative effects are explained in detail and a brief overview of applications of POMs in catalysis and magnetism is given.

Chapter 2 describes the synthesis and characterisation of four novel hybrid organic-inorganic polyoxovanadate compounds based on thiophene-2,5-bisphosphonate as a ligand. The compounds $(NH_4)_{10}[(V_5O_9)_2(C_4H_2P_2O_6)_4(H_2O)(CH_3CN)] \cdot 5\ H_2O$ (**NH4-V_{10}**) and $Na_{10}[(V_5O_9)_2(C_4H_2S(PO_3)_2)_4(H_2O)_2] \cdot 31\ H_2O$ (**Na-V_{10}**)present an advancement to the known $\{V_{10}\}$ capsules, as the bent ligand introduces a source of flexibility into the cage, which leads to variable and adaptable window sizes. The window sizes are hereby influenced by the template molecules within the structure. Slight alteration of the reaction conditions lead to the synthesis of the compounds $Na_{12}[V_{12}O_{12}(OH)_{12}(C_4H_2S(PO_3)_2)_4] \cdot 30\ H_2O$ (**Na-V_{12}**) and $K_{12}[V_{12}O_{12}(OH)_{12}(C_4H_2S(PO_3)_2)_4] \cdot x\ H_2O$ (**K-V_{12}**), which feature a $\{V_{12}\}$ hybrid organic inorganic polyoxovanadate made from three extremely rare V^{IV} cubane units. The magnetically highly anisotropic and intrinsically frustrated molecule has been studied by SQUID magnetometry.

Chapter 3 describes the synthesis and characterisation of the supramolecular hybrid organic-inorganic $[(V_5O_9)_4(C_6H_4(PO_3)_2)_8AM_8]^{12-}$ (AM = Cs, Rb, K) system based on benzene-1,3-bisphosphonate ligands. The attempt to further widen the angles lead to a $\{V_{20}\}$ torus, in which four mixed-valent pentanuclear polyoxovanadate half-capsules are arranged around a cube of alkali metal ions with a sodium ion in the centre of the structure. The alkali metal ions hereby build out stabilising cation-π interactions with the benzene rings of the ligands. The synthesis of three $\{V_{20}\}$ compounds with potassium, rubidium and caesium as the alkali metals are reported. The alkali metal cube is proven to be an integral part of the cluster in both the solid state and aqueous solution by ESI-MS, DOSY-NMR and UV-VIS studies. Magnetic measurements indicate slow relaxation behaviour and preliminary catalytic studies show a difference in the catalysed reaction of CO_2 and epoxides between $\{V_{10}\}$ and $\{V_{20}\}$ systems.

Chapter 4 describes the synthesis and characterisation of $\{V_{20}\}$ analogues. In order to probe the effect of the cation-π interactions within the $\{V_{20}\}$ systems and their general robustness towards electronic and steric changes several variations of the $\{V_{20}\}$ clusters were synthesized. Functionalisation of the benzene-1,3-bisphosphonate ligand with an amine group in the 5-position increases cation-π interactions, which lead to a significantly decreased time of crystallisation. No $\{V_{20}\}$ species was formed by the bromine functionalised ligand, which decreases cation-π interactions. However, the use of pyridine-2,6-bisphosphonate resulted in the formation of the respective $\{V_{20}\}$ compound. In an attempt to increase the solution stability of the cluster the ligand was functionalised with *tert*-butyl groups, which effectively shield the alkali metal cube from the solution. Studies of the solution behaviour *via* DOSY-NMR, ESI-MS and UV-VIS however only slightly indicated improvement.

Chapter 5 describes the expansion of the $\{V_{20}\}$ cluster into $[(V_5O_9)_6(C_6H_3(PO_3)_3)_8AM_{8-x}]^{30-x}$ species by adding a third phosphonate functionality to the ligand. The $\{V_{30}\}$ structures consist of six inward and outward facing pentanuclear half-capsules, which form isomers that differ in their arrangement around the alkali metal cube. From 10 theoretical possible arrangements, six were found to be chemically viable due the disorder present in the structure. Three out of the six isomers were synthesised by using different alkali metals in the synthesis. Isomers, which didn't feature two adjacent inward facing half-capsules were found to feature only part of the alkali metal cube or not at all. This behaviour gives further insight into the role of the cation-π interactions within the $\{V_{20}\}$ systems.

Chapter 6 describes our work on thiomolybdate wheels, which are templated by highly functionalised ligands. The use of aromatic and non-aromatic ligands with four and six carboxylic acid moieties lead to the formation of a $[Mo_2O_2S_2(C_4H_4O(COO)_2(COOH)_2)(C_4H_4O(COO)_3(COOH))]^{3-}$ dimer, a $[Mo_{12}O_{12}S_{12}(OH)_{12}C_6(COO)_6]^{6-}$ and a $[Mo_{16}O_{16}S_{16}(OH)_{16}(C_5H_5(COO)_3(COOH)_1)_2]^{6-}$ wheel as well as unusual mixed-valent $[Mo_{30}O_{104}(OH)_3S_6(C_6(COO)_6)_2K_3(H_2O)_3]^{21-}$double decker compound, which consists of two $\{Mo_{15}\}$ wheels on top of each other.

Chapter 7 describes the experimental details for this thesis.

Chapter 8 provides a comprehensive conclusion of the work carried out and presents possible directions for further research based on the results of this thesis.

Acknowledgements

It is an easy mistake to make to look back at years of work and think of the results as solely your own achievement. As if even just your thoughts or ideas could ever exist independently from the people you've met and the places you've been. This work therefore features the contributions of many and has been influenced by many more.

First and foremost, I'd like to express my gratitude to Wolfgang for giving me the opportunity to carry out my PhD in his group. His trust, guidance and motivation has been a constant help during my time in Ireland, especially during the times, whose work has not found their way into this thesis.

I would like to thank the Wolf Gang and its wonderful people for years of fun, pints, banter and friendship which is the heart and basis of all science. I especially would like to thank Dr. Debobroto Sensharma for in depth discussions about chemistry, life and everything else, Dr. Colm Healy and Swetanshu Tandon for invaluable insight into my work, Friedrich Steuber for being my crystallographer-in-arms holding down the fort in the crystal cave, Luana Martins for the world's best timed coffee breaks during write-up and Éadaoin Whelan for mind boggling patience in countless SEM sessions. I'd also like to thank the rest of the group for making my time enjoyable. In non-alphabetical order: Rory, Kevin, Greg, Lauren, Guanghua, Amal, Ako, Adam, Xiao-Ping, Adam again, Zubair, Camelia, Teresa, Sébastien, Joju, Muhammed, Ximo, Mariah and Yom. Kaderi Karimu and Charlotte Champion did their 4th-year project under my supervision and have done tremendous work, some of which will be discussed in chapter 4.

I wish to thank the school of chemistry, their staff, academics and technicians. Special thanks to Dr. Brendan Twamley for countless hours of answering questions about crystallography and his invaluable help in solving and refinement of the crystal structures, Dr. John O'Brien an Dr. Manuel Rüther for their NMR measurements and their help in interpreting them, Dr. Guanghua Jin for carrying out catalytic studies, Dr. Gary Hessmann for some MS measurements, Fred Cowzer for always having the right advice at the right time and also to Maura, Patsy, Tom, Noelle and Teresa.

I'd like to acknowledge the contributions of our collaborators. Many thanks to Dr. Jennifer Mathieson and the group of Lee Cronin for carrying out the ESI-MS measurements of the

inorganic compounds in this thesis, Kane Esien in the group of Solveig Felton for carrying out the SQUID measurements and Dr. Irina Kühne for help with their interpretation.

During my time as PG representative for the school of chemistry I had the pleasure of working with Shane Collins and Oisin Vince Coulter, who joined me in my fight against student fees and for better conditions of PhD students.

I am very grateful for the financial support I received from the Irish Research Council and the School of Chemistry, who enabled me to carry out my PhD in the first place.

The person I am most indebted to however is my partner Natalie, who always gave me a reason to smile coming home, made the bad times better and good times even more so.

Zu guter Letzt möchte ich meiner Familie danken, die mein Studium der Chemie in Karlsruhe ermöglicht haben. Meinem Vater Michael, meiner Mutter Regine und meinem Bruder Carlo.

Abbreviations

Acac	Acetylacetonate
AM	Alkali metal
ATR	Attenuated total reflection
BVS	Bond valence sum
CSD	Cambridge structural database
CShM	Continuous shape measure
DCM	Dichloromethane
DFT	Density functional theory
DMF	N,N'-Dimethylformamide
DOSY	Diffusion ordered nuclear magnetic resonance spectroscopy
dppf	1,1′-Ferrocenediyl-bis(diphenylphosphine)
EDIPA	Ethyldiisopropylamine
EPR	Electron paramagnetic resonance
esd	Effective standard deviation
ESI	Electronspray ionisation
Fmoc	Fluorenylmethyloxycarbonyl
FT-IR	Fourier transformed infrared spectroscopy
FWHM	Full width half maximum
H_4CPTCA	Cyclopentanetetracarboxylic acid
H_4DPB-Br	Benzene-5-bromo-1,3-bisphosphonic acid
H_4-DPB-H	Benzene-1,3-bisphosphonic acid
H_4DPB-NH_2	Benzene-5-amino-1,3-bisphosphonic acid
H_4DPB-Py	Pyridine-2,5-bisphosphonic acid
H_4DPB-^{t}B	Benzene-5-*tert*-butyl-1,3-bisphophonic acid
H_4PSP	Thiophene-2,5-diphosphonic acid
H_4THFTCA	Tetrahydrofurantetracarboxylic acid
H_6Mel	Mellitic acid
H_6TPB	Benzene-1,3,5-trisphosphonic acid
HCl	Hydrochloric Acid
HPLC	High performance liquid chromatography
HSAB	Hard soft acid base

IVCT	Intervalence charge transfer
LMCT	Ligand metal charge transfer
MeCN	Acetonitrile
MEP	Molecular electrostatic potential
MO	Molecular orbital
MOF	Metal organic frameworks
MS	Mass spectrometry
NCI	Non-covalent interaction
NMR	Nuclear magnetic resonance
Ox. St.	Oxidation state
POM	Polyoxometalate
POMo	Polyoxomolybdate
POV	Polyoxovanadate
POW	Polyoxotungstate
PXRD	Powder x-ray diffraction
QTM	Quantum tunnelling of the magnetization
RT	Room temperature
SG	Space group
SMM	Single molecule magnet
SQUID	Superconducting quantum interference device
SXRD	Single crystal x-ray diffraction
TBAB	Tetrabutylammonium bromide
TM	Transition metal
TMS-Br	Trimethylsilyl bromide
tris	tris(hydroxymethyl)aminomethane
UV-VIS	Ultraviolet – Visible light
XRD	X-ray diffraction

List of Compounds

1	**NH_4-V_{10}**	$(NH_4)_{10}[(V_5O_9)_2(C_4H_2SP_2O_6)_4(H_2O)(CH_3CN)] \cdot 5\ H_2O$
2	**Na-V_{10}**	$Na_{10}[(V_5O_9)_2(C_4H_2S(PO_3)_2)_4(H_2O)_2] \cdot 31\ H_2O$
3	**Na-V_{12}**	$Na_{12}[V_{12}O_{12}(OH)_{12}(C_4H_2S(PO_3)_2)_6] \cdot 30\ H_2O$
4	**K-V_{12}**	$K_{12}[V_{12}O_{12}(OH)_{12}(C_4H_2S(PO_3)_2)_6] \cdot x\ H_2O$
5	**V_{20}H-Cs**	$Cs_{11.5}[(V_5O_9)_4(C_6H_4(PO_3)_2)_8Na_{0.5}Cs_8(H_2O)(CH_3CN)] \cdot 32\ H_2O$
6	**V_{20}H-Rb**	$Rb_{13}[(V_5O_9)_4(C_6H_4(PO_3)_2)_8Rb_8Cl_2] \cdot 30\ H_2O$
7	**V_{20}H-K**	$K_{12}[(V_5O_9)_4(C_6H_4(PO_3)_2)_8K_9(H_2O)_2]N_3 \cdot 25\ H_2O$
8	**$V_{20}NH_2$-Rb**	$[(V_5O_9)_4(C_6H_3(PO_3)_2NH_2)_8NaRb_8Cl_2]^{13-}$
9	**V_{20}Py-Rb**	$[(V_5O_9)_4(C_6H_3N(PO_3)_2)_8NaRb_8Cl_2]^{13-}$
10	**V_{20}^{t}B-Rb**	$Rb_{13}[(V_5O_9)_4(C_6H_3(PO_3)_2C(CH_3)_3)_8NaRb_8Cl_2] \cdot 29\ H_2O$
11	**V_{20}^{t}B-Cs**	$Cs_{13}[(V_5O_9)_4(C_6H_3(PO_3)_2C(CH_3)_3)_8NaCs_8Cl_2] \cdot 26\ H_2O$
12	**V_{20}^{t}B-K**	$K_{13}[(V_5O_9)_4(C_6H_3(PO_3)_2C(CH_3)_3)_8K_9Cl_2] \cdot 25\ H_2O$
13	**V_{30}-K**	$K_{27}[[(V_5O_9)_6(C_6H_3(PO_3)_3)_8K_4]N_3 \cdot 45\ H_2O$
14	**V_{30}-Rb**	$Rb_{27}[(V_5O_9)_6(C_6H_3(PO_3)_3)_8Rb_4]N_3 \cdot 50\ H_2O$
15	**V_{30}-Na**	$Na_{30}[(V_5O_9)_6(C_6H_3(PO_3)_3)_8]N_3 \cdot 53\ H_2O$
16	**V_{30}-Cs**	$Cs_{27}[(V_5O_9)_6(C_6H_3(PO_3)_3)_8]N_3 \cdot 50\ H_2O$
17	**Mo_2**	$K_3[Mo_2O_2S_2(C_4H_4O(COO)_2(COOH)_2)(C_4H_4O(COO)_3(COOH)_1)] \cdot xH_2O$
18	**Mo_{16}**	$K_5(NMe_4)_{1.5}[Mo_{16}O_{16}S_{16}(OH)_{16}(HCPTCA)_2]Cl_{0.5} \cdot 36.5\ H_2O$
19	**Mo_{12}**	$K_5(NMe_4)[Mo_{12}O_{12}S_{12}(OH)_{12}C_6(COO)_6] \cdot x\ H_2O$
20	**Mo_{30}**	$K_{21}[Mo_{30}O_{104}(OH)_3S_6(C_6(COO)_6)_2K_3(H_2O)_3] \cdot x\ H_2O$

Chapter 1

Introduction

1.1 Polyoxometalates

Polyoxometalates (POMs) are a species of discrete anionic polynuclear metal-*oxo* clusters made from early transition metals (V, Nb, Ta, Mo, W)* in their higher oxidation states. The metal centres are decorated by *oxo*-ligands in either terminal position on the outside of the POM or as bridging groups in between them. Their structures are best understood as $\{MO_x\}$ polyhedra, which are connected to each other in either corner-, edge- or face sharing fashion (Figure 1.1.1). Face sharing polyhedra however are seen rather rarely in POMs compared to corner- and edge sharing modes, as the short metal to metal distance becomes unfavourable due to electrostatic repulsion.[1] The typical coordination environments for the $\{MO_x\}$ polyhedra are tetrahedral, square pyramidal and octahedral, giving rise to a plethora of possible structures, both topologically as well as electronically.

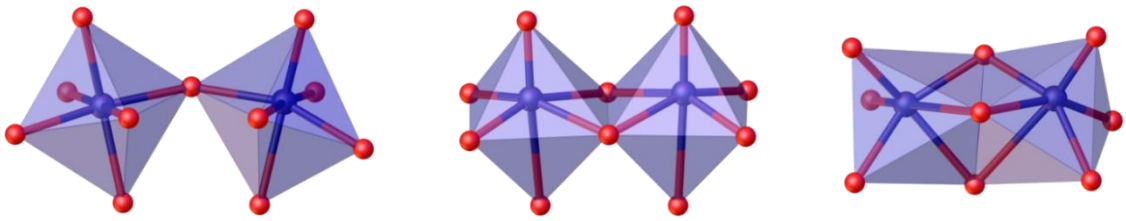

Figure 1.1.1 – Corner-, edge- and face sharing mode of two connected $\{MO_6\}$ octahedra.

As all higher oxidations states of the POM-forming metals such as $Mo^{VI}, Mo^{V}, V^{V}, V^{IV}, W^{VI}, W^{V}$ etc. are able to form those coordination environments, POMs can have the ability to retain their structure upon oxidation or reduction.[2-4] Electrons in POM systems are often not located on a specific metal atom but can rather freely move around the surface of the cluster. This delocalisation of electrons makes POMs highly stable against oxidation and therefore excellent candidates for oxidation catalysis.[5] Because of their stability, rich redox chemistry and fascinating electronic properties, POMs have found their way into areas like magnetism[6], catalysis[7-9], biomedical applications[10, 11], crystallography[12, 13], photo-chemical applications.[14] as well as into green chemistry[15], for gas sequestration[16], waste water decontamination[17], and even quantum computing.[18]

* In recent years this list of elements has been expanded to noble metals like Au, Pd or Pt. POM-like compounds such as *polyoxo*-titanium clusters have also experienced a vast development. In this thesis will however focus on the classical POM metals.

1.1.1 History

The discovery of polyoxometalates dates back to 1783, when the D'Elhuyar brothers discovered a yellow salt with bitter taste that forms from the reaction of ammonium tungstate with an excess of phosphoric acid.[19] The analogous molybdenum salt was later synthesised and reported by J.J Berzelius in 1826.[20] Despite extensive studies by chemists during the 1800s its molecular structure should remain unknown until over a century after its discovery. In 1935 Keggin and Illingworth[21] published their work on the phosphomolybdate anion based on powder x-ray diffraction (PXRD). The authors deduced its structure by comparisons made between the powder patterns of phosphomolybdate and phosphotungstate salts, of which the latter had its structure revealed a year earlier by Keggin and Bragg[22] based on single crystal x-ray diffraction (SXRD) experiments. While Keggin tried to undertake SXRD studies on the 12-phosphomolybdate acid at that time he had to rely on PXRD methods "for crystals of this hydrate could not be grown in sufficient size for single-crystal work".[21] A problem, which, despite tremendous technological advancement, remains persistent to the present day. The composition of the phosphomolybdate anion was found to be $[PMo_{12}O_{40}]^{3-}$. Its structure can be seen in Figure 1.1.2.

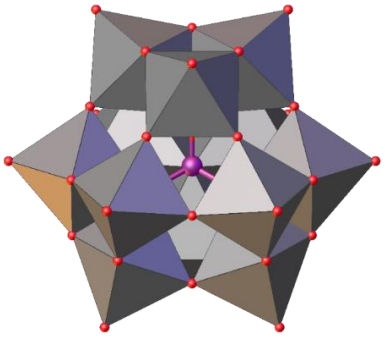

Figure 1.1.2 – Polyhedral representation for the Keggin POM **[**$PMo_{12}O_{40}]^{3-}$. Colour scheme: Purple: P, Grey: Mo.

Twelve $\{MoO_6\}$ octahedra arrange themselves around a central tetrahedral $[PO_4]^{3-}$ anion in groups of three edge-sharing octahedra. Those $\{Mo_3O_{13}\}$ building blocks, called triads, are connected to each other in corner-sharing fashion. The structure has been aptly named the Keggin structure and serves as one of many archetypes of POM structures from which other, more complicated structures can be understood. Variations of $[PMo_{12}O_{40}]^{3-}$, such as silico- $[SiW_{12}O_{40}]^{4-}$ and borotungstates $[BW_{12}O_{40}]^{5-}$ for example, were known in the literature even before its structure was revealed.[23]

1.1.2 Structures

The advancement of XRD instrumentation as well as computer aided structure elucidation within the last century changed the determination of POM structures from a serious scientific feat to a routine task for chemists. This improvement created an explosion in the variety of known POM structures and spurred the development of the field tremendously. Nowadays the most difficult part in creating new POMs is oftentimes the synthesis and crystallisation of the compound instead of solving the structure. A big part in the development of POM chemistry was the focus on understanding the structure, composition and formation of the more than often complicated and intricate POM structures and still is to date. The most important archetypes shall be discussed and serve as examples of different aspects of POM chemistry.

1.1.2.1 Archetypes

One of the earliest classification in POM chemistry describes two general types of structures, namely isopolyanions and heteropolyanions.[24, 25] Isopolyanions solely consist of $\{MO_x\}$ polyhedra, usually of a single metal, which are connected to each other to form anions of the general formula $[H_qM_yO_z]^n$. Heteropolyanions additionally incorporate heteroatoms into their structure, as is the case in the Keggin POM, in which the $\{MO_6\}$ octahedra are arranged around a central tetrahedral $\{XO_4\}$ anion. Heteropolyanions follow the general formula $[H_qX_xM_yO_z]^{n-}$. The most common structural archetypes are shown in Figure 1.1.3.

The Lindqvist ion of the general formula $[M_6O_{19}]^{n-}$ is one of the simplest POM structures and was structurally characterised by Ingvar Lindqvist in the 1950s for the niobium- and tantalum-based POM.[26, 27] Six $\{MO_6\}$ octahedra are arranged in edge sharing fashion to form a super-octahedral structure with O_h geometry. Because of its high *oxo*-ligand to metal ratio the small POM carries a high surface charge, especially for the group 5 metals of niobium and tantalum. ($[M_6O_{19}]^{8-}$, M = Nb, Ta). For the group 6 metals molybdenum and tungsten the charge is greatly reduced due to their higher oxidation state +VI ($[M_6O_{19}]^{2-}$, M = Mo, W). While Lindqvist type structures with vanadium can be realised by substituting the *oxo*-ligands for *alkoxo*-ligands and thus reducing the charge, its "naked" Lindqvist ion $[V_6O_{19}]^{8-}$ has not been synthesized yet.[28-30] Theoretical calculations attribute this to both the high surface charge as well as a small HOMO-LUMO gap compared to $[Nb_6O_{19}]^{8-}$ and $[Ta_6O_{19}]^{8-}$.[31]

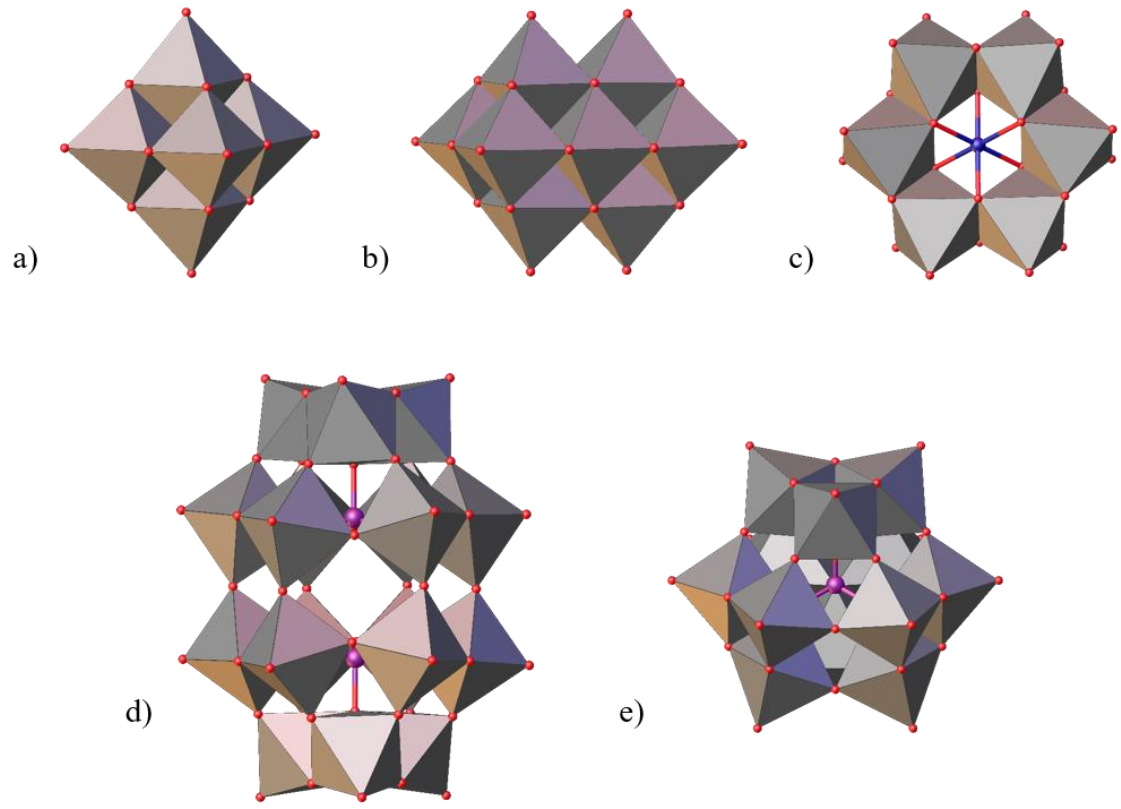

Figure 1.1.3 – Common archetypal POM structures. a) $\{M_6O_{19}\}$, b) Decavanadate $\{V_{10}O_{26}\}$, c) Anderson $\{(XO_6)M_6O_{18}\}$, d) Wells-Dawson $\{(XO_4)_2M_{18}O_{54}\}$ and e) Keggin $\{(XO_4)M_{12}O_{36}\}$.

The most common polyoxovanadate (POV) in acidic medium is therefore the decavanadate anion with the general formula $[V_{10}O_{28}]^{6-}$, pictured next to the Lindqvist structure in Figure 1.1.3. Ten $\{VO_6\}$ octahedra are arranged in edge sharing fashion with six of them forming the centre of the structure, and two of them each being placed at the top and bottom. The structure bears great similarity with the Lindqvist ion and it is easy to imagine the decavanadate structure as two Lindqvist ions, which share two of their $\{MO_6\}$ octahedra. As more *oxo*-ligands are being shared by the $\{VO_6\}$ octahedra, the negative charge per vanadium ion in the decavanadate structure is being greatly reduced compared to the Lindqvist ion and the structure therefore stabilised.[32] The absence of a heteroatom in both of these structures classifies them as isopolyanions.

The third structure is called the Anderson-Evans POM with the general formula of $[H_z(XO_6)M_6O_{18}]^{n-}$.[33] The structure was predicted in 1937 by J.S. Anderson[34] and structurally solved in 1948 by Howard Evans.[35] Here, six $\{MO_6\}$ octahedra are arranged in a ring around a central heteroatom, which is usually a transition metal (TM) ion but can also be a p-block semi-

metal like antimony[36], tellurium[37] or even large non-metals like iodine[38]. The Anderson-Evans POM is an example of a heteropolyanion.

The structure in the lower left of Figure 1.1.3 is the Wells-Dawson heteropolyanion with the general formula $[X_2M_{18}O_{62}]^{n-}$.[39] The structure consists of 18 $\{MO_6\}$ octahedra that are arranged around two $[XO_4]^{n-}$ ions. The top and bottom of the structure consists of three edge sharing $\{MO_6\}$ octahedra to form a $\{M_3O_{13}\}$ motif, which is the same triad unit as in the Keggin structure described above. In the middle of the structure there are two sets of three pairs of edge-sharing $\{MO_6\}$ octahedra, which are connected to each other in corner-sharing fashion. The two internal $[XO_4]^{n-}$ ions have a stabilising effect on the structure. For one, they reduce the charge of the structure because of the oxidation state of their heteroatoms, and secondly, they build out energetically favourable X-O-M bonds. Heteropolyanions are therefore generally more stable than isopolyanions. Similarly to the Lindqvist and decavanadate structure, the Wells-Dawson and the Keggin POM are closely related. The Wells-Dawson structure can be seen as two Keggin structures fused together, each having three corner-sharing $\{MO_6\}$ polyhedra removed.

1.1.2.2 Isomerism

POM structures do not only differ by their composition, size or shape, but also by orientation of their $\{MO_x\}$ polyhedra. A good example is the Keggin ion described above. The $\{M_3O_{13}\}$ triads can each be rotated by 60°, generating rotational isomers of the structure. The connection between the triad's changes from corner-sharing to edge-sharing, when two rotated triads are next to each other. As there are four triads in the structure, five different isomers can be created by successive rotation of the triads as shown in Figure 1.1.4.

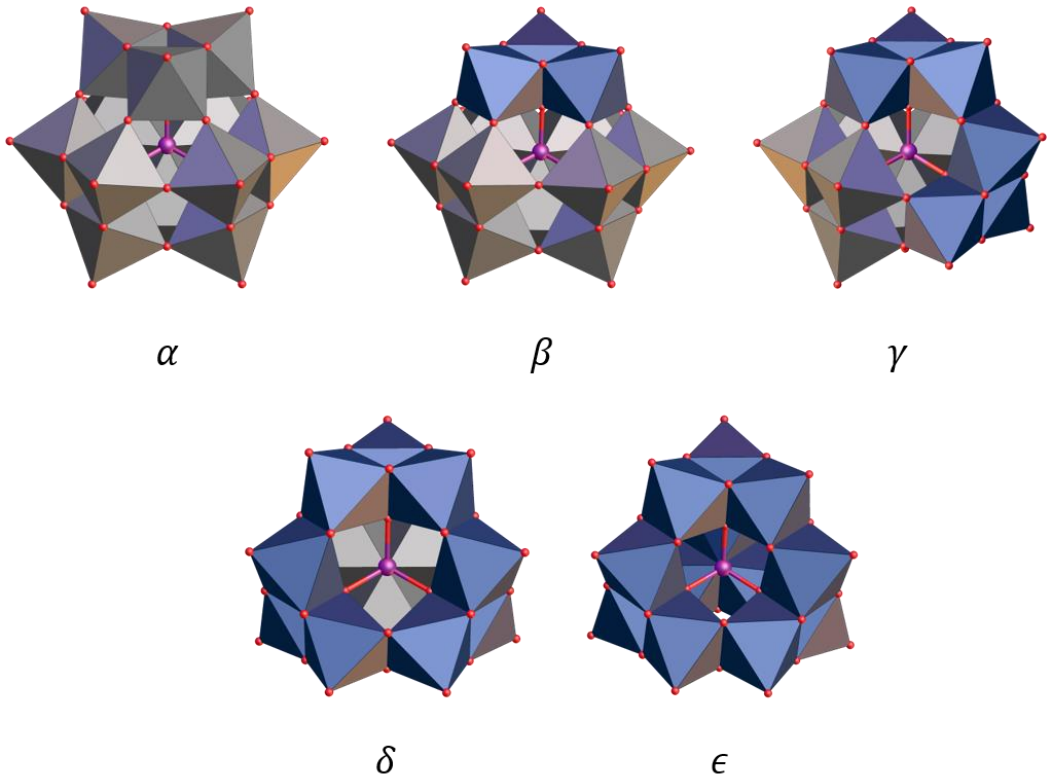

Figure 1.1.4 – The five different isomers of the Keggin ion, named α-, β-, γ-, δ- or ε-Keggin structure, depending on the number of rotated triads. Purple coloured triads have been rotated by 60° in respect to the standard orientation in the α-Keggin ion, which are coloured grey.[40]

1.1.2.3 Reduced species

So far all of the structures described have been made from metals in their highest oxidation state. As stated at the start of this chapter however, one of the most intriguing features of POM chemistry is their ability to undergo multiple redox events without a change in gross structure. It is quite easy to reduce the common POM metals in aqueous solution be it from Mo^{VI} to Mo^{V}, or V^{V} to V^{IV}.[1] One of the most famous examples are the so-called molybdenum blues, which have been of interest in the literature since 1793.[41] Molybdenum blue describes the blue solution that forms when Mo^{VI} is being reduced in aqueous solution at a pH < 3.[42] The structures of the species responsible for the blue colour were unknown for a long time. Only in the mid-1990s the group of Achim Müller in Bielefeld were able to crystallise a number of colossal mixed-valent polyoxomolybdates from solutions of molybdenum blues. Two of the structures can be seen in

Figure 1.1.5. On the left side is an archetypal $\{Mo_{154}\}$ wheel shaped POM, made from an arrangement of different POM fragments that serve as building blocks for the structure. On the right side is the biggest structurally characterised POM to date, a 5.5 nm wide $\{Mo_{368}\}$ nano-lemon. The intense blue colour of the molybdenum blue solution was found to originate from electronically uncoupled $\{Mo_5O_6\}$ incomplete double-cubane motifs, of which each carries two delocalised 4d electrons.[43]

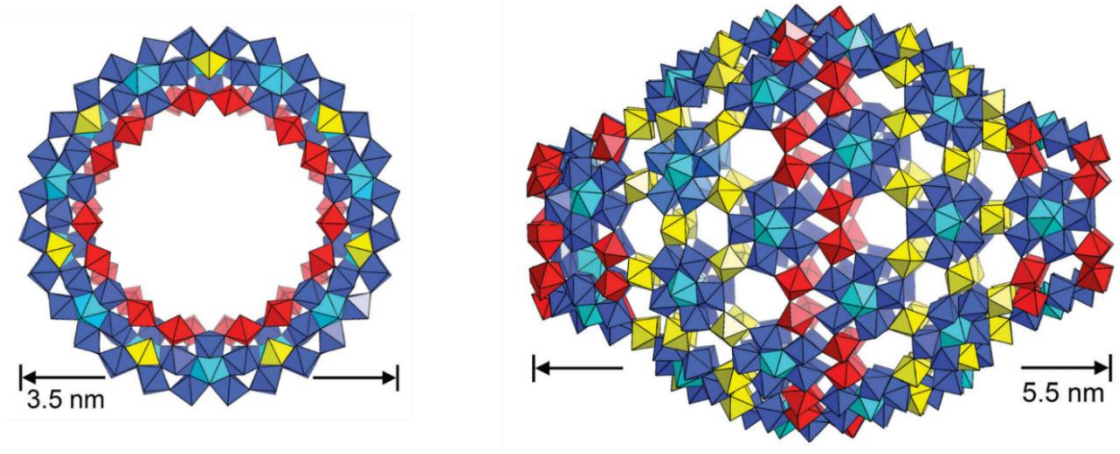

Figure 1.1.5 – The nano-sized POMs $\{Mo_{154}\}$[44] and $\{Mo_{368}\}$[45]. Colour code: $\{(Mo)Mo_5\}$-based building blocks: blue, $\{MoO_7\}$ pentagonal bipyramid: light blue, $\{Mo_2\}$-type building block: red, $\{Mo_1\}$-type: yellow. Picture from ref. [46]

The dominating POV species in acidic medium is the above described decavanadate ion $[V_{10}O_{28}]^{6-}$. Under reducing conditions however, the prevalent species is the archetypal fully reduced POV $[V_{18}O_{42}]^{12-}$, which is depicted in Figure 1.1.6. In this structure 18 square pyramidal vanadyl groups are arranged in edge-sharing fashion with approximate D_{4d} symmetry. The structure can be understood as two $\{V_5O_9\}$ units, which are sitting on top and bottom of the structure while being 90° rotated against each other with a belt of 8 edge-sharing $\{VO_5\}$ polyhedra in between them. The term fully reduced relates to the fact that all 18 vanadium ions are in their reduced form of V^{IV}. POVs can generally be grouped into fully oxidised (V^V), mixed-valent (V^V/V^{IV}), fully reduced (V^{IV}) and highly reduced (V^{III}) species. The last category however is mainly stabilised by *alkoxo*-ligands instead of *oxo*-groups and therefore stretches the definition of a polyoxometalate.

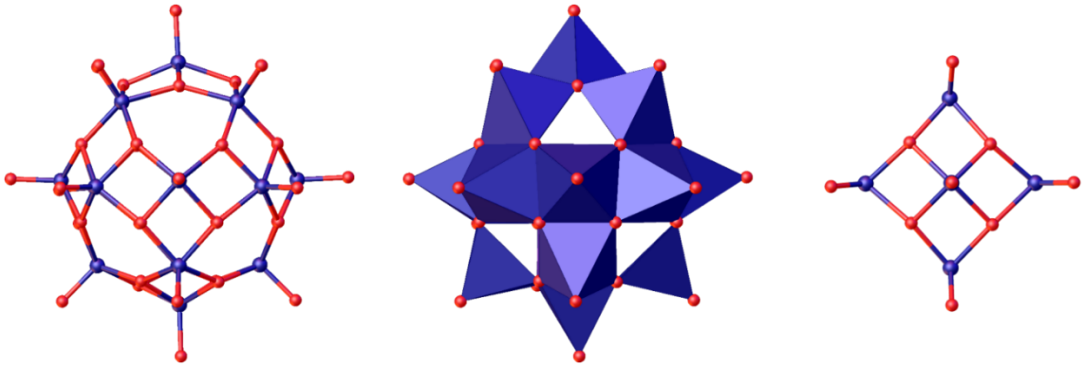

Figure 1.1.6 – The $\{V_{18}O_{42}\}$ archetype of POV chemistry under reducing conditions in normal and polyhedral representation. Right: The $\{V_5O_9\}$ motif within the $\{V_{18}O_{42}\}$ POV.

1.1.3 Synthesis and formation

The classical synthesis of POMs is done as a one-pot synthesis in aqueous solution, in which all necessary reagents are stirred together, optionally filtered, and left to crystallise or precipitate. The formation of POMs can largely be described as a self-assembly mechanism of *oxo*-anions in solution. The details of this process are still to date barely understood, due to the sheer complexity of the system. As a general process however, it is known that the formation of polyoxometalates begins with the protonation of *oxo*-anions in solution, triggering a process of oligomerisation by loss of a water molecule. This reaction, called olation, can be seen exemplified at the orthovanadate anion in the schematic equations below

$$2[VO_4]^{3-} + 2H^+ \rightarrow 2[VO_3OH]^{2-} \rightarrow [V_2O_7]^{4-} + H_2O \qquad \{1.1.1\}$$

$$[V_2O_7]^{4-} + H^+ + [VO_3OH]^{3-} \rightarrow [V_3O_{10}]^{6-} + H_2O \qquad \{1.1.2\}$$

If continued indefinitely this reaction will ultimately lead to the formation of the bulk metal oxide, which is the thermodynamic minimum for all POM reactions. POMs can therefore be seen as kinetically stable intermediates between mononuclear *oxo*-anions and their bulk materials. They are often referred to as discrete molecular metal oxides for that reason and can be used as molecular models for oxide surfaces (Figure 1.1.7).[47-50] The aforementioned gigantic molybdenum blue POMs are an example of this concept, as they are synthesized at low pH under reducing conditions, which leads to their enormous cluster size.

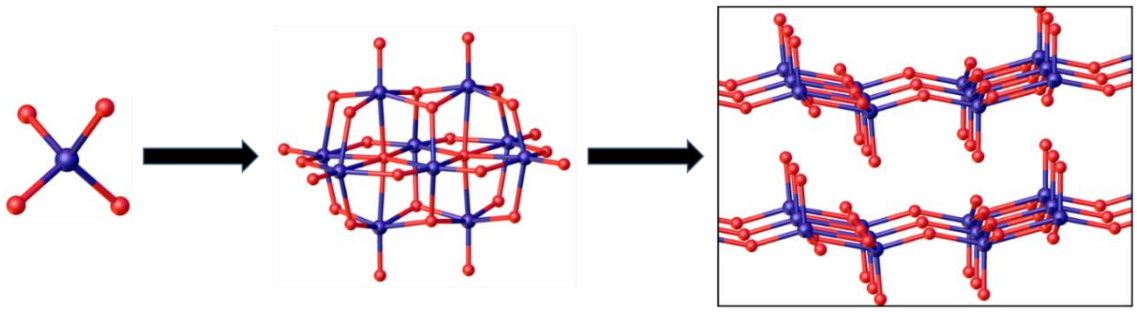

Figure 1.1.7 – Schematic growth mechanism of $[VO_4]^{3-}$ orthovanadate ions in aqueous solution with the decavanadate ion $[V_{10}O_{28}]^{6-}$ an intermediate species towards the bulk vanadium oxide.

The reason for their stability and formation in solution lies in the terminal *oxo*-ligands, which build out highly stable M=O double bonds with the metal ions. Ballhausen and Gray[51] developed a molecular orbital (MO) diagram for the $[VO]^{2+}$ ion in aqueous solution, which proved highly successful in predicting the characteristics of the vanadyl adsorption spectrum as well as its g-value and electron paramagnetic resonance (EPR) spectrum. The molecular orbital (MO) diagram is shown in Figure 1.1.8.

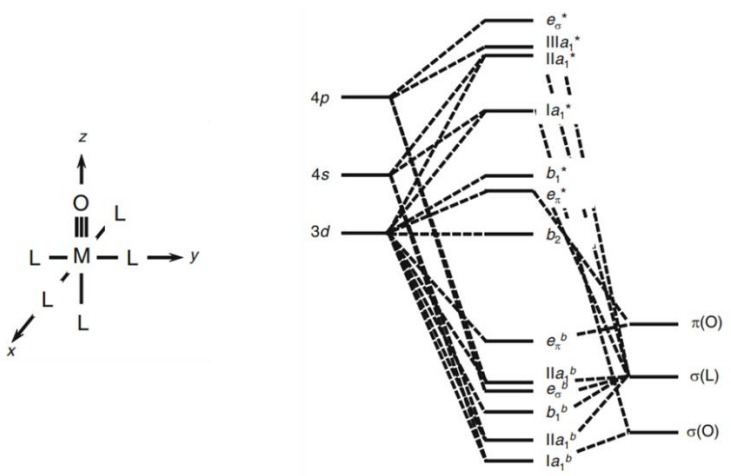

Figure 1.1.8 – MO diagram of the vanadyl bond in $[VO(H_2O)_5]^{2+}$ in octahedral environment with C_4v symmetry.[52]

The bonding orbitals between the vanadium ion and the *oxo*-ligand are a strong σ-bond between the sp_σ hybrid orbital of the oxygen and the $(4s + 3d_z^2)$ hybrid orbital as well as two π-bonds between the oxygen $2p_x$ and $2p_y$ and the vanadium $3d_{xz}$ and $3d_{yz}$ orbitals. This brings the bond

order in the vanadyl group to a total of 3 in the model.* The only oxygen orbital accessible for protonation is a sp_{σ} orbital with heavy s-character, which is energetically unsuited for bonding purposes. The ability to build out strong M=O double bonds therefore renders POMs kinetically inert, which terminates the olation process towards bulk metal oxides.

While the equations {1.1.1} and {1.1.2} seem simple enough from a chemical point of view, reality is much more complicated. The sheer complexity of this system can be exemplified by looking at the different metal oxide species, which are present at any given time in the reaction mixture. Figure 1.1.9 shows the distribution of vanadate species in a 1mM aqueous solution based on pH. The pH however is only one of many variables in the reaction mixture. The distribution as well as the vanadate species themselves will change in this graph with every small change to the system. The challenge of POM chemistry is to steer the reaction towards the desired POM or POM fragment by fine-tuning the conditions. And because detailed mechanisms of POM formation are rare and only applicable within a narrow scope one has to carefully consider and control all possible factors like pH, temperature, choice of metal salts, cations, heteroatoms, solvents, co-solvents, concentrations, reducing agents, crystallisation methods etc… Hence it is understandable, that a lot of discoveries of new structures can be deemed serendipitous at best. Newer approaches in POM synthesis utilise the use of organic solvents[53], hydro- or solvothermal methods[54, 55] or the use of flow chemistry[56] for the discovery of new POM structures.

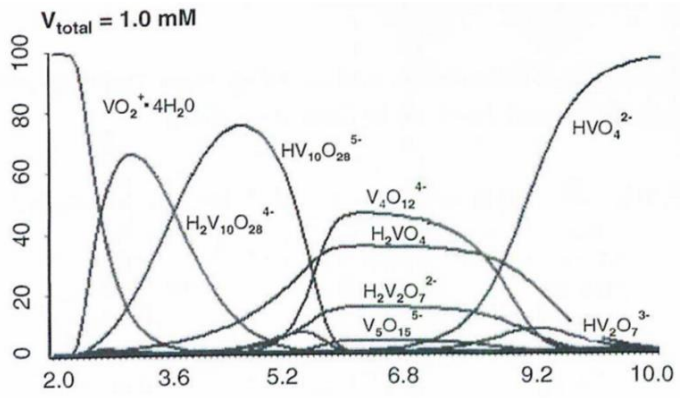

Figure 1.1.9 – Different vanadate species present in an aqueous 1mM solution at different pH values.[57]

* While there are many good reasons to call the bond within the $[VO]^{2+}$ ion a triple bond based on the MO diagram, preference will be given in this report to formulate the bond as a V=O double bond in order to adhere to the octet rule of the oxygen atom.

1.1.3.1 Templates

One of the main strategies to direct the formation of specific POM species is the use of templates, around which the $\{MO_x\}$ polyhedra can assemble themselves to form closed structures. We have seen this approach already in the structures of the Keggin and Wells-Dawson POMs. In both structures, phosphate ions act as the template around which the structures are forming. The syntheses of the Lindqvist and the Keggin POMs are essentially the same with the difference of the templating phosphate ion being present in the synthesis of the Keggin POM. Its effects in the Keggin synthesis are multiple. Most of all, the phosphate ion stabilises the final cluster due to the strong P-O-M bonds, as well as reduces its charge due to the phosphorus ion being in the oxidation state +V, which additionally adds to this stabilisation. Heteropolyanions are therefore more robust than their non-hetero counterparts. This effect can also be seen during the formation. Combined investigations of theoretical calculation and mass spectrometry experiments of Poblet and Cronin give insight in the formation steps of the Keggin ion $[PMo_{12}O_{40}]^{3-}$.[58-61] Figure 1.1.10 shows a part of the results of these calculations. A heteroatom X is inserted into the structure after formation of the $[M_2O_7]^{2-}$ dimer, leading to the energetically favourable anion $[XM_2O_9]^-$. Those calculations however are highly dependent for the specific reaction and are not easily generalizable.

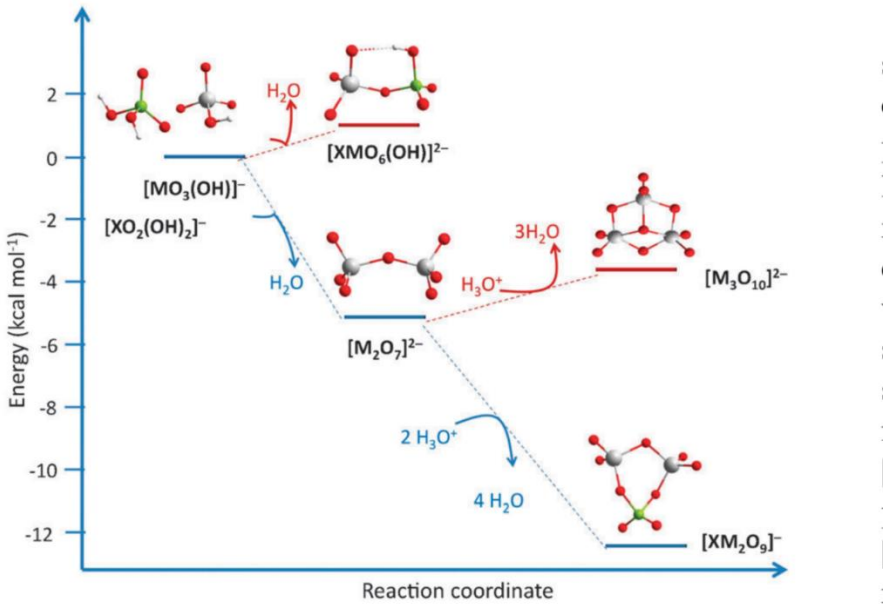

Figure 1.1.10 – Energy calculations of the initially formed oligomers leading to $[PMo_{12}O_{40}]^{3-}$.

Next to a stabilising effect however, the phosphate template is also structure directing, meaning the shape of the template dictates the shape of the resulting POM. While templates for polyoxomolybdates (POMos) and polyoxotungstates (POWs) are usually either tetrahedral or octahedral heteroatoms, POVs display a more diverse variety of available templates. This is mainly due to the square pyramidal geometry which is more common in POVs than in POWs and POMos.[62, 63] Figure 1.1.11 shows a series POVs with different templating anions inside the structure. The structures fully consist of square-pyramidal $\{VO_5\}$ polyhedra. While the chloride template leads to an almost spherical $\{V_{15}\}$ POV the perchlorate template forms an equally tetrahedral shaped $\{V_{22}\}$ POV. The azide and nitrate template both lead to $\{V_{18}\}$ POVs with shapes that mimic their internal template.

The template molecules in the POV examples above differ from the phosphate ion within the Keggin structure. While the phosphate ion did build out strong P-O-M bond the anionic POV template are only weakly bound to the vanadium ions and do not necessarily add to the stabilisation of the cluster Theoretical calculations on a chloride templated divacant open $\{V_{12}Cl\}$ cluster revealed almost no stabilisation of the cluster by the template.[64] In can be assumed in such cases that the templating anions play a role in the formation of the cluster by stabilising intermediates.

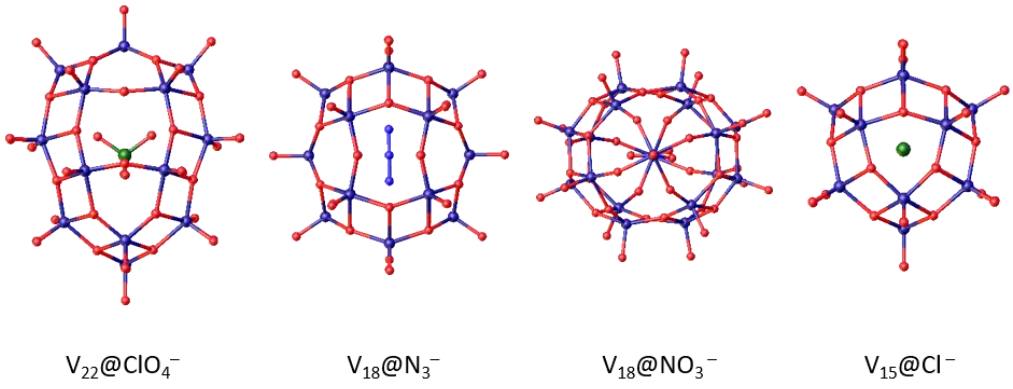

Figure 1.1.11 – POV with different shapes and nuclearites depending on the templating anion.

Aside from anion templating, POVs can also show supramolecular host-guest chemistry with neutral guests. A good example is the basket shaped POV $[(CH_3CN)\subset V_{12}O_{36}]^{4-}$, in which an acetonitrile sits in the middle of the basket. Originally reported by V.W. Day *et.al.* in 1989, its supramolecular chemistry was nicely exemplified in 2018.[65] Hayashi *et. al.* were able to

synthesise the {V_{12}} POV with dichloromethane (DCM) instead of acetonitrile (MeCN). Removal of the DCM within the POV basket under vacuum at 50°C led to the guest free {V_{12}} POV. Figure 1.1.12 shows the structures of {MeCN⊂V_{12}} on the left and the guest free version on the right. Most interestingly, one of the vanadyl groups was flipped from the outside of the structure towards the inside after removal of the guest molecule. This inversion was found to be reversible when the guest free host was exposed to solvent vapours and could be followed by IR spectroscopy.[66] A comprehensive review about the template effects in polyoxometalate system has recently been given by Healy *et.al.* [67]

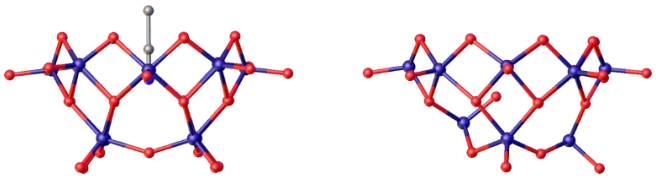

Figure 1.1.12 – The $[V_{12}O_{32}]^{4-}$ POV with and without guest. One of the vanadyl groups is flipped towards the inside in the absence of a guest molecule.

1.1.3.2 Ligands

We have seen how template molecules can simultaneously stabilise and direct the growth of POMs in solution. However, the structures synthesised by this approach are serendipitous at heart with little to no room for modification or design to tailor their physicochemical properties. A way to overcome this limitation is the use of suitable organic molecules, called ligands, which can covalently bind to POM fragments and stop them in their growth. The advantages of this approach are manifold. Firstly it enables the capture of otherwise unattainable structural motifs or, *via* the use of bi- and multifunctional ligands the constructions of larger assemblies from POM fragments.[68-70] Secondly, as organic ligands are easily modified, additional functional groups can be introduced into the material either by using preformed ligands or post-synthetically.[71] The resulting entities made from inorganic POMs and organic ligands are called hybrid organic-inorganic POMs, or hybrid POMs for short.*

* There are two classes of hybrid organic-inorganic POMs in the literature. Class I considers the combination of organic cations and anionic POMs as hybrid materials. Class II encompasses structure, in which organic molecules are covalently bound to POMs. We will solely focus on Class II hybrid POMs in this thesis.

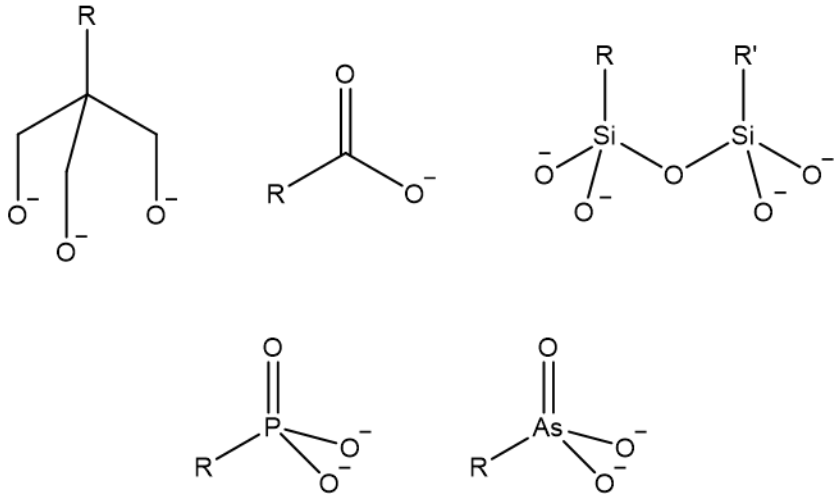

Figure 1.1.13 – Selected ligand motifs used in the construction of Hybrid-POMs. From left to right and top to bottom: Alkoxo-, carboxylate-, organosilicon-, phosphonate- and arsenate ligands.

In order to synthesise hybrid POMs, suitable anchor groups have to be found to covalently or iono-covalently craft the ligands onto the inorganic polyoxometalates. Figure 1.1.13 shows a series of ligands with different functional groups used in the construction of hybrid POMs. The functional groups are closely related to the templating anions we have already discussed (e.g. RPO_3^{2-} / PO_3^{4-}). The similarity in coordination environment and bonding of the functional groups to the metal-*oxo* groups of the POMs facilitates the bonding between them.

Extensive research has been carried out in the area of hybrid organic-inorganic polyoxometalates of the Anderson-Evans POM and the ligand tris(hydroxymethyl)aminomethane (tris) (Figure 1.1.13 – Upper left, R = NH_2). The combination of the tris-alkoxo group, which fits perfectly onto the heteroatom of the Anderson-Evans POM, and the easily functionalised amino group makes this ligand ideal for the construction of hybrid POMs, with applications in nanomaterials[33, 72, 73], photochroism[74], catalysis[75], magnetism[76] and biochemistry[77]. A nice example of the possibilities of the post-functionalisation of ligands has been provided by Cronin *et. al.*, who have investigated the use of high performance liquid chromatography (HPLC) methods for the synthesis of asymmetric bifunctionalised Anderson-Evans POMs.[71] *Via* HPLC columns, it was possible to separate POMs, which were asymmetrically functionalised with both a hydrophobic and hydrophilic groups, from their symmetrically functionalised side products. By using the hydrophobic protecting group fluorenylmethyloxycarbonyl (Fmoc), the authors were able to

generate a universal precursor, which can be functionalised post-synthetically, deprotected, and functionalised again to generate a plethora of possible hybrid POMs (Figure 1.1.14).

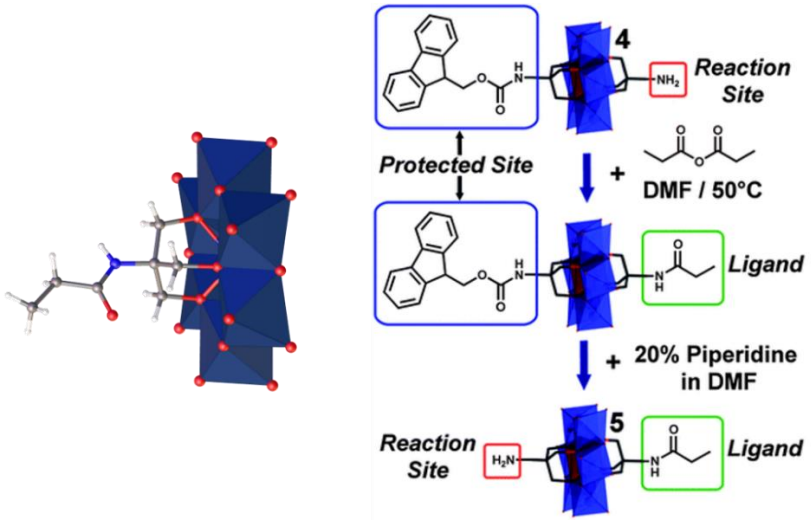

Figure 1.1.14 – Binding mode of tris to the Anderson-Evans POM and synthetic strategy for asymmetric functionalised POMs from ref. [71]

The above described Anderson-Evans hybrid POM is an example of a POM archetype which was functionalised by an organic ligand during its synthesis. The majority of POM structures however cannot be functionalised as easily, as the negative charge, once formed, is delocalized over the whole structure. This renders the terminal *oxo*-ligand chemically inert to electrophilic groups such as phosphonates or arsenates.

1.1.3.3 Lacunary POMs

One way to facilitate the functionalisation is the synthesis of so-called lacunary POMs. These are POM structures, who have one or more $\{MO_x\}$ polyhedra missing from their structure. The term lacunary comes from the Latin "*lacuna*" meaning "gap" or "unfilled space". The gap left behind by removing a metal ion and their terminal *oxo*-ligand creates a nucleophilic pocket, which can be used as anchor point for heteroatoms like transition metals,[54, 78] f-bock elements[79-82] or functional groups of organic ligands.[68] The synthesis of lacunary POMs is controlled *via* the pH of the solution and can be seen as the reverse reaction of POM formation. While POMs form by protonation of *oxo*-anion at low pH, the treatment of POMs with a base results in the removal of $\{MO_x\}$ polyhedra from the structure.

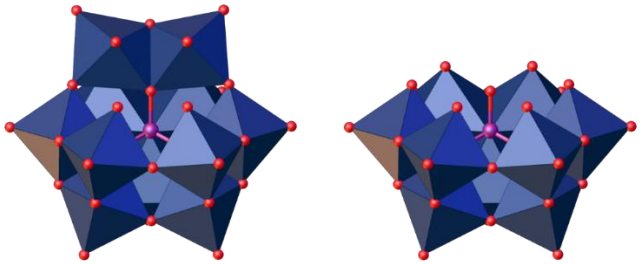

Figure 1.1.15 – Mono- and tri-vacant lacunary structures of the Keggin ion.

A nice example of the possibilities of this approach has been provided by Newton and Oshio. [83] In their study they utilised a divacant lacunary Wells-Dawson POM to functionalise it with different phenylphosphonic acid ligands and were able to manipulate the frontier orbital HOMO-LUMO gap of the Wells-Dawson POM, which increased with a decrease of the electron withdrawing effect of the ligand. The effect of this orbital engineering resulted in an increased photocatalytic activity of the hybrid POMs in the oxidative degradation of indigo under visible light (Figure 1.1.16).[84]

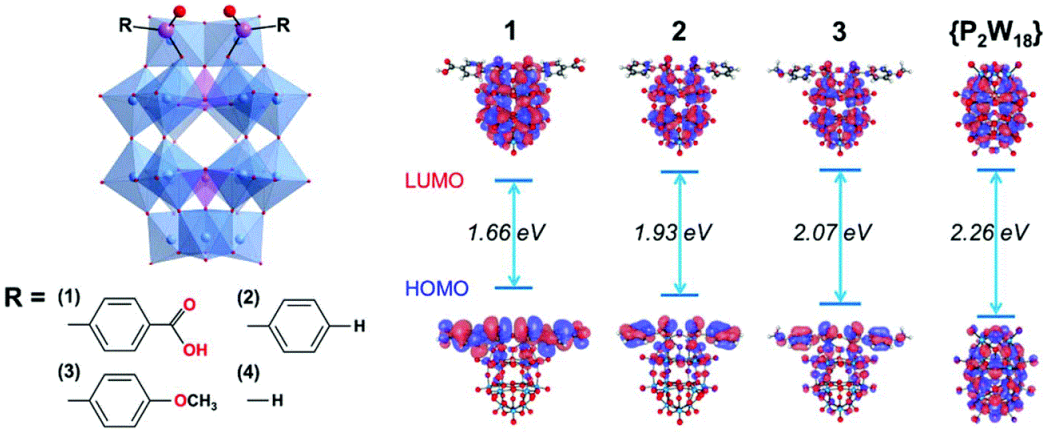

Figure 1.1.16 – Organophosphonate bifunctionalised hybrid Wells-Dawson POMs and frontier orbital energies for the different hybrid species.[84]

Lacunary POMs can also be understood as ligands themselves. Especially in the field transition metal coordination clusters, POMs can be used to stabilise cluster topologies, which were otherwise not achievable. The chemical robustness of POMs makes them ideal to function as non-labile ligands. A big number of transition metal cubanes have been realised by the use of

lacunary POMs as protecting ligands.[85] Cubane motifs are highly sought after because they mimic the oxygen-evolving centre in photosystem II.

1.1.3.4 POM fragments and POM based metal organic materials.

As mentioned earlier, organic ligands can also stop POMs in their growth, capturing otherwise unstable fragments. One example of this method is the pentanuclear polyoxovanadate species $\{V_5O_9X\}$ X = Cl^-, H_2O, N_3^-, MeCN, etc… which will be utilised heavily in this thesis. It was first synthesized in its isolated form by Christou *et al.*[86, 87] in 1989 with the help of thiophenecarboxylic acid. Although only a few examples exist in the literature for the isolated $[V_5O_9X]^{n+}$ motif, it is commonly found in bigger polyoxovanadates like the archetypal $[V_{18}O_{42}]^{6-}$ polyoxovanadate as shown in Figure 1.1.6.[88] The first synthesis using phosphonates as capping groups for the POV fragment was carried out by Müller *et al.*[89] in 1992 in a $\{V_{14}\}$ hybrid polyoxovanadate capsule. The two $\{V_5O_9Cl\}$ half-capsules, both templated by a chloride ion, are connected *via* two central $\{V^{IV}_2O_4\}$ units in the middle of the structure (Figure 1.1.17). The phenylphosphonate ligands are bound to the vanadyl ions in *anti-anti* fashion, which positions the phenyl rings on the outside of the structure. From 2008 on the Schmitt group has utilised the approaches from Müller and Zubieta[89, 90] towards organo-functionalised polyoxovanadates to create $\{V_{10}\}$ hybrid capsules made from bifunctionalised bisphosphonate ligands.[91-94] The capsules, shown in Figure 1.1.18, are connected *via* the aromatic bisphosphonate ligands instead of vanadyl groups. Through the use of differently sized ligands the size of the capsule can so be influenced as well.

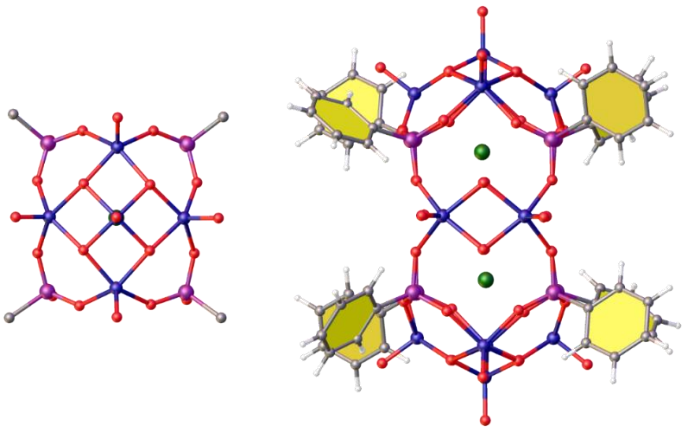

Figure 1.1.17 – The pentanuclear half-capsule $\{V_5\}$ in the polyoxovanadate capsule $\{V_{14}\}$.[89]

In 2014 Zaworotko *et. al.* published an impressive POV based octahedra made from six $\{V_5\}$ units, which were connected *via* trifunctional trimesic acid linkers.[55] The $\{V_5\}$ units are placed at the corners of the octahedra and the organic ligands sitting on its faces. The use of the bifunctionalised isophtalic acid as a ligand was used to generate the torus shaped variation of the octahedra, in which the top and bottom $\{V_5\}$ unit is missing.[95] Inspired by the work of Schmitt and Zaworotko the group around Zhongmin Su published a series of similar compounds which featured di- and tritopic linkers to build out octahedra and tori of three and four $\{V_5\}$ units..[96-99] The authors were able to functionalise the aromatic ligands with bromine and amine functional groups, exemplifying the modifiability of the system. Serendipitously, the solvothermal synthesis from $VOSO_4$ in N,N'-diethylformamide and methanol generated a new alkoxo-stabilised $\{V^{IV}_6\}$ POV, which formed tetrahedral assemblies together with tritopic linkers. The combination of the $\{V_5\}$ and $\{V_6\}$ POV fragments led to the formation of a number of POV based metal-organic polyhedra as shown in Figure 1.1.19.[100-102]

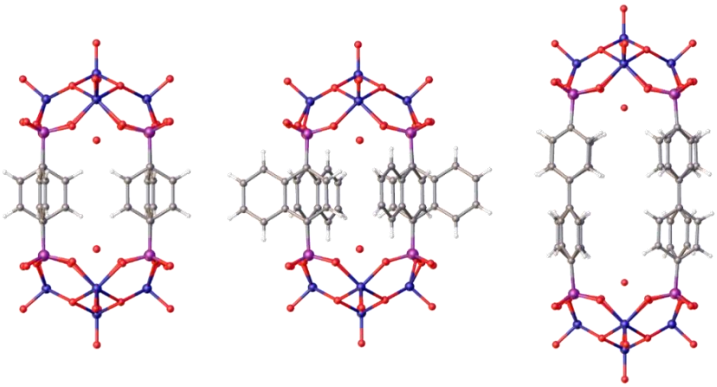

Figure 1.1.18 – The $\{V_{10}\}$ capsules made from two $\{V_5O_9\}$ units, which are linked by aromatic bisphosphonate linkers.

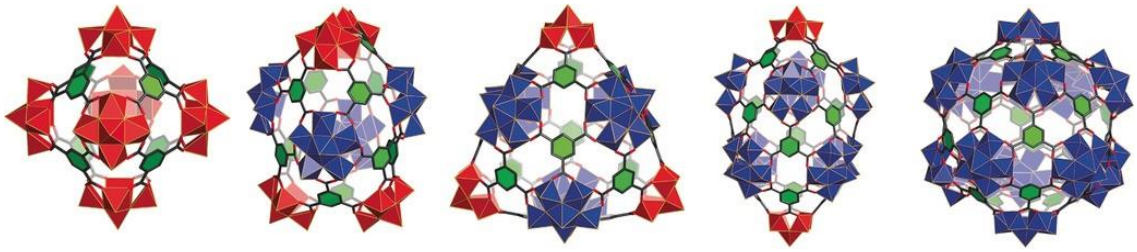

Figure 1.1.19 – POV-based metal-organic polyhedra based on $\{V_5\}$ and $\{V_6\}$ POV fragments.[100, 101]

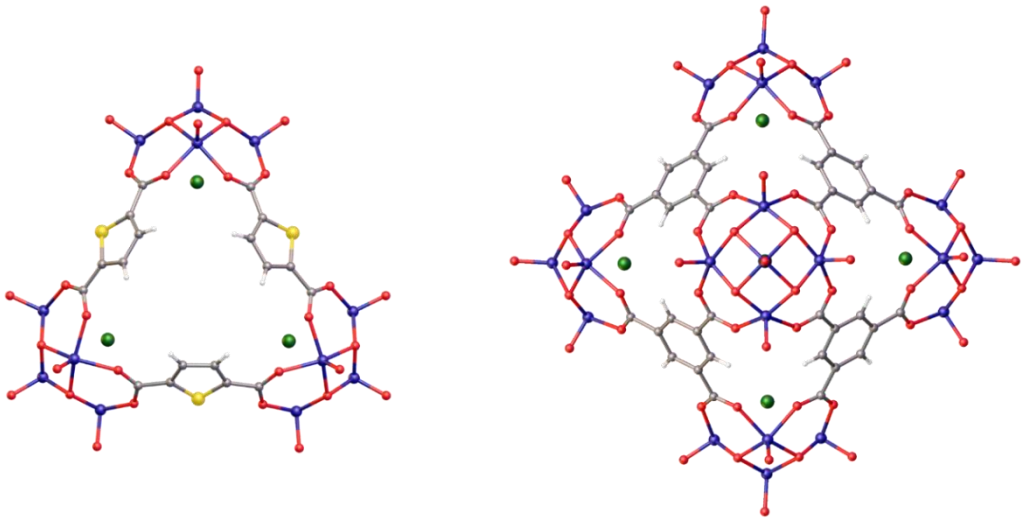

Figure 1.1.20 – POM-based polyhedra of the $\{V_5O_9\}$ half-capsule from Su and Zaworotko.

The field of POM-based metal organic materials expanded dramatically within the last years.[103] Similarly to already discussed metal organic polyhedra, organic linkers of suitable geometry can be used to generate POM based metal organic frameworks (MOFs). Metal organic frameworks are three dimensional polymers made from inorganic nodes and organic linkers, which show a potential for porosity. A nice example of the possibilities of POM based metal organic frameworks (MOFs) has been provided by Lang *et.al.* in 2018.[104] The authors synthesised a MOF made from a reduced ε-Keggin, decorated with four Zn ions and metalloporphyrin linkers functionalised with four 4-carboxyphenyl groups (Figure 1.1.21). The combination of a reduced POM together with the π-electron system of the metalloporphyrin gave rise to excellent CO_2 reduction properties. The cobalt variation catalysed the reaction of CO_2 to CO selectively with a faradaic efficiency of 99% and a turnover frequency of 1656 h^{-1}.

In the field of POV based MOFs Yang *et. al.* reported in 2018 two MOFs utilising a Lindqvist POV, which was stabilised with two tris(hydroxymethyl)-4-picoline ligands, as a linear linker. Reaction with copper and silver led to one interpenetrated and one non-interpenetrated MOF. [105]

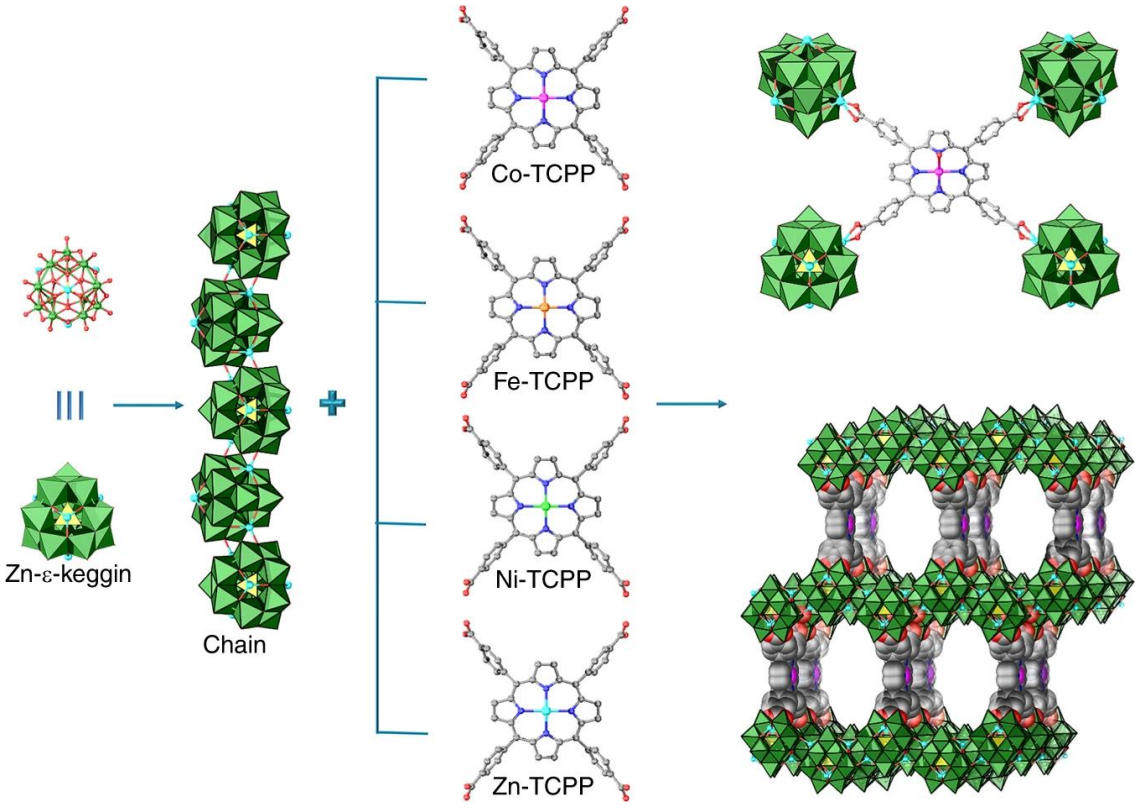

Figure 1.1.21 – Structural composition of the POM-metalloporphyrin MOF by Yang.[104]

1.1.4 Polyoxothiomolybdates

Polyoxothiomolybdates are a subspecies of polyoxometalates, which incorporate either bridging or terminal sulfide anions next to *oxo*-anions. The fundamental anions of *oxo*- and thiomolybdate chemistry ($[MoO_4]^{2-}, [MoS_4]^{2-}$) might seem quite similar, though their reactivity differs drastically.[106] POM synthesis is governed by protonation of small molybdate anions and subsequent fast condensation, which can be steered *via* careful control of the reaction conditions. In contrast, protonating $[MoS_4]^{2-}$ leads quickly to MoS_3, an unfortunately always amorphous polymer, which is, until to date, structurally not fully understood.[107-109] Internal redox processes between the ligand and the metal ions complicate the synthesis of thiomolybdates even further. To obtain usable building blocks in thiomolybdate chemistry another route has to be taken. Low nuclearity species of anionic $[Mo_x^V S_y]^{z-}$ species can be synthesized from $[MoO_4]^{2-}$ through the use of H_2S/NH_3 or ammonium polysulfide in aqueous solution (Figure 1.1.22).

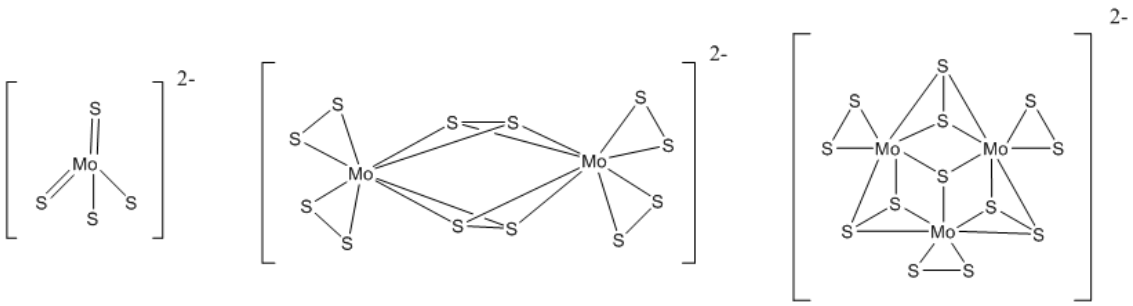

Figure 1.1.22 – Various accessible thiomolybdate compounds. $[MoS_4]^{2-}$, $[Mo_2S_{12}]^{2-}$, $[Mo_3S_{13}]^{2-}$.

The field of polyoxothiomolybdates lies in between POM and thiomolybdate chemistry, which is best exemplified with the stepwise exchange of the oxygen atoms of the molybdate ion $[MoO_4]^{2-}$ with sulphur atoms. This can be done through the use of H_2S gas in an alkaline solution of molybdate anions. These anions are the basis of polyoxothiomolybdate chemistry as they serve as building blocks for subsequent species.

$$[MoO_4]^{2-} \rightarrow [MoO_3S]^{2-} \rightarrow [MoO_2S_2]^{2-} \rightarrow [MoOS_3]^{2-} \rightarrow [MoS_4]^{2-}$$

The precursor used in this work is the oxothiomolybdate cation $[Mo^{V}_2O_2S_2]^{2+}$ which can be synthesized *via* a two-step synthesis from the building block $[Mo^{VI}O_2S_2]^{2-}$. The $[Mo_2O_2S_2]^{2+}$ motif was first used in POM chemistry by F. Sécheresse and E. Cadot in 1996 to cap a divacant lacunary $\{SiW_{10}\}$ POM.[110] Together with the trivacant lacunary POM $[AsW_9O_{33}]^{9-}$ the motif was used to build up dimers, tetramers and even hexamers of the lacunary POM.[111] Aside from the use of the motif with lacunary POMs it has been used extensively to build up ring structures, templated by inorganic anions or organic ligands.[112-129] The first and archetypal thiomolybdate ring was reported by Cadot and Sécheresse in 1998[112], in which six $\{Mo_2O_2S_2\}$ units formed together one $\{Mo_{12}\}$ ring. It quickly became clear that suitable inorganic guests (i.e., $\{MoO_6\}$, I^-, $[PO_4]^{3-}$) could be incorporated in the middle of the rings, which influenced their shape and size.[112, 113, 115] The use of polydentate organic ligands has proven especially successful. Ring sizes from $\{Mo_8\}$ to $\{Mo_{16}\}$ were realised by employing differently sized ligands. In 2010 Cadot *et.al.* achieved the synthesis of an oxothiomolybdate wheel with a nitrilotriacetate stabilised $\{Mo_3S_4\}$ motif as the template.[126]. The first inclusion of a heterometal was achieved in 2011, in form of a bis(dithiooxalato)nickel(II) complex.[127] Figure 1.1.24 shows a selection of differently sized thiomolybdate wheels. Its tendency to build up convex structures stems from its slight bent, which

is due to a distorted octahedral or square pyramidal environment of the molybdenum atoms in $[Mo_2O_2S_2]^{2+}$(Figure 1.1.24). Depending on the ligand *trans* to the terminal *oxo*-ligand this bent can be influenced. The adaptability of the $\{Mo_2O_2S_2\}$ dimer towards the inner template is a consequence thereof.

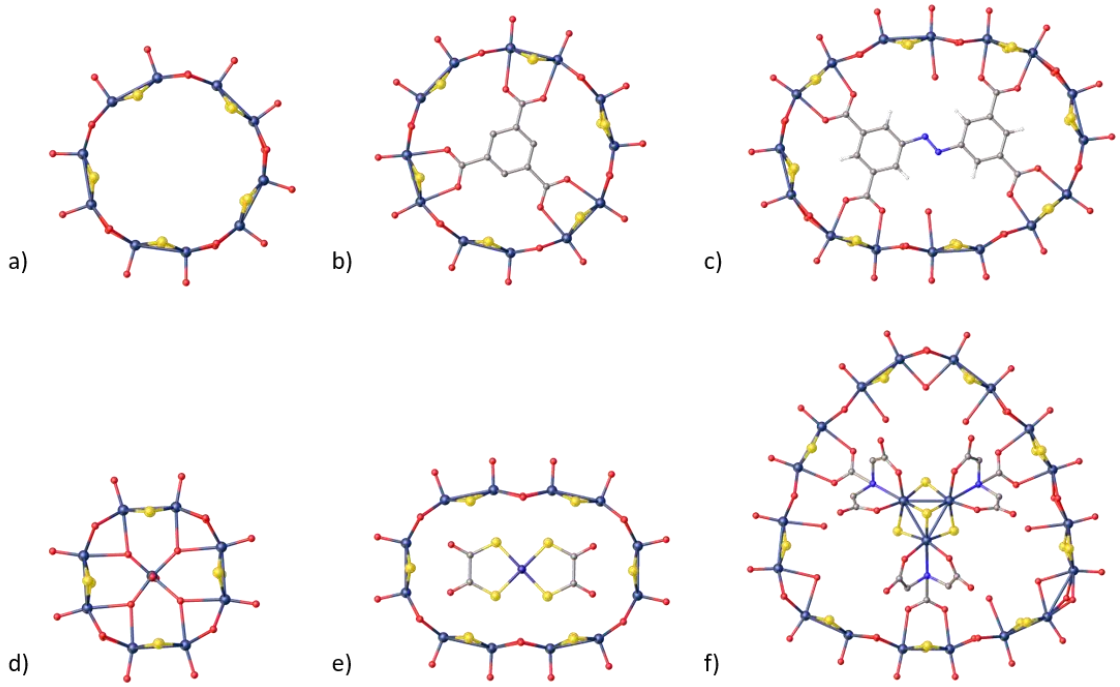

Figure 1.1.23 – Differently sized and shaped oxothiomolybdate wheels. a) $\{Mo_{12}\}$ wheel without template[112], b) $\{Mo_{12}\}$ wheel with trimesic acid[117], c) $\{Mo_{16}\}$ wheel with azo-based tetracarboxylate ligand[129], d) $\{Mo_8\}$ wheel with $\{MoO_6\}$ octahedra[113], e) $\{Mo_{12}\}$ ring with Nickel complex[127], f)$\{Mo_{18}\}$ ring with $\{Mo_3S_4\}$ template.[130]

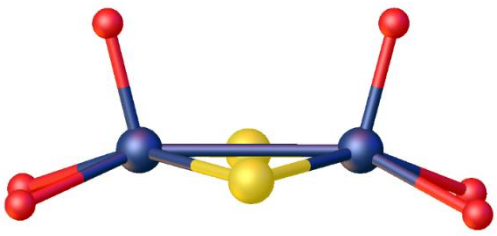

Figure 1.1.24 – The $[Mo_2O_2S_2]^{2+}$ motif with terminal *oxo*-ligands. Purple: Mo, Yellow: S, Red: O.

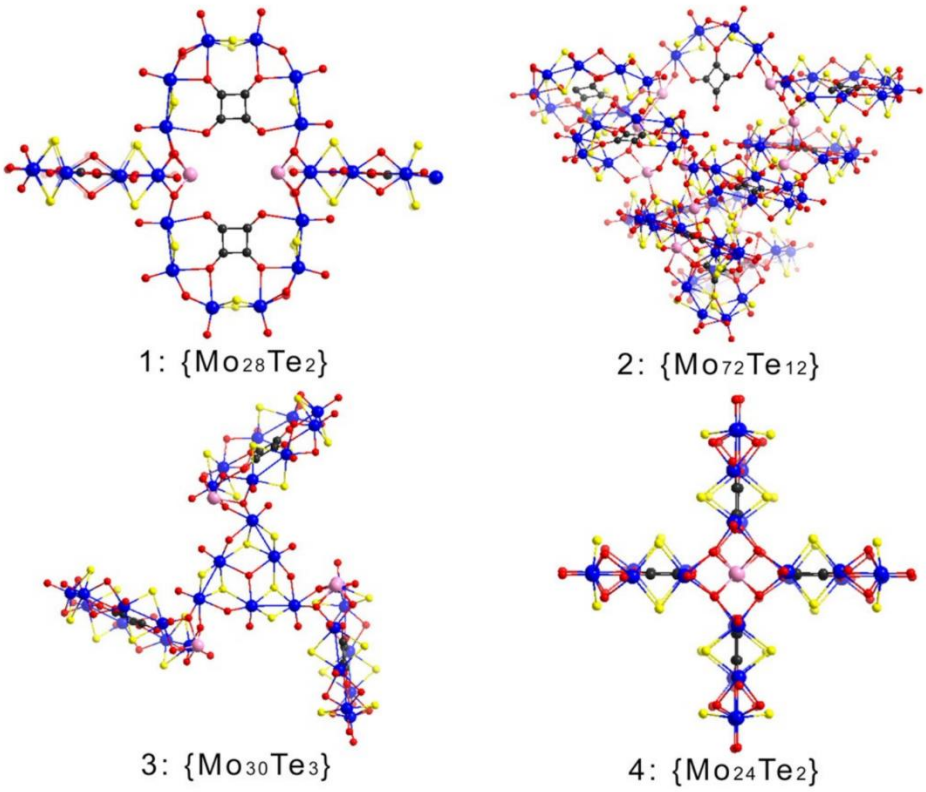

Figure 1.1.25 – Giant $\{Mo_2O_2S_2\}$ assemblies templated by squarates and tellurite anions.[131]

From 2012 on Cronin *et.al.* utilised squaric acid in the synthesis of oxothiomolybdate wheels, which led to a number of open ring building blocks stabilised by the squarate anion.[132-137] Those building blocks could be assembled into clusters with a nuclearity as high as $\{Mo_{96}\}$, which is made up of twelve $\{Mo_8(C_4O_4)\}$ units.[56] Adding selenite or tellurite anions as templating species led to a plethora of new assemblies. Figure 1.1.25 shows the assemblies of $\{Mo_8(C_4O_4)\}$ units and tellurite anions. The $\{Mo_8(C_4O_4)\}$ building block can be nicely seen from the front in $\{Mo_{28}Te_2\}$.

1.2 Non-covalent interactions

The inclusion of aromatic organic ligands does not only offer the possibility of functionalisation and the synthesis of extended structures, but can also give rise to non-covalent interactions (NCI), such as π-π, anion-π, cation-π, halogen bonds or hydrogen bonding. NCIs are rooted in electrostatic, induction and dispersion interactions and while usually seen as weak their strength can range from a few kJ/mol to several hundreds kJ/mol depending on the interaction at hand.[138] π-π interactions and cation-π interactions shall be discussed in detail.

1.2.1 π-π Interactions

Perhaps the most famous and well-studied NCI is the π- π interaction. The interest arises from the ubiquity and importance of π- π interactions in biology, such as DNA[139, 140], proteins structures[141], as well as in drug design and drug recognition.[142] The interaction describes the phenomenon of the attraction between two π-systems in close proximity to each other. Figure 1.2.1 shows some of the possible arrangements between two benzene or toluene molecules. While small aromatic rings are often used as model molecules for π-systems, due to their importance in biological systems,[143, 144] it should be noted that aromaticity is not required for these interactions[145] and can sometimes even hinder them.[146]

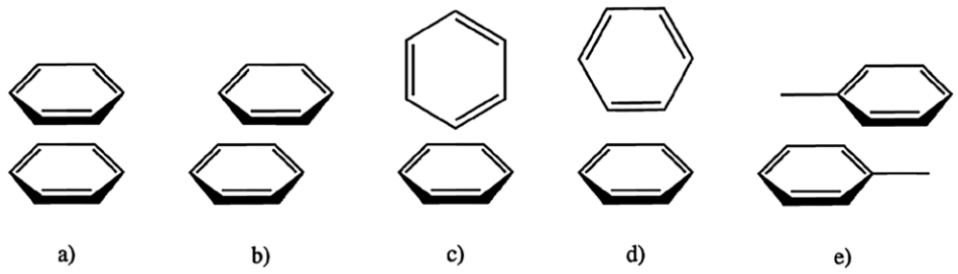

Figure 1.2.1 – Different stacking arrangements of aromatic systems. a) Parallel face-centred, b) Parallel displaced, c) Perpendicular t-shaped, d) Perpendicular y-shaped, e) Parallel offset for toluene.

An early model for the understanding of the interaction between two aromatic systems was provided by Hunter and Sanders in 1990.[147] The authors pointed out, that the π-system of an aromatic ring effectively creates a quadrupole moment, in which a partial negative charge is located above and below the aromatic ring and a partially positive charge is located around it.[148] For two electron-rich aromatic molecules the a) arrangement in Figure 1.2.1 would be

disfavoured by having two negatively charged surfaces close to each other, while the t-shaped or y-shaped arrangement would lead to favourable interactions. Substituents on the aromatic ring result in a polarization of the π-system by either reducing the electron density or enhancing it, depending on whether the substituent is electron-withdrawing or electron-donating. This model predicts a favourable face stacking interaction between an electron-deficient and an electron-rich aromatic system, which was most famously verified by the mixture of benzene and hexafluorobenzene, whose π-π interactions influences the liquid state as well as the solid state.[149-151] The model of Hunter and Sanders has since been challenged however as both computational and experimental studies have emerged over the last 15 years, which contradict the prevalent view of π-π interactions as a dominantly electrostatic interaction.[145] In fact Sherrill reported in 2003 a computational study on mono-substituted benzene dimers, which revealed that all substituents stabilise face-stacked benzene dimers, regardless of their electron-withdrawing or electron-donating properties.[152] Wheeler and Houk were later able to reproduce the findings of Sherrill in a computational study of 24 dimers of substituted and unsubstituted benzene. Additionally, the authors found that, when the benzene ring of the substituted benzene was replaced by a simple hydrogen atom the interaction remained the same as shown in Figure 1.2.2. This indicated that the π-system of the benzene ring was not involved in the stabilising effect of the substituents at all. The correlation of the interactions with the Hammett parameter would arise solely from direct, through-space electrostatic interactions between the substituents and the unsubstituted ring, which means that the polarization effect of the substituent on the aromatic ring is negligible (Figure 1.2.2).[153]

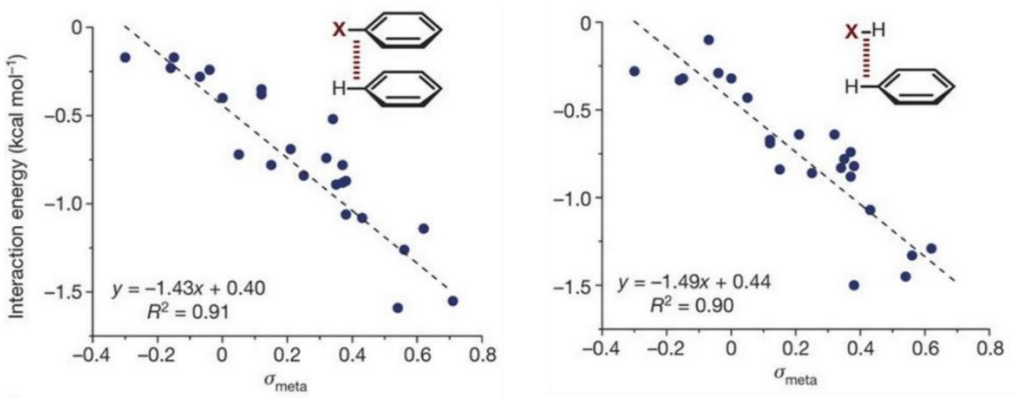

Figure 1.2.2 – Stabilising interactions between substituted and unsubstituted benzene rings and their correlation with the Hammett parameter. The stabilising interaction remains the same when the benzene ring of the substituted benzene is replaced by a hydrogen atom. Picture taken from ref.[154]

It has also been argued that the term π-π interaction should be reserved for larger aromatic systems. Grimme found that the stabilising interaction of a stacking type arrangement was greater for cyclohexane than for benzene with the dominating factor in the interaction being the dispersion component rather than electrostatics. While larger aromatics such as anthracene and tetracene are being significantly more stabilised by a stacking arrangement, their stabilisation has been attributed almost exclusively to dispersion forces, aided by the planarity of the molecules the resulting larger contact area.[155] The perception and our understanding of π-π interactions has therefore change a lot in the last 15 years. And while they have lost a bit of their uniqueness their usefulness in designing and constructing metal-organic materials has not suffered. Aromatic systems like benzene rings are still exceptional platforms to engineer NCIs towards desired properties in supramolecular assemblies.

1.2.2 Cation-π interactions

Cation-π interactions are generally considered the strongest interactions of NCIs and describe the attractive interactions between a cation and a neutral π-system. They were first reported by Kebarle *et.al*. in a 1981 mass spectrometry study of K^+ ions interacting with benzene in gas phase. The experiments showed a preference of the potassium ion for the interaction with a benzene molecule (19 kcal/mol) over water (18 kcal/mol), which was surprising given the large dipole moment of water.[156, 157] Further experimental and computational studies showed a general trend of the binding energy between an alkali metal cation and benzene to decrease with an increase in size. This behaviour resembles classical ion dipole interaction, indicating a mainly electrostatic nature of the effect (Figure 1.2.3).

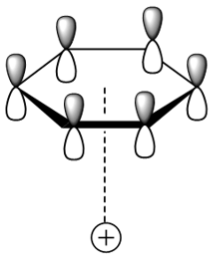

M^+	$-\Delta G^{\circ}_{\mathrm{kcal/mol}}$
Li^+	38.3
Na^+	28.0
K^+	19.2
Rb^+	15.8*

Figure 1.2.3 – Experimental binding energies for cation-π interactions between alkali metals and benzene for Li,[158] Na,[159] and K.[157] * The value for Rb stems from computational studies.[160]

In a first approximation the cation-π interaction can therefore be seen as the interaction between a point charge and an electric quadrupole. We have seen in the discussion of π-π interactions that benzene has a permanent quadrupole moment due to the distribution of its π-electrons. The variation in strength of the cation-π interactions with alkali metal cations can be easily explained by the higher charge density of Li and Na in respect to the bigger cations. Dougherty *et.al.* emphasized the usefulness of molecular electrostatic potential (MEP) plots in explaining the trends for variation of the aromatic species. However, given the close distance of those interactions (< 2-3 Å), it should be clear that, while this simple model reproduces the trends of the cation-π interaction, it cannot account quantitatively for all of the interactions.[161]

The gas phase however is a very foreign place for most chemists, whose rules does not always transfer to the condensed state of matter. Pioneering solution studies using preformed cyclophane receptors in aqueous media have been carried out by Dougherty *et.al.*[162-164] The authors first observed an unusual high binding affinity of the adamantyltrimethylammonium ion to the cyclophane host shown on the left in Figure 1.2.4, which was significantly higher than other reported binding affinities for aliphatic guests in cyclophane hosts. By replacing the two sidewall benzene rings with a saturated cyclohexane ring the association constant was reduced by a factor of 100. This contradicted the possibility that the binding could occur *via* induced dipoles as cyclohexane is more polarisable than benzene. Further studies cemented the view that this interaction was to be understood as a cation-π interaction. Important examples include the higher binding affinity of cationic quinoline guests over their isosteric neutral counterparts, polar NMe_3^+ groups being favoured over hydrophobic CH_3 groups and the replication of the binding affinity of biologically relevant molecules like acetylcholine, which binds to the cyclophane hosts with similar strength as to its biological receptors.[165]

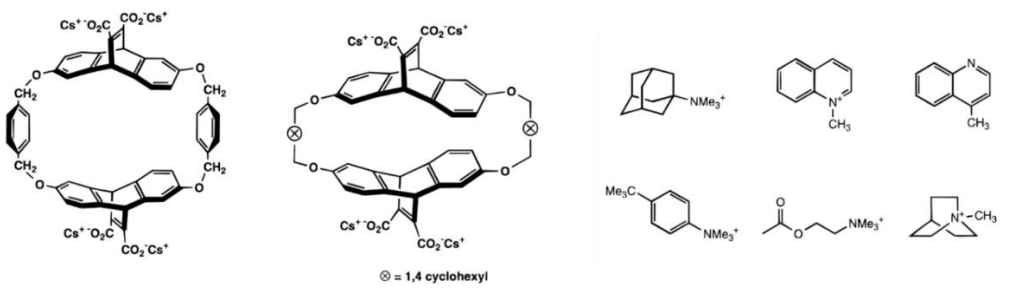

Figure 1.2.4 – Cyclophane hosts and representative organic ammonium ions used in the solution studies of cation-π interactions by Dougherty *et.al.*[162-164] Picture taken from: [161]

This existence of cation-π interactions in aqueous solution is even more remarkable than in the gas-phase as they have to compete with the hydration enthalpy of the cation. The trend of hydration enthalpy for the alkali metal goes down in the periodic table with $\Delta_{\mathrm{hyd}}G^{\circ}(\mathrm{M}^{+},\mathrm{g})$ for $Li^+ > Na^+ > K^+ > Rb^+ > Cs^+$. Due to the electrostatic nature of both effects the cation-π interaction follows the same trend, however not in the same magnitude.

A biologically important example of these trends is the case of ion selective K^+ ion channels, which exist in every living being. Their function is to transport K^+ ions efficiently and selectively through the body. The participating amino acids however make those channels surprisingly hydrophobic, while featuring a large number of aromatic residues. Dougherty *et.al.* were the first to propose a mechanism based on cation-π interactions for the preferential transport of K^+ ions over Na^+ and Li^+ through the channels. The authors conducted a computational study and found the preferential binding of K^+ to two benzene rings over Li^+, Na^+ and Rb^+ in aqueous media.[160] Experimental evidence for this hypothesis came from Lisy *et.al.*, who conducted a mass spectrometry study of alkali metal ion clusters with benzene and water.[166] They found, that the interaction between K^+ and benzene in aqueous solution was strong enough to result in partial dehydration of the K^+ ion, The higher hydration enthalpy of the Na^+ ion prevented it from losing water molecules and therefore the interaction with the benzene molecule. The inability of dehydration of the sodium ion explains the selectivity for K^+ ions of the ion channels as the sodium water cluster would be too big to pass through the channels. This is an example of how potassium-π interactions are favoured over sodium-π interactions in aqueous solution even though the sodium-π interaction is nominally stronger. The biological importance of cation-π interactions is being more and more recognised.[167]

The picture in the solid state however might be again a different one than in the gas phase or liquid state. A study of Kochi *et.al.*[168] of alkali metal complexes with hexakis-(methoxymethyl)benzene showed a reversal of the general trend $Na^+ > K^+ > Rb^+ > Cs^+$. Figure 1.2.5 shows the crystal structures of the complexes. While the Na^+ ions are far away from the benzene rings of the ligand the K^+ ions are slightly gravitating towards the aromatic ring with Rb^+/Cs^+ ions being definitely within reach of a cation-π interaction. The authors deduced the strength of the cation-π interactions to follow the trend $Na < K < Rb \approx Cs$, which is exactly the opposite as expected from the gas and liquid phase.

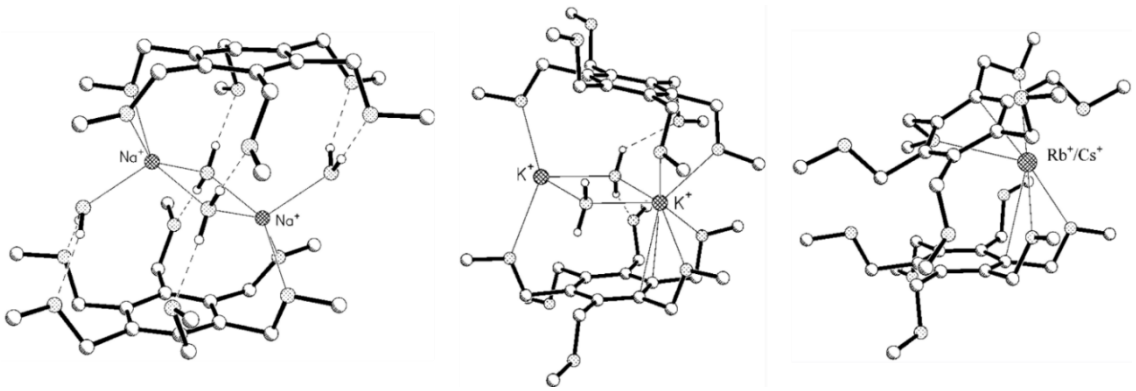

Figure 1.2.5 – Alkali metal complexes of hexakis-(methoxymethyl)benzene with increasing cation-π interaction in the order Na < K < Rb ≈ Cs.

1.2.3 Modifying cation-π interactions

Cation-π interactions are not only the potentially strongest NCI but also the one with the widest range. Wheeler and Houk demonstrated in a 2009 computational study, that the sodium benzene cation-π interaction could be tuned over a range of 20 kcal/mol by changing a single substituent to the ring.[156, 169] There are multiple ways in which cation-π interactions can be influenced. Most obviously the interaction is dependent on both the nature of the cation, for which the trends of the alkali metal cations have already been discussed. As the interaction is predominantly of electrostatic nature, increasing the charge density of the cation increases the interaction. The same principle can be applied to the aromatic ring. Selective substitution of hydrogen atoms with functional groups can influence the electrostatic potential above the ring and thus tuning the cation-π interaction. While the idea of electron-withdrawing and electron-donating groups, who influence the π-system of the aromatic ring, leading to electron-rich and electron-poor systems is intuitive and widespread it does not paint an accurate picture of the situation. Wheeler and Houk have, similar to their studies on π-π interactions, argued that the difference in MEP plots can be explained by through-space interactions of the substituent groups.[169] Interestingly while they found that aromaticity hindered π-π interactions, it actually increases cation-π interactions. Figure 1.2.6 shows the two competing models between π-polarisation due to the electron-withdrawing or donating nature of the substituent and the local dipole model, in which the substituent interacts directly with the cation. Further justification for this view is the recreation of MEPs of substituted aromatic molecules by simple addition of the MEPs of benzene and the lone substiuent.[170]

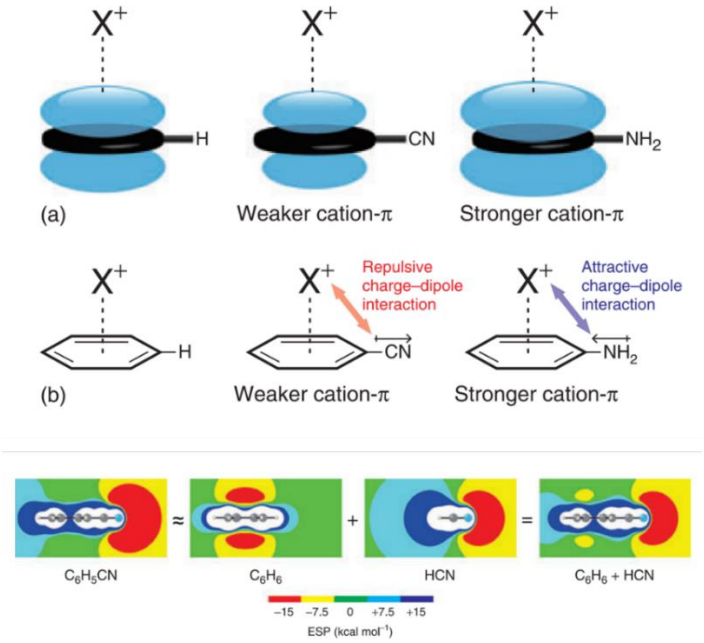

Figure 1.2.6 – Top: Different models of substituent effect in cation-π interactions. (a) modulation of the π-system by electron-withdrawing or donating groups. (b) Through-space interactions in the local dipole model of Wheeler and Houk. Bottom: MEP of benzonitrile as additive model of the MEPs of benzene and hydrogen cyanide. Pictures taken from: [156, 170, 171]

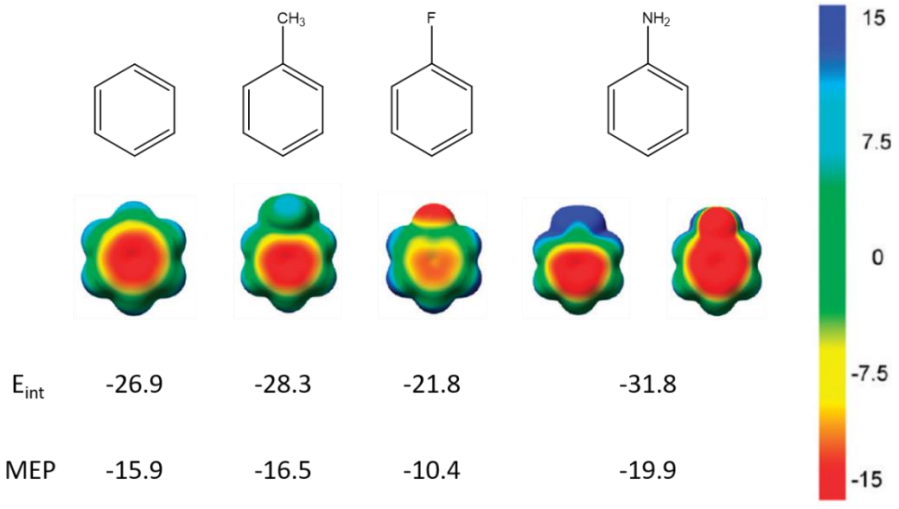

Figure 1.2.7 – MEP surfaces for differently substituted benzene ring. E_{int} are the interaction energies for the sodium-π interaction in the gas phase. MEP values taken at sodium distance. The MEP surface for aniline represents the front and the back. All values in kcal/mol.[169, 170]

Figure 1.2.7 shows the sodium-π interaction energies for differently substituted benzenes and as well as their MEP plots. The stabilisation energy for the sodium benzene interaction is -26.9 kcal/mol, which can be altered by substituting a hydrogen with different functional group. Adding a fluoro-group to the benzene reduces the interaction to -21.8 kcal/mol while an amine group raises it to -31.8 kcal/mol. The methyl group is slightly more stabilising than the hydrogen atom with -28.3 kcal/mol. As can be seen the trend in stabilisation energy is being correlated with the MEP values at the distance of the cation. And while the π-polarization model should not be overestimated the fact that most of electron-withdrawing groups decrease and electron-donating groups increase cation-π interactions makes for a good quick estimation about the electronic effects of substituents.

Another influence on the cation-π interaction is the size of the aromatic system. Sastry *et.al*. did undertake several comprehensive computational studies[172-174] to gauge the effect of increasing the π-system in both cyclic and acyclic molecules. In both cases enlarging the π-system led to a substantial increase in complexation energy. Polarization effects seem to play a more substantial role than in π-π interactions.

As most studies on cation-π interactions are dealing with molecules in the gas-phase, solvation effects are worth considering when trying to apply knowledge from computational and experimental studies. Sastry *et.al.* found a significant reduction in the strength of cation-π interactions by incrementally increasing the number of water molecules around a metal atom interacting with benzene.[175] Cation-π interaction are therefore the strongest in non-polar environments like the gas-phase or the interior of proteins. Their strength even in aqueous solutions is however not to be underestimated as the studies of Dougherty *et.al.* show.

1.2.4 Cooperative effects

A characteristic of covalent interactions is that they are largely unaffected by their environment. The nature of a C-C bond does not change much, whether it is in an ethanol molecule or a complicated protein. Its length and strength remain essentially the same. NCI in contrast are heavily affected by their environment. Supramolecular chemistry and assemblies are the result of all of these interactions acting together. Of special interest to this report is the cooperativity between π-π interactions and cation-π interactions. Sastry *et.al*. investigated the cooperative effects of cation-π and π-π interactions in ternary cation-π-π systems of alkali metals and benzene

ring (Figure 1.2.8). The authors deconstructed the overall interaction energy to investigate the separate π-π and cation-π contribution depending on cation and arrangement. Both interactions showed synergistic effects, meaning the cation-π-π interaction was higher in energy than the cation-π and π-π interaction together. While the cation-π interaction gained only a small increase in the presence of a π-π interaction, the π-π interaction experienced a ~3-fold increase when one of aromatic rings was involved in cation-π interactions with an alkali metal. In the case of Mg^{2+} this increase was found to be even 6-fold in relation to the standalone π-π interaction.

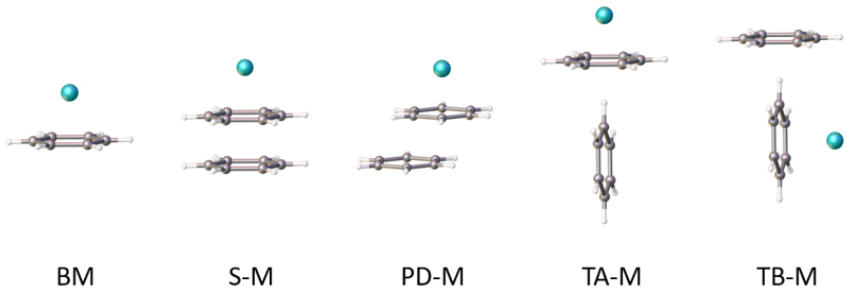

	BM	S-M	PD-M	TA-M	TB-M
-	-	-	-	-	-
Li^+	-34.13	-38.76	-38.36	-33.41	-39.45
Na^+	-20.26	-23.83	-23.52	-19.39	-24.52
K^+	-16.64	-19.81	-19.37	-15.82	-20.40

	S-M	PD-M	TA-M	TB-M
	-1.91	-2.91	-3.00	-3.00
Li^+	-6.54	-7.14	-2.28	-8.32
Na^+	-5.48	-6.17	-2.13	-7.26
K^+	-5.08	-5.68	-2.18	-6.76

Figure 1.2.8 – Cooperative effects between cation-π and π-π interactions. While cation-π interactions receive only a small increase in energy in the ternary cation-π-π system, the π-π interaction can experience a 3fold increase in energy. All values in kcal/mol.[176, 177] Picture reproduced from: [138]

1.2.5 Cation-π interactions in POM chemistry

Although POMs are intrinsically negatively charged and an enormous number of hybrid POMs with aromatic ligands have been synthesized over the last 20 years[178], cation-π effects in POM chemistry have only been observed and studied in recent years. Lu *et.al.* carried out pioneering

studies in the area of cation-π effects on counter-ions and macroionic self-assembly from 2017 on. With the help of an asymmetrically pyrene-functionalised hybrid Lindqvist polyoxovanadate they were able to track dynamic translocation processes of counterions by nuclear magnetic resonance (NMR) spectroscopy in DMSO. The counterions arrange themselves close to the pyrene moiety in solution *via* cation-π interactions and even facilitate the folding of the flexible pyrene group towards the cations.[179] In a study from 2018 the same group found an influence of cation-π interactions towards the self-assembly of rod-shaped hybrid polyoxometalates. The aggregation of polyoxometalates to nanosized blackberries, meaning hollow spheres, is well documented in the literature.[180] A typical characteristic is the formation of larger spheres with a higher ionic strength in solution. By adding aromatic ligands to the polyoxometalate rods, this trend was reversed due to cation-π interactions between Zn^{2+} ions and the aromatic ligands..[181]

POM-based materials, in which cation-π interactions were observed in the solid state are rare. Only three examples have been reported so far, for which cation-π interactions have been identified in the crystal structure. Cui *et.al*. reported the crystal structure of salt between a copper-bispyridine complex, and a Wells-Dawson POW with featuring intriguing Cu-π interaction.[182] Naphthyl-functionalised Keggin derivatives were reported by Gutiérrez-Zorrilla *et.al*. in which the tetrabutylammonium counter-ion build out weak cation-π interactions with the naphthyl ligands.[183] Lastly a fascinating U_{19} uranyl polyoxometalate was reported by Burns *et.al.*, in which the outside potassium ions build out cation-π interaction with a bisphosphonate ligand to form a supramolecular network in the solid state. [184] Those cation-π interaction however do not translate into solution.

1.3 Catalysis

The stability, rich redox chemistry and fascinating electronic properties makes POMs suitable candidates for a range of catalytic applications. After generally describing the catalytic properties of POMs, a few selected examples are given, which are in line with the compounds presented in this thesis.

One of the first catalytic application of polyoxometalates was their use as acid catalysts, due to them being strong Brønsted acids and their ability to form *peroxo*- and *hydroperoxo*-species.[185] Classical Hetero-POMs, such as the triply protonated Keggin-POM $H_3PW_{12}O_{40,}$ are fully dissociated acids in aqueous solution with all three pK_a-values being below those of strong

mineral acids such as sulfuric, nitric or hydrochloric acids.[186] This is mainly due to the low charge density as the negative charge is distributed around the POM cluster. In solution as in the solid-state protons are more likely to reside between solvent molecules than on the POM cluster directly. The removal of solvent molecules can even increase the acidity up to the strength of superacids, as the protons can no longer reside on the solvent molecules and are forced onto the cluster.[187] The bridging *oxo*-ligands generally tend to have a higher electron density then the terminal *oxo*-ligands and are therefore usually the preferred protonation site. The higher acidity of Hetero-POMs results in a significantly higher molar catalytic activity compared to mineral acids. An important example for the industrial use of POM-based acid catalysts is the hydration of olefins. Besides the increased catalytic activity for the reaction, the use of POM-based catalysts also result in higher selectivity and less side reactions.[188]

The use as oxidation catalysts relies on the property of POMs to act as electron sponges. As the coordination environments of the POM building metals can be build out by all higher oxidation states, little structural change is associated with oxidation or reduction of the POM. The delocalisation of electrons on the surface of the POM additionally stabilises reduced species. Early attempts to understand the general redox properties of POMs were therefor based on the charge density of the structures.[24] Pope *et. al.* found a dependence of the reduction potential for isostructural $[XM_{12}O_{40}]^{q-}$ Keggin anions of -0.18 V per additional unit charge. This dependency was later generalised by constructing a simplified molecular charge density.[185] When dividing the overall charge *q* with the number of metal atoms *m*, the resulting ratio *q/m* is linearly related to the energy of the LUMO and therefore the reduction potential of the POM.[189] The LUMO energy is generally lowered by increased size but raised with an increased negative charge on the cluster. This *q/m* ratio is naturally higher for POV species than for molybdenum- or tungsten-based POMs due to the difference of the +V and +VI oxidation state.

The similar structural features of all POMs present an ideal opportunity to create mixed-metal species by substituting one or more metal atoms in the cluster with other POM building metals. This substitution of, for example, tungsten ions with vanadium ions changes the electronic structure of the POM and therefore their redox chemistry. The utilisation of lacunary Keggin POMs to create mixed-metal species dates back to the 70s. Smith and Pope reported in 1973 the synthesis of mono-, di-, tetra- and hexavanado substituted tungsten Keggin structures.[190] The vanadium ions introduce a different catalytic functionality while also being ligated and therefore

stabilised by the lacunary POM. In 2010 Kamata *et.al.*[191] reported the efficient, stereospecific and regioselective hydroxylation of alkanes with H_2O_2, catalysed by a divanadium substituted γ-Keggin polyoxotungstate (Figure 1.3.1). The use of hydrogen peroxide with vanadium complexes in solution usually leads to a large number of *peroxo*-vanadium complexes and therefore to non-selective oxidation or over-oxidation. In the $\{PV_2W_{10}O_{40}\}$ POM, the rigid framework of the Keggin POM prevents this wasteful decomposition of H_2O_2 as well as leading to a high selectivity because of steric hindrance. The catalytically active species is assumed to be a μ_2-η^2:η^2 *peroxo* species.[192]

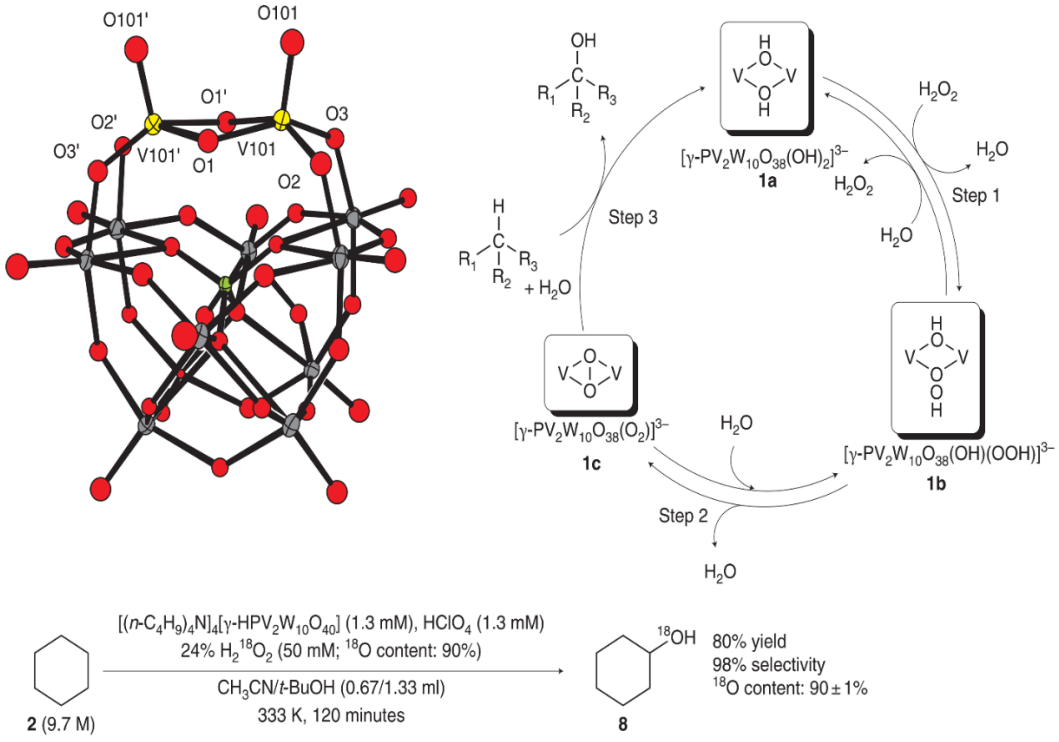

Figure 1.3.1 – Structure, proposed catalytic cycle and example reaction for a divanadium substituted γ-Keggin polyoxotungstate. Picture taken from ref. [191]

In 2016 Whitehead *et.al* reported the room-temperature oxidation of alcohols with the help of a fully reduced arsenate stabilised $Cs_5[V_{14}As_8O_{42}Cl]$ polyoxovanadate.[193] The use of fully reduced polyoxovanadates is rare in oxidation catalysis compared to their oxidized counterparts[194] but none the less the authors reported the selective oxidation of secondary alcohols to ketones with a low catalyst loading of 2 mol%. The catalyst was found to be recyclable up to three times by a

simple filtration step. The $\{V_{14}\}$ cluster is structurally related to the archetypal $\{V_{18}O_{42}\}$ POV, which can be understood by having two vanadium ions of the capping $\{V_5O_9\}$ groups removed.

An example of the catalytic abilities of a hybrid polyoxovanadate has been reported by Niu *et.al*.[195] The authors reported a structurally impressive carboxylate stabilised $\{V_{29}\}$ hybrid POV, consisting of a central $\{V^{V}_{17}\}$ cluster and four auxiliary $\{V^{IV}_{3}\}$ fragments that are connected *via* eight adipate ligands. The hybrid POV was investigated for its oxidation ability of organic sulfides. The catalyst was able to selectively catalyse the oxidation of differently substituted thioethers with *tert*-butyl hydroperoxide to sulfoxides over sulfones. High conversion rates and excellent selectivity were also achieved in the oxidation of dibenzothiophene to the respective sulfone.

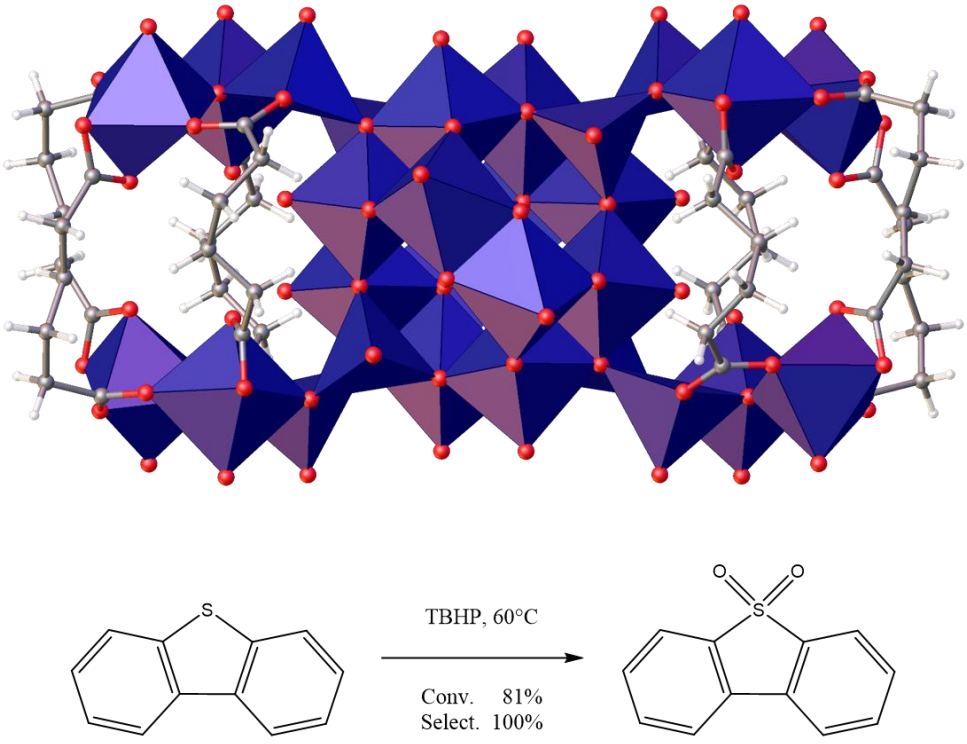

Figure 1.3.2 – Structure and catalytic example of the hybrid POV $\{V_{29}\}$. Pictures reproduced from ref. 195

1.4 Magnetism

Since their discovery polyoxometalates have been fascinating the magnetism community.[6, 196, 197] In first instance they represented molecular models of metal oxides by sharing the same magnetic exchange pathways as well as their delocalization with their bulk equivalents. Most useful for magnetic investigations however is their ability to act as robust ligands for the stabilisation of single or multiple magnetic ions enabled the targeted synthesis of well-defined and possibly gigantic magnetic molecules. In their highest oxidation state (W^{VI}, Mo^{VI}, V^{V}) the polyoxometalate are d^0 ions and therefore magnetically inactive. This approach is nicely exemplified by the magnetic Keplerates of the type $\{M_{30}Mo_{72}\}$[198] (M = V^{IV},[199] Fe^{III},[200] Ln^{II},[201] Cr^{II},[202]). In this cluster family, 30 magnetically active ions are embedded in a Mo^{VI}_{72} matrix, forming an icosidodecahedron of spin centres over the otherwise d^0 cluster.

The ability to act as an electron acceptor without structural rearrangement gives rise to the possibility of having a high variety of d^1 and d^0 combinations in a POM depending on the oxidation states of the metal ions. The degree of control one can achieve is exemplified at the archetypal $[V_{18}O_{48}]^{n-}$ cluster. In a comprehensive study[196] Müller *et.al.* synthesized multiple $\{V_{18}\}$ POVs in different oxidation states by utilising different anionic templates. The clusters ranged from the fully reduced $[V^{IV}_{18}O_{42}]^{12-}$ POV to the partially oxidised $[V^{IV}_{16}V^{V}_{2}O_{42}]^{10-}$, $[V^{IV}_{10}V^{V}_{8}O_{42}]^{4-}$ POV, whose $\chi T/T$ plots are given in Figure 1.4.1. It can be seen, that the system with more unpaired electrons is less antiferromagnetically coupled than the clusters with fewer unpaired electrons.[197] This means, for a growing distance between unpaired electrons a stronger antiferromagnetic coupling is measured. Ab initio calculations show that this behaviour can be traced back to the electron transfer between V^{V} and V^{IV} centres in the cluster, emphasising the importance of delocalisation in these mixed-valence systems.[203]

One of the most fascinating magnetic properties a molecule can have is to display single molecule magnetism. A topic, which recently gained new attention[204, 205] in the literature. Single molecule magnets (SMMs) are molecules, which mimic classical magnetic behaviour at low temperatures, such as slow relaxation and the resulting hysteresis behaviour of their magnetisation. The reason for this behaviour is the interplay between a usually large ground spin state *S* and a negative magnetic anisotropy. The anisotropy shows itself in an easy axis of the magnetization, which describes the energetically preferred orientation for spontaneous magnetization of the spins.

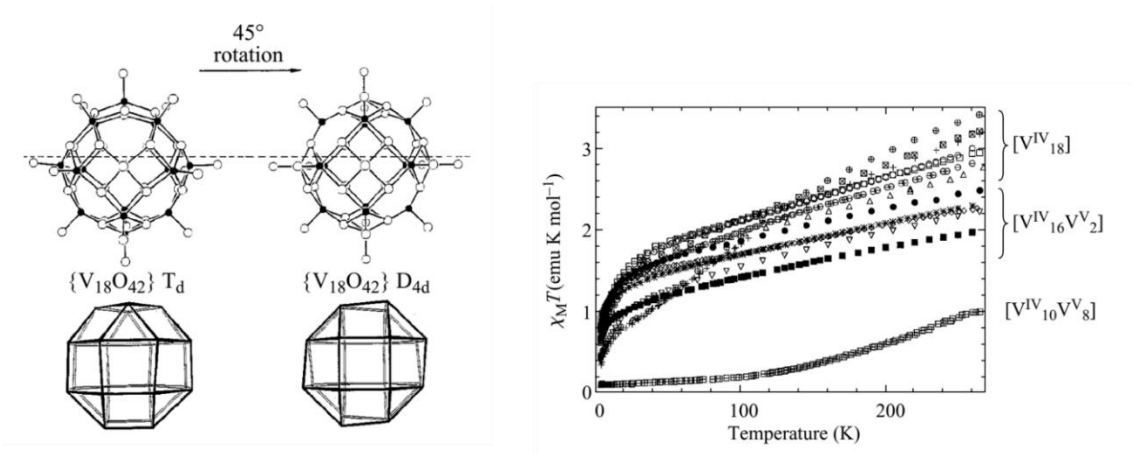

Figure 1.4.1 – Structure and magnetism of differently oxidised $\{V_{18}\}$ POVs. Pictures taken from ref. [196]

This behaviour leads to a double well potential as shown in Figure 1.4.2. The x-axis refers to the spin orientation of 0°, 90° or 180° towards the easy axis for –S, 0 and +S respectively. In the absence of a field both $-M_S$ and $+M_S$ are energetically equal. By applying a field along the easy axis during cooling to low temperature the $-M_S$ states are being stabilised and populated, while the $+M_S$ states are getting destabilised. The removal of the field afterwards leaves the spins in a trapped state, because of the energy barrier ΔE between the states, leading to slow relaxation and hysteresis phenomena.[206]

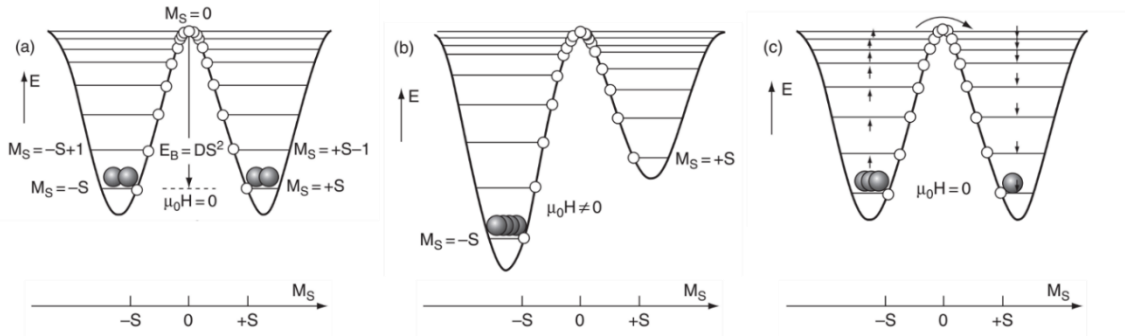

Figure 1.4.2 – Double-well potential of a spin state *S* with an easy axis magnetic anisotropy. a) No magnetic field, equal population of both states +/- M_S, b) Field applied in the direction of the easy axis stabilises M_S = -S, c) After removing the field the energy barrier ΔE prevents spins to relax from the –S to the +S state. Picture taken from ref. [206]

One of the most famous vanadium based SMMs is the $\{V_{15}As_6\}$ POV of Achim Müller.[207] The fully reduced POV consists of 15 vanadium(IV) ions which are arranged as shown in Figure 1.4.3. A triangle of vanadium(IV) ion in the middle of the structure is capped by two $\{V_6\}$ rings on top and bottom. The $\{V_6\}$ are strongly antiferromagnetically coupled, which makes them non-contributing even at higher temperatures. The weakly antiferromagnetically coupled triangle in the middle is therefore spin-frustrated. Spin frustration arises in antiferromagnetic systems in which the spins cannot align themselves completely antiparallel to each other, as is the case in a triangle. A consequence of spin frustration is a strong magnetic anisotropy with the easy axis of the magnetisation along the trigonal axis of the molecule.[208] $\{V_{15}As_6\}$ is one of the best investigated SMMs with over 60 publications to date. One of its most impressive characteristics is the possible application as a qubit in quantum computing. Su *et.al.* first observed quantum oscillation in $\{V_{15}As_6\}$ and were able to distinguish the Rabi-oscillation between the ground and first excited state of the system.[209]

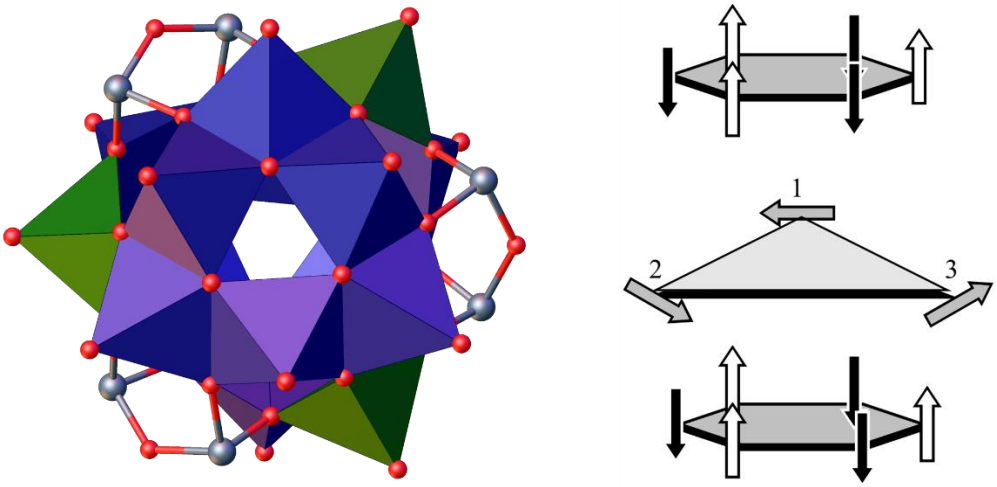

Figure 1.4.3 – Left: Structure of $\{V_{15}As_6\}$. The polyhedra for central vanadium(IV) triangle are coloured green. Right: Schematic drawing of the spin system with the spin-frustrated vanadium(IV) triangle in the middle. Right picture taken from ref. [197]

1.5 Aims and objectives

The aim of this project is the synthesis and characterisation of novel hybrid organic-inorganic POM capsules and ring structures. For this goal, a focus is put on utilising and exploring templating strategies through covalent and non-covalent interactions. We aim to understand those weak but intricate interactions to steer the formation of novel compounds as well as to tune their properties towards desired applications. The design and synthesis of suitable convex precursors and fragments will be used to construct closed POM-based structures and mixed metal systems. The use of easily modifiable organic ligands for this cause will help us investigate the structure-property relationships of novel compounds by tuning the steric and electronic nature of the ligand. Potential applications in areas such as catalysis and magnetism shall be explored for relevant compounds.

In order to achieve these goals, following specific objectives are being set

- To synthesize novel hybrid organic-inorganic POV capsules based on the existing $\{V_{10}\}$ motif from Schmitt *et.al.*
- To structurally characterise those compounds by single crystal x-ray diffractometry (XRD) and supplemental techniques.
- To understand their structure and formation with special focus on the structure directing nature of templating agents and ligands.
- To investigate and utilise the templating effects present in the structure in order to synthesize novel hybrid organic-inorganic POV compounds.
- To determine structure-property relationships and investigate their potential applications.
- To identify usable POM precursor complexes with free functional groups such as phosphonic or carboxylic acids.
- To use those precursor complexes in the construction of mixed metal systems.
- To carry out catalytic studies on the mixed metal systems as well as the cage and ring structures.

1. L. Cronin, in *Comprehensive Coordination Chemistry II*, eds. J. A. McCleverty and T. J. Meyer, Pergamon, Oxford, 2003, pp. 1-56.
2. D. C. Crans and J. J. Smee, in *Comprehensive Coordination Chemistry II*, eds. J. A. McCleverty and T. J. Meyer, Pergamon, Oxford, 2003, pp. 175-239.
3. T. Okamura and N. Ueyama, in *Comprehensive Coordination Chemistry II*, eds. T. J. Meyer and J. A. McCleverty, Pergamon, Oxford, 2003, pp. 529-573.
4. C. G. Young, in *Comprehensive Coordination Chemistry II*, ed. T. J. Meyer, Pergamon, Oxford, 2003, pp. 415-527.
5. J. M. Poblet, X. Lopez and C. Bo, *Chem. Soc. Rev.*, 2003, **32**, 297-308.
6. J. M. Clemente-Juan, E. Coronado and A. Gaita-Arino, *Chem. Soc. Rev.*, 2012, **41**, 7464-7478.
7. N. Mizuno, K. Kamata, S. Uchida and K. Yamaguchi, in *Modern Heterogeneous Oxidation Catalysis*, Wiley-VCH Verlag GmbH & Co. KGaA, Weinheim, 2009, pp. 185-216.
8. H. Lv, Y. V. Geletii, C. Zhao, J. W. Vickers, G. Zhu, Z. Luo, J. Song, T. Lian, D. G. Musaev and C. L. Hill, *Chem. Soc. Rev.*, 2012, **41**, 7572-7589.
9. S.-S. Wang and G.-Y. Yang, *Chem. Rev.*, 2015, **115**, 4893-4962.
10. H. Yanagie, A. Ogata, S. Mitsui, T. Hisa, T. Yamase and M. Eriguchi, *Biomed. Pharmacother.*, 2006, **60**, 349-352.
11. J. T. Rhule, C. L. Hill, D. A. Judd and R. F. Schinazi, *Chem. Rev.*, 1998, **98**, 327-358.
12. A. Bijelic and A. Rompel, *Acc. Chem. Res.*, 2017, **50**, 1441-1448.
13. A. Bijelic and A. Rompel, *Coord. Chem. Rev.*, 2015, **299**, 22-38.
14. T. Yamase, *Chem. Rev.*, 1998, **98**, 307-326.
15. S. Omwoma, C. T. Gore, Y. Ji, C. Hu and Y.-F. Song, *Coord. Chem. Rev.*, 2015, **286**, 17-29.
16. C. Jiang, Y. Guo, C. Wang, C. Hu, Y. Wu and E. Wang, *Appl. Catal.*, 2003, **A256**, 203-212.
17. T. Dizhbite, L. Jashina, G. Dobele, A. Andersone, D. Evtuguin, O. Bikovens and G. Telysheva, *Holzforschung*, 2013, **67**, 539-547.
18. M. J. Martínez-Pérez, S. Cardona-Serra, C. Schlegel, F. Moro, P. J. Alonso, H. Prima-García, J. M. Clemente-Juan, M. Evangelisti, A. Gaita-Ariño, J. Sesé, J. van Slageren, E. Coronado and F. Luis, *Phys. Rev. Lett.*, 2012, **108**, 247213.
19. J. J. D'Elhuyar Lubice and F. C. D'Elhuyar Lubice., in *Extractos de las Juntas Generales celebradas por la Real Sociedad Bascongada de los Amigos del Pais en la Villa de Vergara*, ed. T. d. Robles, San Sebastián, 1783, pp. 46-88.
20. J. J. Berzelius, *Ann. Phys.*, 1826, **82**, 369-392.
21. J. Illingworth and J. Keggin, *J. Chem. Soc.*, 1935, 575-580.
22. J. F. Keggin and W. L. Bragg, *Proc. Royal Soc. A*, 1934, **144**, 75-100.
23. R. Signer and H. Gross, *Helv. Chim.*, 1934, **17**, 1076-1080.
24. M. T. Pope, *Heteropoly and Isopoly Oxometalates*, Springer-Verlag, Berlin, 1983.
25. A. Werner, *Neuere Anschauungen auf dem Gebiete der anorganischen Chemie*, Friedrich Vieweg und Sohn, Braunschweig, 1905.
26. I. Lindqvist, *Arkiv Kemi*, 1952, **5**, 247.
27. I. Lindqvist and B. Aronsson, *Arkiv Kemi*, 1954, **7**, 49.
28. H. K. Chae, W. G. Klemperer and V. W. Day, *Inorg. Chem.*, 1989, **28**, 1423-1424.
29. Y. Hayashi, Y. Ozawa and K. Isobe, *Chem. Lett.*, 1989, **18**, 425-428.
30. L. J. Batchelor, R. Shaw, S. J. Markey, M. Helliwell and E. J. L. McInnes, *Chem. Eur. J.*, 2010, **16**, 5554-5557.
31. X.-F. Su, B. Zhu, C.-X. Wu, L.-K. Yan and Z.-M. Su, *J. Theor. Comput. Chem.*, 2017, **16**, 1750054.

32. N. I. Gumerova and A. Rompel, *Nat. Rev. Chem.*, 2018, **2**, Article number (0112).
33. A. Blazevic and A. Rompel, *Coord. Chem. Rev.*, 2016, **307**, 42-64.
34. J. S. Anderson, *Nature*, 1937, **140**, 850-850.
35. H. T. Evans, *J. Am. Chem. Soc.*, 1948, **70**, 1291-1292.
36. J. Lu, Y. Wang, X. Ma, Y. Niu, V. Singh, P. Ma, C. Zhang, J. Niu and J. Wang, *Dalton Trans.*, 2018, **47**, 8070-8077.
37. C. Robl and M. Frost, *Z. Naturforsch. B*, 1993, **48**, 404.
38. H. Kondo, A. Kobayashi and Y. Sasaki, *Acta Cryst.*, 1980, **B36**, 661-664.
39. B. Dawson, *Acta Cryst.*, 1953, **6**, 113-126.
40. L. C. W. Baker and J. S. Figgis, *J. Am. Chem. Soc.*, 1970, **92**, 3794-3797.
41. C. W. Scheele, *Sämmtliche physische und chemische Werke*, Mayer & Müller, Berlin, 1793.
42. A. Müller and C. Serain, *Acc. Chem. Res.*, 2000, **33**, 2-10.
43. A. Müller, E. Krickemeyer, H. Bögge, M. Schmidtmann, C. Beugholt, S. K. Das and F. Peters, *Chem. Eur. J.*, 1999, **5**, 1496-1502.
44. A. Müller, E. Krickemeyer, J. Meyer, H. Bögge, F. Peters, W. Plass, E. Diemann, S. Dillinger, F. Nonnenbruch, M. Randerath and C. Menke, *Angew. Chem. Int. Ed.*, 1995, **34**, 2122-2124.
45. A. Müller, E. Beckmann, H. Bögge, M. Schmidtmann and A. Dress, *Angew. Chem. Int. Ed.*, 2002, **41**, 1162-1167.
46. B. Botar, A. Ellern and P. Kögerler, *Dalton Trans.*, 2012, **41**, 8951-8959.
47. A. Müller and P. Gouzerh, *Chem. Soc. Rev.*, 2012, **41**, 7431-7463.
48. C. A. Ohlin, E. M. Villa, J. R. Rustad and W. H. Casey, *Nat. Mater.*, 2009, **9**, 11.
49. J. R. Rustad and W. H. Casey, *Nat. Mater.*, 2012, **11**, 223.
50. W. H. Casey and J. R. Rustad, *New J. Chem.*, 2016, **40**, 898-905.
51. C. J. Ballhausen and H. B. Gray, *Inorg. Chem.*, 1962, **1**, 111-122.
52. J. R. Winkler and H. B. Gray, in *Molecular Electronic Structures of Transition Metal Complexes I*, eds. D. M. P. Mingos, P. Day and J. P. Dahl, Springer Berlin Heidelberg, Berlin, Heidelberg, 2012, pp. 17-28.
53. R. J. Errington, in *Polyoxometalate Molecular Science*, eds. J. J. Borrás-Almenar, E. Coronado, A. Müller and M. Pope, Springer Netherlands, Dordrecht, 2003, pp. 55-78.
54. S.-T. Zheng and G.-Y. Yang, *Chem. Soc. Rev.*, 2012, **41**, 7623-7646.
55. Z. Zhang, L. Wojtas and M. J. Zaworotko, *Chem. Sci.*, 2014, **5**, 927-931.
56. C. J. Richmond, H. N. Miras, A. R. de la Oliva, H. Zang, V. Sans, L. Paramonov, C. Makatsoris, R. Inglis, E. K. Brechin, D.-L. Long and L. Cronin, *Nat. Chem.*, 2012, **4**, 1037.
57. A. S. Tracey, G. R. Willsky and E. S. Takeuchi, *Vanadium: Chemistry, Biochemistry, Pharmacology and Practical Applications*, CRC Press, Boca Raton, FL, 2007.
58. L. Vilà-Nadal, A. Rodríguez-Fortea, L.-K. Yan, E. F. Wilson, L. Cronin and J. M. Poblet, *Angew. Chem. Int. Ed.*, 2009, **48**, 5452-5456.
59. L. Vilà-Nadal, A. Rodríguez-Fortea and J. M. Poblet, *Eur. J. Inorg. Chem.*, **2009**, 5125-5133.
60. L. Vilà-Nadal, E. F. Wilson, H. N. Miras, A. Rodríguez-Fortea, L. Cronin and J. M. Poblet, *Inorg. Chem.*, 2011, **50**, 7811-7819.
61. L. Vilà-Nadal, S. G. Mitchell, A. Rodríguez-Fortea, H. N. Miras, L. Cronin and J. M. Poblet, *Phys. Chem. Chem. Phys.*, 2011, **13**, 20136-20145.
62. C. Streb, in *Polyoxometalate-Based Assemblies and Functional Materials*, ed. Y.-F. Song, Springer International Publishing, Cham, 2018, pp. 31-47.
63. A. Müller, H. Reuter and S. Dillinger, *Angew. Chem. Int. Ed.*, 1995, **34**, 2328-2361.
64. K. Kastner, J. T. Margraf, T. Clark and C. Streb, *Chem. Eur. J.*, 2014, **20**, 12269-12273.

65. V. W. Day, W. G. Klemperer and O. M. Yaghi, *J. Am. Chem. Soc.*, 1989, **111**, 5959-5961.
66. Y. Kikukawa, K. Seto, S. Uchida, S. Kuwajima and Y. Hayashi, *Angew. Chem. Int. Ed.*, 2018, **57**, 16051-16055.
67. C. Healy and W. Schmitt, *Coord. Chem. Rev.*, 2018, **371**, 67-85.
68. A. Dolbecq, E. Dumas, C. R. Mayer and P. Mialane, *Chem. Rev.*, 2010, **110**, 6009-6048.
69. D.-L. Long, R. Tsunashima and L. Cronin, *Angew. Chem. Int. Ed.*, 2010, **49**, 1736-1758.
70. Y.-F. Song and R. Tsunashima, *Chem. Soc. Rev.*, 2012, **41**, 7384-7402.
71. C. Yvon, A. Macdonell, S. Buchwald, A. J. Surman, N. Follet, J. Alex, D.-L. Long and L. Cronin, *Chem. Sci.*, 2013, **4**, 3810-3817.
72. J. Zhang, Y.-F. Song, L. Cronin and T. Liu, *J. Am. Chem. Soc.*, 2008, **130**, 14408-14409.
73. Y. Yan, B. Li, Q. He, Z. He, H. Ai, H. Wang, Z. Yin and L. Wu, *Soft Matter*, 2012, **8**, 1593-1600.
74. O. Oms, K. Hakouk, R. Dessapt, P. Deniard, S. Jobic, A. Dolbecq, T. Palacin, L. Nadjo, B. Keita, J. Marrot and P. Mialane, *Chem. Commun.*, 2012, **48**, 12103-12105.
75. S. Tanaka, M. Annaka and K. Sakai, *Chem. Commun.*, 2012, **48**, 1653-1655.
76. X. Feng, W. Zhou, Y. Li, H. Ke, J. Tang, R. Clérac, Y. Wang, Z. Su and E. Wang, *Inorg. Chem.*, 2012, **51**, 2722-2724.
77. R. Raza, A. Matin, S. Sarwar, M. Barsukova-Stuckart, M. Ibrahim, U. Kortz and J. Iqbal, *Dalton Trans.*, 2012, **41**, 14329-14336.
78. D. Li, P. Ma, J. Niu and J. Wang, *Coord. Chem. Rev.*, 2019, **392**, 49-80.
79. F. Hussain, F. Conrad and G. R. Patzke, *Angew. Chem. Int. Ed.*, 2009, **48**, 9088-9091.
80. R. C. Howell, F. G. Perez, S. Jain, J. W. DeW. Horrocks, A. L. Rheingold and L. C. Francesconi, *Angew. Chem. Int. Ed.*, 2001, **40**, 4031-4034.
81. B. S. Bassil, M. H. Dickman, I. Römer, B. von der Kammer and U. Kortz, *Angew. Chem. Int. Ed.*, 2007, **46**, 6192-6195.
82. K. Fukaya and T. Yamase, *Angew. Chem. Int. Ed.*, 2003, **42**, 654-658.
83. S. Fujimoto, J. M. Cameron, R.-J. Wei, K. Kastner, D. Robinson, V. Sans, G. N. Newton and H. Oshio, *Inorg. Chem.*, 2017, **56**, 12169-12177.
84. J. M. Cameron, D. J. Wales and G. N. Newton, *Dalton Trans.*, 2018, **47**, 5120-5136.
85. Z.-J. Liu, X.-L. Wang, C. Qin, Z.-M. Zhang, Y.-G. Li, W.-L. Chen and E.-B. Wang, *Coord. Chem. Rev.*, 2016, **313**, 94-110.
86. D. D. Heinrich, K. Folting, W. E. Streib, J. C. Huffman and G. Christou, *J. Chem. Soc., Chem. Commun.*, 1989, 1411-1413.
87. G. B. Karet, Z. Sun, D. D. Heinrich, J. K. McCusker, K. Folting, W. E. Streib, J. C. Huffman, D. N. Hendrickson and G. Christou, *Inorg. Chem.*, 1996, **35**, 6450-6460.
88. A. Müller, M. Penk, R. Rohlfing, E. Krickemeyer and J. Döring, *Angew. Chem. Int. Ed.*, 1990, **29**, 926-927.
89. A. Müller, K. Hovemeier and R. Rohlfing, *Angew. Chem. Int. Ed.*, 1992, **31**, 1192-1195.
90. M. I. Khan and J. Zubieta, *Angew. Chem. Int. Ed.*, 1994, **33**, 760-762.
91. J. M. Breen, R. Clerac, L. Zhang, S. M. Cloonan, E. Kennedy, M. Feeney, T. McCabe, D. C. Williams and W. Schmitt, *Dalton Trans.*, 2012, **41**, 2918-2926.
92. J. M. Breen and W. Schmitt, *Angew. Chem. Int. Ed.*, 2008, **47**, 6904-6908.
93. J. M. Breen, L. Zhang, R. Clement and W. Schmitt, *Inorg. Chem.*, 2012, **51**, 19-21.
94. M. B. Mahimaidoss, S. A. Krasnikov, L. Reck, C. I. Onet, J. M. Breen, N. Zhu, B. Marzec, I. V. Shvets and W. Schmitt, *Chem. Coomun.*, 2014, **50**, 2265-2267.
95. Z. Zhang, W.-Y. Gao, L. Wojtas, Z. Zhang and M. J. Zaworotko, *Chem. Commun.*, 2015, **51**, 9223-9226.
96. Y.-T. Zhang, X.-L. Wang, S.-B. Li, Y.-R. Gong, B.-Q. Song, K.-Z. Shao and Z.-M. Su, *Chem. Commun.*, 2016, **52**, 9632-9635.

97. Y.-T. Zhang, X.-L. Wang, E.-L. Zhou, X.-S. Wu, B.-Q. Song, K.-Z. Shao and Z.-M. Su, *Dalton Trans.*, 2016, **45**, 3698-3701.
98. Y. Zhang, X. Wang, S. Li, B. Song, K. Shao and Z. Su, *Inorg. Chem.*, 2016, **55**, 8770-8775.
99. Y.-R. Gong, Z.-M. Su and X.-L. Wang, *Acta Cryst.*, 2018, **C74**, 1243-1247.
100. N. Xu, H. Gan, C. Qin, X. Wang and Z. Su, *Angew. Chem.*, 2019, **131**, 4697-4701.
101. Y. Gong, Y. Zhang, C. Qin, C. Sun, X. Wang and Z. Su, *Angew. Chem.*, 2019, **131**, 790-794.
102. Y. Zhang, H. Gan, C. Qin, X. Wang, Z. Su and M. J. Zaworotko, *J. Am. Chem. Soc.*, 2018, **140**, 17365-17368.
103. X.-X. Li, D. Zhao and S.-T. Zheng, *Coord. Chem. Rev.*, 2019, **397**, 220-240.
104. Y.-R. Wang, Q. Huang, C.-T. He, Y. Chen, J. Liu, F.-C. Shen and Y.-Q. Lan, *Nat. Commun.*, 2018, **9**, 4466.
105. X.-X. Li, L.-J. Zhang, C.-Y. Cui, R.-H. Wang and G.-Y. Yang, *Inorg. Chem.*, 2018, **57**, 10323-10330.
106. F. Sécheresse, E. Cadot and C. Simonnet-Jegat, in *Metal Clusters in Chemistry*, eds. P. Braunstein, L. A. Oro and P. R. Raithby, Wiley-VCH, Weinheim, 1999, pp. 124-142.
107. E. Cadot, M. N. Sokolov, V. P. Fedin, C. Simonnet-Jegat, S. Floquet and F. Secheresse, *Chem. Soc. Rev.*, 2012, **41**, 7335-7353.
108. S. J. Hibble and G. B. Wood, *J. Am. Chem. Soc.*, 2004, **126**, 959-965.
109. A. Muller, V. Fedin, K. Hegetschweiler and W. Amrein, *J. Chem. Soc., Chem. Commun.*, 1992, 1795-1796.
110. E. Cadot, V. Béreau, B. Marg, S. Halut and F. Sécheresse, *Inorg. Chem.*, 1996, **35**, 3099-3106.
111. J. Marrot, M. A. Pilette, M. Haouas, S. Floquet, F. Taulelle, X. Lopez, J. M. Poblet and E. Cadot, *J. Am. Chem. Soc.*, 2012, **134**, 1724-1737.
112. E. Cadot, B. Salignac, S. Halut and F. Sécheresse, *Angew. Chem. Int. Ed.*, 1998, **37**, 611-613.
113. A. Dolbecq, E. Cadot and F. Sécheresse, *Chem. Commun.*, 1998, 2293-2294.
114. E. Cadot, B. Salignac, T. Loiseau, A. Dolbecq and F. Sécheresse, *Chem. Eur. J.*, 1999, **5**, 3390-3398.
115. E. Cadot, B. Salignac, J. Marrot, A. Dolbecq and F. Secheresse, *Chem. Commun.*, 2000, 261-262.
116. B. Salignac, S. Riedel, A. Dolbecq, F. Sécheresse and E. Cadot, *J. Am. Chem. Soc.*, 2000, **122**, 10381-10389.
117. A. Dolbecq, E. Cadot and F. Sécheresse, *Comptes Rendus Acad. Sci. II C*, 2000, **3**, 193-197.
118. E. Cadot, A. Dolbecq, B. Salignac and F. Sécheresse, *J. Phys. Chem. Solids*, 2001, **62**, 1533-1543.
119. C. du Peloux, A. Dolbecq, E. Cadot, J. Marrot and F. Sécheresse, *J. Mol. Struct.*, 2003, **656**, 37-44.
120. S. Floquet, J. Marrot and E. Cadot, *Comptes Rendus Acad. Sci. II C*, 2005, **8**, 1067-1075.
121. J.-F. Lemonnier, S. Floquet, A. Kachmar, M.-M. Rohmer, M. Bénard, J. Marrot, E. Terazzi, C. Piguet and E. Cadot, *Dalton Trans.*, 2007, 3043-3054.
122. J.-F. Lemonnier, S. Floquet, J. Marrot, A. Kachmar, M. Bénard, M.-M. Rohmer, M. Haouas, F. Taulelle, M. Henry and E. Cadot, *Inorg. Chem.*, 2007, **46**, 9516-9518.
123. J.-F. Lemonnier, S. Floquet, J. Marrot, E. Terazzi, C. Piguet, P. Lesot, A. Pinto and E. Cadot, *Chem. Eur. J.*, 2007, **13**, 3548-3557.
124. J.-F. Lemonnier, A. Kachmar, S. Floquet, J. Marrot, M.-M. Rohmer, M. Bénard and E. Cadot, *Dalton Trans.*, 2008, 4565-4574.

125. J.-F. Lemonnier, S. Floquet, J. Marrot and E. Cadot, *Eur. J. Inorg. Chem.*, **2009**, 5233-5239.
126. S. Duval, S. Floquet, C. Simonnet-Jégat, J. Marrot, R. N. Biboum, B. Keita, L. Nadjo, M. Haouas, F. Taulelle and E. Cadot, *J. Am. Chem. Soc.*, 2010, **132**, 2069-2077.
127. A. Hijazi, J. C. Kemmegne-Mbouguen, S. Floquet, J. Marrot, C. R. Mayer, V. Artero and E. Cadot, *Inorg. Chem.*, 2011, **50**, 9031-9038.
128. A. Hijazi, J. C. Kemmegne-Mbouguen, S. Floquet, J. Marrot, J. Fize, V. Artero, O. David, E. Magnier, B. Pegot and E. Cadot, *Dalton Trans*, 2013, **42**, 4848-4858.
129. S. Floquet, S. Draoui, J. Marrot, F. Millange, M. Frigoli and E. Cadot, *J. Clust. Sci.*, 2014, **25**, 811-823.
130. S. Duval, F. Dumur, L. Guénée, J. Marrot, C. Simonnet-Jégat and E. Cadot, *Eur. J. Inorg. Chem.*, **2013**, 1149-1156.
131. J. W. Purcell, H. N. Miras, D.-L. Long, P. Markopoulou and L. Cronin, *Chem. Eur. J.*, 2017, **23**, 9683-9689.
132. H. Zang, H. N. Miras, J. Yan, D.-L. Long and L. Cronin, *J. Am. Chem. Soc.*, 2012, **134**, 11376-11379.
133. H.-Y. Zang, J.-J. Chen, D.-L. Long, L. Cronin and H. N. Miras, *Adv. Mater.*, 2013, **25**, 6245-6249.
134. H.-Y. Zang, H. N. Miras, D.-L. Long, B. Rausch and L. Cronin, *Angew. Chem. Int. Ed.*, 2013, **52**, 6903-6906.
135. H.-Y. Zang, A. R. de la Oliva, H. N. Miras, D.-L. Long, R. T. McBurney and L. Cronin, *Nat. Commun.*, 2014, **5**, 3715.
136. H. Zang, A. Surman, D. Long, L. Cronin and H. N. Miras, *Chem. Commun.*, 2016, **52**, 9109-9112.
137. H.-Y. Zang, J. W. Purcell, D.-L. Long, H. N. Miras and L. Cronin, *Chem. Commun.*, 2017, **53**, 8585-8587.
138. A. S. Mahadevi and G. N. Sastry, *Chem. Rev.*, 2016, **116**, 2775-2825.
139. J. D. Watson and F. H. C. Crick, *Nature*, 1953, **171**, 737-738.
140. V. L. Malinovskii, F. Samain and R. Häner, *Angew. Chem. Int. Ed.*, 2007, **46**, 4464-4467.
141. S. K. Burley and G. A. Petsko, *Science*, 1985, **229**, 23-28.
142. A. Weichsel and W. R. Montfort, *Nat. Struct. Biol.*, 1995, **2**, 1095-1101.
143. L. M. Salonen, M. Ellermann and F. Diederich, *Angew. Chem. Int. Ed.*, 2011, **50**, 4808-4842.
144. E. A. Meyer, R. K. Castellano and F. Diederich, *Angew. Chem. Int. Ed.*, 2003, **42**, 1210-1250.
145. R. K. Raju, J. W. G. Bloom, Y. An and S. E. Wheeler, *ChemPhysChem*, 2011, **12**, 3116-3130.
146. J. W. G. Bloom and S. E. Wheeler, *Angew. Chem. Int. Ed.*, 2011, **50**, 7847-7849.
147. C. A. Hunter and J. K. M. Sanders, *J. Am. Chem. Soc.*, 1990, **112**, 5525-5534.
148. C. R. Martinez and B. L. Iverson, *Chem. Sci.*, 2012, **3**, 2191-2201.
149. D. Naae, *Acta Cryst.*, 1979, **B35**, 2765-2768.
150. J. H. Williams, *Acc. Chem. Res.*, 1993, **26**, 593-598.
151. C. R. Patrick and G. S. Prosser, *Nature*, 1960, **187**, 1021-1021.
152. M. O. Sinnokrot and C. D. Sherrill, *J. Phys. Chem. A*, 2003, **107**, 8377-8379.
153. S. E. Wheeler and K. N. Houk, *J. Am. Chem. Soc.*, 2008, **130**, 10854-10855.
154. A. J. Neel, M. J. Hilton, M. S. Sigman and F. D. Toste, *Nature*, 2017, **543**, 637.
155. S. Grimme, *Angew. Chem. Int. Ed.*, 2008, **47**, 3430-3434.
156. Y. An and S. E. Wheeler, in *Encyclopedia of Inorganic and Bioinorganic Chemistry*, ed. R. A. Scott, John Wiley & Sons, 2015.
157. J. Sunner, K. Nishizawa and P. Kebarle, *J. Phys. Chem.*, 1981, **85**, 1814-1820.

158. R. W. Taft, F. Anvia, J. F. Gal, S. Walsh, M. Capon, M. C. Holmes, K. Hosn, G. Oloumi, R. Vasanwala and S. Yazdani, *Pure Appl. Chem.*, 1990, **62**, 17.
159. B. C. Guo, J. W. Purnell and A. W. Castleman, *Chem. Phys. Lett.*, 1990, **168**, 155-160.
160. R. A. Kumpf and D. A. Dougherty, *Science*, 1993, **261**, 1708-1710.
161. J. C. Ma and D. A. Dougherty, *Chem. Rev.*, 1997, **97**, 1303-1324.
162. T. J. Shepodd, M. A. Petti and D. A. Dougherty, *J. Am. Chem. Soc.*, 1986, **108**, 6085-6087.
163. M. A. Petti, T. J. Shepodd, R. E. Barrans and D. A. Dougherty, *J. Am. Chem. Soc.*, 1988, **110**, 6825-6840.
164. T. J. Shepodd, M. A. Petti and D. A. Dougherty, *J. Am. Chem. Soc.*, 1988, **110**, 1983-1985.
165. D. A. Dougherty and D. A. Stauffer, *Science*, 1990, **250**, 1558-1560.
166. O. M. Cabarcos, C. J. Weinheimer and J. M. Lisy, *J. Chem. Phys.*, 1999, **110**, 8429-8435.
167. K. Kumar, S. M. Woo, T. Siu, W. A. Cortopassi, F. Duarte and R. S. Paton, *Chem. Sci.*, 2018, **9**, 2655-2665.
168. G. K. Fukin, S. V. Lindeman and J. K. Kochi, *J. Am. Chem. Soc.*, 2002, **124**, 8329-8336.
169. S. E. Wheeler and K. N. Houk, *J. Am. Chem. Soc.*, 2009, **131**, 3126-3127.
170. S. E. Wheeler and K. N. Houk, *J. Chem. Theory Comput.*, 2009, **5**, 2301-2312.
171. S. E. Wheeler, *Acc. Chem. Res.*, 2013, **46**, 1029-1038.
172. D. Vijay and G. N. Sastry, *Phys. Chem. Chem. Phys.*, 2008, **10**, 582-590.
173. D. Umadevi and G. N. Sastry, *J. Phys. Chem. C*, 2011, **115**, 9656-9667.
174. J. R. Premkumar, D. Vijay and G. N. Sastry, *Dalton Trans.*, 2012, **41**, 4965-4975.
175. A. S. Reddy, H. Zipse and G. N. Sastry, *J. Phys. Chem. B*, 2007, **111**, 11546-11553.
176. A. S. Reddy, D. Vijay, G. M. Sastry and G. N. Sastry, *J. Phys. Chem. B*, 2006, **110**, 2479-2481.
177. D. Vijay and G. N. Sastry, *Chem. Phys. Lett.*, 2010, **485**, 235-242.
178. P. Ma, F. Hu, J. Wang and J. Niu, *Coord. Chem. Rev.*, 2019, **378**, 281-309.
179. D. Li, Z. Liu, J. Song, H. Li, B. Zhang, P. Yin, Z. N. Zheng, J. E. Roberts, M. Tsige, C. L. Hill and T. Liu, *Angew. Chem. Int. Ed.*, 2017, **56**, 3294-3298.
180. P. Yin, D. Li and T. Liu, *Chem. Soc. Rev.*, 2012, **41**, 7368-7383.
181. J. Luo, K. Chen, P. Yin, T. Li, G. Wan, J. Zhang, S. Ye, X. Bi, Y. Pang, Y. Wei and T. Liu, *Angew. Chem. Int. Ed.*, 2018, **57**, 4067-4072.
182. Y. Lü, X. Zhang, X.-B. Cui and J.-Q. Xu, *Inorg. Chem.*, 2018, **57**, 11123-11134.
183. N. Andino, B. Artetxe, S. Reinoso, P. Vitoria, L. San Felices, I. J. Martínez, F. López Arbeloa and M. J. Gutiérrez-Zorrilla, *Inorganics*, 2016, **4**.
184. M. Xu, H. Traustason, F. D. Bo, S. Hickam, S. Chong, L. Zhang, A. G. Oliver and P. C. Burns, *J. Am. Chem. Soc.*, 2019, **141**, 12780-12788.
185. X. López, J. J. Carbó, C. Bo and J. M. Poblet, *Chem. Soc. Rev.*, 2012, **41**, 7537-7571.
186. I. Kozhevnikov, *Catalysts for Fine Chemical Synthesis, Catalysis by Polyoxometalates*, Wiley, 2002.
187. C. L. Hill, in *Comprehensive Coordination Chemistry II*, eds. J. A. McCleverty and T. J. Meyer, Pergamon, Oxford, 2003, pp. 679-759.
188. I. V. Kozhevnikov, *Chem. Rev.*, 1998, **98**, 171-198.
189. X. López, J. A. Fernández and J. M. Poblet, *Dalton Trans.*, 2006, 1162-1167.
190. D. P. Smith and M. T. Pope, *Inorg. Chem.*, 1973, **12**, 331-336.
191. K. Kamata, K. Yonehara, Y. Nakagawa, K. Uehara and N. Mizuno, *Nat. Chem.*, 2010, **2**, 478.
192. Y. Nakagawa and N. Mizuno, *Inorg. Chem.*, 2007, **46**, 1727-1736.
193. M. L. Campbell, D. Sulejmanovic, J. B. Schiller, E. M. Turner, S.-J. Hwu and D. C. Whitehead, *Catal. Sci. Technol.*, 2016, **6**, 3208-3213.

194. M. L. Campbell, D. Sulejmanovic, J. B. Schiller, E. M. Turner, S. J. Hwu and D. C. Whitehead, *Helv. Chim.*, 2017, **100**.
195. K. Wang, Y. Niu, D. Zhao, Y. Zhao, P. Ma, D. Zhang, J. Wang and J. Niu, *Inorg. Chem.*, 2017, **56**, 14053-14059.
196. A. Müller, R. Sessoli, E. Krickemeyer, H. Bögge, J. Meyer, D. Gatteschi, L. Pardi, J. Westphal, K. Hovemeier, R. Rohlfing, J. Döring, F. Hellweg, C. Beugholt and M. Schmidtmann, *Inorg. Chem.*, 1997, **36**, 5239-5250.
197. D. Gatteschi, R. Sessoli and J. Villain, *Molecular Nanomagnets*, Oxford University Press, Oxford, 2011.
198. U. Kortz, A. Müller, J. van Slageren, J. Schnack, N. S. Dalal and M. Dressel, *Coord. Chem. Rev.*, 2009, **253**, 2315-2327.
199. A. Müller, A. M. Todea, J. van Slageren, M. Dressel, H. Bögge, M. Schmidtmann, M. Luban, L. Engelhardt and M. Rusu, *Angew. Chem. Int. Ed.*, 2005, **44**, 3857-3861.
200. A. Müller, S. Sarkar, S. Q. N. Shah, H. Bögge, M. Schmidtmann, S. Sarkar, P. Kögerler, B. Hauptfleisch, A. X. Trautwein and V. Schünemann, *Angew. Chem. Int. Ed.*, 1999, **38**, 3238-3241.
201. A. Müller, H. Bögge, F. L. Sousa, M. Schmidtmann, D. G. Kurth, D. Volkmer, J. van Slageren, M. Dressel, M. L. Kistler and T. Liu, *Small*, 2007, **3**, 986-992.
202. A. M. Todea, A. Merca, H. Bögge, J. van Slageren, M. Dressel, L. Engelhardt, M. Luban, T. Glaser, M. Henry and A. Müller, *Angew. Chem. Int. Ed.*, 2007, **46**, 6106-6110.
203. C. J. Calzado, J. M. Clemente-Juan, E. Coronado, A. Gaita-Arino and N. Suaud, *Inorg. Chem.*, 2008, **47**, 5889-5901.
204. F.-S. Guo, B. M. Day, Y.-C. Chen, M.-L. Tong, A. Mansikkamäki and R. A. Layfield, *Angew. Chem. Int. Ed.*, 2017, **56**, 11445-11449.
205. F.-S. Guo, B. M. Day, Y.-C. Chen, M.-L. Tong, A. Mansikkamäki and R. A. Layfield, *Science*, 2018, **362**, 1400-1403.
206. J.-P. Launay and M. Verdaguer, *Electrons in Molecules : From Basic Principles to Molecular Electronics*, Oxford Univ. Press, Oxford, 2014.
207. A. Müller and J. Döring, *Angew. Chem. Int. Ed.*, 1988, **27**, 1721-1721.
208. P. Kögerler, B. Tsukerblat and A. Müller, *Dalton Trans.*, 2010, **39**, 21-36.
209. J. Yang, Y. Wang, Z. Wang, X. Rong, C.-K. Duan, J.-H. Su and J. Du, *Phys. Rev. Lett.*, 2012, **108**, 230501.

Chapter 2

Thiophene-Based Hybrid Polyoxovanadates

2.1 Introduction

Metal-organic polyhedra are hollow polyhedral molecules composed of inorganic nodes and organic linkers. They are a fascinating and promising class of materials[1-7] with applications in medicine[8], catalysis[9], sensing[10, 11] and gas adsorption.[12] The unique properties of metal-organic polyhedra arise from the confined space of their interior. The size, shape and electronic properties of the internal cavity can be designed by the variation of inorganic node and organic linker. In recent years the field of POM-based polyhedra has gained increased attention.[7, 13] Pioneering work in this field has been carried out by Schmitt *et.al.* From 2008 to 2012 our group published a series of hybrid $\{V_{10}\}$ POV capsules, made from an aromatic bisphosphonate linkers and two mixed-valent $\{V_5O_9\}$ POV fragments (Figure 2.1.1).[14-17] By varying the size of the aromatic ligands the internal volume as well as the cage windows could be altered, which may facilitate the uptake of guest molecules or catalysis within the confined space of the capsule.[7] At the same time the capsules were found to accommodate a variety of different template molecules, exemplifying the adaptability of the system. The mixed-valence pentanuclear half capsule made from four V^{IV} ions and one V^{V} ion is a promising POV fragment for a variety of applications.

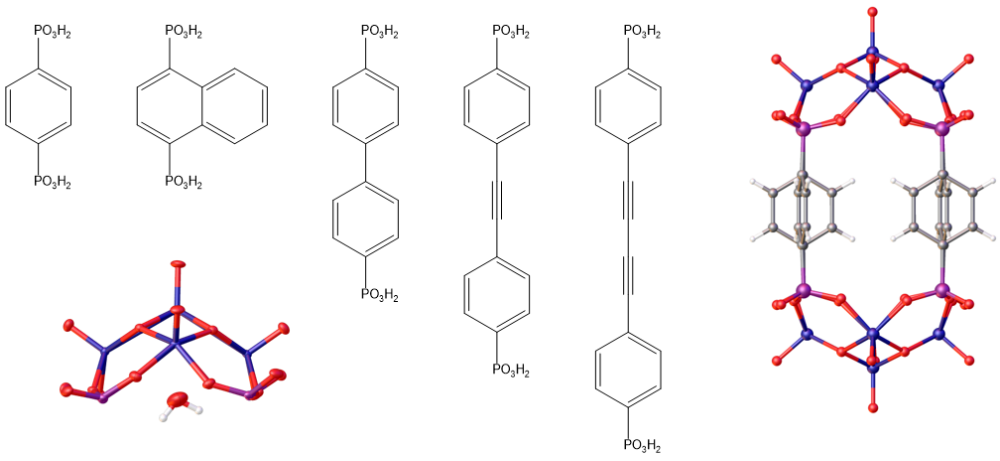

Figure 2.1.1 – Bisphosphonate ligands used in the construction of $\{V_{10}\}$ capsules, prior to 2015. $\{V_5O_9\}$ half-capsule in the lower left. $\{V_{10}\}$ capsule with bezene-1,4-bispshophonate as the ligand.

The drawback of the $\{V_{10}\}$ capsules however is their inaccessible interior. Varying the length of the linker resulted in an elongated but not widened window. In order to increase the width of the windows and make the interior accessible for small molecules, similar aromatic bisphosphonate ligands, with different bend angles between the phosphonate groups were utilised. The angle

hereby has to be large enough to accommodate the $\{V_{10}\}$ motif, which favours an angle of 180°, and is bent enough to significantly widen the window. Figure 2.1.2 shows the different bent angles for benzene-1,4-bisphosphonate, thiophene-2,5-bisphosphonate (H_4PSP) and benzene-1,3-bisphosphonate.

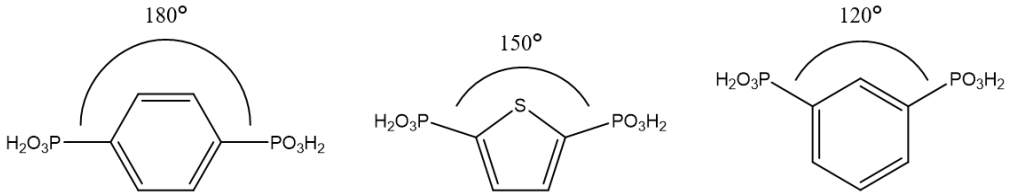

Figure 2.1.2 – Different angles between the phosphonate groups for various aromatic ligands.

Given the P-O-V bond angle for the known $\{V_{10}\}$ systems, H_4PSP was chosen as a suitable ligand to investigate. The inclusion of a heteroatom is interesting as it alters the electronic structure of the interior of the cage, enabling potential additional non-covalent interactions for guest molecules. It could also act as a binding site for soft transition metal atoms, such as Ag, Hg or Cd for the synthesis of new materials.

2.2 $(NH_4)_{10}[(V_5O_9)_2(C_4H_2S(PO_3)_2)_4(H_2O)(CH_3CN)] \cdot 5\ H_2O$ – (NH_4-V_{10}, 1)

The novel compound $(NH_4)_{10}[(V_5O_9)_2(C_4H_2P_2O_6)_4(H_2O)(CH_3CN)] \cdot 5\ H_2O$ (**NH_4-V_{10}**), was synthesized by the partial reduction of ammonium metavanadate with hydrazine in the presence of H_4PSP in water, N,N'-dimethylformamide (DMF) and MeCN (3:1:1 / v:v:v) at pH ~ 7. Green crystals, suitable for SXRD experiments, were obtained after one day, by diffusion of MeCN into the green solution.

2.2.1 Crystallography

The crystal structure of **NH_4-V_{10}** was solved in the orthorhombic space group *Pmna* with unit cell parameters of:

$a = 23.2091(9)$ Å	$\alpha = 90°,$	$Z = 4$
$b = 30.8778(11)$ Å	$\beta = 90°$	$Z' = 0.5$
$c = 12.5188(4)$ Å	$\gamma = 90°$	$V = 8971.5(6)$ Å^3

The structure is a hybrid organic-inorganic $\{V_{10}\}$ polyoxovanadate cage made out of two mixed-valent pentanuclear, anionic $\{(V^{V}O)(V^{IV}O)_4(\mu_3O)_4\}$ half-capsules that are bridged by four PSP^{4-} ligands. The cage is approximately 15.4 Å in length and 10.4 Å in width (Figure 2.2.2).

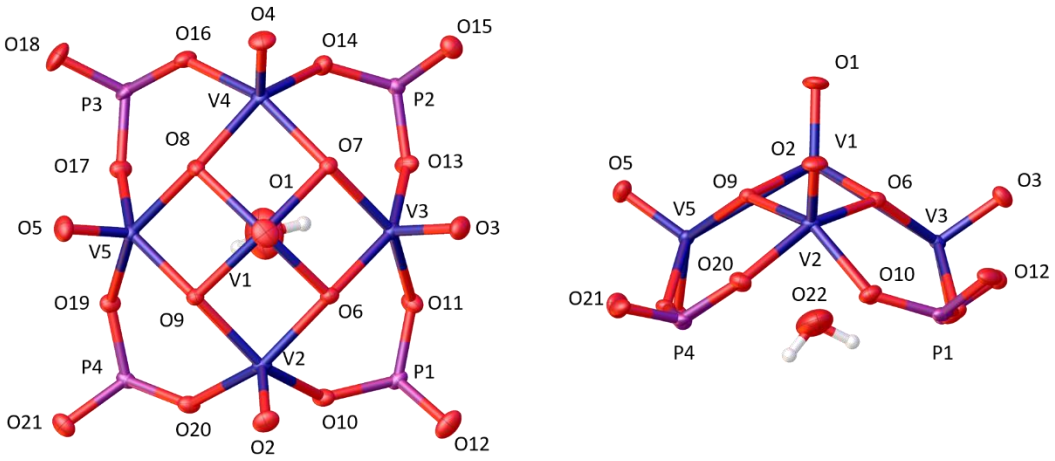

Figure 2.2.1 – The pentanuclear half-capsule in **NH_4-V_{10}**.

All vanadium ions display a square pyramidal coordination environment. The central vanadium(V) ion is bonded to one terminal *oxo*-ligand and four μ_3-O^{2-} ligands. These bridge the central *oxo*-vanadium(V) ion to two of the four peripheral vanadyl groups of the pentanuclear half-capsule (Figure 2.2.1). The four vanadyl groups are each bound to one terminal *oxo*-ligand, two μ_3-O^{2-} ligand as well as two oxygen donors from the doubly deprotonated phosphonate groups of the PSP^{4-} ligand. The terminal *oxo*-ligands of all vanadium ions are pointing towards the outside of the cage, leaving space for a templating agent in the middle of the half-capsule. This templating agent is either a water or an acetonitrile molecule, which were modelled as disordered with an occupancy of 0.5 each. As the acetonitrile molecule is rather long compared to the capsule's interior, there cannot be two acetonitrile molecules within the same capsule for steric reasons. Hence, every capsule features a combination of both templating agents, as shown in Figure 2.2.2. The position of the templating agent is on average 3.17 Å away from the vanadium ions and sits in the focal point of the vanadyl groups. The pentanuclear half-capsule in **NH_4-V_{10}** is hereby essentially identical to the literature known $\{V_{10}\}$ systems.

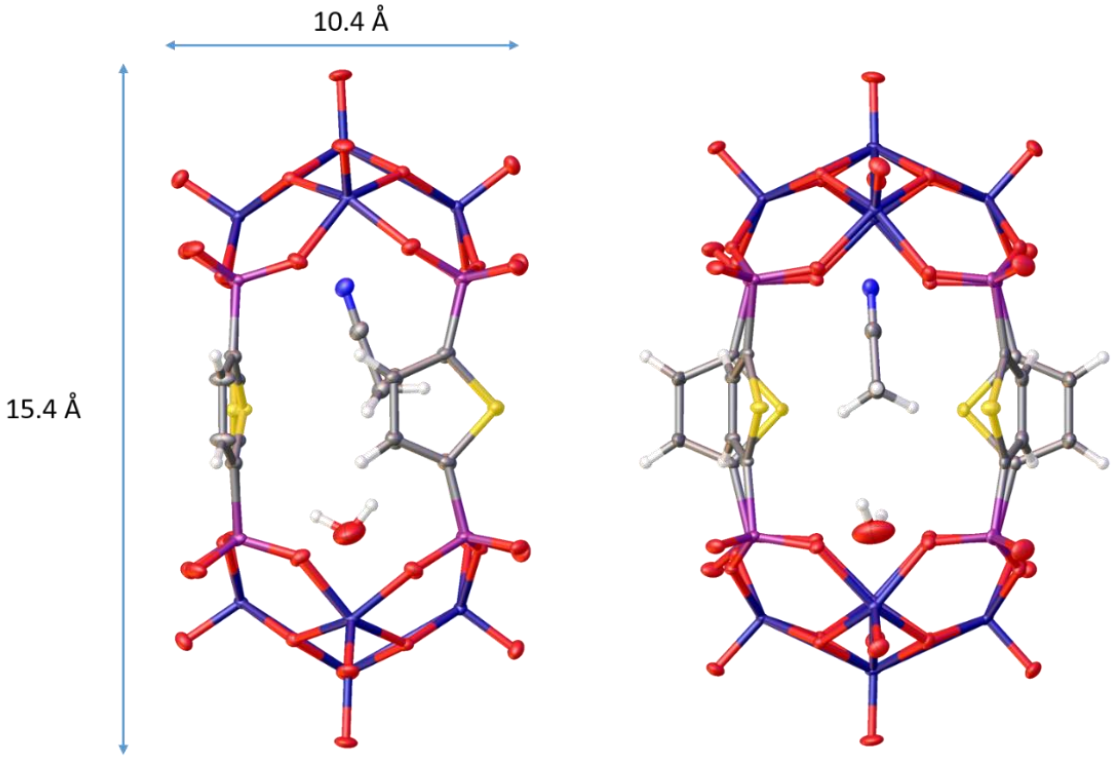

Figure 2.2.2 – Side view of the $\{V_{10}\}$ capsule of **NH_4-V_{10}** with dimensions.

Table 2.2.1 – BVS calculations for the vanadium ions of **NH_4-V_{10}**.

	BVS	Oxidation state
V1	4.42	+5
V2	4.03	+4
V3	4.00	+4
V4	4.04	+4
V5	3.98	+4

The V^{IV}-O bond lengths are in the range of 1.935(2) Å to 2.001(3) Å with the V=O double bonds being between 1.603(3) Å and 1.615(3) Å long. The vanadium oxygen single bond lengths involving the central vanadium(V) ion are slightly shortened compared to the V^{IV}-O bonds with 1.925(2) Å to 1.943(2) Å. The V^{V}=O bond length is unexpectedly longer than its counterpart with 1.625(3) Å. Bond valence sum (BVS) calculations can be seen in Table 2.2.1.

Table 2.2.2 – Bond lengths for the pentanuclear half-capsule in **NH_4-V_{10}**.

Bond	Bond length / Å	Bond	Bond length / Å
V1-O1	1.625(3)	**V3-O11**	2.001(3)
V1-O6	1.925(2)	**V3-O13**	1.974(3)
V1-O7	1.943(2)	**V4-O4**	1.611(3)
V1-O8	1.936(2)	**V4-O7**	1.955(2)
V1-O9	1.938(2)	**V4-O8**	1.935(2)
V2-O2	1.615(3)	**V4-O14**	1.970(3)
V2-O6	1.948(2)	**V4-O16**	2.000(3)
V2-O9	1.935(2)	**V5-O5**	1.604(3)
V2-O10	1.971(2)	**V5-O8**	1.964(2)
V2-O20	1.984(2)	**V5-O9**	1.958(2)
V3-O3	1.603(3)	**V5-O17**	1.976(3)
V3-O6	1.947(2)	**V5-O19**	1.994(2)
V3-O7	1.967(2)		

While the oxidation state of the vanadium(IV) ions are easily confirmed the oxidation state for the central vanadium(V) ion is less defined. This may be an effect of the delocalisation within the mixed-valent polyoxovanadate structure. However, due to the number of counter ions and similar structures in the literature the central vanadium ion can nominally be assigned to be in the oxidation state +V.

The PSP^{4-} ligands are bonded to the vanadyl groups *via* the two deprotonated *oxo*-ions of the phosphonate groups in a *syn-syn* coordination mode, while the non-bonded oxygen atom is pointing away from the structure. The PSP^{4-} ligands possess a large degree of rotational freedom within the cage. Inherent to the ligand itself is the rotation of the thiophene ring around the C-P bond, which is aided by the flexibility of the phosphonate groups to build out a range of different bond angles with the vanadyl groups. One can imagine an axis between the two phosphorus atoms of the ligand, around which the thiophene group can almost freely rotate as indicated by the curved arrow in Figure 2.2.1. The only limitations to this rotation are the other thiophene groups

as well as the templating agent inside the structure. This rotational freedom together with the bent in the diphosphonate ligand gives rise to variable window sizes, which can be observed in the solid-state structure. While the rotation of the ligand is also possible in the literature known $\{V_{10}\}$ capsules, it does not result in the same flexibility because of the missing bent of the used ligands (e.g. 1,4-Benzenediphosphonic acid).

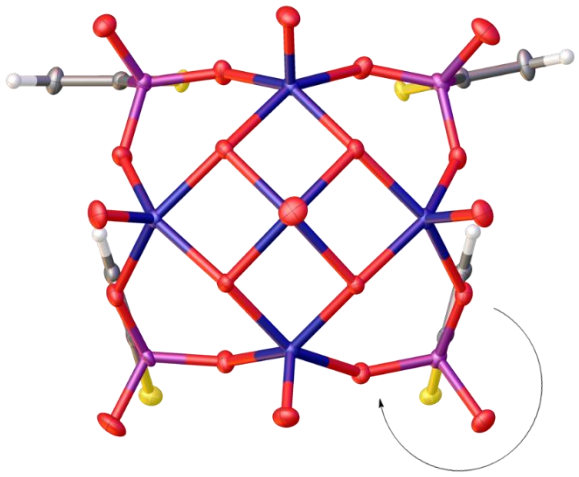

Figure 2.2.3 – Top view of the pentanuclear half-capsule with the PSP^{4-} ligands. The sulfur atoms of the two PSP^{4-} ligands in the upper half are pointing towards the inside, the two in the lower half towards the outside of the structure.

In **NH_4-V_{10}**, the thiophene groups are arranged in two sets of orientations. In the first set the sulfur atom points towards outside the structure, while in the second set the sulfur atom points towards the inside of the structure. Due to the bent nature of the ligand, this leads to different window sizes within the crystal structure, which can be exemplified by measuring the distance between the sulfur atoms of adjacent thiophene groups. The distances are 4.23 Å between the inward facing sulfur atoms and 5.38 Å between the sulfur atoms of outward facing thiophene groups. The other two windows, which can be seen in Figure 2.2.2 on the left side are effectively closed with a distance of 2.97 Å between the hydrogen and carbon atoms of the two neighbouring thiophene groups.

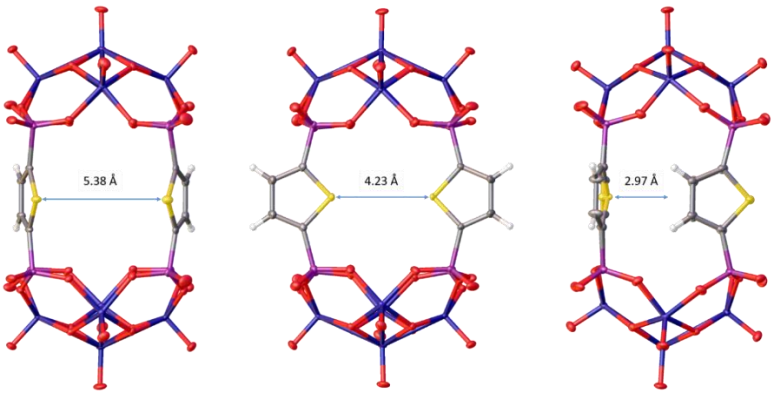

Figure 2.2.4 – Different window sizes for different orientations of the thiophene rings within the {V_{10}} capsule of **NH_4-V_{10}**. Some atoms omitted for clarity.

The cage itself is anionic and carries a charge of -10. This charge is balanced by ammonium ions in the crystal structure, which are building out a hydrogen bonded network with the cages as well as the water molecules around the structure. The ammonium ions arrange themselves above the pentanuclear half-capsule, building out hydrogen bonds with the μ_3-*oxo* ligands and water molecules within the crystal structure. This effectively places the ammonium ions in one layer above and below the capsules as can be seen in Figure 2.2.5 (left). Between the {V10} capsules are water molecules and a disordered acetonitrile.

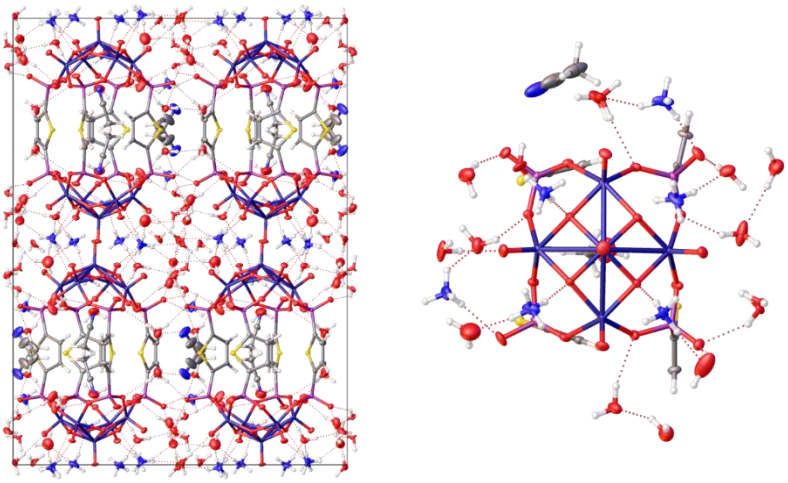

Figure 2.2.5 – Packing diagram of **NH_4-V_{10}** in the crystallographic [001] direction (left). Arrangement of the ammonium ions above the pentanuclear half-capsule (right).

Table 2.2.3 – Crystallographic table of **NH_4-V_{10}**.

Identification code	**NH_4-V_{10}**
Empirical formula	$C_{20}H_{103.2}N_{12}O_{66.6}P_8S_4V_{10}$
Formula weight/(g/mol)	2463.34
Temperature/K	99.98
Crystal system	orthorhombic
Space group	*Pnma*
a/Å	23.2091(9)
b/Å	30.8778(11)
c/Å	12.5188(4)
α/°	90
β/°	90
γ/°	90
Volume/Å^3	8971.5(6)
Z	4
ρ_{calc} g/cm^3	1.824
μ/mm^{-1}	1.342
F(000)	5016
Crystal size/mm^3	0.288 × 0.112 × 0.088
Radiation	MoK_α (λ = 0.71073)
2Θ range for data collection/°	4.964 to 60.372
Index ranges	$-32 \leq h \leq 32$ $-43 \leq k \leq 43$ $-17 \leq l \leq 17$
Reflections collected	162713
Independent reflections	13498 [R_{int} = 0.0638 R_{sigma} = 0.0267]
Data/restraints/parameters	13498/61/626
Goodness-of-fit on F^2	1
Final R indexes [I>=2σ (I)]	R_1 = 0.0553, wR_2 = 0.1237
Final R indexes [all data]	R_1 = 0.0702, wR_2 = 0.1332
Largest diff. peak/hole / e Å^{-3}	1.30/-1.04

2.2.2 Characterisation

2.2.2.1 Powder X-ray diffraction (PXRD)

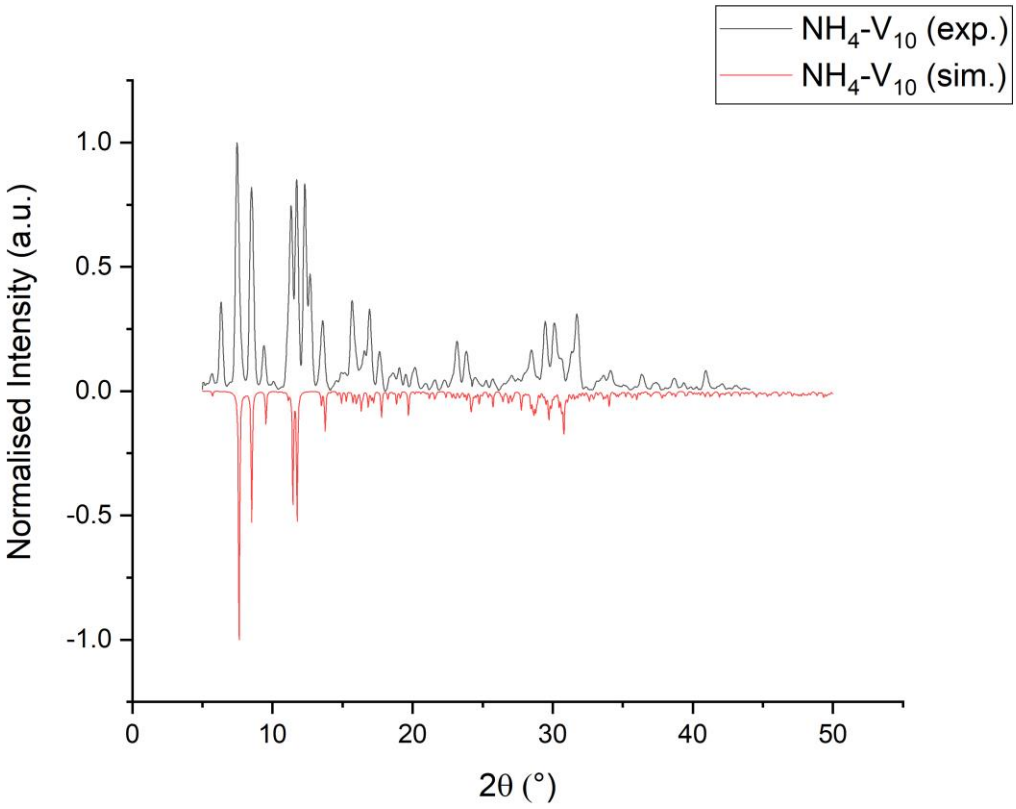

Figure 2.2.6 – Experimental and simulated PXRD pattern of **NH_4-V_{10}**.

A bulk sample of **NH_4-V_{10}** was ground up in the mother liquor and measured in a capillary from 5° to 45° in 2θ and compared to a simulated powder pattern from the crystal structure. All simulated peaks match peaks from the experimental spectrum, proving the presence of the crystalline phase established by SXRD in the bulk sample. While the crystals seemed to be homogenous however, they were not phase pure as multiple peaks in the experimental spectra were not predicted by the simulated pattern. This could be either due to crystalline impurities or due to polymorphs which were not identified by single crystal analysis. Analytical methods, which are depending greatly on phase purity such as magnetic measurements were therefore not carried out.

2.2.2.2 Infrared spectroscopy (IR)

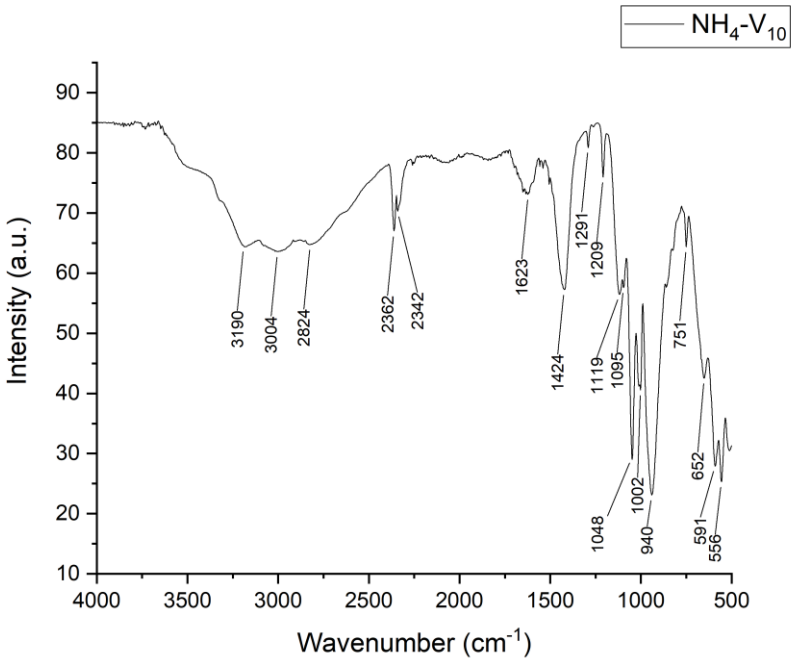

Figure 2.2.7 – IR spectrum of **NH_4 –V_{10}**.

The IR spectrum fits well with literature reported spectra for compounds featuring the {V_5} unit[17-19] as well as compounds featuring the ligand.[20] Assignments were carried out by comparison with literature compounds as well as the spectrum of the pure ligand. The spectrum shows multiple broad bands in the region around 2800 cm^{-1} to 3200 cm^{-1} which can be assigned to the N-H stretch of the ammonium ion.[21] Underlying the ammonium bands is a broad band which can be attributed to the O-H stretch of the crystal water molecules and usually centres around ~3300 cm^{-1}. The scissoring vibration of H_2O can be found at 1623 cm^{-1}.[22] Another signal belonging to a vibrational mode of the ammonium ion can be found at 1424 cm^{-1}.[23] Two characteristic bands at 2362 cm^{-1} and 2342 cm^{-1} belong to the asymmetric stretch of CO_2 and can be considered a measurement artefact, which could not be removed by means of baseline corrections even after multiple attempts. The bands at 1291 cm^{-1}, 1209 cm^{-1}, 1119 cm^{-1} and 1048 cm^{-1} can be attributed to the phosphonate ligand.[18] The V=O stretch is found at 940 cm^{-1} as a rather broadened band, which is indicative of mixed-valent compounds.[24] The absence of unexpected IR bands supports the chemical structure determined by XRD analysis as well as the assignment of the oxidation states by BVS analysis.

2.2.2.3 Thermogravimetric Analysis (TGA)

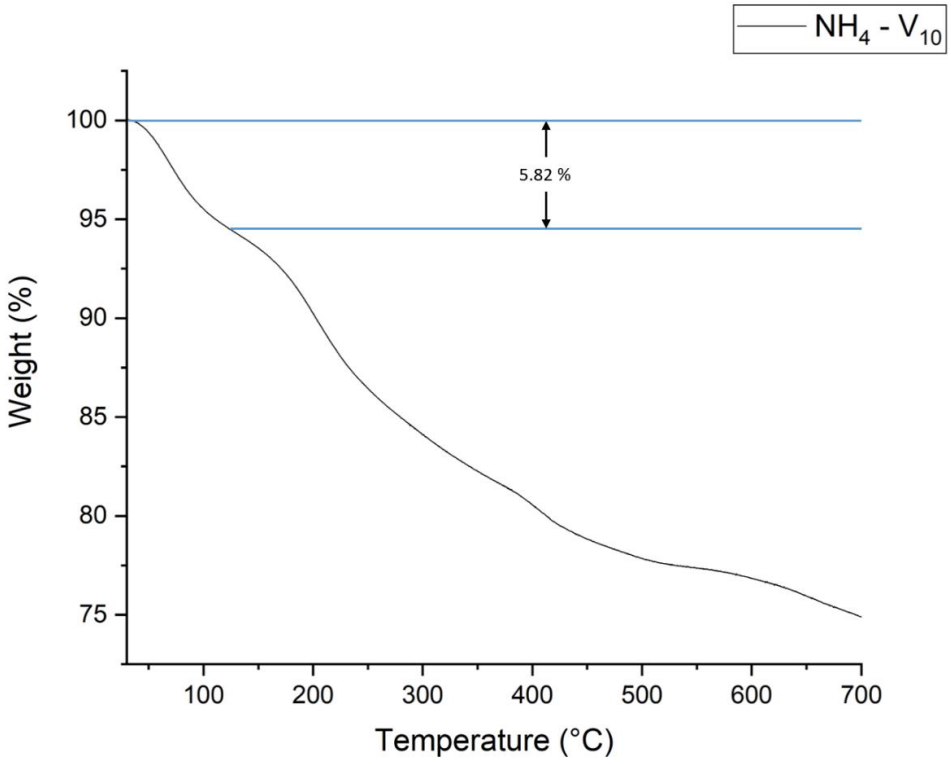

Figure 2.2.8 – TGA curve for **NH_4-V_{10}** from 30°C to 700°C.

To confirm the amount of water molecules in the crystal lattice, as determined by XRD, thermogravimetric analysis of **NH_4-V_{10}** was conducted from 30°C to 700°C at a rate of 5°C per minute under a stream of nitrogen. The sample was held at 30°C for one hour before the measurement to ensure the removal of surface water molecules. The step below about 150°C can be assigned to the loss of approximately six water molecules (Exp: 5.82 %, Calc: 5.64% for five water molecules) by assuming the acetonitrile molecule was removed from the drying process before the measurement. Above 150°C degradation of the ligand occurs, along with the possible decomposition of the ammonium ions into ammonia and subsequent formation of vanadium oxides. Decompositions of this kind have been described in the literature by TGA analysis of ammonium vanadate.[25] The use of ammonium ions as counter ions for the hybrid polyoxovanadate therefore seems to be detrimental to the stability of the compound at higher temperatures. The drop in weight above 500°C is frequently attributed to the formation of vanadium pentoxide.[26]

2.2.2.4 UV-VIS spectroscopy

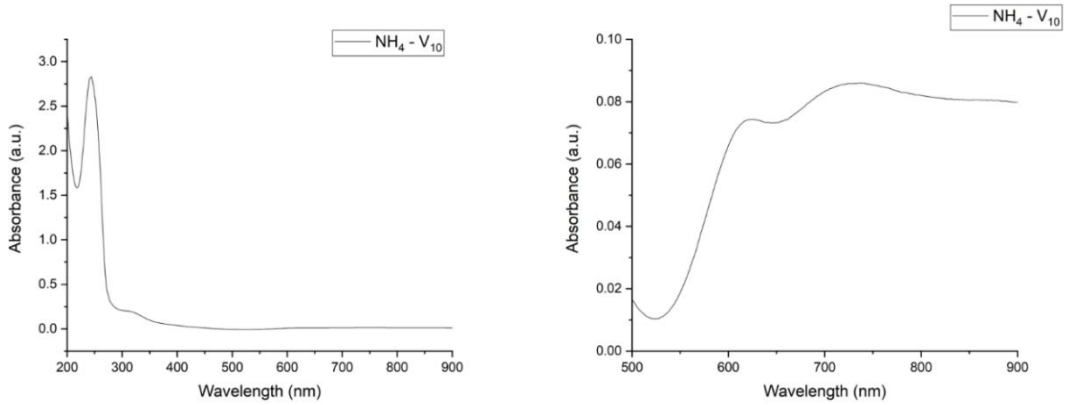

Figure 2.2.9 – UV-VIS spectrum of **NH_4-V_{10}** in Water from 200 to 900 nm (left) and from 500 to 900 nm (right).

The UV-VIS spectrum of the compound **NH_4-V_{10}** was collected in water and shows multiple distinctive features (Figure 2.2.9) and is comparable with the literature known {V_{10}} capsules.[15] The most intense band at 244 nm can be attributed as a ligand centred transition on the basis of the large absorbance value and comparison with similar compounds in the literature.[27, 28] An exact extinction coefficient however could not be calculated due to solubility issues. The second most intense band at 310 nm in form of a shoulder can be attributed to ligand to metal charge transfer (LMCT) bands from the terminal *oxo*-ligands to the vanadium ions.[29] The relatively weak transitions at 624 nm and 727 nm stem from d-d and intervalence charge transfer transitions (IVCT) respectively.[30] The distinction between a d-d transition and an IVCT transition is not straight forward in the case of polyoxovanadates. The broadness of the band at 727 nm indicates however that it is an IVCT transition whereas the band at 624 nm belongs to a d-d transition. The occurrence of an ICVT transition further backs the assignment of the oxidation states of the vanadium ions and exemplifies the mixed-valent nature of pentanuclear half-capsule.

2.3 $Na_{10}[(V_5O_9)_2(C_4H_2S(PO_3)_2)_4(H_2O)_2] \cdot 31\ H_2O$ – (Na-V_{10}, 2)

The compound **Na-V_{10}** was synthesised from sodium orthovanadate in the presence of H_4PSP, sodium azide and hydrazine in water, MeCN and DMF (3:1:1, v:v:v). Green crystals, suitable for XRD measurements, were isolated by diffusing acetonitrile into the solution.

2.3.1 Crystallography

Na-V_{10} was solved as a pseudo-merohedral twin in the orthorhombic space group $Pmna$ with the unit cell dimensions

$a = 29.8506(18)$ Å	$\alpha = 90°,$	$Z = 8$
$b = 17.0863(10)$ Å	$\beta = 90°$	$Z' = 1$
$c = 17.0815(10)$ Å	$\gamma = 90°$	$V = 8712.2(9)$Å^3

The unit cell dimensions indicate a tetragonal space group. Solving the structure in the tetragonal space group $P4/mnc$ however led to impossible symmetry generated H-H distances of d(H-H) < 0.7 Å. Further inspection of the R_{int} values after the adsorption correction with the program SADABS[31] revealed an only slightly higher value for the tetragonal cell than for the orthorhombic cell, which is a common sign of twinning.[32] The structure was solved as a pseudo-merohedral twin in the orthorhombic space group *Pmna* with the twin law

$$\begin{pmatrix} -1 & 0 & 0 \\ 0 & 0 & 1 \\ 0 & 1 & 0 \end{pmatrix}$$

describing a two-fold rotation around the [110] axis. The refined twin ratio is 0.332(2).

2.3.1.1 Structural comparison to NH_4-V_{10}

The structure of **Na-V_{10}** is largely isostructural to **NH_4-V_{10}** and features the same {V_{10}} hybrid polyoxovanadate structure, which is shown in Figure 2.3.1. The differences between the structures lie in the orientation of the thiophene groups, resulting window sizes, the template molecules as well as the counter ions, which have been changed from ammonium to sodium ions. Aside from a brief structural description, only the differences will be discussed in detail.

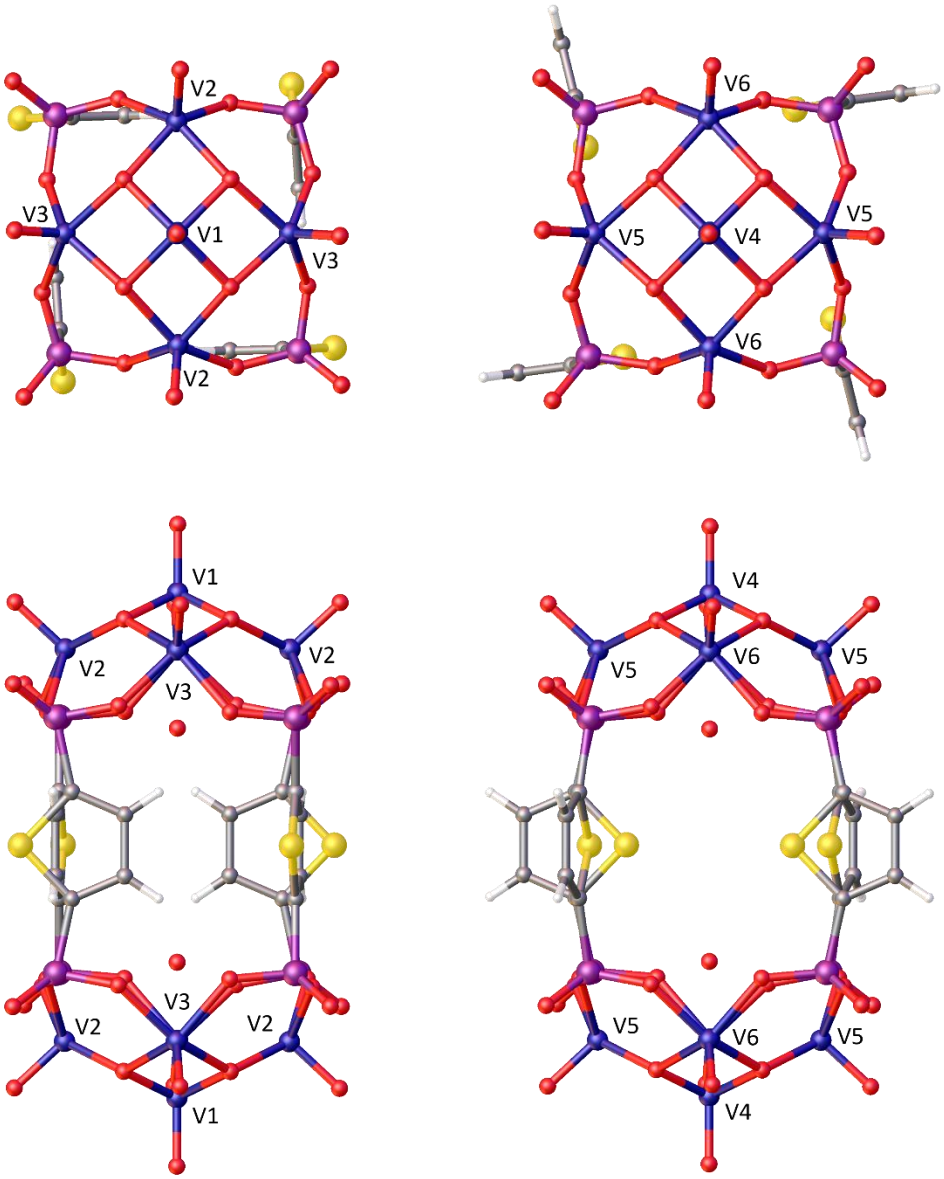

Figure 2.3.1 – Top and side view of the slim (left) and wide variation (right) of the $\{V_{10}\}$ cage in **Na-V_{10}**.

The V^{IV}-O single bonds within the pentanuclear half-capsule range from 1.943(6) Å to 1.996(6) Å with an average of 1.96 Å. The V^{V}-O single bonds are a bit shorter than their V^{IV} counterparts and range from 1.863(5) Å to 1.870(6) Å. For both oxidation states the V=O double bond are around 1.60 Å with only minor derivations. The BVS calculations are shown in Table 2.3.1. As can be seen the oxidation state for both the vanadium(IV) and vanadium(V) ions are now well defined, when compared to the pentanuclear half-capsule in its ammonium counterpart **NH_4-V_{10}**.

Other than in the **NH_4-V_{10}** structure, the thiophene rings of the PSP^{4-} ligands are now arranged in a counterclockwise fashion around the cage. The thiophene ring is hereby disordered over two positions in a 0.90/0.10 ratio, which leads to two different cage arrangements in the crystal structure. The sulfur atoms of the PSP^{4-} ligands point either towards the inside or outside of the cage, influencing its dimensions as well as the window sizes. The result of this behaviour is the occurrence of a widened cage and a slim version of the $\{V_{10}\}$ structure within the crystal structure (Figure 2.3.1 and Figure 2.3.3). The window sizes are shown in Figure 2.3.2, which are similar to the ones seen in **NH_4-V_{10}** but arise from different arrangements of the thiophene rings.

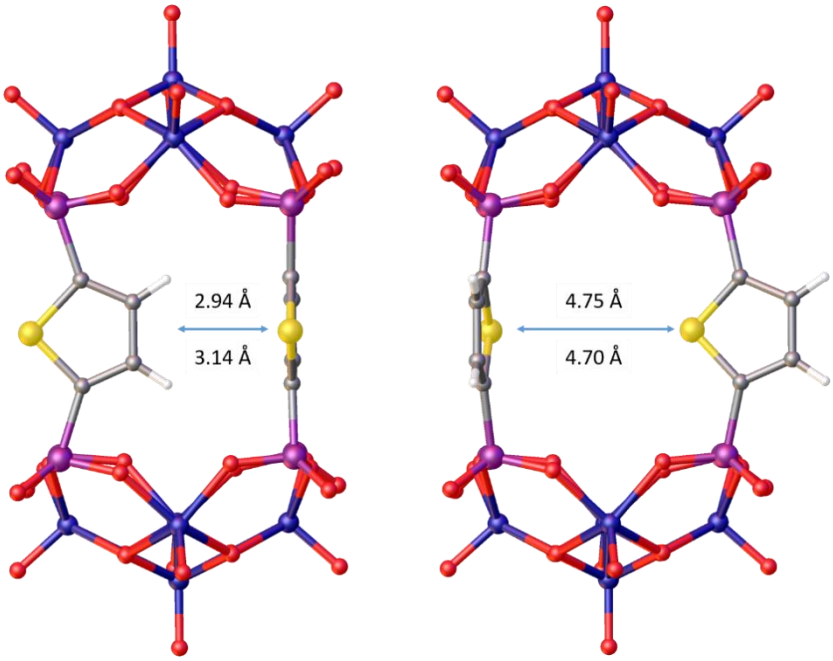

Figure 2.3.2 – Window sizes of the slim cage (left) and the widened cage (right). Only two ligands are shown for clarity.

In the crystal packing the cages are arranged in an ABAB layered structure down the crystallographic *b*-axis as can be seen in Figure 2.3.3. This arrangement can be seen as an orthorhombic face-centred unit cell of cages with the bottom and the top layers populated by slim cages and the middle layer filled with widened cages for 90% of the structure and the other way around for 10 % due to the ligand disorder. The same type of ABAB packing can also be observed in the crystallographic *a*-axis. The $\{V_{10}\}$ cages are hereby rotated against each other by about 33° between the layers, as can be seen in Figure 2.3.4.

Table 2.3.1 – BVS calculations for **Na-V_{10}**.

	BVS	Oxidation state
V(1)	5.08	+5
V(2)	4.01	+4
V(3)	4.06	+4
V(4)	5.10	+5
V(5)	4.03	+4
V(6)	4.06	+4

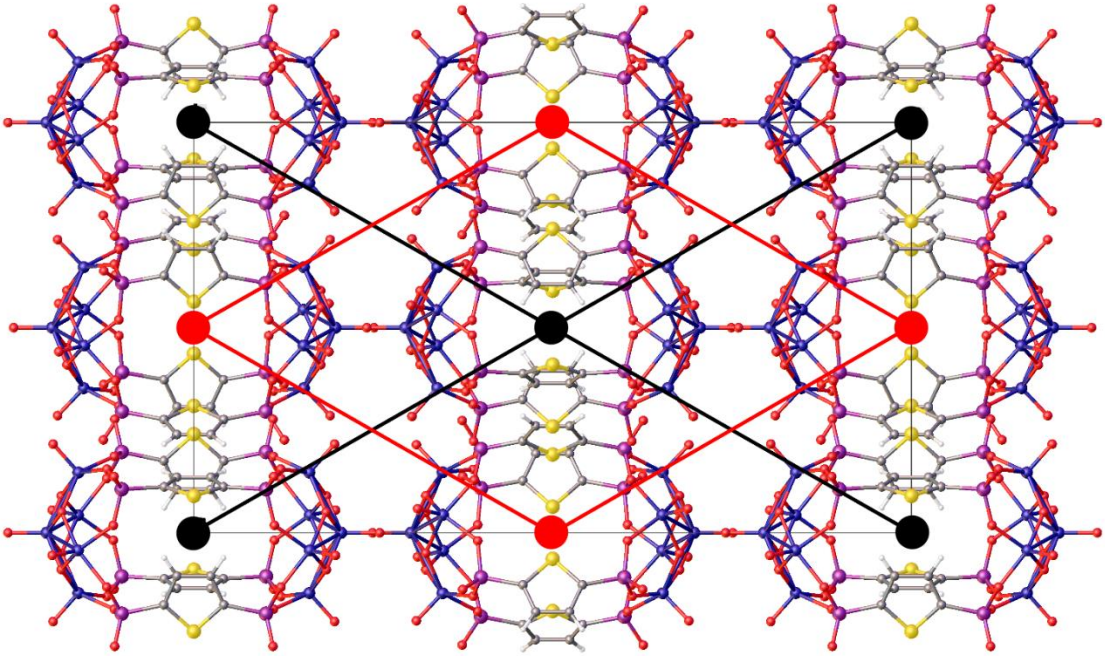

Figure 2.3.3 – Packing of **Na-V_{10}**. View down the crystallographic *b*-axis. The widened cages are marked with a red dot. The slim cages with a black dot.

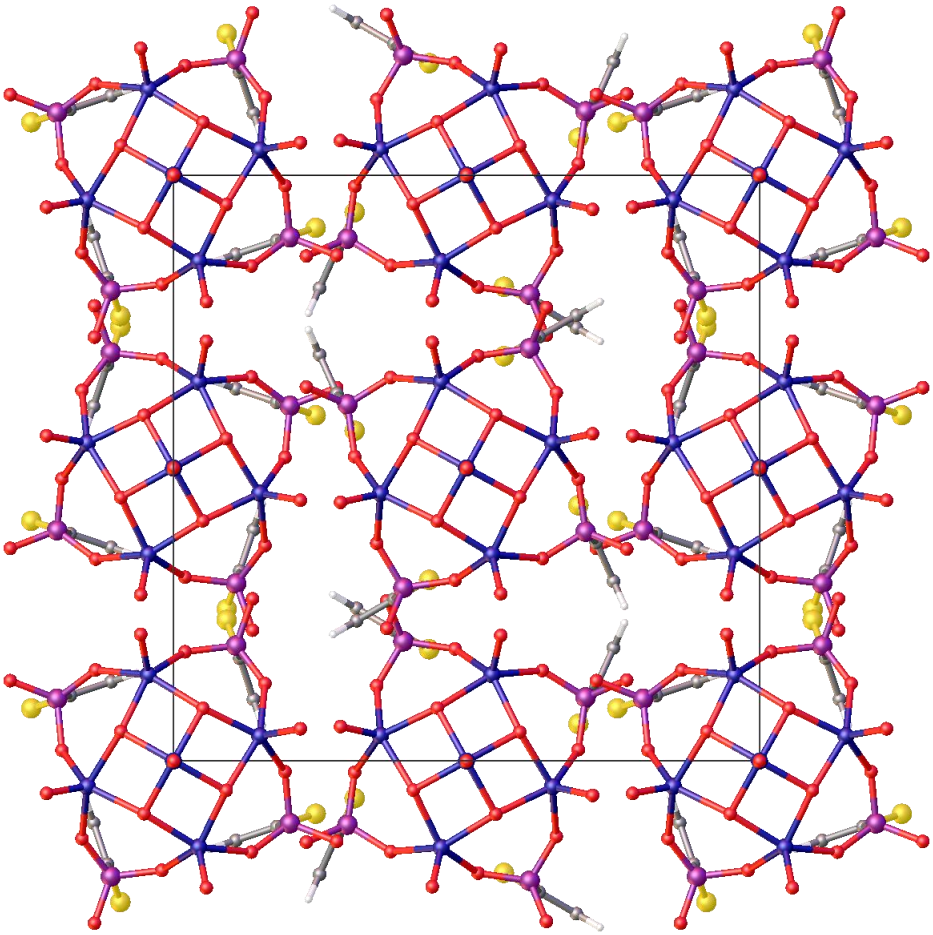

Figure 2.3.4 – Packing of **Na-V$_{10}$**. View down the crystallographic *a*-axis.

The -10 charge of the cages are now balanced by sodium ions in the structure. Three of the five sodium ions within the asymmetric unit are well resolved, while the remaining two are disordered over multiple positions. Two of the well resolved sodium ions build out a dimer, which are bridged by μ_2–water molecules and sits in between the vanadium cages. The other one sits on top of the *oxo*-vanadium(V) group and is connected to two of the sodium dimers *via* a partially occupied sodium ion, which is disordered over two positions. The last sodium ion in the asymmetric unit forms a symmetry generated dimer in the middle of the unit cell. All sodium ions in the structure adopt octahedral or distorted octahedral binding environments.

Table 2.3.2 – Crystallographic table for **Na-V_{10}**.

Identification code	**Na-V_{10}**
Empirical formula	$C_{16}H_8Na_{10}O_{75.11}P_8S_4V_{10}$
Formula weight/(g/mol)	2517.24
Temperature/K	100
Crystal system	orthorhombic
Space group	*Pmna*
a/Å	29.8506(18)
b/Å	17.0863(10)
c/Å	17.0815(10)
α/°	90
β/°	90
γ/°	90
Volume/Å^3	8712.2(9)
Z	4
ρ_{calc} g/cm^3	1.919
μ/mm^{-1}	1.432
F(000)	4915
Crystal size/mm^3	0.21 × 0.09 × 0.05
Radiation	MoKα (λ = 0.71073)
2Θ range for data collection/°	2.746 to 55.844
Index ranges	-38 ≤ h ≤ 39 -16 ≤ k ≤ 22 -22 ≤ l ≤ 17
Reflections collected	42579
Independent reflections	10978 [R_{int} = 0.0660 R_{sigma} = 0.0639]
Data/restraints/parameters	10978/78/612
Goodness-of-fit on F^2	1.011
Final R indexes [I>=2σ (I)]	R_1 = 0.0594, wR_2 = 0.1520
Final R indexes [all data]	R_1 = 0.1086, wR_2 = 0.1834
Largest diff. peak/hole / e Å^{-3}	1.13/-1.65

2.3.2 Characterisation

2.3.2.1 IR spectroscopy

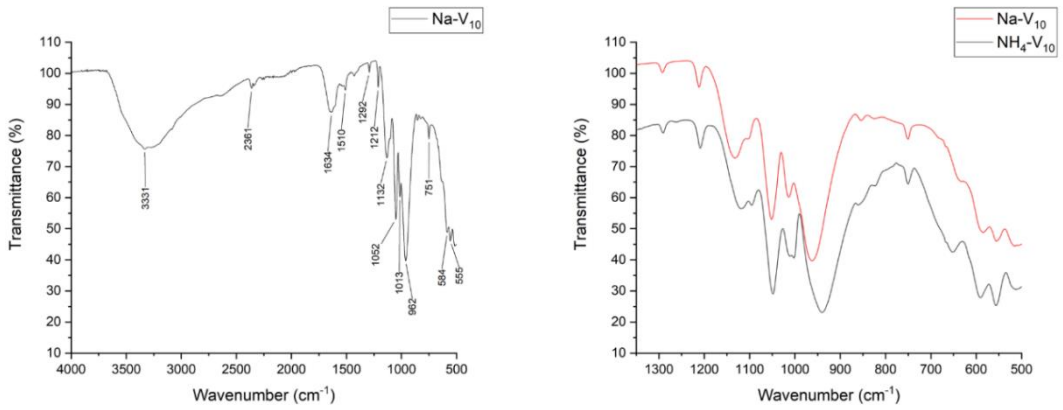

Figure 2.3.5 – IR spectrum of **Na-V_{10}** (left) and comparison with **NH_4-V_{10}** (right).

The IR spectrum of **Na-V_{10}** displays the similar features as **NH_4-V_{10}**. The broad band around 3331 cm^{-1} and another one at 1634 cm^{-1} can be assigned to vibrations stemming from the crystal water. The phosphonate ligand has its bands at 1132 cm^{-1} and 1052 cm^{-1}. Interestingly, the vibration assigned to the V=O stretch has been shifted towards higher wavenumbers from 940 cm^{-1} to 962 cm^{-1} and is less broad than in the IR of **NH_4-V_{10}**. This could indicate that the vibration actually belongs to a V-μ_3O-V vibration as the ammonium ions in **NH_4-V_{10}** build out hydrogen bonds to the μ_3-*oxo* ligands which should influence the vibrational energy compared to the same vibration in **Na-V_{10}**. The Comparison between the IR spectra of **Na-V_{10}** and **NH_4-V_{10}** confirms the identical nature of their polyoxovanadate structure.

2.3.2.2 Mass spectrometry (MS)

The mass spectrum of **Na-V_{10}** was collected via electrospray mass spectrometry (ESI-MS) and can be seen in Table 2.3.3. The spectrum shows its strongest peaks below 300 m/z that can be assigned to the free ligand. This signal could either arise from the ligand in solution or from fragmentation during the ionization process. The ligand assignments are shown in Table 2.3.3.

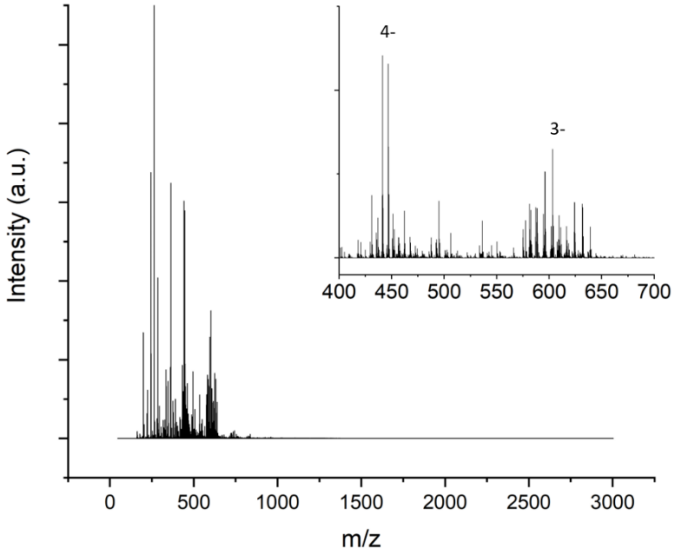

Figure 2.3.6 – ESI-MS spectrum of **Na-V_{10}**.

Table 2.3.3 - Assignment of the MS peaks belonging to the PSP ligand.

Assignment	Calculated (m/z)	Peak (m/z)	Charge
{PSP} + H_3	242.9288	242.9148	1-
{PSP} + H_2Na	264.9107	264.8945	1-
{PSP} + $H_3 - H_2O$	224.9182	224.9051	1-

There are two distinct clusters of signals in the region above 300 m/z at around 450 m/z and 600 m/z, which belong to species with a charge of -4 and -3 respectively. The $\{V^{IV}_8V^{V}_2\}$ cage, as it was characterised in the solid state, carries a charge of -10 and therefore need seven counter ions to reach a charge of -3. However, differently oxidised version of the cage such as $\{V^{IV}_7V^{V}_3\}$ and $\{V^{IV}_6V^{V}_4\}$ were identified in the MS. Those oxidised cages need six and five counter ions for a

charge of -3 respectively. The possible combination of sodium and hydrogen ions along with accompanying water molecules gives rise to a number of signals that can strongly overlap, complicating the analysis. The peaks, for which it was possible to assign a $\{V_{10}\}$ ion, along with their calculated and found m/z values are listed in Table 2.3.4. The calculated peaks differ by a constant 0.036 m/z which indicates a systematic error in the experiment rather than wrong assignment. The matching peak patterns for the assigned peaks can be seen in Figure 2.3.9 and Figure 2.3.8.

While some possible $H_xNa_y\{V_{10}\}^{3-/4-}$ species do fit the m/z values and spacing, they do not fit the peaks in intensity, which is the characteristic aspect of the isotope pattern. An example can be given for two overlapping peaks around 632 m/z, which do belong to the $[Na_6H\{V^{IV}_8V^{V}_2\}]^{3-}$ and the $[Na_6\{V^{IV}_7V^{V}_3\}]^{3-}$ species. Figure 2.3.7 shows the experimental and simulated pattern for both peaks next to each other. None of the species matches the isotopic pattern of the mass spectrum, which is necessary for a confident assignment. A 50/50 combination of both simulated patterns however reproduces the isotope distribution quite nicely. While it was possible to come to a satisfactory model for the peaks around 632 m/z, a lot of the peak patterns were combinations of three or more species with varying distributions to the peak pattern. In these cases, it was not possible to adequately assign a signal to a specific species. The ESI-MS analysis shows both the stability of the hybrid polyoxovanadate in aqueous solution as well as the redox-active nature of the species.

Table 2.3.4 – Assigned peaks in the MS of **Na-V$_{10}$**.

Counter ions	Oxidation state	Calculated (m/z)	Peak (m/z)	Charge
Na_5H_2	$\{V^{IV}_8V^{V}_2\}$	624.6441	624.6054	3-
Na_6H	$\{V^{IV}_8V^{V}_2\}$	631.9714	631.9349	3-
Na_7	$\{V^{IV}_8V^{V}_2\}$	639.2988	639.2623	3-
Na_6	$\{V^{IV}_7V_3\}$	631.636	631.6001	3-
H_5	$\{V^{IV}_6V^{V}_4\}$	587.3357	587.3035	3-
NaH_4	$\{V^{IV}_6V^{V}_4\}$	594.663	594.6262	3-
Na_2H_3	$\{V^{IV}_6V^{V}_4\}$	601.9903	601.9558	3-
Na_3H_2	$\{V^{IV}_6V^{V}_4\}$	609.3176	609.282	3-
Na_4H	$\{V^{IV}_6V^{V}_4\}$	616.6449	616.6086	3-

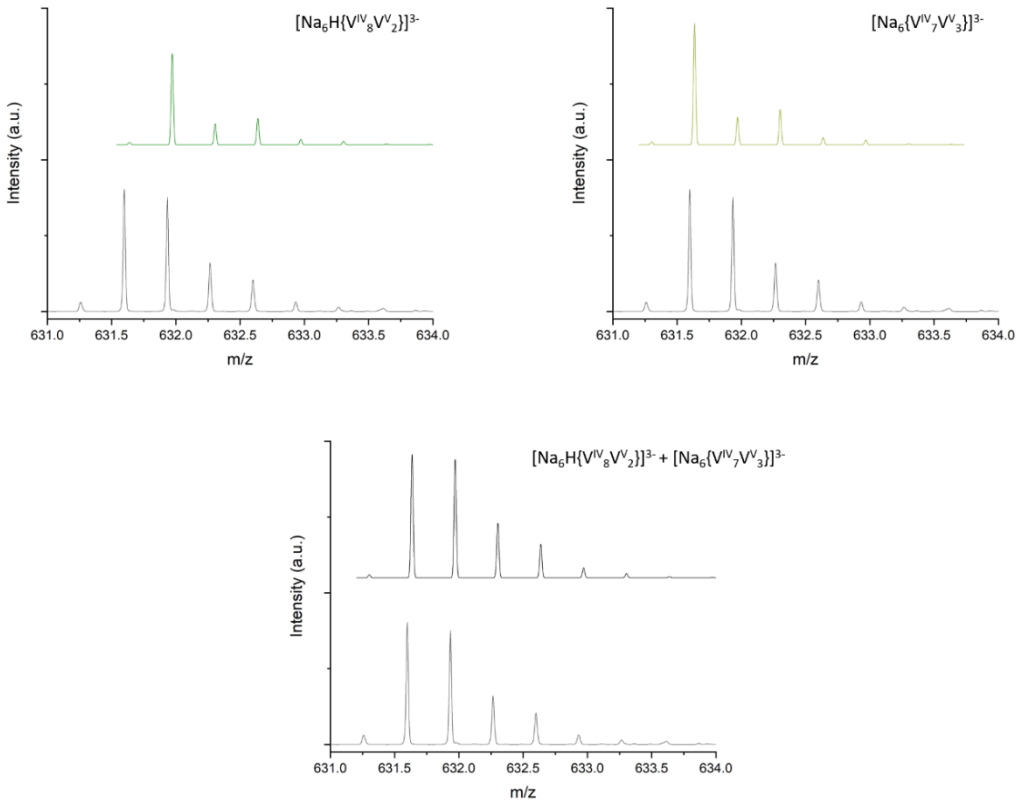

Figure 2.3.7 – Isotope patterns for $[Na_6H\{V^{IV}_8V^{V}_2\}]^{3-}$ and $[Na_6\{V^{IV}_7V^{V}_3\}]^{3-}$ and the combination of both.

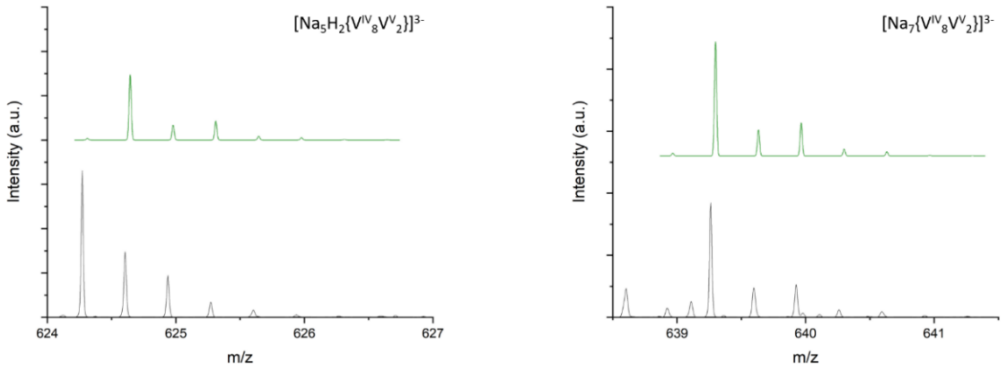

Figure 2.3.8 - Matching peak patterns for the non-oxidised $\{V^{IV}_8V^{V}_2\}$ cage.

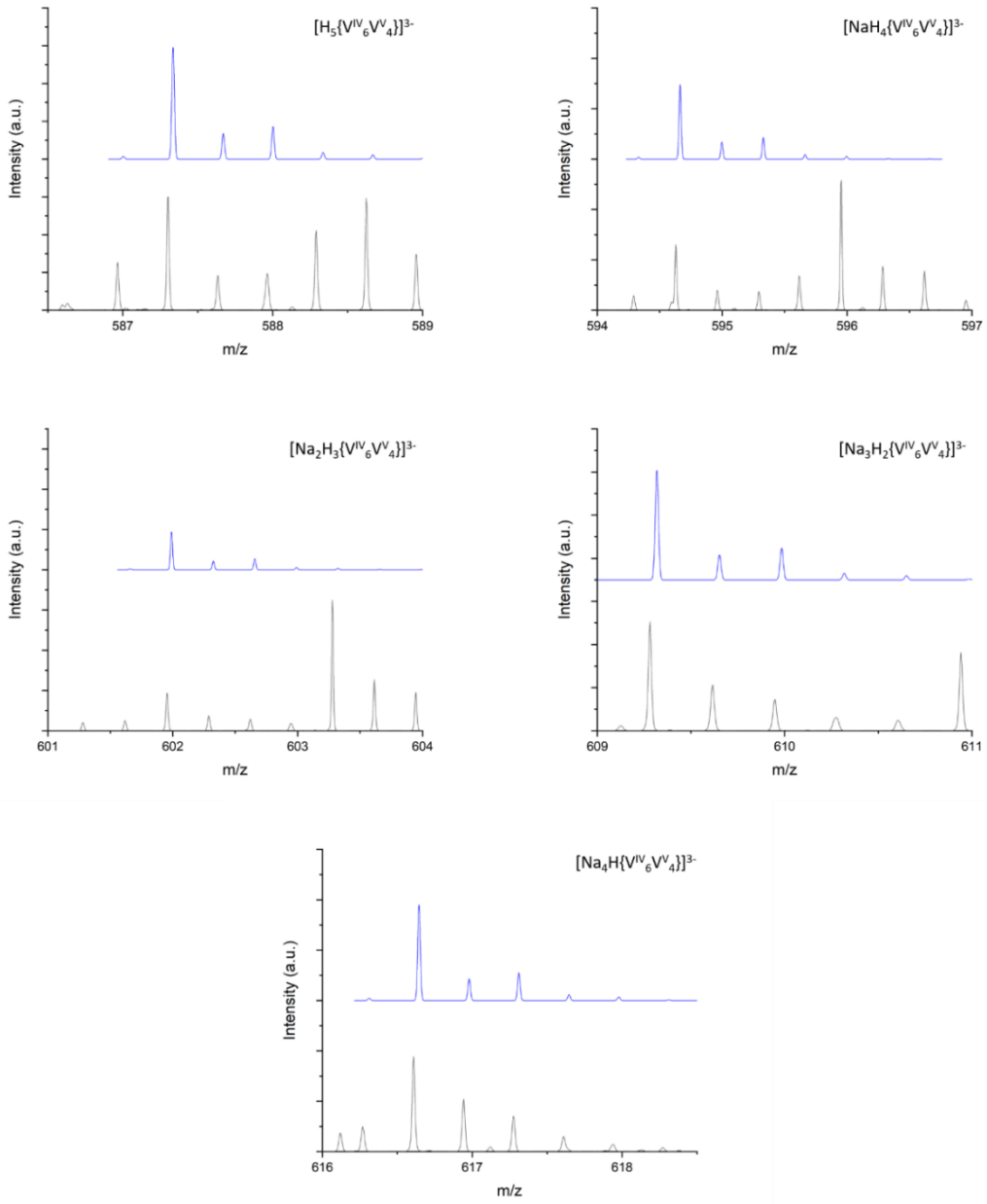

Figure 2.3.9 – Matching peak patterns for the twice oxidised $\{V^{IV}_6V^{V}_4\}$ cage.

2.4 $Na_{12}[V_{12}O_{12}(OH)_{12}(C_4H_2S(PO_3)_2)_6] \cdot 30\ H_2O$ – (Na-V_{12}, 3)

The compound **Na-V_{12}** was synthesized by the partial reduction of sodium orthovanadate with hydrazine in the presence of H_4PSP in water, DMF and MeCN (3:1:1 / v:v:v) at pH ~ 5. Blue crystals were isolated after several days by diffusion of acetonitrile into the green solution, which turned blue over several days.

The synthesis of **Na-V_{12}** is very similar to the synthesis of **Na-V_{10}** with a few differences, namely the exclusion of azide from as well as the lower pH and longer reaction times. At first it was hypothesised the azide anion would act as a template molecule in the synthesis of the {V_5} half-capsule and removing the template would prevent the fragment from forming. Batches of mixed crystals with **Na-V_{10}** and **Na-V_{12}** in reactions without sodium azide refuted this hypothesis (Figure 2.4.1). The key to the crystallisation of pure **Na-V_{12}** was found to be longer reaction times as well as a lower pH. The yield of **Na-V_{10}** is the highest with short reaction times (< 5 minutes) and a pH of ~ 7. It is reduced when the reaction time is increased, and the pH lowered. By adjusting these variables one can prevent **Na-V_{10}** from crystallising out of solution, therefore achieving a pure sample of **Na-V_{12}**.

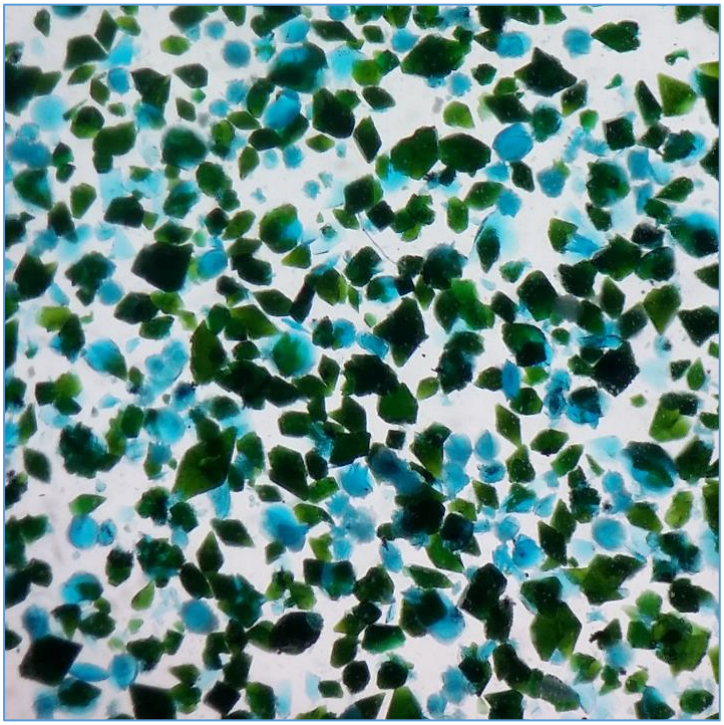

Figure 2.4.1 – Crude mixture of **Na-V_{12}** and **Na-V_{10}** crystals.

2.4.1 Crystallography

Na-V$_{12}$ was solved in the rhombohedral space group $R\bar{3}$ with unit cell parameters of

$a = 30.0698(19)$ Å	$\alpha = 90°$,	$Z = 6$
$b = 30.0698(19)$ Å	$\beta = 90°$	$Z' = 0.33333$
$c = 24.3362(17)$ Å	$\gamma = 120°$	$V = 19057(2)$ Å^3

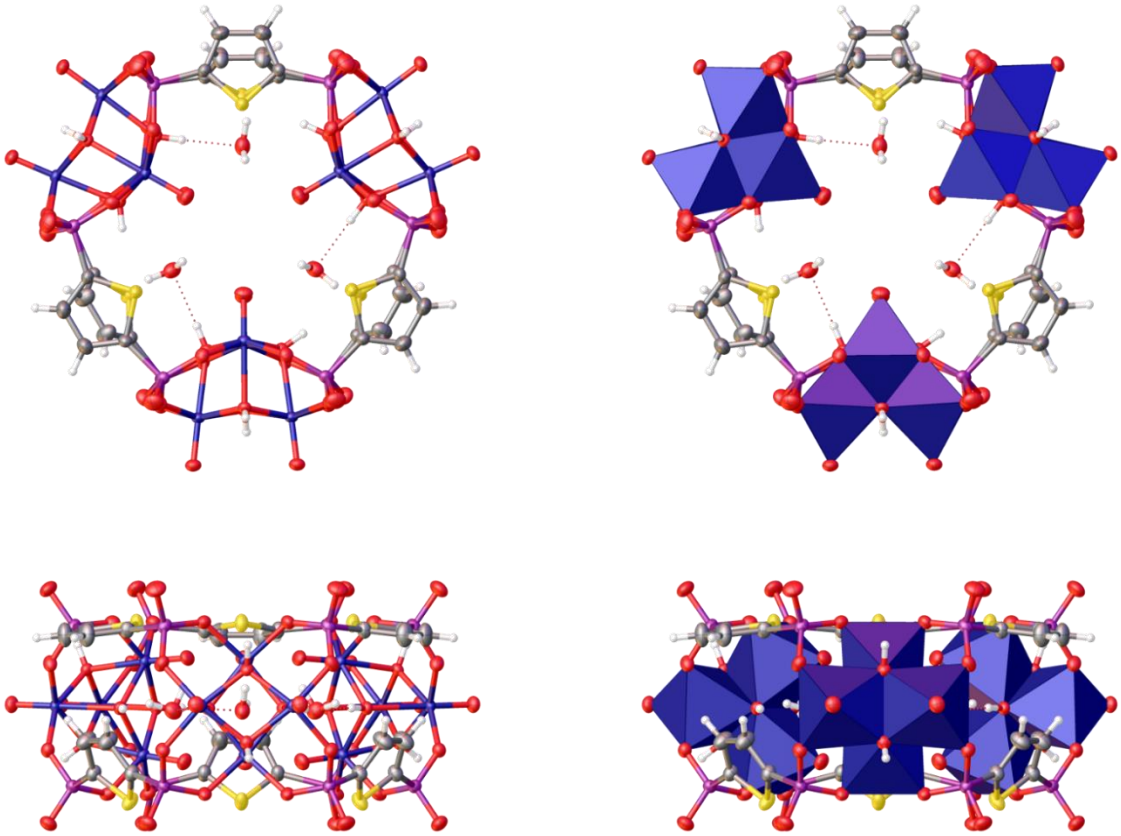

Figure 2.4.2 – Top and side view of the {V_{12}} torus in **Na-V$_{12}$** with and without polyhedral representation of the vanadium(IV) ions.

The general structure of the compound is made up of three tetranuclear vanadium(IV) cubane polyoxovanadate units that are linked together by six PSP^{4-} ligands, creating a torus like shape. The cubane unit consists of four vanadyl ions, which are bridged by four μ_3-hydroxo ions. All vanadium ions display a distorted octahedral geometry and have an oxidation state of +IV as shown by BVS calculations (Table 2.4.2). Each vanadyl ion is bonded to three μ_3-hydroxo

ligands, with two of them being in the equatorial position and one of them being *trans* to the terminal *oxo*-ligand (Figure 2.4.3). The two remaining equatorial positions are filled with oxygen atoms belonging to the phosphonate groups of two PSP^{4-} ligands (Figure 2.4.3). The V=O double bond lengths with the terminal *oxo*-ligands are of typical length, between d(V=O) = 1.600(3) Å and 1.609(3) Å. The bond lengths between the vanadium(IV) ion and the μ_3-hydroxo ligands in the equatorial plane of the distorted VO_6 octahedra are between 2.007(3) Å and 2.043(3) Å while the V-O bonds with the *oxo*-ligands of the phosphonate groups are a bit shorter with distances between 1.986(3) Å and 1.996(3) Å. The V-μ_3OH bond distances *trans* to the V=O double bond are elongated and between 2.269(3) Å and 2.319(3) Å long. Those differences in bond lengths give rise to the slightly distorted octahedral geometry, which is typical for vanadium ions. The coordination environment could also be seen as a square pyramidal coordination environment with an additional, more loosely bonded *oxo*-ion in the position *trans* to the apical *oxo*-ligand.

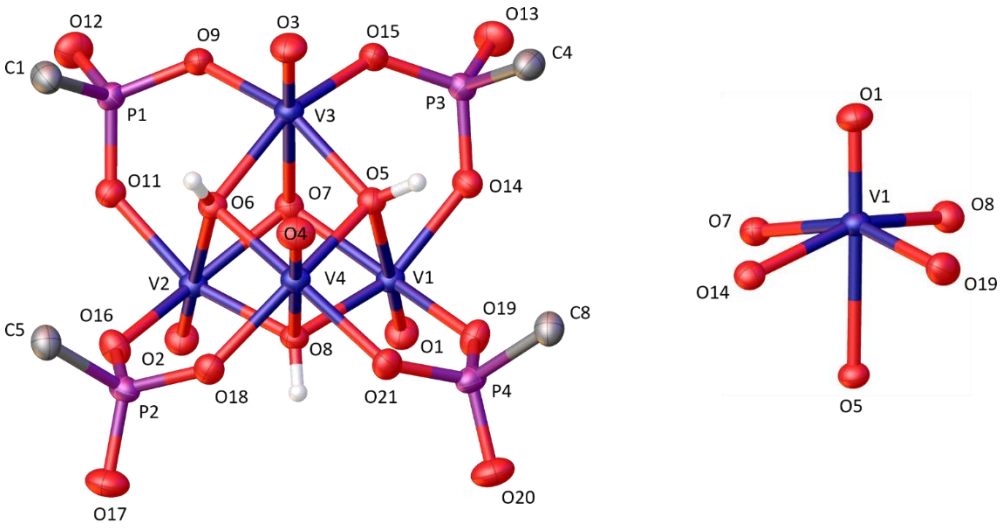

Figure 2.4.3 – The vanadium(IV) cubane unit of **Na-V_{12}** (left) and the distorted octahedral coordination environment of the vanadium ions (right).

Table 2.4.1 – Vanadium – oxygen bond lengths for **Na-V$_{12}$**.

Bond	Bond length / Å	Bond	Bond length / Å
V1-O1	1.607(3)	**V3-O3**	1.600(3)
V1-O5	2.319(3)	**V3-O5**	2.037(3)
V1-O7	2.013(3)	**V3-O6**	2.039(3)
V1-O8	2.015(3)	**V3-O7**	2.285(3)
V1-O14	1.996(3)	**V3-O9**	1.991(3)
V1-O19	1.985(3)	**V3-O15**	1.991(3)
V2-O2	1.609(3)	**V4-O4**	1.609(3)
V2-O6	2.311(3)	**V4-O5**	2.042(3)
V2-O7	2.007(3)	**V4-O6**	2.043(3)
V2-O8	2.011(3)	**V4-O8**	2.269(3)
V2-O11	1.994(3)	**V4-O18**	1.993(3)
V2-O16	1.986(3)	**V4-O21**	1.989(3)

Table 2.4.2 – BVS calculations for the vanadium and hydroxo ions in **Na-V$_{12}$**.

	BVS	Oxidation state		BVS	Assignment
V1	4.03	+4	**O5**	1.22	OH
V2	4.04	+4	**O6**	1.23	OH
V3	4.01	+4	**O7**	1.33	OH
V4	3.97	+4	**O8**	1.33	OH

Geometrical analysis with the program SHAPE (Version 2.1)[33] further illuminates the similarity between the square pyramidal and distorted octahedral environment of the vanadium(IV) ions. With this program, based on continuous shape measure (CShM) calculations[34], a shape constant is generated, which indicates how closely related the coordination environment of a given metal is to an ideal geometrical shape. The closer it is to zero, the better it can be described as a certain polyhedron. These values are shown in Table 2.4.3 for the VO_6 polyhedra of **Na-V$_{12}$** and the VO_5 polyhedra, in which the *hydroxo*-ligand *trans* to the terminal *oxo*-ligand was removed.

Both the square pyramidal geometry for the VO_5 polyhedra and the octahedral geometry for the VO_6 polyhedra are close to their ideal geometries. In both calculations for the VO_5 as well as the VO_6 polyhedra the geometry is closer to an octahedron (or a vacant octahedron in the case of VO_5) than to a spherical square pyramid. To put those numbers into perspective, CShM calculations were carried out for a crystal structure of the truly square pyramidal compound $VO(acac)_2$ from the literature[35] (acac = acetylacetonate). The shape constant for the octahedral coordination environment in the $\{V_{12}\}$ structure lies in between the values for a square pyramidal environment and a vacant octahedral environment in $VO(acac)_2$

Table 2.4.3 – Continuous shape measure calculations of the vanadium(IV) ions in **Na-V12**.

	VO_5		**VO_6**
Atom name	Spherical Square Pyramid	Vacant Octahedron	Octahedron
V1	1.480	1.151	0.934
V2	1.457	1.140	0.925
V3	1.221	1.029	0.836
V4	1.245	0.993	0.808
$VO(acac)_2$	0.433	1.388	

The cubane motif itself is slightly distorted, which can be seen by analysis of the V-O-V and O-V-O bond angles. The O-V-O bond angles lie between 75.24(12)° and 76.61(12)° and therefore differ from the ideal 90° cube angle by about 14°. The V-O-V bond angles range from 101.06(12)° to 103.79(12)° which deviates by about 12-13° from the ideal geometry. CShM analysis was carried out on the cube geometry to probe the extent of the distortion. Table 2.4.4 shows the results for selected geometries, which indicate a slightly distorted cube geometry.

Table 2.4.4 – CShM calculations for the $\{V_4\}$ cubane structure in **Na-V_{12}** for selected geometries.

Geometry	**Shape constant**
Cube	1.729
Triangular Dodecahedron	9.430
Square Antiprism	13.004

Table 2.4.5 – Bond angles within the $\{V_4\}$ cubane motif.

Bonds	Bond angle / °	Bonds	Bond angle / °
O7-V1-O5	75.94(11)	**V3-O5-V1**	101.53(12)
O7-V1-O8	75.24(12)	**V3-O5-V4**	101.91(13)
O8-V1-O5	75.93(11)	**V4-O5-V1**	101.06(12)
O7-V2-O6	75.95(11)	**V3-O6-V2**	101.71(12)
O7-V2-O8	75.44(12)	**V3-O6-V4**	101.81(13)
O8-V2-O6	75.90(11)	**V4-O6-V2**	101.32(12)
O5-V3-O6	76.61(12)	**V1-O7-V3**	103.49(13)
O5-V3-O7	76.29(11)	**V2-O7-V1**	102.37(14)
O6-V3-O7	75.98(11)	**V2-O7-V3**	103.65(13)
O5-V4-O6	76.41(12)	**V1-O8-V4**	103.66(12)
O5-V4-O8	76.56(11)	**V2-O8-V1**	102.17(13)
O6-V4-O8	76.26(11)	**V2-O8-V4**	103.79(12)

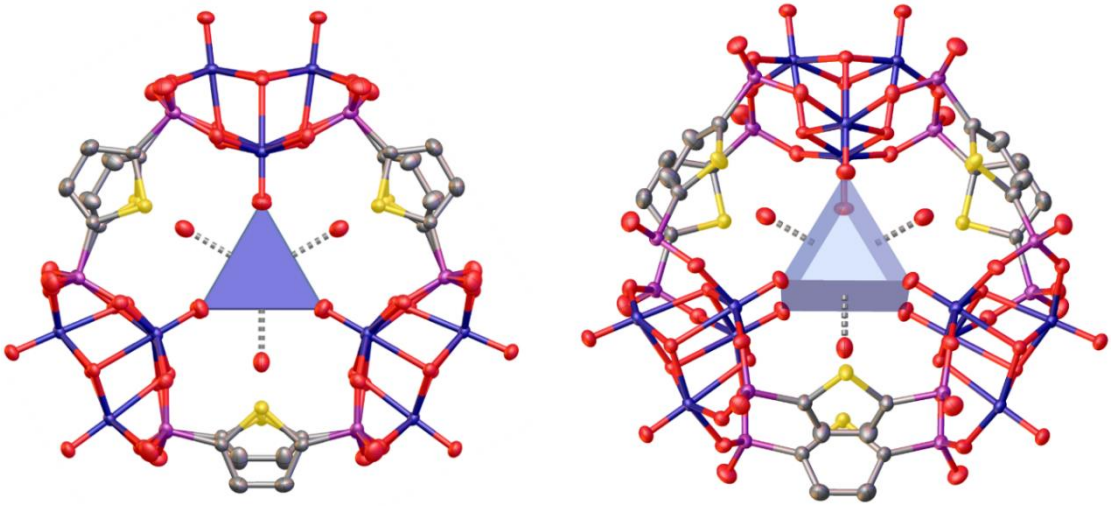

Figure 2.4.4 - Top view for the trigonal prism made up by the terminal *oxo*-ligands of the cubane units. The water molecules are capping the trigonal prism as indicated by the stippled line.

The three cubane units are arranged around a central point with two terminal *oxo*-ligands from each cubane unit pointing towards the inside of the structure. The six terminal *oxo*-groups within the torus build out a tricapped trigonal prism together with three water molecules (Figure 2.4.4). Although the centre of this prism is around 2.8 Å away from the oxygen atoms on the vertices, there is little to no electron density to be found in the crystal structure. As the centre of the structure is surrounded by electronegative ions, this pocket should be ideal to host a sodium or potassium ion in a nine coordinated environment.

The sulfur atoms of the thiophene rings of the ligands are also pointing towards the inside of the structure. Three thiophene rings at the bottom of the torus arrange themselves almost parallel to the horizontal plane in the middle of the torus, which is generated by the vanadyl groups of V1 and V2, whose terminal *oxo*-ligands are pointing towards the outside of the structure. The plane to plane angle between the thiophene rings and the horizontal plane is about 9.08°. The three thiophene groups above the horizontal plane are tilted to generate a plane to plane angle of 58.12° with the horizontal plane in the middle of the structure (Figure 2.4.5).

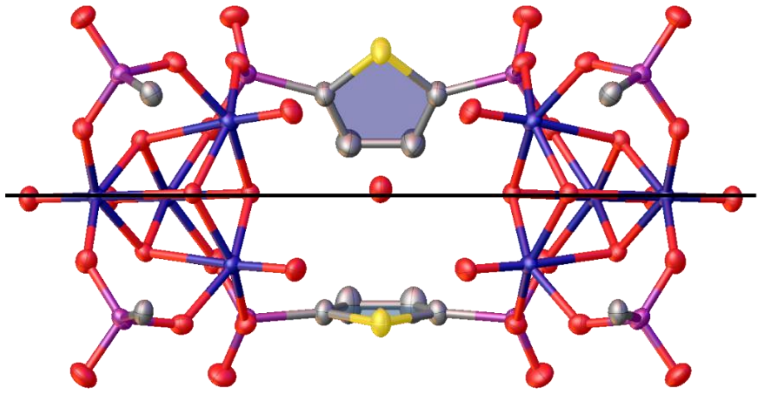

Figure 2.4.5 – Orientation of the thiophene rings in respect to the horizontal plane in the middle of the torus, indicated by the black line.

In the crystal packing the $\{V_{12}\}$ clusters are stacking in the crystallographic [001] direction. Each cluster is hereby rotated 30° towards the next cluster with a distance of about 12.4 Å centre to centre. This 30° rotation leads to an ABAB type of stacking because of the threefold rotation axis inherent in the structure. The stacks of $\{V_{12}\}$ cluster are about 17.36 Å apart and offset by about 4.24 Å. The twelve negative charges are balanced by sodium ions in between the clusters, which

are bridged by water molecules. A few sodium ions within the crystal structure can be resolved without ambiguity. Those are building out classical sodium water chains throughout the crystal structure. Figure 2.4.7 shows well resolved sodium ions in between two stacking $\{V_{12}\}$ cluster. For the most part however, the sodium ions along with the water molecules are heavily disordered.

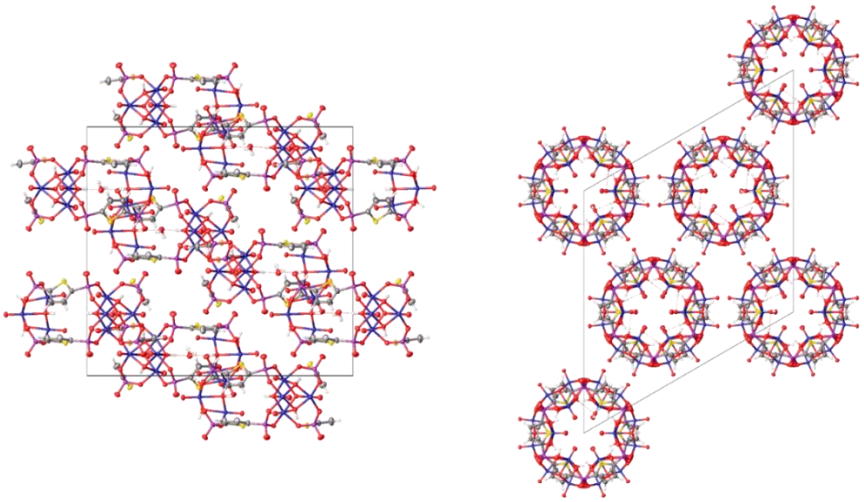

Figure 2.4.6 – Packing of the $\{V_{12}\}$ cluster in the crystallographic [100] and [001] direction.

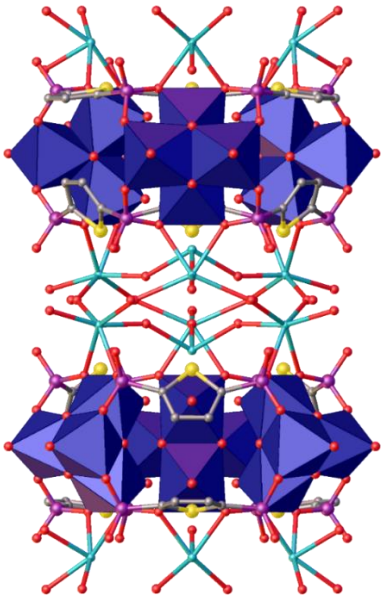

Figure 2.4.7 – Well resolved sodium ions between two stacking clusters.

Table 2.4.6 – Crystallographic table for **Na-V_{12}**.

Identification code	**Na-V_{12}**
Empirical formula	$C_{24}H_{30}Na_{12}O_{91.25}P_{12}S_6V_{12}$
Formula weight/(g/mol)	3229.67
Temperature/K	100
Crystal system	trigonal
Space group	*R-3*
a/Å	30.0698(19)
b/Å	30.0698(19)
c/Å	24.3362(17)
α/°	90
β/°	90
γ/°	120
Volume/Å^3	19057(3)
Z	5.99994
ρ_{calc} g/cm^3	1.689
μ/mm^{-1}	1.233
F(000)	9528
Crystal size/mm^3	0.18 × 0.08 × 0.07
Radiation	MoKα (λ = 0.71073)
2Θ range for data collection/°	2.29 to 58
Index ranges	-41 ≤ h ≤ 41 -41 ≤ k ≤ 41 -33 ≤ l ≤ 33
Reflections collected	247576
Independent reflections	11270 [R_{int} = 0.0529 R_{sigma} = 0.0180]
Data/restraints/parameters	11270/103/619
Goodness-of-fit on F^2	1.05
Final R indexes [I>=2σ (I)]	R_1 = 0.0686, wR_2 = 0.2079
Final R indexes [all data]	R_1 = 0.0851, wR_2 = 0.2303
Largest diff. peak/hole / e Å^{-3}	2.33/-1.19

2.4.2 Characterisation

2.4.2.1 PXRD

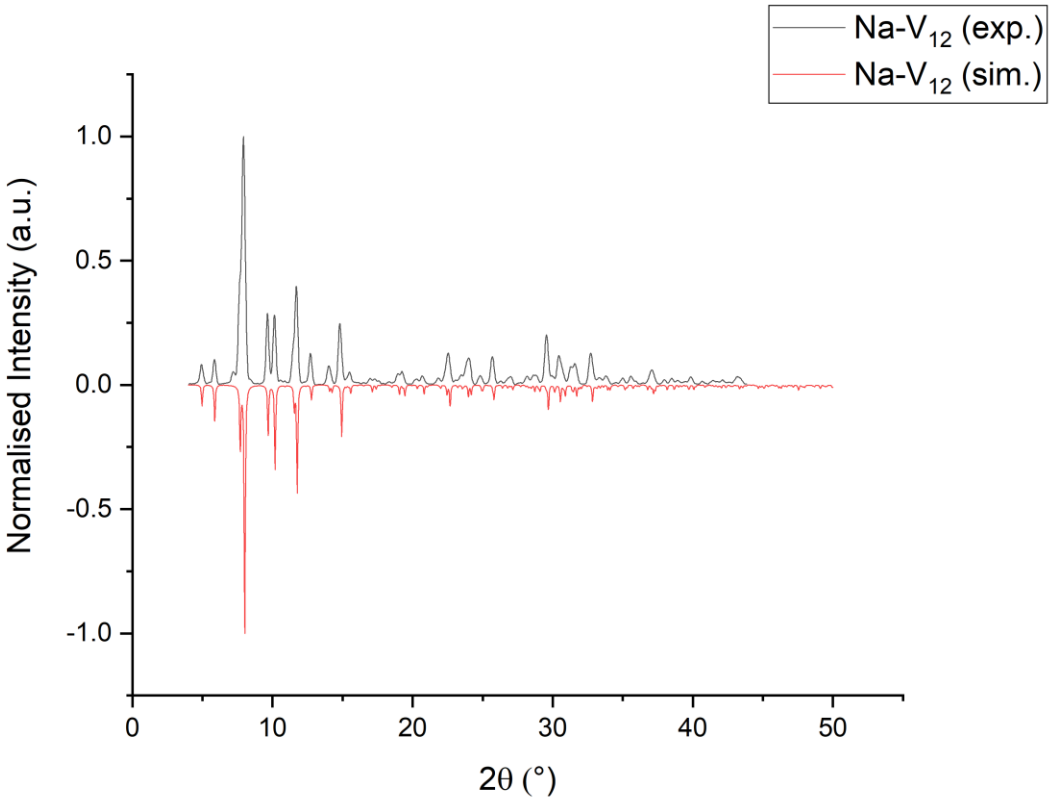

Figure 2.4.8 – PXRD measurement of **Na-V$_{12}$**.

A crystalline sample was ground up in the mother liquor and measured in capillaries over a reservoir of the mother liquor from 5˚ to 55˚θ. The almost perfect overlap between simulated and experimental spectrum indicates phase purity of the bulk sample as well as the absence of crystalline impurities in the sample. Minor differences in Intensity can arise from a slight preferred orientation of the crystals within the sample holder. The matching PXRD pattern to the crystal structure enables us to investigate the bulk magnetic properties of **Na-V$_{12}$** with full knowledge of the molecular structure of the bulk sample.

2.4.2.2 IR spectroscopy

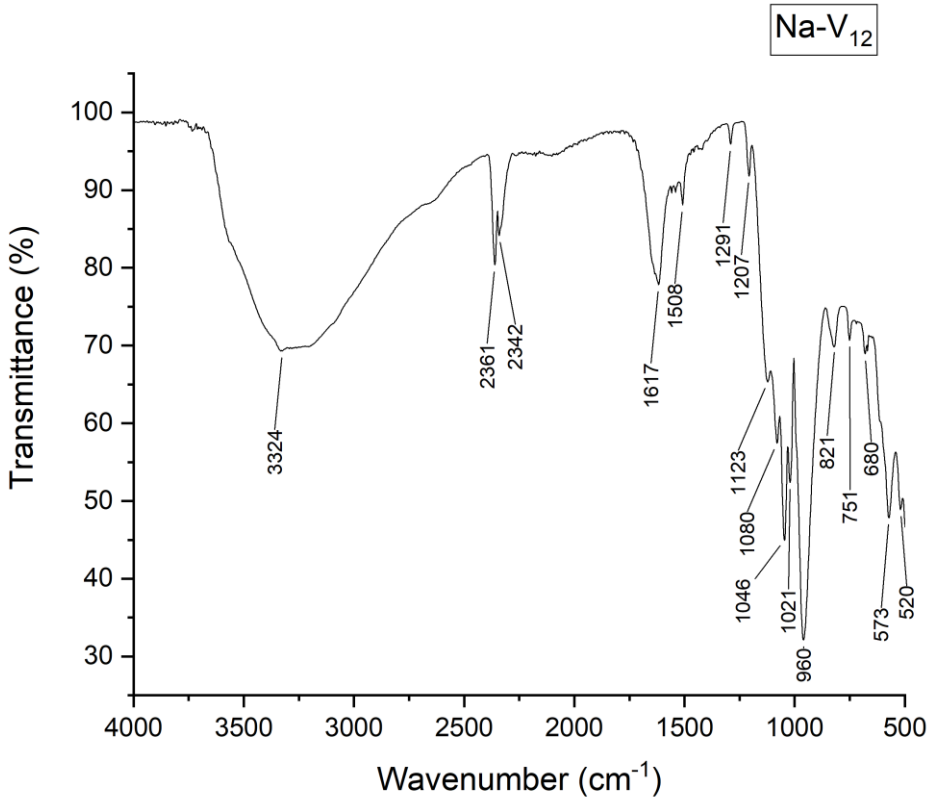

Figure 2.4.9 – IR spectrum of **Na-V$_{12}$**.

The IR spectrum shows two solvent signals from the crystal water at 3324 cm^{-1} and 1617 cm^{-1}. Two characteristic bands at 2361 cm^{-1} and 2342 cm^{-1} belong to the asymmetric stretch of CO_2 which is an artefact of the ATR method used in measurement. A comparison with the IR-spectrum of **Na-V$_{10}$** confirms the assignment of the signals to the phosphonate ligand, which can be found at 1508 cm^{-1}, 1291 cm^{-1}, 1207 cm^{-1}, 1123 cm^{-1}, 1046 cm^{-1} and 1021 cm^{-1}. The V=O double bond stretch is assigned to the signal at 960 cm^{-1}. The absence of any unexpected signals further supports the assumption of sample purity as indicated by the PXRD measurements.

2.4.2.3 TGA

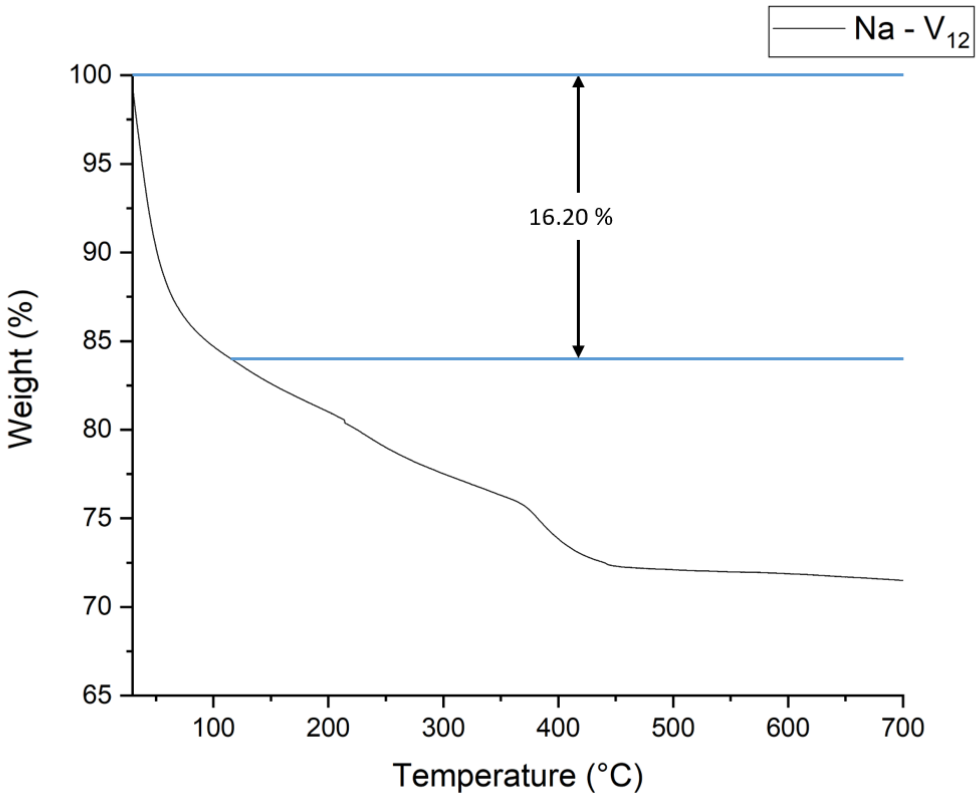

Figure 2.4.10 – TGA curve for **Na-V_{12}** from 30°C to 700°C in N_2.

To investigate the amount of crystal water, whose determination by SXRD was hindered by heavily disordered sodium-water chains, thermogravimetric analysis was conducted on a sample under a stream of nitrogen. The TGA curve shows several weakly defined steps in the range from 30°C to 370°C. Step widths were chosen by careful analysis of the curve derivative. The loss in weight of 16.20 % from 30°C to 120°C can be attributed to the loss of 30 water molecules. (Theoretical value: 16.56 %). This assignment is in agreement with the CHN analysis of the sample, which allows us to accurately determine the molecular weight of the compound. The steady decline after 120°C is likely due to gradual decomposition of the thiophene-based ligand, which is completed after the step at 370°C.[19]

2.4.2.4 MS

The electrospray ionization (ESI) mass spectrum of **Na-V$_{12}$** shows an intense envelope of signals around 612 m/z, which corresponds to the four times negatively charged species of the {V_{12}} cluster. The negative charge of -12 can be countered either by Na^+ and H^+ ions. This leads, together with the possibility of additional solvents as well as possible defragmentation during ionisation, to a large number of signals, which are often partially overlapping. Figure 2.4.11 shows the mass spectrum along with selected peaks and their simulated peak patterns. The assignment to those peaks can be found in Table 2.4.7. Aside from the fully reduced species {V^{IV}_{12}}, some of the peaks were assigned to oxidised version of the cluster with two V^V ions and ten V^{IV} ions, indicating that the cluster is susceptible to partial oxidation in aqueous solution.

Table 2.4.7 – Assignment of the ESI-MS peaks of **Na-V$_{12}$**.

Assignment	Peak (m/z)	Calculated (m/z)	Charge
$\{PSP\}^{4-} + H_3$	242.9288	242.9134	1-
$\{PSP\}^{4-} + H_3 - H_2O$	224.9182	224.9050	1-
$\{PSP\}^{4-} + NaH_2$	264.9107	264.8944	1-
$\{V^{IV}_{12}\}^{12-} + H_8$	613.6979	613.6213	4-
$\{V^{IV}_{12}\}^{12-} + NaH_7$	619.1934	619.1157	4-
$\{V^{IV}_{10}V^{V}_{2}\}^{10-} + H_6(H_2O)$	617.6967	617.6156	4-
$\{V^{IV}_{10}V^{V}_{2}\}^{10-} + H_6(H_2O)_2$	622.1993	622.1115	4-
$\{V^{IV}_{10}V^{V}_{2}\}^{10-} + NaH_5(H_2O)$	623.1922	623.1084	4-
$\{V^{IV}_{10}V^{V}_{2}\}^{10-} + NaH_5(H_2O)_2$	627.6948	627.6095	4-
$\{V^{IV}_{10}V^{V}_{2}\}^{10-} + Na_4H_2$	635.176	635.1044	4-

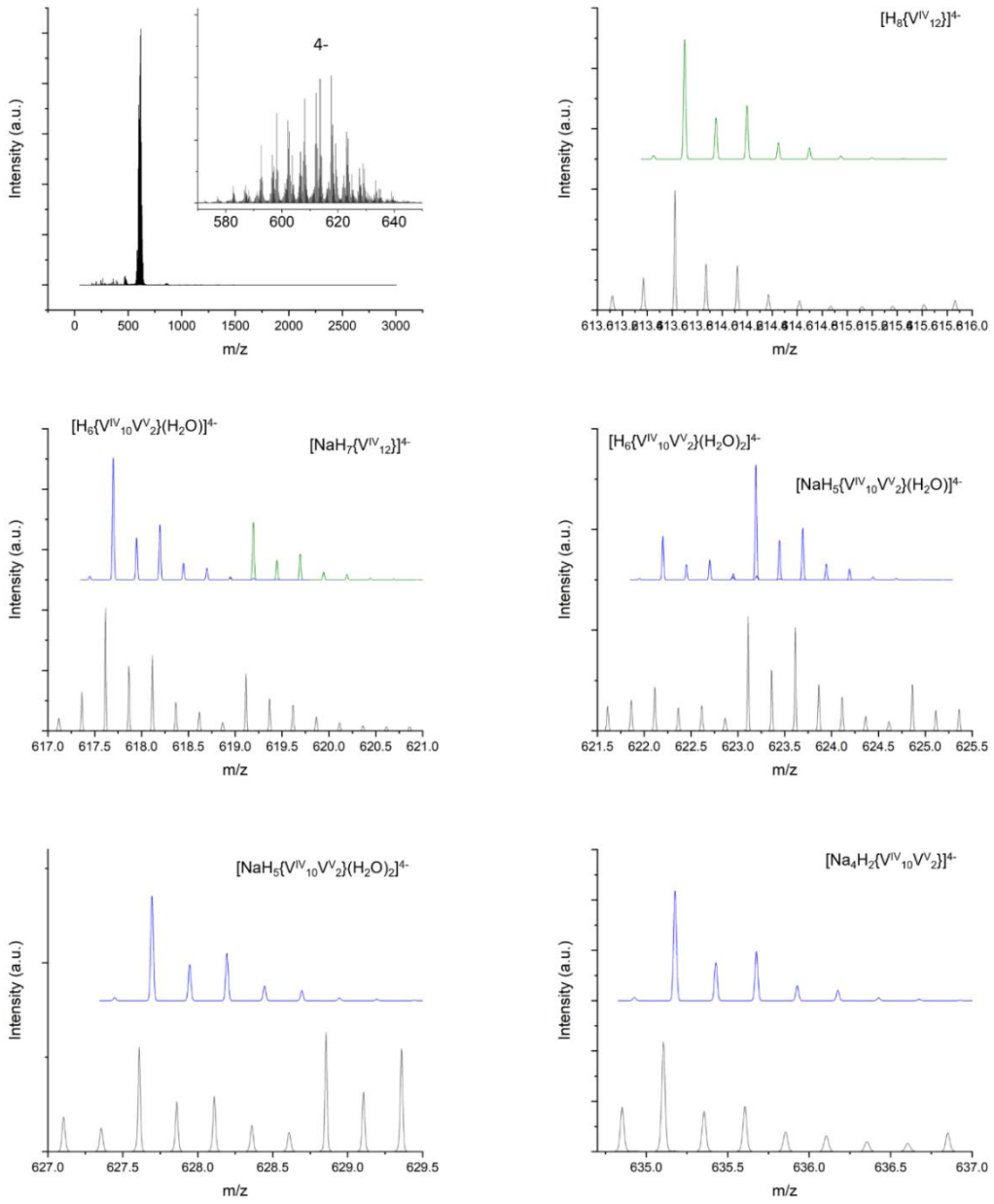

Figure 2.4.11 – ESI-MS of **Na-V_{12}** in water and comparison between simulated (top) and experimental (bottom) peak patterns. $\{V^{IV}_{12}]$ shown in green and $\{V^{IV}_{10}V^{V}_{2}\}$ species shown in blue.

2.4.2.5 UV-VIS

The UV-VIS spectrum of **Na-V_{12}** was carried out in water between 200 nm and 1100 nm. The spectrum shows multiple transitions of which the most intense one at 244 nm belongs to a ligand-centred transition of the thiophene-bisphosphonate ligand as has been seen in the UV-VIS spectrum of **Na-V_{10}** and **NH_4-V_{10}.** The shoulder at around 350 nm belongs to a LMCT transition from a π-orbital of the *oxo*-ligand to the d-orbital of the vanadium ion. Two d-d transitions can be seen at 640 nm at 828 nm in the near infrared region. [29, 30] The {V_{12}} spectrum differs visibly from the {V_{10}} spectra. Most notably is the absence of the IVCT band around 720 nm, which was present in the aqueous solution of the mixed-valent {V_{10}} compound. This indicates the correct assignment of the d-d and IVCT transitions for **Na-V_{10}** and **NH_4-V_{10}.**

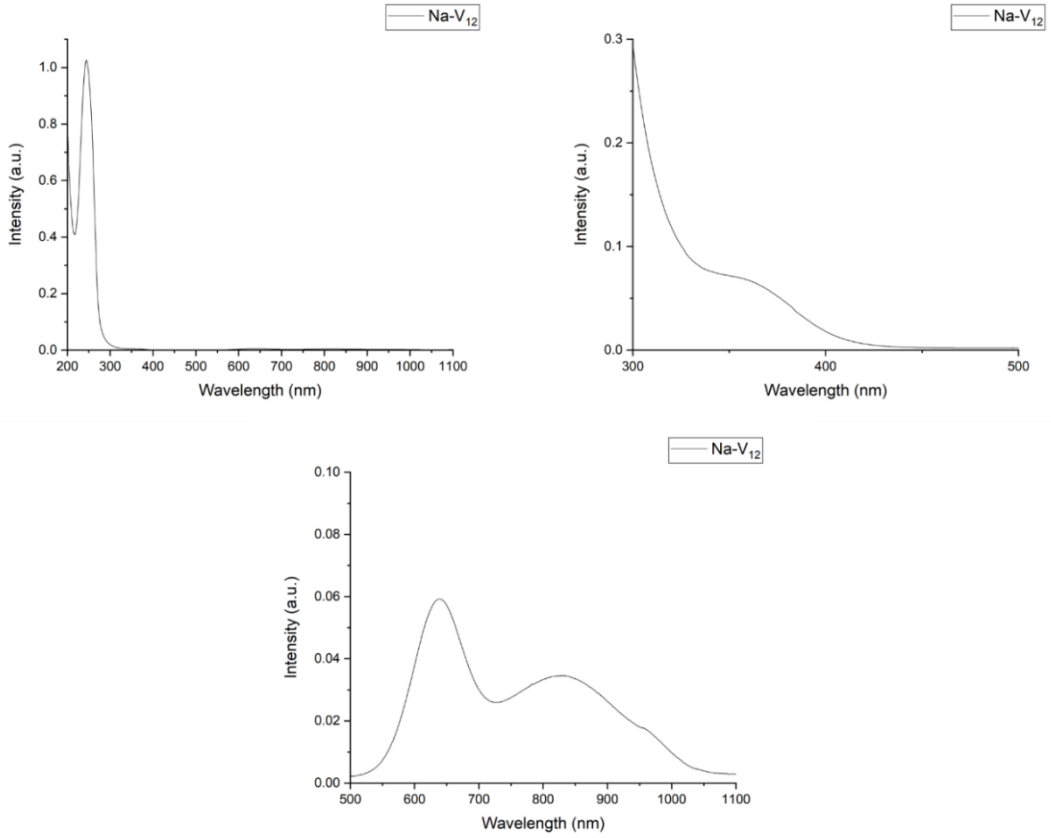

Figure 2.4.12 – UV-VIS spectra of Na-V_{12} in water.

2.4.2.6 Magnetism

Magnetic measurements were conducted on a crystalline sample of **Na-V$_{12}$**. A temperature dependent susceptibility sweep was carried out at a static field 0.1 T from 300 K to 1.8 K. Figure 2.4.13 shows the χT/T plot in linear and logarithmic scale. The room temperature (RT) χT value of about 4.52 cm^{3}K/mol is in good agreement with the value for twelve unpaired electrons (S = ½, g = 2, C = 0.375 cm^{3}K/mol; 12·0.375 cm^{3}K/mol = 4.5 cm^{3}K/mol). The χT product at high temperature is practically constant upon cooling down to about 30 K. Below this point, a sharp decrease in the χT curve is visible, which can be attributed to the combined effect of ligand-field splitting, antiferromagnetic interactions and Zeeman saturation effects. The χT value at 1.8 K is at 0.77 cm^{3}K/mol, which indicates a triplet ground spin state of 2 unpaired electrons (0.75 cm^{3}K/mol). By plotting the χT product against a logarithmic temperature scale (Figure 2.4.13 right), it becomes more obvious that the χT product is heading not towards zero, but rather 0.75 cm^{3}K/mol on lowering the temperature which is indicative of a spin ground state of S = 1 at low temperatures.

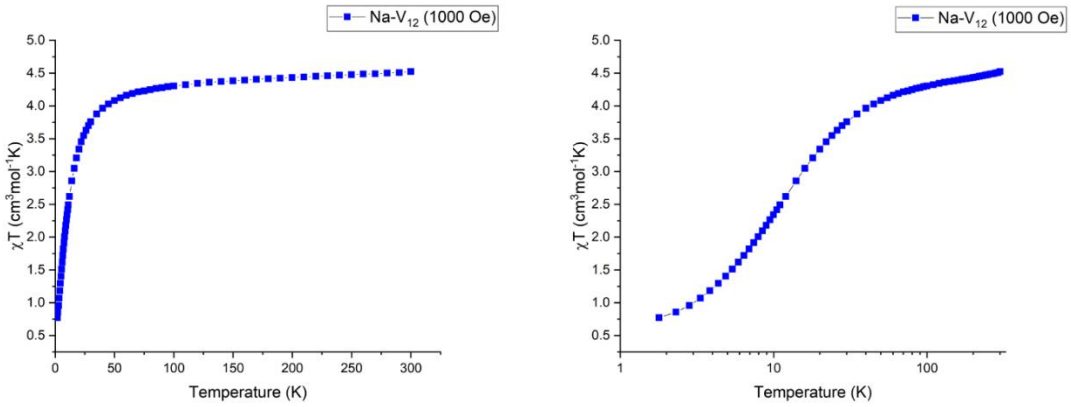

Figure 2.4.13 - χT/T plots for **Na-V$_{12}$** from 300K to 1.8 K at 0.1 T in linear (left) and logarithmic scale (right). Lines are guides to the eye.

The susceptibility was initially fitted with two *J* values, see Figure 1.3.13, for the equatorial and axial connected vanadium ions. As both *J* values were sufficiently close to each other a second model was assumed with only one *J* value, where $J_1 = J_2 = J$, for all interactions within a single vanadium cubane. The vanadium cubanes were assumed to be well separated, and therefore non-interacting which resulted in a *J* value of J = -2.9 cm^{-1}. The small negative value is indicative of

antiferromagnetic interactions within the cubanes. The model and fit to the experimental data can be seen in Figure 2.4.14. While the simulated curve fits the model well it does not recreate the ground spin state of two unpaired electrons, but since the possible long-range intramolecular interactions between the cubanes were not taken into consideration, this could be a possible explanation of a non-zero spin ground state. The model is in partial agreement with a similarly distorted vanadium(IV) cubane unit stabilised by sulfates from the literature. [36]

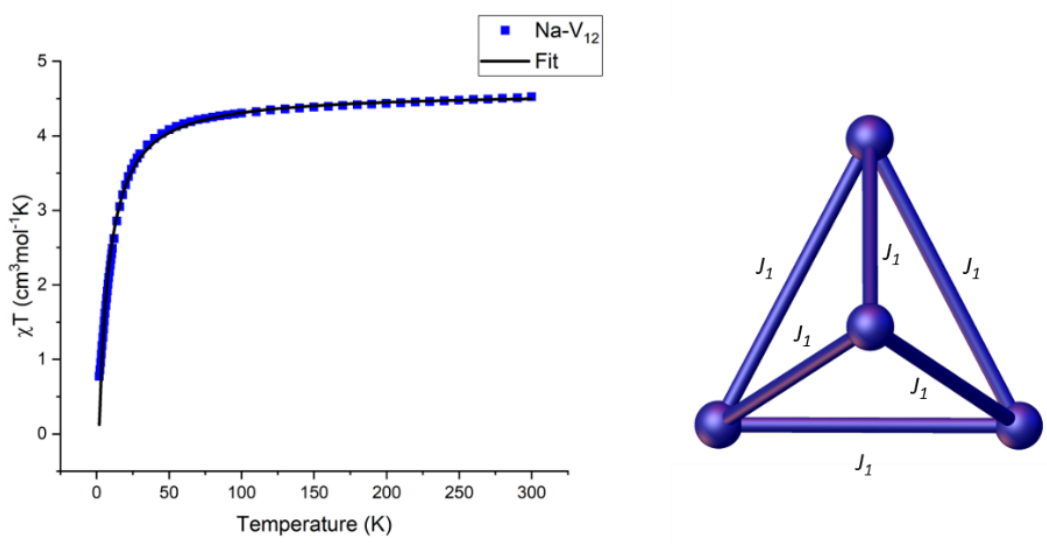

Figure 2.4.14 - χT/T plot with scheme of the magnetic exchange pathways within a $\{V_4\}$ cubane. The susceptibility curve could be fitted satisfactory with only one J value.

The field dependence of magnetisation of **Na-V$_{12}$** was measured from 0 to 7 T at 2, 3 and 5 K and is shown in Figure 2.4.15. Even at the maximum field of 7 T the sample showed no signs of saturation and the lack of saturation in the magnetization values indicates the presence of magnetic anisotropy and/or low-lying excited states. The values of the isotherms increase almost linearly without reaching saturation at 7.0 T and 2.0 K. The linear shape of the magnetization curves measured at various low temperatures suggests that this system must be highly frustrated since saturation to the ground state is never achieved. Plots of the reduced magnetization shown as M vs H/T plots clearly indicate a high anisotropy in the system due to the lack of any superposition of the isotherms.

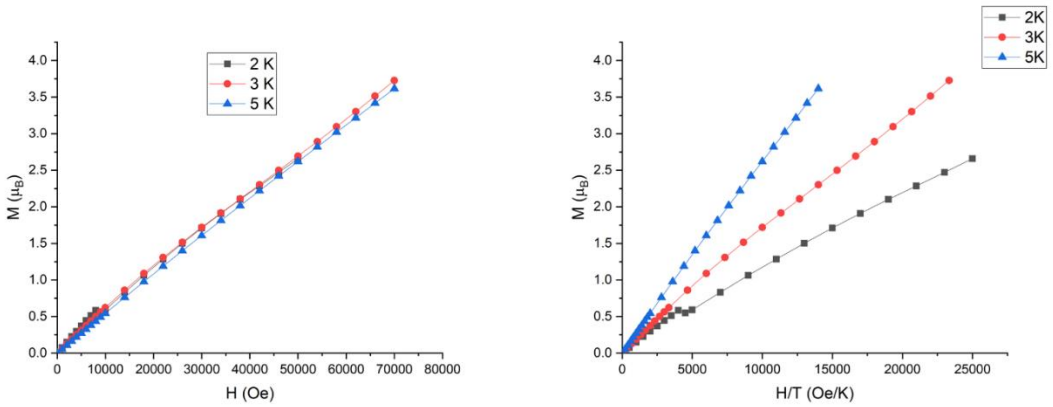

Figure 2.4.15 – M/H plot for **Na-V12** (left) as well as the reduced magnetisation (right) measured at 2, 3 and 5 K from 0 to 7 T.

To test this compound for the presence of slow relaxation of the magnetization which may originate from SMM behavior, ac magnetic susceptibility measurements were performed. Frequency dependence of the ac susceptibility was tested in a variation of applied fields between 0 to 3 T at a given temperature of 1.8 K in attempts to suppress any quantum tunneling of the magnetization (QTM). Neither the in-phase nor the out-of-phase susceptibility show any signs of frequency dependence. The χ value at 0.1 T is 0.47 cm^3/mol which corresponds to a χT value of 0.846 cm^3K/mol in agreement with the measured 0.77 cm^3K/mol for two unpaired electrons.

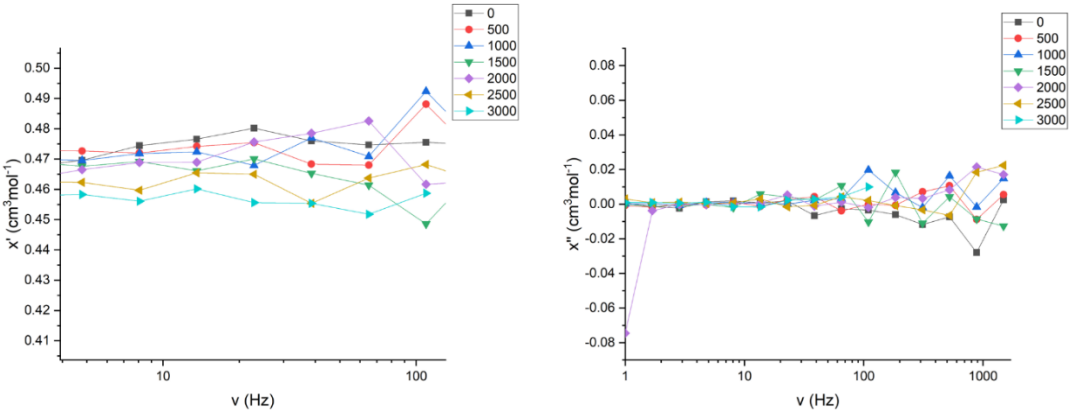

Figure 2.4.16 – In-phase and out-of-phase susceptibility measurements at 1.8 K from 0 to 3 T.

2.5 $K_{12}[V_{12}O_{12}(OH)_{12}(C_4H_2S(PO_3)_2)_6] \cdot x\ H_2O$ – (K-V_{12}, 4)

The absence of any electron density in the centre of the **Na-V_{12}** torus, even though it is surrounded by six nucleophilic *oxo*-groups and three water ligands, posed the question if the $\{V_{12}\}$ structure would behave differently with the incorporation of other alkali metals. As mentioned above, the distances of the *oxo*-ligands are on average about 2.8 Å away from the centre, which is almost the ideal geometry for a potassium ion. Replacing sodium orthovanadate with potassium orthovanadate in the synthesis of **Na-V_{12}** led to blue crystals of the compound **K-V_{12}**, which is largely isostructural to **Na-V_{12}**. The structure will be therefore only briefly discussed, and differences highlighted.

K-V_{12} was solved in the rhombohedral space groups $R\bar{3}m$ with a unit cell of:

$a = 30.019(2)$ Å	$\alpha = 90°,$	$Z = 6$
$b = 30.019(2)$ Å	$\beta = 90°$	$Z' = 0.16667$
$c = 24.2028(19)$ Å	$\gamma = 120°$	$V = 18887(2)$Å^3

Figure 2.5.1 shows the V_{12} torus in the crystal structure of **K-V_{12}**. As can be seen the centre of the structure is now occupied by a potassium ion with an occupancy factor of 0.687. The potassium ions build out K-O bonds from 2.762(12) Å to 2.839(3) Å. The water molecules refine to an occupancy of 0.425.

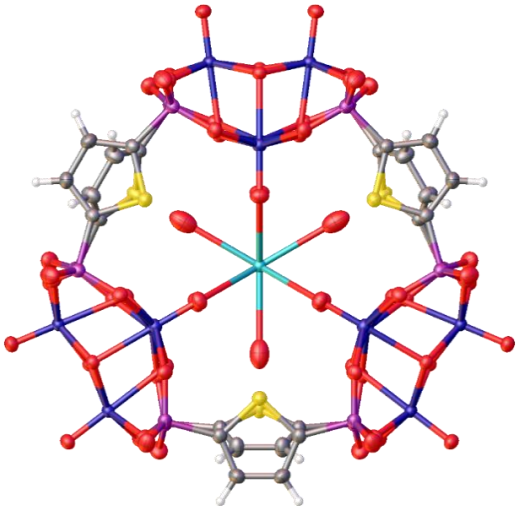

Figure 2.5.1 – {V_{12}**}** torus in the crystal structure of **K-V_{12}**.

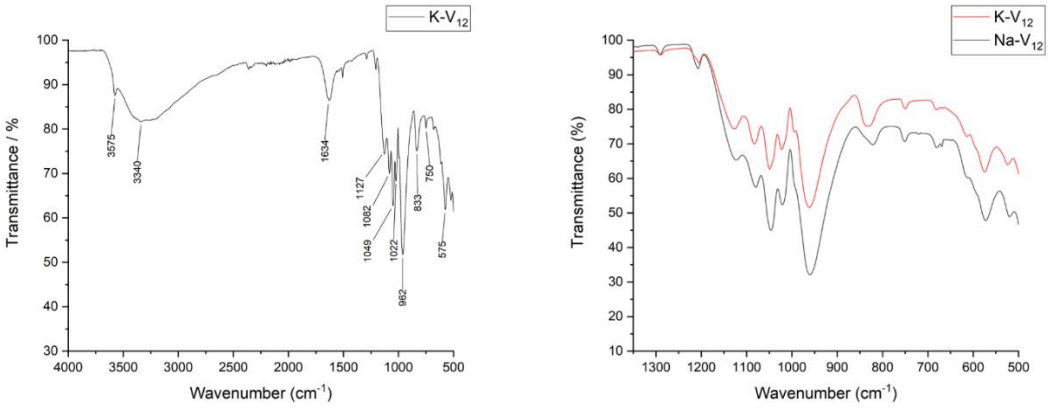

Figure 2.5.2 – IR of **K-V12** (left) and comparison with **Na-V12** (right)

Figure 2.5.2 shows the IR-spectrum of **K-V12** as well as a comparison with the IR-spectrum of **Na-V12**. Both spectra are virtually identical with only minor differences, which exemplifies the similar structure of both compounds. Differences due to the now occupied centre of the $\{V_{12}\}$ torus are not visible in the spectra.

Table 2.5.1 – Crystallographic table for **K-V_{12}**.

Identification code	**K-V_{12}**
Empirical formula	$C_{24}H_{12}K_{0.69}O_{61.28}P_{12}S_6V_{12}$
Formula weight/(g/mol)	2482.84
Temperature/K	99.99
Crystal system	trigonal
Space group	R-3m
a/Å	30.018(2)
b/Å	30.018(2)
c/Å	24.2028(19)
α/°	90
β/°	90
γ/°	120
Volume/Å^3	18887(3)
Z	6.00012
ρ_{calc} g/cm^3	1.31
μ/mm^{-1}	1.192
F(000)	7268
Crystal size/mm^3	0.2 × 0.07 × 0.04
Radiation	MoKα (λ = 0.71073)
2Θ range for data collection/°	3.556 to 61.16
Index ranges	$-42 \leq h \leq 42$, $-42 \leq k \leq 42$, $-34 \leq l \leq 34$
Reflections collected	162915
Independent reflections	6791 [R_{int} = 0.1207, R_{sigma} = 0.0411]
Data/restraints/parameters	6791/0/195
Goodness-of-fit on F^2	1.044
Final R indexes [I>=2σ (I)]	R_1 = 0.0436, wR_2 = 0.1062
Final R indexes [all data]	R_1 = 0.0760, wR_2 = 0.1196
Largest diff. peak/hole / e Å^{-3}	1.54/-0.73

2.6 Conclusions

In this chapter the syntheses, crystal structures and physicochemical characterisations of four novel hybrid POVs based on thiophene-2,5-bisphosphonate ligands were reported. **NH_4-V_{10}**, **Na-V_{10}**, **Na-V_{12}** and **K-V_{12}**.

In pursuit of expanding the range of known $\{V_{10}\}$ capsules,[14-17] while trying to make the interior of the polyoxovanadate capsules more accessible, we showed that we can utilise the bent PSP^{4-} ligand to widen the windows of the capsule. With the synthesis of **NH_4-V_{10}** and **Na-V_{10}** we were able to show that we could use bent ligands while maintaining the general $\{V_{10}\}$ cage structure. The bent in the ligand in combination with the ability of the aromatic ring to rotate around the C-P bond gave rise to a variable window sizes, which are shown to be dependent on the guest molecules. This adaptability will be of advantage in future catalytic applications, in which the capsule is supposed to act as a "molecular flask", as the capture and release of reactants can be influenced by organic reactions inside the cage. The successful inclusion of a heteroatom further demonstrates the possibility to electronically alter the interior to tune the reactivity of the cavity. Mass spectrometry analysis confirmed the structural stability of $\{V_{10}\}$ in solution, while the observation of once and twice oxidised version of the solid-state $\{V^{IV}_8V_2\}$ cage indicates structural stability of the cage against oxidation. These findings show that added flexibility in the $\{V_{10}\}$ systems is a promising route for designing systems that can be used as "molecular flasks" in oxidation catalysis.

A decrease of pH and prolonged reaction times in the synthesis of **Na-V_{10}** led to the synthesis of **Na-V_{12}** featuring a torus of three distorted V^{IV} cubane units that are bridged by six PSP^{4-} ligands. V^{IV} cubane units have so far been reported only once in the literature.[36] As antiferromagnetically coupled cubane units are inherently geometrically frustrated DC and AC magnetic measurements were carried out to investigate the possibility of a degenerate ground spin state. A temperature dependent susceptibility sweep indicated antiferromagnetic interactions and a surprising S=1 ground spin state, which we hypothesize to be caused by long range magnetic interactions between the individual cubane units at low temperatures. The high symmetry combined with the unusual spin ground state presents an interesting magnetic system for which the pathways of the magnetic interactions are yet to be understood. The absence of a sodium in the centre of the $\{V_{12}\}$ torus was hypothesized to be cause by non-ideal distances of the oxygen donors to the centre of the structure. Exchanging the sodium ions to potassium ions lead to the synthesis of **K-V_{12}**, **which**

supported this hypothesis by showing a 0.7 occupancy of potassium in the centre of the structure. This behaviour indicates a selectivity of potassium over sodium of the $\{V_{12}\}$, allowing comparisons of the structure to organic calixarene molecules.

1. J. J. Perry IV, J. A. Perman and M. J. Zaworotko, *Chem. Soc. Rev.*, 2009, **38**, 1400-1417.
2. T. R. Cook, Y.-R. Zheng and P. J. Stang, *Chem. Rev.*, 2012, **113**, 734-777.
3. D. J. Tranchemontagne, Z. Ni, M. O'Keeffe and O. M. Yaghi, *Angew. Chem. Int. Ed.*, 2008, **47**, 5136-5147.
4. Z. Zhang and M. J. Zaworotko, *Chem. Soc. Rev.*, 2014, **43**, 5444-5455.
5. H. Vardhan, M. Yusubov and F. Verpoort, *Coord. Chem. Rev.*, 2016, **306**, 171-194.
6. L. Zhao, X. Jing, X. Li, X. Guo, L. Zeng, C. He and C. Duan, *Coord. Chem. Rev.*, 2019, **378**, 151-187.
7. X.-X. Li, D. Zhao and S.-T. Zheng, *Coord. Chem. Rev.*, 2019, **397**, 220-240.
8. M. Eddaoudi, J. Kim, J. B. Wachter, H. K. Chae, M. O'Keeffe and O. M. Yaghi, *J. Am. Chem. Soc.*, 2001, **123**, 4368-4369.
9. M. Yoshizawa, J. K. Klosterman and M. Fujita, *Angew. Chem. Int. Ed.*, 2009, **48**, 3418-3438.
10. S. Tashiro, M. Tominaga, M. Kawano, B. Therrien, T. Ozeki and M. Fujita, *J. Am. Chem. Soc.*, 2005, **127**, 4546-4547.
11. H. Takezawa, T. Murase, G. Resnati, P. Metrangolo and M. Fujita, *J. Am. Chem. Soc.*, 2014, **136**, 1786-1788.
12. A. C. Sudik, A. R. Millward, N. W. Ockwig, A. P. Côté, J. Kim and O. M. Yaghi, *J. Am. Chem. Soc.*, 2005, **127**, 7110-7118.
13. M. Stuckart and K. Y. Monakhov, *Chem. Sci.*, 2019, **10**, 4364-4376.
14. J. M. Breen, R. Clerac, L. Zhang, S. M. Cloonan, E. Kennedy, M. Feeney, T. McCabe, D. C. Williams and W. Schmitt, *Dalton Trans.*, 2012, **41**, 2918-2926.
15. J. M. Breen and W. Schmitt, *Angew. Chem. Int. Ed.*, 2008, **47**, 6904-6908.
16. J. M. Breen, L. Zhang, R. Clement and W. Schmitt, *Inorg. Chem.*, 2012, **51**, 19-21.
17. M. B. Mahimaidoss, S. A. Krasnikov, L. Reck, C. I. Onet, J. M. Breen, N. Zhu, B. Marzec, I. V. Shvets and W. Schmitt, *Chem. Commun.*, 2014, **50**, 2265-2267.
18. J. M. Breen, PhD Thesis, Trinity College Dublin, 2010.
19. Y. Zhang, X. Wang, S. Li, B. Song, K. Shao and Z. Su, *Inorg. Chem.*, 2016, **55**, 8770-8775.
20. C.-Y. Gao, F. Wang, H.-R. Tian, L.-J. Li, J. Zhang and Z.-M. Sun, *Inorg. Chem.*, 2016, **55**, 537-539.
21. K. Nakamoto, in *Infrared and Raman Spectra of Inorganic and Coordination Compounds Part A*, John Wiley & Sons, Inc., Hoboken, New Jersey, 2008, pp. 149-354.
22. K. Nakamoto, in *Infrared and Raman Spectra of Inorganic and Coordination Compounds Part B*, John Wiley & Sons, Inc., Hoboken, New Jersey, 2008, pp. 1-273.
23. D. de Waal, A. M. Heyns, K. J. Range and C. Eglmeier, *Spectrochim. Acta A*, 1990, **46**, 1649-1657.
24. C. Daniel and H. Hartl, *J. Am. Chem. Soc.*, 2005, **127**, 13978-13987.
25. S. A. Selim, C. A. Philip and R. S. Mikhail, *Thermochim. Acta*, 1980, **36**, 287-297.
26. G. Yucesan, V. Golub, C. J. O'Connor and J. Zubieta, *Dalton Trans.*, 2005, 2241-2251.
27. T. L. Stott, M. O. Wolf and B. O. Patrick, *Inorg. Chem.*, 2005, **44**, 620-627.
28. Y. Gong, J. Li, J. Qin, T. Wu, R. Cao and J. Li, *Cryst. Growth Des.*, 2011, **11**, 1662-1674.
29. A. Müller, K. Hovemeier, E. Krickemeyer and H. Bögge, *Angew. Chem. Int. Ed.*, 1995, **34**, 779-781.
30. A. Müller, K. Hovemeier and R. Rohlfing, *Angew. Chem. Int. Ed.*, 1992, **31**, 1192-1195.
31. G. Sheldrick, SADABS, Bruker ASX Inc., Madison, Wisconsin, USA., 2014.
32. R. Herbst-Irmer and G. M. Sheldrick, *Acta Cryst.*, 1998, **B54**, 443-449.

33. D. C. M. Llunell, J. Cirera, P. Alemany, S. Alvarez, SHAPE, Version 2.1, Universitat de Barcelona, 2013.
34. D. Casanova, J. Cirera, M. Llunell, P. Alemany, D. Avnir and S. Alvarez, *J. Am. Chem. Soc.*, 2004, **126**, 1755-1763.
35. M. A. K. Ahmed, H. Fjellvåg, A. Kjekshus and B. Klewe, *Z. Anorg. Allg. Chem.*, 2004, **630**, 2311-2318.
36. A. Ignaszak, N. Patterson, M. Radtke, M. R. J. Elsegood, J. W. A. Frese, J. L. Z. F. Lipman, T. Yamato, S. Sanz, E. K. Brechin, T. J. Prior and C. Redshaw, *Dalton Trans.*, 2018, **47**, 15983-15993.

Chapter 3

Supramolecular Hybrid Organic-Inorganic Polyoxovanadate Systems

3.1 Introduction

After the successful synthesis of the $\{V_{10}\}$ cage with H_4PSP the question arose if the flexibility within the windows of the polyoxovanadate capsule induced by the slightly bent thiophene ligand could be expanded upon. The next narrower angle that is synthetically easily accessible is the 120° angle in 1,3-disubstituted benzene derivatives (Figure 3.1.1). Narrowing the angle could hereby lead to wider windows in the $\{V_{10}\}$ capsule as well as an increased effect of the flexibility on the window size. In the case of the $\{V_{12}\}$ system narrower angles would mean a different sized interior of the torus which could be selective for different cations.

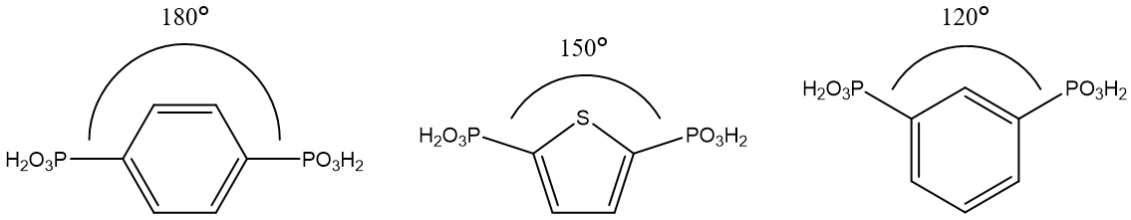

Figure 3.1.1 – Idealised bond angles in Benzene-1,4-bisphosphonic acid, H_4PSP and Benzene-1,3-bisphosphonic acid.

The benzene ring in benzene-1,3-bisphosphonic acid (DPB-H) is also a good organic platform for further functionalisation, be it as heteroatom within the rings or functional groups attached to the outside. Possible applications influenced by the electronic structure of the ligand can so be influenced with relative ease.

In this chapter a family of novel supramolecular hybrid organic-inorganic $\{V_{20}\}$ polyoxovanadate structures is presented, which are held together by cation-π interactions in the solid state as in solution. The synthesis, crystal structures, physicochemical characterisation as well as their catalytic and magnetic behaviour are reported.

3.2 Ligand synthesis

The ligand benzene-1,3-bisphosphonic acid was synthesized from 1,3-dibromobenzene *via* a Michael-Arbuzov reaction with triethylphosphite and nickel bromide in 1,3-diisopropylbenzene at 180°C under a nitrogen atmosphere (Figure 3.2.1).

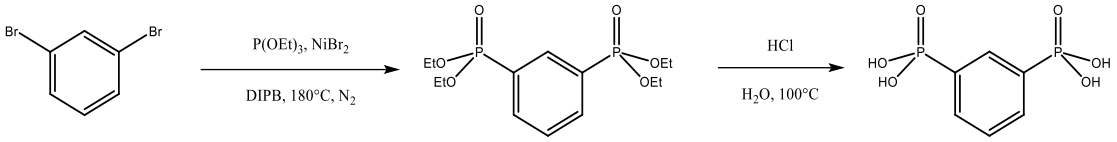

Figure 3.2.1 – Reaction scheme for the synthesis of DPB-H. DIBP: Diisopropylbenzene.

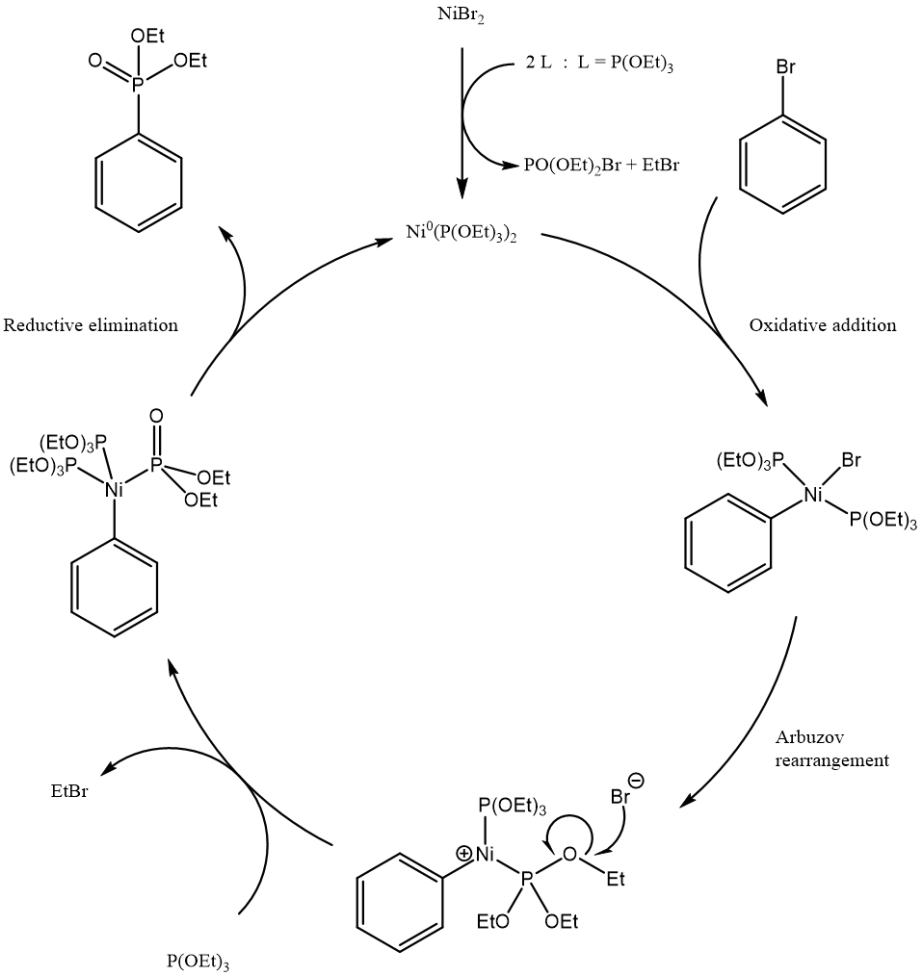

Figure 3.2.2 – Catalytic Cycle for the Michael-Arbuzov reaction of aryl bromides.[241, 242]

Figure 3.2.2 shows a possible catalytic cycle for the reaction. The active catalyst is a Ni^0 species, which is highly air-sensitive but can be generated in situ with relative ease from $NiBr_2$ at temperatures higher than 120°C. After the catalyst generation, the aryl bromide is added to the nickel complex *via* an oxidative addition, which is followed by the Arbuzov rearrangement, in which ethyl bromide is formed and the phosphonate group generated. Addition of another triethylphosphite group to the nickel species and a reductive elimination completes the catalytic cycle. The gaseous ethyl bromide, which is formed during the reaction is being removed constantly by a gentle stream of nitrogen that flows through the reaction vessel. This is necessary to complete the reaction by shifting the equilibrium towards the products and also for safety reasons as ethyl bromide has a flash point in nitrogen which is lower than the reaction temperature. The phosphonate ester is then being hydrolysed with hydrochloric acid to produce the free phosphonic acid.

3.3 The supramolecular organic-inorganic V_{20}H-AM system (AM = Cs, Rb, K)

The reaction of benzene-1,3-bisphosphonic acid with a source of orthovanadate ions yielded a family of novel supramolecular {V_{20}} hybrid organic inorganic polyoxovanadate clusters. Three closely related compounds were obtained, which mainly differ by their alkali metal cations inside and outside of the structure.

The compounds **V_{20}H – AM** (**AM = Cs, Rb, K**) were synthesized by the partial reduction of sodium orthovanadate with hydrazine in the presence of benzene-1,3-bisphosphonic acid (H_4DPB-H), sodium azide and the respective alkali metal chloride in the solvent system water, DMF and MeCN (3:1:1 / v:v:v) at pH ~ 7. Green crystals, suitable for single crystal x-ray crystallography were obtained after several days by diffusion of MeCN into the solution. In the case of **V_{20}H-K** potassium orthovanadate was used instead of sodium orthovanadate.

As the structures are almost identical a full structural description shall be given for the caesium-based compound **V_{20}H-Cs** and only comparisons made for **V_{20}H-Rb**, and **V_{20}H-K**.

3.3.1 $Cs_{11.5}[(V_5O_9)_4(C_6H_4(PO_3)_2)_8Na_{0.5}Cs_8] \cdot CH_3CN \cdot 33\ H_2O$ - (V_{20}H-Cs, 5)

The crystal structure of **V_{20}H-Cs** was solved in the tetragonal space group *P*4/*mnc* with unit cell parameters of:

$a = 19.9912(6)$ Å	$\alpha = 90°,$	$Z = 2$
$b = 19.9912(6)$ Å	$\beta = 90°$	$Z' = 0.125$
$c = 22.9901(7)$ Å	$\gamma = 90°$	$V = 9187.9(6)$ Å^3

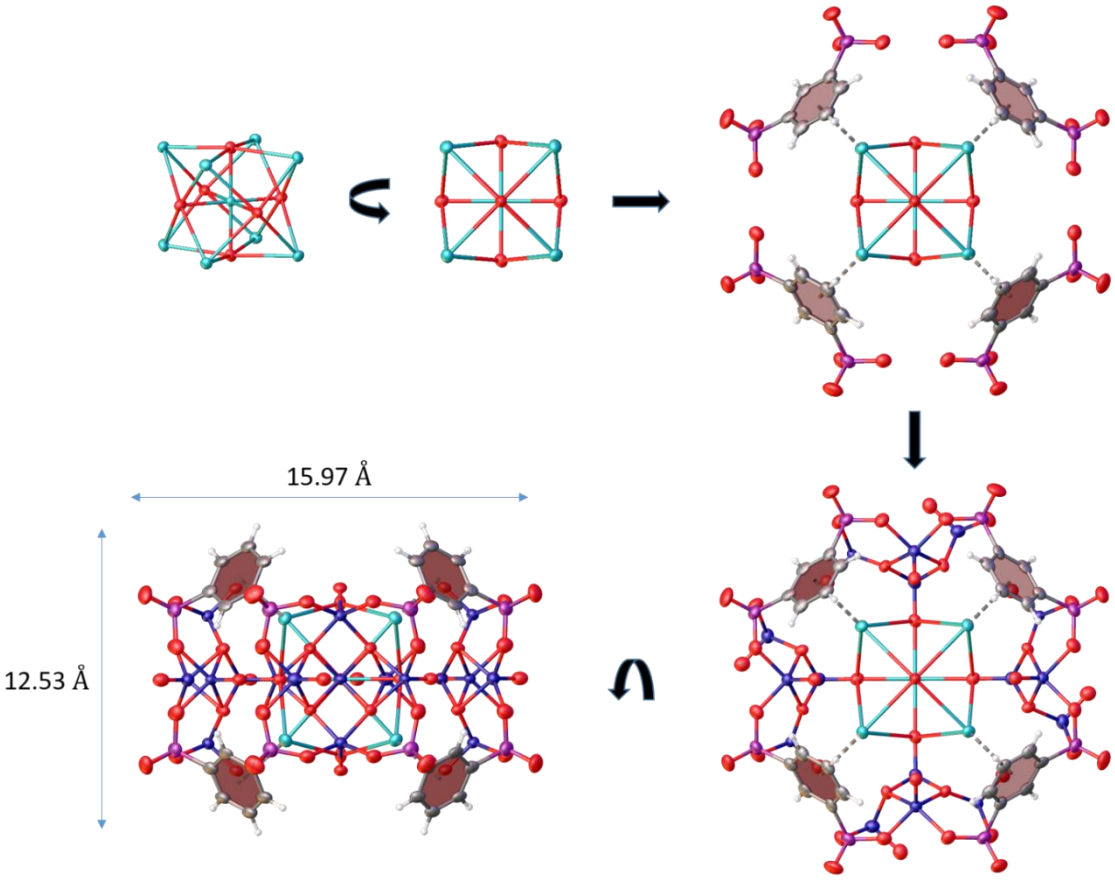

Figure 3.3.1 - Successive build-up of the structure of **V_{20}H-Cs**. Around a cube of alkali metal cations are four pentanuclear polyoxovanadate half-capsules that are connected *via* eight DPB-H^{4-} ligands.

The general structure of **V_{20}H-Cs** consists of an anionic {V_{20}} hybrid organic-inorganic polyoxovanadate cluster. Four mixed-valent pentanuclear polyoxovanadate half-capsules are

arranged around a cube of alkali metal ions with a sodium ion sitting in the centre of the structure. The cluster is approximately 15.97 Å · 15.97 Å · 12.53 Å in size. Its structure can be best understood by successively assembling it from the inside to the outside as depicted in Figure 3.3.1. The structure description will follow this approach by first describing the alkali metal cube and their relation to the ligands, followed by the pentanuclear half capsules and lastly the packing of the cluster in the crystal structure.

3.3.1.1 The alkali metal cube

The centre of the structure is a cube of caesium cations that forms around a half-occupied sodium ion (Na1) in a distorted octahedral environment (Figure 3.3.2). The caesium cations (Cs1) are placed on the corners of the cube and build out Cs–O bonds with the terminal *oxo*-ligands (O1) of *oxo*-vanadium(V) groups. Those *oxo*-ligands are located in the centre of the four equatorial faces of the cube. The two axial faces were modelled as occupied by water molecules if the sodium ion is present or by acetonitrile molecules if not. Due to the high symmetry of the *P*4/*mnc* space group the asymmetric unit contains only one caesium ion and one *oxo*-ligand with the cube being symmetry generated by a fourfold rotation axis and a mirror plane. The Cs–O distances are between 3.003(4) Å and 3.476(18) Å long, whereas the Na–O distances are 2.468(6) Å and 3.04(3) Å. The caesium ions additionally build out Cs–O bonds with the μ_3–O^{2-} ions (O5,O6) and two other terminal *oxo*-ligands (O2,O3A,O4) of the pentanuclear half-capsule (
Table 3.3.1).

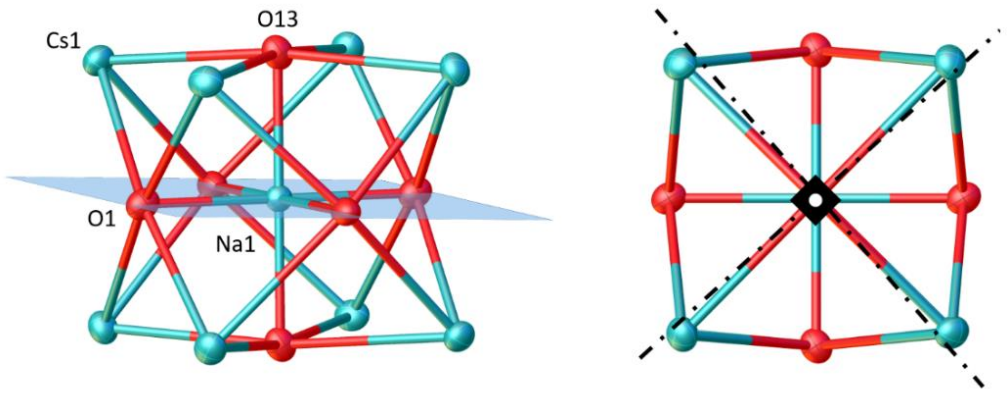

Figure 3.3.2 – The alkali metal cube of **V_{20}H – Cs**.

Table 3.3.1 - Bond lengths for the alkali metal oxygen bonds.

Bond	Bond length / Å	Bond	Bond length / Å
Cs1–O1[1]	3.365(4)	**Cs1–O4**	3.446(18)
Cs1–O1	3.389(4)	**Cs1–O3A**	3.476(16)
Cs1–O2[1]	3.260(4)	**Cs1–O13[3]**	3.237(4)
Cs1–O2	3.278(4)	**Na-O13**	3.04(3)
Cs1–O6	3.003(4)	**Na-O1**	2.468(6)
Cs1–O5[2]	3.013(4)		
[1]1-Y,+X,+Z; [2]1-Y,+X,1-Z; [3]1-X,1-Y,1-Z			

3.3.1.2 Ligands

The aromatic benzene rings of the ligand are positioned over the edges of the cube and build out cation-π interactions with the caesium ions. The distance between them is d(Cs-π) = 3.227(3) Å, which indicates strong cation-π interactions.[243] The phosphonate groups of the ligand are bound to the vanadyl groups in *anti-anti* fashion *via* P–O–V bonds, in contrast to the *syn-syn* binding mode seen in the {V_{10}} system in chapter 3. The P=O double bonds of the ligands points towards the outside of the structure and remain non-bonding. Around a cube of alkali metal cations are four pentanuclear polyoxovanadate half-capsules that are connected *via* the eight DPB-H^{4-} ligands (Figure 3.3.1).

3.3.1.3 The pentanuclear half-capsule

The half-capsule in **V_{20}H-Cs** is strongly related to the half capsule in compound **NH_4-V_{10}**. All vanadium ions display the typical square pyramidal coordination environment. The central vanadium ion V1 is in the oxidation state +V and is surrounded by four μ_3-*oxo* ions and one terminal *oxo*-ligand, which points towards the centre of the structure and is part of the alkali metal cube. As in **NH_4-V_{10}**, the central *oxo*-vanadium(V) group is surrounded by four vanadyl ions which share two μ_3-*oxo* groups each with the central vanadium ion and fill their coordination

sphere with two μ_2-*oxo* ions from two phosphonate groups which bind to the vanadyl ions in *anti-anti* fashion. The difference between the pentanuclear half capsule in **NH_4-V_{10}** and **V_{20}H-Cs** is the orientation of one of the peripheral vanadyl groups.

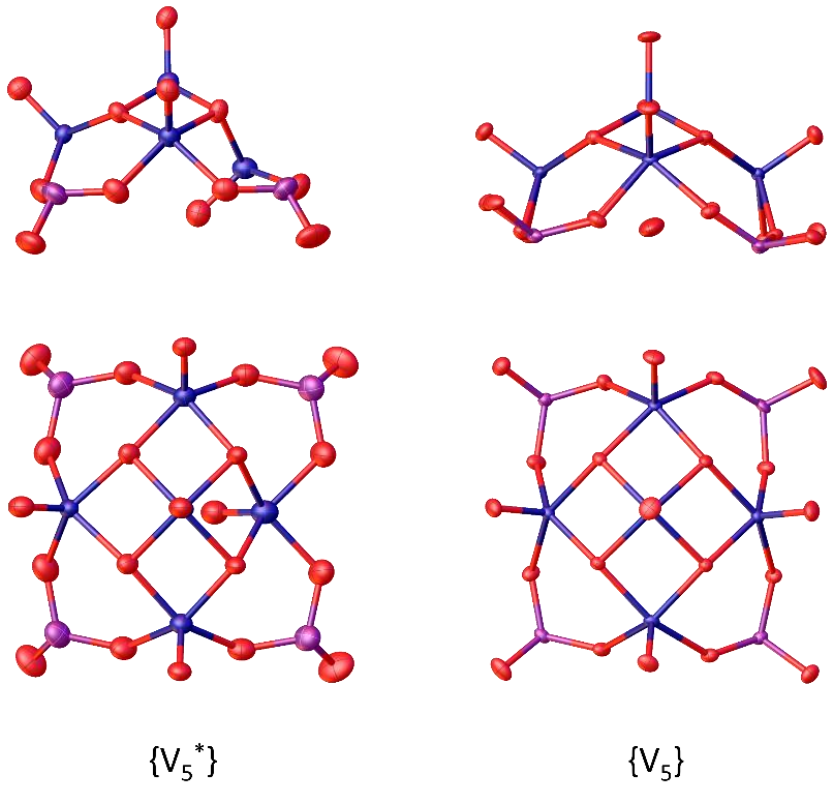

Figure 3.3.3 – The pentanuclear half capsules for the {V_{20}}-systems ({V_5^*}, left) and the {V_{10}}-systems ({V_5,} right) from the side (top row) and the top (bottom row). The templating agent present in the half-capsule of {V_{10}} is missing in the {V_{20}}-system.

In Figure 3.3.3 the two variations of the half-capsule can be seen side by side. Whereas all terminal *oxo*-ligands point towards the outside of the half-capsule for the {V_{10}}-systems, one of the vanadyl groups is flipped and points towards the inside of the half capsule in the {V_{20}} structure. This effect is due to steric hindrance that would otherwise be present in the structure. Because the phosphonate groups bind to the vanadyl groups in *anti-anti* fashion the half-capsules arrange themselves around the cube in an inverted way in regard to the {V_{10}} system. If all terminal *oxo*-ligands would point towards the outside of the half-capsule as in {V_{10}} two vanadyl groups of neighbouring half-capsules would occupy almost the same position in the structure (Figure 3.3.1). To avoid this one of the vanadyl groups is flipped towards the inside of the half-

capsule. As we will encounter those two motifs frequently in later parts of this thesis they shall be labelled {V_5} for the "normal" half-capsule with all terminal *oxo*-ligands pointing towards the outside and {V_5^*} for the half-capsule, in which one vanadyl group is flipped towards the inside. Another difference between the two systems is the presence of a templating agent in the {V_{10}} system. The known structures in the literature, which feature the pentanuclear half-capsule as it appears in the {V_{10}} system, have a nucleophilic templating agent sitting in the focal point of the vanadyl groups. This can be a halide, azide, water, DMF molecule or principally any other nucleophilic species.[67] This templating agent is not present anymore in the {V_{20}} structure. Instead, a terminal *oxo*-ligand occupies its position. As there is no directing force which favours one vanadyl groups on the inside over the other they are disordered in a 50:50 fashion, resulting in either a clockwise and counter-clockwise arrangement in the crystal structure (Figure 3.3.4).

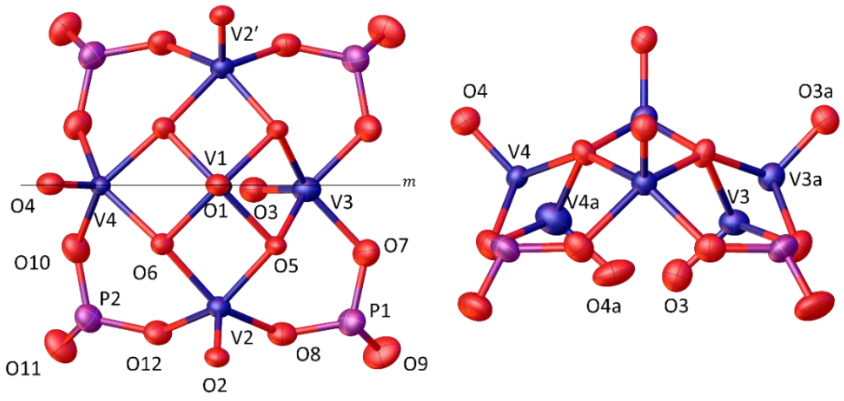

Figure 3.3.4 – Naming scheme of the {V_5} unit in **V_{20}H-Cs** with a mirror plane *m* going through the middle as indicated by solid line (left) and disorder present in the half-capsule.

The bond length for the V^V=O double bond is 1.637(6) Å while the V^V–O single bonds are 1.912(4) and 1.911(4) Å long. Around the central vanadium ion there are four vanadium(IV) ions of which three are present in the asymmetric unit. The fourth vanadium ion V2′ is symmetry generated by a mirror plane going through the middle of the half-capsule as seen in Figure 3.3.4. The bond lengths for the non-disordered V^{IV}=O bonds are around 1.61 Å whereas the bond lengths for V4=O and V4′=O deviate from the usual value of ~ 1.6 Å for vanadyl groups with 1.584(15) Å and 1.676(16) Å. Indicated by the rather larger effective standard deviation (esd) these values are to be taken with caution as the disorder present in the structure is the likely cause

of the seemingly shortened and elongated bonds. The V^{IV}–O single bonds range from 1.910(4) Å to 2.056(5) Å. All oxidation states were confirmed by BVS calculations (Table 3.3.2).

Table 3.3.2 – BVS calculations for **V_{20}H-Cs**.

	BVS	Oxidation state
V1	4.56	5
V2	4.03	4
V3	3.86	4
V3a	3.73	4
V4	4.02	4
V4a	3.78	4

Table 3.3.3 – Table of bond lengths for the pentanuclear half-capsule. See Figure 3.3.4 for scheme.

Bond	Bond length / Å	Bond	Bond length / Å
V1-O1	1.637(6)	**V3A-O3A**	1.616(18)
V1-O5	1.910(4)	**V3A-O5^{1}**	1.953(5)
V1-O5^{4}	1.910(4)	**V3A-O5^{2}**	1.953(5)
V1-O6	1.911(4)	**V3A-O7**	2.056(5)
V1-O6^{4}	1.911(4)	**V3A-O7^{4}**	2.056(5)
V2-O2	1.609(4)	**V4-O10**	2.027(5)
V2-O5^{4}	1.935(4)	**V4-O10^{4}**	2.027(5)
V2-O6	1.941(4)	**V4-O4**	1.584(15)
V2-O8^{6}	1.998(5)	**V4-O6**	1.946(5)
V2-O12	1.978(5)	**V4-O6^{4}**	1.946(5)
V3-O3	1.612(15)	**V4A-O10**	1.953(6)
V3-O5	2.015(5)	**V4A-O10^{4}**	1.953(6)
V3-O5^{4}	2.015(5)	**V4A-O4A**	1.676(16)
V3-O7^{5}	1.960(5)	**V4A-O6**	1.974(5)
V3-O7^{6}	1.960(5)	**V4A-O6^{4}**	1.974(5)

[1]1-Y,+X,+Z; [2]1-Y,+X,1-Z; [4]+X,+Y,1-Z; [5]+Y,1-X,1-Z; [6]+Y,1-X,+Z

3.3.1.4 Packing

The structure crystallizes in the tetragonal space group *P*4/*mnc* and arranges itself in an apparent body centred lattice with a cluster on every edge as well as in the centre of the unit cell. The highly negative charge of 11- is balanced by caesium ions which lie disordered in the unit cell along with water molecules. It was not possible to resolve the positions of the highly disordered caesium cations outside of the anionic cluster, hence the squeeze routine[244] was applied in the refinement of the crystal structure to account for missed electron density. In total the squeeze routine accounted for 1862 e^- in a volume of 3888 Å^3 in the unit cell, which roughly fit the electron count for the caesium counter ions and solvent molecules in the structure of 1902 e^- for 23 Cs^+ ions and 66 water molecules. And while the electron count of the squeeze routine in general cannot be used as a proof for the contents within the unit cell, as it highly depends on good high angle data, it can be used as a feasibility check.

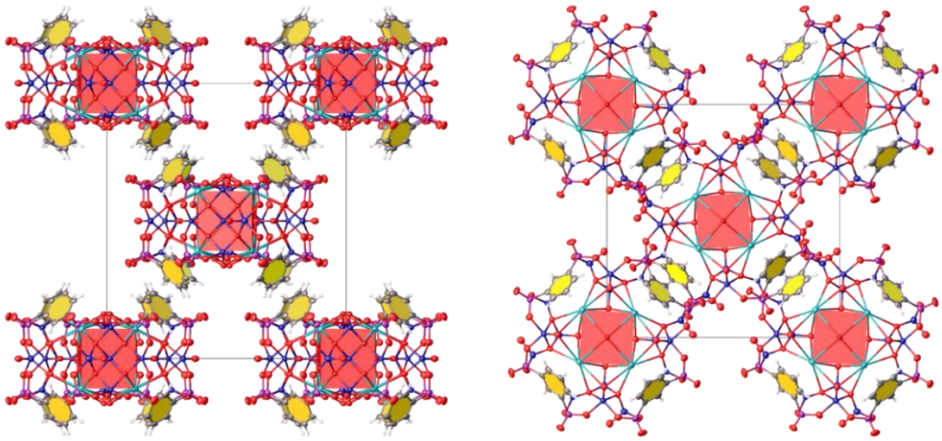

Figure 3.3.5 – Packing of **V_{20}H-Cs** looking down the crystallographic *a*-axis [100] (left) and *c*-axis [001] (right).

The highly symmetric packing of **V_{20}H-Cs** enables an extension to the cation-π interactions present in the cluster. All eight DPB-H^{4-} ligands are building out π-π interactions in a parallel displaced fashion with eight neighbouring capsules. The distances for these interactions are d(π-π) = 3.412(11) Å with a centroid to centroid distance of 3.741(8) Å and an off-set of 1.534(16) Å as shown in Figure 3.3.6. It has been demonstrated in the literature that the sequential

interaction of cation-π interactions and π-π interactions behave in a cooperative instead of an additive fashion.[138] Computational studies have shown that the presence of a cation can lead to a three to six fold increase of the energy of the π- π interactions.[177] Additionally the presence of a π- π interaction increases the energy of the cation-π interaction, however by only a small amount. To view those interactions isolated from each other would therefore paint a false picture of the nature of the interaction. The combined interaction has to be seen as one cation-π-π-cation interaction.

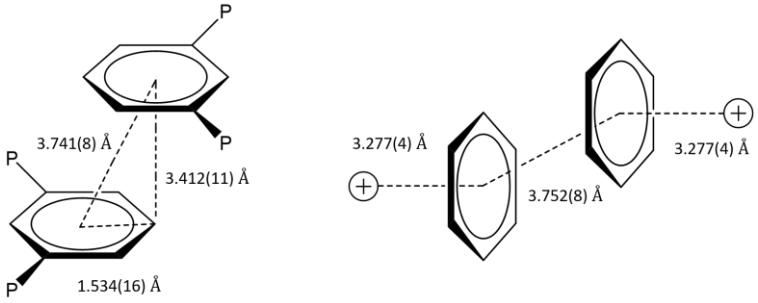

Figure 3.3.6 – Schematic ***π*-*π*** stacking and extended cation-***π*-*π***-cation interactions with distances in **V_{20}H-Cs**.

3.4 Structural comparison between V_{20}H-Cs, V_{20}H-Rb and V_{20}H-K

In the following section the structure and composition of **V_{20}H-Cs** shall be compared with the compounds

$Rb_{13}[(V_5O_9)_4(C_6H_4(PO_3)_2)_8NaRb_8Cl_2] \cdot 30\ H_2O$ - (**V_{20}H-Rb, 6**)
$K_{12}[(V_5O_9)_4(C_6H_4(PO_3)_2)_8K_9]N_3 \cdot 27\ (H_2O)$ - (**V_{20}H-K, 7**).

3.4.1 The alkali metal cube

The alkali metal cube has two labile ligands in the axial positions, which can be occupied by a range of different ligands or anions, such as water, acetonitrile or chloride ions. In the case of **V_{20}H-Rb** these positions were resolved to be occupied by two chloride ions as shown in Figure 3.4.1, whereas in **V_{20}H-K** two water molecules were modelled a disordered over multiple positions. As mentioned before the alkali metal cube of **V_{20}H-Cs** features a half-occupied sodium ion in the middle of the structure which is attached to two water molecules as shown in Figure 3.3.2.

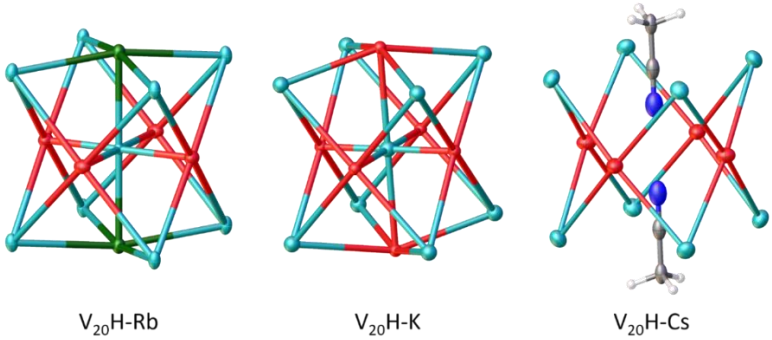

Figure 3.4.1 – Different ligands in the axial positions of the alkali metal cube. Disorder omitted for clarity.

Whenever the sodium ion is not present in the structure however, two acetonitrile molecules are occupying the axial positions. Different from V_{20}H-Rb and V_{20}H-Cs the middle of the cube in V_{20}H-K is fully occupied by a potassium ion instead of a sodium ion. This is possible due to the difference in size of the alkali metal (AM) ions and the respective alkali metal oxygen bond lengths within the cluster. With increasing ion radius of the alkali metal cation, the positive charge becomes more diffuse and the cation becomes softer by means of the hard-soft acid-base principle (HSAB). This elongates the preferred alkali metal oxygen bond lengths, which can be exemplified by a survey within the Cambridge structural database (CSD) for $AM(H_2O)_6$ octahedra. Table 3.4.1 shows the preferred bond lengths of the different alkali metal cations with oxygen donors. It can be seen that only sodium and potassium are observed to build out AM-O distances shorter than 2.7 Å. As the inside of the $\{V_{20}\}$ torus is constraint in size by the organic ligands and the pentanuclear half-capsules neither rubidium nor caesium are able to occupy the centre of the alkali metal cube. The alkali metal oxygen bond lengths for V_{20}H-K and V_{20}H-Rb can be found in Table 3.4.2 and Table 3.4.3.

Table 3.4.1 – Minimum, maximum and mean distances for AM-O bonds in $AM(H_2O)_6$ octahedra found in the CSD.

Cation	Min / Å	Mean / Å	Max / Å	Observations
Na^+	1.896	2.322	3.024	88
K^+	1.944	2.676	3.090	52
Rb^+	2.783	2.942	3.173	14
Cs^+	3.037	3.211	3.394	17

Table 3.4.2 – Selected K-O bond lengths in **V_{20}H-K**.

Bond	Bond length / Å	Bond	Bond length / Å
K2-O10	2.842(5)	**O9-K1**	2.848(5)
K2-O2	3.198(5)	**O11-K1^{2}**	2.867(5)
K2-O6	3.197(6)	**O4-K1**	3.199(5)
K2-O3	3.34(5)	**O4-K1^{1}**	3.199(5)
K2-O1	3.370(8)	**O6-K1^{2}**	3.238(5)
K2-C6	3.404(7)	**O3-K1**	3.42(5)
K2-O7A	3.36(5)	**O1-K3**	2.268(7)
K2-O8^{1}	2.814(5)	**O5-K1^{2}**	3.4221(17)
K2-O24	2.34(2)	**O5-K1**	3.4222(17)
K2-O25	2.75(3)	**O5-K3**	2.291(8)
K1-O26	2.52(3)	**O7A-K1**	3.42(5)
^{1}+X,-Y,+Z; ^{2}1-X,+Y,-Z			

Table 3.4.3 – Bond lengths for the alkali metal cube in **V_{20}H-Rb**.

Bond	Bond length / Å	Bond	Bond length / Å
Rb1-Cl^{1}	3.2529(7)	**Rb1-O2^{2}**	3.160(3)
Rb1-O4^{1}	2.871(3)	**Rb1-O3A**	3.478(7)
Rb1-O4	2.871(3)	**Rb1-O3A^{3}**	3.478(7)
Rb1-O1^{2}	3.4010(6)	**Cl1-Na1**	2.863(3)
Rb1-O1	3.4010(6)	**O1-Na1**	2.340(7)
Rb1-O2	3.160(3)		
^{1}+Y,+X,+Z; ^{2}1-Y,+X,+Z; ^{3}+Y,+X,1-Z			

3.4.2 The pentanuclear half-capsule

In all three compounds the pentanuclear half-capsule shows positional disorder of the vanadyl groups which were modelled as disordered over two positions with 50:50 occupancy. Selected bond lengths for V_{20}H-Rb and V_{20}H-K can be seen in Table 3.4.5 and Table 3.4.6. The bond valence sum analysis for **V_{20}H-K** is less straight forward then for **V_{20}H-Rb** and **V_{20}H-Cs**. Its results can be seen in Table 3.4.4. The positional disorder of the vanadyl groups as well as delocalisation of electrons within the half-capsules leads to less defined and less resolved bond lengths and consequently less accurate BVS calculations. The central vanadium ion V1 (Figure 3.4.2) with the nominal oxidation state 5 features a V=O bond length of 1.653(8) Å which is uncommonly long for this type of bond. The reason for this bond elongation is the positive charge of the potassium cation which is only 2.268(7) Å away from the terminal *oxo*-ligand and pulls the *oxo*-ligand away from the vanadium(V) ion. While the bond length of 1.653(8) Å can be explained in this way the V=O bond lengths of the disordered *oxo*-vanadium(V) ions in the middle of the torus should show more common bond lengths of 1.60 Å as they are usually found in polyoxovanadates and vanadium compounds. Wherever needed those bond lengths were chosen to be restrained to a target value of 1.600 Å +/- 0.01 Å.

Table 3.4.4 – BVS Calculations for **V_{20}H-K** (left) and **V_{20}H-Rb** (right).

V_{20}H-K	**BVS**	**Oxidation state**	**V_{20}H-Rb**	**BVS**	**Oxidation state**
V1	4.36	5	V1	4.55	5
V2	4.14	4	V2	4.00	4
V3	3.85	4	V3	3.82	4
V3a	3.88	4	V3a	3.95	4
V4	4.06	4			
V5	4.40	5			
V6	4.11	4			
V7	4.02	4			
V7a	3.84	4			

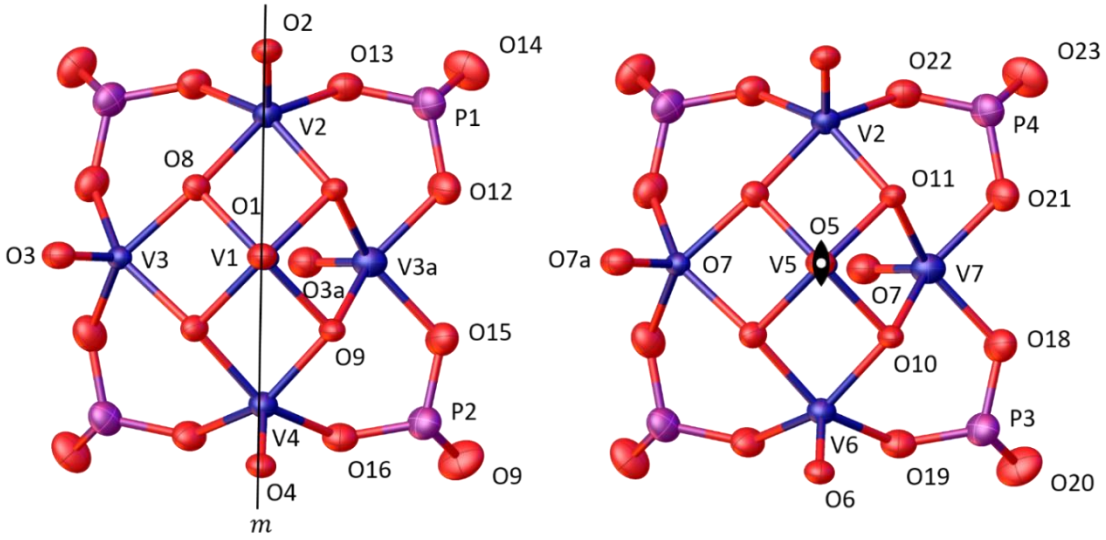

Figure 3.4.2 - Naming scheme for the pentanuclear half-capsules of **V_{20}H-K**. One half-capsule is symmetry generated by a mirror plane (left) and one half-capsule by a two-fold rotation axis with a centre of symmetry (right).

Table 3.4.5 – V-O bond lengths for **V_{20}H-K**.

Bond	Bond length / Å	Bond	Bond length / Å	Bond	Bond length / Å
V1-O1	1.653(8)	**V2-O2**	1.587(7)	**V6-O6**	1.603(5)
V1-O9^{1}	1.926(5)	**V2-O13^{1}**	1.978(5)	**V6-O11**	1.947(5)
V1-O9	1.926(5)	**V2-O13**	1.978(5)	**V6-O22^{2}**	1.960(5)
V1-O8	1.929(5)	**V2-O8^{1}**	1.944(5)	**V6-O19**	1.984(5)
V1-O8^{1}	1.929(5)	**V2-O8**	1.944(5)	**V6-O10**	1.933(5)
V5-O5	1.624(8)	**V3-O3**	1.600(14)	**V7-O7**	1.625(10)
V5-O10^{2}	1.943(5)	**V3-O9**	1.943(5)	**V7-O10**	2.023(6)
V5-O10	1.943(5)	**V3-O8^{1}**	1.958(5)	**V7-O11^{2}**	1.946(5)
V5-O11^{2}	1.932(5)	**V3-O15**	2.042(5)	**V7-O21**	1.895(6)
V5-O11	1.932(5)	**V3-O12**	2.049(5)	**V7-O18**	1.961(6)

V4-O4	1.609(7)	**V3A-O3A**	1.645(11)	**V7A-O7A**	1.602(14)
V4-O9	1.941(5)	**V3A-O9**	1.988(5)	**V7A-O10**	1.914(5)
V4-O9[1]	1.941(5)	**V3A-O8[1]**	1.984(5)	**V7A-O11[2]**	1.952(5)
V4-O16	1.977(5)	**V3A-O12**	1.925(5)	**V7A-O21**	2.090(6)
V4-O16	1.977(5)	**V3A-O15**	1.956(6)	**V7A-O18**	2.027(6)
[1]+X,-Y,+Z; [2]1-X,+Y,-Z					

Table 3.4.6 – Vanadium oxygen bond lengths in the pentanuclear half-capsule of **V_{20}H-Rb**.

Bond	Bond length / Å	Bond	Bond length / Å
V1-O1	1.638(8)	**V3-O3**	1.624(9)
V1-O4	1.911(3)	**V3-O4[5]**	2.002(4)
V1-O4[5]	1.911(3)	**V3-O4**	2.002(4)
V1-O4[6]	1.911(3)	**V3-O5[5]**	1.971(4)
V1-O4[4]	1.911(3)	**V3-O5**	1.971(4)
V2-O2	1.619(5)	**V3A-O3A**	1.577(7)
V2-O4	1.929(3)	**V3A-O4[5]**	1.958(4)
V2-O4[4]	1.929(3)	**V3A-O4**	1.958(4)
V2-O6	1.994(3)	**V3A-O5**	2.044(4)
V2-O6[4]	1.994(3)	**V3A-O5[5]**	2.044(4)
		V3A-O3A[3]	2.244(8)
[3]+Y,+X,1-Z; [4]+X,1-Y,+Z; [5]+X,+Y,1-Z; [6]+X,1-Y,1-Z			

3.4.3 Space group and packing

Although identical in their core structure, **V_{20}H – Cs, Rb, K** were solved in three different space groups. **V_{20}H-Cs** and **V_{20}H-Rb** were solved in the high symmetry tetragonal space groups *P4/mnc* and *I4/mmm* whereas **V_{20}H-K** was solved in the lower symmetry monoclinic space group *C2/m*. The unit cells are compared in Table 3.4.7.

It is apparent that **V_{20}H-Cs** and **V_{20}H-Rb** are quite similar in unit cell dimensions and space group. The only difference being the difference in the length of the cell axes of **V_{20}H-Cs**, which are a bit smaller and the cell volume therefore a bit less. The symmetry is however slightly reduced, changing from the body-centred cell of *I*4/*mmm* for **V_{20}H-Rb** to the primitive tetragonal cell of *P*4/*mnc*. The reason for this change in symmetry is a slight rotation of the cluster in the centre against its neighbouring clusters sitting on the edges of the unit cell. This is shown in Figure 3.4.3 in which the crystal packing diagrams in [100] direction for **V_{20}H-Cs** and **V_{20}H-Rb** are shown next to each other. The black lines are indicating the orientation of the clusters within the unit cell. One can see that for **V_{20}H-Cs** the cluster are rotated 6.2(3)° against each other, which reduces the symmetry of the crystal structure. The relation between the space groups is shown as a Bärnighausen diagram in Figure 3.4.4. It can be seen that *P*4/*mnc* is a klassengleiche k-subgroup to *I*4/*mmm* with index 2. This means that *P*4/*mnc* and *I*4/*mmm* share the same point group but not all translations. In this case the slight rotation of the central {V_{20}} cluster leads to the removal of all body-centred translations of *I*4/*mmm*, resulting in *P*4/*mnc*.

Table 3.4.7 – Comparison of the unit cells for **V_{20}H-Cs**, **-Rb**, **-K**.

AM	***a*** / Å	***b*** / Å	***c*** / Å	***α*** / °	***β*** / °	***γ*** / °	***V*** /Å^3
Cs	19.9912(6)	19.9912(6)	22.9901(7)	90	90	90	9187.9(5)
Rb	20.5137(5)	20.5137(5)	23.0839(7)	90	90	90	9714.0(5)
K	30.2412(12)	20.5427(8)	17.2658(7)	90	110.393(2)	90	10053.9(7)
AM	***Z***	***Z′***	**SG**				
Cs	2	0.125	*P4/mnc*				
Rb	2	0.0625	*I4/mmm*				
K	2	0.25	*C2/m*				

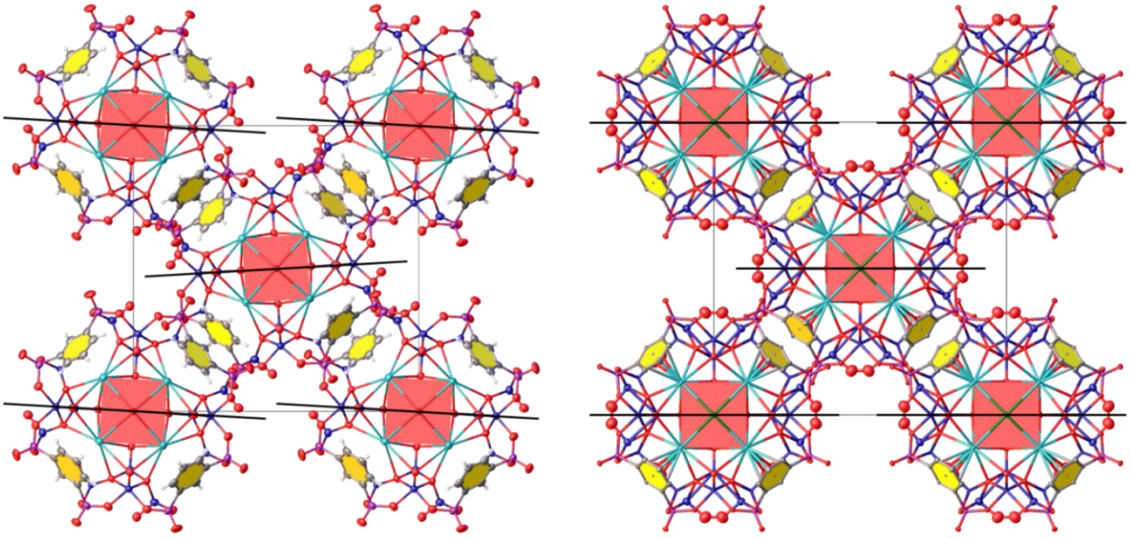

Figure 3.4.3 – Comparison of the packing in 100 direction between **V_{20}H-Cs** (left) and **V_{20}H-Rb** (right). The lines are drawn in the middle of the cluster and indicate their orientation.

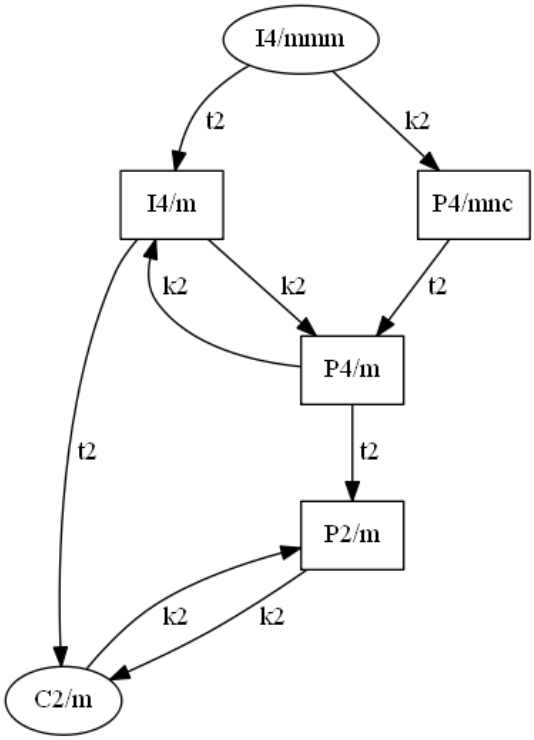

Figure 3.4.4 – Bärnighausen diagram of the space group relations between *I4/mmm*, *P4/mnc* and *C2/m* (kx = klassengleiche, tx = translationengleiche, x = Index).

This slight difference likely has its origin the geometric arrangement of the π-π interaction. The plane to plane angle between the two aromatic benzene rings is 5.1(3)°, which causes the skewed alignment of the {V_{20}} clusters. Different from **V_{20}H-Cs**, the crystal packing for **V_{20}H-Rb** is completely symmetric as can be clearly seen in Figure 3.4.3. The plane-plane angle of 0.0(3)° in the π-π interactions.

Table 3.4.8 – Comparison between the cation-π and π-π distances.

	π - π	**π-C**	**Displacement**	**Cation-π**	**π –π-angle**
Cs^+	3.741(8) Å	3.412(11) Å	1.534(16) Å	3.277(4) Å	5.1(3) °
Rb^+	3.912(5) Å	3.624(6) Å	1.475(10) Å	3.271(3) Å	0.0(3) °
K^+	-	-	-	3.232(4) Å	-

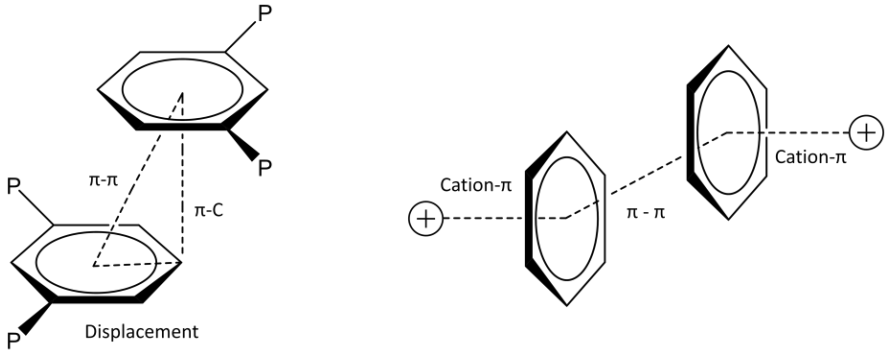

Figure 3.4.5 - General scheme for the cation-π and π-π interactions (c = centre).

The biggest difference in the packing of the three isostructural polyoxovanadate clusters can be seen in **V_{20}H-K**. The *π-π* interactions between neighbouring clusters present in **V_{20}H-Rb** and **V_{20}H-Cs** are missing in **V_{20}H-K**. This manifests itself in the reduced symmetry of the crystal lattice. The anionic {V_{20}} polyoxovanadate clusters are not held together by intramolecular forces anymore and arrange themselves on half of the twelve edges of a monoclinic unit cell stacking in *ABCABC* fashion in the crystallographic [101] direction. This can be seen on the right side of Figure 3.4.6.which shows the packing in [010] direction. The distance between A, B and C is 13.323(3)Å, measured centre to centre. Within a layer the distance between two clusters is 21.2202(7) Ã. The missing π-π interactions led to a reduction in symmetry within the crystal

structure. The space group is now the monoclinic body centred *C*2/*m*, with a reduced point group of 2/*m* compared to *4*/*mmm* of *I*4/*mmm*. The reason for the missing cation-π-π-cation interactions could lie in the difference of strength in the interaction within the three clusters, which is dependent on the cation. Because the cation-π interaction can be seen as a simple ion-quadrupole interaction in a first approximation it might seem intuitive that the strength of this interaction decreases for alkali metal down the periodic table, i.e. Na > K > Rb > Cs. Computational and experimental studies of $AM^{+}\cdots\pi$-arene interactions in the gas phase confirm this trend. The picture in solution or the solid state however might look differently. Indeed, Kochi et. al. have studied the affinity of alkali metal cations towards a hexakis(methoxymethyl)benzene ligand in the solid state and saw an increase in affinity with $Cs^{+} \approx Rb^{+} > K^{+} > Na^{+}$. The fact that we do not see any π-π interactions in the monoclinic crystal structure plus the known effect of cooperativity between cation-π interactions and π-π interactions might be the reason for the reduced symmetry in **V_{20}H-K**. However, as we will see further down, the powder pattern for the bulk sample indicates the presence of a tetragonal phase for **V_{20}H-K** and therefore the possible presence of π-π interactions.

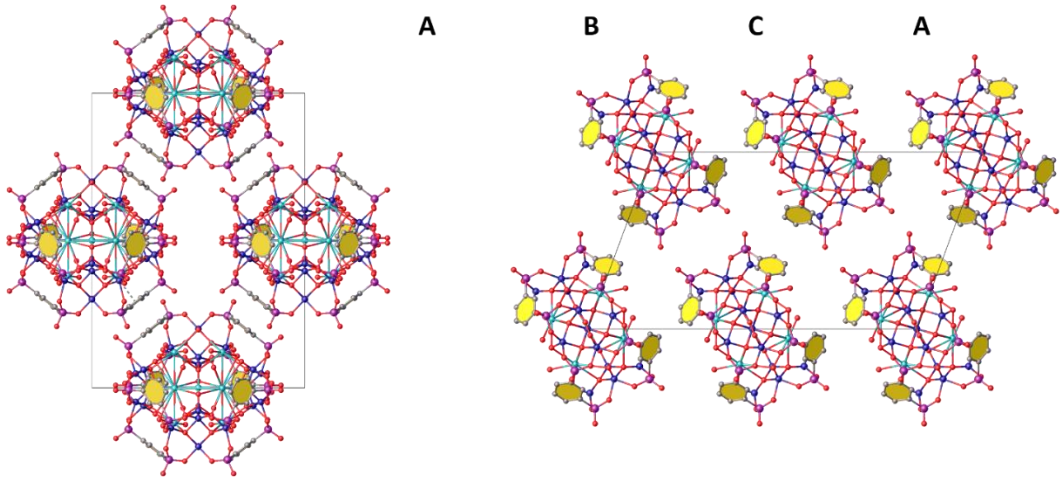

Figure 3.4.6 – Packing of **V_{20}H-K** in the crystallographic [001] direction looking down the *c*-axis (left) and in [010] direction looking down the *b*-axis.

In none of the **V_{20}H-AM** structures was it possible to resolve the positions of the alkali metal cations and water molecules in between the capsules in a meaningful way. Therefore the squeeze routine[244] was applied with the program package PLATON.[245]

Table 3.4.9 – Crystallographic tables for **V_{20}H-Cs**, **-Rb** and **-K**.

Identification code	**V_{20}H-Cs**	**V_{20}H-Rb**	**V_{20}H-K**
Empirical formula	$C_{50}H_{35}Cs_8NNa_{0.5}O_{85}P_{16}V_{20}$	$C_{48}H_{32}Cl_2NaO_{88}P_{16}Rb_8V_{20}$	$C_{48}H_{32}K_9O_{88.02}P_{16}V_{20}Na_{0.5}$
Formula weight(g/mol)	4598.88	4308.7	3894.77
Temperature/K	100	99.99	100
Crystal system	tetragonal	tetragonal	monoclinic
Space group	*P*4/*mnc*	*I*4/*mmm*	*C*2/*m*
a/Å	19.9912(6)	20.5137(5)	30.2412(12)
b/Å	19.9912(6)	20.5137(5)	20.5427(8)
c/Å	22.9901(7)	23.0839(7)	17.2658(7)
α/°	90	90	90
β/°	90	90	110.393(2)
γ/°	90	90	90
Volume/Å^3	9187.9(6)	9714.0(6)	10053.9(7)
Z	2	2	2
ρ_{calc} g/cm^3	1.662	1.473	1.287
μ/mm^{-1}	2.739	3.135	1.263
F(000)	4335	4130	3801
Crystal size/mm^3	0.14 × 0.1 × 0.08	0.18 × 0.1 × 0.04	0.13 × 0.13 × 0.13
Radiation	MoKα (λ = 0.71073)	MoKα (λ = 0.71073)	MoKα (λ = 0.71073)
2Θ range for data collection/°	4.568 to 55.168	4.778 to 59.366	4.85 to 54.642
Index ranges	-26 ≤ h ≤ 25, -25 ≤ k ≤ 26, -29 ≤ l ≤ 29	-28 ≤ h ≤ 28 -28 ≤ k ≤ 28 -32 ≤ l ≤ 32	-38 ≤ h ≤ 38 -26 ≤ k ≤ 26 -22 ≤ l ≤ 22
Reflections collected	201697	149504	110330
Independent reflections	5459 [R_{int} = 0.1310, R_{sigma} = 0.0253]	3832 [R_{int} = 0.0885 R_{sigma} = 0.0199]	11569 [R_{int} = 0.1457, R_{sigma} = 0.0682]
Data/restraints/ parameters	5459/27/246	3832/8/127	11569/13/467
Goodness-of-fit on F^2	1.033	1.004	1.046
Final R indexes [I>=2σ (I)]	R_1 = 0.0507, wR_2 = 0.1143	R_1 = 0.0615, wR_2 = 0.1671	R_1 = 0.0782, wR_2 = 0.2303
Final R indexes [all data]	R_1 = 0.0736, wR_2 = 0.1297	R_1 = 0.0783, wR_2 = 0.1854	R_1 = 0.1250, wR_2 = 0.2638
Largest diff. peak/hole / e Å^{-3}	2.17/-1.26	3.07/-2.63	1.38/-0.71

3.5 Solid state characterisation

The structures and composition of the $\{V_{20}\}$ compounds in the solid state were further confirmed by IR, CHN, TGA and PXRD. Solution studies were carried out by UV-VIS, NMR and MS.

3.5.1 PXRD

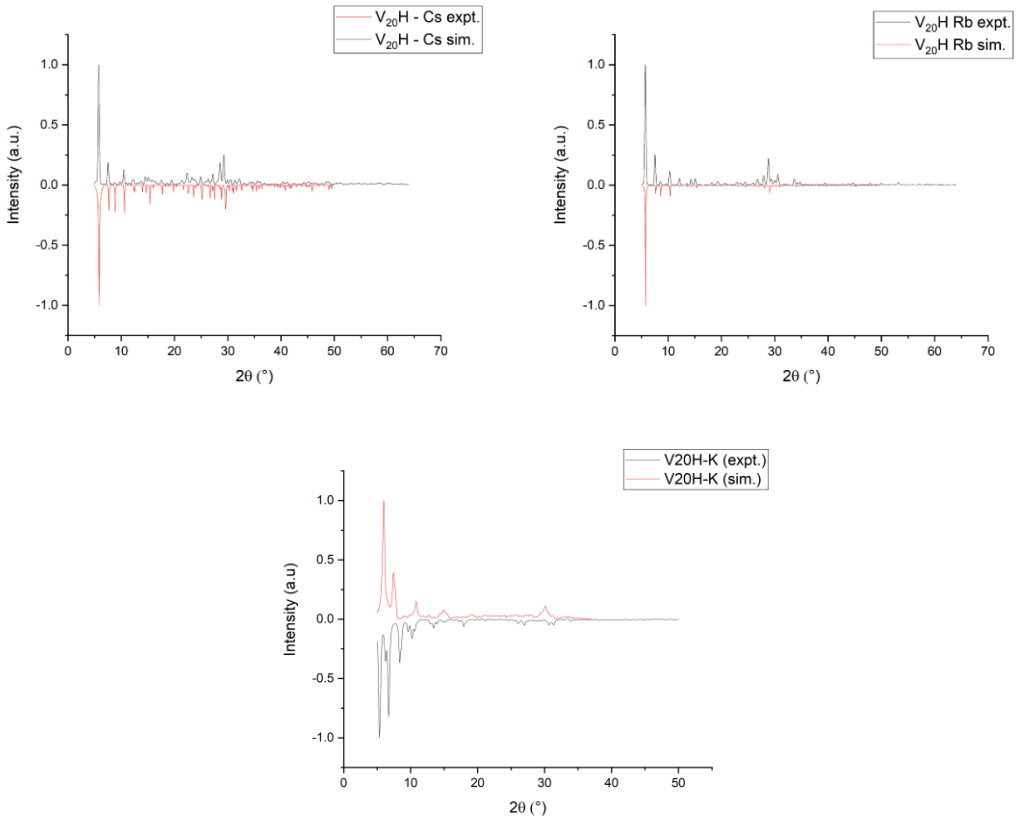

Figure 3.5.1 – PXRD of 1-3. Experimental (red, positive). Simulated (black, negative).

To investigate the phase purity of the crystalline samples as well as the absence of crystalline impurities PXRD patterns were recorded for **V_{20}H-Cs**, **-Rb** and **-K**. Because the samples lost crystallinity upon solvent loss and grinding rather quickly, they were measured in capillaries with minimal grinding in their mother liquor. Differences in intensity of the peaks therefore are due to one or multiple preferred orientation of the crystals. All simulated peaks were found in the PXRD spectra of **V_{20}H-Cs** and **V_{20}H-Rb**, indicating phase purity of the tetragonal phase determined by SXRD. The spectra for **V_{20}H-K** was collected in a capillary filled with neat DMF instead of mother liquor. The quality of the spectra is therefore reduced, possibly due to loss of crystal water

to the DMF solution. While phase purity cannot be established for **V_{20}H-K**, the peak pattern does loosely match the simulated pattern. By comparison the powder pattern for **V_{20}H-K** looks similar to the powder patterns for **V_{20}H-Rb** and **V_{20}H-Cs**. This indicates that apart from the monoclinic phase determined by SXRD there might be tetragonal phase present in the sample. Further analysis requiring phase purity such as magnetic measurements could therefore not be carried out on **V_{20}H-K**.

3.5.2 IR-spectroscopy

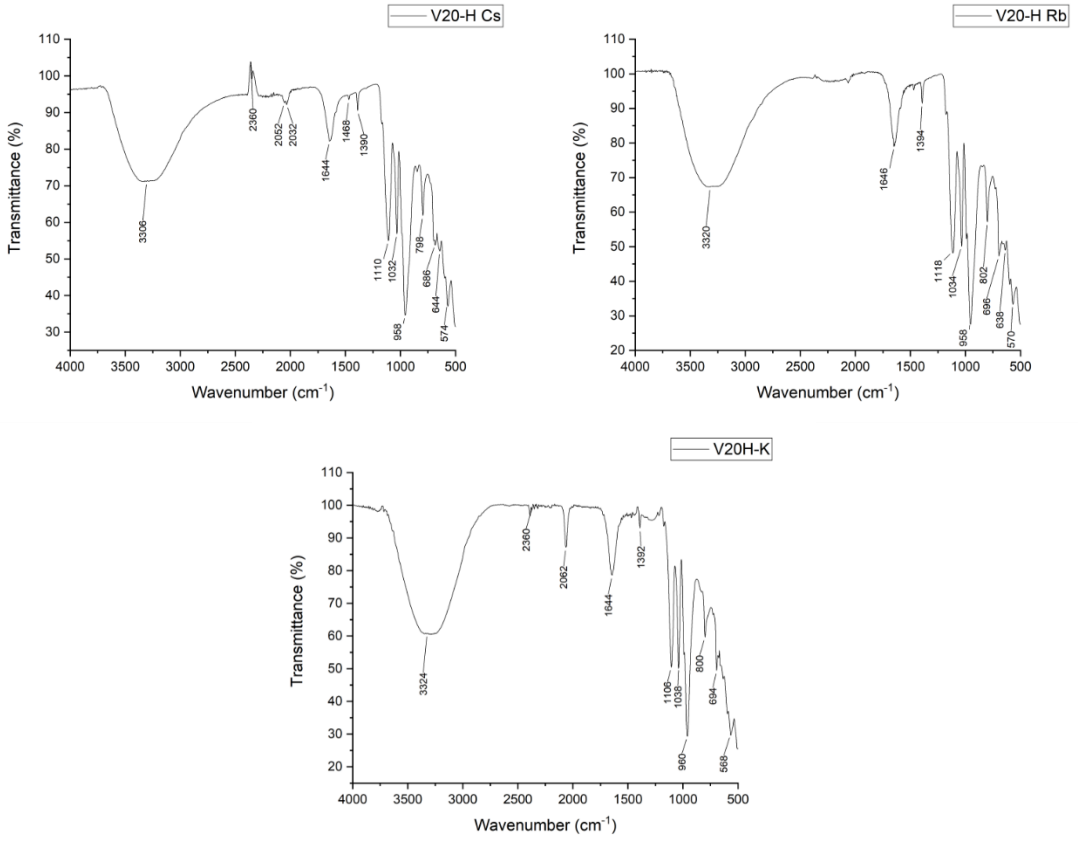

Figure 3.5.2 – IR spectrum of {V_{20}} from 4000 to 480 cm^{-1}.

Infrared spectra were recorded from 4000 cm^{-1} to 500 cm^{-1}. All three compounds display largely the same spectra, as was expected from the similar molecular structures. Differences due to the change in counter ions were not observed. All signals were assigned by comparisons with the ligand spectra and comparisons with literature known compounds.[92, 246] The broad signals at

around 3300 cm^{-1} and 1644 cm^{-1} are due to crystal water. The small amount of acetonitrile molecules in the structure give rise to the signal at 2032 cm^{-1}. Signals from 1468 cm^{-1} and 1390 cm^{-1} (CH_3 deformation) indicate the presence of small amounts of acetonitrile in the structure as well. The signal at around 1110 cm^{-1} and 1032 cm^{-1} can be attributed to the phosphonate ligand while the broad signals at around 958 cm^{-1} are stemming from the V=O double bonds with vanadium(IV) and vanadium(V). A slight anomaly is visible in some spectra around 2360 cm^{-1}, which stems from CO_2 and is due to air bubbles trapped in the layer of material on the diamond of the ATR attachment (attenuated total reflectance). Overall the IR analysis supports the assignment of the molecular composition by SXRD analysis.

3.5.3 TGA

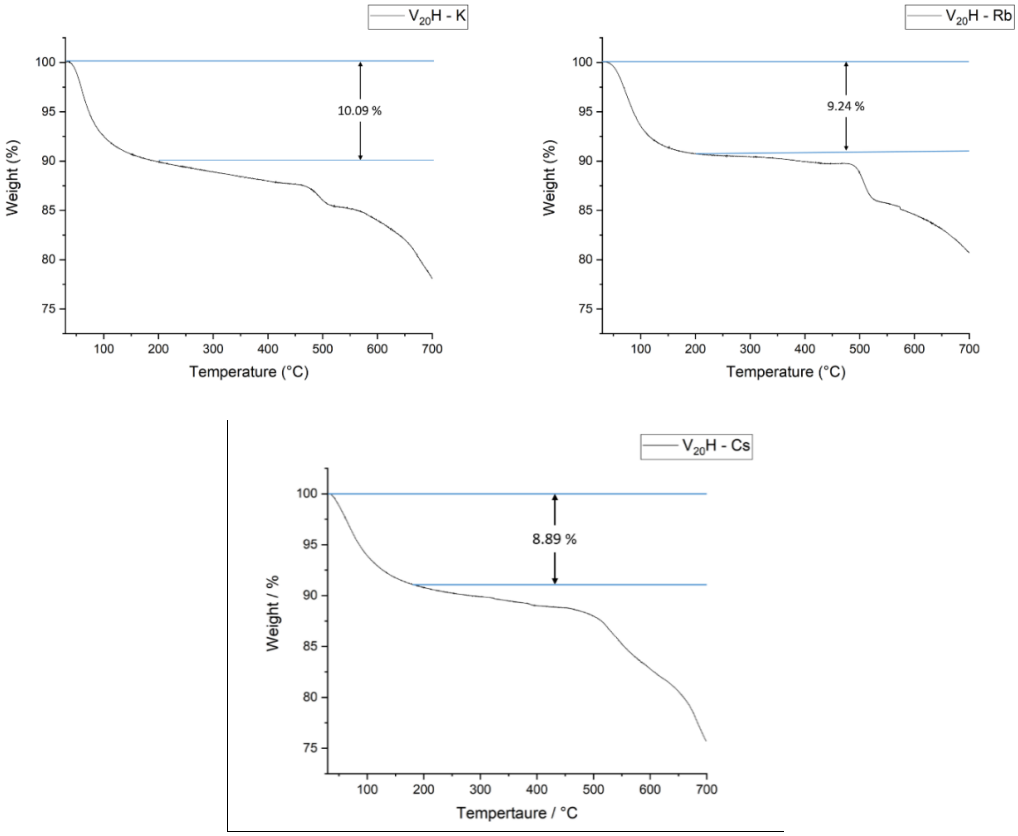

Figure 3.5.3 – Thermogravimetric analysis of **V_{20}H-K**, **-Rb** and **-Cs**.

To determine the amount of crystal water in the samples as well as to investigate their thermal stability TGA curves of **V_{20}H-K**, **-Rb** and **-Cs** were collected in a nitrogen atmosphere from 30°C to 700°C at a rate 5°C per minute. Of all TGA graphs the curve for **V_{20}H-Rb** shows the

sharpest step behaviour. The first drop of 9.24 % between 30°C and 200°C in the **V_{20}H-Rb** graph corresponds to 30 H_2O molecules (theoretical value 9.17 %) of water molecules within the unit cell. The subsequent drop from 290°C to 470°C and from 470°C to 525°C can be attributed to ligand degradation. The formation of metal oxides can be seen in from 500°C onwards. The TGA curve of **V_{20}H-K** and **V_{20}H-Cs** are less pronounced and therefore difficult to quantify. Analysis of the curve derivatives however show similar steps sizes from 30°C to 200°C. **V_{20}H-K** loses 10.09 % of its weight which corresponds to 30 water molecules (theoretical value 10.10 %). The weight loss of 8.89 % in **V_{20}H-Cs** corresponds to 33 water molecules (theoretical value 8.87 %). All values are in line with CHN analyses as can be seen in the experimental and therefore confirm the molecular compositions of the compounds.

3.5.4 NMR-spectroscopy

After solid state characterisation revealed cation-π interactions as integral part of the $\{V_{20}\}$ structures the question arose if these non-covalent interactions would exist in solution or if they were just a phenomenon in the solid state. As attempts in-house to investigate the complexes by mass spectrometry failed the focus was laid on NMR spectroscopy of the paramagnetic clusters.

The ^{1}H, ^{13}C and ^{31}P-NMR spectra of the free ligand H_4DPB-H are shown in Figure 3.5.4. The ^{1}H-NMR spectrum of DPB-H shows three sets of signals in the aromatic region. The signal for the H^4 is a triplet at 8.00 ppm with a coupling constant of $^{3}J(^{1}H^{1}H)$ = 13.24 Hz. H^3 is split up in a doublet of doublet of doublet at 7.84 ppm with coupling constants of $^{3}J(^{1}H^{31}P)$ = 14.46 Hz, $^{3}J(^{1}H^{1}H)$ = 7.68 Hz and $^{5}J(^{1}H^{31}P)$ = 1.40 Hz. H^4 presents itself as a multiplet from 7.52 – 7.57 ppm. The signals are hereby split up by the coupling between protons as well as between protons and the NMR active ^{31}P nucleus. The ^{13}C-NMR shows 4 signals of which C^2 is observed as a doublet of doublet at 139.53 ppm with coupling constants of $^{1}J(^{13}C^{31}P)$ = 166.34 Hz and $^{3}J(^{13}C^{31}P)$ = 10.76 Hz. The signals for C^1 and C^4 split up in triplets at 131.11 ppm and 126.92 ppm with coupling constants of $^{2}J(^{13}C^{31}P)$ = 9.51 Hz and $^{3}J(^{13}C^{31}P)$ = 24.71 Hz respectively. The ^{31}P-NMR only features one signal for the two symmetry-related ^{31}P phosphorus nuclei.

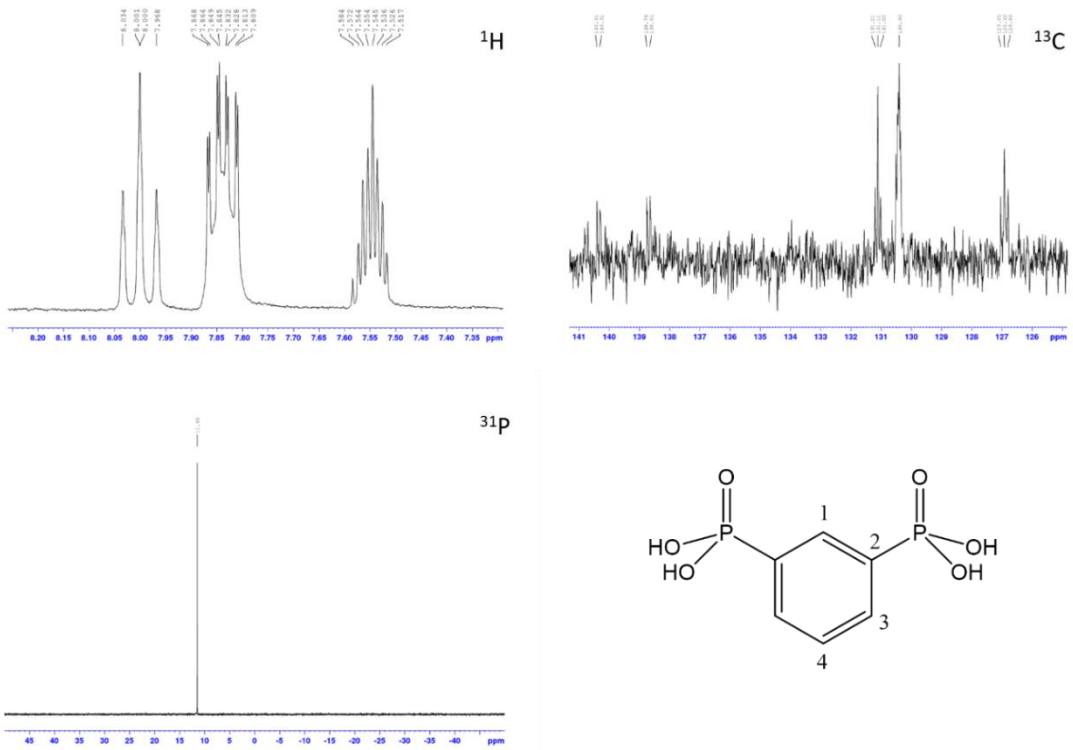

Figure 3.5.4 – ^{1}H, ^{13}C and ^{31}P-NMR spectra of DPB-H in D_2O.

A sample of **V_{20}H-Cs** in D_2O was prepared. The ^{1}H-NMR spectra of **V_{20}H-Cs** can be seen in Figure 3.5.5 and is showing multiple features. The signal at 4.72 ppm is the solvent peak of D_2O. In the aromatic region are three sharp and somewhat defined signals which evidently belong to the aromatic protons of the ligand. The three signals are slightly but not significantly shifted upfield in comparison to the NMR spectrum of the free ligand, which might be because of the difference in concentration in solution. Downfield next to the ligand signals is an intense broad signal at 8.59 ppm. Peak broadening is a characteristic phenomenon of paramagnetic species in NMR spectroscopy. As the $\{V_{20}\}$ cluster contains 16 V(IV) and therefore d^1-ions it is highly paramagnetic in nature. The broad signals therefore are likely to belong to aromatic protons, who are in the vicinity of the paramagnetic V(IV) ions.

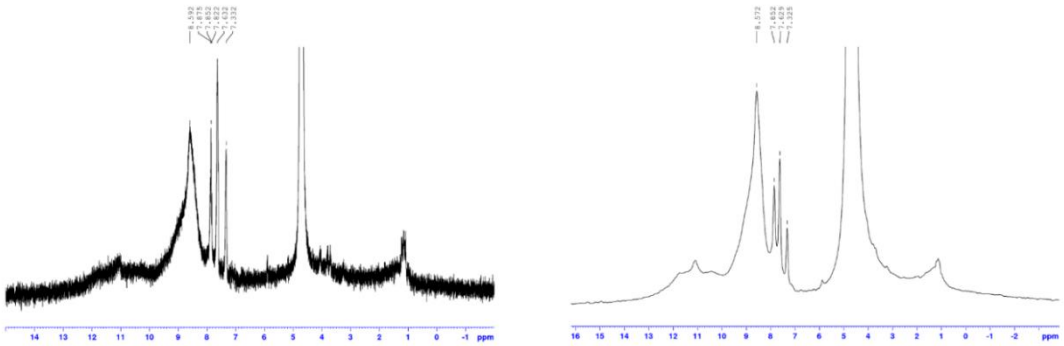

Figure 3.5.5 – ^{1}H-NMR spectrum of **V_{20}H-Cs** in D_2O.

The reason for peak broadening is the fast relaxation of the nuclear spins in the presence of unpaired electrons compared to a non-paramagnetic environment. The parameters of the pulse sequence for the NMR experiment can be altered to account for this effect to produce a clearer spectrum, which can be seen in Figure 3.5.5 on the right side. Apart from the intense peak at 8.59 ppm there are a series of even broader signals with low intensity. These could stem from protons sitting directly on the polyoxovanadate half-capsules on the oxygen ions attached to the paramagnetic vanadium(IV) centres.

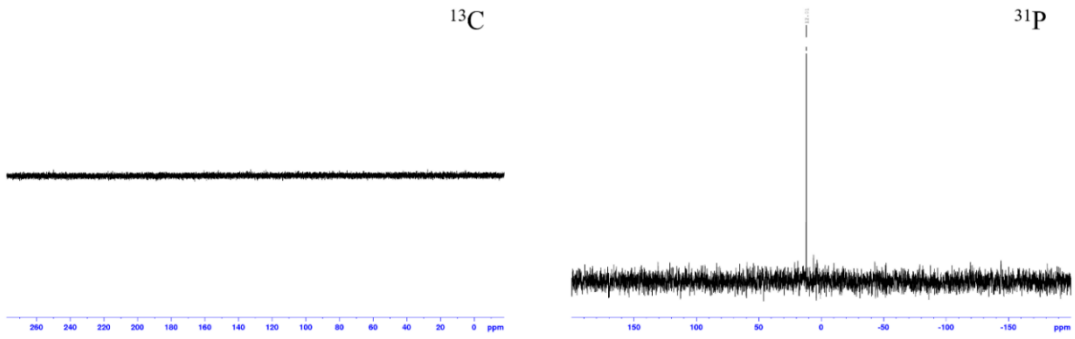

Figure 3.5.6 – ^{13}C and ^{31}P-NMR spectra of **V_{20}H-Cs**.

Because of the difference in spin density arising from p orbitals heteronuclei are affected differently by paramagnetic species. Surprisingly still, the ^{13}C-NMR does not show any signals at all, which is likely because of the relaxation processes being too fast for the measurement. The ^{31}P-NMR shows one sharp signal at 12.01 ppm which is slightly but not significantly shifted

downfield in comparison to the free ligand in solution. The ^{1}H-NMR spectra of **V_{20}H-Rb** and **V_{20}H-K** were identical to **V_{20}H-Cs** with the exception of a DMF solvent signal in the spectra of **V_{20}H-K**.

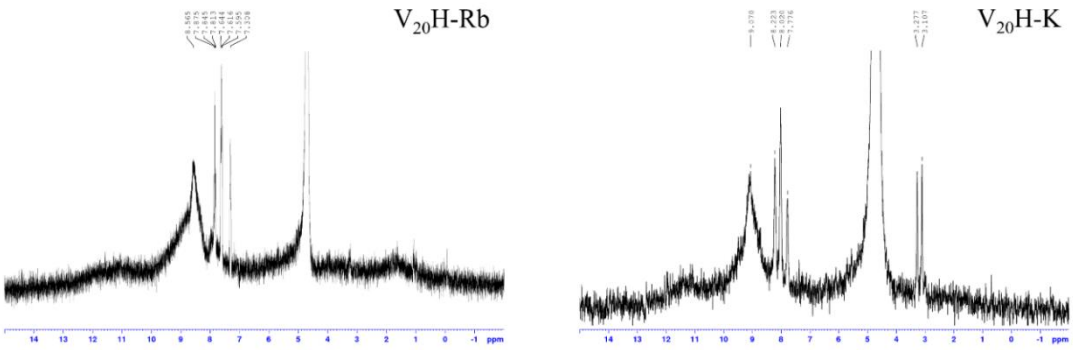

Figure 3.5.7 – ^{1}H-NMR spectra of **V_{20}H-Rb** and **V_{20}H-K**.

The question arose if the signals are stemming from the paramagnetic {V_{20}} system or the free ligand. Therefore diffusion-ordered (DOSY) NMR experiments were chosen to investigate the nature of these signals. This NMR technique allows the determination of the diffusion coefficient, by measuring multiple NMR spectra with varying field gradients. With increasing field gradient the intensity of a signal becomes gradually smaller and is dependent on the diffusion coefficient, which can be seen in the Stejskal-Tanner equation {3.5.1}.

The DOSY-NMR data was fitted with the Stejskal-Tanner equation with an additional term I_0 for the initial intensity.

$$E(b) = I_0 \cdot \exp\left(--\gamma^2 g^2 \delta^2 \left(\Delta - \frac{\delta}{3}\right) D\right) = I_0 \cdot \exp(-bD) \qquad \{3.5.1\}$$

with

$$\gamma = 26752 \frac{rad}{s \cdot Gauss}, \;\; \delta = 0.003\, s, \;\; \Delta = 0.095400\, s$$

for all measurements. When $E(b)$ is plotted against b on a logarithmic scale the slope of the curve is the negative self-diffusion coefficient D. If we further assume the molecule to be approximately

a spherical particle in solution, we can use the Stokes-Einstein equation to calculate the hydrodynamic radius *via*:

$$D = \frac{k_B T}{6\pi\,\eta\,r} \qquad \{3.5.2\}$$

With k_B being the Boltzman constant, T the temperature, η the viscosity of the deuterated solvent and r the hydrodynamic radius.

In Figure 3.5.8 we see the DOSY-NMR plots for DPB-H and **V_{20}H-Rb**. The values for $E(b)$ of the Steijskal-Tanner equation are the integration values over each peak in the NMR spectrum. Three similar but slightly different values for D can be derived that way. The importance to integrate over single peaks and not over multiple peaks can be seen in the DOSY-NMR for **V_{20}H-Rb** on the right hand side of Figure 3.5.8. The rightmost peak has a drastically different value than the two other peaks in the aromatic region. This is due to overlap from a DMF solvent signal with the aromatic peaks. This influences the slope of the curve and therefore averages the D value.

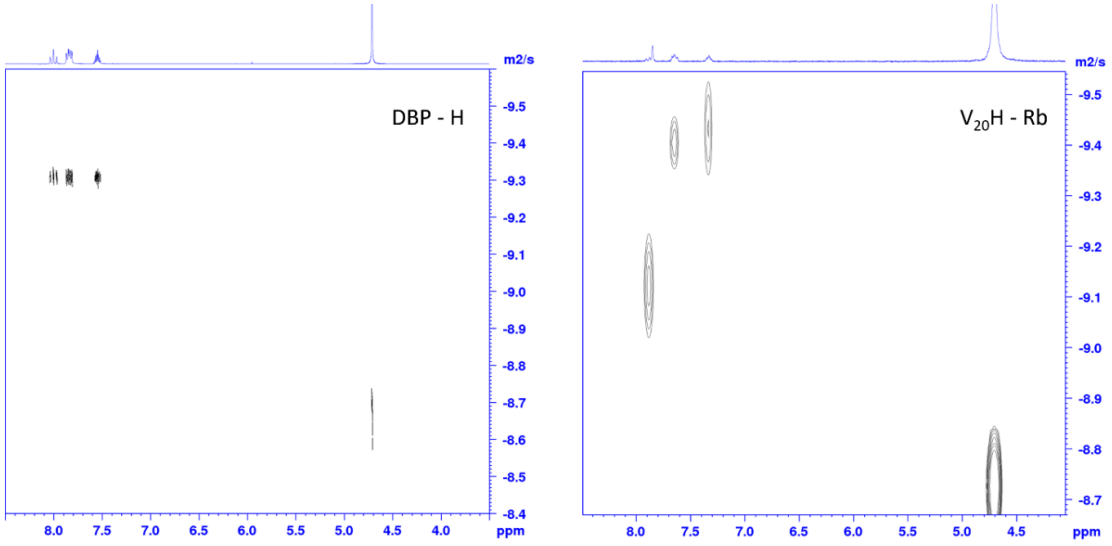

Figure 3.5.8 – ^{1}H-DOSY-NMR plot for DPB-H (left) and **V_{20}H-Rb** (right).

The D values for DPB-H and **V_{20}H-Rb** were calculated to $D = 4.92\ m^2/s$ and $D = 3.52\ m^2/s$ respectively. The fitted curves are shown in Figure 3.5.9. The hydrodynamic radii are calculated

after equation {3.5.2} to $R_H(\mathrm{DPB-H}) = 3.49$ Å and $R_H(\mathrm{V_{20}H-Rb}) = 4.87$ Å. This constitutes a slight difference in hydrodynamic radius for the sharp aromatic signals in the ^{1}H-NMR spectrum of the free ligand and the polyoxovanadate species.

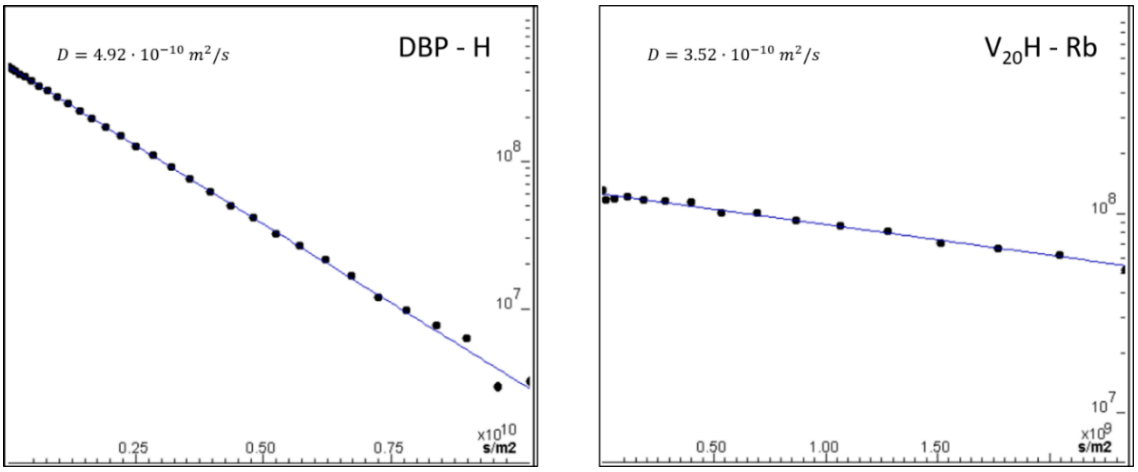

Figure 3.5.9 – Fits with the Skjelstal-Tanner equation of the DOSY NMR measurements of DPB-H and **V_{20}H-Rb**.

The hydrodynamic radius R_H describes the radius of a hard sphere that has the same diffusion properties as the particle being described by the hydrodynamic radius. In general, the hydrodynamic radius for a particle is bigger in size than the radius of the particle itself as surrounding solvent molecules are part of the species moving through the solution. We know from the crystal structure that the polyoxovanadate has got diameters of approximately 15.97 Å · 15.97 Å · 12.53 Å. The calculated hydrodynamic radius for the species, which gives rise to the sharp aromatic peaks in the spectra of **V_{20}H-Rb** was $r_H(\mathrm{V_{20}H-Rb}) = 4.87$ Å. This radius is too small to belong to the $\{V_{20}\}$ polyoxovanadate cluster. It therefore is likely to belong to the free ligand in solution. Partial decomposition of the cluster in solution is a feasible explanation for this. The broader peaks however could not be investigated by DOSY-NMR spectroscopy due to their paramagnetic nature. DOSY-NMR alone can therefore not give a definitive answer to the question if the $\{V_{20}\}$ cluster is present in solution.

3.5.5 ESI-MS

After carrying out the DOSY-NMR studies in-house a collaboration with the research group of Lee Cronin enabled us to identify the{V_{20}} cluster in solution by mass spectrometry.

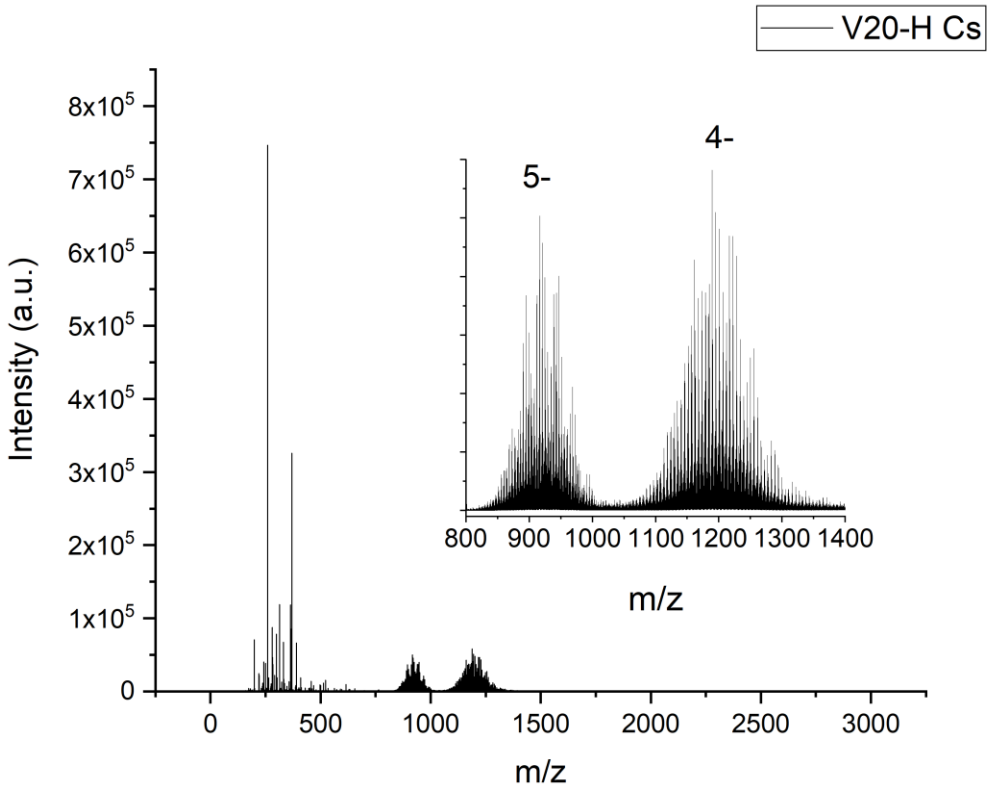

Figure 3.5.10 – **ESI**-MS of **V_{20}H-Cs** in water. Two broad envelopes corresponding to the 5- and 4- species can be seen along with fragments in the lower mass region.

The electrospray ionization (ESI) mass spectrum of **V_{20}H-Cs** (Figure 3.5.10) shows two broad envelopes around 920 m/z and 1200 m/z which correspond to the five times and four times negatively charged species of the polyoxovanadate cluster. The high negative charge of -11, which can be countered by Cs^+, H^+ or Na^+ in combination with labile groups such as water or MeCN molecules gives rise to a myriad of different m/z combinations. Unexpectedly, the {V_{20}} cluster displayed a large variety of different oxidation states, of which six can be assigned in the ESI-MS of **V_{20}H-Cs**. The peaks below 500 belong mostly to the free ligand and its combinations with Na^+, H^+ and Cs^+. Their assignment can be seen in Table 3.5.3.

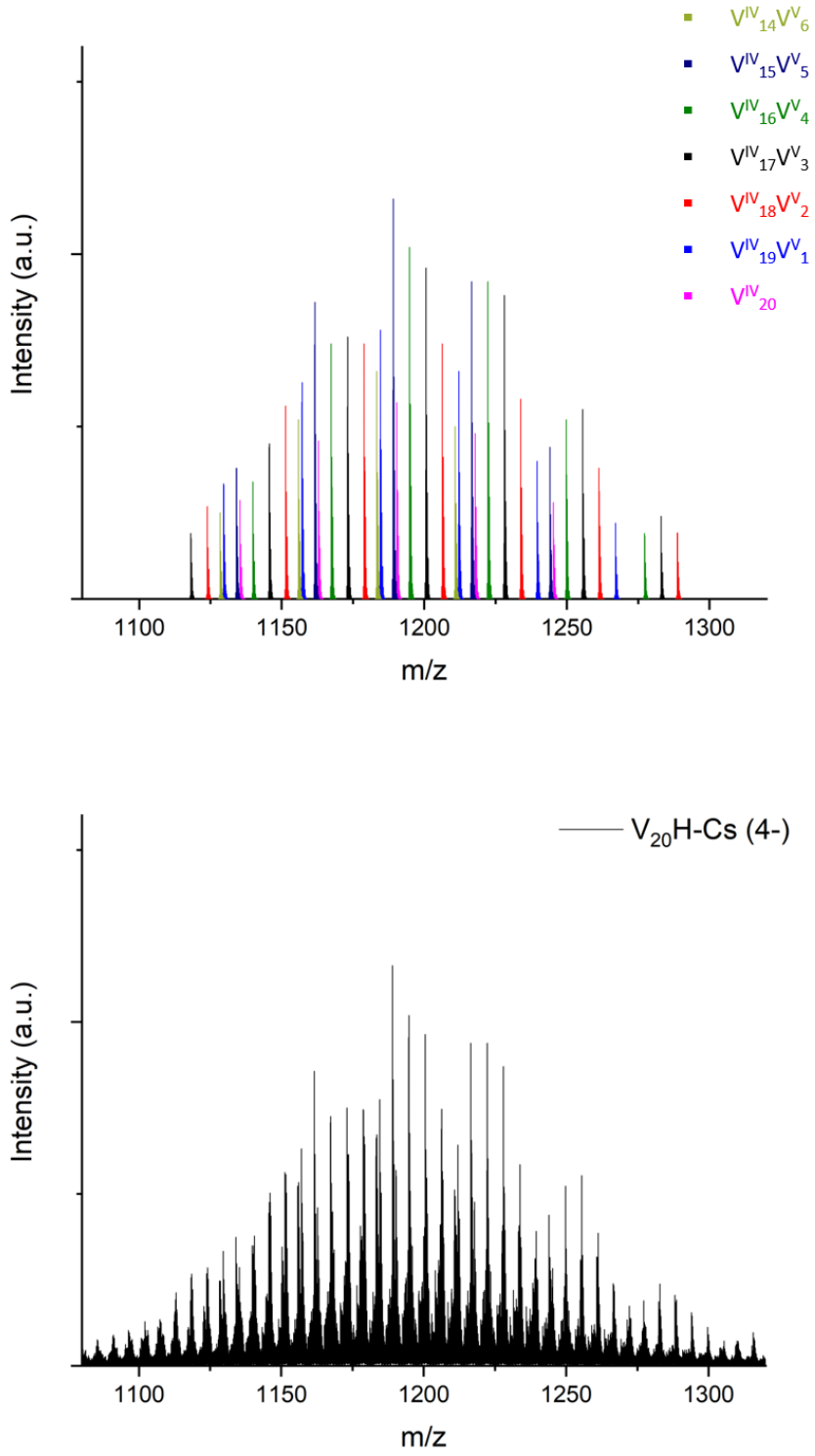

Figure 3.5.11 – The 4- envelope in the ESI-MS spectrum (bottom) of **V_{20}H-Cs** and its modelled peaks (top). Each colour stands for one oxidation state.

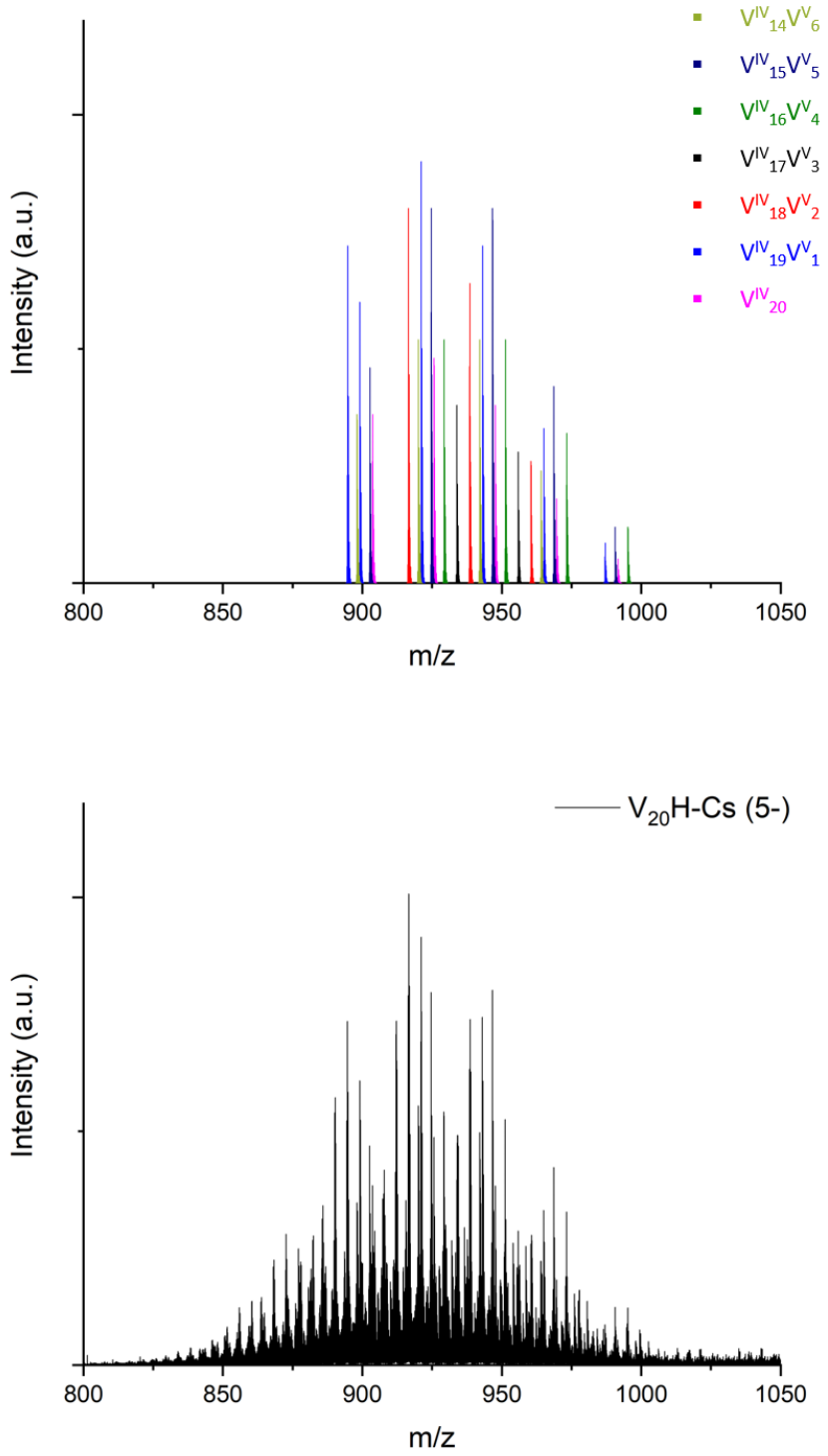

Figure 3.5.12 - The 5- envelope in the ESI-MS spectrum (bottom) of **V_{20}H-Cs** and its modelled peaks (top). Each colour stands for one oxidation state.

Table 3.5.1 – Table of assigned peaks in the 5- envelope in the MS of **V_{20}H-Cs**.

Counter ions	Oxidation state	Calculated (m/z)	Peak (m/z)	Charge
$Na_{10}H_2$ -2Cs	V^{IV}_{20}	903.7235	903.6642	5-
Na_9H_2 -Cs	V^{IV}_{20}	925.7067	925.6422	5-
Na_8H_2	V^{IV}_{20}	947.6898	947.6272	5-
$CsNa_7H_2$	V^{IV}_{20}	969.6729	969.6077	5-
$Cs_2Na_6H_2$	V^{IV}_{20}	991.6561	991.5917	5-
Na_8H_3 -2Cs	$V^{IV}_{19}V^{V}_{1}$	894.7292	894.6691	5-
Na_9H_2 -2Cs	$V^{IV}_{19}V^{V}_{1}$	899.1256	899.0634	5-
Na_8H_2 -Cs	$V^{IV}_{19}V^{V}_{1}$	921.1087	921.0477	5-
Na_7H_2	$V^{IV}_{19}V^{V}_{1}$	943.0919	943.0295	5-
$CsNa_6H_2$	$V^{IV}_{19}V^{V}_{1}$	965.075	965.0128	5-
$Cs_2Na_5H_2$	$V^{IV}_{19}V^{V}_{1}$	987.0581	986.9935	5-
Na_7H_2 -Cs	$V^{IV}_{18}V^{V}_{2}$	916.5108	916.4522	5-
Na_6H_2	$V^{IV}_{18}V^{V}_{2}$	938.4939	938.4322	5-
$CsNa_5H_2$	$V^{IV}_{18}V^{V}_{2}$	960.477	960.4168	5-
Na_5H_2	$V^{IV}_{17}V^{V}_{3}$	933.896	933.8383	5-
$CsNa_4H_2$	$V^{IV}_{17}V^{V}_{3}$	955.8791	955.8252	5-
Na4H_2	$V^{IV}_{16}V^{V}_{4}$	929.299	929.246	5-
$CsNa_3H_2$	$V^{IV}_{16}V^{V}_{4}$	951.2811	951.2285	5-
$Cs_2Na_2H_2$	$V^{IV}_{16}V^{V}_{4}$	973.2643	973.2105	5-
Cs_3NaH_2	$V^{IV}_{16}V^{V}_{4}$	995.2474	995.1916	5-
Na_4H_2 -Cs	$V^{IV}_{15}V^{V}_{5}$	902.7169	902.6663	5-
Na_3H_2	$V^{IV}_{15}V^{V}_{5}$	924.7	924.6485	5-
$CsNa_2H_2$	$V^{IV}_{15}V^{V}_{5}$	946.6832	946.6309	5-
Cs_2NaH_2	$V^{IV}_{15}V^{V}_{5}$	968.6663	968.6137	5-
Cs_3H_2	$V^{IV}_{15}V^{V}_{5}$	990.6494	990.5959	5-
Na_3H_2 -Cs	$V^{IV}_{14}V^{V}_{6}$	898.119	898.0673	5-
Na_2H2	$V^{IV}_{14}V^{V}_{6}$	920.1021	920.0495	5-
$CsNaH_2$	$V^{IV}_{14}V^{V}_{6}$	942.0852	942.0315	5-
Cs_2H_2	$V^{IV}_{14}V^{V}_{6}$	964.0684	964.0142	5-

Table 3.5.2 - Table of assigned peaks in the 4- envelope in the MS of **V_{20}H-Cs**.

Counter ions	Oxidation state	Calculated (m/z)	Peak (m/z)	Charge
$Na_{11}H_2$ - 2Cs	V^{IV}_{20}	1135.402	1135.328	4-
$Na_{10}H_2$ - Cs	V^{IV}_{20}	1162.881	1162.807	4-
Na_9H_2	V^{IV}_{20}	1190.36	1190.283	4-
$CsNa_8H_2$	V^{IV}_{20}	1217.839	1217.766	4-
$Cs_2Na_7H_2$	V^{IV}_{20}	1245.318	1245.241	4-
$Na_{10}H_2$ - 2Cs	$V^{IV}_{19}V^{V}_{1}$	1129.655	1129.581	4-
Na_9H_2 - Cs	$V^{IV}_{19}V^{V}_{1}$	1157.134	1157.057	4-
Na_8H_2	$V^{IV}_{19}V^{V}_{1}$	1184.613	1184.54	4-
$CsNa_7H_2$	$V^{IV}_{19}V^{V}_{1}$	1212.092	1212.018	4-
$Cs_2Na_6H_2$	$V^{IV}_{19}V^{V}_{1}$	1239.57	1239.493	4-
$Cs_3Na_5H_2$	$V^{IV}_{19}V^{V}_{1}$	1267.049	1266.977	4-
Na_9H_2 - 2Cs	$V^{IV}_{18}V^{V}_{2}$	1123.907	1123.829	4-
Na_8H_2 - Cs	$V^{IV}_{18}V^{V}_{2}$	1151.386	1151.308	4-
Na_7H_2	$V^{IV}_{18}V^{V}_{2}$	1178.865	1178.79	4-
$CsNa_6H_2$	$V^{IV}_{18}V^{V}_{2}$	1206.344	1206.273	4-
$Cs_2Na_5H_2$	$V^{IV}_{18}V^{V}_{2}$	1233.823	1233.756	4-
$Cs_3Na_4H_2$	$V^{IV}_{18}V^{V}_{2}$	1261.302	1261.232	4-
$Cs_4Na_3H_2$	$V^{IV}_{18}V^{V}_{2}$	1288.781	1288.708	4-
Na_8H_2 - 2Cs	$V^{IV}_{17}V^{V}_{3}$	1118.16	1118.085	4-
Na_7H_2 - Cs	$V^{IV}_{17}V^{V}_{3}$	1145.639	1145.567	4-
Na_6H_2	$V^{IV}_{17}V^{V}_{3}$	1173.118	1173.048	4-
$CsNa_5H_2$	$V^{IV}_{17}V^{V}_{3}$	1200.597	1200.528	4-
$Cs_2Na_4H_2$	$V^{IV}_{17}V^{V}_{3}$	1228.076	1228.005	4-
$Cs_3Na_3H_2$	$V^{IV}_{17}V^{V}_{3}$	1255.555	1255.486	4-
$Cs_4Na_2H_2$	$V^{IV}_{17}V^{V}_{3}$	1283.033	1282.964	4-
Na_6H_2 - Cs	$V^{IV}_{16}V^{V}_{4}$	1139.891	1139.82	4-
Na_5H_2	$V^{IV}_{16}V^{V}_{4}$	1167.37	1167.306	4-
$CsNa_4H_2$	$V^{IV}_{16}V^{V}_{4}$	1194.849	1194.781	4-
$Cs_2Na_3H_2$	$V^{IV}_{16}V^{V}_{4}$	1222.328	1222.26	4-
$Cs_3Na_2H_2$	$V^{IV}_{16}V^{V}_{4}$	1249.807	1249.74	4-
Cs_4NaH_2	$V^{IV}_{16}V^{V}_{4}$	1277.286	1277.218	4-
Na_5H_2 - Cs	$V^{IV}_{15}V^{V}_{5}$	1134.144	1134.075	4-
Na_4H_2	$V^{IV}_{15}V^{V}_{5}$	1161.623	1161.051	4-

$CsNa_3H_2$	$V^{IV}_{15}V^{V}_{5}$	1189.102	1189.031	4-
$Cs_2Na_2H_2$	$V^{IV}_{15}V^{V}_{5}$	1216.581	1216.515	4-
Cs_3NaH_2	$V^{IV}_{15}V^{V}_{5}$	1244.06	1243.993	4-
Na_4H_2 -Cs	$V^{IV}_{14}V^{V}_{6}$	1128.396	1128.331	4-
Na_3H_2	$V^{IV}_{14}V^{V}_{6}$	1155.875	1155.805	4-
$CsNa_2H_2$	$V^{IV}_{14}V^{V}_{6}$	1183.354	1183.286	4-
Cs_2NaH_2	$V^{IV}_{14}V^{V}_{6}$	1210.833	1210.763	4-

Table 3.5.3 – Table of the assigned peaks in the MS of **V_{20}H-Cs** below 400 m/z.

Assignment	Calculated (m/z)	Peak (m/z)	Charge
$\{DPB\text{-}H\}^{4-} - H_2O + H_3$	218.9618	218.9492	1-
$\{DPB\text{-}H\}^{4-} + Cs_2$	249.8802	249.8767	2-
$\{DPB\text{-}H\}^{4-} + NaH_2$	258.9543	258.9405	1-
$\{DPB\text{-}H\}^{4-} + Na_2H$	280.9362	280.9202	1-
$\{DPB\text{-}H\}^{4} + H_2O + Na_2H$	299.9468	298.9297	1-
$\{DPB\text{-}H\}^{4-} + CsH_3$	368.8700	368.8505	1-
$\{DPB\text{-}H\}^{4-} + CsNaH$	390.8519	390.8308	1-

Figure 3.5.11 and Figure 3.5.12 show a close-up of the 4- and 5- envelope respectively along with the modelled peaks in the top half of the picture. Each separate colour represents an oxidation state of the $\{V_{20}\}$ cluster in the ESI-MS pattern, whereby multiple peak patterns, caused by differing counter ions, belong to each oxidation state. The $\{V_{20}\}$ species found in the MS range from the twice oxidised $\{V^{IV}_{14}V^{V}_{6}\}$ to the fully reduced $\{V^{IV}_{20}\}$ species, exemplifying the rich redox chemistry of the cluster. 29 peaks patterns were assigned to their respective species in the 5- envelope and can be seen in Table 3.5.1. A series of peaks belonging to a single oxidation state follows a clear series, which can be exemplified by looking at the original $\{V^{IV}_{16}V^{V}_{4}\}$ oxidations state as it was determined by solid state measurements. Four ions can be seen for the $\{V^{IV}_{16}V^{V}_{4}\}$ species in the ESI-MS, which follows the series:

$$[Na_4H_2\{V_{20}\}]^{5-} \rightarrow [CsNa_3H_2\{V_{20}\}]^{5-} \rightarrow [Cs_2Na_2H_2\{V_{20}\}]^{5-} \rightarrow [Cs_3NaH_2\{V_{20}\}]^{5-}$$

The peak pattern matches for the ion series can be seen in Figure 3.5.13. Overlapping signals partially obscure some of the peak patterns. It is worth noting that no peak patterns could be identified which featured either additional water molecules or MeCN molecules. The $\{V_{20}\}$ cluster hereby refers to the cluster without the labile axial ligands. Additionally, almost all signals identified follow the general formula $[Cs_xNa_yH_2\{V_{20}\}]^{q-}$. Only for some species three protons were identified as part of the counter ions of the species. Of special interest are the signals below the molecular weight of the $\{V_{20}\}$ cluster itself without counter ions attached to it. Figure 3.5.14 shows the part of the spectrum below this point in blue colour. The peaks below this point have to belong to partially disintegrated species. Matching peak pattern for ions with less than eight caesium ions could be found for almost all of the oxidation states, as can be seen in Table 3.5.1 and Table 3.5.2. It is not clear however if those signals arise from species in solution or if they form during the ionisation process.

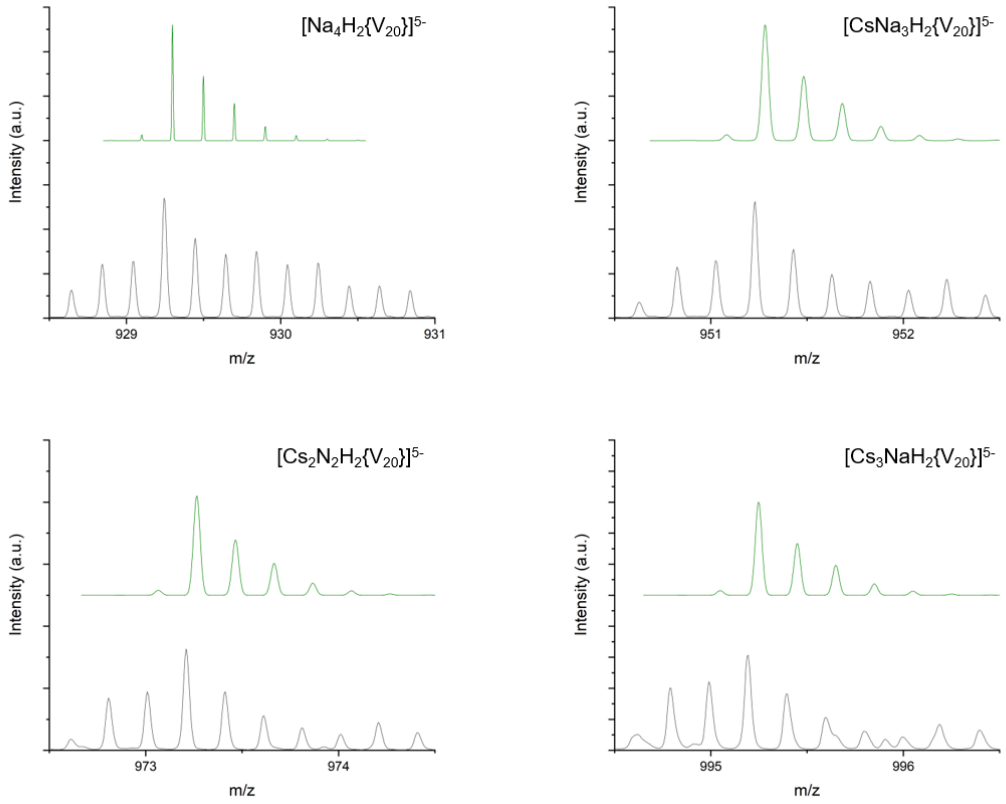

Figure 3.5.13 – Simulated (top) and experimental (bottom) peak patterns for the $\{V^{IV}_{16}V^{V}_{4}\}$ ions in the 5- envelope.

The successful identification of the $\{V_{20}\}$ cluster in the ESI-MS spectrum proves its stability in water. The alkali metal cube is therefore undoubtedly an integral part of the cluster. More importantly however it proves that cation-π interactions are stable in aqueous solutions and its cations can resist diffusing into the solvent. This behaviour exemplifies the strength of the cation-π interactions within this system as the hydration energy of the alkali metal cations are quite high. The occurrence of cation-π interactions in coordination complexes under non-anaerobic conditions is therefore rare in the literature with only a few examples to this date.[247-252]

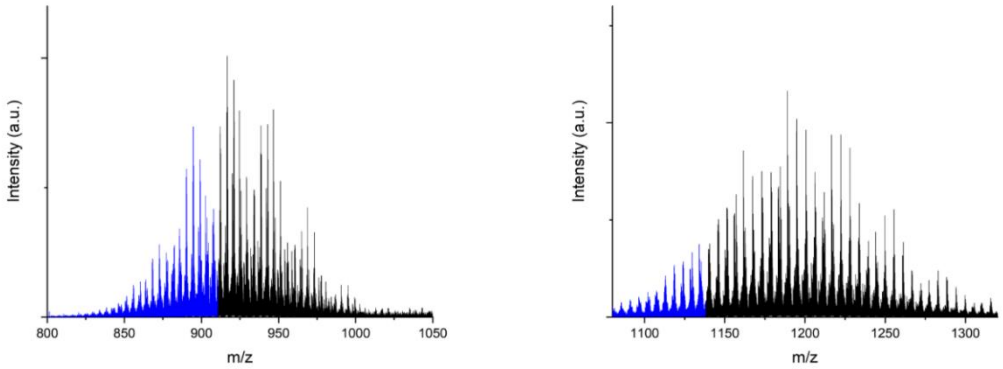

Figure 3.5.14 – 5- and 4- envelope of **V_{20}H-Cs**. The blue part of the spectrum shows the peaks for the species which have to have lost caesium ions from the alkali metal cube.

Figure 3.5.15 shows the ESI-MS spectrum of **V_{20}H-Rb**. As in **V_{20}H-Cs** we see two broad envelopes of 5- and 4- charge along with a number of peaks below 400 m/z. The broad envelopes can be assigned to $\{V_{20}\}$ clusters in different oxidation states along with differing combinations of counter ions. Signals below 400 m/z belong to ligands species. The modelled peaks for the envelope can be seen in Figure 3.5.17 and Figure 3.5.18 with their assigned peaks listed in Table 3.5.4 and Table 3.5.5. The ion series of $\{V^{IV}_{16}V^{V}_{4}\}$ can be seen in Figure 3.5.19. The ESI-MS spectrum of **V_{20}H-Rb** follows the same trends in their series.

Unfortunately, the $\{V_{20}\}$ concentration in the MS sample of **V_{20}H-K** turned out to be too low in order to produce a clear spectrum with distinct pattern. Background noise and overlap of many different signals obscure the peak pattern of the $\{V_{20}\}$ species in **V_{20}H-K**. While the peaks can be made to fit the experimental m/z values, no clear assignment can be made because of the missing pattern matches. The positioning and shape of the 4- and 5- envelope in the MS of **V_{20}H-**

K strongly indicates however that the {V_{20}} cluster in **V_{20}H-K** exhibits the same solution behaviour as in **V_{20}H-Rb** and **V_{20}H-Cs**.

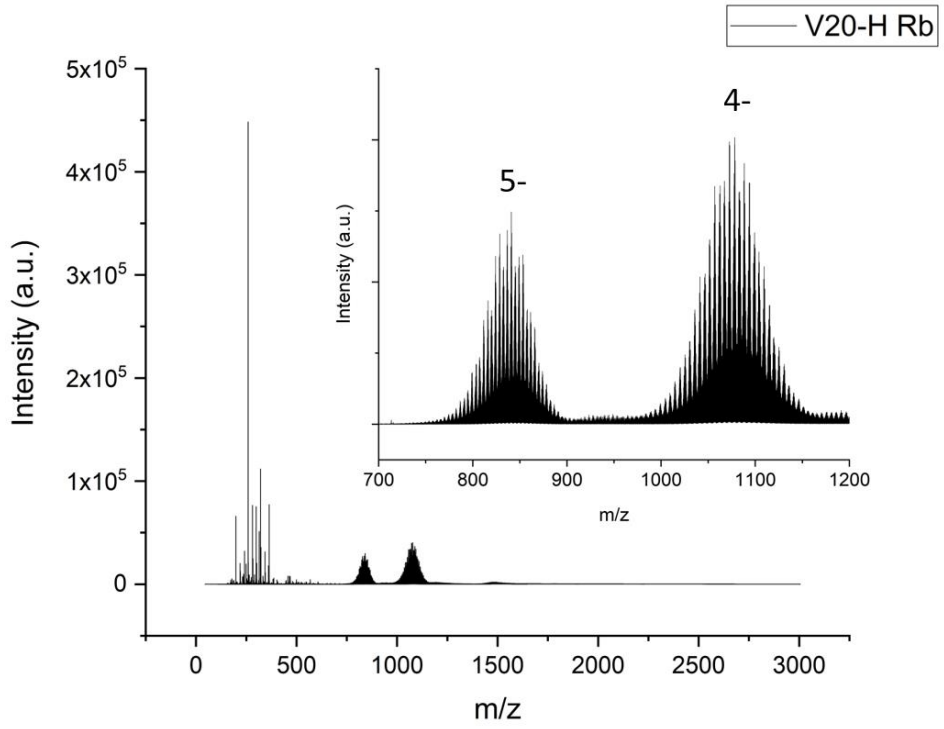

Figure 3.5.15 – ESI-MS spectrum of **V_{20}H-Rb**.

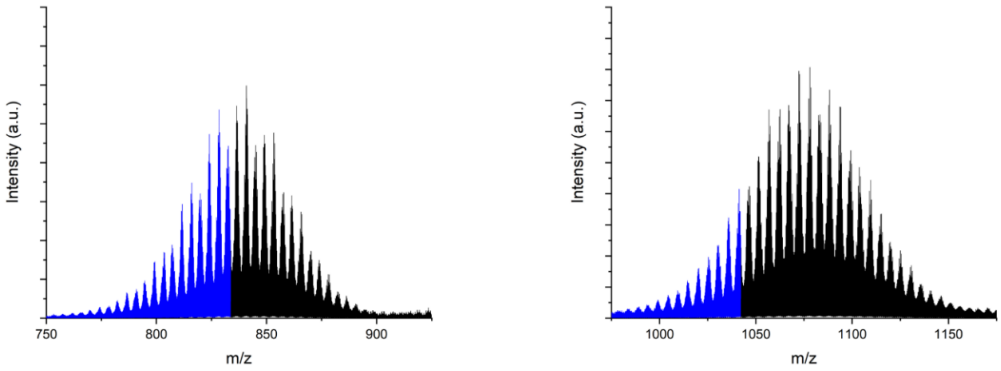

Figure 3.5.16 - 5- and 4- envelope of **V_{20}H-Rb**. The blue part of the spectrum shows the peaks for the species which have to have lost rubidium ions from the alkali metal cube.

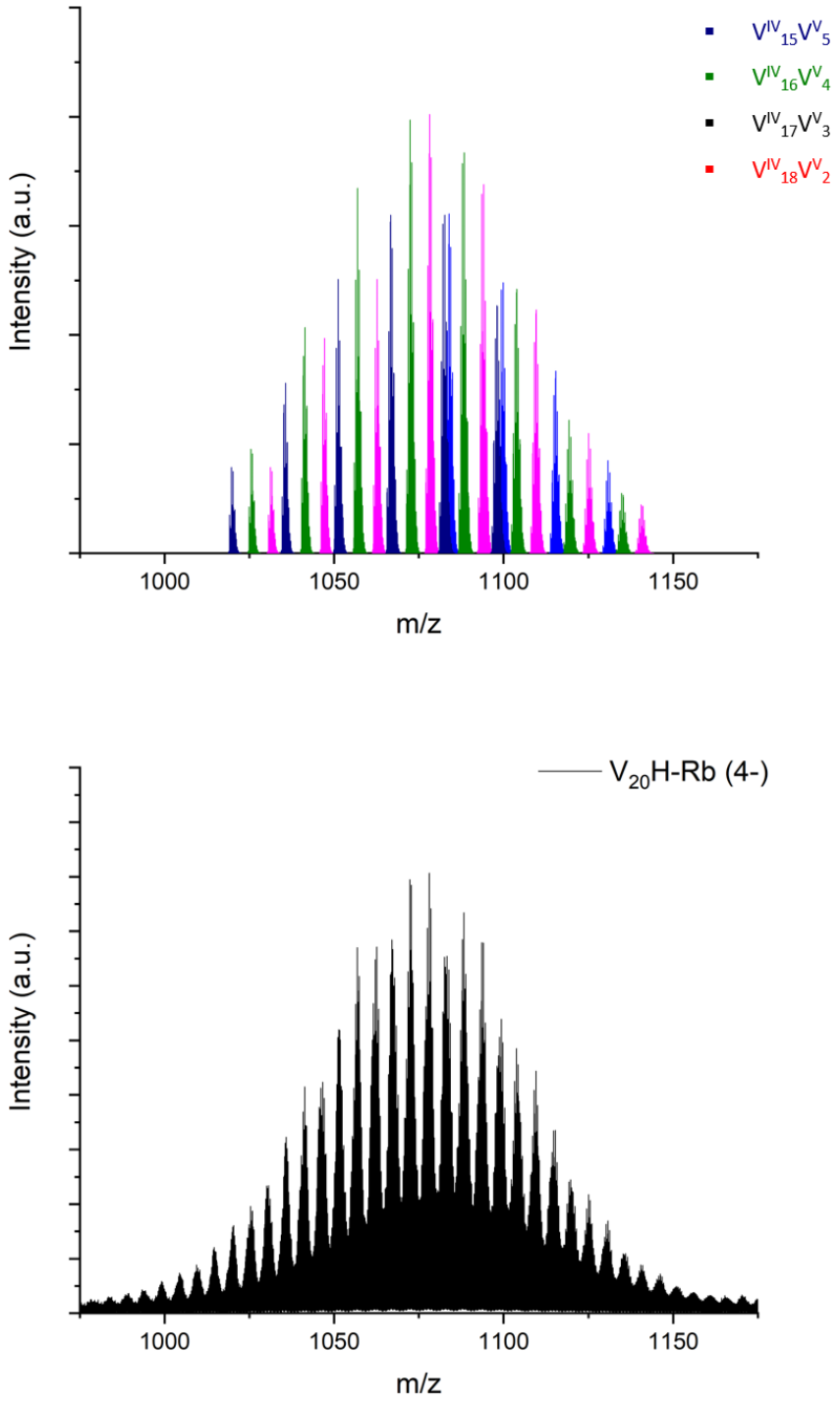

Figure 3.5.17 – The 4- envelope in the ESI-MS spectrum (bottom) of **V_{20}H-Rb** and its modelled peaks (top).

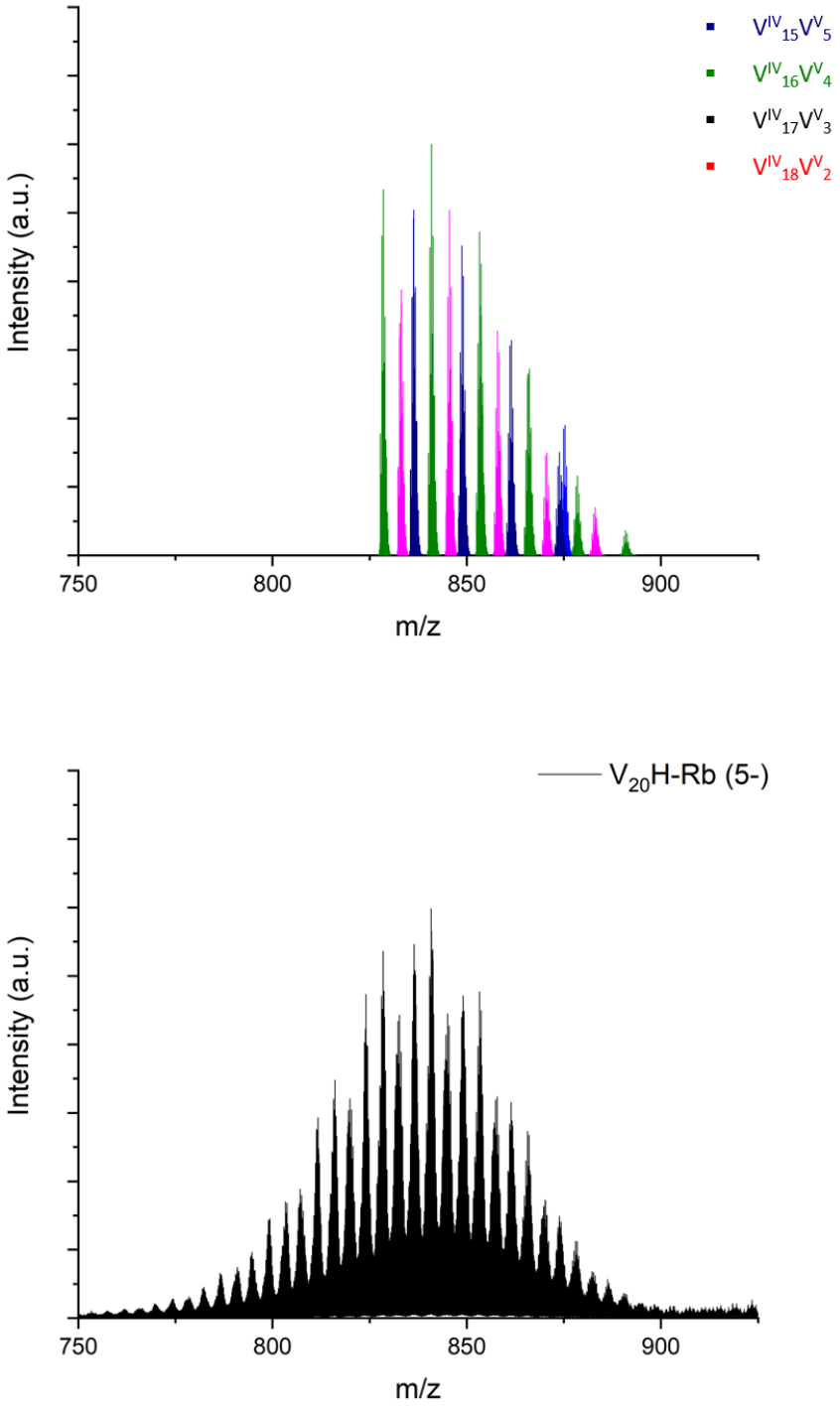

Figure 3.5.18 – The 4- envelope in the ESI-MS spectrum (bottom) of **V_{20}H-Rb** and its modelled peaks (top).

Table 3.5.4 – Table of assigned peaks in the 4- envelope of the MS of **V_{20}H-Rb**.

Counter ions	Oxidation state	Calculated (m/z)	Peak (m/z)	Charge
Na_7H_2	$V^{IV}_{18}V^{V}_{2}$	1083.877	1083.814	4-
$RbNa_6H_2$	$V^{IV}_{18}V^{V}_{2}$	1099.858	1099.792	4-
$Rb_2Na_5H_2$	$V^{IV}_{18}V^{V}_{2}$	1115.338	1115.279	4-
$Rb_3Na_4H_2$	$V^{IV}_{18}V^{V}_{2}$	1130.819	1130.762	4-
Na_9H_2 - 3 Rb	$V^{IV}_{17}V^{V}_{3}$	1031.188	1031.116	4-
Na_8H_2 - 2 Rb	$V^{IV}_{17}V^{V}_{3}$	1047.169	1047.101	4-
Na_7H_2 - Rb	$V^{IV}_{17}V^{V}_{3}$	1062.649	1062.584	4-
Na_6H_2	$V^{IV}_{17}V^{V}_{3}$	1078.13	1078.064	4-
RbNa5H_2	$V^{IV}_{17}V^{V}_{3}$	1094.11	1094.045	4-
$Rb_2Na_4H_2$	$V^{IV}_{17}V^{V}_{3}$	1109.591	1109.531	4-
$Rb_3Na_3H_2$	$V^{IV}_{17}V^{V}_{3}$	1125.071	1125.013	4-
$Rb_4Na_2H_2$	$V^{IV}_{17}V^{V}_{3}$	1140.552	1140.504	4-
Na_8H_2 – 3 Rb	$V^{IV}_{16}V^{V}_{4}$	1025.441	1025.369	4-
Na_7H_2 – 2 Rb	$V^{IV}_{16}V^{V}_{4}$	1041.421	1041.354	4-
Na_6H_2 – Rb	$V^{IV}_{16}V^{V}_{4}$	1056.902	1056.839	4-
Na_5H_2	$V^{IV}_{16}V^{V}_{4}$	1072.382	1072.316	4-
$RbNa_4H_2$	$V^{IV}_{16}V^{V}_{4}$	1088.363	1088.3	4-
Rb2Na_3H_2	$V^{IV}_{16}V^{V}_{4}$	1103.843	1103.784	4-
$Rb_3Na_2H_2$	$V^{IV}_{16}V^{V}_{4}$	1119.324	1119.272	4-
Rb_4NaH_2	$V^{IV}_{16}V^{V}_{4}$	1134.804	1134.757	4-
Na_7H_2 – 3 Rb	$V^{IV}_{15}V^{V}_{5}$	1019.693	1019.62	4-
Na_6H_2 – 2 Rb	$V^{IV}_{15}V^{V}_{5}$	1035.674	1035.611	4-
Na_5H_2 – Rb	$V^{IV}_{15}V^{V}_{5}$	1051.154	1051.091	4-
Na_4H_2	$V^{IV}_{15}V^{V}_{5}$	1066.635	1066.578	4-
$RbNa_3H_2$	$V^{IV}_{15}V^{V}_{5}$	1082.615	1082.557	4-
$Rb_2Na_2H_2$	$V^{IV}_{15}V^{V}_{5}$	1098.096	1098.039	4-

Table 3.5.5 – Table of assigned peaks in the 5- envelope of **V_{20}H-Rb**.

Counter ions	Oxidation state	Calculated (m/z)	Peak (m/z)	Charge
$RbNa_5H_2$	$V^{IV}_{18}V^{V}_{2}$	875.2878	875.2343	5-
Na_7H_2 - 2 Rb	$V^{IV}_{17}V^{V}_{3}$	833.1367	833.0803	5-
Na_6H_2 - Rb	$V^{IV}_{17}V^{V}_{3}$	845.5211	845.4665	5-
Na_5H_2	$V^{IV}_{17}V^{V}_{3}$	857.9055	857.8522	5-
$RbNa_4H_2$	$V^{IV}_{17}V^{V}_{3}$	870.6899	870.6371	5-
$Rb_2Na_3H_2$	$V^{IV}_{17}V^{V}_{3}$	883.0743	883.0244	5-
Na_6H_2 - 2 Rb	$V^{IV}_{16}V^{V}_{4}$	828.5387	828.4852	5-
Na_5H_2 - Rb	$V^{IV}_{16}V^{V}_{4}$	840.9231	840.8713	5-
Na_4H_2	$V^{IV}_{16}V^{V}_{4}$	853.3075	853.2578	5-
$RbNa_3H_2$	$V^{IV}_{16}V^{V}_{4}$	866.0919	866.0403	5-
$Rb_2Na_2H_2$	$V^{IV}_{16}V^{V}_{4}$	878.4763	878.4271	5-
Rb_3NaH_2	$V^{IV}_{16}V^{V}_{4}$	890.8607	890.8148	5-
Na_4H_2 - Rb	$V^{IV}_{15}V^{V}_{5}$	836.3252	836.2773	5-
Na_3H_2	$V^{IV}_{15}V^{V}_{5}$	848.7096	848.6643	5-
$RbNa_2H_2$	$V^{IV}_{15}V^{V}_{5}$	861.494	861.4527	5-
Rb_2NaH_2	$V^{IV}_{15}V^{V}_{5}$	873.8784	873.833	5-

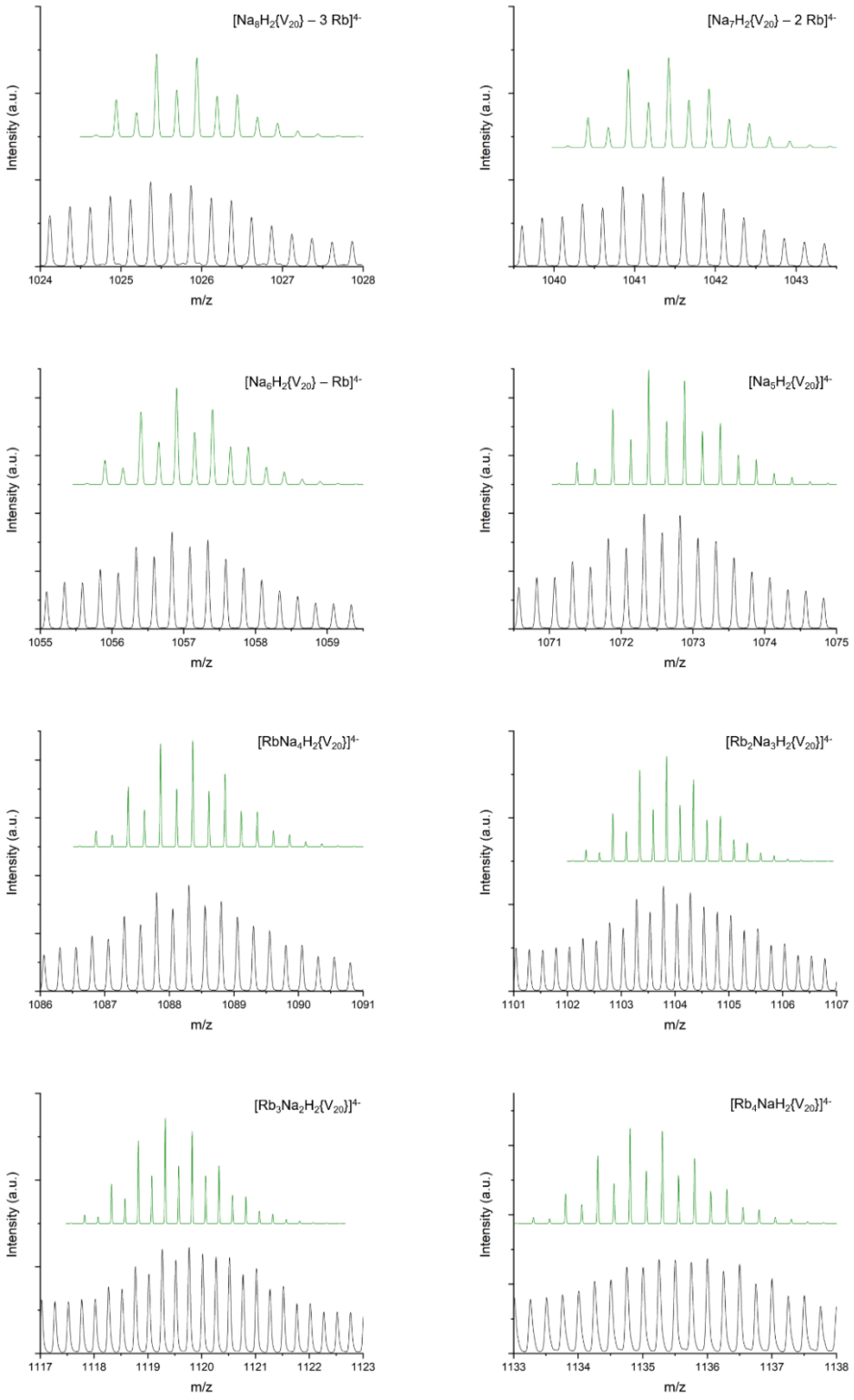

Figure 3.5.19 – Pattern match for the $\{V^{IV}_{16}V^{V}_{4}\}$ ions in the 4- envelope of the MS of **V_{20}H-Rb**.

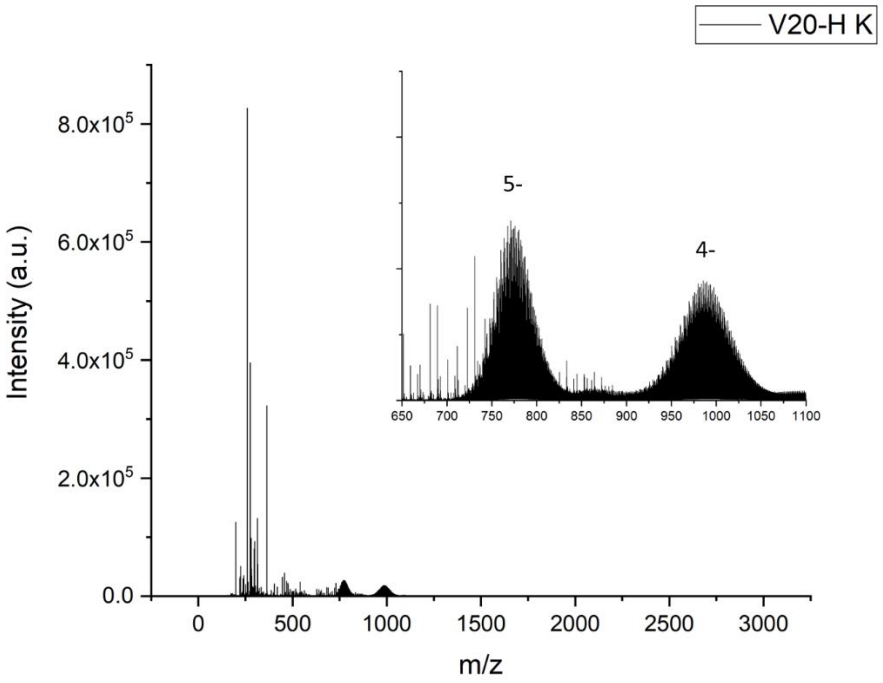

Figure 3.5.20 – Mass spectrum of **V_{20}H-K** in water.

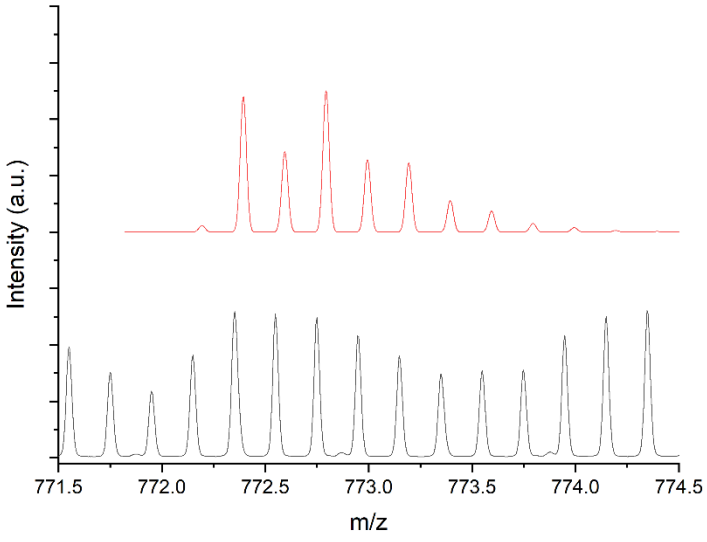

Figure 3.5.21 – Example of the simulated (top) and experimental (bottom) peak pattern for **V_{20}H-K** Even though the general shape and peak positions can be matched, no definitive assignment of the peak pattern for one species can be made.

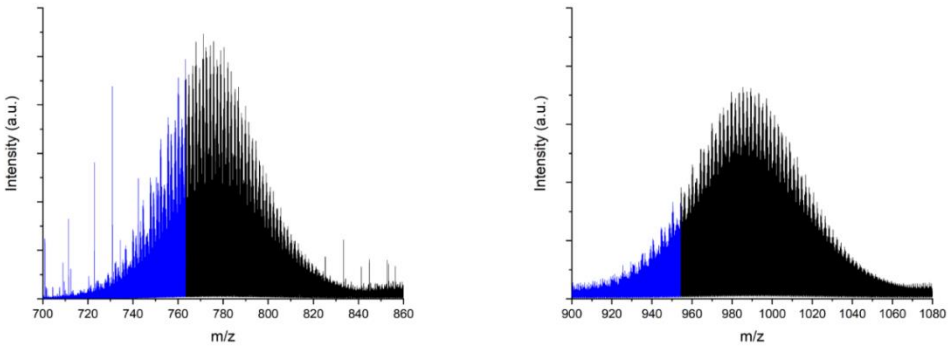

Figure 3.5.22 – 5- and 4- envelope of **V_{20}H-K**. The blue part of the spectrum shows the peaks for the species which have to have lost potassium ions from the alkali metal cube.

3.5.6 UV-VIS

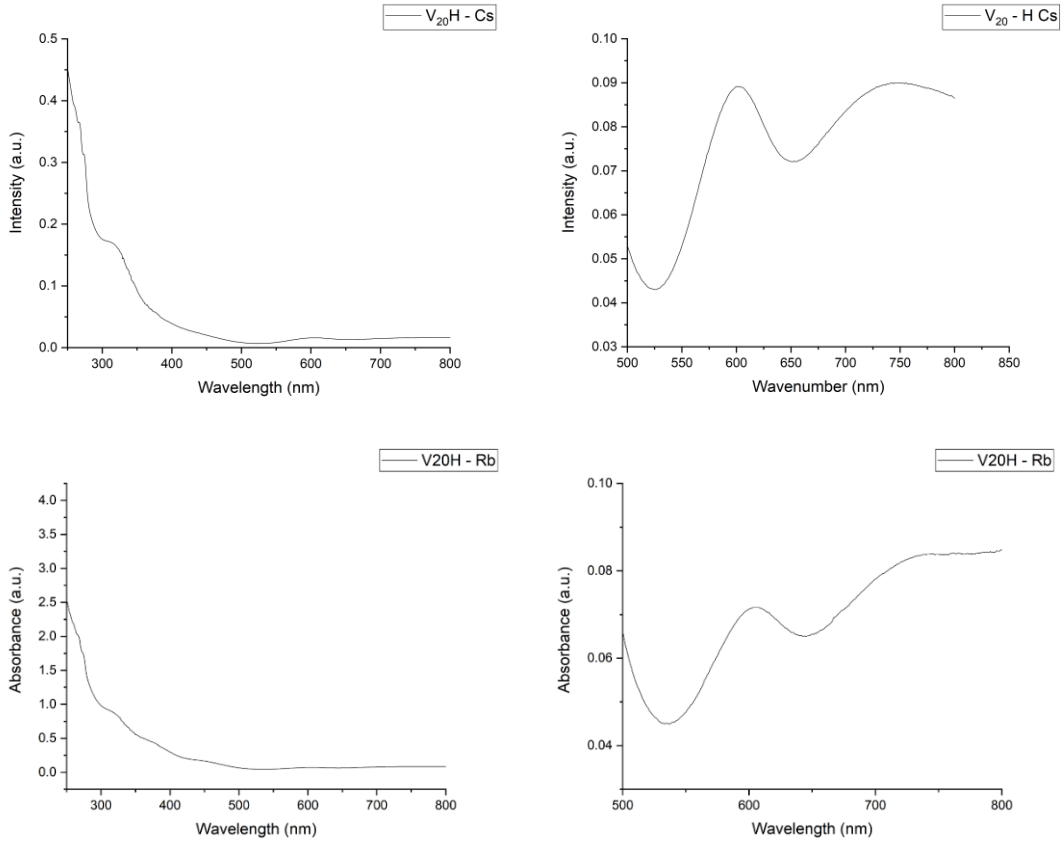

Figure 3.5.23 – UV-VIS spectrum of **V_{20}H-Cs** (top row) and **V_{20}H-Rb** (bottom row) from 250 to 800 nm (left) and 500 to 800 nm (right).

The UV-VIS spectra for **V_{20}H-Cs** and **V_{20}H-Rb** show intense π-π* transitions arising from the ligand near the UV region. The shoulder at around 320 nm for **V_{20}H-Cs** and 315 nm for **V_{20}H-Rb** can be attributed to LMCT bands from the *oxo*-ligand to the vanadium ion in the V=O groups.[253] Around 606 nm one can see a d-d transition with a broader signal at 750 nm next to it. The broader signal could either arise from a d-d transition or an IVCT transition due to the mixed-valent nature of the compound. As d-d and IVCT transitions can be very similar in energy and intensity for mixed-valent polyoxovanadates it is not straight forward to assign signals in the UV-VIS spectra without further analysis. A characteristic difference however between them is the bandwidth of the signal, which can be expressed *via* the full width at half maximum (FWHM) of the signal. As the signals overlap significantly spectral deconvolution was performed for the spectrum of **V_{20}H-Cs** between 500 and 800 nm assuming Gaussian shape of the signals. The

FWHM parameter for the d-d transition at 606 nm and the transition at 750 nm were found to be $\Delta\nu_{1/2}$ = 1779 cm-1 and 3894 cm-1 respectively (Figure 3.5.24). A FWHM of around 4000 cm-1 hereby fits the characteristic of a localised Class II mixed valent system according to the Robin and Day classification, which shows weak intensities, solvent dependency and large bandwidths of $\geq$ 2000 cm-1.[254] The signal around 750 nm is therefore most likely assigned to an IVCT band rather than a d-d transition.

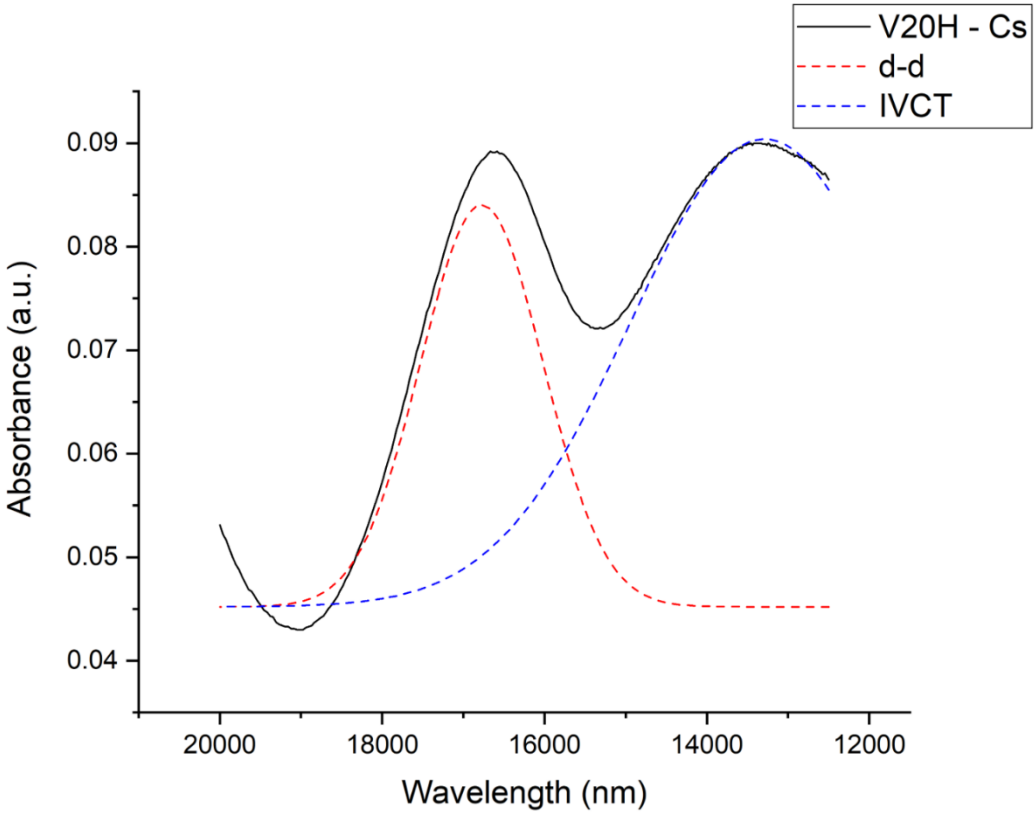

Figure 3.5.24 – Spectral deconvolution of the UV-VIS spectra of **V_{20}H-Cs**.

3.6 Theoretical calculations

After establishing the existence of cation-π interactions in both solid state and solution the question arose to which extent the cation-π interactions play a role in the stabilisation and formation of the structure. As the $\{V_{20}\}$ consists of more than 200 atoms, Density Functional Theory (DFT) calculations on the whole structure would have been too computationally intensive. Therefore, the first target for DFT calculations was to investigate if the partially inverted $\{V_5^*\}$ unit as it exists in the $\{V_{20}\}$ structures differs energetically from the pentanuclear half-capsule in the $\{V_{10}\}$ structures. To create a chemically sensible model for the $\{V_5O_9\}^{5-}$ units the initial atom coordinates were taken from the structures of **NH_4-V_{10}** and **V_{20}H-Cs** and the aromatic benzene rings of the phosphonate ligands were replaced by methyl groups. The converged structures for the $\{V_{10}\}$ half-capsule and the inverted counterpart can be seen in Figure 3.6.1. The models reproduced both the bond-distances as well as the bond-angles of both pentanuclear polyoxovanadate unit accurately.

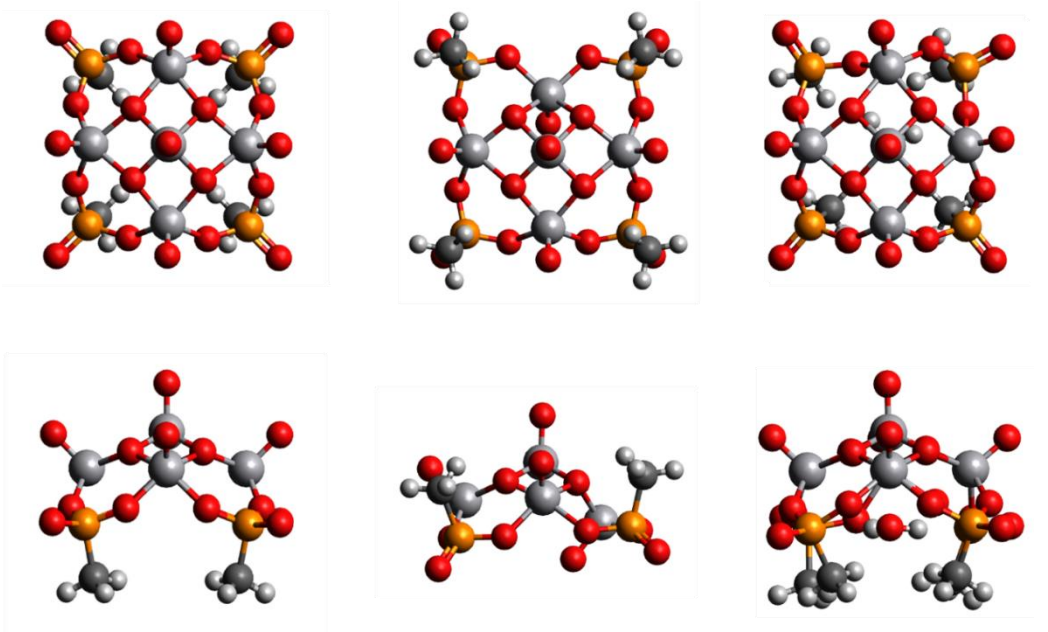

Figure 3.6.1 – Converged model structures for the pentanuclear half-capsule in $\{V_{10}\}$, its partially inverted counterpart in $\{V_{20}\}$ and the $\{V_{10}\}$ half-capsule with water as a template molecule.

Three sets of frequency calculations were carried out to determine the free energy of the $\{V_{10}\}$ half-capsule, the $\{V_{20}\}$ half-capsule as well as the $\{V_{10}\}$ capsule with water as a templating agent. The water molecule was constrained to be 3.1 Å away from the V^V centre in the middle of the structure. The results are summarised in Table 3.6.1.

Table 3.6.1 – Theoretical calculations for the pentanuclear half-capsule in $\{V_{10}\}$, $\{V_{20}\}$ and $\{V_{10}\}$ with water as a templating agent.

Model	Free Energy / Hartrees	Stabilisation / (kJ/mol)
Water	-76.331661	
$\{V_5O_9\}$	-3461.41635	
$\{V_5O_9\}$ inverted	-3461.405869	+ 27.5 vs. $\{V_5O_9\}$ + 63.8 vs. $\{V_5O_9(H_2O)\}$
$\{V_5O_9(H_2O)\}$	-3537.761812	-36.2 vs. $\{V_5O_9\}+H_2O$

The calculations show that the partially inverted half-capsule is about 27 kJ/mol less stable than its $\{V_{10}\}$ counterpart, even without a templating molecule in the electrophilic pocket of the standard pentanuclear half-capsule. The addition of a water molecule as a templating agent further stabilises the standard pentanuclear half-capsule by about 36 kJ/mol to a total of 64 kJ/mol. This means that the inverted half-capsule becomes energetically even less favourable in respect to the standard half-capsule because of the loss of a templating molecule. In order for the system to favour a $\{V_{20}\}$ structure with four inverted $\{V_5^*\}$ half-capsules over a $\{V_{20}\}$ structure with four normal $\{V_5\}$ half-capsules, this loss in stabilisation has to be overcome.

3.7 Magnetic Measurements

Magnetic measurements were conducted on samples of **V_{20}H-Cs** and **V_{20}H-Rb**. A temperature dependent susceptibility sweep was conducted for **V_{20}H-Cs** from 300 K to 1.8 K with an applied static external dc field of 0.1 T and can be seen in Figure 3.7.1 The χT value at room temperature of about 6.04 cm^3K/mol fits well with the value for 16 unpaired electrons (S = ½, g = 2, C = 0.375 cm^3K/mol; 16 · 0.375 cm^3K/mol = 6.0 cm^3K/mol), stemming from the 16 V^{IV} d^1 ions. The χT product stays almost constant at 6.04 cm^3K/mol upon lowering the temperature from 300 K down to 20 K. Upon further cooling, the χT product exhibits a sharp decrease which can be attributed to the combined effect of ligand-field splitting, dominant antiferromagnetic interactions and Zeeman saturation effects. The χT value at 1.8 K lies at 5.27 cm^3K/mol, which is close to the χT value for 14 unpaired electrons. This high χT value at 1.8 K could be indicative of a non-zero ground state and the presence of ferromagnetic interactions.

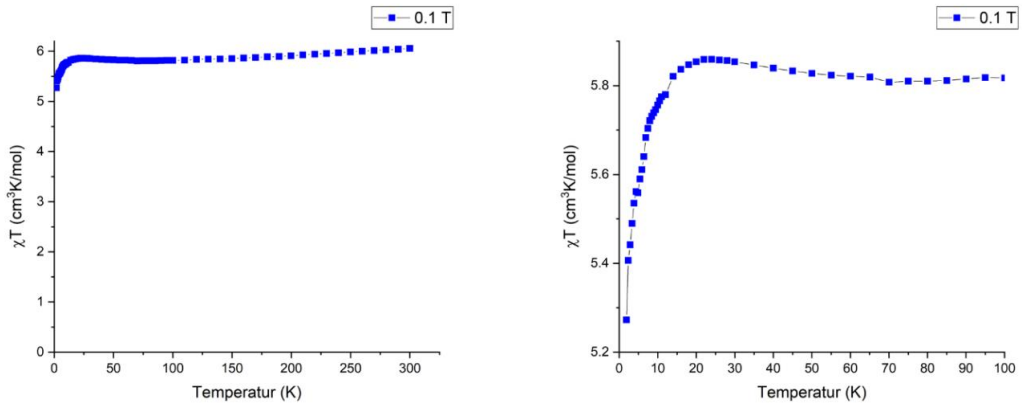

Figure 3.7.1 – χT/T plot for **V_{20}H-Cs** from 300 K to 1.8 K at 0.1 T.

The field-dependence of magnetisation of V_{20}H-Cs was measured from 0 T to 7 T at 2, 3 and 5K and can be seen in Figure 3.7.2. At none of the measured temperatures magnetic saturation could be achieved and the lack of saturation in the magnetisation values indicates the presence of magnetic anisotropy and/or low-lying excited states. The 2 K isotherm shows a typical shape of a magnetization curve, with a rapid increase at low field before following a more gradual linear increase beyond 1.0 T, without reaching saturation at 7.0 T and a value of 10.79 μ_B. This value is smaller than the expected 16.0 μ_B for sixteen V^{IV} (S = ½), which are uncoupled or completely ferromagnetically coupled. The 5 K isotherm shows an almost linear increase with the filed, and only starts bending after 5.0 T. The reduced magnetisation on the right side of Figure 3.7.2

indicates isotropic behaviour of the system at fields below 1T as indicated by the superposition to one single master curve of the temperature isotherms. Above 1T the reduced magnetisation curves slightly drift apart indicating a weak anisotropic behaviour at higher fields.

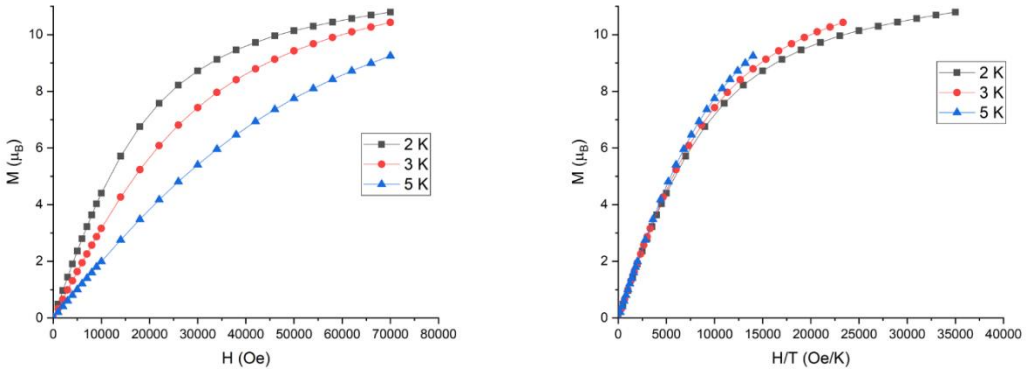

Figure 3.7.2 – M/H plot from 0 T to 7 T at 2, 3 and 5K (left). Right: Plot of the reduced magnetisation.

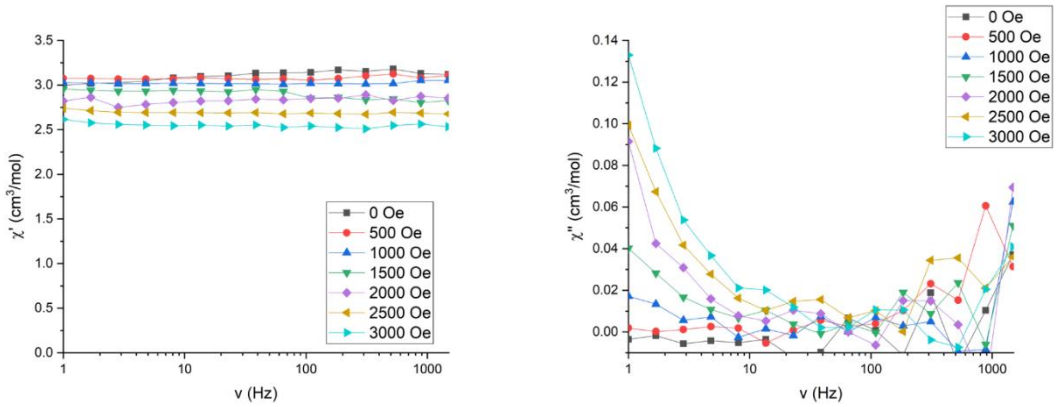

Figure 3.7.3 – Frequency dependent in-phase and out-of-phase susceptibility measurements for **V_{20}H-Cs**.

AC magnetic susceptibility measurements were performed in order to investigate the presence of slow relaxation of the magnetization which may originate from SMM behavior. In attempts to suppress any QTM, the frequency-dependent ac susceptibility was tested with varying applied field from 0 to 0.3 T at 1.8 K. The χ' value of 3.02 cm^3/mol at 0.1 T and 1.8K corresponds to a χT value of 5.44 cm^3K/mol. The out-of-phase susceptibility shows a small but visible frequency dependence, which rises with higher frequencies, indicating slow relaxation behaviour. Although,

there are field-dependent signals, the optimum field could not be established, due to the absence of visible maxima, which are not within the measurable frequency window. In order to check for possible relaxation processes at higher temperatures, the in-phase and out-of-phase susceptibility was also measured as temperature-dependency using 1000 Hz as a set frequency (Figure 3.7.4), which were found to be absent. Below the so-called blocking temperature T_B, both the in-phase and out-of-phase AC susceptibility should show maxima which are frequency- and temperature-dependent. As can be seen in Figure 3.7.4 the AC susceptibility shows a temperature dependent in-phase signal, while the out-of-phase susceptibility exhibits a rather flat line and does not show maxima at temperatures above 1.8 K.

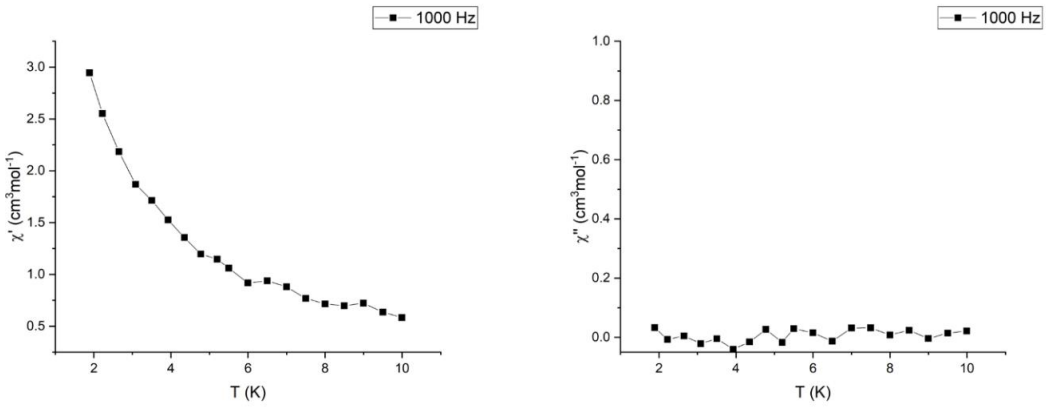

Figure 3.7.4 – Zero field temperature dependent AC in-phase and out-of-phase susceptibility plots for **V_{20}H-Cs**.

The same set of magnetic measurements were conducted for **V_{20}H-Rb**. As for **V_{20}H-Cs** the room temperature χT value for **V_{20}H-Rb** is with 6.08 cm^3K/mol close to the theoretical value of 6 cm^3K/mol for 16 unpaired electrons (S = ½, g = 2, C = 0.375 cm^3K/mol; 16 · 0.375 cm^3K/mol = 6.0 cm^3K/mol). (Figure 3.7.5). On lowering the temperature, the $\chi_M T$ product decreases almost linearly until it reaches the minimum value of 4.99 cm^3K/mol at 26 K. On further cooling, the $\chi_M T$ value increases to reach a maximum value of 5.21 cm^3 K/mol at 4 K, before it drops upon further cooling to 5.11 cm^3K/mol at 1.8 K. This behavior of a clear visible increase at low temperatures is indicative of ferromagnetic interactions between the metal ions. The drop of the $\chi_M T$ product at low temperatures can be again attributed to the combined effect of ligand-field splitting, dominant antiferromagnetic interactions and Zeeman saturation effects.

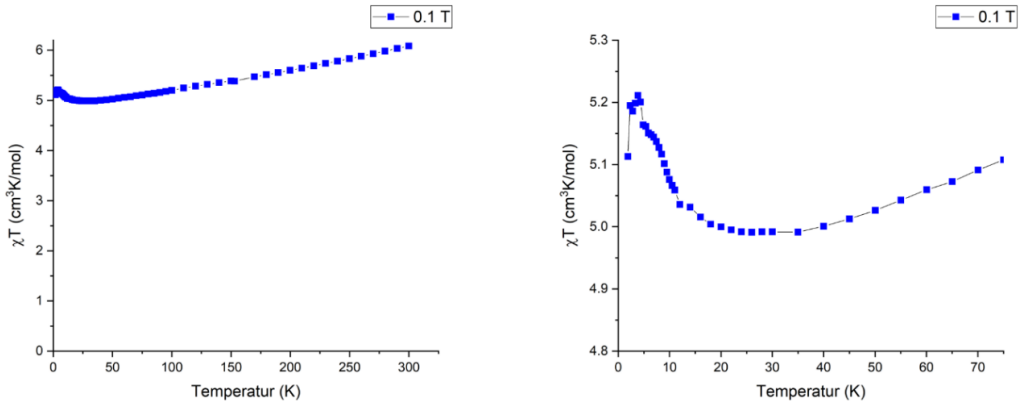

Figure 3.7.5 – χT/T plot for **V_{20}H-Rb** from 300 K to 1.8 K at 0.1 T and close up from 0 K to 75 K.

Field dependence of the magnetisation curves at 2, 3 and 5 K do not show saturation up to 7 T, but a similar behaviour as V_{20}H-Cs. The lack of clear saturation in the magnetization values indicates the presence of magnetic anisotropy and/or low-lying excited states. The values of the 2K-isotherms rapidly increase at low field before following a more gradual linear increase after 1.0 T without saturation reaching at 7.0 T and 2.0 K a value of 9.24 μ_B. The reduced magnetisation plots shown as M vs. H/T for **V_{20}H-Rb** highlight again, that the system displays isotropic behaviour below 1T and slightly anisotropic behaviour above 1T where the isotherms stop to superimpose and start diverging.

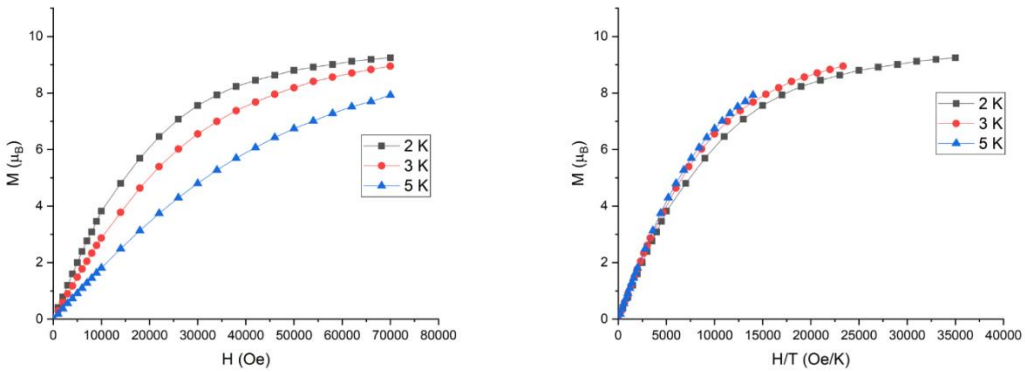

Figure 3.7.6 – M/H curves for **V_{20}H-Rb.**

In order to investigate this compound for possible SMM behavior, ac magnetic susceptibility measurements were performed and the out-of-phase signal **V_{20}H-Rb** shows frequency

dependence, which increase with field strength, indicating a slow relaxation behaviour. The maximum, which is about to be visible at low frequencies (1.0 Hz), seems frequency-independent since there is no shifting towards lower or higher frequencies, just the intensity of the peak is increasing. This might be due to fast relaxation processes, such as QTM. At higher frequencies, there is a field-dependence in the signal visible, which is quite weak, and an optimum field could not be established. The peak at 2500 Oe and 200 Hz was assigned to a noise signal during the measurement.

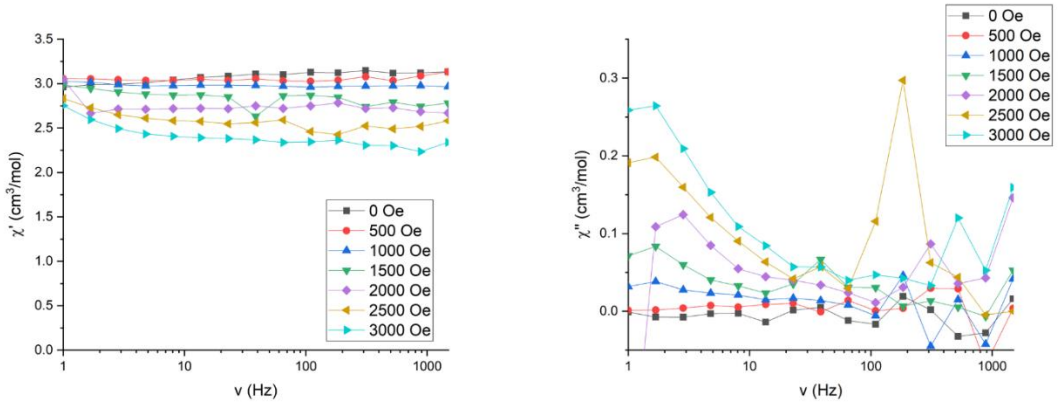

Figure 3.7.7 – Frequency dependent AC measurements for **V_{20}H-Rb**.

As in **V_{20}H-Cs** no maximum in the temperature dependence of the in-phase or out-of-phase susceptibility was observed for temperatures above 1.8 K.

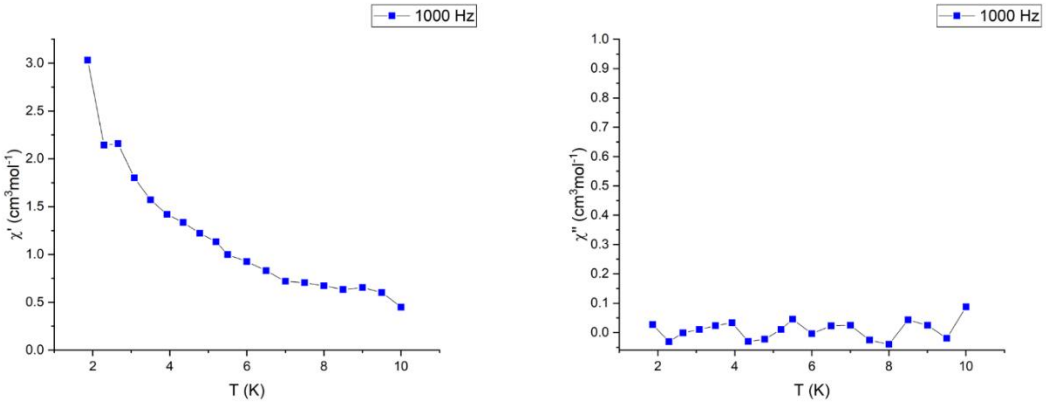

Figure 3.7.8 – Zero field temperature dependent AC measurements for **V_{20}H-Rb**.

3.8 Conclusions

In this chapter the synthesis, characterisation and properties of a family of novel supramolecular hybrid organic-inorganic polyoxovanadate clusters was reported. In order to expand on the flexibility of the $\{V_{10}\}$ system and to further test its variability benzene-1,3-diphosphonate was chosen as a ligand because of the narrower angle between the phosphonate groups in comparison to the PSP^{4-} ligand used in chapter 2. The use of benzene-1,3-diphosphonic acid together with a source of orthovanadate and an alkali metal chloride salt (K, Rb, Cs) under reducing conditions led to the formation of a $\{V_{20}\}$ torus, in which four inverted pentanuclear $\{V_5^*\}$ half-capsules are arranged around a cube of alkali metal cations in an inverted fashion.

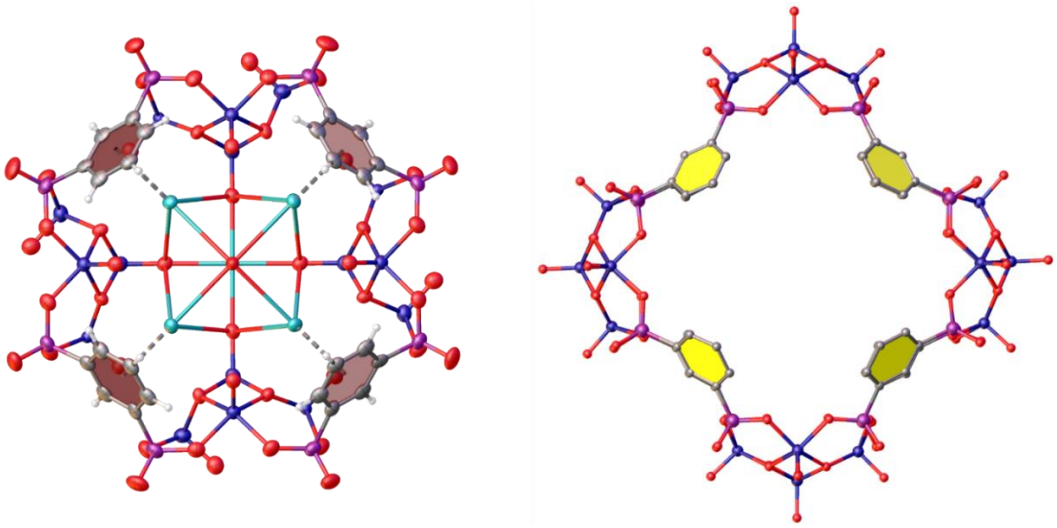

Figure 3.8.1 – Left: The synthesised $\{V_{20}\}$ system. Right: The possible $\{V_5\}_4$ system with four outward facing half-capsules. All attempts to synthesise the $\{V_5\}_4$ structures failed.

The conformational change of the $\{V_5*\}$ half-capsule compared to the $\{V_5\}$ half-capsule is accompanied by a loss in stabilisation energy, as theoretical investigations show. This is surprising as one could imagine a $\{V_{20}\}$ system in which four normal $\{V_5\}$ capsules are arranged in an outward facing fashion as shown in Figure 3.8.1. The loss in stabilisation energy has to be compensated in order for the system to favour the $\{V_{20}\}$ system with the inverted $\{V_5^*\}$ half-capsule. We hypothesize that the numerous cation-π interactions, which are build out between the alkali metal cube and the aromatic benzene rings of the ligand are the reason for the existence of the $\{V_{20}\}$ capsule. Aiding this conclusion is the fact that we are able to synthesise **V_{20}H-Cs**, **-Rb**, and **-K** but not the sodium version of the $\{V_{20}\}$ structure, which can be explained by the

strong solvation energy of the sodium cation in the aqueous solvent system. This drawback was utilised however in the syntheses of **V_{20}H-Rb**, and **V_{20}H-Cs**, in which Na_3VO_4 was used as the vanadium source together with the respective alkali metal chloride.

Further proof for the importance of the cation-π interactions is the existence of the $\{V_{20}\}$ species in aqueous solution as proven by ESI-MS. The measurements show a wide range of different oxidation states, ranging from four times reduced to twice oxidised when compared to the $\{V^{IV}_{16}V^{V}_{4}\}$ oxidation state in the solid state as it was assigned by XRD and SQUID measurements. It is not entirely clear if those oxidation states were a product of the ionisation process or exist in solution. It is indicative however that the cluster can accommodate these oxidation states without breaking apart. The same can be said for the loss of up to three alkali metal ions from the cluster core.

We therefore synthesised the first example of a supramolecular hybrid polyoxometalate cluster in which cation-π interactions constitute an integral part of the molecule. As the design and synthesis of polyoxometalate clusters are incredibly complex, hard to understand and even harder to predict the understanding and the utilisation of novel non-covalent interactions is important to path the way for novel compounds. We demonstrated that cation-π interactions can be strong enough to compensate both structural change in hybrid polyoxometalates as well as the loss of template molecules. The careful design of organic linkers that maximise cation-π interactions can aid the synthesis of hybrid polyoxometalate species or stabilise intermediates in solution that would have otherwise not been achievable.

1. Q. Yao and S. Levchik, *Tetrahedron Lett.*, 2006, **47**, 277-281.
2. V. Iaroshenko, *Organophosphorus Chemistry: From Molecules to Applications*, Wiley-VCH, Weinheim, 2019.
3. A. S. Mahadevi and G. N. Sastry, *Chem. Rev.*, 2013, **113**, 2100-2138.
4. C. Healy and W. Schmitt, *Coord. Chem. Rev.*, 2018, **371**, 67-85.
5. A. Spek, *Acta Cryst.*, 2015, **C71**, 9-18.
6. A. S. Mahadevi and G. N. Sastry, *Chem. Rev.*, 2016, **116**, 2775-2825.
7. D. Vijay and G. N. Sastry, *Chem. Phys. Lett.*, 2010, **485**, 235-242.
8. A. Spek, *Acta Cryst.*, 2009, **D65**, 148-155.
9. T. Zheng, Y. Gao, L. Chen, Z. Liu, J. Diwu, Z. Chai, T. E. Albrecht-Schmitt and S. Wang, *Dalton Trans.*, 2015, **44**, 18158-18166.
10. J. M. Breen and W. Schmitt, *Angew. Chem. Int. Ed.*, 2008, **47**, 6904-6908.
11. J.-P. Morel and N. Morel-Desrosiers, *Org. Biomol. Chem.*, 2006, **4**, 462-465.
12. M. Cametti, M. Nissinen, A. Dalla Cort, L. Mandolini and K. Rissanen, *J. Am. Chem. Soc.*, 2005, **127**, 3831-3837.

13. G. W. Bates, P. A. Gale, M. E. Light, M. I. Ogden and C. N. Warriner, *Dalton Trans.*, 2008, 4106-4112.
14. J. A. Przyojski, M. L. Kiewit, K. L. Fillman, H. D. Arman and Z. J. Tonzetich, *Inorg. Chem.*, 2015, **54**, 9637-9645.
15. L.-J. Zhou, W.-H. Deng, Y.-L. Wang, G. Xu, S.-G. Yin and Q.-Y. Liu, *Inorg. Chem.*, 2016, **55**, 6271-6277.
16. W. Schmitt, C. E. Anson, J. P. Hill and A. K. Powell, *J. Am. Chem. Soc.*, 2003, **125**, 11142-11143.
17. T. D. Keene, D. M. D'Alessandro, K. W. Krämer, J. R. Price, D. J. Price, S. Decurtins and C. J. Kepert, *Inorg. Chem.*, 2012, **51**, 9192-9199.
18. D. M. D'Alessandro and F. R. Keene, *Chem. Soc. Rev.*, 2006, **35**, 424-440.

Chapter 4

Modulating Cation-π Interactions in Hybrid Polyoxovanadates

4.1 Introduction

In chapter 3 it was established that cation-π interactions were an integral part of the {V_{20}} systems, both in the solid state as in solution. However, the overall effect on the hybrid POVs in terms of stability and formation was not entirely clear from the **V_{20}H-AM** compounds. Changing the alkali metal cation in **V_{20}H-AM** resulted only in minor differences, such as difficulties in the synthesis of **V_{20}H-K** and possible effects on the crystal packing. In this chapter the intention is to probe the nature and effect of these interactions within the {V_{20}} systems by modulating the electronic nature of the aromatic ring. As discussed in chapter 1.2.3 cation-π interactions can be influenced by adding substituents to the aromatic ring. A combination of through-space interactions and π-polarization results in changes of the molecular electrostatic potential above the benzene ring. Based on the calculations of Wheeler and Houk[169, 170] five additional ligands based on the benzene-1,3-bisphosphonic acid ligand were chosen for synthesis. The ligands and their abbreviations are shown in Figure 4.1.1.

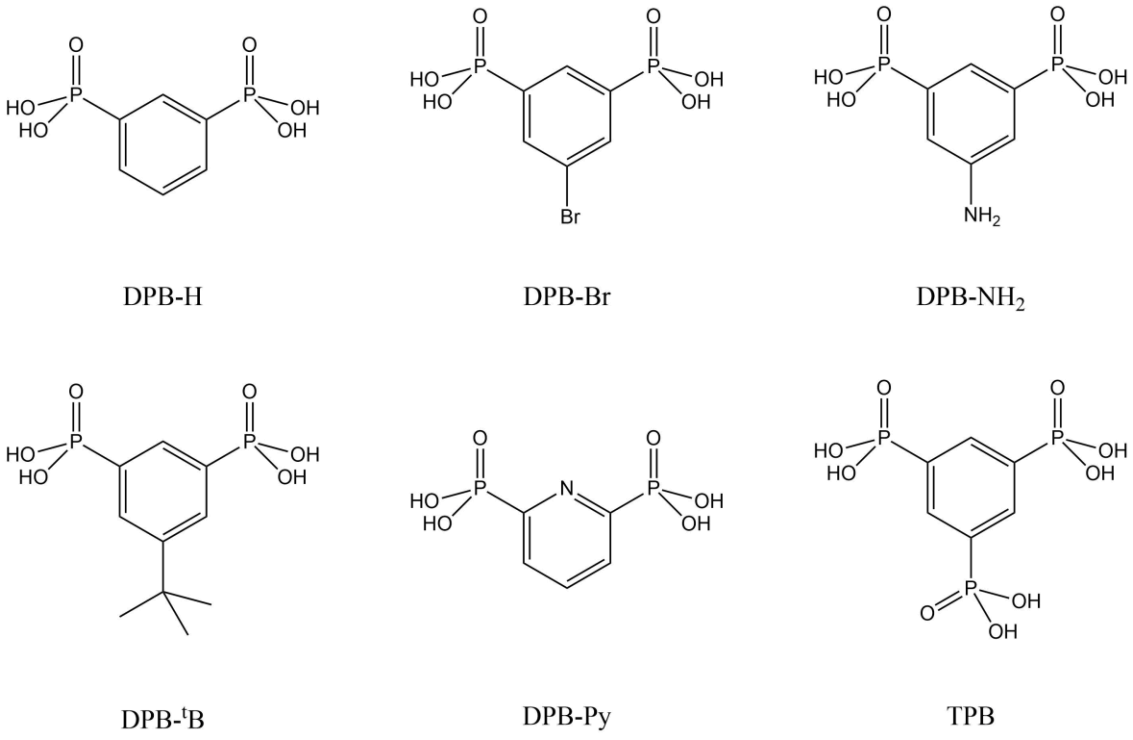

Figure 4.1.1 – Variations of the DPB-H ligands used in this thesis.

The ligands can be grouped by their effect on the cation-π interactions. Benzene-5-bromo-1,3-bisphosphonic acid (DPB-Br) and benzene-5-amino-1,3-bisphosphonic acid (DPB-NH_2) were

chosen to respectively decrease and enhance the molecular electrostatic potential (MEP) of the ligand. An example for this effect can be seen in Figure 4.1.2, which shows the MEP surfaces, values and gas-phase sodium-π interactions for mono-substituted benzene rings. A halogen substituent, such as F^-, Cl^- or Br^- reduces the interaction energy while the amino ligand increases it.

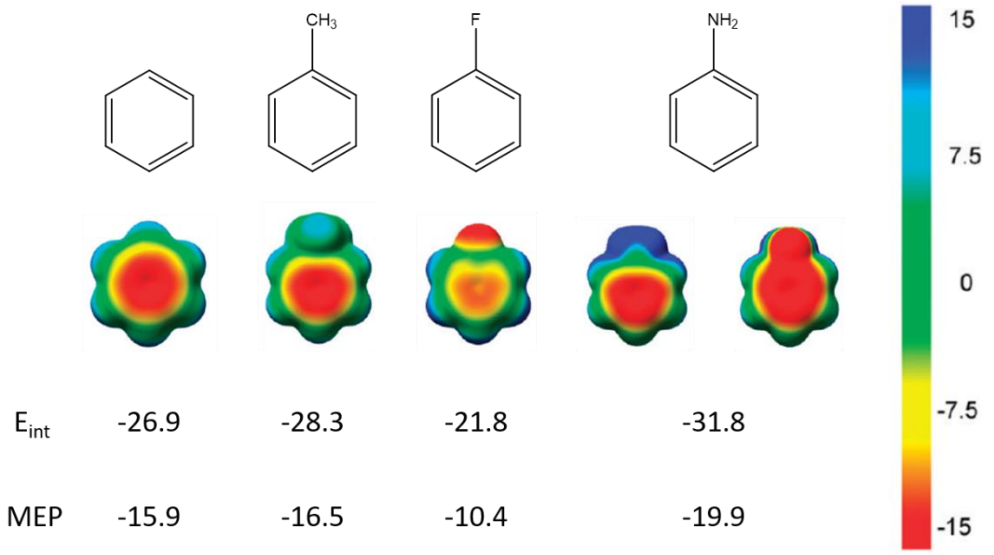

Figure 4.1.2 – MEP surfaces for differently substituted benzene ring. E_{int} are the interaction energies for the sodium-π interaction in the gas phase. MEP values taken at sodium distance. The MEP surface for aniline represents the front and the back. All values in kcal/mol.[169, 170]

The DPB-^{t}B ligand, in which the benzene-1,3-bisphosphonic acid ligand is functionalised with a *tert*-butyl group in the 5-poisiton was chosen to test if it was possible to inhibit the leaching of alkali metal cations as observed in the ESI-MS of the V_{20}H-AM systems. The incorporation of bulkier ligands additionally tests the general versatility of the {V_{20}} system. Alkyl substituents have a slight MEP enhancing effect on aromatic rings as demonstrated by the value for toluene in Figure 4.1.2. The incorporation of heteroatoms into the aromatic ring of hybrid POVs has been a goal of this thesis from the very beginning. Substituting the benzene ring with a pyridine ring in the DPB-H ligand should slightly reduce the MEP value at the cation-π distance. The tri-functionalised ligand Benzene-1,3,5-trisphosphonic acid (H_6TPB), featuring three phosphonate groups will be topic of chapter 5.

4.2 Ligand synthesis

The ligands DPB-Br, DPB-^{t}B and TPB were synthesized *via* a modified Michael-Arbuzov reaction as described for DPB-H in chapter 3.2. Applying this synthesis route for TPB has the additional benefit of producing the phosphonate ester of DPB-Br as a side product in the first step. The side product can be separated by column chromatography before deprotection with aqueous hydrochloric acid (HCl). The harsh conditions of the Michael-Arbuzov reaction, however, were found to be unsuited for the synthesis of the nitrogen containing ligands DPB-Py and DPB-NH_2. In these cases, the related but milder palladium-catalysed Hirao cross-coupling reaction[255] was utilised for the phosphonylation of the respective aryl bromide. In this named reaction an aryl bromide is reacted with a dialkylphosphite under a nitrogen atmosphere in the presence of a palladium catalyst, a phosphine and a base to yield functionalised phosphonate esters. The reaction scheme for the phosphonylation and deprotection of 2,6-dibrompyridine (DPB-Py) is shown in Figure 4.2.1.

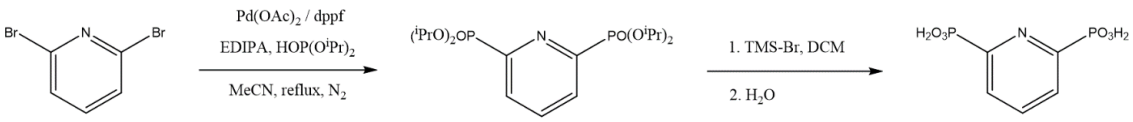

Figure 4.2.1 – Reaction scheme for the phosphonylation and deprotection of 2,6-dibromopyridine. Abbreviations: Ethyldiisopropylamine (EDIPA), 1,1′-Ferrocenediyl-bis(diphenylphosphine) (dppf).

Because of the heteroatom present in the ligand, deprotection of the phosphonate ester *via* aqueous HCl would not lead to the desired product. The reaction of phosphonate esters with an excess of trimethylsilyl bromide (TMS-Br) in DCM under a nitrogen atmosphere generates the trimethylsilyl ester in situ, which can subsequently be deprotected by the simple addition of water to the reaction.

4.3 $[(V_5O_9)_4(C_6H_3(PO_3)_2(NH_2))_8NaRb_8Cl_2]^{13-}$, ($V_{20}NH_2$-Rb, 8)

$V_{20}NH_2$-Rb was synthesized by the reaction of benzene-5-amino-1,3-bisphosphonic acid with sodium orthovanadate in the presence of rubidium chloride, sodium azide and hydrazine in the solvent system water, DMF and MeCN (3:1:1 / v:v:v) at pH = 7. By diffusing acetonitrile into the solution, green crystals, suitable for X-ray crystallography, formed in a matter of hours together with an inseparable white sticky impurity of unidentified nature. Noteworthy is the shortened time of crystallisation compared to **V_{20}H-Rb**, for which crystals formed after several days.

4.3.1 Crystallography

The crystal structure of **$V_{20}NH_2$-Rb** was solved in the tetragonal space group *P*4/*mnc* with following unit cell parameters.

$a = 19.7754(7)$ Å	$\alpha = 90°,$	$Z = 2$
$b = 19.7754(7)$ Å	$\beta = 90°$	$Z' = 0.125$
$c = 23.1729(9)$ Å	$\gamma = 90°$	$V = 9062.1(6)Å^3$

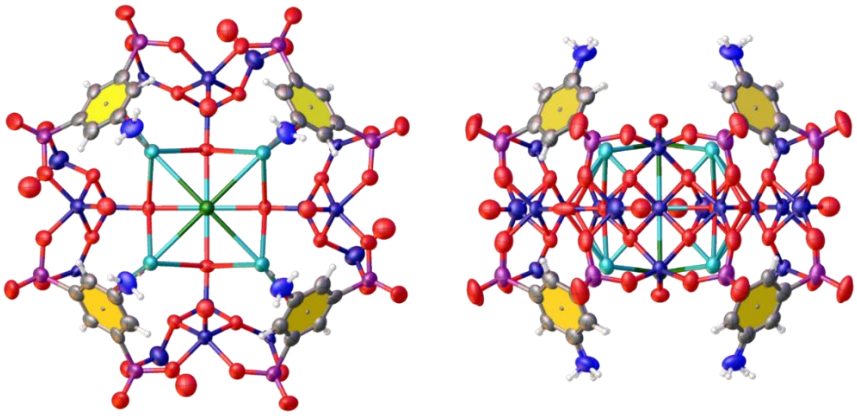

Figure 4.3.1 - Top and Side view of **$V_{20}NH_2$-Rb**.

The structure is almost identical to **V_{20}H-Rb** and will therefore be discussed in less detail with differences highlighted. As **V_{20}H-Rb**, the general structure consists of four mixed-valent pentanuclear half-capsules that are arranged around a cube of rubidium ions being bridged by

eight DPB-Py^{4-} ligands with a sodium ion in the centre of the structure. The {V_{20}} cluster is approximately 15.9 Å · 15.91 Å · 12.14 Å in size. The axial positions of the rubidium cube are occupied by two chloride ions. Because of the high symmetry space group *P4/mnc*, there is only one rubidium, one chloride and one sodium ion in the asymmetric unit. The cube is symmetry generated by a series of mirror planes as well as 2-fold rotation axes and a 4-fold rotational axis with a centre of symmetry at the sodium atom (Figure 4.3.2). The bonds lengths between the rubidium cations and the terminal *oxo*-ligands of the *oxo*-vanadium(V) ions are 3.2719(10) Å and the rubidium chloride bonds 3.508(7) Å long. The sodium ion in the middle of the structure builds out sodium oxygen bonds with a length of 2.382(8) Å and Na-Cl bonds with a length of 2.862(7) Å as is typical for sodium.

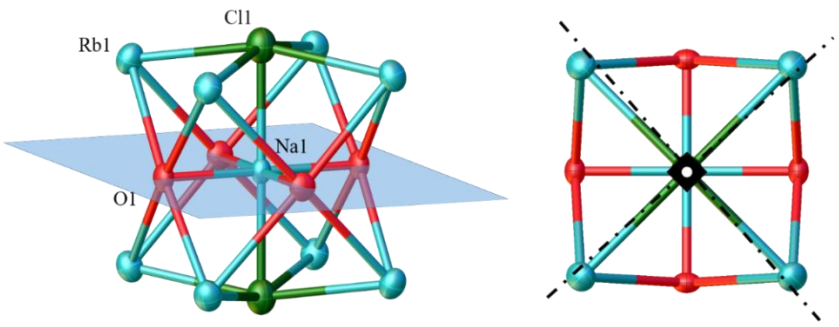

Figure 4.3.2 – The alkali metal cube of **$V_{20}NH_2$-Rb** with symmetry elements.

Table 4.3.1 - Bond lengths in the alkali metal cube for **$V_{20}NH_2$-Rb**.

Bond	Bond length / Å	Bond	Bond length / Å
Rb1-Cl1	3.2538(10)	**Rb1-O2^1**	3.217(7)
Rb1-O1^1	3.341(6)	**Rb1-O4B^1**	3.36(3)
Rb1-O1	3.390(6)	**Rb1-O3A**	3.42(4)
Rb1-O5	2.869(7)	**Cl1-Na1**	2.773(4)
Rb1-O61	2.879(6)	**O1-Na1**	2.388(8)
Rb1-O2^2	3.203(7)		
^{1}+Y,1-X,1-Z; ^{2}+X,+Y,1-Z; ^{3}+Y,1-X,+Z			

The pentanuclear half-capsule shows the same disorder as **V_{20}H-Rb**. The vanadyl groups in the middle of the structure were modelled as disordered over two positions in 50:50 fashion (Figure 4.3.3). The V=O bond lengths range from 1.592(19) Å to 1.651(17) Å and the V-O single bonds from 1.910(6) Å to 2.076(9) Å. BVS calculations confirm the oxidation state of +V for the central V1 and +IV for the neighbouring vanadium ions (Table 4.3.2).

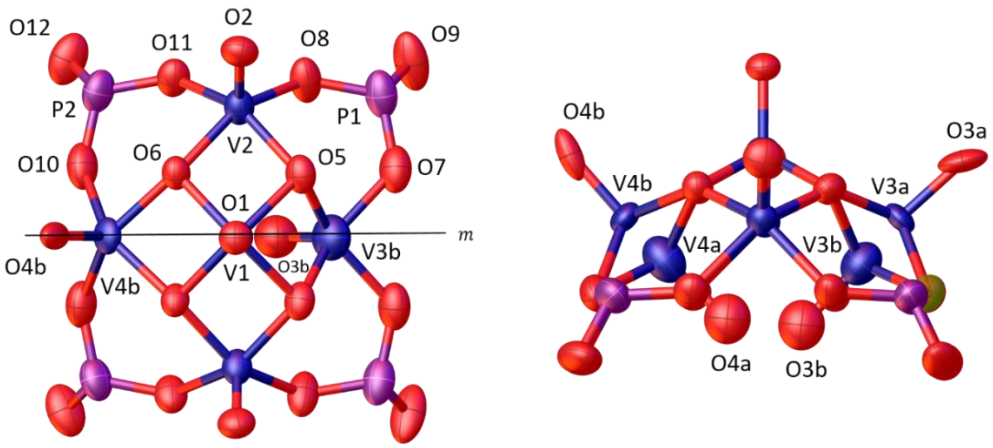

Figure 4.3.3 - Naming scheme of the pentanuclear half-capsule in **$V_{20}NH_2$-Rb**.

Table 4.3.2 – BVS calculations for **$V_{20}NH_2$ – Rb**.

	BVS	Oxidation state
V1	4.56	5
V2	3.99	4
V3a	3.82	4
V3b	3.81	4
V4a	3.69	4
V4b	3.77	4

The {V_{20}} clusters arrange themselves in tetragonal body centred fashion within the crystal structure. As in **V_{20}H-Cs** a slight rotation of the central {V_{20}} cluster reduces the apparent body-centred symmetry to primitive tetragonal. Due to heavy disorder, counter ions and solvent molecules could not be refined and were accounted for using the PLATON squeeze routine.

Table 4.3.3 – Bond lengths of the pentanuclear half-capsules in **$V_{20}NH_2$ – Rb**.

Bond	Bond length / Å	Bond	Bond length / Å
V1-O1	1.620(8)	**V3A-O7**	2.064(9)
V1-O5^2	1.930(7)	**V3A-O3A**	1.620(19)
V1-O5	1.930(7)	**V3B-O5**	2.003(8)
V1-O6	1.910(6)	**V3B-O7**	1.960(9)
V1-O6^2	1.910(6)	**V3B-O3B**	1.631(17)
V2-O5^2	1.937(7)	**V4A-O6**	1.977(8)
V2-O6	1.933(6)	**V4A-O10**	2.002(9)
V2-O8	1.977(7)	**V4A-O4A**	1.651(17)
V2-O2	1.621(7)	**V4B-O6**	1.968(7)
V2-O11^2	2.002(7)	**V4B-O6^2**	1.968(7)
V3A-O5^2	1.929(8)	**V4B-O10**	2.076(9)
V3A-O5	1.929(8)	**V4B-O10^2**	2.076(9)
V3A-O7^2	2.064(9)	**V4B-O4B**	1.592(19)
^{2} +X,+Y,1-Z			

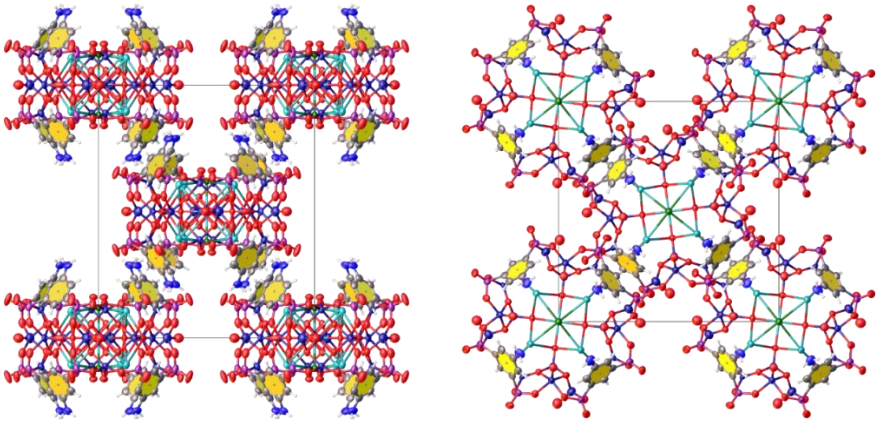

Figure 4.3.4 - Packing diagrams for **$V_{20}NH_2$-Rb** in [100] direction (left) and [001] direction (right).

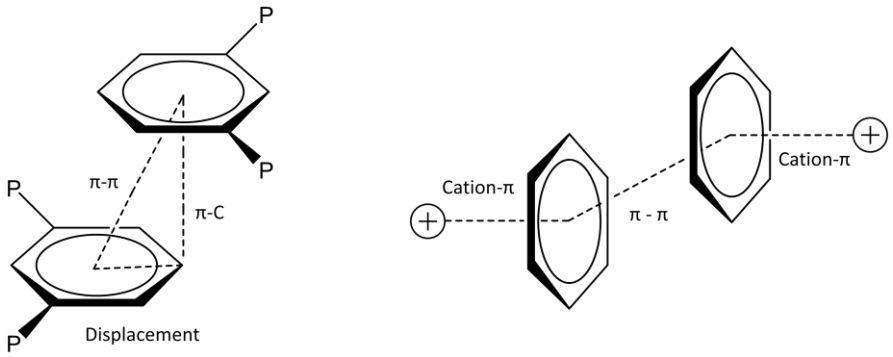

Figure 4.3.5 - General scheme for the cation-π-π-cation interactions.

The tetragonal space groups allow for the formation of cation-π-π-cation interactions. The cation-π distances are 3.225(3) Å, while the π-π interactions can be described by a centroid to centroid distance of d(π-π) = 3.780(5) Å, resulting from a plane to centroid distance of d(π-C) =3.424(6) Å with a displacement of 1.602(10) Å. The aromatic benzene rings involved in the π-π interactions are essentially parallel aligned with a plane-plane angle of 10.9(3)°. A comparison of these distances with the distances from **V_{20}H-Rb** shows that the cation-π distance was reduced from 3.271(3) Å in **V_{20}H-Rb** to 3.225(3) Å in **V_{20}H-NH_2**. While this is only a slight contraction the change in distance is outside the margin of the statistical errors for the distance measurements. The difference in the π-π interactions are more pronounced, and are significantly reduced from 3.912(5) Å to 3.780(5) Å. The reason for this seems to be rooted in the space group and the corresponding crystal packing as can be seen by comparing **$V_{20}NH_2$-Rb** and **V_{20}H-Cs**, which share the space group *P*4/*mnc*.

Table 4.3.4 – Comparison between **$V_{20}NH_2$-Rb**. SG = space group.

	π-π	**π-C**	**Displacement**	**Cation-π**	**Angle**	**SG**
$V_{20}NH_2$-Rb	3.780(5) Å	3.424(6) Å	1.602(10) Å	3.225(3) Å	10.9(3) °	*P*4/*mnc*
V_{20}H-Rb	3.912(5) Å	3.624(6) Å	1.475(10) Å	3.271(3) Å	0.0(3) °	*I*4/*mmm*
V_{20}H-Cs	3.741(8) Å	3.412(11) Å	1.534(16) Å	3.277(4) Å	5.1(3) °	*P*4/*mnc*

Table 4.3.5 –Crystallographic table for **$V_{20}NH_2$-Rb**.

Identification code	**$V_{20}NH_2$-Rb**
Empirical formula	$C_{48}H_{40}Cl_2N_8NaO_{84}P_{16}Rb_8V_{20}$
Formula weight/(g/mol)	4364.85
Temperature/K	99.99
Crystal system	tetragonal
Space group	$P4/mnc$
a/Å	19.7754(7)
b/Å	19.7754(7)
c/Å	23.1729(9)
α/°	90
β/°	90
γ/°	90
Volume/Å^3	9062.1(7)
Z	2
ρ_{calc} g/cm^3	1.6
μ/mm^{-1}	13.14
F(000)	4194
Crystal size/mm^3	0.1 × 0.07 × 0.06
Radiation	CuKα (λ = 1.54178)
2Θ range for data collection/°	5.876 to 125.016
Index ranges	$-21 \leq h \leq 21$, $-22 \leq k \leq 22$, $-26 \leq l \leq 26$
Reflections collected	53331
Independent reflections	3721 [R_{int} = 0.0721, R_{sigma} = 0.0341]
Data/restraints/parameters	3721/11/231
Goodness-of-fit on F^2	1
Final R indexes [I>=2σ (I)]	R_1 = 0.0767, wR_2 = 0.2075
Final R indexes [all data]	R_1 = 0.0834, wR_2 = 0.2123
Largest diff. peak/hole / e Å^{-3}	1.07/-1.27

4.4 $[(V_5O_9)_4(C_6H_3N(PO_3)_2)_8NaRb_8Cl_2]^{13-}$ (V_{20}Py-Rb, 9)

$[(V_5O_9)_4(C_6H_3N(PO_3)_2)_8NaRb_8Cl_2]^{13-}$ (**V_{20}Py-Rb**) was synthesized by the reaction of pyridine-1,6-bisphosphonic acid with sodium orthovanadate in the presence of rubidium chloride, sodium azide and hydrazine in the solvent system water, DMF and MeCN (3:1:1 / v:v:v) at pH = 7. By diffusing MeCN into the solution, green crystals, suitable for X-ray crystallography formed after several days together with a non-removable white residue.

4.4.1 Crystallography

The structure of **V_{20}Py-Rb** was solved in the tetragonal space group *I*4/*mmm*

$a = 19.7216(8)$ Å	$\alpha = 90°,$	$Z = 2$
$b = 19.7216(8)$ Å	$\beta = 90°$	$Z' = 0.0625$
$c = 22.3083(11)$ Å	$\gamma = 90°$	$V = 8676.6(7)$Å^3

The structure, shown in Figure 4.4.1, contains the same structural motif as **V_{20}H-Rb**, in which four $\{V_5^*\}$ half-capsules are arranged around a rubidium cube, being bridged by eight pyridine-1,6-bisphosphonic acid ligands. The cluster is approximately 12.16 Å · 16.14 Å · 16.14 Å in size

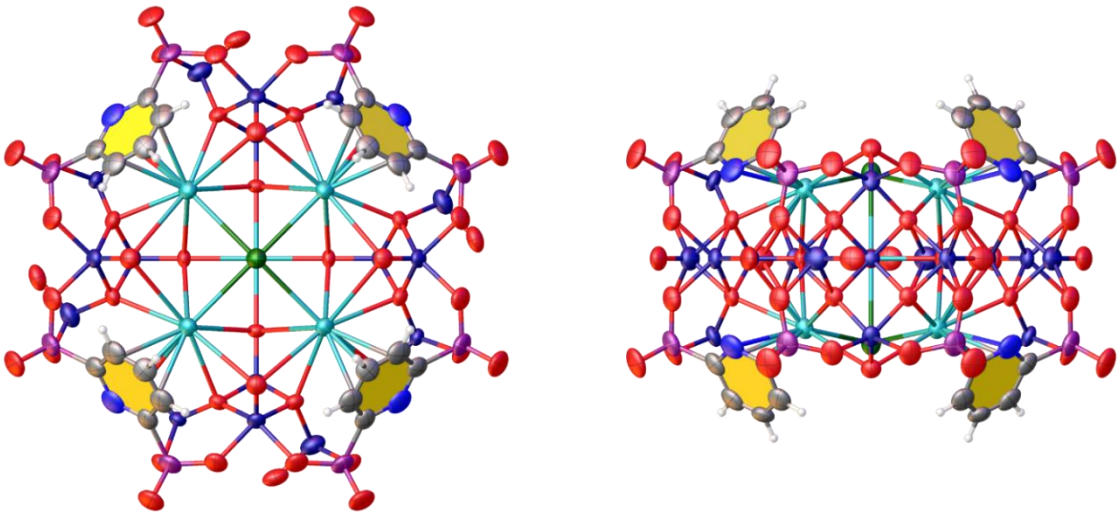

Figure 4.4.1 – Top and side view of the $\{V_{20}\}$ cluster in **V_{20}Py-Rb**.

Two chloride ions are located in the axial positions of the rubidium cube in the centre of the structure. The cube is symmetry generated by a series of mirror planes as well as 2-fold rotation

axes and a rotoinversion axis with the inversion centre on the sodium ion within the *I*4/*mmm* space group. (Figure 4.4.2).

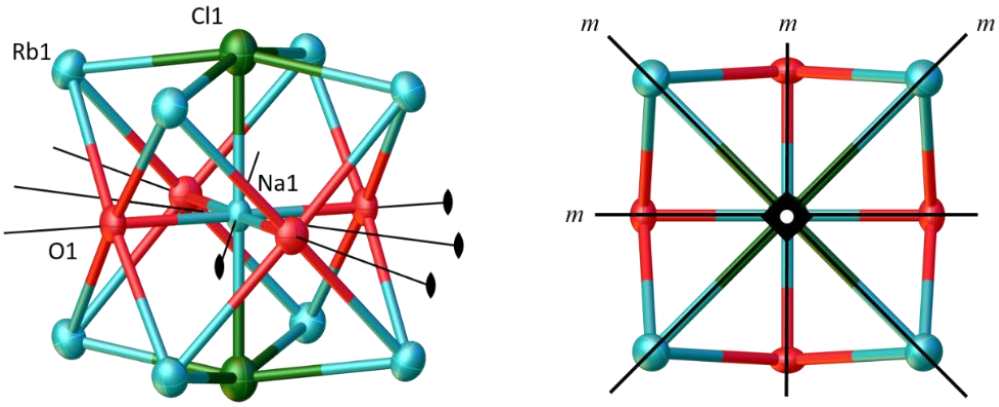

Figure 4.4.2 – The alkali metal cube with symmetry elements in **V_{20}Py-Rb**.

Table 4.4.1 – Bond lengths for the alkali metal cube in **V_{20}Py-Rb**.

Bond	Bond length / Å	Bond	Bond length / Å
Rb1-Cl1	3.2257(15)	**Rb1-N1**	3.505(10)
Rb1-O4[1]	2.872(5)	**Rb1-O3A[3]**	3.364(10)
Rb1-O4	2.872(5)	**Rb1-O3A[4]**	3.364(10)
Rb1-O1[2]	3.2717(9)	**Rb1-O3A**	3.364(10)
Rb1-O1	3.2717(9)	**Cl1-Na1**	2.864(7)
Rb1-O2[2]	3.254(5)	**O1-Na1**	2.378(8)
Rb1-O2	3.254(5)		
[1]+Y,+X,+Z; [2]1-Y,+X,+Z; [3]+X,+Y,1-Z; [4]+Y,+X,1-Z			

The bonds lengths between the rubidium cations and the terminal *oxo*-ligands of the *oxo*-vanadium(V) ions are 3.2717(9) Å and the Rb-Cl bonds are 3.2257(15) Å long. The sodium ion in the middle of the structure builds out sodium oxygen bonds with a length of 2.378(8) Å and Na-Cl bonds with a length of 2.864(7) Å. The Rb-O bond lengths vary between 2.872(5) Å and

3.364(10) Å. The bonds involving the sodium ion in the middle are 2.378(8) Å and 2.864(7) Å for the oxygen and chloride ions respectively. The disordered pentanuclear half-capsule can be seen in Figure 4.4.3. The bond lengths for the V=O double bonds range from 1.601(8) Å to 1.632(8) Å while the V-O single bonds range from 1.933(5) Å to 2.063(6) Å. Interestingly, BVS calculations seem to indicate that the central *oxo*-vanadium ion is in the oxidation state +IV (Table 4.4.2). This is unusual given the vast amounts of known structures with this motif, in which the central vanadium ion is clearly in the oxidation state +V, as proven by the number of counter ions, IVCT bands in UV-VIS spectra and magnetic measurements.

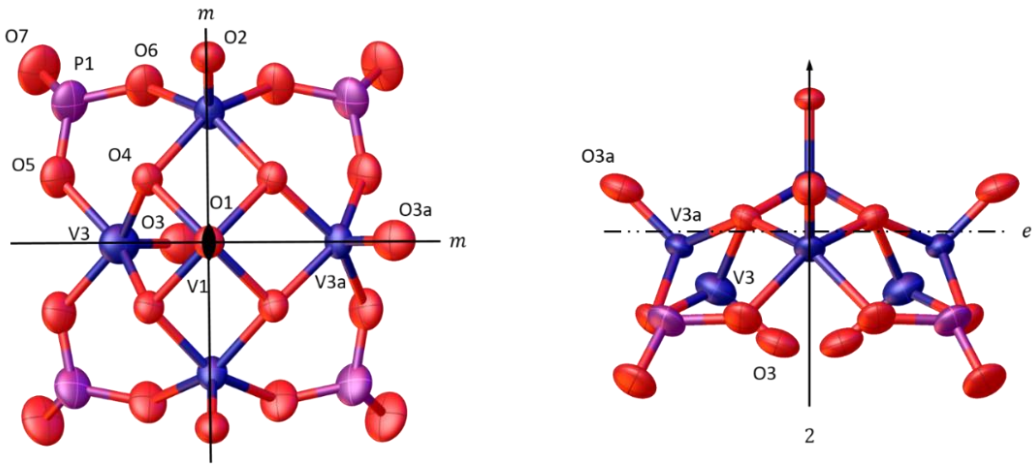

Figure 4.4.3 – Naming scheme for the disordered pentanuclear half-capsule of **V_{20}Py-Rb**.

Table 4.4.2 – BVS calculations for **V_{20}Py-Rb**.

	BVS	Oxidation state
V1	4.12	4
V2	4.06	4
V3	3.91	4
V3a	3.85	4

Table 4.4.3 – Bond lengths for the pentanuclear half-capsule of **V_{20}Py-Rb**.

Bond	Bond length / Å	Bond	Bond length / Å
V1-O1	1.632(8)	**V2-O65**	1.991(5)
V1-O4	1.936(5)	**V3A-O3A**	1.607(7)
V1-O4^{3}	1.936(5)	**V3A-O3A^{3}**	1.607(7)
V1-O4^{5}	1.936(5)	**V3A-O4**	1.933(5)
V1-O4^{6}	1.936(5)	**V3A-O5**	2.063(6)
V2-O2	1.601(8)	**V3-O3**	1.624(9)
V2-O4	1.939(5)	**V3-O4**	2.005(6)
V2-O4^{5}	1.939(5)	**V3-O5**	1.942(7)
V2-O6	1.991(5)	**V3-O5**	1.942(7)
^{3}+X,+Y,1-Z; ^{5}+X,1-Y,+Z; ^{6}+X,1-Y,1-Z			

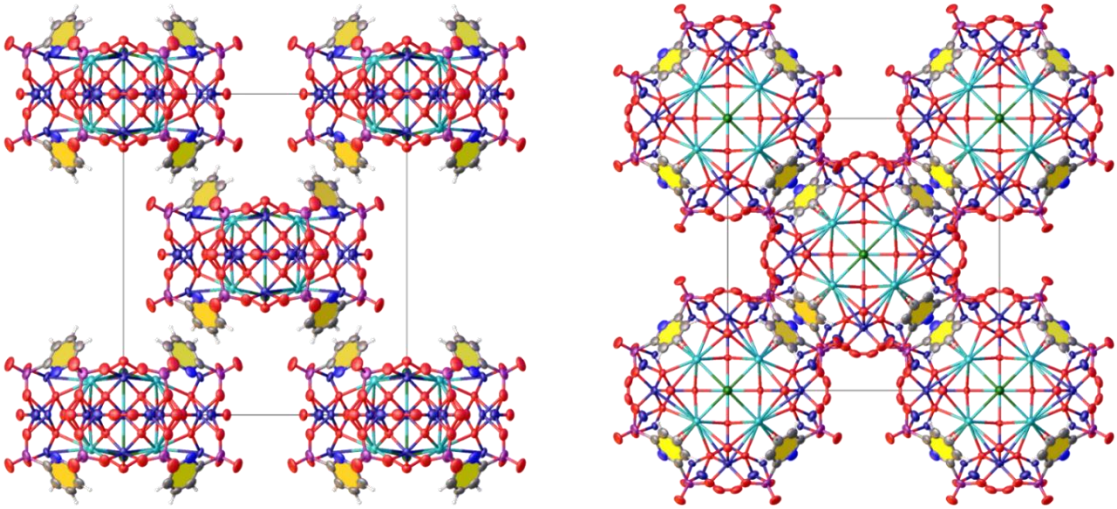

Figure 4.4.4 – Packing diagram of **V_{20}Py-Rb** in [100] (left) and [001] direction (right).

V_{20}Py-Rb was solved in the crystallographic space group *I*4/*mmm*, for which Figure 4.4.4 shows the packing diagram in [100] and [001] direction. The clusters pack in the same way as in the structure of **V_{20}H-Rb**. The higher symmetry body-centred space group leads to alignment of the

clusters in the unit cell, which resonates into the geometry of the cation-π-π-cation interactions. The plane-plane angle between the benzene rings of the ligands are therefore 0.0(7)°. Interestingly, both the cation-π distances and the π-π distances are significantly shortened in comparison to **V_{20}H-Rb**. The cation-π distance is reduced by 0.031 Å and the π-π distance by 0.341 Å. This compression is seen in the unit cell as well, in which **V_{20}Py-Rb** is on average 0.79 Å shorter per unit cell axis. As the counter ions could not be resolved in the crystal structure it is hard to determine if this correlation follows a causation in either direction.

Table 4.4.4 – Comparison of the cation-π-π-cation interactions and unit cells in **V_{20}H-Rb** and **V_{20}Py-Rb**.

	π-π	π-C	Displacement	Cation-π	Angle	SG
V_{20}Py-Rb	3.571(10) Å	3.353(12) Å	1.229(19) Å	3.240(5) Å	0.0(7) °	*I*4/*mmm*
V_{20}H-Rb	3.912(5) Å	3.624(6) Å	1.475(10) Å	3.271(3) Å	0.0(3) °	*I*4/*mmm*
	a / Å	***b*** / Å	***c*** / Å	**α = β = γ / °**	***V*** / Å^3	**SG**
V_{20}H-Rb	20.5147(5)	20.5137(5)	23.089(7)	90	9714.0(5)	*I*4/*mmm*
V_{20}Py-Rb	19.7216(8)	19.7216(8)	22.3038(11)	90	8676.6(7)	*I*4/*mmm*

Table 4.4.5 –Crystallographic table for **V_{20}Py-Rb**.

Identification code	**V_{20}Py-Rb**
Empirical formula	$C_{40}H_{24}Cl_2N_8NaO_{84}P_{16}Rb_8V_{20}$
Formula weight/(g/mol)	4252.64
Temperature/K	100
Crystal system	tetragonal
Space group	$I4/mmm$
a/Å	19.7216(8)
b/Å	19.7216(8)
c/Å	22.3083(11)
α/°	90
β/°	90
γ/°	90
Volume/Å^3	8676.6(8)
Z	2
ρ_{calc} g/cm^3	1.628
μ/mm^{-1}	13.707
F(000)	4066
Crystal size/mm^3	0.06 × 0.05 × 0.03
Radiation	CuKα (λ = 1.54178)
2Θ range for data collection/°	5.982 to 136.618
Index ranges	-20 ≤ h ≤ 23, -18 ≤ k ≤ 23, -26 ≤ l ≤ 25
Reflections collected	30037
Independent reflections	2261 [R_{int} = 0.0635, R_{sigma} = 0.0329]
Data/restraints/parameters	2261/3/127
Goodness-of-fit on F^2	1.003
Final R indexes [I>=2σ (I)]	R_1 = 0.0634, wR_2 = 0.1874
Final R indexes [all data]	R_1 = 0.0701, wR_2 = 0.1930
Largest diff. peak/hole / e Å^{-3}	0.92/-1.43

4.5 The $V_{20}{}^{t}B$-AM system (AM = Cs, Rb, K)

4.5.1 Synthesis

The three compounds **$V_{20}{}^{t}B$-AM** (AM = Cs, Rb, K) were synthesized from sodium orthovanadate in presence of DPB-^{t}B, sodium azide and the respective alkali metal chloride under reducing conditions in a solution of water, DMF and MeCN at pH ~ 7. In the case of **$V_{20}{}^{t}B$-K** the combination of sodium orthovanadate and alkali metal chloride was substituted with the use of potassium orthovanadate. All compounds were obtained by diffusing MeCN into the solution as green crystals after several days. Single crystals of **$V_{20}{}^{t}B$-Cs** and **$V_{20}{}^{t}B$-Rb** were suitable for XRD, while no crystals of sufficient quality could be obtained of **$V_{20}{}^{t}B$-K**.

4.5.2 $Rb_{13}[V_{20}P_{16}O_{84}NaRb_8C_{80}H_{96}Cl_2] \cdot 29\ H_2O$ ($V_{20}{}^{t}B$ – Rb, 10)

4.5.2.1 Crystallography

The crystal structure of **$V_{20}{}^{t}B$-Rb** was solved in the monoclinic space group *C*2/*m* with following unit cell parameters.

$a = 20.4471(12)$ Å	$\alpha = 90°$	$Z = 2$
$b = 33.574(2)$ Å	$\beta = 105.2820(10)°$	$Z' = 0.25$
$c = 17.9993(18)$ Å	$\gamma = 90°$	$V = 11919.4(16)$ Å^3

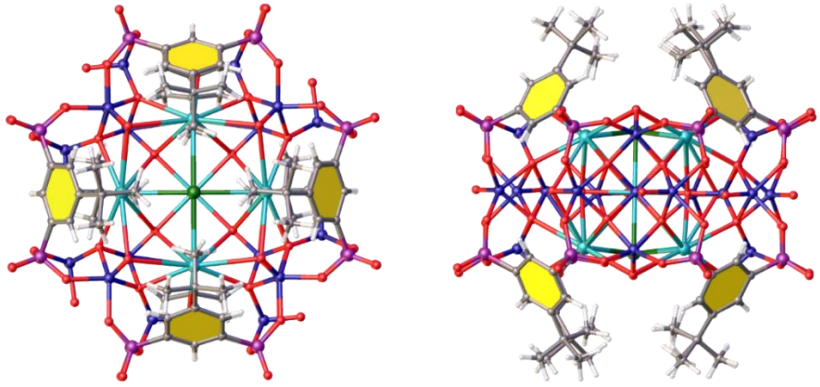

Figure 4.5.1 – Top and side view of the {V_{20}} cluster in **$V_{20}{}^{t}B$-Rb**.

The {V_{20}} cluster is, with the exception of the ligand, identical with the already discussed {V_{20}} cluster and can be seen in Figure 4.5.1. Because of the bulky *tert*-butyl group the cluster is

approximately 14.99 Å · 17.24 Å · 17.31 Å in size and therefore a bit bigger than its DPB-H counterpart **V_{20}H-Rb**.

The alkali metal cube in the unit cell is symmetry generated by a mirror plane and an inversion centre on the position of the central sodium ion as shown in Figure 4.5.2. Both axial positions are occupied by chloride ions, for which the Rb-Cl bond lengths are between 3.1906(10) Å and 3.393(7) Å long. The Rb-O bond lengths lie between 3.533(7) Å and 3.393(7) Å (Table 4.5.1).

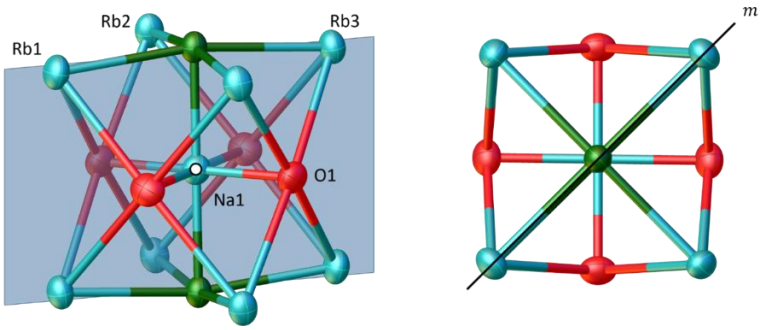

Figure 4.5.2 – Alkali metal cube for **V_{20}^{t}B-Rb** with a mirror plane and an inversion centre as symmetry elements.

Table 4.5.1 – Bond lengths for the alkali metal cube of **V_{20}^{t}B-Rb**.

Bond	Bond length / Å	Bond	Bond length / Å
Rb1-Cl1^{1}	3.221(3)	**Rb2-O1**	3.385(7)
Rb1-O1	3.393(7)	**Rb2-O1^{3}**	3.383(7)
Rb1-O1^{2}	3.393(7)	**Rb3-Cl1**	3.225(3)
Rb2-Cl1^{1}	3.1906(10)	**Rb3-O1**	3.353(7)
Na1-Cl1	2.759(3)	**Na1-O1**	2.396(6)
^{1}1-X,1-Y,1-Z; ^{2}+X,1-Y,+Z; ^{3}1-X,+Y,1-Z			

The pentanuclear half-capsule can be seen in Figure 4.5.3. The V=O double bonds range from 1.572(12) Å to 1.660(3) Å and average to 1.61 Å while the V-O single bond are between 1.851(6) Å and 2.198(11) Å long and average to 1.99 Å (Table 4.5.2). Bad data quality combined with the disorder in the structure is likely the cause for unusual high minimum and maximum values of the vanadium oxygen bond lengths. BVS calculations can be seen in Table 4.5.3.

Table 4.5.2 – Bond lengths for the pentanuclear half-capsule in **V_{20}-^{t}B-Rb**.

Bond	Bond length / Å	Bond	Bond length / Å
V1-O1	1.620(6)	**V4-O4**	1.635(8)
V1-O8	1.851(6)	**V4-O7**	2.021(8)
V1-O6	1.913(7)	**V4A-O7**	1.945(7)
V1-O9	1.858(6)	**V4A-O6**	1.942(7)
V1-O7	1.905(6)	**V4A-O16**	2.059(9)
V2-O7	1.952(7)	**V4A-O15**	2.039(9)
V2-O8	1.953(7)	**V4A-O4A**	1.572(12)
V2-O2	1.593(6)	**V5-O8**	2.010(7)
V2-O10	1.968(6)	**V5-O9**	1.994(7)
V2-O18	1.963(6)	**V5-O12**	2.089(12)
V3-O6	1.948(7)	**V5-O5**	1.660(3)
V3-O3	1.616(6)	**V5-O19^{3}**	2.120(11)
V3-O9	1.958(6)	**V5-O8**	2.010(7)
V3-O20^{3}	1.961(7)	**V5A-O12**	2.198(11)
V3-O13	1.979(7)	**V5A-O8**	1.983(6)
V4-O7	2.021(8)	**V5A-O9**	1.919(6)
V4-O6	2.029(7)	**V5A-O5A**	1.653(9)
V4-O15	1.975(9)	**V5A^{3}-O19**	2.177(10)
V4-O7	2.021(8)		
^{3}1-X,+Y,1-Z			

Table 4.5.3 – BVS calculations for **V_{20}^{t}B-Rb**.

	BVS	Oxidation state		BVS	Oxidation state
V1	4.89	5	**V4A**	3.99	4
V2	4.13	4	**V5**	3.32	4
V3	4.01	4	**V5A**	3.34	4
V4	3.71	4			

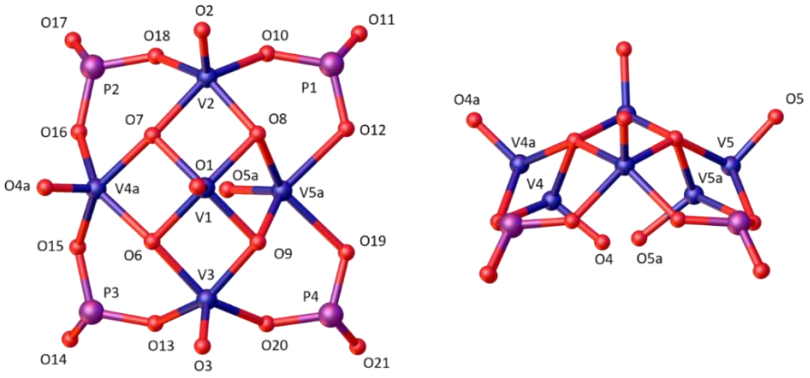

Figure 4.5.3 – Naming scheme for the pentanuclear half-capsule in **$V_{20}{}^{t}$B-Rb.**

Due to the bulky *tert*-butyl substituents on the ring the {V_{20}} cluster does not engage in π-π interactions between clusters in the crystal structure. The cation-π distances average to 3.20 Å, which is slightly, but significantly shorter than the 3.24 Å in **V_{20}H-Rb**. The {V_{20}} structures arrange themselves in layers within the crystallographic *ab*-plane, which leads to the classical separation of inorganic and organic domains in the crystal structure. Figure 4.5.4 shows the packing diagram in [100] and [010] direction, which show the layers of organic *tert*-butyl groups and the inorganic POV clusters. The red and yellow dots visualise different positions in view direction. Cations and solvent water molecules could not be modelled due to data quality issues and were accounted for with the PLATON squeeze routine.

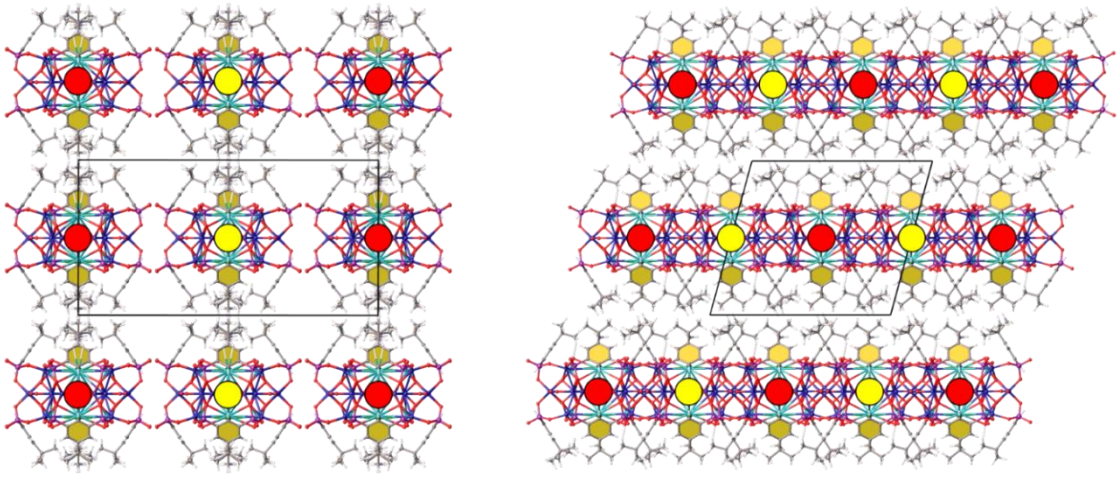

Figure 4.5.4 – Packing diagram of **$V_{20}{}^{t}$B-Rb** in [100] and [010] direction.

Table 4.5.4 –Crystallographic table for **V_{20}^{t}B-Rb**.

Identification code	**V_{20}^{t}B-Rb**
Empirical formula	$C_{80}H_{96}Cl_2NaO_{84}P_{16}Rb_8V_{20}$
Formula weight/(g/mol)	4849.76
Temperature/K	100.01
Crystal system	monoclinic
Space group	C2/m
a/Å	20.4471(12)
b/Å	33.574(2)
c/Å	17.9993(18)
α/°	90
β/°	105.2820(10)
γ/°	90
Volume/Å^3	11919.4(16)
Z	2
ρ_{calc} g/cm^3	1.351
μ/mm^{-1}	2.58
F(000)	4628
Crystal size/mm^3	0.204 × 0.105 × 0.099
Radiation	MoKα (λ = 0.71073)
2Θ range for data collection/°	5.056 to 50.992
Index ranges	$-24 \leq h \leq 24$, $-40 \leq k \leq 40$, $-21 \leq l \leq 21$
Reflections collected	92548
Independent reflections	11251 [R_{int} = 0.1427, R_{sigma} = 0.0798]
Data/restraints/parameters	11251/98/525
Goodness-of-fit on F^2	1.025
Final R indexes [I>=2σ (I)]	R_1 = 0.0814, wR_2 = 0.2325
Final R indexes [all data]	R_1 = 0.1375, wR_2 = 0.2776
Largest diff. peak/hole / e Å^{-3}	1.82/-1.84

4.5.3 $Cs_{13}[V_{20}P_{16}O_{84}NaCs_8C_{80}H_{96}Cl_2] \cdot 26\ H_2O$ ($V_{20}{}^{t}$B-Cs, 11)

4.5.3.1 Crystallography

The crystal structure of **$V_{20}{}^{t}$B-Cs** was solved in the triclinic space group $P\bar{1}$ with unit cell parameters of:

$a = 17.8917(8)$ Å	$\alpha = 116.487(3)°$	$Z = 1$
$b = 19.7119(9)$ Å	$\beta = 102.900(4)°$	$Z' = 0.5$
$c = 20.1522(10)$ Å	$\gamma = 96.335(3)°$	$V = 6018.6(6)$ Å^3

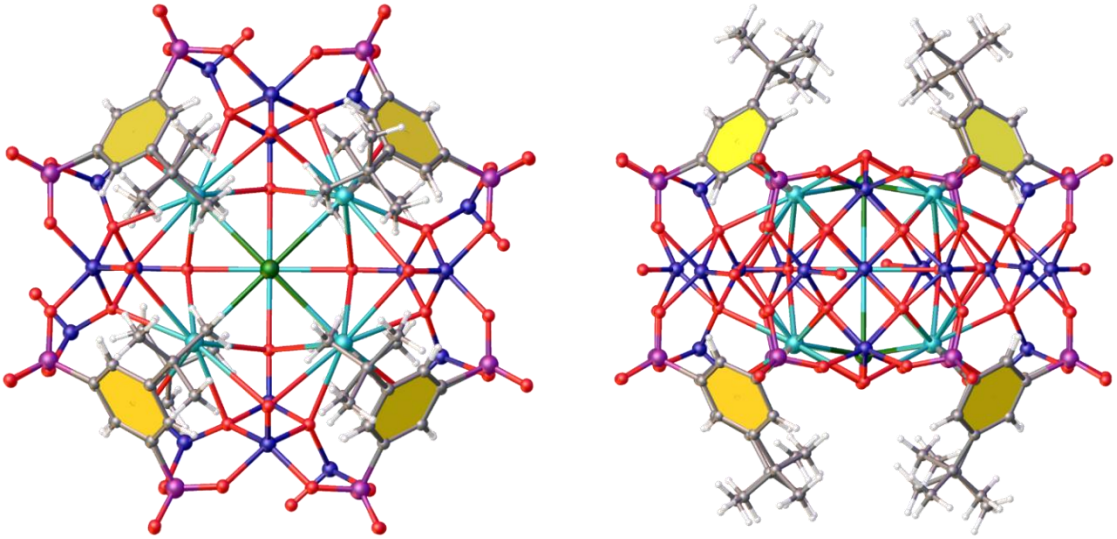

Figure 4.5.5 - Top and side view of the {V_{20}} cluster in **$V_{20}{}^{t}$B-Cs**.

The {V_{20}} cluster in **$V_{20}{}^{t}$B-Cs** is structurally identical to the POV in **$V_{20}{}^{t}$B-Rb** and about 15.29 Å · 17.39 Å · 17.39 Å in size. The alkali metal cube is only symmetry generated by an inversion centre due to the low symmetry space group $P1$. The axial positions are occupied by chloride ions, which build out Cs-Cl bonds, whose lengths average to 3.26 Å. The Cs-O bond lengths range from 2.961(7) Å to 3.50(4) Å. As in **V_{20}H-Cs** a sodium ion is located in the centre of the structure.

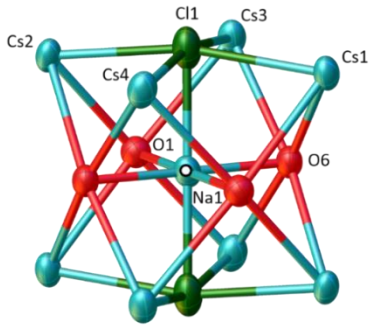

Figure 4.5.6 – The alkali metal cube in **$V_{20}{}^{t}$B-Cs** with an inversion centre on the sodium ion.

Table 4.5.5 - Bond lengths for the alkali metal cube of **$V_{20}{}^{t}$B-Cs**.

Bond	Bond length / Å	Bond	Bond length / Å	Bond	Bond length / Å
Cs1-Cl1[1]	3.278(3)	**Cs2-O6**	3.331(6)	**Cs4-Cl1**	3.254(3)
Cs1-O1	3.364(7)	**Cs2-O7**	3.329(9)	**Cs4-O1[1]**	3.397(7)
Cs1-O6	3.351(8)	**Cs2-O14**	2.986(8)	**Cs4-O6**	3.372(8)
Cs1-O13	2.961(7)	**Cs2-O10A**	3.361(15)	**Cs4-O7**	3.272(7)
Cs1-O16	3.002(8)	**Cs3-Cl1**	3.258(4)	**Cs4-O3[1]**	3.296(8)
Cs1-O3	3.306(10)	**Cs3-O2**	3.299(7)	**Cs4-O12[1]**	2.976(7)
Cs1-O8	3.275(7)	**Cs3-O1**	3.361(7)	**Cs4-O18**	2.974(7)
Cs1-O10A	3.488(17)	**Cs3-O6[1]**	3.366(6)	**Cs4-O5A[1]**	3.46(3)
Cs1-O4	3.35(3)	**Cs3-O11**	2.975(8)	**Cs4-O9**	3.45(4)
Cs2-Cl1	3.254(3)	**Cs3-O17[1]**	2.993(7)	**Na1-Cl1**	2.813(4)
Cs2-O2	3.252(7)	**Cs3-O8[1]**	3.280(8)	**Na1-O1**	2.495(6)
Cs2-O1	3.381(7)	**Cs3-O5A**	3.42(2)	**Na1-O6**	2.555(6)
Cs2-O15	2.996(6)	**Cs3-O9[1]**	3.50(4)		

[1]1-X,1-Y,1-Z

The mixed valence pentanuclear half-capsules shows the same positional disorder as in the previously discussed compounds. The V=O double bond lengths range from 1.582(6) Å to 1.634(10) Å, while the single bonds range from 1.884(12) Å to 2.149(11) Å. BVS analysis confirms the typical oxidation states $\{V^{V}V^{IV}_{4}\}$, which can be seen in Table 4.5.6.

Table 4.5.6 – BVS calculation for **$V_{20}{}^{t}$B-Cs**.

	BVS	Oxidation state		BVS	Oxidation state
V1	4.55	5	**V6**	4.51	5
V2	3.99	4	**V7**	4.13	4
V3	3.99	4	**V8**	4.16	4
V4	3.94	4	**V9**	3.66	4
V4a	3.96	4	**V9a**	3.78	4
V5	3.83	4	**V10**	4.04	4
V5a	3.78	4	**V10a**	3.92	4

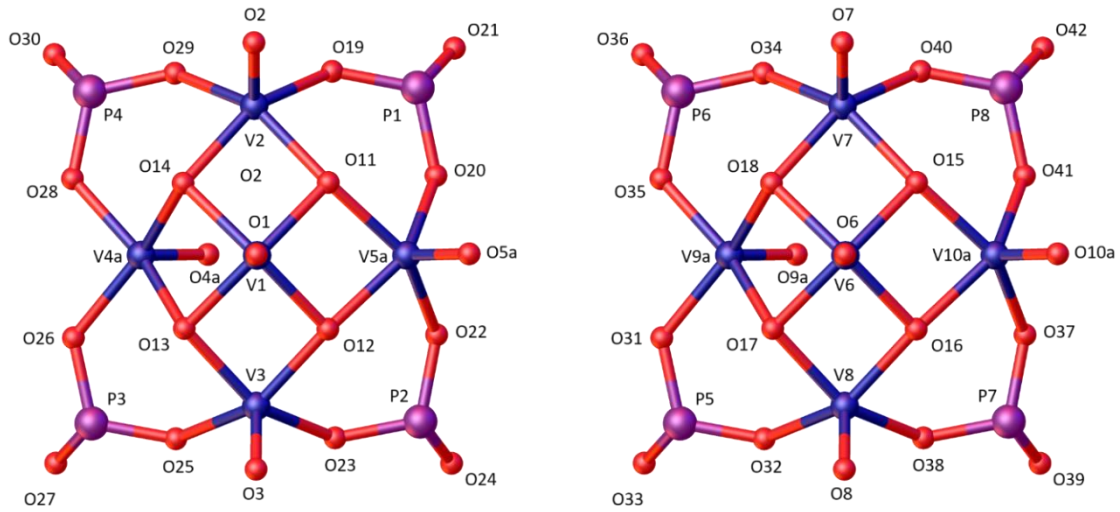

Figure 4.5.7 – Naming scheme for the pentanuclear half-capsule in **$V_{20}{}^{t}$B-Cs**.

Table 4.5.7 – Bond lengths for the pentanuclear half-capsule in **V_{20}H-Cs**.

Bond	Length / Å	Bond	Length / Å	Bond	Length / Å
V1-O1	1.627(6)	**V4A-O26**	1.973(10)	**V8-O32[1]**	1.993(9)
V1-O13	1.920(8)	**V5-O20**	1.977(11)	**V8-O38**	2.003(8)
V1-O11	1.909(7)	**V5-O5**	1.634(10)	**V8-O8**	1.584(7)
V1-O14	1.935(7)	**V5-O11**	1.988(13)	**V9-O17**	1.948(10)
V1-O12	1.908(9)	**V5-O12**	1.995(10)	**V9-O31[1]**	2.086(10)
V2-O2	1.598(7)	**V5-O22**	1.952(14)	**V9-O18**	1.966(8)
V2-O29	2.002(7)	**V5A-O11**	1.952(9)	**V9-O35[1]**	2.149(11)
V2-O11	1.962(7)	**V5A-O12**	1.975(8)	**V9-O9**	1.602(10)
V2-O14	1.937(7)	**V5A-O22**	2.051(11)	**V9A-O17**	2.066(10)
V2-O19	2.004(8)	**V5A-O20**	2.070(10)	**V9A-O31[1]**	1.951(9)
V3-O13	1.948(8)	**V5A-O5A**	1.600(9)	**V9A-O18**	2.021(8)
V3-O3	1.605(6)	**V6-O15**	1.922(7)	**V9A-O35[1]**	1.925(12)
V3-O12	1.933(8)	**V6-O6**	1.621(6)	**V9A-O9A**	1.633(8)
V3-O25	2.006(8)	**V6-O16**	1.926(8)	**V10-O10**	1.622(9)
V3-O23	1.999(9)	**V6-O17**	1.922(7)	**V10-O16**	1.919(9)
V4-O4	1.593(9)	**V6-O18**	1.930(9)	**V10-O41**	2.002(10)
V4-O13	1.890(9)	**V7-O15**	1.925(9)	**V10-O37**	1.884(12)
V4-O14	1.965(9)	**V7-O7**	1.582(6)	**V10-O15**	2.017(10)
V4-O28	2.102(9)	**V7-O40**	1.984(7)	**V10A-O15**	1.916(9)
V4-O26	2.021(11)	**V7-O18**	1.941(7)	**V10A-O16**	1.969(7)
V4A-O4A	1.639(9)	**V7-O34[1]**	2.020(10)	**V10A-O41**	2.044(10)
V4A-O13	1.986(7)	**V8-O16**	1.927(7)	**V10A-O37**	2.062(10)
V4A-O14	1.946(9)	**V8-O17**	1.924(8)	**V10A-O10A**	1.590(9)
V4A-O28	1.922(9)				
[1]1-X,1-Y,1-Z					

The packing diagram can be seen in Figure 4.5.8. As in **$V_{20}{}^{t}$B-Rb**, the clusters build out layers in the crystallographic *bc* plane, which leads to separate domains of the organic *tert*-butyl groups and the inorganic POV clusters. The network of caesium ions and water molecules could not be modelled due to high degree of disorder and bad data quality. The PLATON squeeze routine[244] was therefore employed.

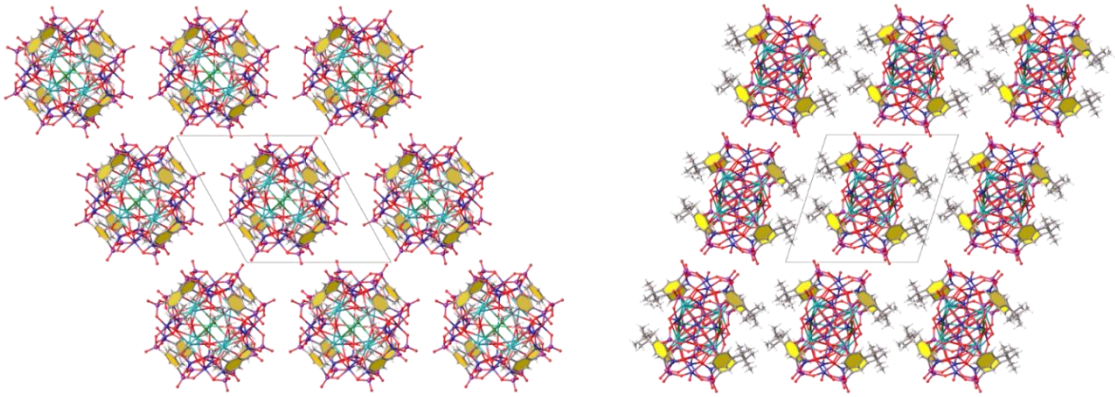

Figure 4.5.8 – Packing diagram of **$V_{20}{}^{t}$B-Cs** in [100] and [010] direction.

Table 4.5.8 – Crystallographic table for **$V_{20}{}^{t}$B-Cs.**

Identification code	**$V_{20}{}^{t}$B-Cs**
Empirical formula	$C_{80}H_{96}Cl_2Cs_8NaO_{84}P_{16}V_{20}$
Formula weight/(g/mol)	5073.05
Temperature/K	99.99
Crystal system	triclinic
Space group	P-1
a/Å	17.8917(8)
b/Å	19.7119(9)
c/Å	20.1522(10)
α/°	116.487(3)
β/°	102.900(4)
γ/°	96.335(3)
Volume/Å^3	6018.5(5)
Z	1
ρ_{calc} g/cm^3	1.4
μ/mm^{-1}	17.255
F(000)	2433
Crystal size/mm^3	0.11 × 0.09 × 0.06
Radiation	CuKα (λ = 1.54178)
2Θ range for data collection/°	5.22 to 117.86
Index ranges	-18 ≤ h ≤ 19, -21 ≤ k ≤ 21, -22 ≤ l ≤ 22
Reflections collected	47961
Independent reflections	17211 [R_{int} = 0.0837, R_{sigma} = 0.1058]
Data/restraints/parameters	17211/321/960
Goodness-of-fit on F^2	1.02
Final R indexes [I>=2σ (I)]	R_1 = 0.0687, wR_2 = 0.1875
Final R indexes [all data]	R_1 = 0.1015, wR_2 = 0.2087
Largest diff. peak/hole / e Å^{-3}	1.05/-1.00

4.5.4 Characterisation

4.5.4.1 IR spectroscopy

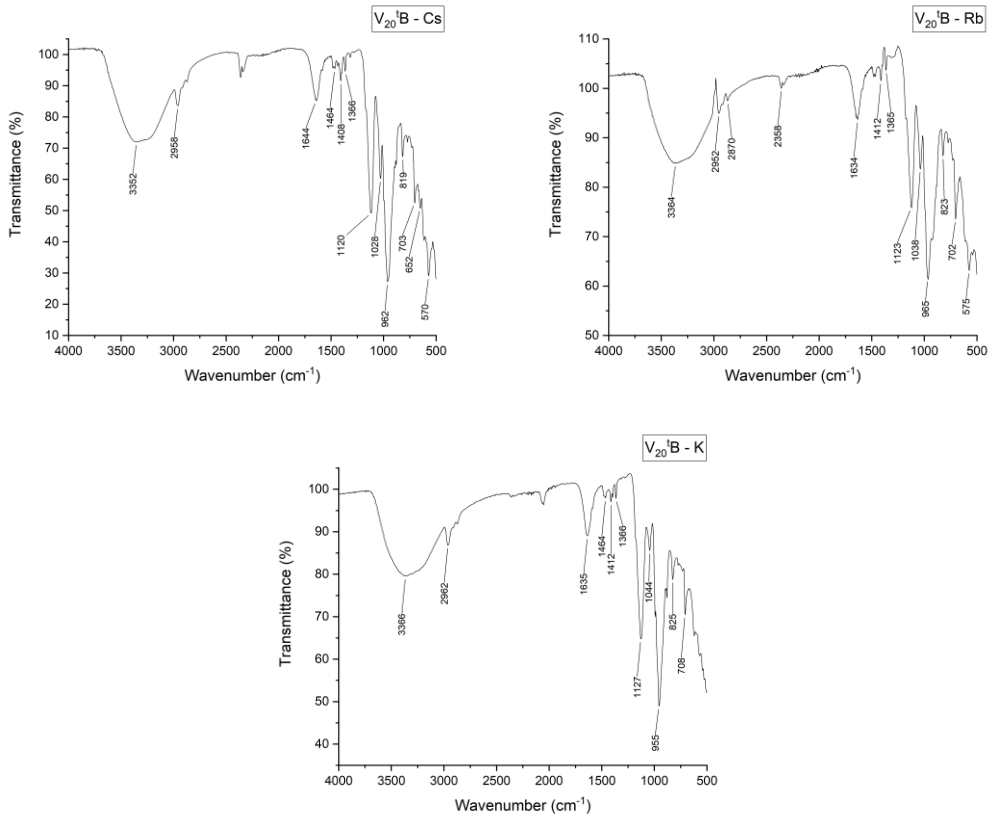

IR spectra of **V_{20}^{t}B-AM** (AM = **Cs**, **Rb**, **K**) were recorded from 4000 cm^{-1} to 500 cm^{-1}. As with the **V_{20}H-AM** series all IR spectra are virtually identical due to the similar structure of the compounds. The absence of unexpected peaks backs the structure elucidation by SXRD. The broad signals around 3360 cm^{-1} and 1640 cm^{-1} are stemming from constitutional water molecules. The signal at around 2958 cm^{-1} can be assigned to the *tert*-butyl group of the DPB-^{t}B ligand as can the signals between 1360 cm^{-1} and 1470 cm^{-1}. The signals at around 1120 cm^{-1} and 1030 cm^{-1} can be attributed to the phosphonate group of the ligand while the signal around 965 cm^{-1} stems from the V=O double bonds with vanadium(IV) and vanadium(V).

4.5.4.2 TGA

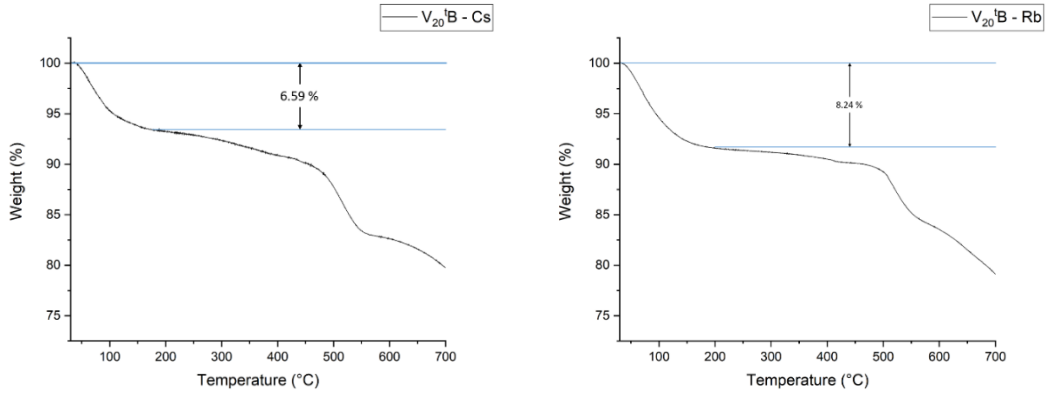

To investigate the amount of water molecules as identified by IR spectroscopy and to test the thermal stability of the compounds, TGA curves were recorded for **$V_{20}{}^{t}$B-Cs** and **$V_{20}{}^{t}$B-Rb** from 30°C to 700°C under a nitrogen atmosphere. The first drop in weight of 6.59 % from 30°C to 180°C in the TGA of **$V_{20}{}^{t}$B-Cs** corresponds to 26 water molecules (theoretical value: 6.44 %). The loss in weight from 30°C to 180°C in the TGA of **$V_{20}{}^{t}$B-Rb** of 8.24% can be attributed to the loss of 29 water molecules (theoretical value: 8.26 %). Ligand decomposition can be seen in both TGA curves from about 450°C with additional oxide formation after approximately 600°C. All TGA results correspond well with the results from CHN analysis and therefore prove the molecular composition of the compounds.

4.5.4.3 PXRD

To investigate the phase-purity of the compound as well as the absence of crystalline impurities a PXRD pattern was recorded from 5˚ to 55˚ θ. The simulated pattern of **$V_{20}{}^{t}$B-Rb** based on the monoclinic phase determined by SXRD fits well with the experimental pattern. Differences in intensity can be explained by crystals orienting themselves in a preferred orientation within the capillary. The structure determined by SXRD is therefore representative for all crystals within the bulk sample of **$V_{20}{}^{t}$B-Rb**.

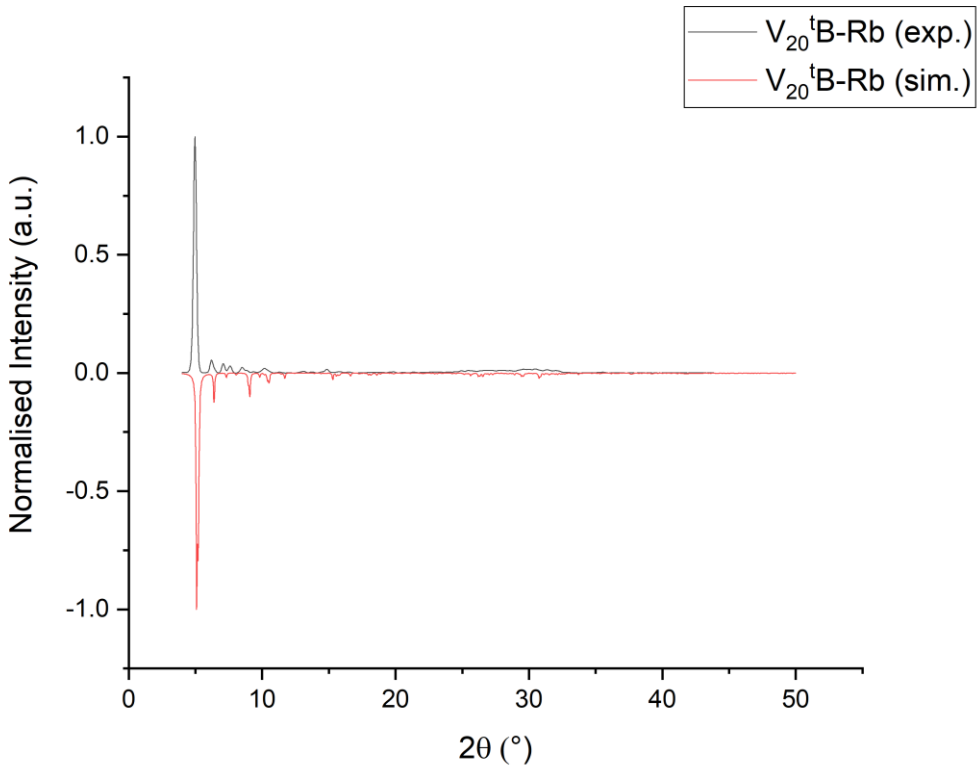

Figure 4.5.9 – Simulated and calculated PXRD pattern for **$V_{20}{}^{t}$B-Rb**.

4.5.4.4 MS

ESI-MS spectra were recorded for all three **$V_{20}{}^{t}$B-AM** (AM = Cs, Rb, K) compounds in water. All spectra show the typical broad envelopes of 5- and 4- charged species of the {V_{20}} polyoxovanadates in different oxidation states and composed of various numbers of counter ions. The strongest signals can be found below 500 m/z, which belong to the free ligand.

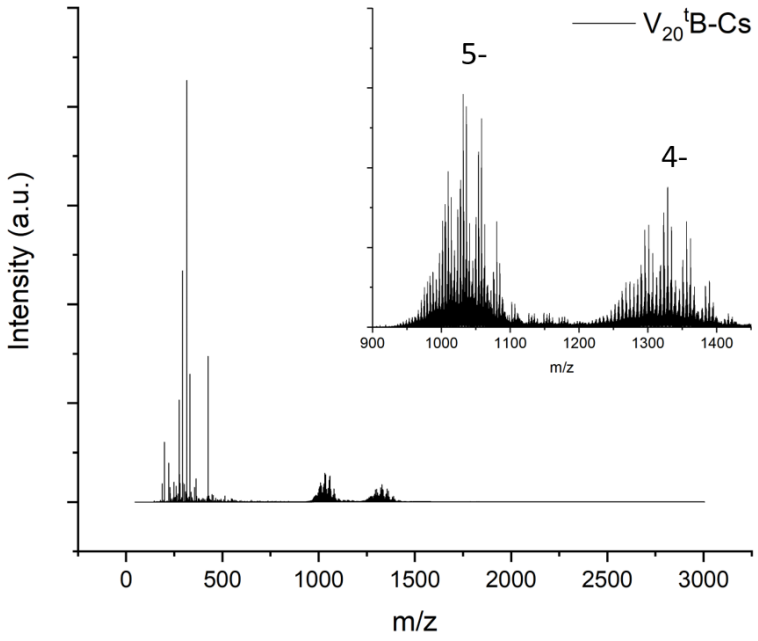

Figure 4.5.10 – ESI-MS spectrum of **$V_{20}{}^{t}$B-Cs**.

Figure 4.5.10 shows the full ESI-MS spectrum of **$V_{20}{}^{t}$B-Cs** up to 3000 m/z. The 5- and 4- envelopes can be seen together with their assigned peaks in Figure 4.5.11 and Figure 4.5.12. The observed oxidation states range from three times reduced to three times oxidised in the 5- envelope and from four times reduced to four times oxidised in the 4- envelope. The matching peak patterns for the non-oxidised {$V^{IV}_{16}V^{V}_{4}$} species are shown in Figure 4.5.13. Figure 4.5.14 shows the part of the ESI-MS spectrum, which can only stem from species that have lost caesium ions from their alkali metal cube in the centre of the structure. The existence of peaks with less than eight rubidium ions proves that the *tert*-butyl group does not completely prevent the alkali metal cube to dissociate either in solution or during the ionisation process. As in the V_{20}H-AM compounds however, the alkali metal cube is still an integral part of the molecule in $V_{20}{}^{t}$B-AM compounds in the solid state as well as in aqueous solution.

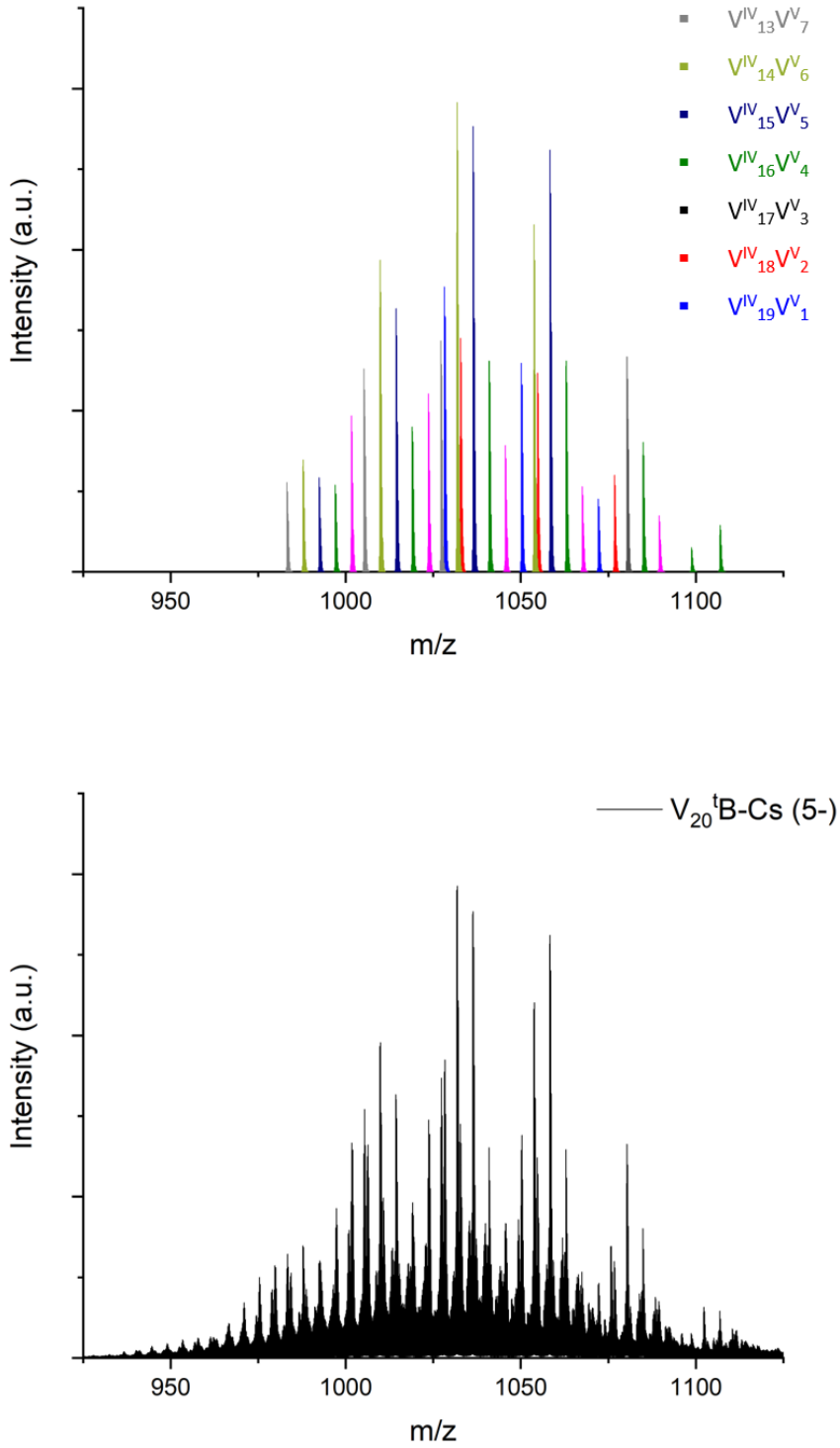

Figure 4.5.11 – Modelled peaks for the 5- envelope of **$V_{20}{}^{t}$B-Cs**.

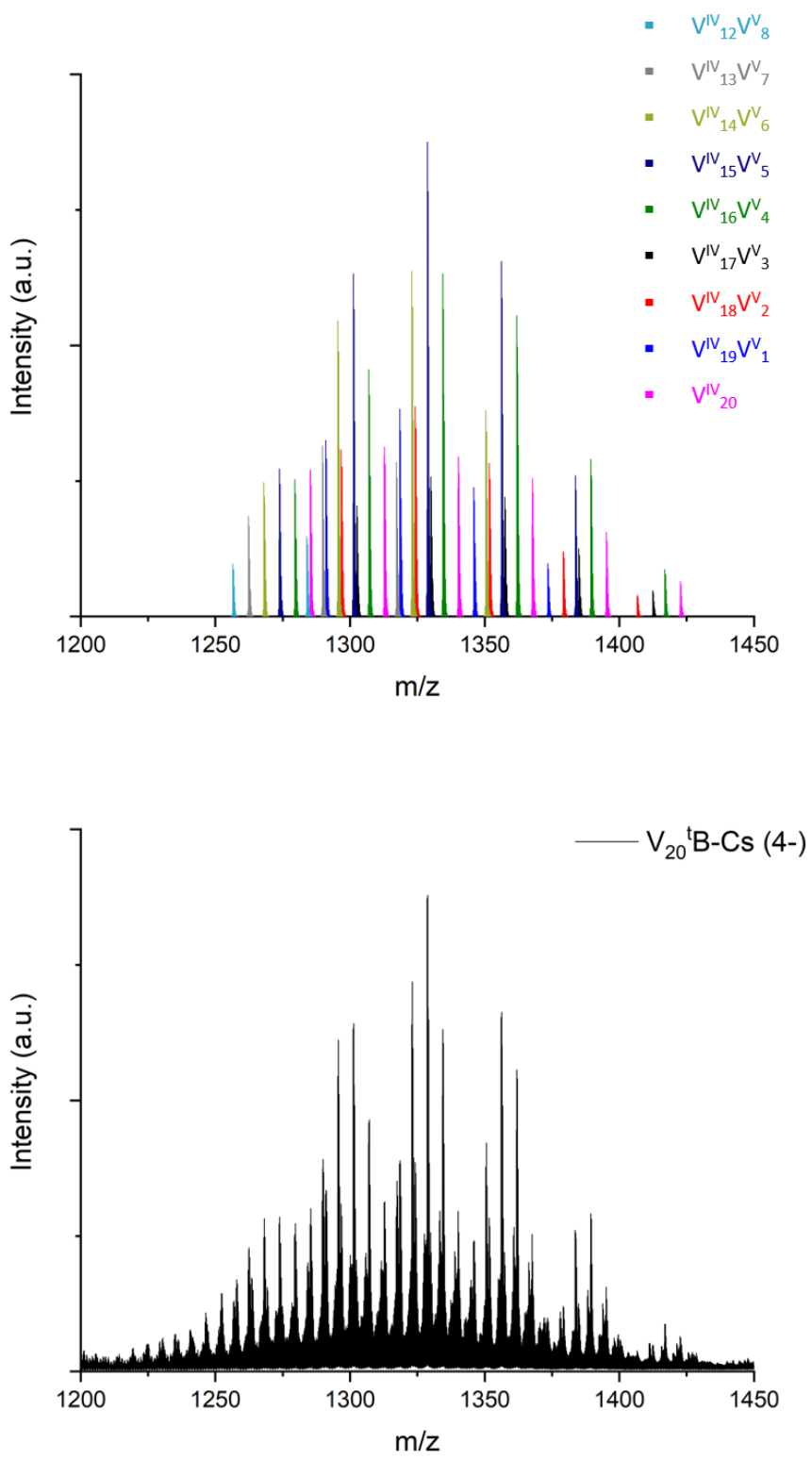

Figure 4.5.12 - Modelled peaks for the 5- envelope of **$V_{20}{}^{t}$B-Cs**.

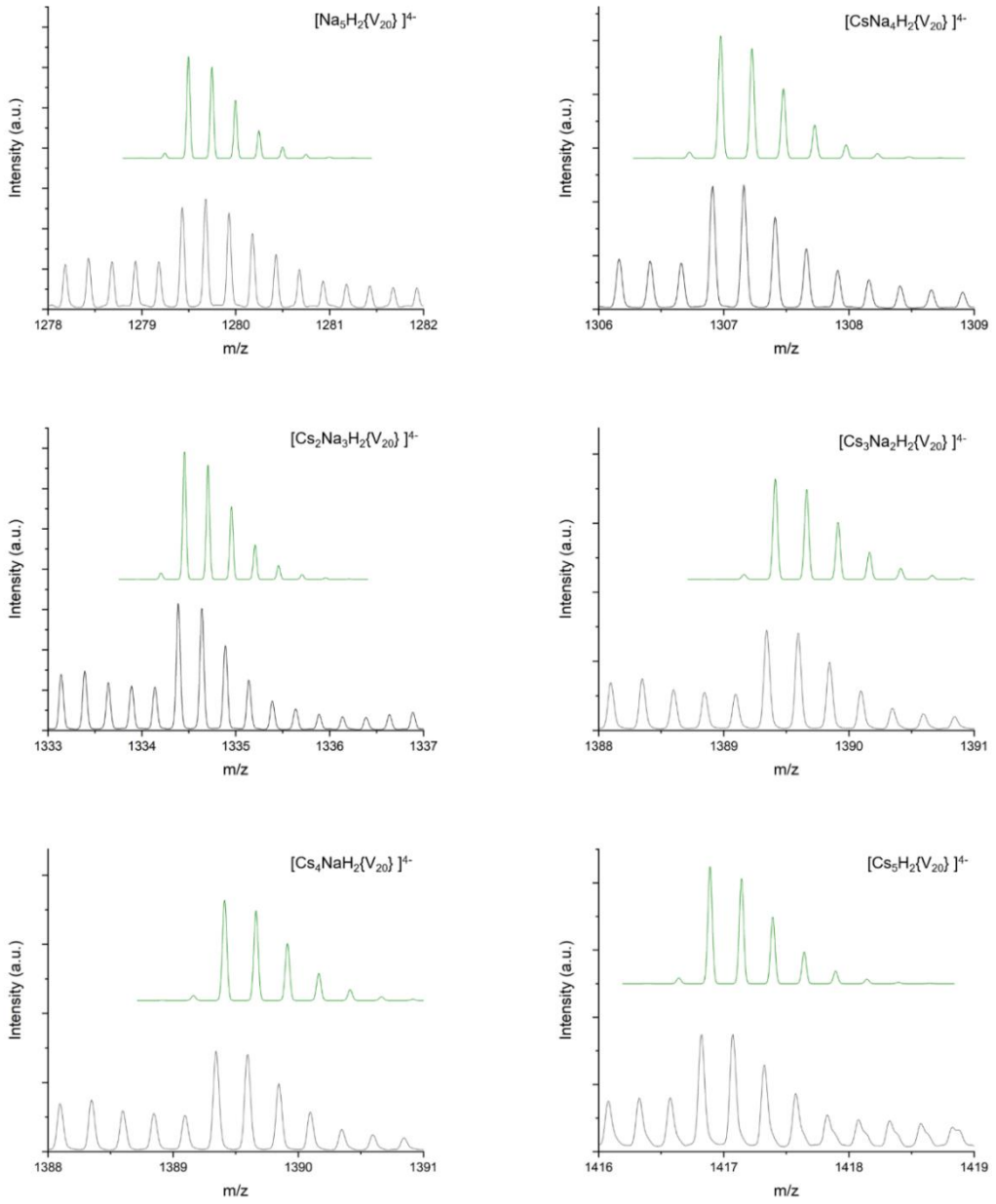

Figure 4.5.13 – Matching peak patterns for the $\{V^{IV}_{16}V^{V}_{4}\}$ oxidation state in the 4- envelope of **V_{20}^{t}B-Cs**.

Table 4.5.9 – Assigned peaks in the 4- envelope in the ESI-MS of **$V_{20}{}^{t}$B-Cs**.

Counter ions	Oxidation state	Calculated (m/z)	Peak (m/z)	Charge
Na_9H_2	V^{IV}_{20}	1302.485	1302.413	4-
$CsNa_8H_2$	V^{IV}_{20}	1329.964	1329.889	4-
$Cs_2Na_7H_2$	V^{IV}_{20}	1357.443	1357.367	4-
$Cs_3Na_6H_2$	V^{IV}_{20}	1384.922	1384.845	4-
$Cs_4Na_5H_2$	V^{IV}_{20}	1412.4	1412.323	4-
Na_8H_2	$V^{IV}_{19}V^{V}_{1}$	1296.738	1296.666	4-
$CsNa_7H_2$	$V^{IV}_{19}V^{V}_{1}$	1324.217	1324.139	4-
$Cs_2Na_6H_2$	$V^{IV}_{19}V^{V}_{1}$	1351.696	1351.619	4-
$Cs_3Na_5H_2$	$V^{IV}_{19}V^{V}_{1}$	1379.175	1379.098	4-
$Cs_4Na_4H_2$	$V^{IV}_{19}V^{V}_{1}$	1406.654	1406.58	4-
Na_7H_2	$V^{IV}_{18}V^{V}_{2}$	1290.99	1290.917	4-
$CsNa_6H_2$	$V^{IV}_{18}V^{V}_{2}$	1318.469	1318.394	4-
$Cs_2Na_5H_2$	$V^{IV}_{18}V^{V}_{2}$	1345.948	1345.871	4-
$Cs_3Na_4H_2$	$V^{IV}_{18}V^{V}_{2}$	1373.427	1373.357	4-
Na_6H_2	$V^{IV}_{17}V^{V}_{3}$	1285.243	1285.168	4-
$CsNa_5H_2$	$V^{IV}_{17}V^{V}_{3}$	1312.722	1312.647	4-
$Cs_2Na_4H_2$	$V^{IV}_{17}V^{V}_{3}$	1340.201	1340.133	4-
$Cs_3Na_3H_2$	$V^{IV}_{17}V^{V}_{3}$	1367.68	1367.615	4-
$Cs_4Na_2H_2$	$V^{IV}_{17}V^{V}_{3}$	1395.159	1395.093	4-
Cs_5NaH_2	$V^{IV}_{17}V^{V}_{3}$	1422.638	1422.568	4-
Na_5H_2	$V^{IV}_{16}V^{V}_{4}$	1279.495	1279.424	4-
$CsNa_4H_2$	$V^{IV}_{16}V^{V}_{4}$	1306.974	1306.91	4-
$Cs_2Na_3H_2$	$V^{IV}_{16}V^{V}_{4}$	1334.453	1334.385	4-
$Cs_3Na_2H_2$	$V^{IV}_{16}V^{V}_{4}$	1361.932	1361.863	4-
Cs_4NaH_2	$V^{IV}_{16}V^{V}_{4}$	1389.411	1389.343	4-
Cs_5H_2	$V^{IV}_{16}V^{V}_{4}$	1416.89	1416.823	4-
Na_4H_2	$V^{IV}_{15}V^{V}_{5}$	1273.748	1273.679	4-
$CsNa_3H_2$	$V^{IV}_{15}V^{V}_{5}$	1301.227	1301.163	4-
$Cs_2Na_2H_2$	$V^{IV}_{15}V^{V}_{5}$	1328.706	1328.64	4-
Cs_3NaH_2	$V^{IV}_{15}V^{V}_{5}$	1356.185	1356.119	4-
Cs_4H_2	$V^{IV}_{15}V^{V}_{5}$	1383.664	1383.596	4-
Na_3H_2	$V^{IV}_{14}V^{V}_{6}$	1268.001	1267.933	4-
$CsNa_2H_2$	$V^{IV}_{14}V^{V}_{6}$	1295.479	1295.411	4-

Cs_2NaH_2	$V^{IV}_{14}V^{V}_{6}$	1322.959	1322.895	4-
Cs_3H_2	$V^{IV}_{14}V^{V}_{6}$	1350.437	1350.373	4-
Na_2H_2	$V^{IV}_{13}V^{V}_{7}$	1262.253	1262.193	4-
$CsNaH_2$	$V^{IV}_{13}V^{V}_{7}$	1289.732	1289.665	4-
Cs_2H_2	$V^{IV}_{13}V^{V}_{7}$	1317.211	1317.142	4-
NaH_2	$V^{IV}_{12}V^{V}_{8}$	1256.506	1256.445	4-
CsH_2	$V^{IV}_{12}V^{V}_{8}$	1283.985	1283.926	4-

Table 4.5.10 - Assigned peaks in the 5- envelope in the ESI-MS of **$V_{20}{}^{t}B$-Cs**.

Counter ions	Oxidation state	Calculated (m/z)	Peak (m/z)	Charge
Na_7H_2	$V^{IV}_{19}V^{V}_{1}$	1032.792	1032.732	5-
$CsNa_6H_2$	$V^{IV}_{19}V^{V}_{1}$	1054.775	1054.713	5-
$Cs_2Na_5H_2$	$V^{IV}_{19}V^{V}_{1}$	1076.758	1076.694	5-
$Cs_3Na_4H_2$	$V^{IV}_{19}V^{V}_{1}$	1098.741	1098.681	5-
Na_6H_2	$V^{IV}_{18}V^{V}_{2}$	1028.194	1028.136	5-
$CsNa_5H_2$	$V^{IV}_{18}V^{V}_{2}$	1050.177	1050.116	5-
$Cs_2Na_4H_2$	$V^{IV}_{18}V^{V}_{2}$	1072.16	1072.098	5-
Na_6H_2 - Cs	$V^{IV}_{17}V^{V}_{3}$	1001.613	1001.558	5-
Na_5H_2	$V^{IV}_{17}V^{V}_{3}$	1023.596	1023.538	5-
$CsNa_4H_2$	$V^{IV}_{17}V^{V}_{3}$	1045.579	1045.523	5-
$Cs_2Na_3H_2$	$V^{IV}_{17}V^{V}_{3}$	1067.562	1067.511	5-
$Cs_3Na_2H_2$	$V^{IV}_{17}V^{V}_{3}$	1089.546	1089.492	5-
Na_5H_2 - Cs	$V^{IV}_{16}V^{V}_{4}$	997.015	996.964	5-
Na_4H_2	$V^{IV}_{16}V^{V}_{4}$	1018.998	1018.951	5-
$CsNa_3H_2$	$V^{IV}_{16}V^{V}_{4}$	1040.981	1040.931	5-
$Cs_2Na_2H_2$	$V^{IV}_{16}V^{V}_{4}$	1062.964	1062.915	5-
Cs_3NaH_2	$V^{IV}_{16}V^{V}_{4}$	1084.948	1084.894	5-
Cs_4H_2	$V^{IV}_{16}V^{V}_{4}$	1106.931	1106.876	5-
Na_4H_2 - Cs	$V^{IV}_{15}V^{V}_{5}$	992.4171	992.3684	5-
$CsNa_2H_2$	$V^{IV}_{15}V^{V}_{5}$	1036.383	1036.335	5-
Cs_2NaH_2	$V^{IV}_{15}V^{V}_{5}$	1058.366	1058.316	5-
Cs_3H_2	$V^{IV}_{15}V^{V}_{5}$	1080.35	1080.296	5-
Na_3H_2	$V^{IV}_{15}V^{V}_{5}$	1014.4	1014.348	5-
Na_3H_2 - Cs	$V^{IV}_{14}V^{V}_{6}$	987.8191	987.7711	5-
Na_2H_2	$V^{IV}_{14}V^{V}_{6}$	1009.802	1009.75	5-

$CsNaH_2$	$V^{IV}_{14}V^{V}_{6}$	1031.785	1031.738	5-
Cs_2H_2	$V^{IV}_{14}V^{V}_{6}$	1053.769	1053.721	5-
Na_2H_2 - Cs	$V^{IV}_{13}V^{V}_{7}$	983.2212	983.1722	5-
NaH_2	$V^{IV}_{13}V^{V}_{7}$	1005.204	1005.156	5-
CsH_2	$V^{IV}_{13}V^{V}_{7}$	1027.187	1027.138	5-

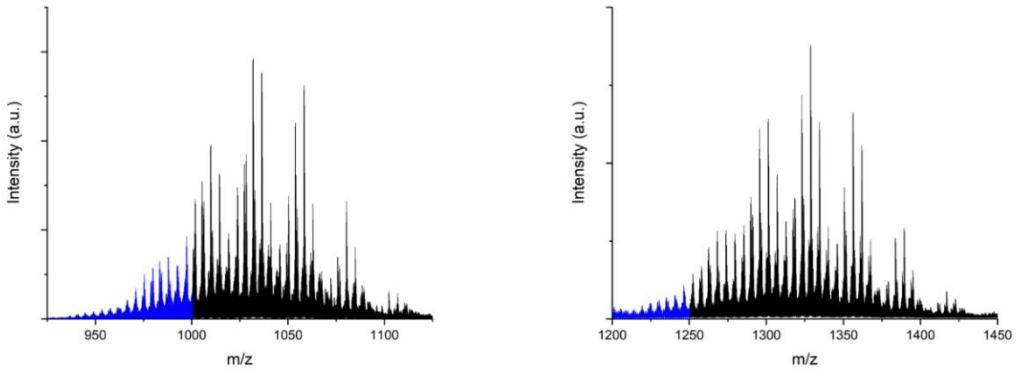

Figure 4.5.14 – The 5- and 4- envelope of **$V_{20}{}^{t}$B-Cs**. The blue part of the spectrum shows the peaks for the species which have to have lost caesium ions from the alkali metal cube.

Figure 4.5.15 shows the full ESI-MS spectrum of **$V_{20}{}^{t}$B-Rb**. The oxidation states visible in the 5- and 4- envelope range from the twice reduced $\{V^{IV}_{18}V^{V}_{2}\}$ to the twice oxidised $\{V^{IV}_{14}V^{V}_{6}\}$ species The assigned peaks, which can be seen in Figure 4.5.17 and Figure 4.5.18, are listed in Table 4.5.11 and Table 4.5.12 for the 5- and 4- envelope respectively. Matching peak patterns can be seen in Figure 4.5.19. Figure 4.5.16 visualises the part of the spectrum which belong to species with a non-intact alkali metal cube in the centre of the structure.

Figure 4.5.20 and Figure 4.5.21 show the ESI-MS spectrum of **$V_{20}{}^{t}$B-K**. The quality of the mass spectrum unfortunately prevents a definitive assignment of the individual species. However, the spectrum clearly identifies the same 5- and 4- envelopes as observed in the ESI-MS spectra of **$V_{20}{}^{t}$B-Cs** and **$V_{20}{}^{t}$B-Rb** together with the ligand signals below 500 m/z.

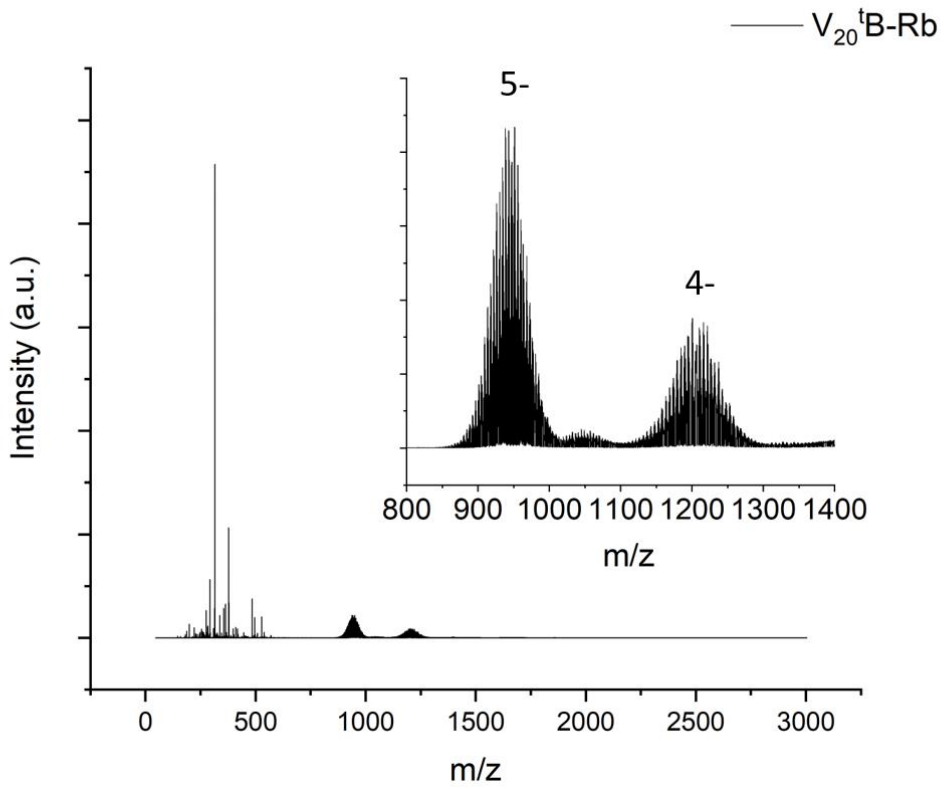

Figure 4.5.15 – ESI-MS of **V_{20}^{t}B-Rb** in water. Two broad envelopes can be seen around 900-1000 m/z of 5- charge and 1150 – 1300 m/z with 4- charge.

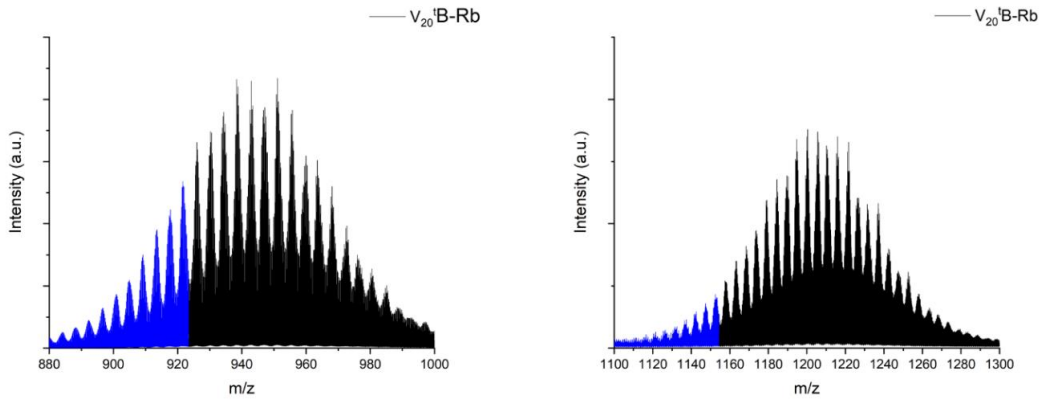

Figure 4.5.16 – Signals of the 5- and 4- envelope of **V_{20}^{t}B-Rb**. The blue part of the spectrum shows the peaks for the species which have to have lost rubidium ions from the alkali metal cube.

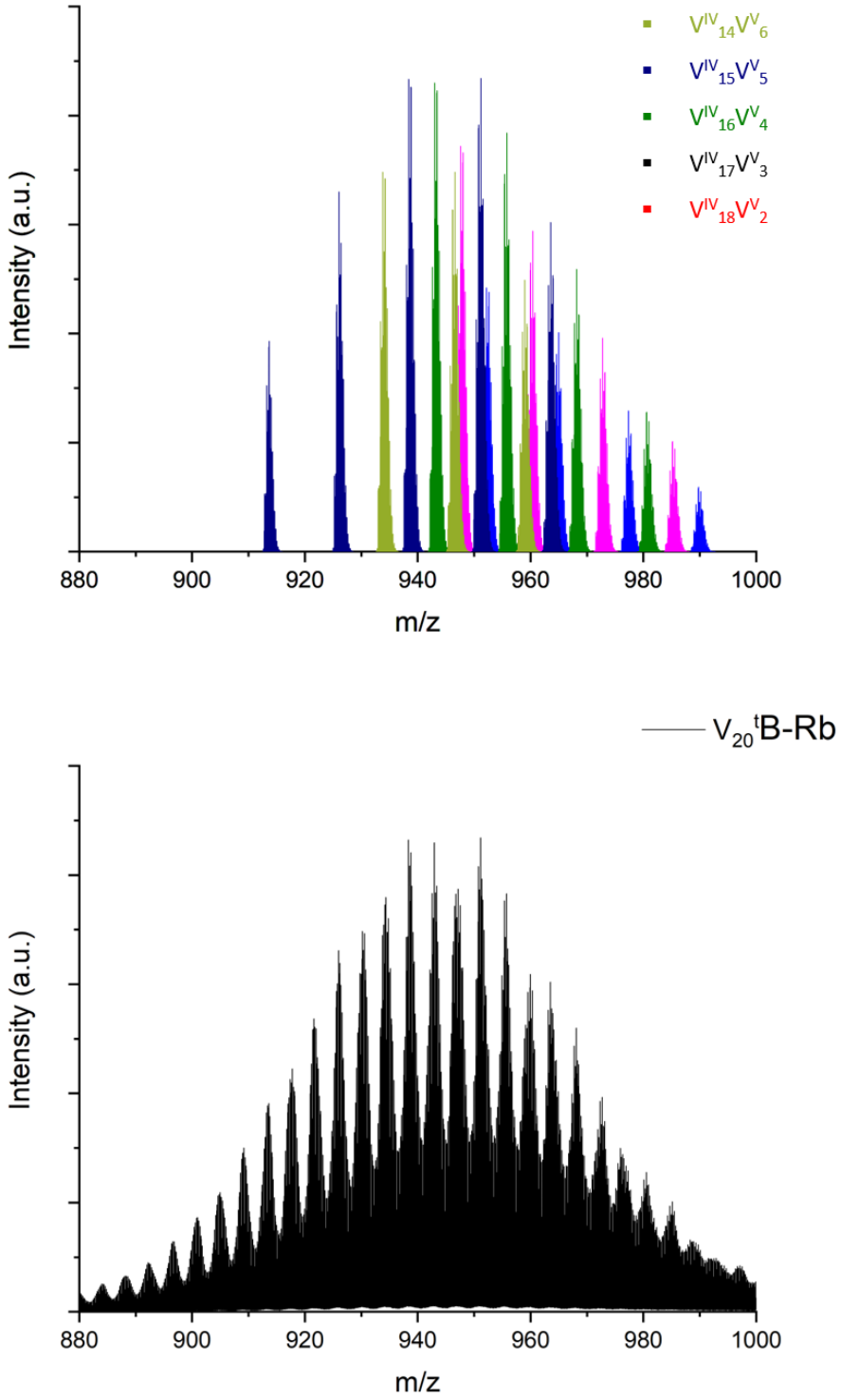

Figure 4.5.17 – ESI-MS spectra of the 5- envelope of **$V_{20}{}^{t}$B-Rb** and modelled peaks.

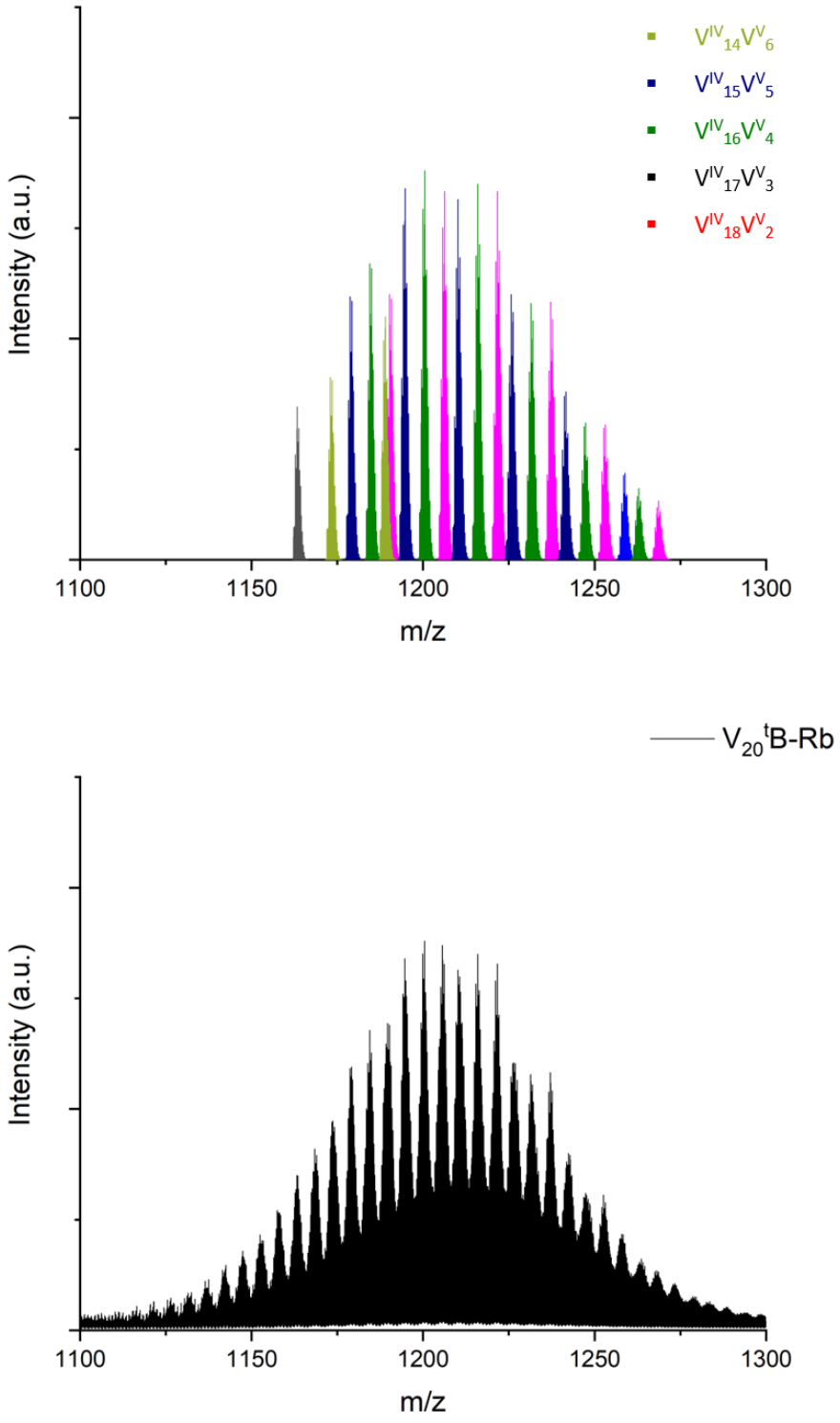

Figure 4.5.18 - ESI-MS spectra of the 4- envelope of **$V_{20}{}^{t}$B-Rb** and modelled peaks.

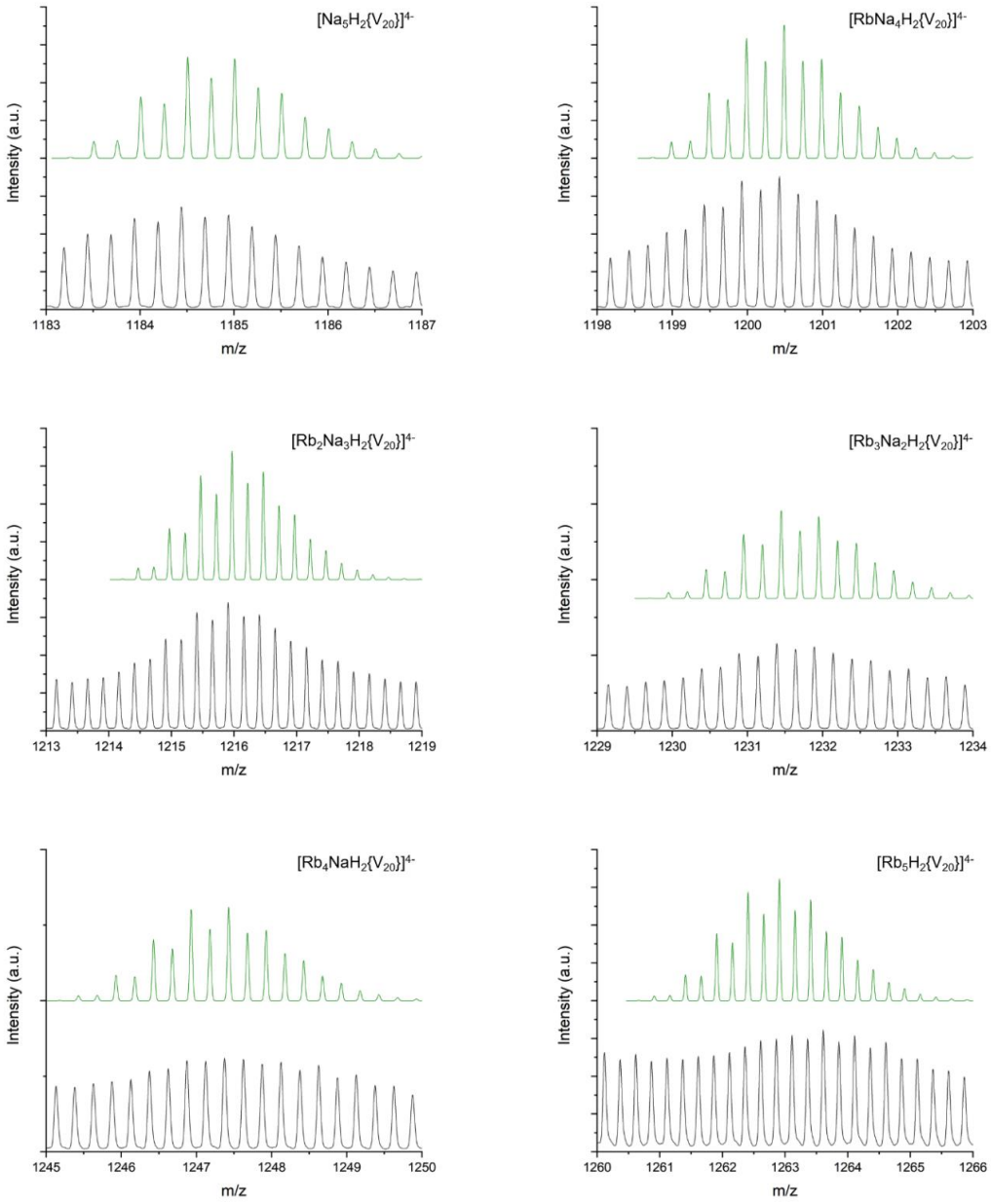

Figure 4.5.19 – Matching peak patterns for the $\{V^{IV}_{16}V^{V}_{4}\}$ oxidation state in the 4- envelope of the MS of **V_{20}^{t}B-Rb.**

Table 4.5.11 – Assigned peaks in the 5- envelope of the ESI-MS spectrum of **$V_{20}{}^{t}$B-Rb**.

Counter ions	Oxidation state	Calculated (m/z)	Peak (m/z)	Charge
Na_6H_2	$V^{IV}_{18}V^{V}_{2}$	952.2036	952.1489	5-
$RbNa_5H_2$	$V^{IV}_{18}V^{V}_{2}$	964.9880	964.9372	5-
$Rb_2Na_4H_2$	$V^{IV}_{18}V^{V}_{2}$	977.3724	977.3209	5-
$Rb_3Na_3H_2$	$V^{IV}_{18}V^{V}_{2}$	989.7568	989.7096	5-
Na_5H_2	$V^{IV}_{17}V^{V}_{3}$	947.6056	947.5494	5
$RbNa_4H_2$	$V^{IV}_{17}V^{V}_{3}$	960.3900	960.3372	5-
$Rb_2Na_3H_2$	$V^{IV}_{17}V^{V}_{3}$	972.7744	972.7220	5-
$Rb_3Na_2H_2$	$V^{IV}_{17}V^{V}_{3}$	985.1588	985.1123	5-
Na_4H_2	$V^{IV}_{16}V^{V}_{4}$	943.0077	942.9550	5-
$RbNa_3H_2$	$V^{IV}_{16}V^{V}_{4}$	955.7921	955.7421	5-
$Rb_2Na_2H_2$	$V^{IV}_{16}V^{V}_{4}$	968.1765	968.1278	5-
Rb_3NaH_2	$V^{IV}_{16}V^{V}_{4}$	980.5609	980.5135	5-
Na_5H_2 - 2Rb	$V^{IV}_{15}V^{V}_{5}$	913.6429	913.5854	5-
Na_4H_2 - Rb	$V^{IV}_{15}V^{V}_{5}$	926.0253	925.9699	5-
Na_3H_2	$V^{IV}_{15}V^{V}_{5}$	938.4097	938.3597	5-
$RbNa_2H_2$	$V^{IV}_{15}V^{V}_{5}$	951.1936	951.1460	5-
Rb_2NaH_2	$V^{IV}_{15}V^{V}_{5}$	963.5780	963.5323	5-
Na_2H_2	$V^{IV}_{14}V^{V}_{6}$	933.8118	933.7637	5-
$NaRbH_2$	$V^{IV}_{14}V^{V}_{6}$	946.5962	946.5489	5-
Rb_2H_2	$V^{IV}_{14}V^{V}_{6}$	958.9806	958.9357	5-

Table 4.5.12 – Assigned peaks in the 4- envelope of the ESI-MS spectrum of **$V_{20}{}^{t}$B-Rb**.

Counter ions	Oxidation state	Calculated (m/z)	Peak (m/z)	Charge
$Rb_4Na_3H_2$	$V^{IV}_{18}V^{V}_{2}$	1258.9243	1258.8654	4-
Na_6H_2	$V^{IV}_{17}V^{V}_{3}$	1190.2548	1190.1884	4-
$RbNa_5H_2$	$V^{IV}_{17}V^{V}_{3}$	1206.2354	1206.1742	4-
$Rb_2Na_4H_2$	$V^{IV}_{17}V^{V}_{3}$	1221.7159	1221.6505	4-
$Rb_3Na_3H_2$	$V^{IV}_{17}V^{V}_{3}$	1237.1964	1237.1359	4-
$Rb_4Na_2H_2$	$V^{IV}_{17}V^{V}_{3}$	1253.1769	1253.1209	4-
Rb_5NaH_2	$V^{IV}_{17}V^{V}_{3}$	1268.6574	1268.6016	4-
Na_5H_2	$V^{IV}_{16}V^{V}_{4}$	1184.5074	1184.4386	4-

$RbNa_4H_2$	$V^{IV}_{16}V^{V}_{4}$	1200.4879	1200.4266	4-
$Rb_2Na_3H_2$	$V^{IV}_{16}V^{V}_{4}$	1215.9684	1215.9070	4-
$Rb_3Na_2H_2$	$V^{IV}_{16}V^{V}_{4}$	1231.4489	1231.3905	4-
Rb_4NaH_2	$V^{IV}_{16}V^{V}_{4}$	1247.4294	1247.3730	4-
Rb_5H_2	$V^{IV}_{16}V^{V}_{4}$	1262.9099	1262.8604	4-
Na_5H_2 - Rb	$V^{IV}_{15}V^{V}_{5}$	1163.2795	1163.2145	4-
Na_4H_2	$V^{IV}_{15}V^{V}_{5}$	1178.7600	1178.6959	4-
$RbNa_3H_2$	$V^{IV}_{15}V^{V}_{5}$	1194.7405	1194.6791	4-
$Rb_2Na_2H_2$	$V^{IV}_{15}V^{V}_{5}$	1210.2210	1210.1635	4-
Rb_3NaH_2	$V^{IV}_{15}V^{V}_{5}$	1225.7015	1225.6447	4-
Rb_4H_2	$V^{IV}_{15}V^{V}_{5}$	1241.6820	1241.6314	4-
Na_3H_2	$V^{IV}_{14}V^{V}_{6}$	1173.0125	1172.9539	4-
$RbNa_2H_2$	$V^{IV}_{14}V^{V}_{6}$	1188.9930	1188.9320	4-

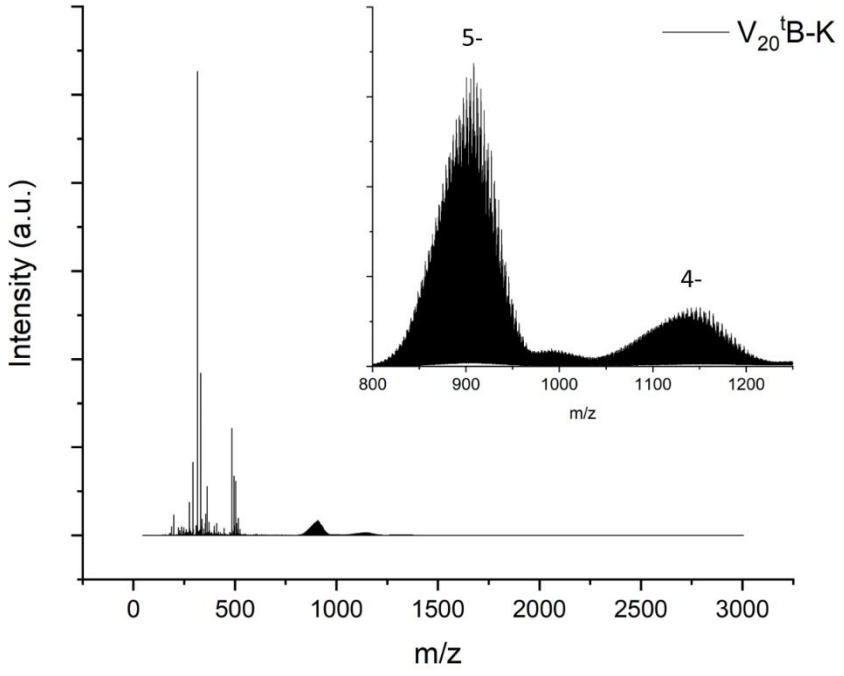

Figure 4.5.20 – ESI-MS spectrum of **$V_{20}{}^{t}$B-K**.

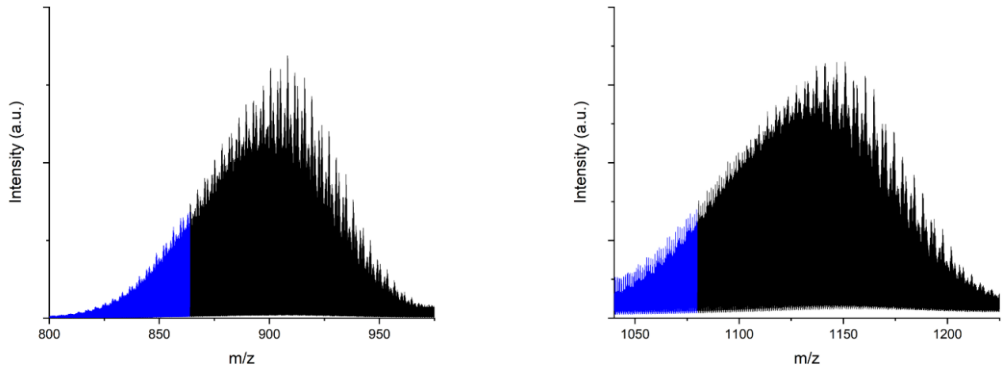

Figure 4.5.21 – MS spectrum of **$V_{20}{}^{t}$B-K**. The blue coloured part belongs to species with a non-intact alkali metal cube.

4.5.4.5 UV-VIS

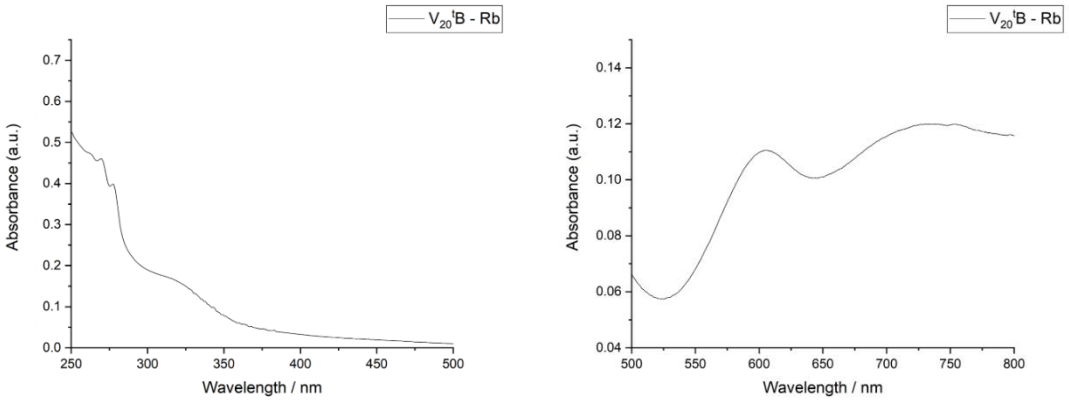

Figure 4.5.22 – UV-VIS spectra of **$V_{20}{}^{t}$B-Rb** from 200-500 nm and 500-800 nm.

The UV-VIS spectrum of **$V_{20}{}^{t}$B-Rb** can be seen in Figure 4.5.22 and shows intense signals that likely arise from two ligand centred transitions at 269 nm and 277 nm. The shoulder at around 320 nm can be attributed to LMCT bands from the *oxo*-ligand to the vanadium ion in the V=O groups.[253] At *ca.* 606 nm one can see a d-d transition with a broader adjacent signal at *ca.* 730 nm. As in the **V_{20}H-AM** compounds the broad signal at 730 nm is assigned as an IVCT transition band. All assignments were made on the basis of the absorbance value and in comparison with similar compounds from previous chapters.

4.5.4.6 NMR

To probe the solution stability of the *tert*-butyl protected {V_{20}} hybrid POVs, the DOSY-NMR studies from chapter 3 were repeated with **V_{20}^{t}B-Cs**.

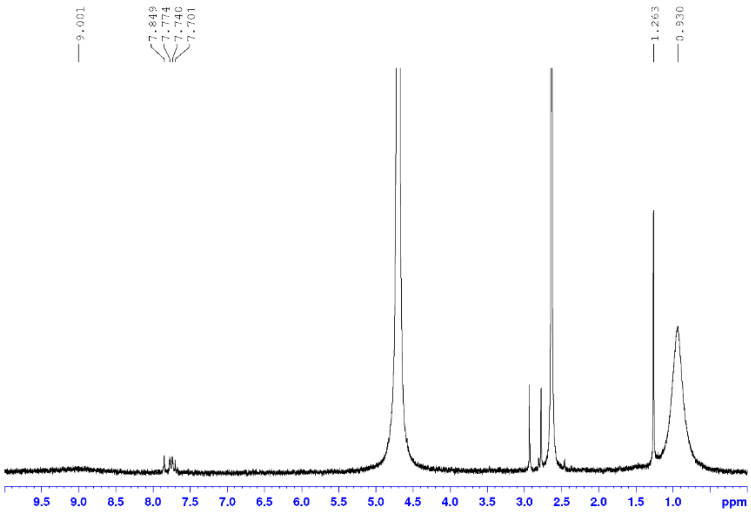

Figure 4.5.23 – ^{1}H-NMR spectrum of **V_{20}^{t}B-Cs**.

The ^{1}H-NMR spectrum of the paramagnetic {V_{20}} compound shows a series of sharp and broad signals along with signals for DMSO, DMF and the D_2O solvent peak. DOSY-NMR studies were carried out observing the integral change of the sharp signal at 1.26 ppm, which can be assigned to the *tert*-butyl group. The broad signal could not be investigated by DOSY-NMR because of its paramagnetic nature and fast relaxation. The DOSY-NMR data was fitted with the Stejskal-Tanner equation[38] with an additional term I_0 for the initial intensity.

$$E(b) = I_0 \cdot \exp\left(--\gamma^2 g^2 \delta^2 \left(\Delta - \frac{\delta}{3}\right) D\right) = I_0 \cdot \exp(-bD) \qquad \{4.5.1\}$$

with

$$\gamma = 26752 \frac{rad}{s \cdot Gauss}, \;\; \delta = 0.002\ s, \;\; \Delta = 0.04673\ s$$

When $E(b)$ is plotted against b the slope of the curve is the negative self-diffusion coefficient D, which was calculated to be $D = 3.07 \cdot 10^{-10}$ for **V_{20}[t]B-Cs** and $D = 2.91 \cdot 10^{-10}\ m^2 s^{-1}$ for the free ligand.

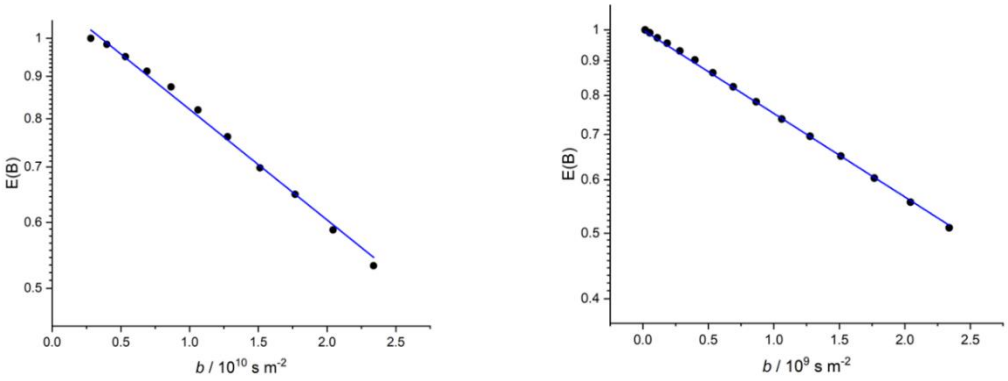

Figure 4.5.24 – DOSY-NMR graphs for **V_{20}[t]B-Cs** (left) and the free ligand DPB-tB (right).

If we assume the molecule to be approximately a spherical particle in solution we can use the Stokes-Einstein equation[39] to calculate the hydrodynamic radius *via*:

$$D = \frac{k_B T}{6\pi\,\eta\,r} \qquad \{4.5.2\}$$

With k_B being the Boltzman constant, T the temperature, η the viscosity of the deuterated solvent and r the hydrodynamic radius. The hydrodynamic radius for **V_{20}[t]B-Cs** is r_H = 5.69 Å and r_H = 6.00 Å for the free ligand. The difference in radii is within the accuracy of the measurement and they can be seen as of equal value. As the {V_{20}} hybrid POV is about 18 to 19 Å in diameter and the measurements for **V_{20}[t]B-Cs** and the free ligand closely match, it can be concluded that the sharp NMR signals arise from the free organic ligand. The DOSY measurement proves that at least some of the free ligand is present in the solution. It does not rule out the possibility, that the observed broad paramagnetic signals belong to the ligand bound to the paramagnetic polyoxovanadate.

4.6 Conclusions

In this chapter the use of four different ligands based on the DPB-H ligand for the synthesis of novel supramolecular {V_{20}} hybrid polyoxovanadates is reported. The ligands were chosen to probe the adaptability of the {V_{20}} system towards electronic and steric changes which influence the stabilising cation-π interactions within the cluster. We successfully demonstrated that the {V_{20}} cluster can accommodate a variety of differently substituted ligands, which exemplifies the versatility of the system and their potential use in further supramolecular assemblies. The ability to introduce more functional groups enables a route for the synthesis of higher nuclearity species as well as the possibility to specifically tailor the electronic and possibly catalytic abilities of those systems.

The ligand DPB-NH_2 and DPB-Br were chosen as their additional substituents significantly increase (DPB-NH_2) or decrease (DPB-Br) the strength of the cation-π interactions between the alkali metal cation and the aromatic benzene ring of the ligand. Decreased cation-π distances in **$V_{20}NH_2$-Rb** as well as a rapid crystallisation rate compared to **V_{20}H-Rb** can be attributed to increased cation-π interactions. These observations are exemplifying the effect of increased cation-π interaction on both the formation and the stabilisation of the{V_{20}} system. The use of a pyridine ring instead of a benzene ring however should also result in a reduction of the strength of the cation-π interactions. Nonetheless **V_{20}Py-Rb** was successfully synthesized by utilising the DPB-Py ligand.

Initially, before MS analysis confirmed the existence and stability of the compound in solution DOSY-NMR studies were utilised to prove their existence in water. As the NMR studies for the **V_{20}H-AM** proved the existence of free ligand in solution it was hypothesised that the leeching of alkali metal cation into the solvent were the cause of the partial degradation of the compound in water. To prevent this behaviour the DPB-^{t}B ligand was synthesized to effectively close the system and protect the alkali metal cube from leeching out into solution. Three different compounds were synthesized of which **$V_{20}{}^t$B-Rb** and **$V_{20}{}^t$B-Cs** were analysed by XRD. The crystal quality of **$V_{20}{}^t$B-K** was found to be not good enough for single crystal XRD analysis. All **$V_{20}{}^t$B-AM** compounds were proven to be stable in solution by ESI-MS. As the decomposition of the alkali metal cube observed in the ESI-MS spectrum was similar for the **$V_{20}{}^t$B-AM** compounds as for the **V_{20}H-AM** compounds we cannot conclude that the presumed leeching has been successfully avoided as intended. As it is not clear however which of the ESI-MS signals arise

from species in solution and which arise from the ionisation process, this hypothesis has not been disproven yet.

1. S. E. Wheeler and K. N. Houk, *J. Am. Chem. Soc.*, 2009, **131**, 3126-3127.
2. S. E. Wheeler and K. N. Houk, *J. Chem. Theory Comput.*, 2009, **5**, 2301-2312.
3. Y. Belabassi, S. Alzghari and J.-L. Montchamp, *J. Organomet. Chem.*, 2008, **693**, 3171-3178.
4. A. Spek, *Acta Cryst.*, 2015, **C71**, 9-18.
5. T. D. Keene, D. M. D'Alessandro, K. W. Krämer, J. R. Price, D. J. Price, S. Decurtins and C. J. Kepert, *Inorg. Chem.*, 2012, **51**, 9192-9199.

Chapter 5

Isomerism in Expanded V_{30} Hybrid Polyoxovanadates

5.1 Introduction

In the previous chapters 3 and 4 we reported the synthesis and characterisation of a novel family of supramolecular{V_{20}} hybrid POVs with differently functionalised ligands. The synthesis of the amino-, *tert*-butyl and pyridine varieties proved the {V_{20}} system to be adaptable to electronic and steric changes to the ligand. This apparent robustness of the synthesis led us to explore the possibilities of extending the {V_{20}} torus into hybrid POVs with a higher nuclearity. The use of polyoxovanadate building blocks for the synthesis of larger polyhedra assemblies has been pioneered by the Schmitt group[256], and has been extended on by the groups of Mike Zaworotko[55] and Zhongmin Su[98, 101, 102]. While the synthetic aspect is challenging the rationalisation of the obtained polyhedra is relatively straight forward as ligands and POV building blocks can be seen as simple geometrical shapes such as squares, pentagons and triangles. Because of the rigid angles of the building blocks the outcome of using one kind of building block and one kind of linker is largely predetermined.[212] With the {V_{20}} system however the situation is more complex as the pentanuclear half-capsule reacts to steric hindrance by generating isomers of itself, e.g. {V_5} vs. {V_5^*} or inverted vs. normal oriented.

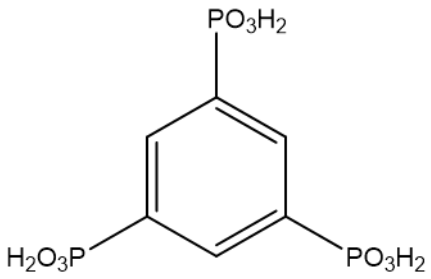

Figure 5.1.1 – Benzene-1,3,5-trisphosphonic acid.

The most obvious choice for an extension of the {V_{20}} system is the addition of another phosphonate group to the DPB-H ligand as pictured in Figure 5.1.1. In the {V_{20}} systems we have seen so far, that four sides of the central alkali metal cube are occupied by {V_5^*} half capsules, leaving two sides of the cube unoccupied. The addition of a third phosphonate group to the ligand creates perfect binding sites for two other pentanuclear half-capsules at the top and bottom of the structure. The geometrical alignment of the third phosphonate group should hereby be predetermined by the formation of the {V_{20}} POV.

This arrangement however does not decide if the system would prefer the outward-facing $\{V_5\}$ or the inward-facing $\{V_5^*\}$ half-capsule. In fact, it is an interesting question as to which combination of $\{V_5\}$ and $\{V_5^*\}$ capsules are allowed, as it is not possible to arrange six inward-facing capsules around the alkali metal cube due to space restrictions. The steric hindrance present in the $\{V_{20}\}$ system was solved by the flipping of one vanadyl group from the outside to the inside of the pentanuclear half-capsule. The situation in a possible $\{V_{30}\}$ system however is more complex as this mechanism of avoidance is not possible anymore. In the following section a comprehensive analysis of the possible and impossible $\{V_{30}\}$ structures is given.

5.2 Isomers of $\{V_{30}\}$

The situation can be understood by analysing the possible allowed combinations of arranging six polyoxovanadate half-capsules around a cube. Without steric hindrance present in the system, there would be ten possible combinations of placing inverted and non-inverted pentanuclear units around the alkali metal cube. Those possibilities are illustrated in Figure 5.2.1 using a cube net representation, in which N stands for the normal and I stands for inverted orientation of the pentanuclear half-capsule.

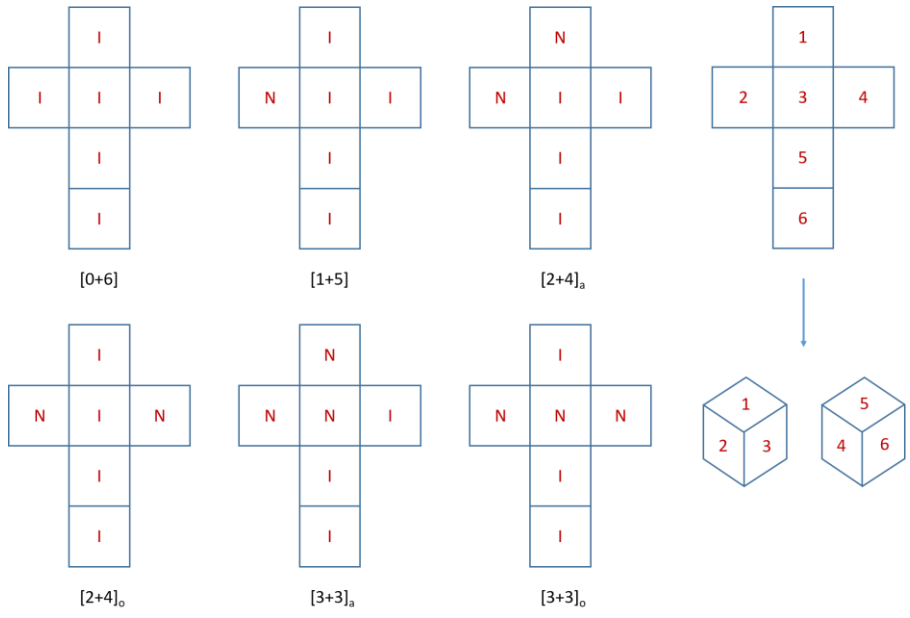

Figure 5.2.1 – Possible arrangements of normally oriented (N) and inverted half-capsules (I) around the alkali metal cube for the different theoretical isomers of the $\{V_{30}\}$ structure. The other four isomers can be constructed by switching N with I and *vice versa*.

To label the different isomers in the text following bracket notation will be used throughout this thesis. The general label for the isomers shall be:

$$[N+I]_x$$

N stands for the number of normal or outward pointing half-capsules and *I* stands for the number of inverted or inward facing half-capsules within the structure. The symbol *x* denotes a modifier to the arrangement which can either be *a* for adjacent or *o* for opposite. This helps to distinguish the two possible combinations of two normal and four inverted half-capsules, in which the two normal half-capsules occupy opposite faces of the cube, as in $[2+4]_o$, or adjacent faces of the cube, as in $[2+4]_a$. In the [3+3] arrangement *a* denotes the variant, in which the three normal half-capsules are all adjacent to each other, whereas *o* denotes the possibility of two normal half-capsules being opposite to each other. All possibilities are shown in Figure 5.2.1. Please note that the [4+2] isomer can be constructed but simply exchanging N for I and vice versa from the [2+4] configuration.

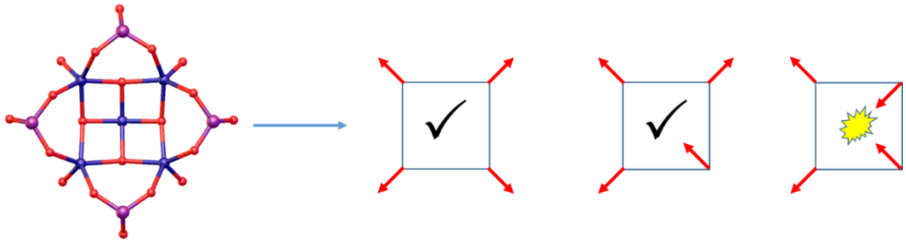

Figure 5.2.2 – Illustration of the steric hindrance of two vanadyl groups flipped to the inside caused by three adjacent half-capsules.

Not all of the ten possible combinations can be synthesised as isomers of the $\{V_{30}\}$ system. As described in chapter 3, the reason for the flipping of one vanadyl group from the outside to the inside of the pentanuclear half-capsule within the $\{V_{20}\}$ systems was steric hindrance that otherwise would be present in the structure. This led to an either clockwise or counter-clockwise arrangement of the vanadyl groups in the middle of the structure. The same principle is also the reason for the existence or non-existence of different possible isomers but with additional restrictions. The difference between the $\{V_{20}\}$ structure and possible $\{V_{30}\}$ structures is that steric hindrance is now present in two directions at once, around the bend and towards the top and bottom of the structure. While we already saw that the system is able to flip one vanadyl group

from the outside to the inside it cannot happen twice as shown in Figure 5.2.2. The same problem would arise now within the half-capsule as the *oxo*-groups would again occupy approximately the same space. Under these considerations the theoretical isomers [0+6], [1+5] , $[2+4]_{a,}$ and $[3+3]_a$ are impossible to achieve, as they have more than two inverted half-capsules adjacent to each other. This leaves us with six possible isomers, namely $[2+4]_{o,}$ $[3+3]_{o,}$ $[4+2]_a$, $[4+2]_o$,[5+1] and [6+0].

5.3 $K_{27}[(V_5O_9)_6(C_6H_3(PO_3)_3)_8K_4]N_3 \cdot 45\ H_2O$ (V_{30}-K, 13)

The compound **V_{30}-K** was prepared by the partial reduction of potassium orthovanadate with hydrazine in the presence of benzene-1,3,5-trisphosphonic acid in a solvent mixture of water, DMF and MeCN (3:1:1 v:v:v) along with sodium azide at a pH of about 7. A dark green precipitate formed after about 30 minutes, which was dissolved in water and recrystallised by adding a minor amount of DMF into the solution. Green crystals, suitable for XRD formed after several days to weeks. This method differs from the synthetic approaches of the earlier chapters in that the compound is recrystallised from the crude precipitate, whose rapid formation was avoided in the syntheses for the $\{V_{10}\}$ and $\{V_{20}\}$ systems.

5.3.1 Crystallography

The compound **V_{30}-K** was solved in the triclinic space group $P\bar{1}$ with the following unit cell parameters:

$$\begin{array}{lll} a = 19.6124(10)\ \text{Å} & \alpha = 62.822(2)^\circ & Z = 1 \\ b = 20.8088(11)\ \text{Å} & \beta = 65.124(2)^\circ & Z' = 0.5 \\ c = 21.2020(12)\ \text{Å} & \gamma = 88.747(3)^\circ & V = 6826.1(7)\ \text{Å}^3 \end{array}$$

The structure consists of a heavily disordered hybrid polyoxovanadate which was refined as a mixture of two distinct isomeric structures that are occupying the same position within the unit cell. Using the notation introduced earlier the isomers are the $[4+2]_o$ and $[2+4]_o$ isomers, which differ by the orientation of the POV half-capsules as well as the presence of the alkali metal cube. Both structures were modelled to have an occupancy of 50 % and are shown in Figure 5.3.1. They will be discussed separately before a more detailed description of the crystal structure and the disorder within is given afterwards.

5.3.1.1 The $[2+4]_o$ isomer

The $[2+4]_o$ isomer is about 22.0 Å · 15.9 Å · 15.8 Å in size. It consists of six half-capsules that are arranged around a cube of potassium ions and are connected *via* eight benzene-1,3,5-trisphosphonate ligands. The centre of the structure is made up of the same $\{V_{20}\}$ hybrid POV structure, which has been described in chapter 3 and 4. Four pentanuclear $\{V_5^*\}$ half-capsules are arranged around the alkali metal cube in an inverted fashion, which display a disorder of the central vanadyl groups leading to either a clockwise or counter clockwise arrangement. Additionally to the $\{V_{20}\}$ structure however, the third phosphonate group on the ligands is now in the position of binding two more pentanuclear half-capsules as can be seen in Figure 5.3.1. The two additional half-capsules arrange themselves in a non-inverted fashion with their terminal *oxo*-ligands pointing towards the outside of the structure. With four inverted $\{V_5^*\}$ units and two outward facing half-capsules, which are placed on opposite sides of the cube, this isomer is the $[2+4]_o$ isomer as conceptualised in section 5.2.

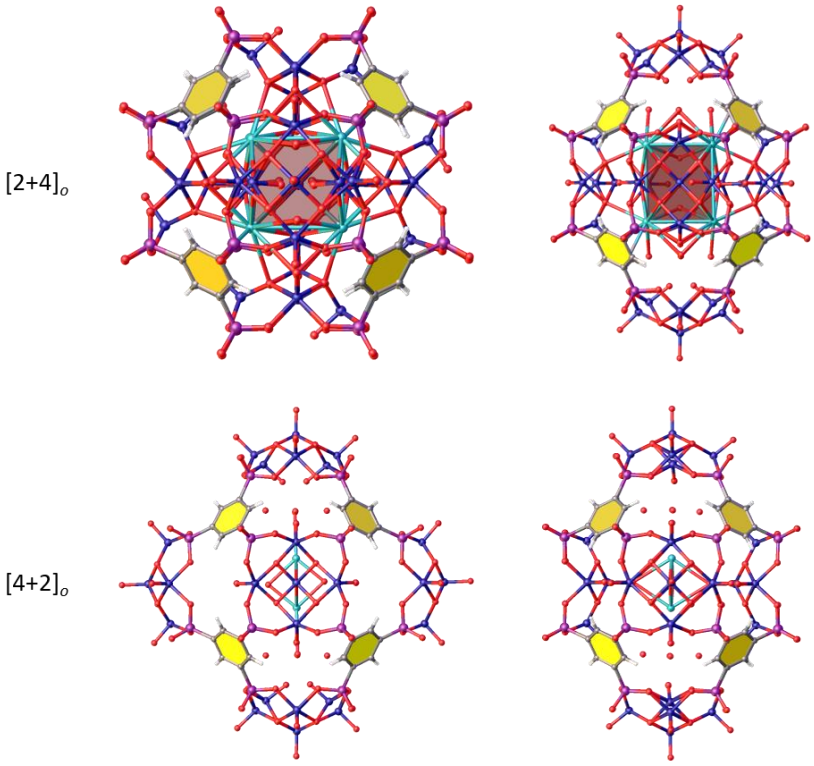

Figure 5.3.1 – The two isomers found in the crystal structure of **V_{30}-K** as viewed from the top (left) and the side (right). Top row: $[2+4]_O$ isomer. Bottom row: $[4+2]_O$ isomer. The alkali metal cube is missing in the $[4+2]_o$ isomer.

Other than the four central $\{V_5^*\}$ units the two outward-facing half-capsules are free from any steric influence caused by adjacent vanadyl groups. Interestingly however they do show disorder of two vanadyl groups, which were modelled to be 90 % on the outside and 10 % on the inside. These occupancies can be resolved to a distribution of 80 % $\{V_5^*\}$ and 20 % $\{V_5\}$ configuration as shown in Figure 5.3.2. The reason for this remains unclear, but it might be a slight indication about the formation of those structures, which is worthwhile to investigate in the future. As those two pentanuclear half-capsules are part of both the $[4+2]_o$ and $[2+4]_o$ isomer it cannot be determined from the crystal structure to which extent the $\{V_5^*\}$ and $\{V_5\}$ belong to either of the two isomers. It is entirely possible, although pure speculation, that all of the $\{V_5^*\}$ half-capsules belong to only one of the two isomers.

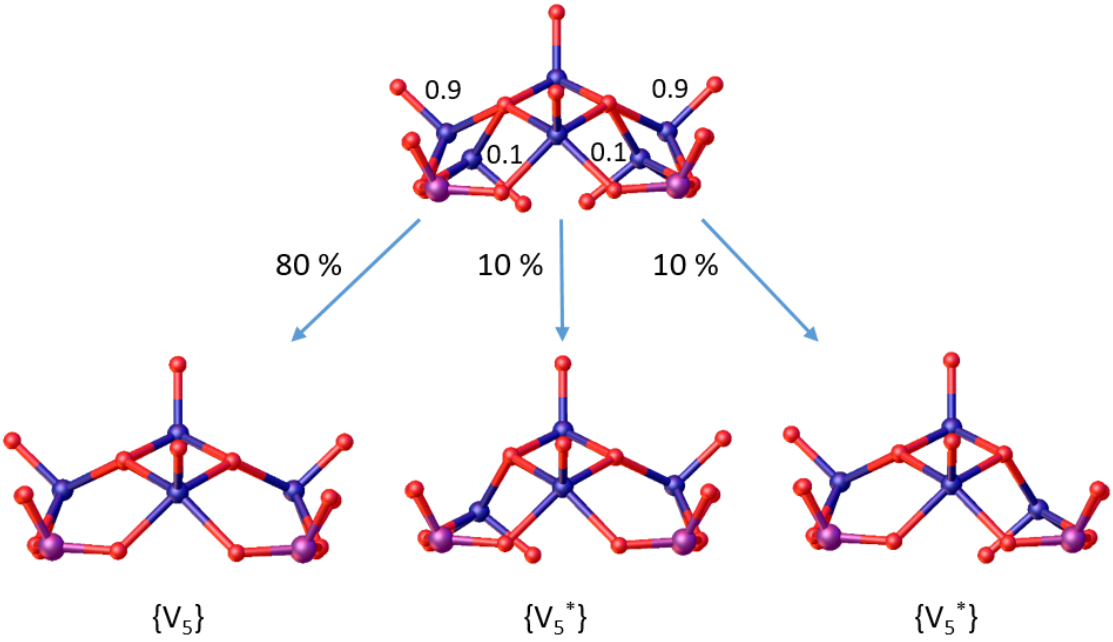

Figure 5.3.2 – Disorder of the vanadyl groups present in the capping top and bottom half-capsules of the $[2+4]_o$ isomer and the resulting distribution of the different half-capsules.

The six polyoxovanadate half-capsules carry a combined charge of -30, which is partly countered by the potassium cations within the structure. The potassium cube within the $[2+4]_o$ isomer is almost identical in size compared to the $\{V_{20}\}$ structures in chapter 3 and 4. The K-O distances within the cube are on average 3.16 Å long and therefore a bit longer than the preferred potassium oxygen distance of about 2.7 Å. Different from the $\{V_{20}\}$ structures however is the absence of

any electron density in the centre of the cube indicating the presence of a central sodium or potassium ion. There is the possibility however that this might be due to the highly disordered nature of the structure. The cation-π distances between the potassium ions and the benzene rings of the ligand are slightly larger than in **V_{20}H-K** with distances between 3.31(2) and 3.395(11) Å.

5.3.1.2 The $[4+2]_o$ isomer

The second isomer in the crystal structure features four outward-facing {V_5} half-capsules and two inverted {V_5} half-capsules, the latter of which occupy opposite sides of the structure. Two of the half-capsules in the central {V_{20}} structure have now been inverted compared to the $[2+4]_o$ isomer, leading to a central {V_{20}} ring with outward facing half-capsules that are being capped by two inward facing half-capsules at the top and bottom. Due to this the size of the $[2+4]_o$ isomer is increased compared to the $[4+2]_o$ isomer with dimensions of 22.2 Å · 22.0 Å · 15.8 Å.

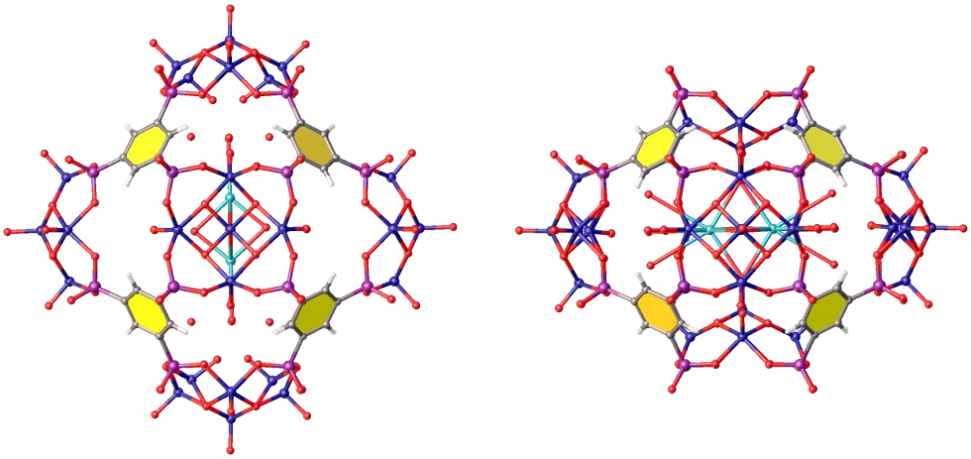

Figure 5.3.3 – Top and side view of the $[4+2]_o$ isomer in **V_{30}-K**.

Aside from their general orientation (normal vs. inverted) the pentanuclear half-capsules in the $[4+2]_o$ and $[2+4]_o$ isomers also differ by the orientation of their vanadyl groups ({V_5} vs. {V_5^*}). In the $[4+2]_o$ isomer, the two inverted half-capsules and two of the outwards facing half-capsules were resolved to have all *oxo*-ligands of the vanadyl groups point towards the outside of the half-capsule. Only the aforementioned outward facing half-capsule from Figure 5.3.2 could indicate the presence of the {V_5^*} variation within the isomer. Only for two of the {V_5} half-capsules was it possible to model a templating water molecule in the focal point. This is likely due to the heavy disorder, which is obscuring electron density within the disordered regions of the crystal

structure. The biggest difference between the isomers difference however is the missing alkali metal cube from the inside of the $[4+2]_o$ isomer. The alkali metal cube is only present in the $[2+4]_o$ isomer and was modelled to have an occupancy of 0.5 within the crystals structure. The centre of the $[4+2]_o$ isomer is occupied by a potassium dimer which is bridged by water ligands as well as the two terminal *oxo*-ligands from the inverted $\{V_5\}$ units. Due to the disorder it was not possible to further resolve the inside of the $[4+2]_o$ isomer in a meaningful way.

5.3.1.3 Crystallographic disorder

The main disorder present in the structure is the disorder of the polyoxovanadate half-capsules, which gives rise to the two distinct isomers. There are four crystallographic independent half-capsules in the asymmetric unit, which were resolved to be disordered with different occupancies and are shown in Figure 5.3.2, Figure 5.3.4 and Figure 5.3.5. The four half-capsules are made up of the vanadium ions V1 to V5, V1a to V5b, V6 to V10 and V11 to V15. As mentioned above the half-capsule of V11 to V15 has its vanadyl groups disordered over two positions with an occupancy of 0.9 / 0.1 which corresponds to 80 % $\{V_5\}$ and 10 % of each orientation of $\{V_5^*\}$ (Figure 5.3.2).

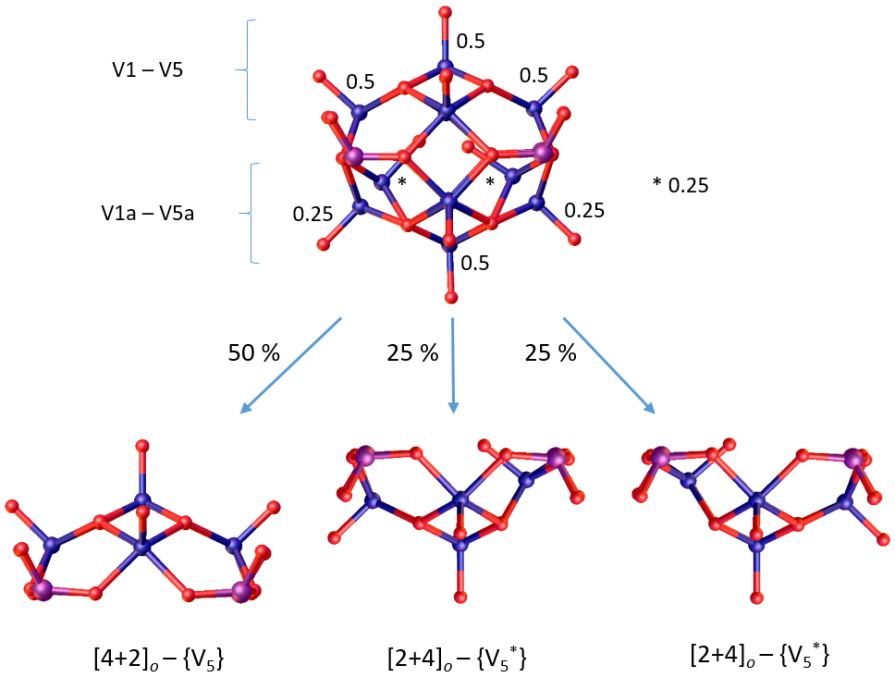

Figure 5.3.4 – Resolved disorder in the pentanuclear half-capsule V1-V5 / V1a-V5b.

The second and third half-capsule, made up of the vanadium ions V1-V5 and V1a-V5a respectively, is shown in Figure 5.3.4. Here, the half-capsule shows disorder within disorder. The first disorder is resolved with the half-capsule being 50 % outward-facing (V1-V5) and 50 % inverted (V1a-V5a). Within the inverted half-capsule two vanadyl groups are disordered over two positions with an occupancy of 0.25 each. This leads to a distribution of having an outward-facing $\{V_5\}$ capsule 50 % of the time, which belongs to the $[4+2]_o$ isomer and 25 % of each orientation of an inverted $\{V_5^*\}$ capsule, belonging to the $[2+4]_o$ isomer.

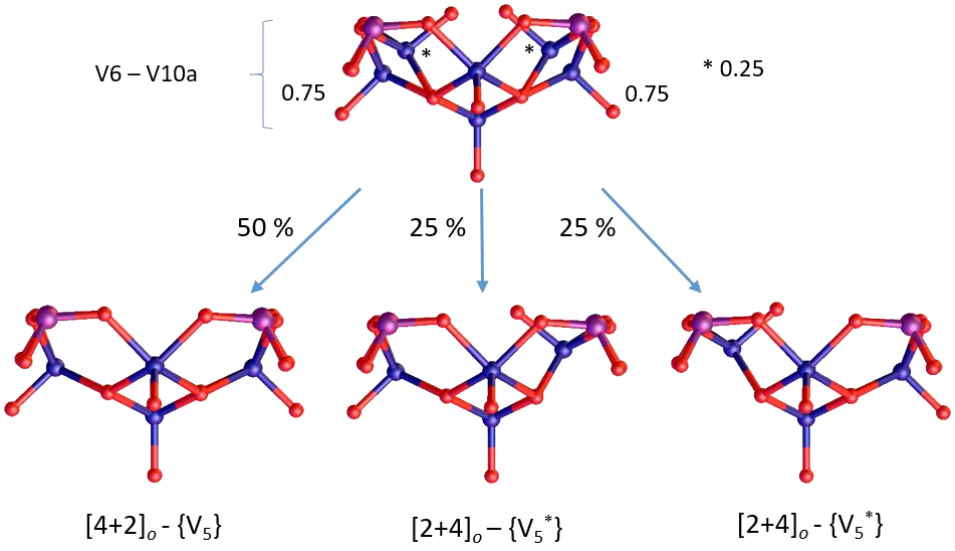

Figure 5.3.5 – Resolved disorder in the pentanuclear half-capsule V6-V10.

The last half-capsule made from V6 to V10 has two of its vanadyl groups disordered over two positions with an occupancy of 0.75 to 0.25 (Figure 5.3.5). This distribution resolves to an inverted $\{V_5\}$ capsule 50 % of the time ($[4+2]_o$) and each orientation of an inverted $\{V_5^*\}$ capsule 25 % of the times ($[2+4]_o$).

5.3.1.4 Bond lengths and angles

The vanadium-oxygen bond lengths of the pentanuclear half-capsules are of expected length for a highly disordered structure with an average of 1.61 Å for the V=O double bonds and 1.94 Å for V-O single bonds. Vanadium oxygen double bond lengths were restricted to 1.6 Å where necessary. The BVS calculations for the vanadium ions with the assigned oxidation states are shown in Table 5.3.1.

Table 5.3.1 – BVS calculation for both isomers of **V_{30}-K**. "OS" – Oxidation state.

	BVS	OS		BVS	OS		BVS	OS		BVS	OS
V1	4.88	5	**V1a**	4.94	5	**V6**	4.95	5	**V11**	5.24	5
V2	4.26	4	**V2a**	3.7	4	**V7**	3.92	4	**V12**	3.94	4
V3	3.97	4	**V3a**	4.17	4	**V8**	4.08	4	**V12a**	4.09	4
V4	3.83	4	**V3b**	4.02	4	**V8a**	4.07	4	**V13**	3.86	4
V5	3.8	4	**V4a**	3.87	4	**V9**	3.98	4	**V14**	3.96	4
			V5a	4.08	4	**V10**	3.97	4	**V14A**	4.07	4
			V5b	3.71	4	**V10a**	3.84	4	**V15**	4.06	4

The binding mode of the phosphonate groups in both isomers depend on the orientation of the half-capsules. For the inverted half-capsules in the structure the phosphonate groups show the *anti-anti* binding mode as it occurs in the $\{V_{20}\}$ structures. The outward-facing half-capsules have the phosphonate groups bound to them in a *syn-syn* binding mode. The P-O-V bond angle doesn't change significantly between both binding modes, being on average insignificantly larger for the outward-facing half-capsules with 127.2° than for the inverted half-capsules with 126.0° (Figure 5.3.6).

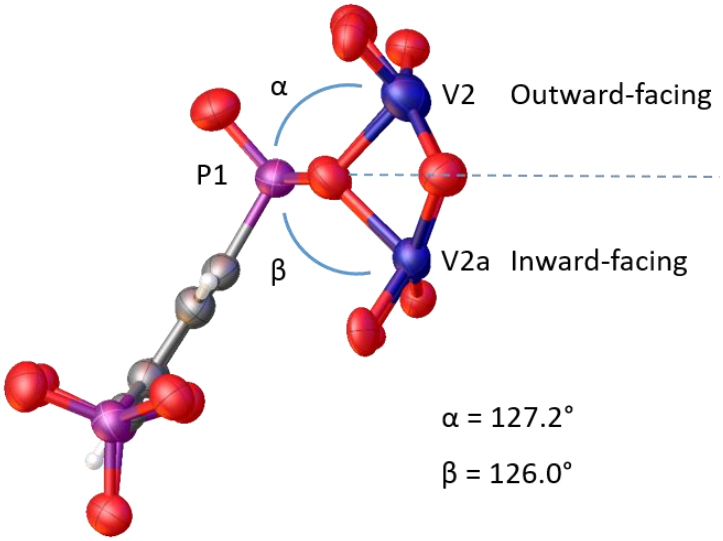

Figure 5.3.6 – Phosphonate binding mode and bond angles for outward-facing and inverted half-capsules.

5.3.1.5 Packing

As both isomers occupy the same position within the crystal structure their packing is also identical. The hybrid polyoxovanadate arranges itself in sheets along the crystallographic direction [110] (Figure 5.3.7). Within those sheets the clusters are showing an *ABAB* style packing, as shown in Figure 5.3.8. Notably the inclusion of two addition polyoxovanadate half-capsule prevents the system from building out π-π interactions between the clusters. The outside environment around the {V_{30}} polyoxovanadate is made up of potassium and possibly sodium counter ions that are being bridged by water molecules. Because of the heavy disorder present in the crystal structure, those positions could not be resolved and the PLATON SQUEEZE routine was applied.

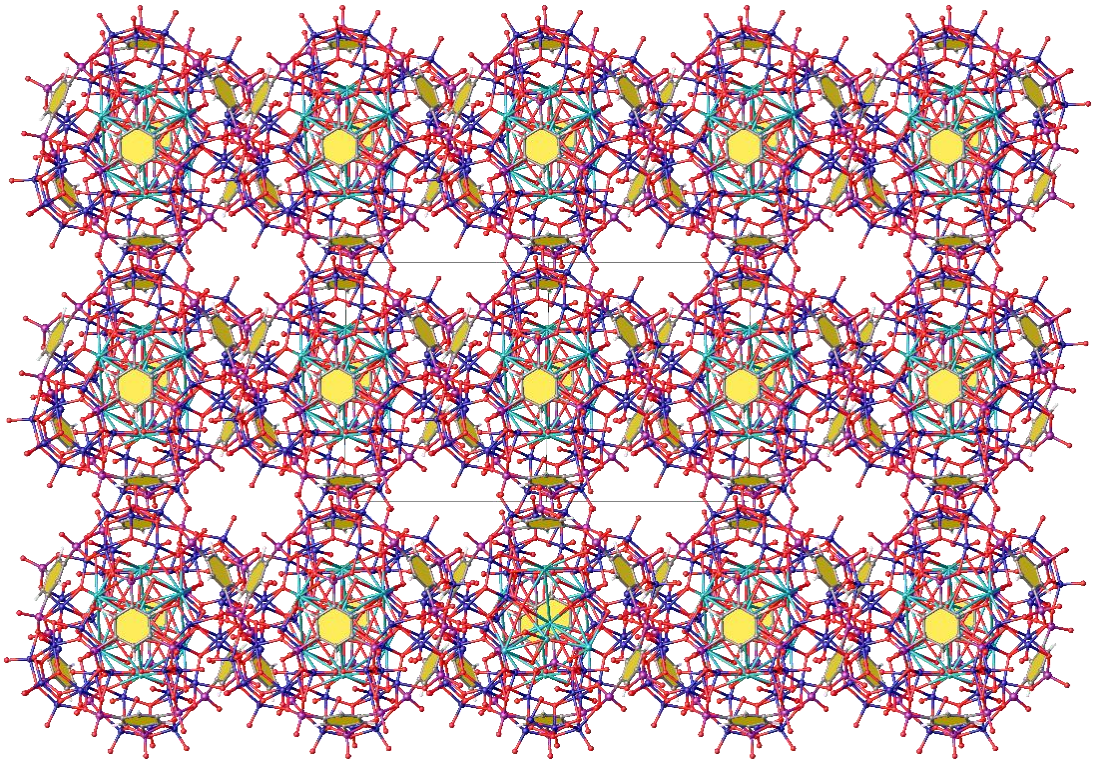

Figure 5.3.7 – Packing of **V_{30}-K**. View down the crystallographic [110] axis.

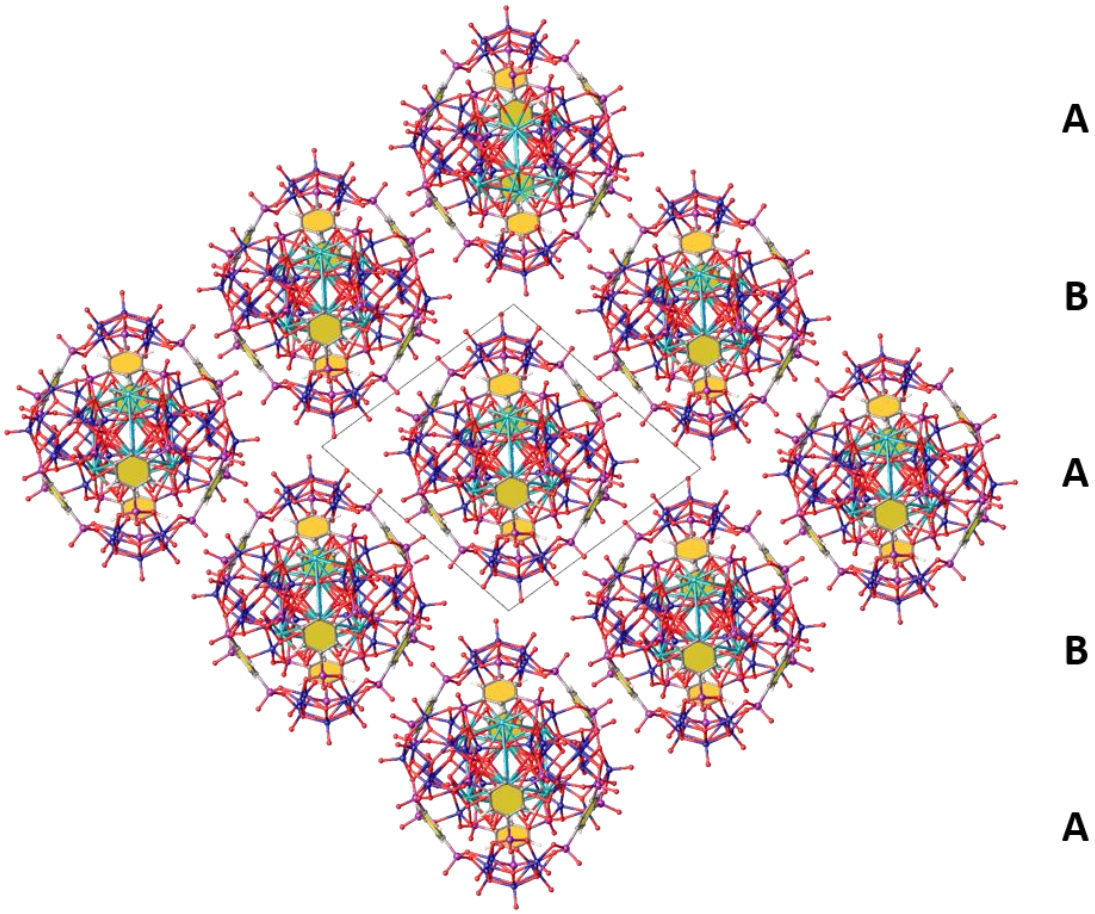

Figure 5.3.8 – Packing for the disordered structure of **V_{30}-K**. View down the crystallographic *c*-axis. The clusters stack in [110] direction in *ABAB* fashion.

Table 5.3.2 – Crystallographic table for **V_{30}-K**.

Identification code	**V_{30}-K**
Empirical formula	$C_{48}H_{24}K_5O_{137}P_{24}V_{30}$
Formula weight/(g/mol)	5211.46
Temperature/K	100
Crystal system	triclinic
Space group	*P*-1
a/Å	19.6124(10)
b/Å	20.8088(11)
c/Å	21.2020(12)
α/°	62.822(2)
β/°	65.124(2)
γ/°	88.747(3)
Volume/Å^3	6826.1(7)
Z	1
ρ_{calc} g/cm^3	1.268
μ/mm^{-1}	10.86
F(000)	2517
Crystal size/mm^3	0.14 × 0.07 × 0.04
Radiation	CuKα (λ = 1.54178)
2Θ range for data collection/°	4.884 to 137.14
Index ranges	-23 ≤ h ≤ 23 -25 ≤ k ≤ 25 -25 ≤ l ≤ 25
Reflections collected	102224
Independent reflections	24903 [R_{int} = 0.0679 R_{sigma} = 0.1002]
Data/restraints/parameters	24903/46/1306
Goodness-of-fit on F^2	1.033
Final R indexes [I>=2σ (I)]	R_1 = 0.0944, wR_2 = 0.2817
Final R indexes [all data]	R_1 = 0.1105, wR_2 = 0.2976
Largest diff. peak/hole / e Å^{-3}	2.54/-0.89

5.4 $Rb_{26}[[(V_5O_9)_6(C_6H_3(PO_3)_3)_8Rb_4] \cdot 40\ H_2O$ (V_{30}-Rb, 14)

The compound **V_{30}-Rb** was prepared in the same manner as **V_{30}-K** by replacing potassium orthovanadate with sodium orthovanadate and rubidium chloride.

5.4.1 Crystallography

The compound **V_{30}-Rb** was solved in the monoclinic space group $C2/c$ with the following unit cell parameters.

$a = 34.212(3)$ Å	$\alpha = 90°$	$Z = 4$
$b = 28.369(2)$Å	$\beta = 91.704(5)°$	$Z' = 0.5$
$c = 28.435(3)$ Å	$\gamma = 90°$	$V = 27586(4)$ Å^3

The crystal structure of **V_{30}-Rb** is almost identical with the crystal structure of **V_{30}-K**. As in **V_{30}-K** the disordered polyoxovanadate structure in **V_{30}-Rb** is made up of the two isomers $[2+4]_o$ and $[4+2]_o$, which were modelled to have an occupancy of 0.5 each. The major difference between the two structures is the presence of rubidium ions instead of potassium ions in the inside and outside of the structure. Apart from a brief description, only differences will be discussed.

5.4.1.1 The $[2+4]_O$ isomer

The $[2+4]_o$ isomer consists of two outward-facing POV half-capsules, which are occupying opposite faces of the cube and four inverted half-capsules, which are creating the $\{V_{20}\}$ torus in the middle of the structure. Identical to the $[2+4]_o$ isomer in **V_{30}-K** the isomer is 21.8 Å · 15.9 Å · 15.9 Å in size. The crystallographic disorder within the half-capsules, which gives rise to the two isomers is the same as for **V_{30}-K** and can be seen in Figure 5.3.4 and Figure 5.3.5. The only notable difference is the absence of any disorder in the outward facing half-capsule. The half-capsule was modelled to full occupancy without showing any signs of disorder present (Figure 5.4.1). The distances within the rubidium cube are between 3.144(10) Å and 3.37(2) Å long with an average of 3.25 Å. The cation-π distances are between 3.222(10) Å and 3.257(10) Å long, indicating strong interactions.

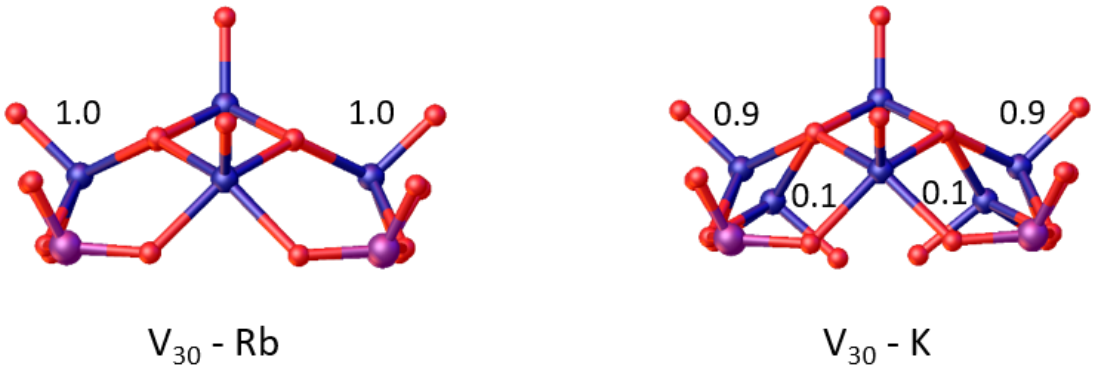

Figure 5.4.1 – Change in disorder in **V_{30}-Rb** in comparison to **V_{30}-K**.

5.4.1.2 The $[4+2]_o$ isomer

The $[4+2]_o$ isomer is made up of four outward-facing half-capsules and two inverted half-capsules, which occupy opposite faces of the structure. The size of the cluster is bigger than the $[2+4]_o$ isomer with 21.9 Å ·21.8 Å· 15.9 Å. Unfortunately, the inside of the $[4+2]_o$ isomer could not be modelled due to generally low intensity reflections and low resolution of the x-ray diffraction experiment. It can be assumed that **V_{30}-Rb** is also identical to **V_{30}-K** in this respect.

5.4.2 Bond lengths and angles

The vanadium oxygen double bond lengths range from 1.573(15) Å to 1.673(15) Å with an average of 1.61 Å while V-O single bond lengths range from 1.77(4) Å to 2.216(14) Å and average at 1.95 Å. The BVS calculation confirm the oxidation states for the mixed-valence pentanuclear half-capsule and are shown in Table 5.4.1. The BVS value of 4.75 for V9b is affected by the disorder in the structure, leading to inaccurate bond lengths with large error margins

5.4.3 Packing

The biggest difference between **V_{30}-K** and **V_{30}-Rb** is the space group and subsequent packing in the crystal structure. While **V_{30}-K** was solved in the triclinic space group $P\bar{1}$, **V_{30}-Rb** was solved in the higher symmetry monoclinic space group $C2/c$.

Table 5.4.1 – BVS calculations for **V_{30}-Rb**. (OS = Oxidation state)

	BVS	OS.		BVS	OS		BVS	OS		BVS	OS
V1	4.91	5	**V6**	5.06	5	**V6a**	5.29	5	**V11**	5.1	5
V2	3.97	4	**V7**	4.2	4	**V7a**	3.67	4	**V12**	3.84	4
V3	4.25	4	**V8**	4.09	4	**V7b**	4.08	4	**V12a**	4.01	4
V4	4.13	4	**V9**	4.22	4	**V8a**	4.11	4	**V13**	3.95	4
V5	4.53	4	**V10**	3.97	4	**V9a**	4.12	4	**V14**	4.13	4
						V9b	4.75	4	**V14A**	3.36	4
						V10a	3.85	4	**V15**	4.15	4

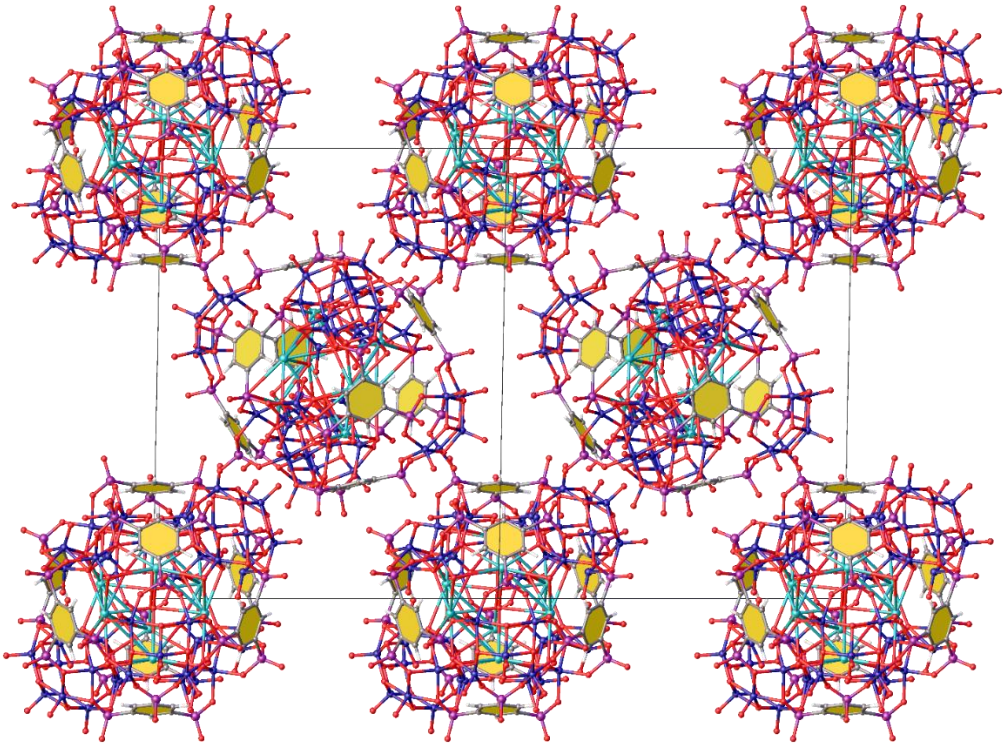

Figure 5.4.2 – Packing of **V_{30}-Rb**. View in the crystallographic [110] direction.

In the monoclinic unit cell, there are two full clusters and four half clusters, which are sitting on inversion centres. Clusters of the same orientation within the unit cell arrange themselves in layers in the [110] plane as can be seen in Figure 5.4.2. There are two different orientations of clusters within the unit cell leading to an ABAB style packing down the crystallographic *c*-axis.

The cluster of layer B are hereby rotated by 109.6(13)° towards the clusters of layer A and vice versa. The reason for this change in space group is probably the outside of the polyoxovanadate cluster, which likely consists of rubidium ions that are bridged by water molecules. With the quality of the dataset and the highly disordered nature of the structure it was not possible to resolve the counter ions and crystal water molecules. Hence, the Olex2 solvent mask routine was applied, which utilises the BYPASS[257] algorithm for the treatment of disordered cations and solvent molecules. This routine applied for 5334 electrons in a solvent accessible void of 12740 $Å^3$ in the unit cell. Those numbers roughly fit the necessary 104 rubidium counter ions for the residual 104- charge of the four {V_{30}} hybrid polyoxovanadates in the unit cell along with 40 water molecules per cluster.

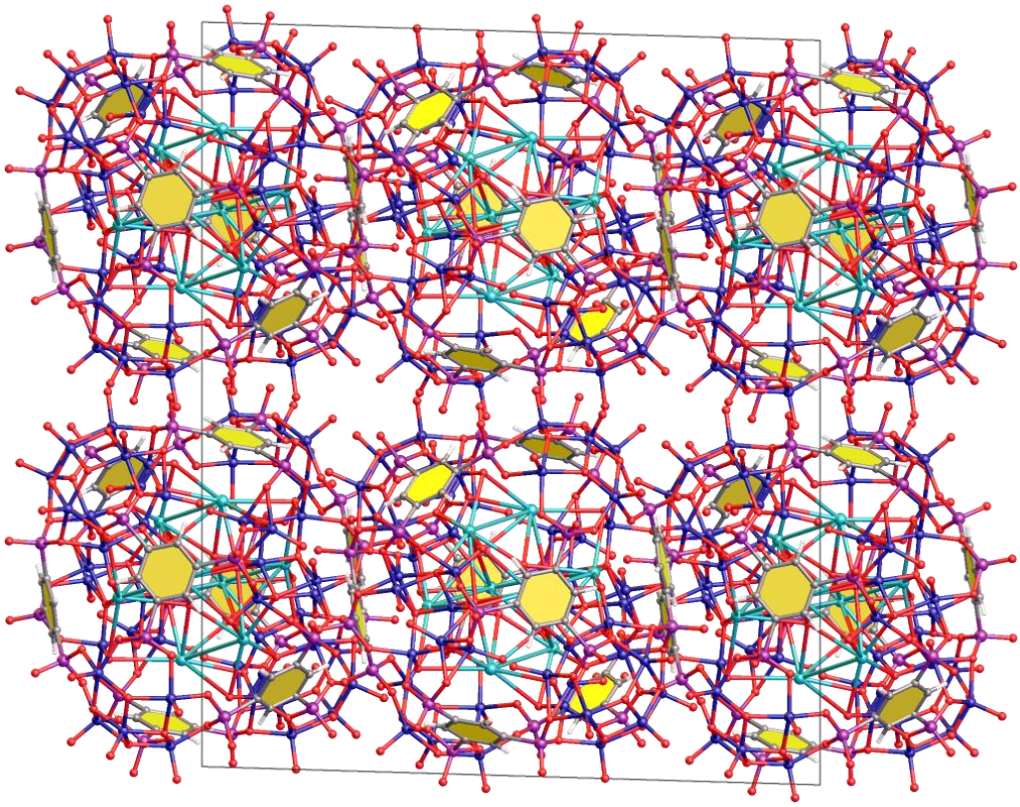

Figure 5.4.3 – Packing of **V_{30}-Rb**. View down the crystallographic *b*-axis.

Table 5.4.2 – Crystallographic table for **V_{30}-Rb**.

Identification code	**V_{30} - Rb**
Empirical formula	$C_{48}H_{24}O_{130}P_{24}Rb_4V_{30}$
Formula weight/(g/mol)	5294.03
Temperature/K	100
Crystal system	monoclinic
Space group	*C*2/*c*
a/Å	34.212(3)
b/Å	28.369(2)
c/Å	28.435(3)
α/°	90
β/°	91.704(5)
γ/°	90
Volume/Å^3	27586(4)
Z	4
ρ_{calc} g/cm^3	1.275
μ/mm^{-1}	10.892
F(000)	10200
Crystal size/mm^3	0.08 × 0.06 × 0.02
Radiation	CuKα (λ = 1.54178)
2Θ range for data collection/°	4.046 to 105.226
Index ranges	-34 ≤ h ≤ 35 -29 ≤ k ≤ 29 -29 ≤ l ≤ 29
Reflections collected	105045
Independent reflections	15699 [R_{int} = 0.1076 R_{sigma} = 0.0720]
Data/restraints/parameters	15699/89/962
Goodness-of-fit on F^2	1.006
Final R indexes [I>=2σ (I)]	R_1 = 0.1684, wR_2 = 0.4093
Final R indexes [all data]	R_1 = 0.2027, wR_2 = 0.4403
Largest diff. peak/hole / e Å^{-3}	5.30/-1.80

5.5 $Na_{30}[[(V_5O_9)_6(C_6H_3(PO_3)_3)_8]N_3 \cdot 53\ H_2O$, ($V_{30}$-Na, 15)

The compound was prepared *via* the same synthesis as **V_{30}-Rb** by replacing rubidium chloride with sodium chloride. **V_{30}-Na** was solved in the triclinic space group $P\bar{1}$ with the following unit cell parameters.

$a = 20.0441(13)$ Å	$\alpha = 94.060(4)°$	$Z = 2$
$b = 22.6954(11)$ Å	$\beta = 90.666(4)°$	$Z' = 1$
$c = 36.629(2)$ Å	$\gamma = 115.026(3)°$	$V = 14920.5(14)$ Å^3

The core structure is the $[4+2]_o$ isomer of the $\{V_{30}\}$ structure as seen in **V_{30}-K** as well as **V_{30}-Rb**. Other than in previous crystal structures however the **V_{30}-Na** structure features almost solely the $[4+2]_o$ isomer with only a minor amount of the $[2+4]_o$ isomer present in the structure. When trying to model the disorder leading to the two isomers it was found that the [4+2] isomer was present around 95 % of the time, which thwarted every attempt to successfully resolve the disorder. The structure was therefore refined with only the $[4+2]_o$ isomer present while treating the interior of the $\{V_{30}\}$ as disordered water molecules. The structure can be seen in Figure 5.5.1.

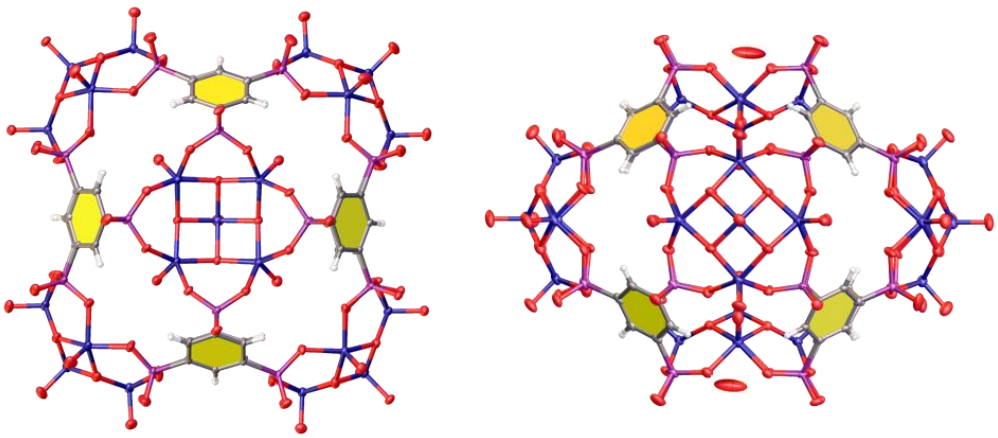

Figure 5.5.1 – The $[4+2]_o$ isomer in the **V_{30}-Na** structure from the top (left) and side (right)**.**

As can be seen from Figure 5.5.1 the $[4+2]_o$ isomer in the **V_{30}-Na** crystal structure is well resolved, which allows us to adequately compare the structure to the same isomers in **V_{30}-Rb**, and **V_{30}-K**. The vanadium oxygen double bond lengths range from 1.592(5) Å to 1.623(5) Å with

an average of 1.60 Å. The V-O single bonds range from 1.841(4) Å to 1.998(4) Å with an average of 1.95 Å. Due to the well resolved bon distances, the oxidation states of the vanadium ions within the pentanuclear half-capsules are now unambiguously determinable by BVS calculations, as can be seen in Table 5.5.1. The disorder present in **V_{30}-Rb** and **V_{30}-K** led to artificially elongated or shortened bond lengths, which were impeding the bond valence sum analysis.

Table 5.5.1 – BVS calculations for the vanadium ions of **V_{30}-Na**. (Ox.St. = Oxidation State)

	BVS	Ox.St.		BVS	Ox.St.		BVS	Ox.St.
V1	5.03	5	**V11**	5.07	5	**V21**	4.96	5
V2	4.00	4	**V12**	3.97	4	**V22**	3.95	4
V3	4.03	4	**V13**	4.02	4	**V23**	3.95	4
V4	4.04	4	**V14**	4.01	4	**V24**	3.96	4
V5	4.01	4	**V15**	4.01	4	**V25**	3.95	4
V6	4.98	5	**V16**	5.04	5	**V26**	5.09	5
V7	3.94	4	**V17**	4.03	4	**V27**	4.03	4
V8	3.93	4	**V18**	3.99	4	**V28**	4.00	4
V9	3.98	4	**V19**	4.02	4	**V29**	3.99	4
V10	3.95	4	**V20**	3.98	4	**V30**	4.00	4

The alkali metal cube in the crystal structures of **V_{30}-Rb** and **V_{30}-K** was modelled with 0.5 occupancy, as was the occupancy of the two isomers. From a crystallographic point of view, it was not entirely clear if the cube belonged to the $[2+4]_o$ or $[4+2]_o$ isomer. A disordered crystal structure is always to be understood as an average, be it over time (i.e. rotational disorder of a $-CH_3$ group) or space as in the case of positional disorder. The crystal structure of **V_{30}-Na** answers this question by showing no signs of any cation-π interactions with the benzene rings from within the cube. While it is possible that disordered sodium ions are present within the cavity of the cube, none of them are to be found in the position of the rubidium or potassium ions the **V_{30}-Rb** and **V_{30}-K** structures. This means, that the assignment of the alkali metal cube to the $[2+4]_o$ isomer was correct.

The missing disorder in the **V_{30}-Na** structure along with a resolution of 0.83 Å with an average intensity of 24.8 I/σ made it also possible to resolve the counter ions and water molecules in the crystal structure. The sodium oxygen Na-O single bonds range from 2.173(12) Å to 2.993(10) Å

with an average of 2.55 Å, which is in good agreement with literature data. The packing diagram split into the {V_{30}} structures and sodium-water chains can be seen in Figure 5.5.2. The {V_{30}} cluster arrange themselves on four edges and two faces of the triclinic unit cell and stacking in direction of the *b*-axis (Figure 5.5.3).

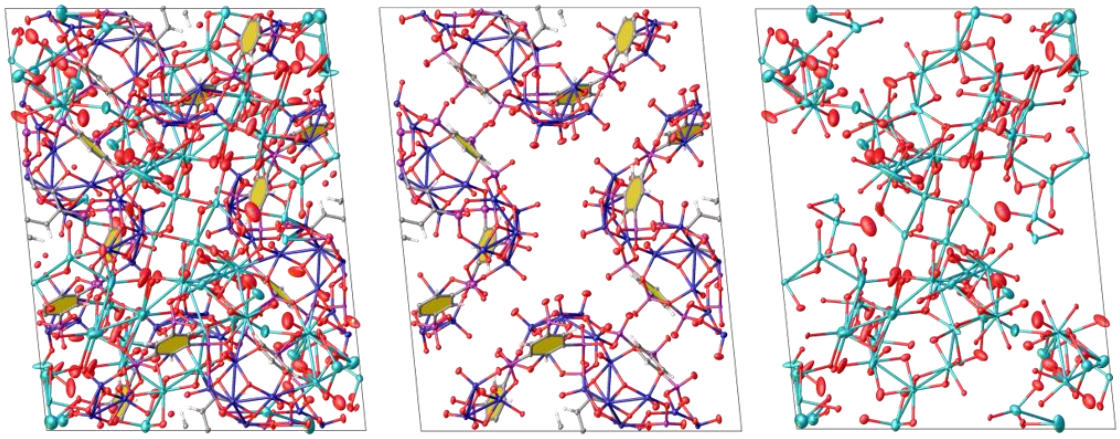

Figure 5.5.2 – Packing diagram of **V_{30}-Na** in [100] direction (left), split up in hybrid polyoxovanadates (middle) and the network of sodium ions and water molecules (right).

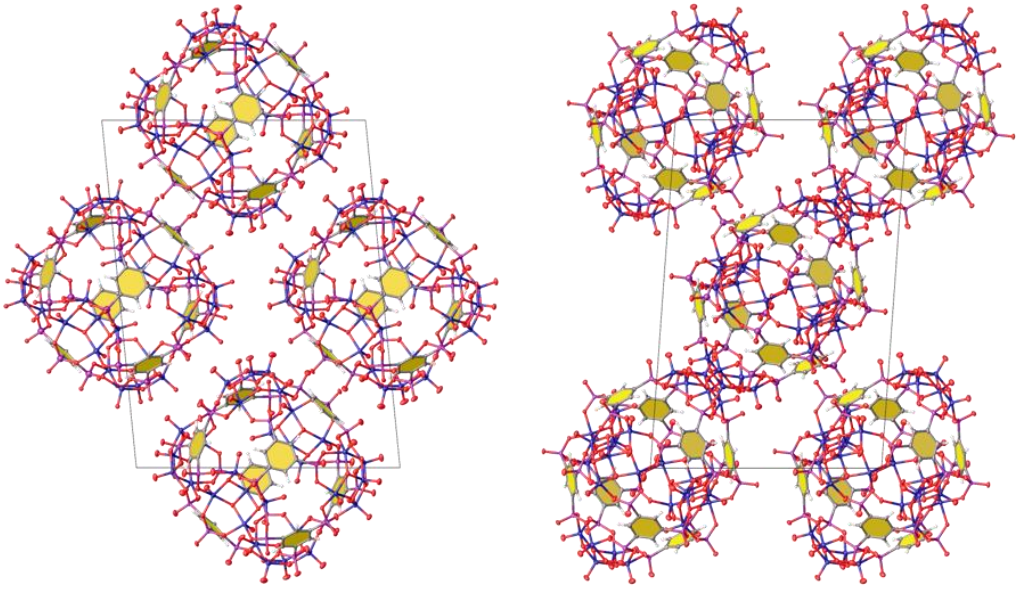

Figure 5.5.3 – Packing diagram of **V_{30}-Na** in [100] direction (left) and [010] direction (right).

Table 5.5.2 – Crystallographic table for **V_{30}-Na**.

Identification code	**V_{30} - Na**
Empirical formula	$C_{48}H_{24}Na_{30}O_{193.14}P_{24}V_{30}$
Formula weight/(g/mol)	6652.09
Temperature/K	99.99
Crystal system	triclinic
Space group	*P*-1
a/Å	20.0441(13)
b/Å	22.8822(15)
c/Å	30.198(2)
α/°	95.239(2)
β/°	93.498(2)
γ/°	96.247(2)
Volume/Å^3	13675.6(16)
Z	2
ρ_{calc} g/cm^3	1.615
μ/mm^{-1}	10.901
F(000)	6474
Crystal size/mm^3	0.15 × 0.07 × 0.05
Radiation	CuKα (λ = 1.54178)
2Θ range for data collection/°	2.946 to 137.552
Index ranges	$-24 \leq h \leq 24$ $-27 \leq k \leq 27$ $-36 \leq l \leq 36$
Reflections collected	206830
Independent reflections	50019 [R_{int} = 0.0443, R_{sigma} = 0.0404]
Data/restraints/parameters	50019/51/3061
Goodness-of-fit on F^2	1.068
Final R indexes [I>=2σ (I)]	R_1 = 0.0883, wR_2 = 0.2641
Final R indexes [all data]	R_1 = 0.1021, wR_2 = 0.2796
Largest diff. peak/hole / e Å^{-3}	4.06/-2.92

5.6 $Cs_{27}[[(V_5O_9)_6(C_6H_3(PO_3)_3)_8Cs_4]N_3 \cdot 50\ H_2O$ (V_{30}-Cs, 16)

The compound **V_{30}-Cs** was synthesized *via* the same procedure as **V_{30}-Rb** by replacing rubidium chloride with caesium chloride. **V_{30}-Cs** was solved in the triclinic space group $P\bar{1}$ with unit cell parameters of :

$a = 19.8787(10)$ Å	$\alpha = 95.239(2)°$	$Z = 2$
$b = 22.8822(15)$ Å	$\beta = 93.498(2)°$	$Z' = 1$
$c = 30.198(2)$ Å	$\gamma = 96.247(2)°$	$V = 13675.4(16)$ Å^3

5.6.1 The $[3+3]_o$ isomer

The core structure of **V_{30}-Cs** is a $\{V_{30}\}$ isomer, in which three outward-facing half-capsules are arranged next to each other with two of them occupying opposite sides of the structure. The other three half-capsules are inverted and arranged in the same manner (Figure 5.6.1). Using the notation from before this isomer is the $[3+3]_o$, as described in chapter 5.2. This arrangement leads to an asymmetrical isomer of $\{V_{30}\}$ with dimensions of about 15.6 Å · 18.1 Å · 22.0 Å.

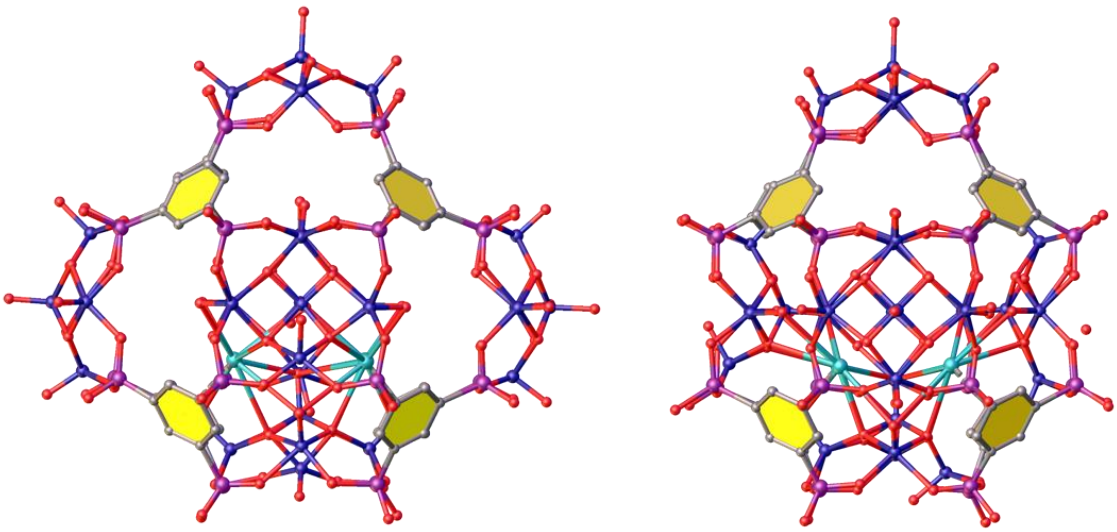

Figure 5.6.1 – Side views of the $[3+3]_o$ isomer of **V_{30} – Cs**.

The most interesting part of the structure is the alkali metal cube, which has been cut in half and is only present in the lower half of the structure. Four caesium ions are building out cation-π

interactions with the four TPB ligands, which are bonded to two inverted half-capsules. The top half of the structure shows no indication of the caesium ions sitting in their usual position on the corner of the cube. To understand this behaviour, one has to not only factor in the stabilising cation-π interactions but also the *oxo*-ligand environment of the alkali metal ions. The caesium ions are positioned directly above the μ_3-*oxo* groups of the pentanuclear half-capsules as illustrated in Figure 5.6.2. This behaviour can be seen in the $\{V_{10}\}$, $\{V_{20}\}$ and $\{V_{30}\}$ structures and has part of its origin the electrostatic potential of the polyoxovanadate half-capsule. A map of the molecular electrostatic potential at $\rho(r) = 0.02$ a. u. for the $\{V_5\}$ and $\{V_5^*\}$ half-capsule from -0.51 to -0.2 $e^-/(r_{Bohr})^3$ can be seen in Figure 5.6.3. This map which was calculated *via* DFT calculations on models of $\{V_5\}$ and $\{V_5^*\}$, in which the benzene ring attached to the phosphonate group was replaced by a methyl group to lower the time of the computation. The areas of higher electron density are coloured red, the areas of lower electron density green to blue.

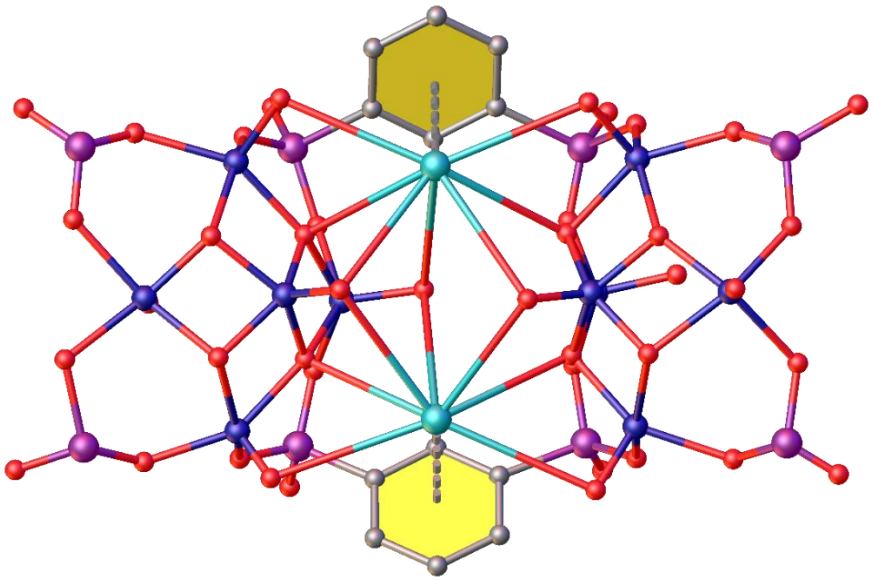

Figure 5.6.2 – View on the caesium ion environment between two inverted half-capsules.

It can be clearly seen from Figure 5.6.3 that the highest electrostatic potential resides at the top of the half-capsules is placed at the μ_3-*oxo* groups. This position is achieved twice for every alkali metal cation in the $\{V_{20}\}$ and $\{V_{30}\}$ structures as can be seen in Figure 5.6.2. Additionally, the caesium ion can build out bonds in this position with the terminal *oxo*-ligands of two central *oxo*-vanadium(V) ions and four vanadyl groups of the two adjacent polyoxovanadate half-capsules. The bond lengths of the caesium ion to the μ_3-*oxo* groups range from 3.01(3) Å to 3.25(3) Å with

an average of 3.1 Å. Those additional stabilizing cesium oxygen bonds are only possible if the capsule is inverted. By imagining a cesium ion occupying a corner in the upper half of the cube in the {V_{30}}-Cs structure one can see how this cesium ion could only build out cesium oxygen bonds with the *oxo*-groups of inverted one half-capsule instead of two. The coordination sphere of the cesium ions in this position would likely be filled by water molecules inside the {V_{30}}-Cs structure.

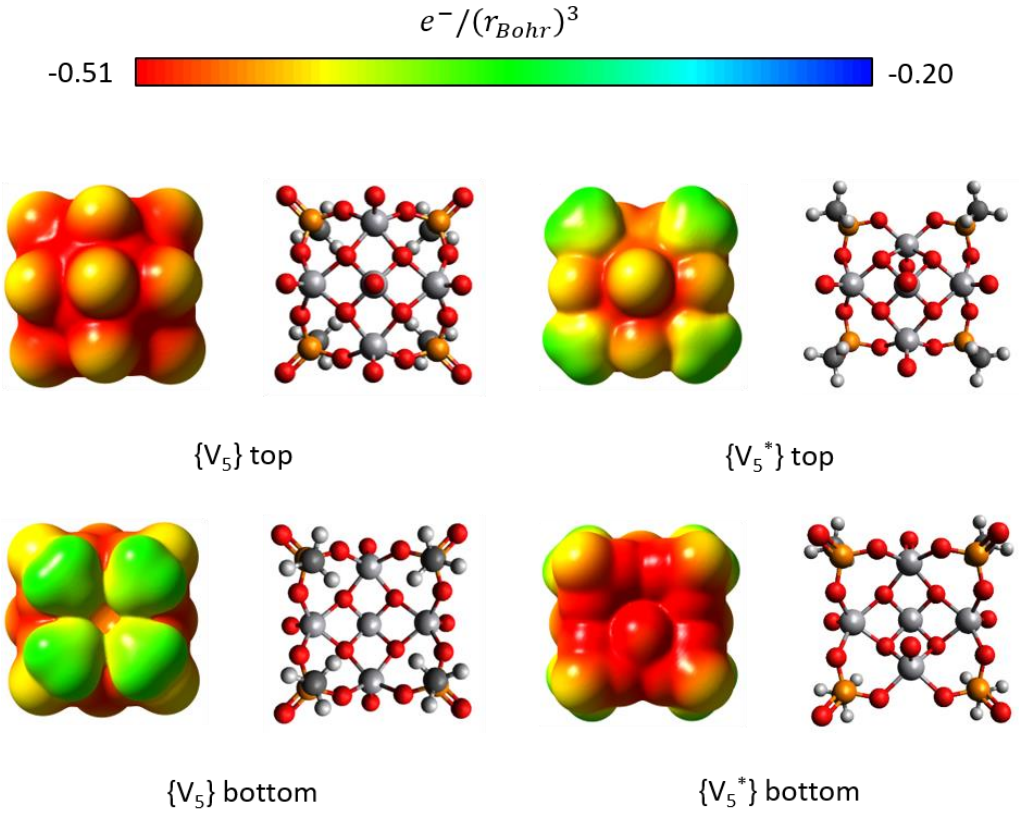

Figure 5.6.3 – Electrostatic Potentials on the {V_5} and {V_5^*} half-capsule.

5.6.2 Crystallography

As in the other {V_{30}} structures, steric hindrance results in disorder present in the pentanuclear half-capsules. The central inverted {V_5^*} half-capsule, which is in the middle between two adjacent inverted half-capsule displays a 50/50 disorder of two vanadyl groups as shown in Figure 5.6.4.

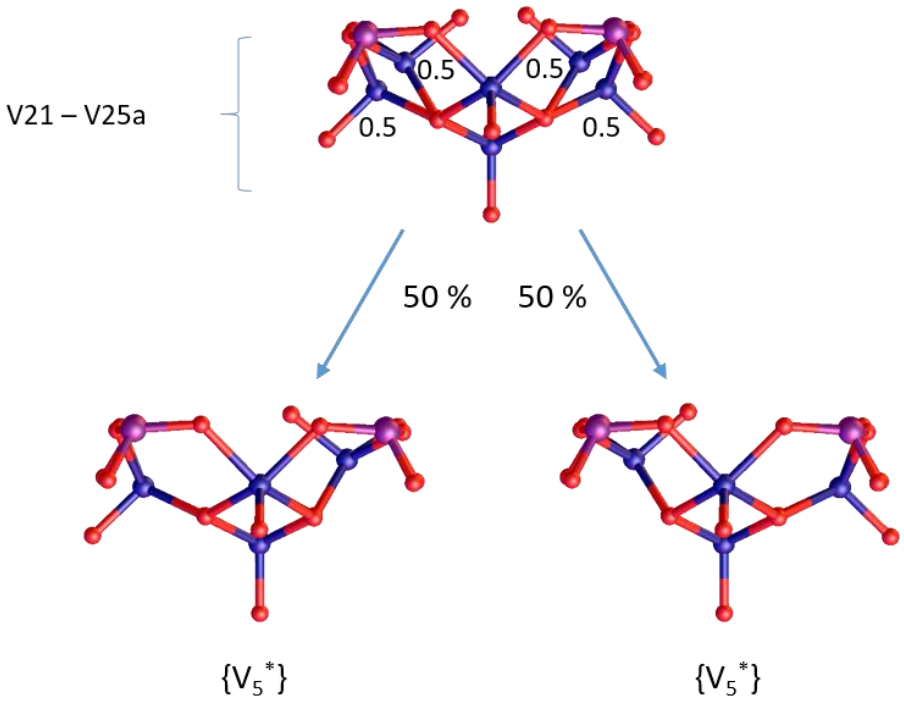

Figure 5.6.4 – Disorder of the pentanuclear half-capsule V21-V25a.

The two inverted pentanuclear half-capsules, which have only one neighbouring inverted half-capsule show disorder within the vanadyl group nearest to it. The vanadyl group on the other side is not affected by steric hindrance and therefore not disordered. This leads to a 50/50 distribution of a $\{V_5^*\}$ and a $\{V_5\}$ half-capsule (Figure 5.6.5).

The V=O double bonds range from 1.55(5) Å to 1.66(4) Å with an average of 1.6 Å. The V=O distances where restrained to a distance of 1.6 Å wherever needed. The V-O single bond distances were not restrained and range from 1.67(3) Å to 2.17(4) Å giving an average bond length of 1.9 Å. The extreme short and long V-O distances are indicative of the low resolution of the diffraction pattern and should be viewed with caution.

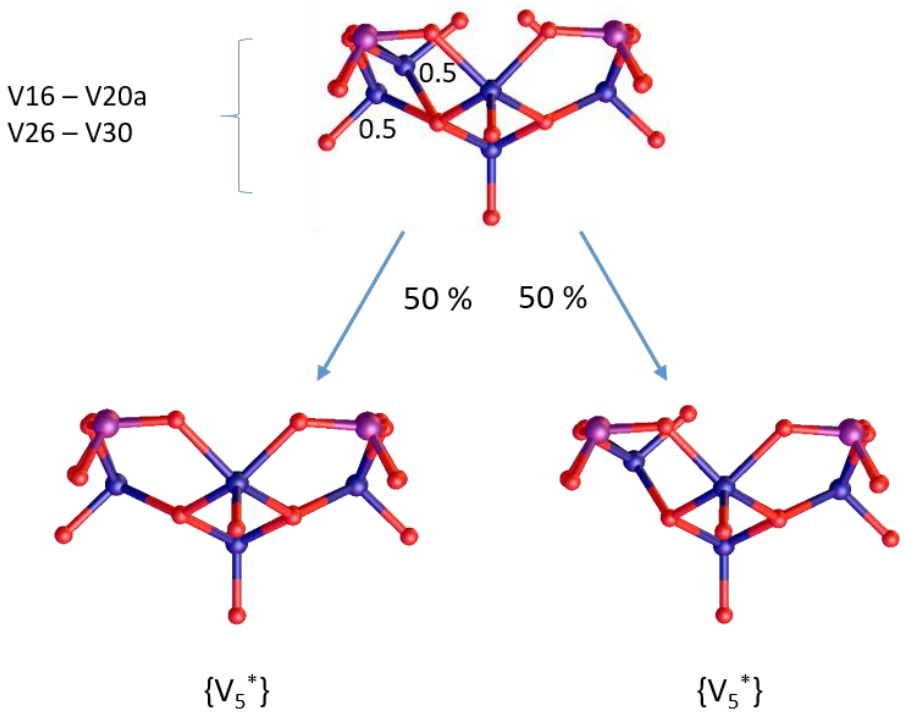

Figure 5.6.5 – Disorder of pentanuclear half-capsule V16-V20a and V26-V30.

The packing of the $[3+3]_o$ isomer can be seen in Figure 5.6.6 and Figure 5.6.7. Other than the $\{V_{30}\}$ clusters in **V_{30}-Na**, **-K** and **-Rb** the $\{V_{30}\}$ cluster in **V_{30}-Cs** is asymmetric. It arranges itself in a head to head/tail to tail arrangement down the crystallographic *c*-axis as can be seen in Figure 5.6.7. This arrangement leads to layers of outward-facing half-capsules and inverted half-capsules. In general, throughout the crystal structure, outward-facing half-capsules are in the vicinity to other outward-facing half-capsules. The same applies for inverted half-capsules, as can be seen in Figure 5.6.6.

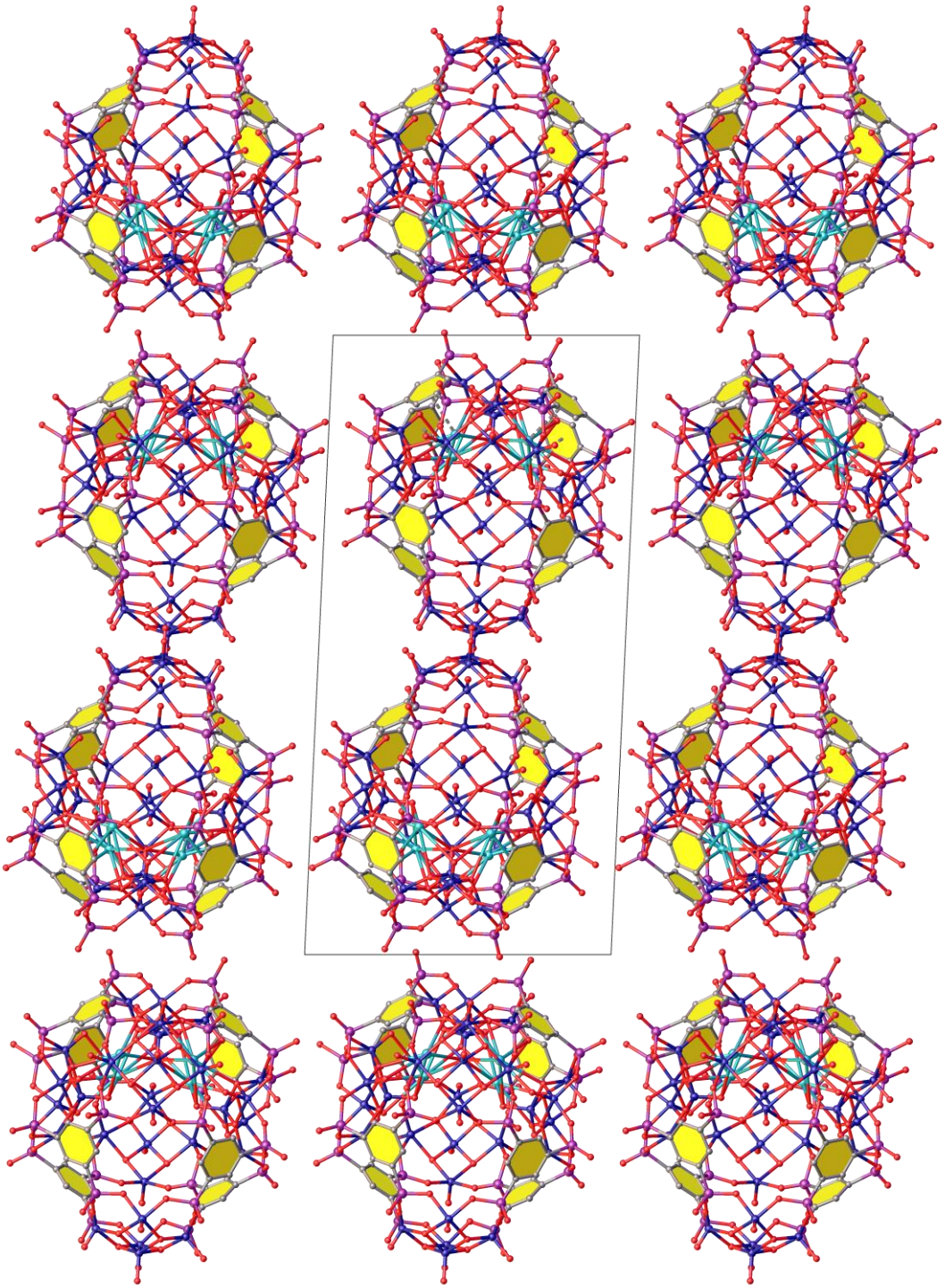

Figure 5.6.6 – Packing of **V_{30}-Cs** in [010] direction.

It is highly likely that the residual charge of -26 from the {V_{30}} structure is balanced by caesium ions, which are bridged by water molecules in between the crystal structure. Because of the low resolution of the diffraction data however those could not be resolved from the XRD experiment.

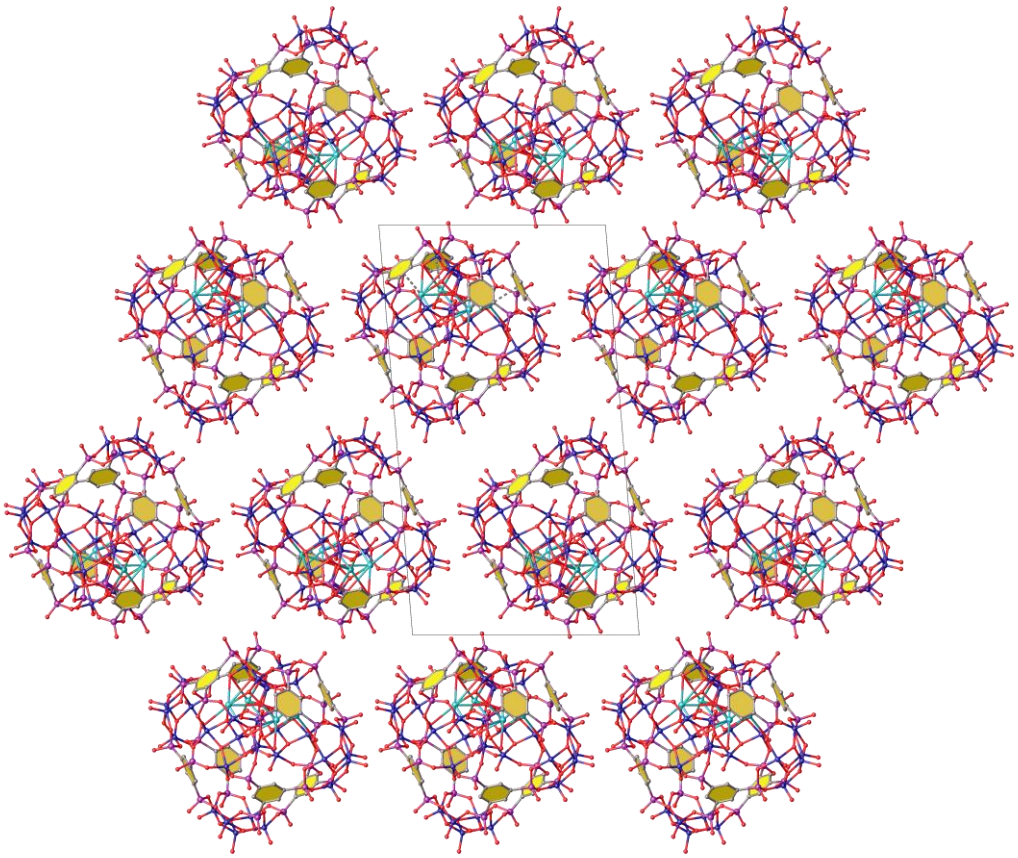

Figure 5.6.7 – Packing of **V_{30}-Cs** in [001] direction.

Table 5.6.1 – Crystallographic table for **V_{30}-Cs**.

Identification code	**V_{30} – Cs**
Empirical formula	$C_{48}Cs_4O_{127.5}P_{24}V_{30}$
Formula weight/(g/mol)	5419.6
Temperature/K	100
Crystal system	triclinic
Space group	*P*-1
a/Å	19.8787(10)
b/Å	22.6954(11)
c/Å	36.629(2)
α/°	94.060(4)
β/°	90.666(4)
γ/°	115.026(3)
Volume/Å^3	14920.6(14)
Z	2
ρ_{calc} g/cm^3	1.206
μ/mm^{-1}	13.018
F(000)	5156
Crystal size/mm^3	0.16 × 0.06 × 0.05
Radiation	CuKα (λ = 1.54178)
2Θ range for data collection/°	4.312 to 87.54
Index ranges	$-17 \leq h \leq 17$ $-20 \leq k \leq 20$ $-32 \leq l \leq 32$
Reflections collected	35834
Independent reflections	20865 [R_{int} = 0.0648, R_{sigma} = 0.1212]
Data/restraints/parameters	20865/230/812
Goodness-of-fit on F^2	1.011
Final R indexes [I>=2σ (I)]	R_1 = 0.2210, wR_2 = 0.5007
Final R indexes [all data]	R_1 = 0.2630, wR_2 = 0.5300
Largest diff. peak/hole / e Å^{-3}	3.71/-3.22

5.7 Characterisation

5.7.1 IR

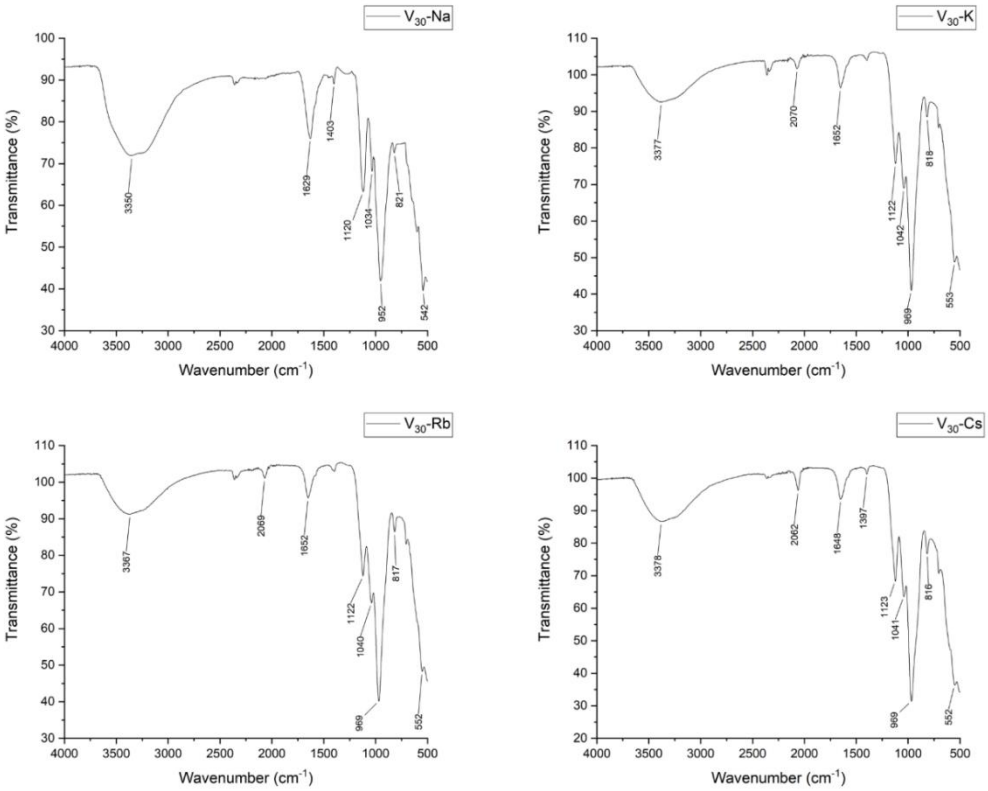

Figure 5.7.1 – IR spectrums of the **V_{30}-AM** compounds.

IR spectra of all four compounds were recorded from 4000 cm^{-1} to 500 cm^{-1}. All compounds display largely the same spectra, as is not unexpected given the similar molecular compositions. The overall symmetry of the compounds seems to make no difference in the IR spectra, despite the differences between the highly symmetric **V_{30}-Na** and the lesser symmetric **V_{30}-Cs** for example. All spectra show two broad signals around 3370 cm^{-1} and 1652 cm^{-1}, which derive from constitutional water molecules in the crystal structure. All compounds except **V_{30}-Na** show a signal around 2060 cm^{-1}, which results from the N≡N=N stretch, indicating small quantities of azide ions in the structure. The signal around 1400 cm^{-1} can be assigned to a CH_3 deformation vibration of MeCN. The signals around 1122 cm^{-1} and 1040 cm^{-1} can be attributed to the phosphonate ligand while the strongest signal around 969 cm^{-1} belongs to the V=O stretch. Overall the IR analysis supports the general assignment of the molecular composition by SXRD analysis.

5.7.2 PXRD

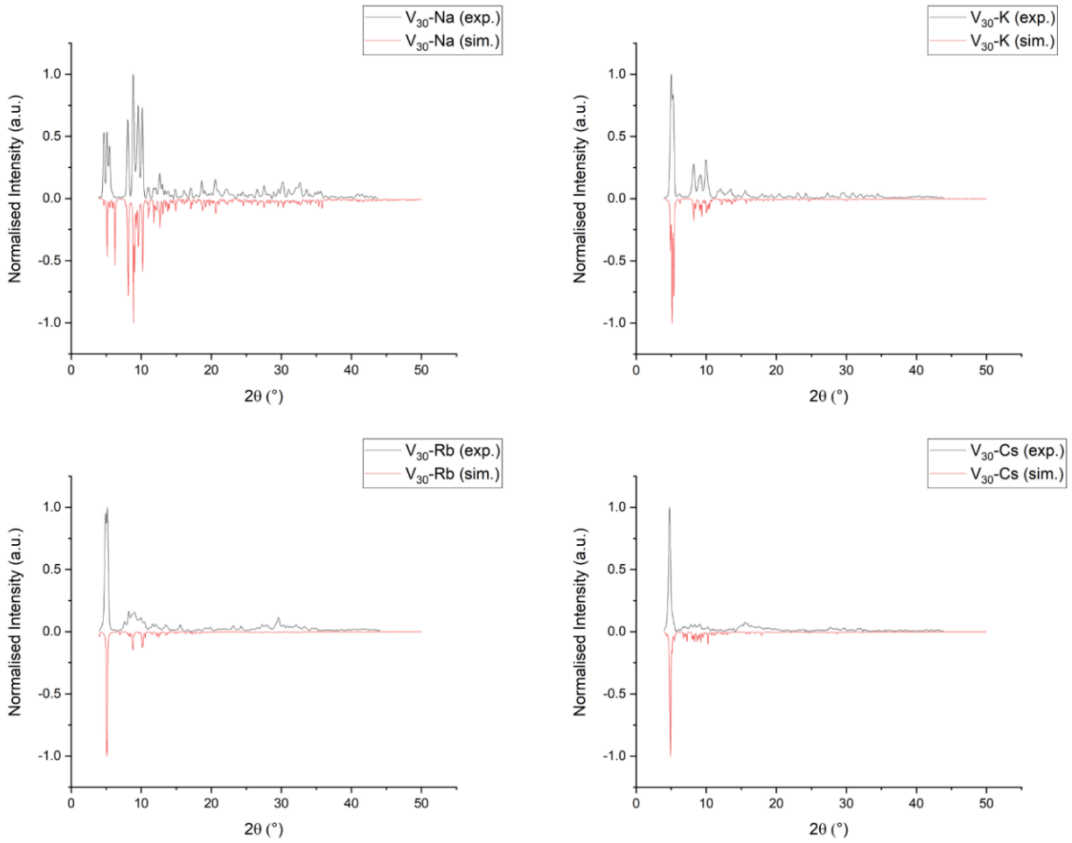

Figure 5.7.2 – PXRD patterns of the **V_{30}-AM** compounds.

To investigate the phase purity of the crystalline samples as well as the absence of crystalline impurities PXRD patterns were recorded between 5˚ and 55˚ θ. The PXRD patterns for **V_{30}-Cs** and **V_{30}-K** fit well to the simulated patterns of their crystal structures, indicating phase purity of the bulk materials. **V_{30}-Na** and **V_{30}-Rb** do show additional peaks in the experimental patterns which are likely due to the presence of different crystalline phases in the samples. In the case of **V_{30}-Rb** it is likely that a triclinic phase, as found in **V_{30}-K**, exists alongside the monoclinic phase. Of interest is the phase purity of **V_{30}-Cs** as the low symmetry $[3+3]_o$ isomer is likely to be less stable than the more symmetric $[2+4]_o$ and $[4+2]_o$ isomers. The absence of other isomers in the bulk material indicates an unexpected preference of caesium for the $[3+3]_o$ isomer, which might provide a path to more insight into the formation of these POV clusters in future studies.

5.7.3 MS

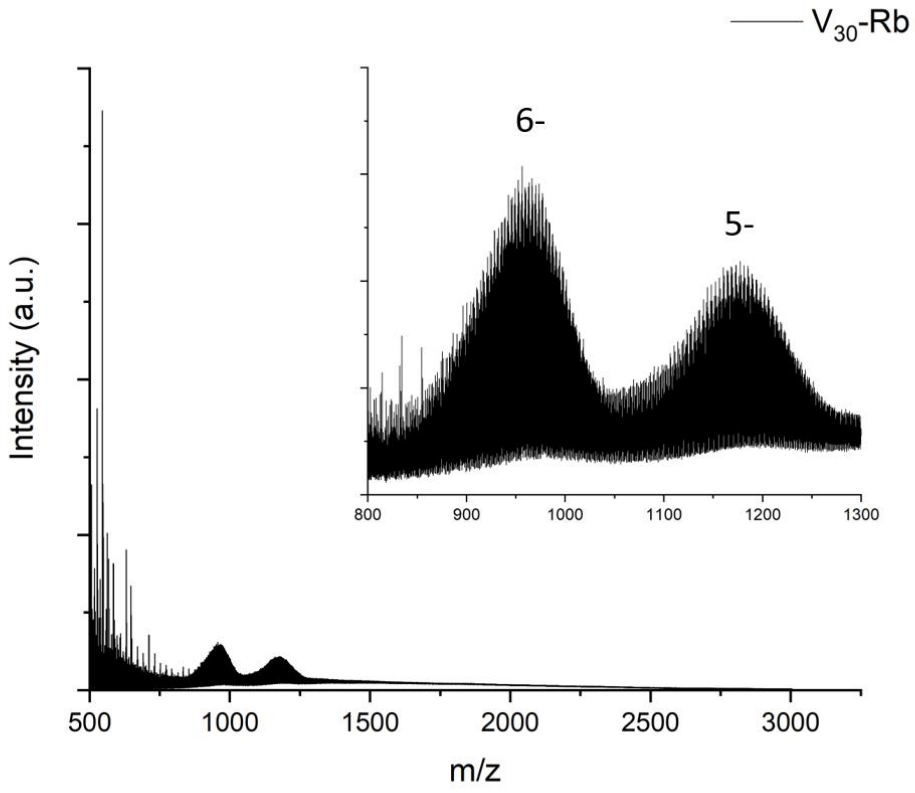

Figure 5.7.3 – MS of **V_{30}-Rb** in water.

To investigate the solution stability of the {V_{30}} clusters an ESI-MS spectrum **V_{30}-Rb** of was recoded in aqueous solution. The mass spectrum of **V_{30}-Rb** shows two broad envelopes of 6- and 5- charge, determined by the number of signals between 1 m/z. Due to the significant overlap of different species the isotope distributions are not well resolved and a definitive assignment as in the case of the **V_{20}H-AM** compounds could not be made. Attempts were also hindered by the inside of the structure not being fully resolved from the XRD measurements. The 6- envelope centres around 956.36 m/z, while the 5- envelope centres around 1177.21 m/z. The similar charge, position and shape of the peak envelopes compared to the **V_{20}H-AM** family however hint at the presence of the {V_{30}} cluster in solution. This would mean that the {V_{30}} cluster displays a similar stability against dissociation in water as well as the same rich redox chemistry visible in the ESI-MS spectra of the {V_{20}} clusters.

5.8 Conclusions

In this chapter the synthesis and characterisation of four novel {V_{30}} hybrid POVs was presented. The structures represent an expansion of the {V_{20}} systems described in chapter 3 and 4. Different from the {V_{20}} clusters the {V_{30}} structures feature varying arrangements of six inward-facing or outward-facing {V_5} and {V_5^*} units. The resulting structures were conceptualised as three out of six chemically viable isomers.

Most interestingly, the arrangement of the differently oriented pentanuclear half-capsules had an influence on the presence of the alkali metal cube in the centre of the structure and thus provided insight into the formation of the {V_{20}} and {V_{30}} capsules. While the alkali metal cube was fully present in the $[2+4]_o$ isomer, it was missing completely from the $[4+2]_o$ isomer while the [3+3] isomer featured half a cube on the inside of the structure. Backed by theoretical calculations, we can conclude from this observation that the cation-π interactions are aided by favourable AM-μ_3O^{2-} bonds from two adjacent inverted half-capsules, which is the case in the $[2+4]_o$ and partly in the $[3+3]_o$ isomer. We hypothesize that this energetically favourable situation is the reason why inverted half-capsules are favoured in the {V_{20}} and {V_{30}} systems. As sodium ions do not participate in cation-π interactions in these clusters due to the higher hydration energy the case of **V_{30}-Na** validates this assumption by building out the $[4+2]_o$ isomer without two adjacent half-capsules in the structure.

The {V_{30}} structures can be seen as templated metal organic polyhedra with an added level of complexity due to the variation in the POV building blocks. The isomerism present in the system can be explained by the cation-π interactions, which govern the formation and stability of the cluster. Insights gained by the system are transferable to not only the {V_{20}} systems but also to future POV-based assemblies. The added stabilisation of the AM-μ_3O^{2-} will play an important role in the design and synthesis of tetrahedral POV-based polyhedra and other platonic architectures based on cation-π interactions.

1. L. Zhang and W. Schmitt, *J Am Chem Soc*, 2011, **133**, 11240-11248.
2. Z. Zhang, L. Wojtas and M. J. Zaworotko, *Chem. Sci.*, 2014, **5**, 927-931.
3. Y. Gong, Y. Zhang, C. Qin, C. Sun, X. Wang and Z. Su, *Angew. Chem.*, 2019, **131**, 790-794.
4. Y. Zhang, H. Gan, C. Qin, X. Wang, Z. Su and M. J. Zaworotko, *J. Am. Chem. Soc.*, 2018, **140**, 17365-17368.

5. Y. Zhang, X. Wang, S. Li, B. Song, K. Shao and Z. Su, *Inorg. Chem.*, 2016, **55**, 8770-8775.
6. D. J. Tranchemontagne, Z. Ni, M. O'Keeffe and O. M. Yaghi, *Angew. Chem. Int. Ed.*, 2008, **47**, 5136-5147.
7. P. van der Sluis and A. L. Spek, *Acta Cryst.*, 1990, **A46**, 194-201.

Chapter 6

Oxothiomolybdate wheels with highly functionalised ligand

6.1 Introduction

The synthesis of closed hybrid POM structures such as rings, capsules and polyhedra requires convex POM fragments, which can be assembled *via* organic ligands into discrete, non-periodic structures. Aside from suitable POV fragments like the $\{V_5\}$ half-capsule we were interested in convex precursors of other POM building metals as well. The combination of these different building blocks could potentially give rise to chemically and electronically interesting mixed-metal systems. A fascinating building block in POM chemistry for these purposes is the oxothiomolybdenum cation $[Mo^{V}_2O_2S_2(H_2O)_4]^{2+}$, which can be seen in Figure 6.1.1. The $\{Mo_2O_2S_2\}$ building block has been utilised extensively by Cadot *et.al.* to generate a large number of ring structures with a wide variety of different internal templates. It also proved suitable as a heteronuclear capping group for lacunary POMs in mixed metal systems.[107, 110] The $\{Mo_2O_2S_2\}$ motif is inherently bent and therefore ideal for the construction of rings, capsules or polyhedra.[§] This preference to build out ring structures is almost unrivalled in POM chemistry. Aside from to the possibility of synthesising mixed-metal systems we were therefore drawn to its ability to accommodate a plethora of different templating agents and interested in seeing how far this system could be stretched by using geometrically challenging ligands.

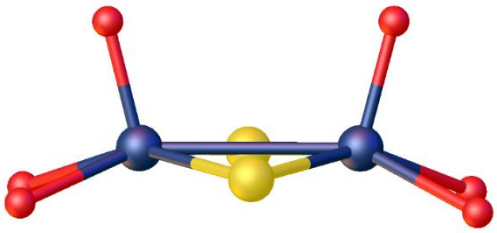

Figure 6.1.1 - The $[Mo_2O_2S_2]^{2+}$ motif with terminal *oxo*-ligands.

The majority of the oxothiomolybdate wheels known in the literature are synthesised with di- or tri-functionalised carboxylate ligands based on short alkyl chains or planar aromatic rings. The first two ligands that were chosen for investigation were the commercially available cyclopentanetetracarboxylic acid (H_4CPTCA) and the closely related tetrahydrofurantetracarboxylic acid (H_4THFTCA), which are shown in Figure 6.1.2. The main difference between the two ligands is the potential binding site at the oxygen atom of the tetrahydrofuran ring in H_4THFTCA. The saturated cyclopentane ring present in the ligands is

[§] A more extensive review of the chemistry of the $\{Mo_2O_2S_2\}$ group is given in the chapter 1.1.4.

likely to display the envelope conformation within the structures, positioning the carboxylate ligands into a challenging arrangement for the preferably planar ring systems. Another structurally potentially interesting ligand for the oxothiomolybdate rings is mellitic acid (H_6Mel), in which a benzene ring is functionalised by six carboxylic acid groups. Although the benzene ring is essentially planar the six carboxylic acid groups have the tendency to rotate out of the aromatic plane due to electronic repulsion of their oxygen atoms. This should inhibit the formation of a classical $\{Mo_2O_2S_2\}$ based ring, in which the carboxylic acid groups are parallel to the ring plane.

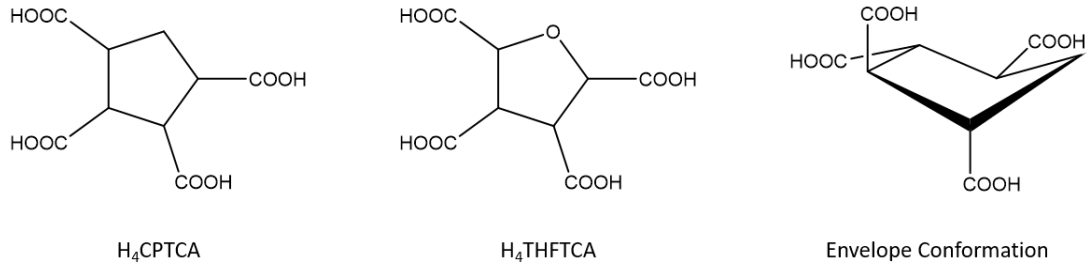

Figure 6.1.2 – Initial ligands used in the synthesis of polyoxothiomolybdate wheels and possible conformation for H_4CPTCA.

The use of highly functionalised ligands has the additional purpose of increasing the chance to obtain oxothiomolybdate structures with free carboxylate groups in order to use them as precursors for larger POM based assemblies. The ability of the $\{Mo_2O_2S_2\}$ systems to accommodate almost any carboxylic acid makes it difficult to generate usable precursor structures with di- or trifunctionalised carboxylate ligands.

6.2 $K_3[Mo_2O_2S_2(C_4H_4O(COO)_2(COOH)_2)(C_4H_4O(COO)_3(COOH))] \cdot 6\ H_2O$ – (**Mo₂, 17**)

The compound $K_3[Mo_2O_2S_2(C_4H_4O(COO)_2(COOH)_2)(C_4H_4O(COO)_3(COOH))] \cdot 6\ H_2O$ (**Mo₂, 1**) was synthesised by adjusting the pH of an aqueous solution of tetrahydrofurantetracarboxylic acid (H_4THFTCA) with K_2CO_3 to pH = 7. After addition of an aqueous solution of $\{K_{0.40}(NMe_4)_{0.1}I_{0.5}[Mo_2O_2S_2(OH)_2(H_2O)] \cdot 6.3\ H_2O\}_n$ the pH was adjusted to pH = 4.5 and the resulting solution was stirred for an hour at room temperature, filtered and left to crystallise. The product was obtained as orange-yellow crystals after several months.

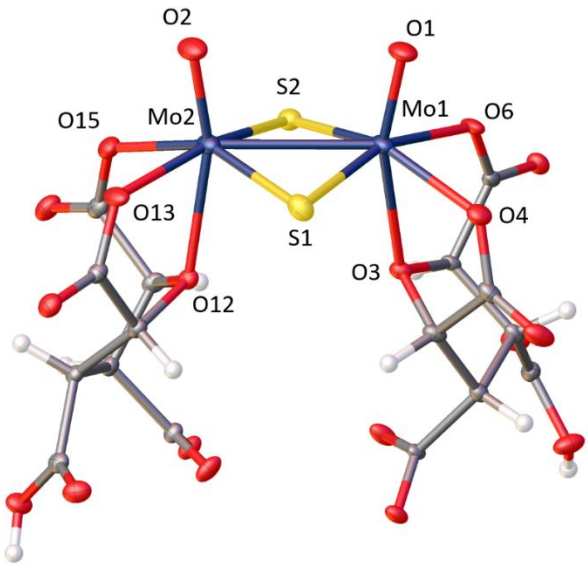

Figure 6.2.1 – Structure of the thiomolybdate dimer in **Mo₂**.

6.2.1 Crystallography

Mo₂ was solved in the monoclinic space group $P2_1/c$ with following unit cell parameters:

$a = 7.6214(7)$ Å	$\alpha = 90°$,	$Z = 4$
$b = 21.1151(18)$ Å	$\beta = 95.305(2)°$	$Z' = 1$
$c = 20.3345(18)$ Å	$\gamma = 90°$	$V = 3258.3(5)$ Å^3

The structure consists of a molybdenum dimer, in which two *oxo*-molybdenum(V) ions of distorted octahedral geometry are connected in edge-sharing fashion. Bridged by two μ_2-sulfide

ions the coordination sphere is completed by a singly protonated $(H_1THFTCA)^{3-}$ or a doubly protonated $(H_2THFTCA)^{2-}$ ligand.

Different from the literature known thiomolybdate ring system the wo carboxylate moieties bind in the equatorial position of the dimer in *anti*-fashion and therefore block the extension of the dimer to form into a ring system. The position *trans* to the terminal *oxo*-group is occupied by the oxygen donor of the tetrahydrofuran ring. The flexibility of the tetrahydrofuran ring allows the carboxylate groups to position their oxygen donors in the equatorial plane. Removal of the oxygen donor from the ring should therefore diminish the chances of the dimer formation.

The bond lengths for the Mo=O double bonds are 1.682(3) Å and 1.684(3) Å long while the Mo-O single bonds with the carboxylate ions range from 2.118(3) Å to 2.157(4) Å. The oxygen donor of the tetrahydrofuran ring is rather loosely bound to the molybdenum ion and builds out Mo-O bonds with a length of 2.332(3) Å and 2.359(3) Å (Table 6.2.1). Longer than the Mo-O bonds are the Mo-S bonds with distances between 2.3122(12) Å and 2.3193(1) Å. The Mo-S-Mo bond angles are characteristically sharp with 75.16(4)° and 75.25(4)°, leading to a short Mo-Mo bond distance of 2.8265(6) Å. Both molybdenum ions are in the oxidation state +V, as confirmed by BVS calculations (Table 6.2.2).

Table 6.2.1 - Bond distances for the molybdenum(V) ions in **Mo2**.

Bond	Bond length / Å	Bond	Bond length / Å	Bond	Bond length / Å
Mo1-S1	2.3122(12)	**Mo2-S1**	2.3180(14)	**Mo1-Mo2**	2.8265(6)
Mo1-S2	2.3193(13)	**Mo2-S2**	2.3155(12)		
Mo1-O1	1.682(3)	**Mo2-O2**	1.684(3)		
Mo1-O3	2.359(3)	**Mo2-O12**	2.322(3)		
Mo1-O4	2.142(3)	**Mo2-O13**	2.118(3)		
Mo1-O6	2.120(3)	**Mo2-O15**	2.157(4)		

Table 6.2.2 – BVS calculations for the molybdenum ions in **Mo2**.

	BVS	Oxidation state
Mo1	5.08	+5
Mo2	5.08	+5

As can be seen in Figure 6.2.1 the octahedral environment of the molybdenum ions is distorted to the point, in which the structure resembles a square pyramidal coordination environment if the oxygen donor of the tetrahydrofuran ring would be removed. Geometrical analysis using the program SHAPE[237] was carried out in order to compare the coordination environment to ideal square pyramidal and octahedral geometries (Table 6.2.3). In both cases the coordination environment for the molybdenum ions is closer to an octahedral than a square pyramidal geometry, while the low CShM values (< 3) indicate that both geometries are valid views of the structure.

Table 6.2.3 – Continuous shape measure calculations of the molybdenum(V) ions in Mo_{12}.

	MoO_4S_2		**MoO_3S_2**
Atom name	Spherical Square Pyramid	Vacant Octahedron	Octahedron
Mo1	2.569	1.798	2.005
Mo2	2.971	2.069	2.272

As an effect of the almost square pyramidal environment, the $\{Mo_2\}$ – dimer is not planar but slightly bent. The angle between O13-Mo2 and Mo1-O4 bonds is about 35°, as illustrated in Figure 6.2.2. This slight bend is the reason behind the prevalence of this dimer to build out ring structures, as will be demonstrated later in the chapter. The molybdenum dimer is hereby also not fully symmetrical. By looking along the Mo-Mo axis, one can see that both MoL_6 octahedra are slightly rotated against each other by about 14° (Figure 6.2.2).

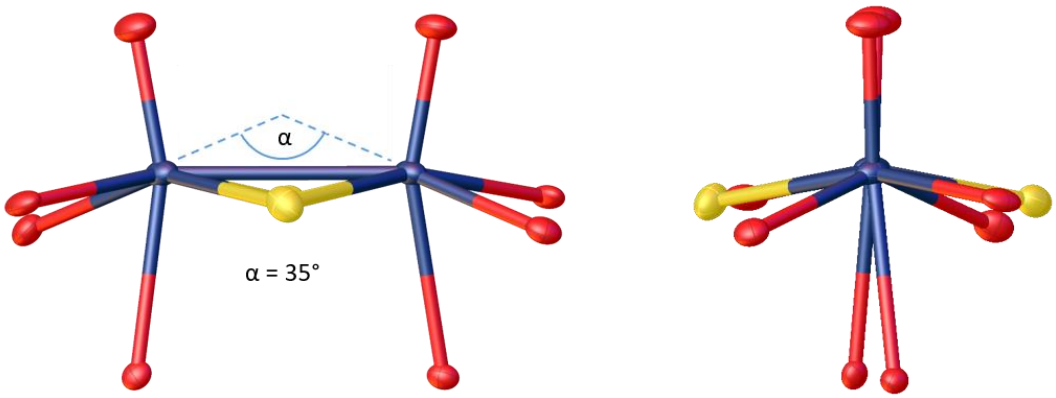

Figure 6.2.2 – The molybdenum dimer in **Mo_{12}**.

L1		L2	
C1	S	**C9**	R
C2	S	**C10**	R
C3	R	**C11**	S
C4	R	**C12**	S

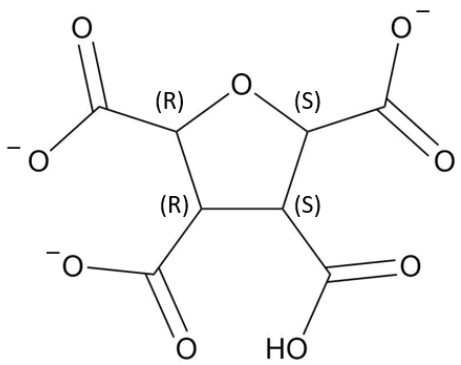

Figure 6.2.3 - Absolute configuration for the THFTCA ligands in **Mo_2**.

The $H_1THFTCA^{3-}$ ligands have four stereogenic centres each and are present in their *meso* form in the $\{Mo_2\}$ cluster. The absolute configuration of the tetrahydrofuran rings can be seen in Figure 6.2.3. Each ligand is at least doubly deprotonated and binds with its carboxylate groups to the molybdenum ions as described above. The free carboxylic acid groups in the structure build out hydrogen bonds to water molecules, while the deprotonated carboxylate group binds to a potassium ion which is located between the two molybdenum dimers. The fourth carboxylate group has to be partially protonated in order for crystal structure to achieve charge balance. This, however, could not be modelled from the obtained data.

The -4 charge of the molybdenum dimer is balanced by three potassium ions in the asymmetric unit, which arrange themselves in dimers in between the molybdenum clusters as shown in Figure 6.2.4. They are bridged by water molecules of which some lie disordered in the structure. Figure 6.2.5 shows the arrangement of the molybdenum dimers within the crystal structure.

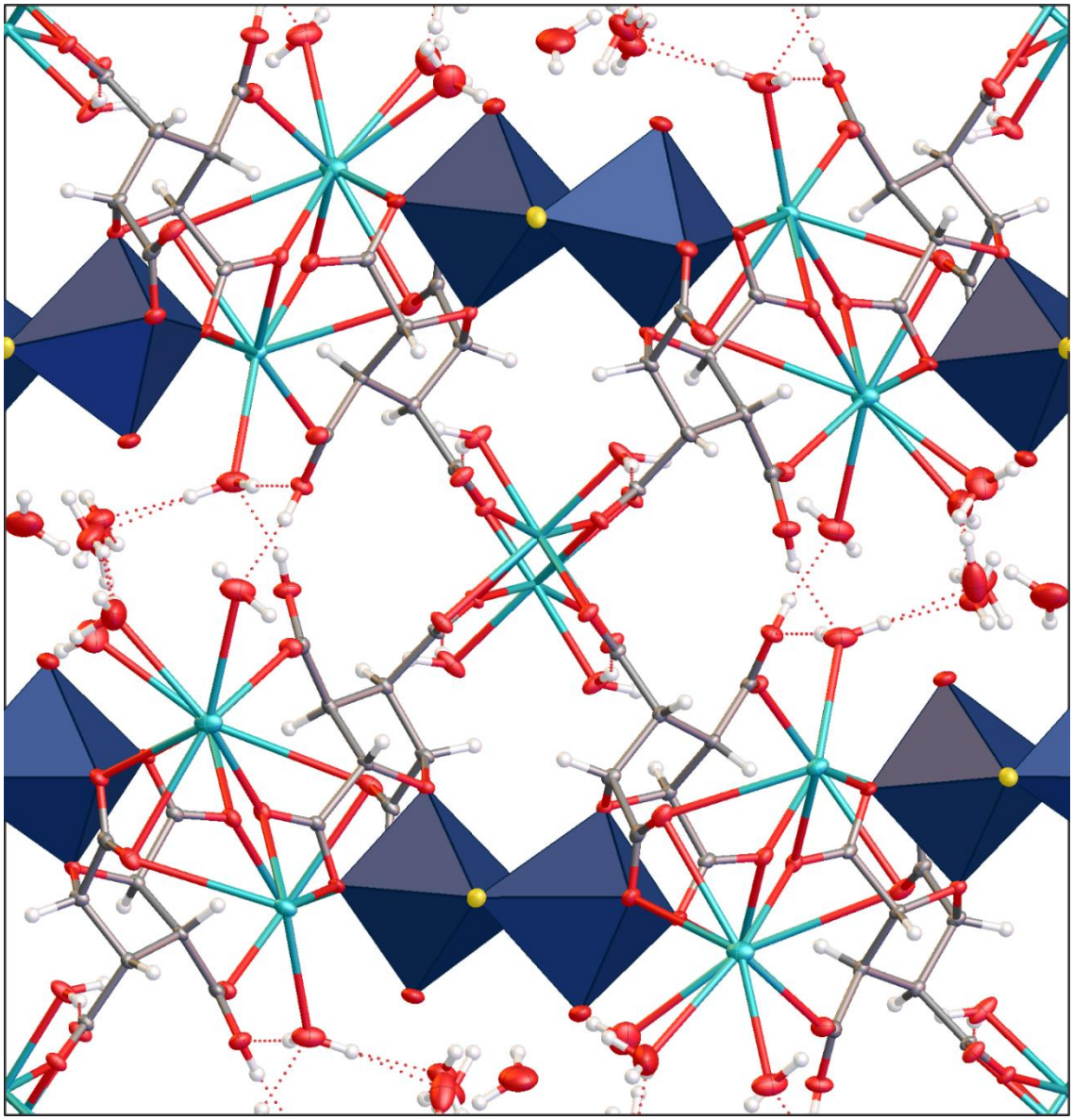

Figure 6.2.4 – Packing diagram of **Mo$_2$**. View in [100] direction.

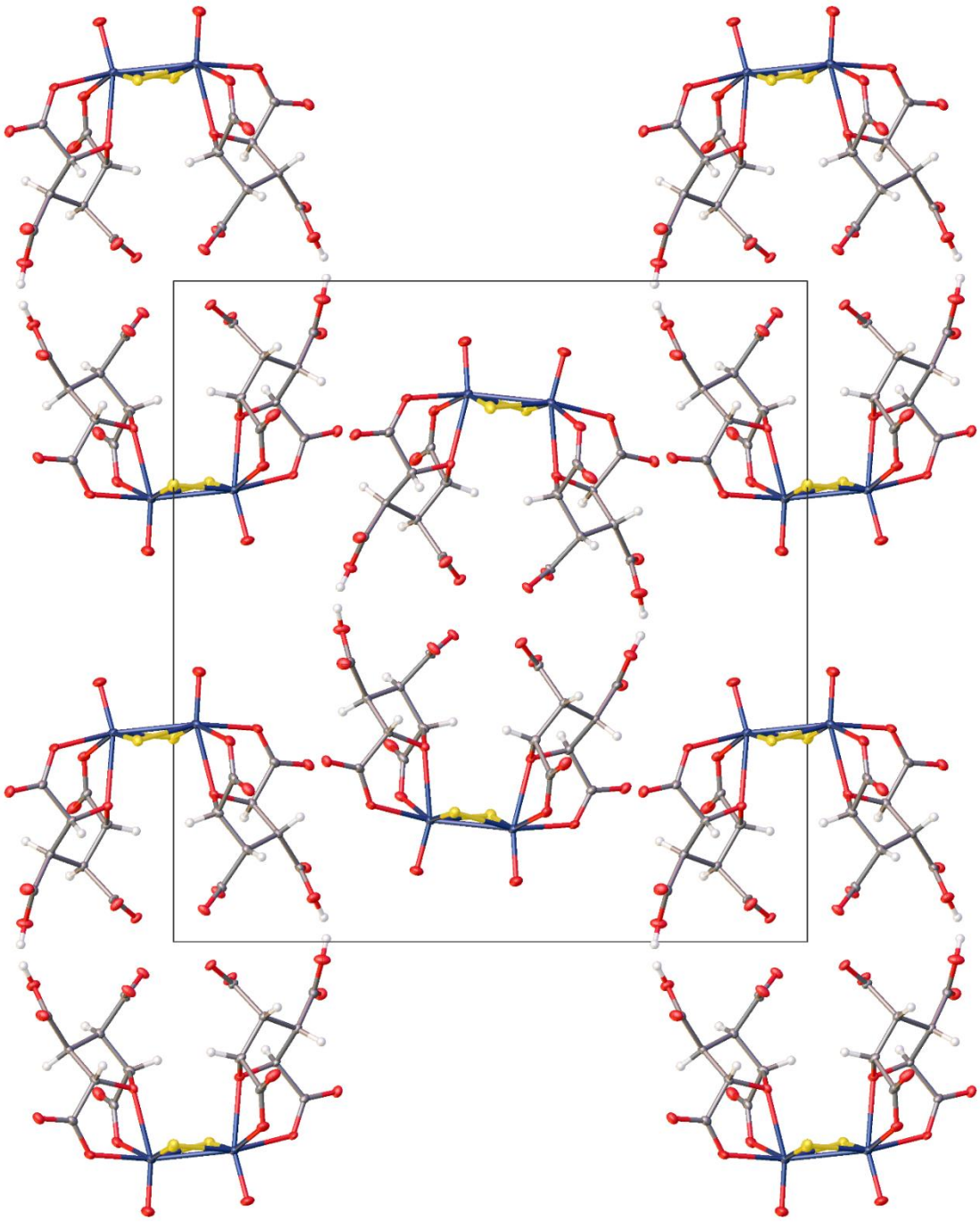

Figure 6.2.5 – Packing diagram of the molybdenum dimers in **Mo$_2$**. View in [100] direction.

Table 6.2.4 – Crystallographic table for **Mo_2**.

Identification code	**Mo_2**
Empirical formula	$C_{16}H_{24}K_3Mo_2O_{27}S_2$
Formula weight/(g/mol)	1021.65
Temperature/K	99.98
Crystal system	monoclinic
Space group	$P2_1/c$
a/Å	7.6214(7)
b/Å	21.1151(18)
c/Å	20.3345(18)
α/°	90
β/°	95.305(2)
γ/°	90
Volume/Å^3	3258.3(5)
Z	4
ρ_{calc} g/cm^3	2.083
μ/mm^{-1}	1.386
F(000)	2036
Crystal size/mm^3	0.13 × 0.04 × 0.04
Radiation	MoKα (λ = 0.71073)
2Θ range for data collection/°	3.858 to 68.778
Index ranges	$-11 \leq h \leq 12$ $-33 \leq k \leq 33$ $-32 \leq l \leq 32$
Reflections collected	186195
Independent reflections	13686 [R_{int} = 0.1397 R_{sigma} = 0.0652]
Data/restraints/parameters	13686/26/501
Goodness-of-fit on F^2	0.971
Final R indexes [I>=2σ (I)]	R_1 = 0.0642, wR_2 = 0.1214
Final R indexes [all data]	R_1 = 0.1043, wR_2 = 0.1374
Largest diff. peak/hole / e Å^{-3}	1.46/-2.04

6.2.2 Characterisation

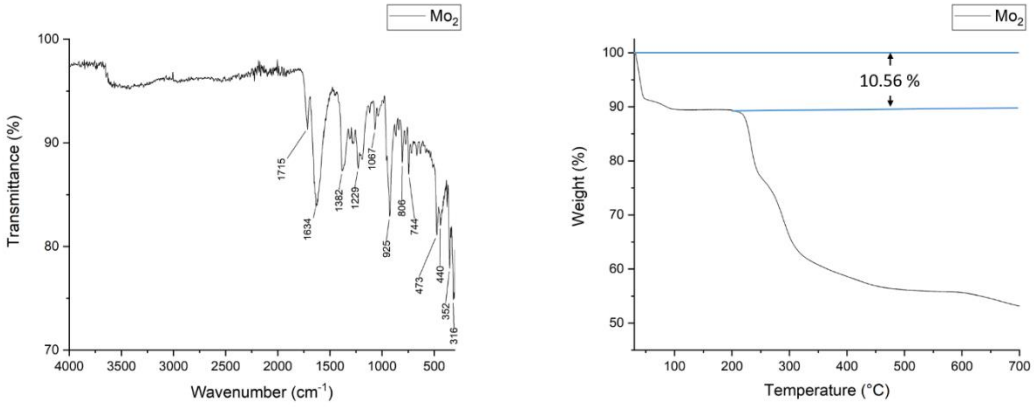

Figure 6.2.6 – IR spectrum and TGA curve of **Mo2**.

The IR spectrum of **Mo2** shows a characteristic band for the carbonyl stretch of the free carboxylic acid at 1715 cm^{-1}. The asymmetric and symmetric COO^- stretches for the bonded carboxylate groups can be found at $\nu_{as}(COO) = 1634\ cm^{-1}$ and $\nu_{as}(COO) = 1382\ cm^{-1}$. The difference between the asymmetric and symmetric stretch is the so called Deacon-Philips Δ value.[258] The value of $\Delta(\nu_{as}\text{-}\nu_{sym}) = 252\ cm^{-1}$ is consistent with the monodentate binding mode of the carboxylate ligands. By comparison with literature values the Mo=O group can be assigned to the intense signal at 925 cm^{-1}. The Mo-S-Mo bridge can be found at $\nu(\text{Mo-S-Mo}) = 473\ cm^{-1}$.[259]

To confirm the amount of solvent in the crystals a TGA curve was recorded from 30°C to 700°C in a nitrogen atmosphere. The 10.56 % drop in weight from 30°C to 100°C in the TGA curve of **Mo2** correspond to 6 water molecules (Theoretical value: 10.75 %). Ligand decomposition can be seen from 205°C onwards and metal oxide formation from about 600°C.

6.3 $K_5(NMe_4)_{1.5}[Mo_{16}O_{16}S_{16}(OH)_{16}(HCPTCA)_2]Cl_{0.5} \cdot 23\ H_2O$ (**Mo_{16}**, 18)

The compound $K_5(NMe_4)_{1.5}[Mo_{16}O_{16}S_{16}(OH)_{16}(HCPTCA)_2]Cl_{0.5} \cdot 23\ H_2O$ (**Mo_{16}**) was synthesised from a reaction of cyclopentanetetracarboxylic acid (H_4CPTCA) with K_2CO_3 in water at pH = 4.5. The product was obtained as orange crystals after several months.

6.3.1 Crystallography

Mo_{16} was solved in the triclinic space group $P\bar{1}$ with the unit cell dimensions of

$a = 17.5672(12)$ Å	$\alpha = 115.068(1)°$,	$Z = 2$
$b = 19.7328(14)$ Å	$\beta = 91.535(2)°$	$Z' = 1$
$c = 20.2612(14)$ Å	$\gamma = 115.163(2)°$	$V = 5570.3(7)$Å^3

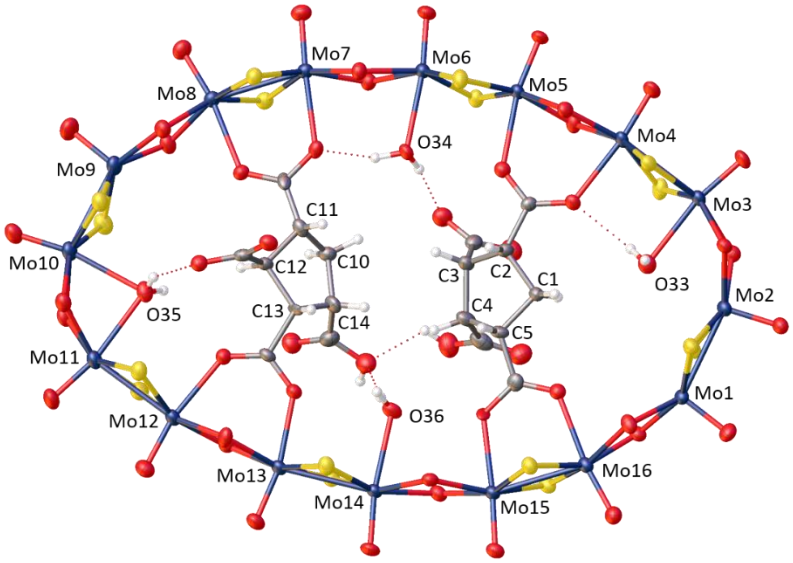

Figure 6.3.1 – {Mo_{16}} thiomolybdate ring in **Mo_{16}**.

The H_4CPTCA ligand was chosen as removal of the oxygen donor of the tetrahydrofuran ring in H_4THFTCA was suspected to diminish the chances of dimer formation in favour of the classical thiomolybdate ring system. The structure consists of an oval shaped {$Mo^{V}_{16}O_{16}(OH)_{16}S_{16}$} ring of neutral charge, made up of eight {$Mo_2O_2S_2$} building blocks, in which one doubly deprotonated and one triply deprotonated CPTCA ligand are placed in the centre of the ring. As

there is no oxygen donor in the cyclopentane ring anymore to position the carboxylate groups into the equatorial position of the thiomolybdate building block the system reverts to its standard ring formation. Four coordinating water molecules are incorporated inside the ring and complete the coordination sphere for five of the molybdenum ions. As in **Mo$_2$** the molybdenum polyhedra are connected in edge-sharing fashion. The size and shape of the ring is characterised by an inner cross-sectional diameter of d(Mo14-Mo6) = 12.2223(14) Å and d(Mo10-Mo2) = 19.0088(15) Å, leading to the overall oval shape of the molecule. Each molybdenum ion possesses a terminal *oxo*-ligand, which points towards the outside of the ring. The molybdenum ions are alternately bridged by two μ_2-OH^- and two S^{2-} ions. Although the hydrogen atoms for the hydroxy groups could not be resolved, they are confirmed by BVS calculations as can be seen in Table 6.3.1. Three out of the 16 molybdenum ions (Mo1, Mo2 and Mo9) are five coordinated, while the other 13 have their coordination sphere completed by water ligands (either singly bonded or bridging) or by carboxylate O-donor atoms of the two CPTCA ligands. Because of the difference in curvature around the ring, the molybdenum ions adopt either an octahedral or a square pyramidal geometry, depending on the sixth oxygen donor and the position in the ring. CShM analysis gives an indication about the coordination environment of each molybdenum ion. As carried out before the CShM values were calculated for the {MoO_4S_2} polyhedra as well as the {MoO_3S_2} polyhedra, in which the oxygen donor *trans* to the terminal *oxo*-ligand was removed, if present. The results can be seen in Table 6.3.2 and Figure 6.3.2.

Table 6.3.1 – BVS parameters for the molybdenum and oxygen ions in the ring of **Mo$_{16}$**. Ox. : Oxidation state.

	BVS	Ox.		BVS	Ox.		BVS	Ass.		BVS	Ass.
Mo1	5.11	+5	**Mo9**	5.00	+5	**O17**	1.23	-OH	**O25**	1.27	-OH
Mo2	4.88	+5	**Mo10**	5.10	+5	**O18**	1.19	-OH	**O26**	1.19	-OH
Mo3	4.97	+5	**Mo11**	5.13	+5	**O19**	1.22	-OH	**O27**	1.17	-OH
Mo4	5.19	+5	**Mo12**	5.13	+5	**O20**	1.18	-OH	**O28**	1.07	-OH
Mo5	5.08	+5	**Mo13**	5.07	+5	**O21**	1.2	-OH	**O29**	1.15	-OH
Mo6	5.10	+5	**Mo14**	5.03	+5	**O22**	1.24	-OH	**O30**	1.23	-OH
Mo7	5.05	+5	**Mo15**	5.12	+5	**O23**	1.24	-OH	**O31**	1.25	-OH
Mo8	5.13	+5	**Mo16**	5.14	+5	**O24**	1.23	-OH	**O32**	1.29	-OH

Table 6.3.2 – CShM analysis of the molybdenum ions in **Mo16**.

	MoO_3S_2		MoO_4S_2
Atom name	Spherical Square Pyramid	Vacant Octahedron	Octahedron
Mo1	2.511	3.313	-
Mo2	2.640	2.644	-
Mo3	3.057	2.718	2.470
Mo4	3.352	2.171	1.853
Mo5	3.408	2.091	1.789
Mo6	3.274	2.445	2.008
Mo7	3.392	2.578	2.191
Mo8	3.432	2.522	2.134
Mo9	2.409	3.194	-
Mo10	2.790	2.578	2.207
Mo11	2.889	2.626	2.27
Mo12	3.299	1.999	1.755
Mo13	3.436	1.967	1.759
Mo14	3.397	2.508	2.081
Mo15	3.490	2.566	2.173
Mo16	3.674	2.630	2.229

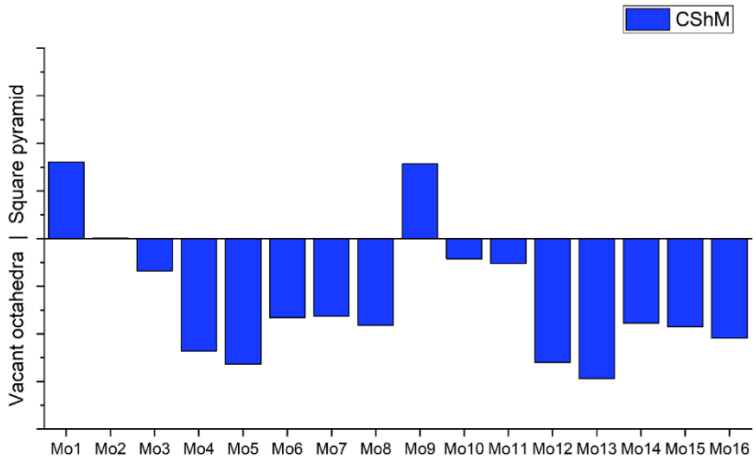

Figure 6.3.2 – Comparative CShM analysis. The further the bars reach one side, the clearer is the assignment of the respective polyhedra.

The molybdenum bond lengths for the Mo-(μ_2-OH) bonds average to 2.09 Å, while the Mo-S bond lengths average to 2.32 Å, with little variations around the ring for both. The Mo-O-Mo bond angles are distinctly different to the Mo-S-Mo bond angles and average to 106.7° while the Mo-S-Mo angles average to 74.7°. This leads to an average Mo-Mo distance between the sulphur bridged molybdenum ions of about 2.82 Å, which is characteristic for a Mo-Mo single bonds present in the cluster. The average bond length for the Mo=O double bond is 1.69 Å. The longest bonds for the molybdenum ions are associated with Mo-O bonds involving the water ligands and oxygen atoms inside the ring. The Mo-OH_2 distances range from 2.379(6) Å for the Mo14-O36 bond to 2.472(6) Å for the Mo10-O35 bond.

Both organic ligands in the asymmetric unit bind with two of their carboxylate groups to the ring. The remaining carboxylate and protonated carboxylic acid moieties are located above or below the ring plane. Ligand 1 (L1, C1-C5) binds with the carboxylates in 1 and 4 position to the ring while Ligand 2 (L2, C11-C14) binds to the ring with its carboxylate groups in 1 and 3 position (Figure 6.3.1). As can be seen in Figure 6.3.3 the free carbonyl groups from L1 are located on opposite sides of the ring while those of L2 are on the same side. The protonated carboxylic acid group is located at position 3 for L1 and 4 for L2. Figure 6.3.4 shows the structural formula of the ligands.

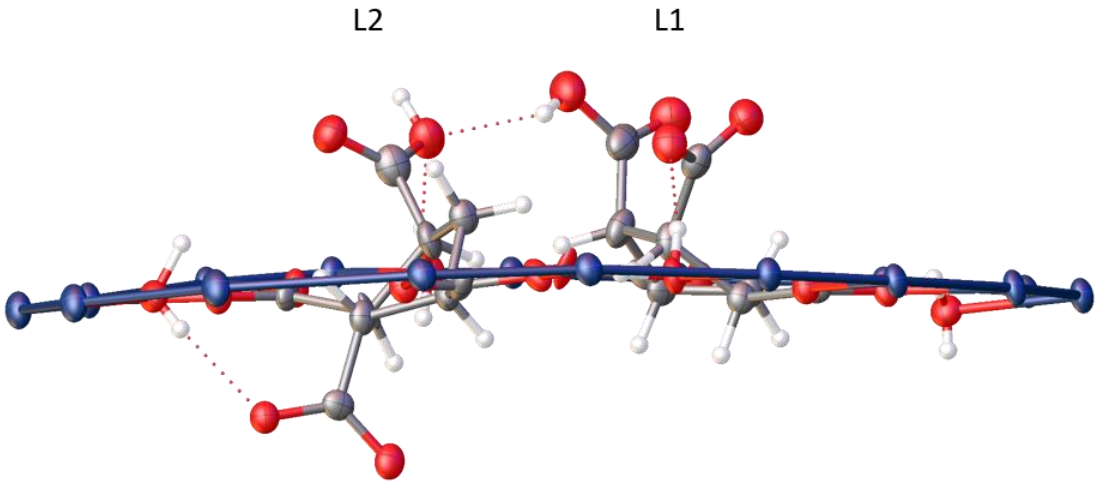

Figure 6.3.3 – Schematic view of the positions of the carboxylate group above and below the **Mo_{16}** ring.

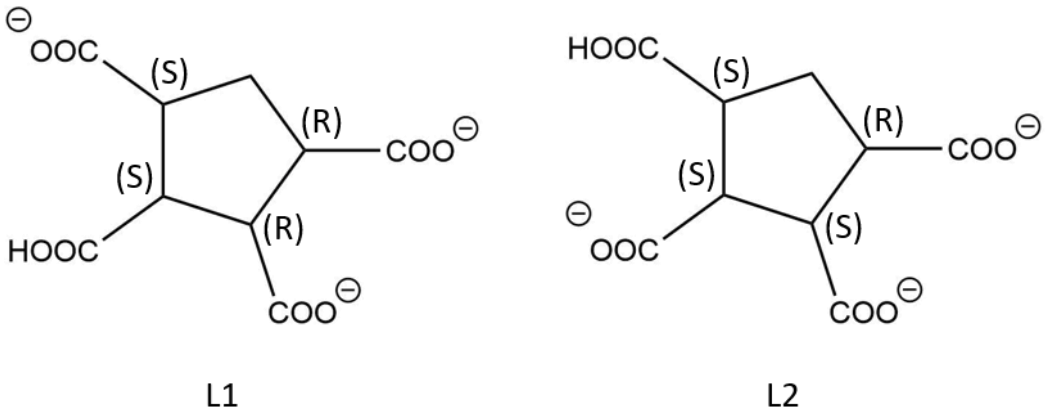

Figure 6.3.4 – Structural formulas for L1 and L2 with absolute configuration of the stereocentres.

Although there are only two unique ligands in the asymmetric unit, there are three unique stereoisomers in the unit cell, with the third being generated by the inversion centre of the $P\bar{1}$ space group. The three organic ligands have four stereogenic centres each with the conformations as shown in Table 6.3.3. C2 to C5 are the stereogenic centres of L1 and C11 to C14 those of L2 respectively. The dollar symbols represented in Table 6.3.3 indicate the rings and the carbon atoms in the unit cell that are generated by the inversion centre. Considering the stereochemistry, L1 is the *meso* form of CPTCA, and therefore not chiral as the ligand L1$ can be transformed back into L1 by an improper rotation. L2$ on the other hand is the enantiomer of L2. The unit cell therefore contains three different ligands, of which L2$ is generated by the inversion centre from the L2 in the asymmetric unit.

Table 6.3.3 – Absolute configurations for the carbon atoms of the CPTCA ligands in **Mo_{16}**. The dollar sign $ indicates the ligands generated by the inversion centre.

L1		**L1$**		**L2**		**L2$**	
C2	R	**C2$**	S	**C11**	R	**C11$**	S
C3	R	**C3$**	S	**C12**	S	**C12$**	R
C4	S	**C4$**	R	**C13**	S	**C13$**	R
C5	S	**C5$**	R	**C14**	S	**C14$**	R

The Mo_{16} rings lie in the plane orthogonal to the crystallographic [110] direction and form pairs, which are about 5.92 Å apart in stack direction and shifted by about 3.26 Å (Figure 6.3.5). The pairs stack approximately in [101] direction with slight deviation in ABAB fashion. The distance in stack direction between the top ring of the lower pair and the bottom ring of the upper pair is 7.43 Å. The pairs in general are shifted by 13.35 Å in stacking direction and 15.24 Å perpendicular to the stacking direction.

The negative charge of the two inner $HCPTCA^{3-}$ ligands is countered by potassium and tetramethylammonium ions, which lie disordered in the structure. The potassium ions were modelled with partial occupancies to sum up to five potassium ions, while two separate tetramethylammonium ions were modelled as fully and half-occupied. Charge balance is achieved with a half-occupied chloride ion in the structure. The potassium ions are arranged in typical chains, which are bridged by water molecules.

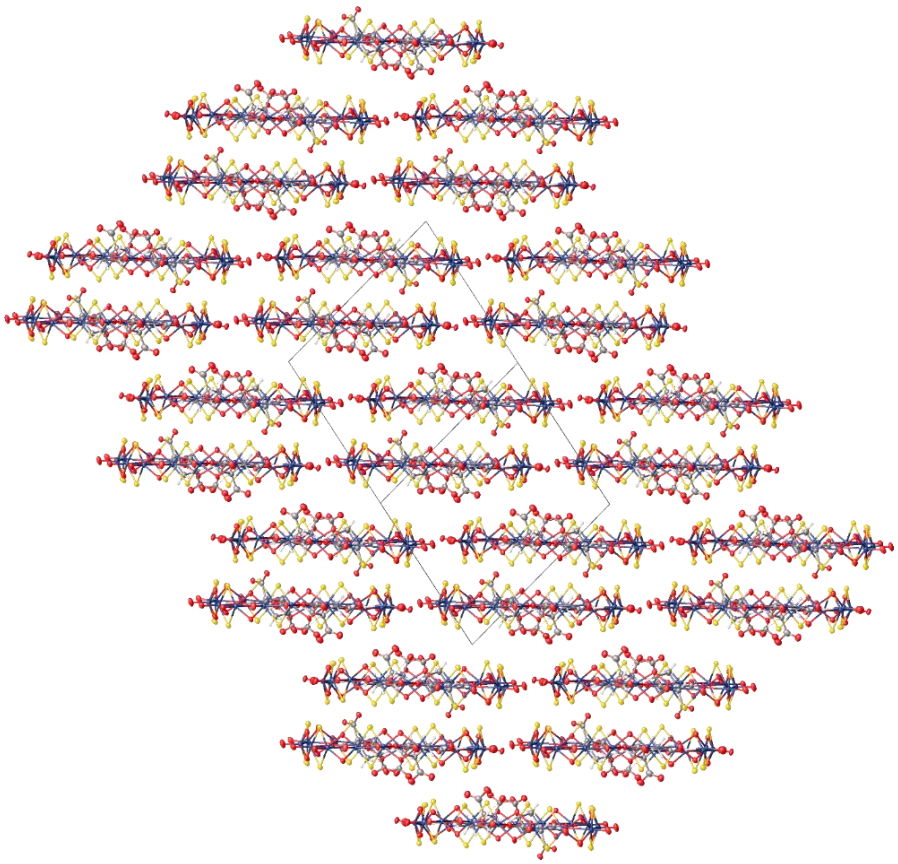

Figure 6.3.5 – Packing of the **Mo_{16}** rings. View along [110]

Table 6.3.4 – Crystallographic table for **Mo_{16}**.

Identification code	**Mo_{16}**
Empirical formula	$C_{24}H_{40}Cl_{0.5}K_5Mo_{16}N_{1.5}O_{72.5}S_{16}$
Formula weight/(g/mol)	3770.19
Temperature/K	100.01
Crystal system	triclinic
Space group	P-1
a/Å	17.5517(12)
b/Å	19.7171(14)
c/Å	20.2461(14)
α/°	115.0617(14)
β/°	91.5486(16)
γ/°	115.1630(15)
Volume/Å^3	5558.2(7)
Z	2
ρ_{calc} g/cm^3	2.253
μ/mm^{-1}	2.331
F(000)	3611
Crystal size/mm^3	0.16 × 0.05 × 0.04
Radiation	MoKα (λ = 0.71073)
2Θ range for data collection/°	2.51 to 55.276
Index ranges	-21 ≤ h ≤ 22 -25 ≤ k ≤ 25 -26 ≤ l ≤ 26
Reflections collected	117943
Independent reflections	24418 [R_{int} = 0.0537, R_{sigma} = 0.0533]
Data/restraints/parameters	24418/156/1338
Goodness-of-fit on F^2	1.038
Final R indexes [I>=2σ (I)]	R_1 = 0.0598, wR_2 = 0.1555
Final R indexes [all data]	R_1 = 0.0998, wR_2 = 0.1824
Largest diff. peak/hole / e Å^{-3}	3.35/-1.31

6.3.2 Characterisation

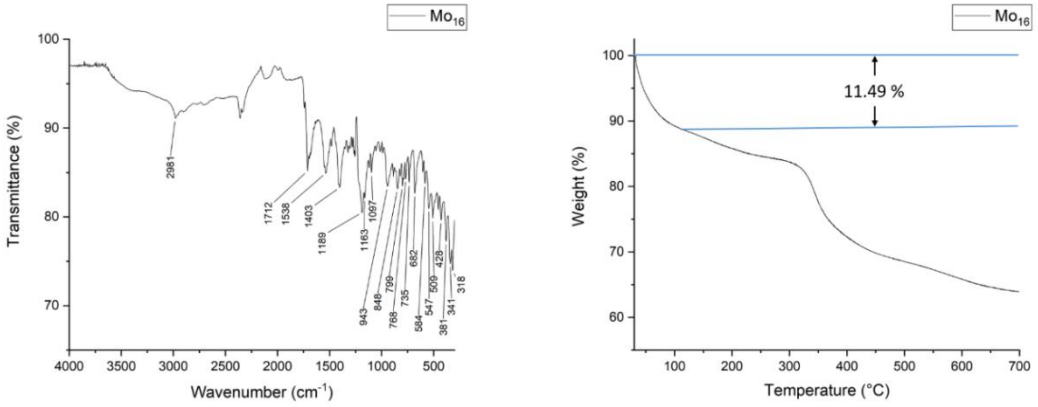

Figure 6.3.6 – IR spectrum and TGA curve of **Mo_{16}**.

Although quite messy due to the possible body vibrations from ligand and ring systems all important signals expected from the structure could be found in the IR. The signals for the asymmetric stretches of the free and bonded carboxylates can be found at 1712 cm^{-1} and 1538 cm^{-1} respectively. The corresponding symmetric stretch for the bonded carboxylate gives rise to the signal at 1403 cm^{-1}. The interpretation of the fingerprint region is made difficult by the complicated IR spectrum of the ligand. By comparisons with the literature however the signals at 943 cm^{-1} can be assigned to the Mo=O stretch, the signal at 454 cm^{-1} to the ν(Mo-S-Mo) stretch and the signal at 509 cm^{-1} to the ν(Mo-OH-Mo) vibrations. [259]

To determine the amount of solvent within the system a TGA curve was recorded from 30°C to 700°C under a nitrogen atmosphere. The TGA curve of **Mo_{16}** shows multiple, not clearly defined steps, which might be attributed to the overlap of the decomposition of the tetramethylammonium cations and the loss of water molecules. Step width was therefore determined by careful analysis of the curve derivative. The loss in weight between 30°C to 120°C corresponds to 23 water molecules (Theoretical value: 11.58 %.). Ligand decomposition can be seen from 300°C on with oxide formation starting at around 600°C.

6.4 $K_5(NMe_4)[Mo_{12}O_{12}S_{12}(OH)_{12}C_6(COO)_6] \cdot 39\ H_2O$ (Mo_{12}, 19)

The compound $K_5NMe_4[Mo_{12}O_{12}S_{12}(OH)_{12}C_6(COO)_6] \cdot x\ H_2O$ (**Mo_{12}**) was synthesized by adjusting the pH of an aqueous solution of mellitic acid with K_2CO_3 to pH = 7. After addition of an aqueous solution of $\{K_{0.40}(NMe_4)_{0.1}I_{0.5}[Mo_2O_2S_2(OH)_2(H_2O)] \cdot 6.3\ H_2O\}_n$ the pH was adjusted to pH = 4.5 and the resulting solution was stirred for an hour at room temperature, filtered and left to crystallise. The product was obtained as yellow crystals.

6.4.1 Crystallography

Mo_{12} was solved in the tetragonal space group $P4_2/ncm$ with following unit cell parameters:

$a = 26.1768(12)$ Å	$\alpha = 90°$	$Z = 4$
$b = 26.1768(12)$Å	$\beta = 90°$	$Z' = 0.25$
$c = 13.1951(6)$ Å	$\gamma = 90°$	$V = 9041.6(7)$ Å^3

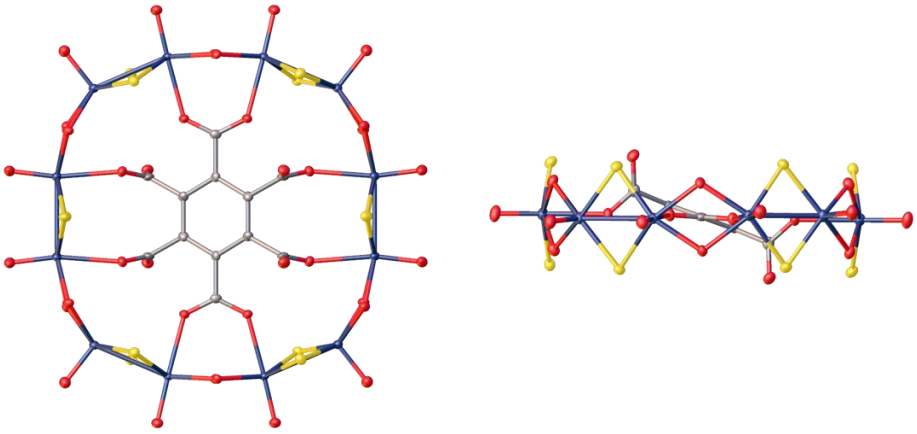

Figure 6.4.1 – Top and side view of the $\{Mo_{12}\}$ thiomolybdate cluster in **Mo_{12}**.

The central structure of **Mo_{12}** is a ring shaped thiomolybdate cluster, which is made up of six $[Mo_2O_2S_2(OH)_2]$ dimers, that arrange themselves around a fully deprotonated mellitate anion as shown in Figure 6.4.1. As in **Mo_{16}** the molybdenum ions build out either octahedral or square pyramidal coordination environments. Because of the more symmetrical shape and smaller ring size of $\{Mo_{12}\}$ compared to $\{Mo_{16}\}$ the coordination environments can be unambiguously assigned to either of them. CShM calculations can be found in Table 6.4.2. BVS calculations show that all molybdenum ions are in the oxidation state +V (Table 6.4.1).

Table 6.4.1 – BVS calculations for the molybdenum and hydroxy ions in **Mo_{12}**.

	BVS	**Ox.**		**BVS**	**Ass.**
Mo1	5.10	+5	**O4**	1.21	-OH
Mo2	4.89	+5	**O5**	1.12	-OH
Mo3	5.04	+5	**O6**	1.21	-OH

Table 6.4.2 – CShM-calculations for **Mo_{12}**.

	MoO_3S_2		**MoO_4S_2**
Atom name	Spherical Square Pyramid	Vacant Octahedron	Octahedron
Mo1	3.232	2.433	2.134
Mo2	2.554	2.918	-
Mo3	3.507	2.303	1.974

The coordination sphere of the octahedral molybdenum ions is completed by oxygen donors of the carboxylate ions. There are two distinct binding modes of the carboxylate ions observed in the structure. Two of the carboxylate ions in the cluster bind to two molybdenum ions in a *syn-syn* bidentate fashion. This binding mode seems to be preferred in thiomolybdate systems, since it is exclusively observed in the literature as well as in the {Mo_{16}} structure. Interestingly, the two bidentate carboxylate groups in {Mo_{12}} are not entirely in plane with the benzene ring, but slightly twisted by about 16°, which is slightly unfavourable as there is less p-orbital overlap with the aromatic system of the benzene ring. This flat angle together with the close proximity of the carboxylate groups in the ligand hinders two neighbouring groups to orient themselves in a similar fashion next to each other to minimise the lone pair – lone pair repulsion of the carboxylate groups. In the alkali metal salts of mellitic acid, the carboxylate ions are twisted by about 65° against the ring[260], which can be considered the energetic minimum of the free ligand. As the 16° twist in the {Mo_{12}} structure is far away from this minimum the neighbouring carboxylate groups build out a 90° degree angle to the benzene ring and bind with one oxygen donor to the molybdenum ion while the other oxygen atom is pointing above or below the ring (Figure 6.4.1, right). The oxygen donors, which are bound to molybdenum ions are lying all in the plane of the ring, which, together with the binding modes of the carboxylate ions results in the twisting of the benzene ring against the plane of the thiomolybdate ring.

The packing of the thiomolybdate clusters in the crystal structure can be seen in Figure 6.4.2 and Figure 6.4.4. The rings are lying at the corners and faces of the tetragonal unit cell in different orientations. All corners are occupied by thiomolybdates of the same orientation, whereas the faces are split in three sets of opposite faces, which are each occupied by thiomolybdates in different orientations. As can be seen in Figure 6.4.2, the thiomolybdates arrange themselves loosely in layers across the crystallographic *ab* plane. The plane to plane angles between the different orientations depends on, if two clusters are being compared within the same layer or in between layers. Within the same layers the rings are twisted 33.17° against each other while they are twisted 23.29° against each other in between layers.

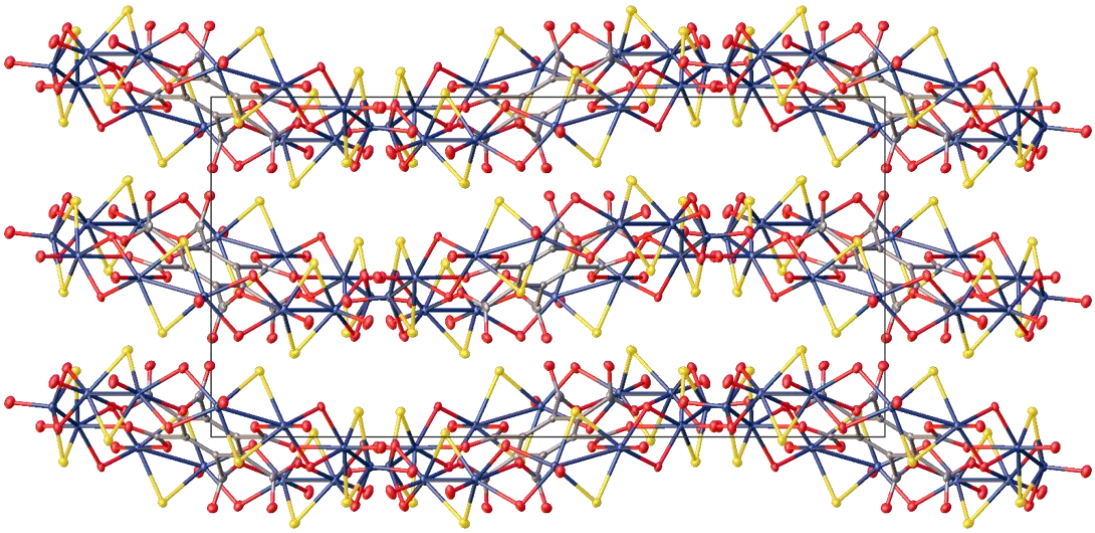

Figure 6.4.2 – Packing of the thiomolybdate rings in Mo_{12}. View in [100] direction.

The six times negative charge of the mellitate anion is balanced by five potassium ions and one tetramethylammonium ion in the crystal structure. The tetramethylammonium ions is well resolved while the potassium ions are heavily disordered, building out potassium water chains throughout the crystal structure (Figure 6.4.4).

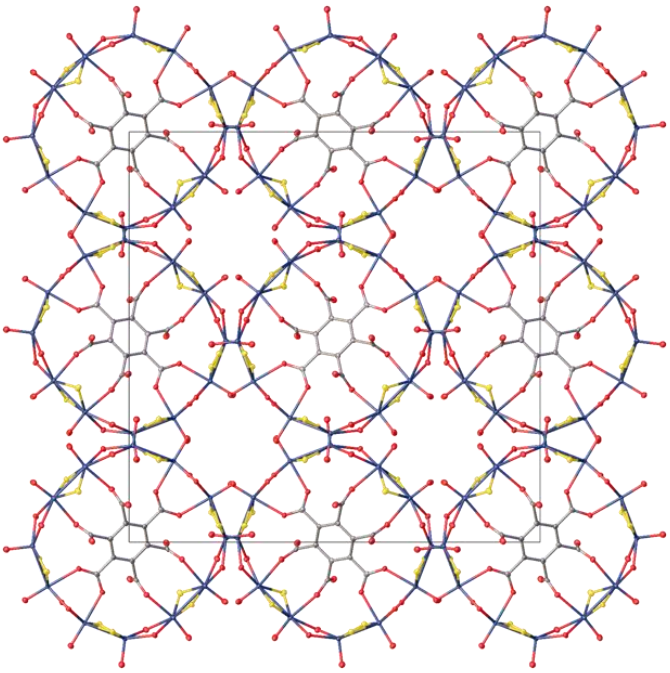

Figure 6.4.3 – Packing of the thiomolybdate clusters. View in [001] direction.

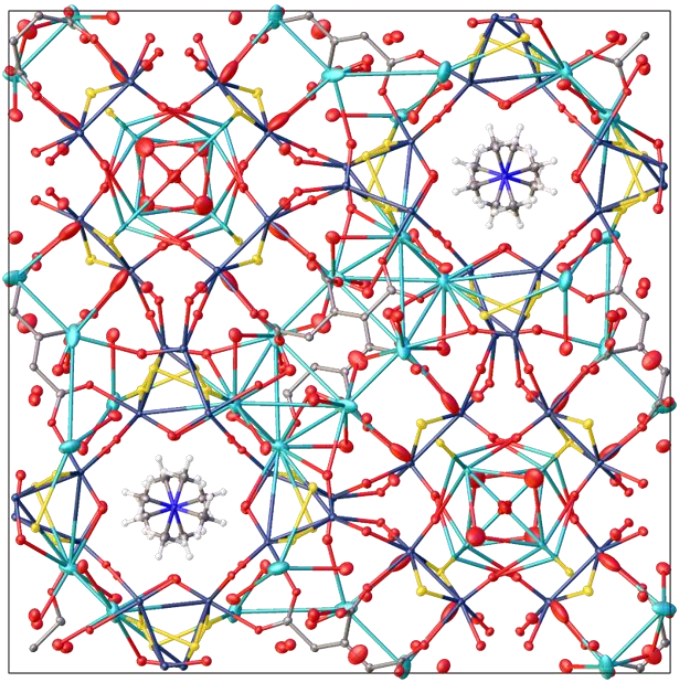

Figure 6.4.4 – Packing of the thiomolybdate cluster with and without counter ions and solvent molecules. View in [001] direction.

Table 6.4.3 – Crystallographic table for **Mo_{12}**.

Identification code	**Mo_{12}**
Empirical formula	$C_{16}H_{12}K_7Mo_{12}NO_{64.5}S_{12}$
Formula weight/(g/mol)	3059.97
Temperature/K	100
Crystal system	tetragonal
Space group	$P4_2/ncm$
a/Å	26.1768(12)
b/Å	26.1768(12)
c/Å	13.1951(6)
α/°	90
β/°	90
γ/°	90
Volume/Å^3	9041.6(9)
Z	4
ρ_{calc} g/cm^3	2.248
μ/mm^{-1}	2.302
F(000)	5840
Crystal size/mm^3	0.06 × 0.06 × 0.04
Radiation	MoKα (λ = 0.71073)
2Θ range for data collection/°	3.112 to 55
Index ranges	$-33 \leq h \leq 34$, $-33 \leq k \leq 34$, $-17 \leq l \leq 17$
Reflections collected	253944
Independent reflections	5352 [R_{int} = 0.1743, R_{sigma} = 0.0384]
Data/restraints/parameters	5352/25/291
Goodness-of-fit on F^2	0.938
Final R indexes [I>=2σ (I)]	R_1 = 0.0419, wR_2 = 0.1015
Final R indexes [all data]	R_1 = 0.0678, wR_2 = 0.1167
Largest diff. peak/hole / e Å^{-3}	1.46/-1.49

6.4.2 Characterisation

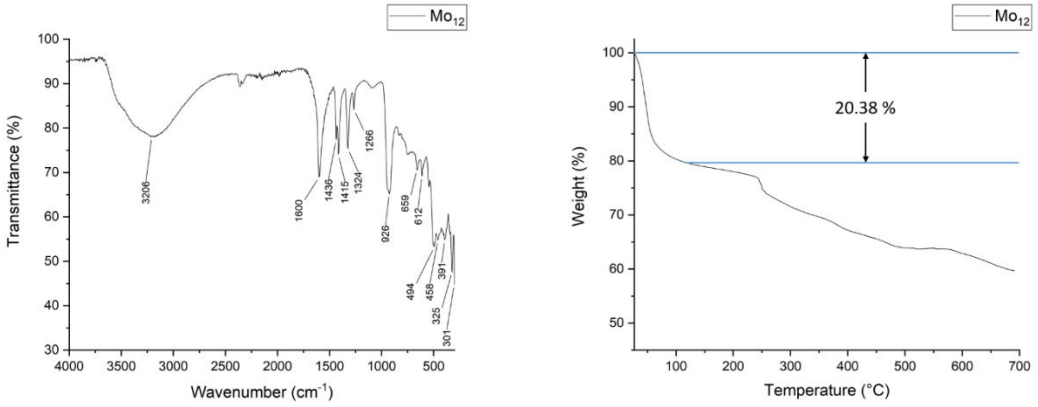

Figure 6.4.5 – IR spectrum and TGA curve of **Mo$_{12}$**.

The IR spectrum for **Mo$_{12}$** fits well with literature known compounds.[117] It shows a broad signals at 3206 cm^{-1}, which can be attributed to crystal water. The signals for the asymmetric and symmetric stretches of the free and bonded carboxylates can be found at 1600 cm^{-1} and 1436 cm^{-1} / 1415 cm^{-1} respectively. The strong signal at 926 cm^{-1} can be assigned to the Mo=O stretch. The ν(Mo-S-Mo) stretch can be assigned to the band at 458 cm^{-1} and the ν(Mo-OH-Mo) stretch to the signal at 494 cm^{-1}.

To determine the amount of solvent present in the crystals a TGA curve from 30°C to 700°C was recorded under a nitrogen atmosphere. It shows a sharp drop in weight between 30°C to 120°C of 20.38 %, which corresponds to the loss of 36 water molecules. (Theoretical value: 20.36 %). Ligand decomposition can be seen from 240°C onwards and oxide formation from around 570°C.

6.5 $K_{21}[Mo_{30}O_{104}(OH)_3S_6(C_6(COO)_6)_2K_3(H_2O)_3]\cdot x\ H_2O$ (**Mo_{30}**, 20)

The compound $K_{21}[Mo_{30}O_{104}(OH)_3S_6(C_6(COO)_6)_2K_3(H_2O)_3]\cdot x\ H_2O$ (**Mo_{30}**) was synthesized by adjusting the pH of an aqueous solution of mellitic acid with K_2CO_3 to pH = 8.5. After addition of an aqueous solution of $\{K_{0.40}(NMe_4)_{0.1}I_{0.5}[Mo_2O_2S_2(OH)_2(H_2O)] \cdot 6.3\ H_2O\}_n$ and sodium molybdate the pH was adjusted to pH = 4.5 *via* acetic acid and the resulting solution was stirred for an hour at room temperature, filtered and left to crystallise. The product was obtained as deep blue crystals.

6.5.1 Crystallography

Mo_{30} was solved in the triclinic space group $P\bar{1}$ with following unit cell parameters:

$a = 17.1415(8)$ Å	$\alpha = 97.921(2)°$	$Z = 2$
$b = 18.4475(8)$ Å	$\beta = 91.199(2)°$	$Z' = 1$
$c = 28.5348(13)$ Å	$\gamma = 114.619(2)°$	$V = 8093.9(7)$ Å^3

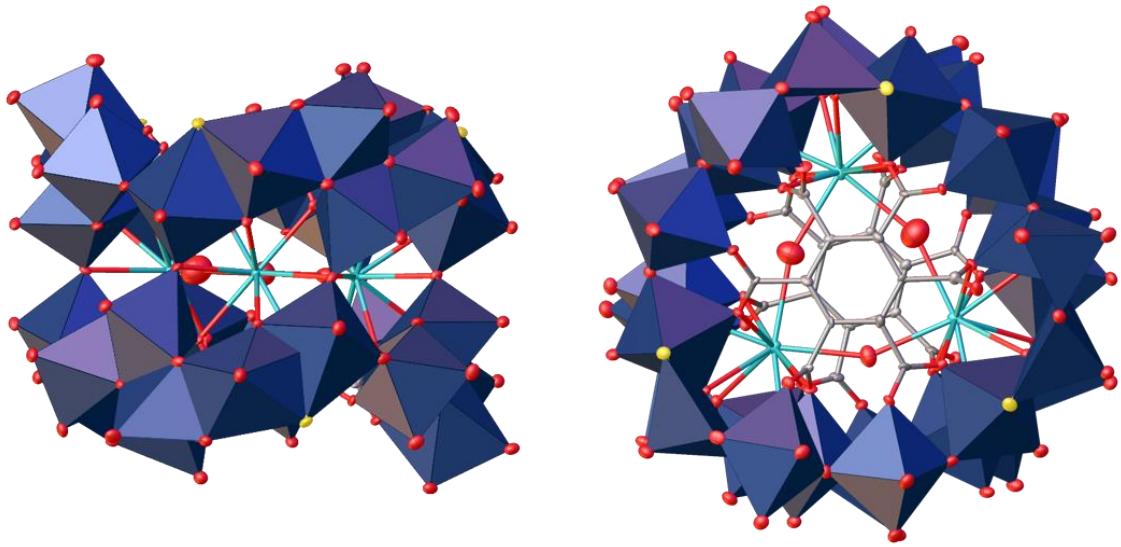

Figure 6.5.1 – Side view of $\{Mo_{30}\}$ with polyhedral representation for the molybdenum ions.

The structure can be understood as a fused double decker compound made from two $\{Mo_{15}\}$ polyoxothiomolybdate rings, each with a mellitate anion in the middle of the ring. The two rings are connected to each other at six points *via* corner sharing MoO_6 octahedra, as well as three

hydrogen bonds between *oxo*- and *hydroxo* groups. In the centre of the structure is a triangle of potassium ions which are bridged by water molecules.

The $\{Mo_{15}\}$ rings, which can be seen in Figure 6.5.4, consist of three repeating $\{Mo_5\}$ units, that are arranged around a fully deprotonated mellitate anion. The $\{Mo_5\}$ unit can be seen in Figure 6.5.2. It consists of three edge sharing $\{MoO_6\}$ octahedra, a $\{MoO_4S\}$ square pyramid and a $\{MoO_5S\}$ octahedron. The $\{Mo_5\}$ units themselves are connected to each other *via* corner sharing octahedral in the ring. The molybdenum ions Mo1 and Mo2, which are bonded to the S^{2-} ion are in the oxidation state +V while the molybdenum ions Mo3-Mo5 are in the oxidation state +VI. Table 6.5.1 and Table 6.5.2 are showing the BVS calculations for the molybdenum ions as well as μ_2- and μ_3-oxygen donors in all six $\{Mo_5\}$ units within the $\{Mo_{30}\}$ structure. Atoms in the same row hereby correspond to the same atoms according to the general scheme in Figure 6.5.2.

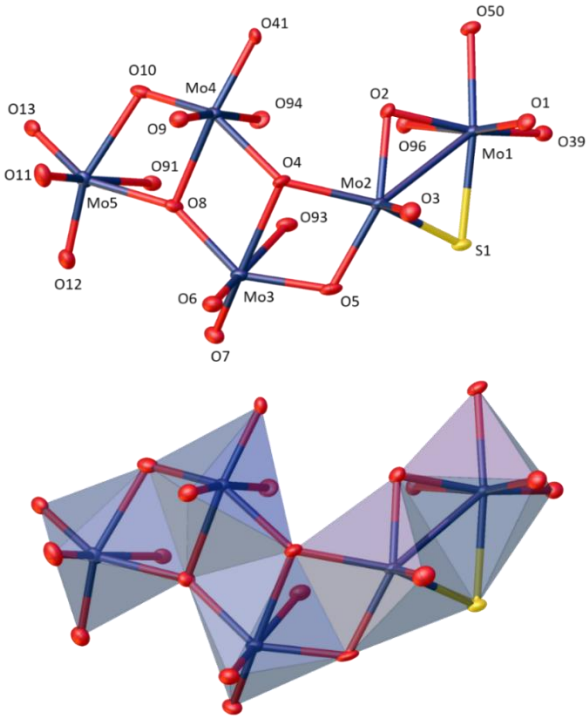

Figure 6.5.2 – The $\{Mo_5\}$ unit in **Mo_{30}**.

The Mo^{VI} octahedra are bound to two terminal *oxo*-groups for which the Mo=O double bond lengths range from 1.672(6) Å to 1.738(6) Å with an average of 1.71 Å. They are connected *via*

μ_2- and μ_3-*oxo* groups to each other. The Mo^{VI}-O single bonds hereby range from 1.756(6) Å to 2.289(6) Å with an average of 1.99 Å. In the case of three of the six {Mo_5} repeating units, the *oxo* group corresponding to O10 in

Figure **6.5.2** is a hydroxo group (O36, O66, O81), which likely builds out hydrogen bonds to the *oxo*-groups (O10, O23, O51) in the same respective position of the other three {Mo_5} units. The hydrogen atoms could not be resolved from the Fourier map and were only identified by BVS calculations. Figure 6.5.3 shows their position within the structure, as illustrated by the dotted blue lines. The distances between the donor and acceptor atoms are around 2.7 Å, indicating strong hydrogen bonding. The two Mo^{V} ions are connected to the other Mo^{VI} ions *via oxo*-groups and to each other *via* one *oxo*-group and one sulfide bridge. The bond angle for the Mo-S-Mo bonds averages to 70.46 Å, which results in shortened Mo-Mo distances of about 2.68 Å, indicating the presence of a Mo-Mo single bond. The octahedral molybdenum ions have their coordination sphere filled by the oxygen donor of the carboxylate groups of the mellitate ligand, which can be seen in Figure 6.5.4.

Table 6.5.1 - BVS calculations for the {Mo_5} units in **Mo_{30}**.

	BVS	**Ass**		**BVS**	**Ass**		**BVS**	**Ass**
Mo1	5.24	+5	**Mo6**	5.20	+5	**Mo11**	5.16	+5
Mo2	5.11	+5	**Mo7**	5.11	+5	**Mo12**	4.97	+5
Mo3	6.00	+6	**Mo8**	5.80	+6	**Mo13**	6.06	+6
Mo4	5.97	+6	**Mo9**	6.04	+6	**Mo14**	5.93	+6
Mo5	6.02	+6	**Mo10**	6.01	+6	**Mo15**	6.10	+6
O39	1.17	-O-	**O13**	1.98	-O-	**O26**	1.98	-O-
O50	1.98	-O-	**O80**	1.95	-O-	**O64**	1.99	-O-
O2	1.86	-O-	**O15**	1.90	-O-	**O28**	1.85	-O-
O4	1.77	-O-	**O18**	1.80	-O-	**O31**	1.78	-O-
O5	1.82	-O-	**O17**	1.78	-O-	**O30**	1.86	-O-
O8	1.86	-O-	**O21**	1.93	-O-	**O34**	1.95	-O-
O10	1.61	-O-	**O23**	1.69	-O-	**O36**	1.17	-OH-
O41	1.94	-O-	**O70**	1.99	-O-	**O56**	1.93	-O-
O13	1.98	-O-	**O26**	1.98	-O-	**O39**	1.98	-O-

Table 6.5.2 – BVS calculations for **Mo_{30}**.

	BVS	Ass		BVS	Ass		BVS	Ass
Mo16	5.18	+5	**Mo21**	5.11	+5	**Mo26**	5.31	+5
Mo17	5.01	+5	**Mo22**	5.08	+5	**Mo27**	5.04	+5
Mo18	6.07	+6	**Mo23**	6.04	+6	**Mo28**	5.97	+6
Mo19	6.02	+6	**Mo24**	6.04	+6	**Mo29**	5.92	+6
Mo20	6.06	+6	**Mo25**	5.91	+6	**Mo30**	5.97	+6
O84	1.96	-O-	**O54**	2.03	-O-	**O69**	1.95	-O-
O41	1.94	-O-	**O56**	1.93	-O-	**O70**	1.99	-O-
O42	1.90	-O-	**O57**	1.86	-O-	**O72**	1.90	-O-
O45	1.78	-O-	**O62**	1.90	-O-	**O75**	1.84	-O-
O44	1.75	-O-	**O59**	1.78	-O-	**O74**	1.82	-O-
O48	1.94	-O-	**O65**	1.92	-O-	**O78**	1.92	-O-
O51	1.67	-O-	**O66**	1.20	-OH-	**O81**	1.22	-OH-
O50	1.98	-O-	**O64**	1.99	-O-	**O80**	1.95	-O-
O54	2.03	-O-	**O69**	1.95	-O-	**O84**	1.96	-O-

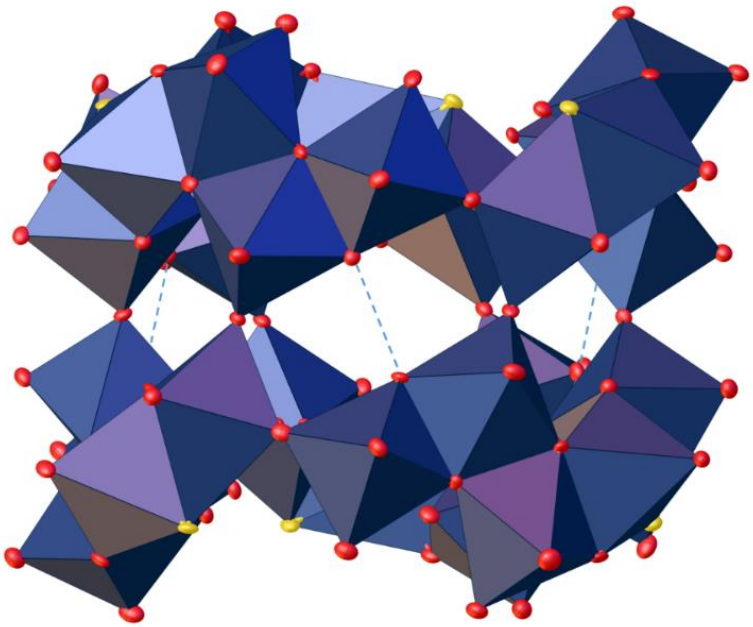

Figure 6.5.3 – H-Bonds between the {Mo_{15}} rings indicated by dotted lines. Potassium ions omitted for clarity.

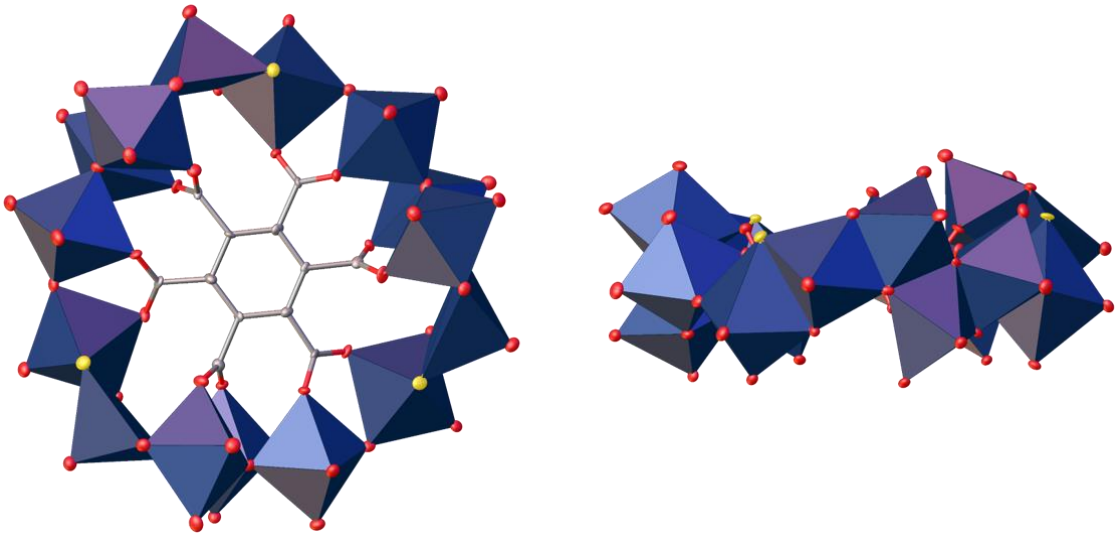

Figure 6.5.4 – {Mo_{15}} rings with polyhedral representation.

The angles of the carboxylate group are twisted against the central benzene ring between 37.1° and 75.4° as can be seen in Figure 6.5.5. The carboxylates hereby twist themselves to accommodate the positions of the MoO_6 octahedra as can be seen in Figure 6.5.4. This results in alternating twist angles of the carboxylate groups of about 37° and 70°.

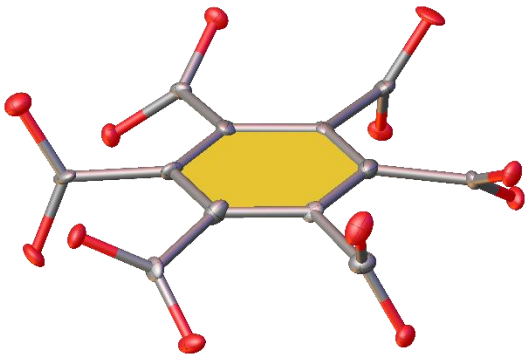

Figure 6.5.5 – Mellitate anion in one of the Mo_{15} rings.

This situation, how it presents itself in {Mo_{30}}, is almost the opposite as we saw in {Mo_{12}}. While the benzene ring of the mellitate anion in {Mo_{12}} was twisting itself to accommodate the flat {Mo_{12}} ring, the mellitate ion is now lying rather flat in the {Mo_{30}} structure with the molybdenum ring twisting itself around the benzene ring.

The packing of the {Mo_{30}} clusters can be seen in Figure 6.5.6 and Figure 6.5.7. The clusters arrange themselves in layers within the crystallographic *ab* plane. The clusters exhibit a distance of 17.14 Å and 18.42 Å from their nearest neighbour in the plane. The layers are about 14.7 Å apart and the clusters are shifted by about 5.7 Å within them. The overall 21- charge is balanced by 21 potassium ions that lie disordered in the structure and build out the classical potassium water network that is typical for polyoxometalates.

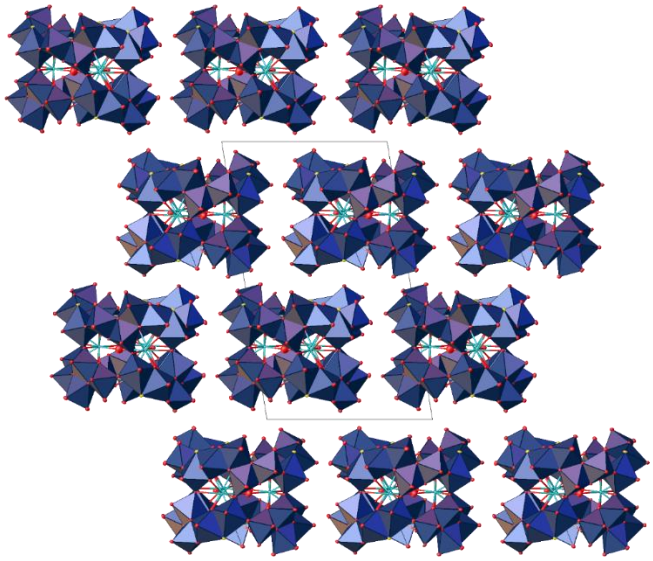

Figure 6.5.6 – Packing diagram of {Mo_{39}} in **Mo_{30}** in [100] direction.

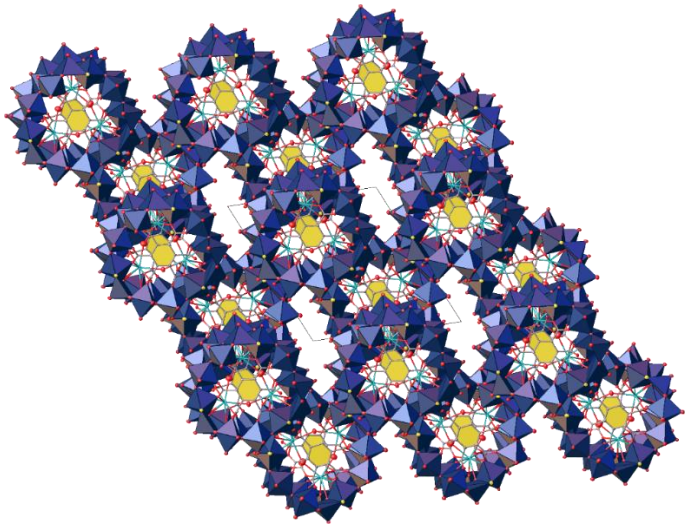

Figure 6.5.7 – Packing diagram of {Mo_{30}} in **Mo_{30}** in [001] direction.

Table 6.5.3 – Crystallographic table for **Mo_{30}**.

Identification code	**Mo_{30}**
Empirical formula	$C_{24}K_{21}Mo_{30}O_{150.03}S_6$
Formula weight/(g/mol)	6580.38
Temperature/K	99.98
Crystal system	triclinic
Space group	P-1
a/Å	17.1415(8)
b/Å	18.4475(8)
c/Å	28.5348(13)
α/°	97.921(2)
β/°	91.199(2)
γ/°	114.619(2)
Volume/Å^3	8093.9(6)
Z	2
ρ_{calc} g/cm^3	2.7
μ/mm^{-1}	25.031
F(000)	6198
Crystal size/mm^3	0.1 × 0.04 × 0.04
Radiation	CuKα (λ = 1.54178)
2Θ range for data collection/°	3.138 to 136.922
Index ranges	-20 ≤ h ≤ 20 -22 ≤ k ≤ 22 -33 ≤ l ≤ 34
Reflections collected	89090
Independent reflections	29525 [R_{int} = 0.1088, R_{sigma} = 0.0817]
Data/restraints/parameters	29525/1518/2225
Goodness-of-fit on F^2	1.022
Final R indexes [I>=2σ (I)]	R_1 = 0.0544, wR_2 = 0.1479
Final R indexes [all data]	R_1 = 0.0636, wR_2 = 0.1550
Largest diff. peak/hole / e Å^{-3}	3.49/-1.86

6.5.2 Characterisation

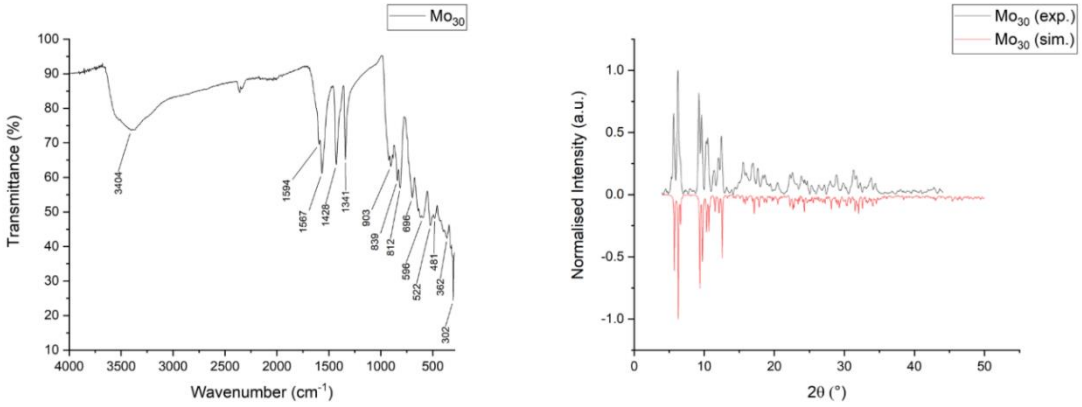

Figure 6.5.8 – IR spectrum and PXRD pattern of **Mo$_{30}$**.

The IR spectrum of **Mo$_{30}$** is predictably similar to the IR spectrum of **Mo$_{12}$** and shows broadly the same features such as the broad peak at 3404 cm^{-1}, which can be assigned to crystal water, as well as the signals for the asymmetric and symmetric stretches of the free and bonded carboxylates, which can be found at 1594/1567 cm^{-1} and 1428 cm^{-1} respectively. The signal at 903 cm^{-1} can be assigned to the Mo=O stretch.

Surprisingly, as the only compound of the four oxothiomolybdate structures **Mo$_{30}$** crystallised phase-pure as can be seen from the PXRD pattern on the right side of Figure 6.5.8. Batches of **Mo$_2$**, **Mo$_{12}$** and **Mo$_{16}$** regularly featured multiple polymorphs, which crystallised in different space groups as well as lattice systems due to the possible combination of counter ions, solvent molecules and possible packing arrangements.

6.6 Conclusion

In this chapter the synthesis and characterisation of four novel oxothiomolybdate compounds, which featured the $\{Mo_2O_2S_2\}$ building block is reported. The use of highly functionalised ligands with four and six carboxylic acids led to the formation of one oxothiomolybdate dimer and three ring systems with differing nuclearites.

The use of the H_4THFTCA ligand in the synthesis of oxothiomolybdate rings resulted in the formation of the simple $\{Mo_2O_2S_2(H_1THFTCA)_2\}$ dimer **Mo$_2$**. The dimer has four partially protonated carboxylate groups, which makes it a candidate to act as a precursor for the synthesis of mixed-metal systems. Unfortunately, however, the long time it takes the compound to form diminishes its usefulness for this purpose.

To prevent dimer formation, the oxygen donor of the tetrahydrofuran ring was replaced by a CH_2 group by using the ligand H_4THFTCA in the same reaction. This thwarted the formation of the molybdenum dimer and resulted in a **Mo$_{16}$** ring, which was templated by two THFTCA ligands in the centre of the structure. The preference of the $\{Mo_2O_2S_2\}$ building block to form ring structures outweighed any new structural motifs the CPTCA ligand could have accommodated. Additional functional groups which could have bonded to more $\{Mo_2O_2S_2\}$ groups are left dangling in the structure. As it is the case with **Mo$_{12}$**, the possible use of **Mo$_{16}$** as a precursor complex is prevented by long crystallisation times.

To test the limits of the planar ring structure formation mellitic was used to force the coordination of more than four carboxylate groups. As in **Mo$_{16}$** the compound consists of an oxothiomolybdate ring of neutral charge that is templated by one mellitate anion. The sterical challenge, posed by mellitate, was solved in the structure by tilting the mellitate anion in respect to the oxothiomolybdate ring plane. The planar ring structure was again favoured over possible new structural motifs. Only the addition of a Mo^{VI} source to the synthesis resulted in the loss of planarity, as seen in **Mo$_{30}$**. The unusual mixed-valent $\{Mo_{30}\}$ oxothiomolybdate double decker ring compound made from $\{MoO_6\}$, $\{MoO_5S\}$ and $\{MoO_5S\}$ polyhedra is templated by two fully deprotonated mellitate anions. The sterical challenge posed by the mellitate anion has been solved in **Mo$_{30}$** in the opposite way than in **Mo$_{12}$**. While the mellitate ion in **Mo$_{12}$** was tilted to accommodate the planar oxothiomolybdate ring structure, the mellitate ions in **Mo$_{30}$** now appears planar with two $\{Mo_{15}\}$ rings twisting around their carboxylate groups. $\{Mo_{30}\}$ structure features

dimers of molybdenum ions which are bridged by both a sulfide and an *oxo* group. As this motif has likely been formed by the substitution of a sulfide ion for an *oxo* group from the $\{Mo_2O_2S_2\}$ precursor, it poses the interesting question if this substitution happened before or after complexation of the molybdenum dimer by a carboxylate group. Investigation into this system could lead to insight into the slow oxidation under aerobic conditions of the thiomolybdate rings.

1. E. Cadot, M. N. Sokolov, V. P. Fedin, C. Simonnet-Jegat, S. Floquet and F. Secheresse, *Chem. Soc. Rev.*, 2012, **41**, 7335-7353.
2. E. Cadot, V. Béreau, B. Marg, S. Halut and F. Sécheresse, *Inorg. Chem.*, 1996, **35**, 3099-3106.
3. D. C. M. Llunell, J. Cirera, P. Alemany, S. Alvarez, SHAPE, Version 2.1, Universitat de Barcelona, 2013.
4. G. B. Deacon and R. J. Phillips, *Coord. Chem. Rev.*, 1980, **33**, 227-250.
5. J. Ellermeier, PhD Thesis, Christian-Albrechts-Universität, 2002.
6. J. A. Harnisch, L. M. Thomas, I. A. Guzei and R. J. Angelici, *Inorganica Chim. Acta*, 1999, **286**, 207-214.
7. A. Dolbecq, E. Cadot and F. Sécheresse, *Comptes Rendus Acad. Sci. II C*, 2000, **3**, 193-197.

Chapter 7

Experimental

Materials and equipment

Reagents: All chemicals were purchased from commercial sources and were used without further purification. Water was deionised and distilled before use.

Single Crystal X-Ray Diffraction Analysis:

Single crystal x-ray analysis and refinement were performed by the author using a Bruker APEX2 Duo diffractometer. X-ray intensity data were measured at 100K using an Oxford Cryosystem Cobra low temperature device using a MiTeGen micromount. Frames were integrated with the Bruker SAINT software package[261] and the data corrected for absorption effects using the multi-scan method (SADABS)[235]. Structures were solved by direct methods using XT[262] and refined with the programs Olex2[263] and XL[264] least squares refinement. All non-hydrogen atoms were refined anisotropically unless otherwise mentioned. If highly disordered cations or solvent molecules could not be resolved the Paton-SQUEEZE[244] routine was employed to account for not resolved electron density.

General refinement details of crystal structures

All non-hydrogen atoms were refined anisotropically unless otherwise mentioned. All hydrogen atoms in C-H bonds were place in idealized positions as riding with $U_{iso}(H) = 1.2\ U_{eq}(C)$. Hydrogen atoms in water molecules and carboxylic acid groups were included as a rotating group riding on the oxygen with $U_{iso}(H) = 1.2\ U_{eq}(C)$. Hydrogen atoms in water molecules were place in idealised position to generate a sensible hydrogen bonded network, if possible. If no meaningful network could be found, they were not modelled. Ammonium ions were modelled as a rigid group.

Special refinement details for the structures can be found on the attached CD, which includes the cif, res, hkl, ins and fcf files, the crystallographic tables as well as the checkcif report for all structures. The following restraints and constraints were used in the refinement of the crystal structures and shall be explained briefly.[265]

DANG	The distance between two atoms is restraint at a distance d with an estimated standard deviation of s. This command is used for 1,3 distances where the standard deviation is usual twice the standard deviation as in the DFIX command.
DELU	The components of the anisotropic displacement parameters of bonded atoms are restrained to be equal within the direction of the bond within an effective standard variation s1.

DFIX	The distance between two atoms is restraint at a distance d with an estimated standard deviation of s.
EADP	The anisotropic displacement parameters of all named atoms are restrained to be the same.
EXYZ	The x, y and z parameters of all named atoms are restrained to be the same
FLAT	The named atoms are restrained to lie in a common plane
ISOR	The U_{ij} components of the named atoms are restrained to approximate isotropic behaviour within an effective standard deviation s.
RIGU	This command applies a rigid bond restrained with effective standard deviations for 1,2 and 1,3-distances.
SADI	The distances between two or more sets of atoms are restrained to be equal within an effective standard deviation of s.
SIMU	The U_{ij} components for two atoms closer than a distance d_{max} are restrained to be equal within a standard deviation.
SUMP	The free variables of the named atoms sum up to a given value c within standard deviation.

Powder x-ray diffraction analysis:

Samples for PXRD measurement were ground up in the mother liquor and sealed in a glass capillary. The capillaries were mounted using a goniometer head on a Bruker APEX2 Duo diffractometer. Data was collected at 2θ values of 10° and 20° by a 360° φ-rotation with 10 minutes per frame at 25 °C. The data was integrated and processed using the Bruker APEX II routine XRD2-Eval subprogram.

Mass spectrometry

ESI-MS spectra of the inorganic compounds were recorded by Dr. Jennifer Mathieson at the University of Glasgow on a Waters Synapt G2 HDMS using water as a solvent. ESI-MS spectra of organic compounds were measured by Dr. Gary Hessman using a Micromass time of flight spectrometer. All mass spectra were analysed using the mMass software.

UV-VIS spectroscopy

UV-VIS spectra were recorded on a Perkin Elmer Lambda 35 spectrometer using a quartz cuvette with a path length of 10mm at room temperature. All spectra were analysed using the UVWinlab software.

IR-spectroscopy

Infrared spectroscopy experiments were performed from 4000 cm^{-1} to 500 cm^{-1} on a Perkin Elmer Spectrum One FT-IR spectrometer with an Attenuated Total Reflectance sampling attachment. Following abbreviations are used in the experimental: vs, very strong: s, strong; m, medium; w, weak; vw, very weak; sh; shoulder, br; broad, and vbr; very broad.

CHN analysis

Elemental Analysis was undertaken by the Microanalysis Lab of the School of Chemistry and Chemical Biology in the University College Dublin with an Exeter Analytical CE 440 instrument.

TGA

TGA measurements were performed using a Perkin Elmer Pyriss 1 TGA instrument. 1-5 mg of sample were heated in ceramic crucible under a nitrogen atmosphere from 30 °C to 700 °C at a heating rate of 5 °C/min.

Magnetic measurements

Magnetic Measurements were performed by Dr. Kane Esien at the University of Belfast using a Quantum Design MPMS XL SQUID, utilizing the reciprocal sample option (RSO).

NMR spectroscopy

NMR experiments were performed by Dr. John O'Brien using a Bruker Avance III 400 or a Bruker Avance II 600 NMR. DOSY-NMR experiments were performed by Dr. Manuel Rüther on a Bruker Avance HD 400 NMR.

Theoretical calculations

Theoretical calculations were carried out by Swetanshu Tandon. The $\{V_5O_9\}^{5-}$ unit was modelled in a non-periodic environment using density function theory. The calculations were carried out with the cluster code gaussian09[266] using PBE0[267, 268] functional in conjunction with SDDALL[269] basis set with and effective core potential for V, 6-31G(2d)[270] basis set for phosphorus, the 6-31G(d)[271] basis set for O, C and N and 6-31G(p)[271] basis set for H. The default convergence criteria and a larger integration grid containing 225 radial shells with each shell containing 974 angular points were used. For each system, only the ferromagnetic configuration was modelled. Frequency calculations were carried out to determine the free energy of the different systems. For the $\{V_5O_9\}^{5-}$ unit, one of the oxo-groups on the V(IV) centres was flipped (pointing inwards towards the cavity) to determine the relative stability of the $\{V_5O_9\}^{5-}$ unit in the two different configurations. It was observed that the $\{V_5O_9\}^{5-}$ unit with all the oxo-groups pointing in the

same direction is more stable by ~27 kJ/mol. Additionally, this unit was further modelled with a water molecule in the cavity and it was found to stabilise the system by ~49 kJ/mol although it moved away from the V centres. The water molecule was later restrained to be ~3.1 Å away from V(V) centre in which case it was found to stabilise the system by ~36 kJ/mol.

7.1 Synthetic procedures

All reactions under nitrogen were carried out using standard Schlenk techniques. Solvents were degassed before use by bubbling nitrogen through the solvent.

7.1.1 Organic compounds

Synthesis of DPB-OEt (Tetraethyl-1,3-benzenedisphosphonate)[246]

10 g of 1,3-dibromobenzene (42.4 mmol, 1 eq) was dissolved in 20 mL 1,3-diisopropylbenzene under a nitrogen atmosphere and stirred at 180 °C for 30 minutes. The temperature of the solution was lowered to 120 °C and 1.17 g $NiBr_2$ (5.4 mmol, 0.13 eq) were added to the mixture after which the solution was heated up again to 180 °C for 20 minutes. 25 mL triethyl phosphite (24.2 g, 133.0 mmol, 3.14 eq) in 20 mL of 1,3-dibromobenzene were slowly dropped in the solution over the next 5 hours. A steady stream of nitrogen gas over the solution was maintained during the reaction to remove ethyl bromide from the atmosphere. The reaction was stirred at 180 °C for 24 hours before cooled to room temperature before triethyl phosphite, solvent and other by-products were distilled of under a high vacuum. The residue was purified by column chromatography with an eluent of DCM:MeOH (20:1). The product was obtained as a slightly yellow oil. Yield: 10.8 g (30.8 mmol, 72.7 %) ^{1}H-NMR ($CDCl_3$, 400 MHz) σ_H (ppm): 8.26 (1H, t, ^{3}J = 13.19 Hz), 7.99 – 8,05 (2H, m), 7.57 – 7.63 (1H, m), 4.10 – 4.23 (8H, m), 1.36 (12H, t, ^{3}J = 7.69 Hz), ^{31}P-NMR ($CDCl_3$, 162 MHz) σ_P (ppm): 16.92 (s).

Synthesis of DPB-H (benzene-1,3-diphosphonic acid)

10.8 g (30.8 mmol, 1 eq) of tetraethyl-1,3-benzenedisphosphonate were dissolved in 50 mL half-concentrated hydrochloric acid and refluxed overnight. The solution was filtered, and the solvent removed under vacuum. The product was obtained as a white powder (6.94 g, 94.6 %). ^{1}H-NMR (D_2O+NaOD, 400 MHz) σ_H (ppm): 8.00 (1H, t, ^{3}J = 13.24 Hz), 7.81-7.87 (2H, m), 7.52 – 7.57 (1H, m). ^{13}C-NMR (D_2O+NaOD, 100 MHz) σ_c (ppm): 126.92 (t, ^{3}J = 24.71 Hz), 130.4 (m), 131.11 (t, ^{2}J = 9.51 Hz), 139.53 (dd, ^{1}J = 166.34 Hz, ^{3}J = 10.76 Hz). ^{31}P-NMR (D_2O+NaOD, 162 MHz) σ_P (ppm): 14.53 (s) FT-IR (ATR) $\tilde{\nu}$ (cm^{-1}): 1593 (w), 1402 (m), 1197 (w), 1152 (w), 1087

(m), 982 (s), 939(s), 845(m), 808 (m), 799 (m), 727(m), 693 (s), 675(s), 569 (m), 526(m). ESI-MS: $[M-H]^-$: calculated m/z: 293.0349, observed m/z: 293.0352.

Synthesis of DPB-^{t}B-OEt (5-tert-butyl-tetraethyl-1,3-benzenediphosphonate)[246]

10 g of 5-*tert*-Butyl-1,3-dibromobenzene (34.2 mmol, 1 eq) was dissolved in 10 mL of 1,3-diisopropylbenzene under nitrogen. This mixture was stirred at 180 °C for 30 minutes after which 1.07 g of Nickel(II) bromide (4.90 mmol, 0.14 eq) was added. A solution of 20 mL of triethyl phosphite (20 mL, 117 mmol, 3.42 eq) in 8 mL of 1,3-diisopropylbenzene was slowly added in steps. After 1 mL was added, the reaction was allowed to stir for 30 minutes after which the rest of the triethyl phosphite solution was added dropwise over a period of 5 hours. The reaction mixture was stirred over 24hr before being cooled to room temperature. Triethyl phosphate, the solvent and other by-products of the reaction were removed under vacuum. The residue was taken up in a 100 mL of ethyl acetate and washed three times with 100 mL of water each. The yellow oil was purified by column chromatography (Eluent: EtOAc:MeOH v/v 20:1). The product was retrieved as a yellow oil (10.58 g, 26.1 mmol, 76.31 %). ^{1}H-NMR ($CDCl_3$, 400 MHz) σ_H(ppm): 1.27-1.30 (12H, t, ^3J = 7.08 Hz), 1.31 (9H, s), 4.00 - 4.17 (8H, m), 7.93-7.99 (3H, m). ^{13}C-NMR ($CDCl_3$, 100 MHz) σ_C (ppm): 16.27 (t, ^3J = 3.15 Hz), 31.05 (s), 35.06 (m), 62.26-62.29 (m), 128.96 (dd, J_1 = 101.49 Hz, J_2 = 14.40 Hz), 131.94 (t, ^3J = 10.53 Hz), 132.47-132.55 (m), 151.94 (s). ^{31}P NMR ($CDCl_3$, 162 MHz) σ_p (ppm): 17.96 (s).

Synthesis of DPB-^{t}B (5-tert-butyl-1,3-benzenediphosphonic acid)

A mixture of 10.58 g 5-*tert*-butyl-tetraethyl-1,3-benzenediphosphonate (26.0 mmol, 1eq) and 80 mL of half-concentrated hydrochloric acid (40 mL) was refluxed overnight. The solution was filtered, and the filtrate removed under vacuum. The product was obtained as an off-white powder (7.12 g, 92 %). ^{1}H NMR (D_2O+NaOD, 400 MHz) σ_H (ppm): 3.52 (9H, s), 4.71-4.72 (4H,m), 10.01 – 10.11(3H, dd, J=14.4883 Hz). ^{13}C NMR (D_2O+NaOD, 100 MHz) σ_C (ppm): 31.43 (s), 35.01 (s), 130.59 (s), 133.3 (s), 135.29 (s), 150.51-150.64 (m). ^{31}P NMR (D_2O+NaOD, 162 MHz) σ_p (ppm): 14.53. FT-IR(ATR) $\tilde{\nu}$ (cm^{-1}): 3585 (vw), 2973 (w), 1651 (w), 1584 (w), 1479 (w), 1412 (w), 1364 (w), 1092 (m), 1005 (s), 938 (s), 887 (m), 819 (m) 774 (m), 698 (s), 613 (w), 563 (m) 524(s). ESI-MS: $[M-H]^-$: calculated m/z: 236.9723, observed 236.9701

Synthesis of DPB-P-OEt (*hexethyl-1,3,5-benzenetriphosphonate*)[246]

10 g of 1,3,5-tribromobenzene (31.8 mmol, 1 eq) were dissolved in 20 mL of 1,3-diisopropylbenzene under a nitrogen atmosphere and stirred at 180 °C for 30 minutes. 1 g of $NiBr_2$ (4.58 mmol, 0.14 eq) were added and the solution was stirred for another 20 minutes after which, 25 mL triethyl phosphite (24.2 g, 133.0 mmol, 4.00 eq) in 20 mL of 1,3-dibromobenzene

were slowly dropped in the solution over the next 5 hours. A steady stream of nitrogen gas over the solution was maintained during the reaction to remove ethyl bromide from the atmosphere. The reaction was stirred at 180 °C for 24 hours before cooled to room temperature before triethyl phosphite, solvent and other by-products were distilled of under a high vacuum. The residue was purified by column chromatography with an eluent of DCM:MeOH (20:1). The product was obtained as a slightly yellow oil. Yield: 4.52 g (29.3 %).^{1}H-NMR ($CDCl_3$, 400 MHz) σ_H (ppm): 8.37 – 8.44 (3H, m), 4.10 – 4.26 (12H, m), 1.36 (18H, t, ^{3}J = 7.07 Hz). ^{31}P-NMR ($CDCl_3$, 162 MHz) σ_P (ppm): 15.34.

Synthesis of DPB-P (1,3-5-benzenetriphosphonic acid)

4.5 g of hexethyl-1,3,5-benzenetriphosphonate were dissolved in 50 mL of half-concentrated hydrochloric acid and refluxed overnight. After filtration the solvent was removed under vacuum and the product obtained as a white powder. Yield: (2.62 g, 89 %) ^{1}H-NMR (D_2O+NaOD, 400 MHz) σ_H (ppm): 8.06 – 8.12 (3H, m) ^{13}C-NMR (D_2O, 100 MHz) σ_c (ppm): 133.48 (tt, J_{CP} = 180.42 Hz, J_{CP} = 12.29 Hz), 134.76 – 134.08 (m). ^{31}P-NMR (D_2O+NaOD, 162 MHz) σ_P (ppm): 12.79 (s). FT-IR(ATR) $\tilde{\nu}$ (cm^{-1}): 1586 (m), 1416 (m), 1227 (w), 1178 (m), 1123 (m), 1065 (m), 992 (s), 932 (s), 891 (m), 734 (m), 684(s), 574 (w), 509 (s).

Synthesis of DPB-Br-OEt (tetraethyl-5-bromo-1,3-benzenediphosphonate)[246]

1,3,5-Tribromobenzene (10 g; 31.85 mmol, 1 eq) was dissolved in 1,3-diisopropylbenzene (10 mL) and degassed with nitrogen. This mixture was stirred at 180 °C for 20 mins under a nitrogen atmosphere. To the reaction mixture, 1.07 g of Nickel(II) bromide(4.90 mmol, 0.15 eq) was added. A solution of 20 mL of triethyl phosphite (12 mL; 63.8 mmol, 2.1 eq) in 8 mL of diisopropylbenzene was added next. After 1 mL was added, the reaction was allowed to stir for 30 minutes after which the rest of the triethyl phosphite solution was added dropwise over a period of 5 hours. The reaction mixture was stirred for 24hr before being cooled to room temperature. Triethyl phosphite, solvent and other by-products were removed under high vacuum. The residue was purified by column chromatography with an eluent of EtOAc:MeOH (20:1). The product yielded as a yellow oil. Yield: 2.77 g, 20 % ^{1}H NMR ($CDCl_3$, 400 MHz) σ_H (ppm): 1.37 (12H, t, ^{3}J = 7.07 Hz), 4.09 - 4.26 (8H,m), 8.10 - 8.19 (3H, m). ^{13}C NMR ($CDCl_3$, 100 MHz) σ_C (ppm): 16.31 - 16.34 (m), 62.71 - 62.77 (m), 123.26 (s), 130.90-131.03 (m), 132.91 - 133.10 (m), 138.13 - 138.16 (m). ^{31}P NMR ($CDCl_3$, 162 MHz) σ_p (ppm): 14.62.

Synthesis of DPB-Br (5-bromo-1,3-benzenediphosphonic acid)

2.77 g of tetraethyl-5-bromo-1,3-benzenediphosphonate (6.45 mmol) was refluxed in 20 mL of half-concentrated hydrochloric acid overnight. The solution was filtered, and the filtrate

evaporated under vacuum. The product was obtained as an off-white powder (2.03 g, 99 %). ^{1}H NMR (D_2O+NaOD, 400 MHz) σ_H (ppm): 7.87-7.89(3H, m). ^{13}C NMR (D_2O+NaOD, 100 MHz) σ_C (ppm): 122.68 (d, J = 17.71 Hz), 130.60 (t, ^{3}J = 10.47 Hz), 135.79 (d, 3J = 8.21Hz), 129.62 (dd, J1 = 178.20 Hz, J2 = 13.21Hz). ^{31}P NMR (D_2O+NaOD, 162 MHz) σ_p (ppm): 11.75. FT-IR(ATR) $\tilde{\nu}$ (cm^{-1}): 2737 (br), 2270 (br), 1581 (vw), 1564 (vw), 1413 (vw), 1394 (w) 1114 (m), 1084 (s), 1101 (s), 988 (s), 933 (s), 878 (m) 780 (m), 766 (m), 677 (s), 556 (m), 540 (m), 524 (s), 512 (m). ESI-MS: $[M-H]^-$: calculated m/z: 314.8840, observed m/z: 314.8828.

Synthesis of DPPy-O^{i}Pr (tetraisopropyl-2,6-pyridinediphosphonate)[272]

3 g of 2,6-dibromopyridine (12.7 mmol, 1 eq), 5 g of diisopropyl phosphite (5.1 mL, 30.4 mmol, 2.4 eq), 4.26 g of ethyldiisopropyl amine (5.74 mL, 32.9 mmol, 2.60 eq), 57 mg of palladium(II)acetate (0.253 mmol, 0.02 eq) and 154 mg of bis(diphenylphosphino)ferrocene (0.279 mmol, 0.02 eq) were dissolved under a nitrogen atmosphere in 12 mL of acetonitrile and refluxed for 24 hours. The solution was filtered, and the residue extracted three times with ethyl acetate. The residue was purified by column chromatography with DCM as the eluent. The product was obtained as a yellow oil. Yield: 1.1 g (25 %) ^{1}H-NMR (CDCD2Ol$_3$, 400 MHz) σ_H (ppm): 1.35 (24H, dd, ^{2}J = 54.15 Hz, ^{3}J = 6.19 Hz), 4.75 – 4.83 (4H, m) 8.47 (dt, 2H, ^{3}J = 13.2 Hz, J_{HP} = 6.19 Hz), 9.09 – 9.12 (1H, m). ^{31}P-NMR ($CDCl_3$, 162 MHz) σ_P (ppm): 12.1 (s).

Synthesis of DPPy (pyridine-2,6-diphosphonic acid)

1.1 g of tetraisopropyl-2,6-pyridinediphosphonate was dissolved in 20 mL DCM under nitrogen and treated with 2.5 mL of trimethylsilyl bromide (2.90 g, 18.9 mmol, 7.02 eq). The mixture was stirred for 2 days, after which it was treated with 20 mL of water and stirred for another hour. The solution was evaporated under vacuum and the product obtained as an off-white powder. Yield: 0.352 g (54 %)

^{1}H-NMR (D_2O+NaOD, 400 MHz) σ_H (ppm): 8.11 (tt, 1H, ^{3}J = 11.1 Hz, J_{HP} = 1.87 Hz), 8.54 – 8.57 (2H, m)^{13}C-NMR (D_2O+NaOD, 100 MHz) σ_c (ppm): 135.29 (dd, J = 163.88 Hz, J = 8.27 Hz), 140.13 (t, J = 7.33 Hz), 149.67 (d, J = 11.88 Hz). ^{31}P-NMR (D_2O+NaOD, 162 MHz) σ_P (ppm): 8.25. FT-IR(ATR) $\tilde{\nu}$ (cm^{-1}): 3301 (w), 3102 (m), 2660 (m), 2077 (w), 1619 (m), 1400 (m), 1204 (w), 1124 (m), 931 (s), 860 (m), 673 (s), 525 (s).

Synthesis of DPB-NH$_2$-O^{i}Pr (tetrakisisopropyl-3,5-aniline-diphosphonate)[273]

2 g of 3,5-dibromoaniline (7.97 mmol, 1 eq) together with 0.179 mg of palladium(II)acetate (0.797 mmol, 0.1 eq) and 105 mg of triphenylphosphine (0.398 mg, 0.05 eq) were combined under a nitrogen atmosphere. 5 mL of diisopropyl phosphite (4.99 g. 32.26 mmol, 4.8 eq) in 10 mL Ethanol and 5.12 mL of N,N'-dicyclohexylmethylamine (4.67 g, 23.9 mmol, 3 eq) in 10 mL

Ethanol were added subsequently. The mixture was refluxed overnight, cooled down to room temperature and evaporated under nitrogen. The residue was purified *via* column chromatography using DCM/MeOH (10:1) as an eluent. Yield : 0.78 g (27 %). ^{1}H-NMR (DMSO-d^{6}, 400 MHz) σ_H (ppm): 1.23 (24H, dd, ^{2}J = 41.6 Hz, ^{3}J = 6.18 Hz), 4.50 – 4.55 (4H, m), 5.78 (2H, s), 7.08 – 7.12 (3H, m). ^{13}C-NMR (DMSO-d^{6}, 100 MHz) σ_c (ppm): 24.09 (d, J = 31.4 Hz), 70.58, 119.58 – 119.75 (m), 131.14 (dd, J = 185.17 Hz, J = 15.32 Hz, 149.42 (t, J = 16.16 Hz). ^{31}P-NMR (DMSO-d^{6}, 162 MHz) σ_P (ppm): 16.01.

Synthesis of DPB-NH$_2$ (3,5-anilinediphosphonic acid)

0.780 g (1.85 mmol, 1 eq) of tetrakisisopropyl-3,5-aniline-diphosphonate was dissolved in 5 ml DCM under a nitrogen atmosphere and treated with 1.5 mL of trimethylsilyl bromide (1.74 g, 11.3 mmol, 6.14 eq). The mixture was stirred for 2 days after which it was treated with 10 mL of water. The solvents were removed under reduced pressure and the product obtained as an off-white powder. Yield: 0.298 g (63 %). ^{1}H-NMR (DMSO-d$_6$, 400 MHz) σ_H (ppm): 7.01 – 7.05 (2H, m), 7.22 (t, J = 12.73 Hz). ^{31}P-NMR (DMSO-d$_6$, 162 MHz) σ_P (ppm): 13.33. FT-IR(ATR) $\tilde{\nu}$ (cm^{-1}): 3375 (w), 2777 (br), 1683 (m), 1623 (m), 1585 (m), 1410 (m), 1278 (w), 1153 (m), 1132(m), 1077 (m), 996 (m), 932 (m), 917 (s), 882 (m), 810 (w), 714 (w), 683 (s), 599 (w), 583 (w), 539 (m), 503 (m).

7.1.2 Inorganic compounds

*Synthesis of **NH$_4$-V$_{10}$ (1)***

0.044 g NH_4VO_3 (0.381 mmol, 1 eq), 0.070 g NaN_3 (1.08 mmol, 2.83 eq) and 0.050 g H_4PSP (0.205 mmol, 0.538 eq) were dissolved in 1 mL H_2Om 3 mL DMF and 1 mL MeCN. The yellow solution was heated to 70 °C before the pH was adjusted to pH = 7.0 *via* concentrated HCl. After the addition of 16 µL of $N_2H_4 \cdot H_2O$ the solution turned green and was readjusted to pH = 7.0. The solution was stirred for 3 minutes before it was cooled down to room temperature and filtered. The solution was split to 1mL samples. 0.5 mL MeCN was diffused into each sample. Green crystals formed after two days, which were filtered and dried in air at 40 °C overnight. Yield: 0.045 g (60 % based on vanadium). Selected FT-IR signals (ATR-Diamond) / (cm^{-1}): 3190 (m), 3004 (m), 2824 (m), 1623 (w), 1424 (m), 1291 (w), 1209 (w), 1119 (m), 1095 (m), 1048 (s), 1002 (m), 940 (s), 751 (m), 652 (m), 591 (s), 556 (s). CHN analysis for $C_{18}H_{63}N_{11}O_{48}P_8V_{10}$; Expected: C: 9.47, H: 2.88, N: 6.90, S: 6.32; Found: C: 9.41, H: 3.00, N: 7.83, S: 6.57.

Synthesis of ***Na-V$_{10}$ (2)***

Na-V$_{10}$ is synthesized *via* the same procedure as **NH$_4$-V$_{10}$** by replacing NH_4VO_3 with 0.044 g of Na_3VO_4 (0.381 mmol). Green crystals formed several 2 days. Yield: 0.003 g (3 % based on vanadium) Selected FT-IR signals (ATR-Diamond) / (cm^{-1}): 3331 (br), 1634(m), 1501 (w), 1292 (vw), 1212 (vw), 1132 (m), 1052 (m), 1013 (m), 962 (s), 751(w), 584 (m), 555(m).

Synthesis of ***Na-V$_{12}$ (3)***

0.070 g Na_3VO_4 (0.381 mmol, 1 eq) and 0.050 g H_4PSP (0.205 mmol, 0.538 eq) were dissolved in 1 mL H_2O, 3 mL DMF and 1 mL MeCN. The yellow solution was heated to 70 °C before the pH was adjusted to pH = 5 *via* concentrated HCl. After the addition of 16 µL of $N_2H_4{\cdot}H_2O$ the solution turned green and was readjusted to pH = 5. After stirring for 30 minutes at 70 °C, it was cooled down to room temperature and the blue precipitate filtered off. The green solution was split to 1mL samples. 0.5 mL MeCN was diffused into each sample. The green solution turned blue after several days, after which blue crystals formed, which were filtered and dried in at 40 °C overnight. Yield: 0.030 g (27 % based on vanadium) Selected FT-IR signals (ATR-Diamond) / (cm^{-1}): 3324 (br), 1617 (m), 1508 (w), 1291 (vw), 1207 (vw), 1123 (m), 1080 (m), 1046 (s), 1021 (m), 960 (s), 821 (m), 751 (m), 680 (m), 573 (s). CHN analysis for $C_{16}H_{80}Na_{12}O_{78}P_8S_4V_{12}$; Expected: C: 8.83, H: 2.59, S: 5.89, Found: C: 8.12, H: 2.30, N: 2.43, S: 5.81.

Synthesis of ***K-V$_{12}$ (4)***

K-V$_{12}$ is synthesized *via* the same procedure as **Na-V$_{12}$** by replacing Na_3VO_4 with 0.088 g of NH_4VO_3 (0.381 mmol). Blue crystals formed after several days. Yield: 0.004 g. Selected FT-IR signals (ATR-Diamond) / (cm^{-1}): 3575 (w), 3340 (br), 1634 (m), 1127 (m), 1082 (m), 1049 (s), 1022 (m), 962 (s), 883 (m), 750 (w), 575 (m).

Synthesis of ***V$_{20}$H-Cs (5)***

0.070 g Na_3VO_4 (0.381 mmol, 1 eq) and 0.070 g NaN_3 (1.08 mmol, 2.83 eq) and 0.193 g CsCl (1.14 mmol, 3 eq) were dissolved in 3 mL H_2O. In a second solution 0.050 g H_4DPB-H (0.210 mmol, 0.55 eq) was dissolved in 1 mL DMF. Both solutions were combined and 1 mL MeCN was added to the mixture. The yellow solution was heated to 70 °C before the pH was adjusted to pH = 7 *via* concentrated HCl. After the addition of 16 µL of $N_2H_4{\cdot}H_2O$ the solution turned green and was readjusted to pH = 7. After stirring for 1 minute at 70 °C, the solution was cooled down to room temperature. The green solution was split to 1mL samples, into which 0.5 mL MeCN was diffused into each sample. Green crystals formed after 2 days, which were filtered and dried at 40 °C overnight. Yield: 0.054 g (41 % based on vanadium). CHN analysis for

$Cs_{11.5}(V_{20}P_{16}O_{84}Na_{0.5}Cs_8C_{48}H_{32})(CH_3CN)(H_2O)_{33}$; Expected: C: 8.96, H: 1.52, N: 0.21, Found: C: 9.15, H: 1.42, N: 0.23. Selected FT-IR signals (ATR-Diamond) / (cm^{-1}): 3306 (br), 2052 (w), 2032 (w), 1644 (br), 1468 (w), 1390 (w), 1110 (m), 1032 (m), 958 (s), 798 (m), 686 (m). 644 (m), 574 (m).

Synthesis of ***V_{20}H-Rb (6)***

V_{20}H-Rb was synthesised in the same way as **V_{20}H-Cs** by substituting CsCl with 0.138 g RbCl (1.14 mmol, 3 eq). Yield: 0.048 g (43 % based on vanadium) CHN analysis for $Rb_{13}[V_{20}P_{16}O_{84}NaRb_8C_{48}H_{32}Cl_2](H_2O)_{30}$; Expected: C: 9.77, H: 1.57, N: 0.00, Found: C: 9.58, H: 1.71, N: 0.00. Selected FT-IR signals (ATR-Diamond) / (cm^{-1}): 3320 (br), 1646 (br), 1394 (w), 1118 (m), 1034 (m), 958 (s), 802 (m), 696 (m). 638 (m), 570 (m).

Synthesis of ***V_{20}H-K (7)***

V_{20}H-K was synthesised in the same way as **V_{20}H-Cs** by substituting Na_3VO_4 with 0.088 g K_3VO_4 (0.380 mmol, 1 eq) and not using CsCl. Yield: 0.003 g (3 % based on vanadium) CHN analysis for $K_{12}[V_{20}P_{16}O_{84}K_9C_{48}H_{32}](N_3)(H_2O)_{27}$; Expected: C: 11.96, H: 1.80, N: 0.87, Found: C: 11.91, H: 1.91, N: 0.99. Selected FT-IR signals (ATR-Diamond) / (cm^{-1}): 3324 (br), 2062 (m), 1644 (br), 1392 (w), 1106 (m), 1038 (m), 960 (s), 800 (m), 694 (m), 568 (m).

Synthesis of ***$V_{20}NH_2$-Rb (8)***

$V_{20}NH_2$-Rb was synthesized in the same way as **V_{20}H-Rb** by substituting H_4DPB-H with 0.053 g H_4DPB-NH_2 (0.210 mmol, 0.55 eq). The product was obtained as green crystals after several hours together with a non-removable side-product, which prevented further characterisation.

Synthesis of ***V_{20}Py-Rb (9)***

V_{20}Py-Rb was synthesized in the same way as **V_{20}H-Rb** by substituting H_4DPB-H with 0.050 g H_4DPB-Py (0.210 mmol, 0.55 eq). The product was obtained as green crystals together with a non-removable side-product, which prevented further characterisation.

Synthesis of ***$V_{20}{}^{t}$B-K (10)***

$V_{20}{}^{t}$B-K was synthesized in the same way as **V_{20}H-K** by substituting H_4DPB-H with 0.062 mg H_4DPB-^{t}B (0.210 mmol, 0.55 eq). Yield: 0.010 g (10 % based on vanadium). CHN analysis for $K_{13}[V_{20}P_{16}O_{84}NaK_8C_{80}H_{96}Cl_2] \cdot 25\ H_2O$: Expected: C: 15.93 H: 2.44 N: 0.00, Found: C: 16.03, H: 2.39, N: 0.20. Selected FT-IR signals (ATR-Diamond) / (cm^{-1}): 3366 (br), 2962 (m), 1635 (br), 1464 (w), 1412 (w), 1366 (w), 1127 (s), 1044 (m), 955 (s), 825 (w), 708 (m).

Synthesis of ***$V_{20}{}^{t}$B-Rb (11)***

$V_{20}{}^{t}$B-Rb was synthesized in the same way as **V_{20}H-Rb** by substituting H_4DPB-H with 0.062 mg H_4DPB-^{t}B (0.210 mmol, 0.55 eq). Yield: 0.008 g (8 % based on vanadium). CHN analysis for $Rb_{13}[V_{20}P_{16}O_{84}NaRb_8C_{80}H_{96}Cl_2] \cdot 29\ H_2O$: Expected: C: 15.18 H: 2.45 N: 0.00, Found: C: 15.31, H: 2.07, N: 0.09. Selected FT-IR signals (ATR-Diamond) / (cm^{-1}): 3352 (br), 2958 (m), 1644 (br), 1412 (w), 1365 (w), 1123 (s), 1038 (m), 965 (s), 823 (w), 702 (m), 575 (m).

Synthesis of ***$V_{20}{}^{t}$B-Cs (12)***

$V_{20}{}^{t}$B-Cs was synthesized in the same way as **V_{20}H-Cs** by substituting H_4DPB-H with 0.062 mg H_4DPB-^{t}B (0.210 mmol, 0.55 eq). Yield: 0.012 g (9 % based on vanadium). CHN analysis for $Cs_{13}[V_{20}P_{16}O_{84}NaCs_8C_{80}H_{96}Cl_2] \cdot 26\ H_2O$: Expected: C: 13.22 H: 2.05 N: 0.00, Found: C: 13.57, H: 1.89, N: 0.09. Selected FT-IR signals (ATR-Diamond) / (cm^{-1}): 3364 (br), 2952 (m), 2870 (w), 1634 (br), 1464 (w), 1408 (w), 1366 (w), 1120 (s), 1028 (m), 962 (s), 819 (w), 703 (m), 652 (w), 570 (m).

Synthesis of ***V_{30}-K (13)***

0.070 g Na_3VO_4 (0.380 mmol, 1 eq) was dissolved in 3mL of water and 1mL of MeCN together with 0.070 g NaN_3 (1.08 mmol, 2.83 eq) and 0.086 g KCl (1.14 mmol, 3 eq). In a second solution 0.066 g benzene-1,3,5-triphosphonic acid was dissolved in in 1mL DMF. Both solutions were combined and heated to 70 °C. 16 µL of $N_2H_4 \cdot H_2O$ was added to the solution, which subsequently turned green. The solution was stirred for one hour, during which a dark green precipitate formed. The solution was cooled down to room temperature before the colourless supernatant solution was removed. The precipitate was dissolved in 3mL of water. Non-dissolved residuals were filtered of and 0.5 mL of DMF was added to the solution. Green crystals of **V_{30}-K** formed after several weeks, which were sorted by hand in the mother liquor. Yield: 0.004 g (4.5 %). CHN analysis for $K_{27}[V_{30}P_{24}O_{140}C_{48}H_{24}K_4]N_3 \cdot 45\ H_2O$; Expected: C: 8.03, H: 1.60, N: 0.58, Found: C: 6.73, H: 1.58, N: 0.72. Selected FT-IR signals (ATR-Diamond) / (cm^{-1}): 3350 (br), 1629 (br), 1403 (w), 1120 (m), 1034 (m), 952 (s), 821 (w), 542 (m).

Synthesis of ***V_{30}-Rb (14)***

V_{30}-Rb was synthesized in the same way as **V_{30}-K** by substituting KCl for 0.138 g RbCl (1.14 mmol, 3 eq).Yield: 0.003 g (2.8 %) CHN analysis for $Rb_{27}[V_{30}P_{24}O_{140}C_{48}H_{24}K_4]N_3 \cdot 50\ H_2O$; Expected: C: 6.62, H: 1.44, N: 0.48, Found: C: 5.96, H: 1.4, N: 0.54. Selected FT-IR signals (ATR-Diamond) / (cm^{-1}): 3350 (br), 1629 (br), 1403 (w), 1120 (m), 1034 (m), 952 (s), 821 (w), 542 (s). 3367 (br), 2069 (w), 1652 br), 1122 (m), 1040 (m), 969 (s), 817 (w), 552 (s).

*Synthesis of **V_{30}-Na (15)***

V_{30}-Na was synthesized in the same way as **V_{30}-K** without KCl. Yield: 0.006 g (7 %). CHN analysis for $Na_{30}[V_{30}P_{24}O_{140}C_{48}H_{24}]N_3 \cdot 53\ H_2O$; Expected: C: 8.47, H: 1.92, N: 0.61, Found: C: 7.35, H: 1.85, N: 0.69. Selected FT-IR signals (ATR-Diamond) / (cm^{-1}): 3350 (br), 1629 (br), 1403 (w), 1120 (m), 1034 (m), 952 (s), 821 (w), 542 (m).

*Synthesis of **V_{30}-Cs (16)***

V_{30}-Cs was synthesized in the same way as **V_{30}-K** by substituting KCl with 0.193 g CsCl (1.14 mmol, 3 eq) Yield: 0.002 mg (1.6 %). CHN analysis for $Cs_{27}[V_{30}P_{24}O_{140}C_{48}H_{24}Cs_4]N_3 \cdot 50\ H_2O$; Expected: C: 5.66, H: 1.22, N: 0.41, Found: C: 5.01, H: 1.00, N: 0.38. Selected FT-IR signals (ATR-Diamond) / (cm^{-1}): 3378 (br), 2062 (w), 1649 (br), 1397 (w), 1123 (m), 1041 (m), 969 (s), 816 (w), 552 (m).

*Synthesis of **Mo_2 (17)***

Solution 1 was prepared from 1.57 g $\{K_{0.40}(NMe_4)_{0.1}I_{0.5}[Mo_2O_2S_2(OH)_2(H_2O)] \cdot 6.3\ H_2O\}_5$ [112] in 58 mL 0.3 M HCl. 0.446 g tetrahydrofurantetracarboxylic acid (18.0 mmol, 206 eq) was dissolved 10 mL of water. The pH was adjusted to $pH = 7$ with an aqueous 1 M K_2CO_3 solution. 8.8 mL of solution 1 (0.0873 mmol, 1 eq.) was added and the pH adjusted to $pH = 4$ with 1 M HCl. The orange solution was stirred for one hour at room temperature before it was filtered and left to crystallise. After 1 year orange crystals of **Mo_2** formed, which were washed with water and methanol. Yield: 45 mg (10 % based on molybdenum). Selected FT-IR signals (ATR-Diamond) / (cm^{-1}): 1715 (m), 1634 (s), 1382 (m), 1229 (m), 1067 (w), 925 (m), 806 (w), 744(w), 473 (m), 440 (m), 352 (m), 316 (s).

*Synthesis of **Mo_{16} (18)***

100 mg cyclopentanetetracarboxylic acid (0.406 mol, 10.9 eq) were dissolved in 5 mL of water. 100 mg of $\{K_{0.40}(NMe_4)_{0.1}I_{0.5}[Mo_2O_2S_2(OH)_2(H_2O)] \cdot 6.3\ H_2O\}_5$ (37.1 mmol, 1 eq) were added to the solution and the suspension sonicated until a clear solution was formed. The pH was adjusted to $pH = 4.5$ with 1 M K_2CO_3 and the solution was stirred for one hour at room temperature. The solution was filtered and left to crystallise. After 1 year orange crystals of the product were formed which were washed with water and methanol. Yield: 20 mg (21 %). Selected FT-IR signals (ATR-Diamond) / (cm^{-1}): 2981 (w), 1712 (m), 1538 (m), 1403 (m), 1189 (s), 1163 (m), 1097 (w), 943 (w), 848 (w), 799 (w), 768 (w), 735 (w), 682 (m), 584 (w), 547 (w), 509 (w), 428 (w), 381 (w), 341 (w), 318 (w).

Synthesis of ***Mo₁₂*** ***(19)***

A solution of 250 mg of $\{K_{0.40}(NMe_4)_{0.1}I_{0.5}[Mo_2O_2S_2(OH)_2(H_2O)] \cdot 6.3\ H_2O\}_5$ (0.0926 mmol, 1 eq) in 3 mL of 0.5 M HCl was added to a solution of 0.038 g mellitic acid (0.111 mmol, 1.2 eq) in 3 mL of water. The pH of the solution was adjusted to pH = 4.5 and stirred at 50 °C for one hour before it was filtered and left to crystallise. The product was obtained as yellow-orange crystals. Yield: 34 mg (17 % based on molybdenum). Selected FT-IR signals (ATR-Diamond) / (cm^{-1}): 3206 (br), 1600 (s), 1436 (m), 1415 (m), 1324 (m), 1266 (w), 926 (s), 659 (w), 612 (w), 494 (w), 458 (w), 391 (w), 325 (m), 301 (s).

Synthesis of ***Mo₃₀*** ***(20)***

0.113 g mellitic acid (0.330 mmol, 1.1 eq) was dissolved in 2mL water and the pH adjusted to pH = 8.65 *via* a 1 M K_2CO_3 solution. After addition of 0.028 Na_2MoO_4 (0.136 mmol, 0.45 eq) in 0.5 mL H_2O a solution of 0.044 g $\{K_{0.40}(NMe_4)_{0.1}I_{0.5}[Mo_2O_2S_2(OH)_2(H_2O)] \cdot 6.3\ H_2O\}_5$ (0.0163 mmol, 0.55 eq) and 0.025 g KCl in 1mL of water was added to the solution. After addition of 1.6 mL of a 0.3 M HCl solution the pH was adjusted to pH = 4.4 *via* a 60 % aqueous solution of acetic acid. The solution was stirred at room temperature for one hour, filtered and left to crystallise. Dark blue crystals of **Mo₃₀** formed after several weeks. The crystals were sorted by hand and washed with DCM. Yield: 3 mg (< 1 % based on molybdenum). Selected FT-IR signals (ATR-Diamond) / (cm^{-1}): 3404 (br), 1594 (m), 1567 (s), 1428 (s), 1341 (s), 903 (m), 839 (m), 812 (m), 696 (m), 596 (m), 522 (m), 482 (w), 362 (w), 302 (s).

Synthesis of $(NH_4)_2MoO_2S_2$ [274]

10.0 g of ammonium molybdate tetrahydrate (8.09 mmol, 1 eq) was dissolved in 30 mL water and 50 mL of a 35 % aqueous ammonia solution. The solution was cooled in an ice bath and a steady stream of H_2S gas was passed over the stirring solution. After 1 hour the solution turned yellow and an orange precipitate formed. After enough precipitate formed the solution was left to stand for 10 minutes under an H_2S atmosphere. After filtration the orange precipitate was washed with cold ethanol and cold ether. The product was dried under vacuum and stored under nitrogen. Yield: 9.05 g (70 % based on molybdenum). Selected IR signals (ATR-Diamond) / (cm^{-1}): 3108 (m, br) 2938 (m, br), 2748 (m), 2375 (w), 1747 (w), 1651 (m), 1385 (w), 779 (s, M=O), 470 (s, Mo=S).[274]

Synthesis of $(NMe_4)_2Mo_2O_2S_6$ [275]

9.05 g $(NH_4)_2MoO_2S_2$ (34.4 mmol, 1 eq) was dissolved in 100 mL water and boiled for 10 minutes. After that a solution of sodium hydroxide (2.51g, 62.8 mmol, 1.82 eq) and tetramethylammonium chloride (4.02g, 36.7 mmol, 1.06 eq) dissolved in 400 mL water was added slowly to the solution and the solution was left to cool down and stored overnight on ice. The product formed overnight as an orange crystalline precipitate, which was filtered, washed with water, methanol and ether and dried in air. Yield: 1.67 g (26 % based on sulfur). Selected IR signals (ATR-Diamond) / (cm^{-1}): 3382 (br), 3010 (w), 1476 (m), 1441 (m), 1407 (m), 1281 (w), 1165(w), 1067 (w), 924 (s, Mo=O), 506 (m, S-S), 467 (m), 354 (s), 320 (m), 279 (m), 250 (m). [276]

Synthesis of $\{K_{0.40}(NMe_4)_{0.1}I_{0.5}[Mo_2O_2S_2(OH)_2(H_2O)] \cdot 6.3\ H_2O\}_5$ [112]

2.67 g of KI (16.1 mmol, 5.43 eq) were dissolved with 1.50 g I_2 (5.90 mmol, 2 eq) in 11.7 mL of 1 M HCl. This solution was added under vigorous stirring to a suspension of 1.67 g of $(NMe_4)_2Mo_2O_2S_6$ (2.96 mmol, 1 eq) in 10 mL of 0.7 M KI (7.00 mmol, 2.36 eq). The solution was heated to 50 °C for 10 minutes and the precipitates filtered. The red filtrate was kept on ice for an hour and was filtered again. The pH was adjusted to $pH = 1.5$ with 4 M KOH solution upon which a yellow precipitate formed. The solution was kept on ice for another hour, filtered and washed with cold ethanol and ether. Yield: 0.860 g (54 % based on molybdenum). Selected FT-IR signals (ATR-Diamond) / (cm^{-1}): 3562 (w), 3314 (m, br), 1603 (m), 1483 (w), 1082 (w), 969 (m, M=O), 948 (m), 519 (s, Mo-OH=Mo), 487 (Mo-S-Mo) 409 (m), 342 (s), 289 (m), 264 (m).[112]

1. SAINT+, Bruker AXS Inc., Madison, Wisconsin, USA, 2012.
2. G. Sheldrick, SADABS, Bruker ASX Inc., Madison, Wisconsin, USA., 2014.
3. G. Sheldrick, *Acta Cryst.*, 2015, **A71**, 3-8.
4. O. V. Dolomanov, L. J. Bourhis, R. J. Gildea, J. A. K. Howard and H. Puschmann, *J. Appl. Crystallogr.*, 2009, **42**, 339-341.
5. G. Sheldrick, *Acta Cryst.*, 2015, **C71**, 3-8.
6. A. Spek, *Acta Cryst.*, 2015, **C71**, 9-18.
7. G. M. Sheldrick, Alphabetical list of SHELXL instructions, http://shelx.uni-goettingen.de/shelxl_html.php, (accessed 13/10/2019, 2019).
8. M. J. Frisch, G. W. Trucks, H. B. Schlegel, G. E. Scuseria, M. A. Robb, J. R. Cheeseman, G. Scalmani, V. Barone, B. Mennucci, G. A. Petersson, H. Nakatsuji, M. Caricato, X. Li, H. P. Hratchian, A. F. Izmaylov, J. Bloino, G. Zheng, J. L. Sonnenberg, M. Hada, M. Ehara, K. Toyota, R. Fukuda, J. Hasegawa, M. Ishida, T. Nakajima, Y. Honda, O. Kitao, H. Nakai, T. Vreven, J. J. A. Montgomery, J. E. Peralta, F. Ogliaro, M. Bearpark, J. J. Heyd, E. Brothers, K. N. Kudin, V. N. Staroverov, R. Kobayashi, J. Normand, K. Raghavachari, A. Rendell, J. C. Burant, S. S. Iyengar, J. Tomasi, M. Cossi, N. Rega, J. M. Millam, M. Klene, J. E. Knox, J. B. Cross, V. Bakken, C. Adamo, J. Jaramillo, R. Gomperts, R. E. Stratmann, O. Yazyev, A. J. Austin, R. Cammi, C. Pomelli, J. W.

Ochterski, R. L. Martin, K. Morokuma, V. G. Zakrzewski, G. A. Voth, P. Salvador, J. J. Dannenberg, S. Dapprich, A. D. Daniels, Ö. Farkas, J. B. Foresman, J. V. Ortiz, J. Cioslowski and D. J. Fox, Gaussian 09, Guassian Inc., Wallingford CT, 2009.
9. J. P. Perdew, K. Burke and M. Ernzerhof, *Phys Rev Lett*, 1996, **77**, 3865-3868.
10. C. Adamo and V. Barone, *J Chem Phys*, 1999, **110**, 6158-6170.
11. M. Dolg, U. Wedig, H. Stoll and H. Preuss, *J Chem Phys*, 1987, **86**, 866-872.
12. M. J. Frisch, J. A. Pople and J. S. Binkley, *J Chem Phys*, 1984, **80**, 3265-3269.
13. M. M. Francl, W. J. Pietro, W. J. Hehre, J. S. Binkley, M. S. Gordon, D. J. Defrees and J. A. Pople, *J Chem Phys*, 1982, **77**, 3654-3665.
14. T. Zheng, Y. Gao, L. Chen, Z. Liu, J. Diwu, Z. Chai, T. E. Albrecht-Schmitt and S. Wang, *Dalton Trans.*, 2015, **44**, 18158-18166.
15. J. Zon, V. Videnova-Adrabinska, J. Janczak, M. Wilk, A. Samoc, R. Gancarz and M. Samoc, *CrystEngComm*, 2011, **13**, 3474-3484.
16. A. Bessmertnykh, C. M. Douaihy and R. Guilard, *Chem. Lett.*, 2009, **38**, 738-739.
17. E. Cadot, B. Salignac, S. Halut and F. Sécheresse, *Angew. Chem. Int. Ed.*, 1998, **37**, 611-613.
18. P. Basu and M. Johnson, *The Integrated Approach to Chemistry Laboratory: Selected Experiments*, Destech Publications Incorporated, Lancaster, 2009.
19. W. Rittner, A. Müller, A. Neumann, W. Bäther and R. C. Sharma, *Angew. Chem. Int. Ed.*, 1979, **18**, 530-531.
20. A. Mueller, E. Krickemeyer and U. Reinsch, *Z. Anorg. Allg. Chem.*, 1980, **470**, 35-38.

Chapter 8

Conclusions and Outlook

8.1 Summary and Conclusions

The main objective of this thesis was the synthesis and characterisation of novel hybrid organic-inorganic polyoxovanadate capsules and ring structures by utilising templating strategies involving covalent and non-covalent interactions. In summary the synthesis and characterisation of 20 novel hybrid organic-inorganic polyoxovanadate and polyoxothiomolybdate compounds is reported, of which 19 were structurally characterised by SXRD. All compounds were further characterised, wherever possible, by supplemental techniques such as IR spectroscopy, CHN analysis, TGA, ESI-MS, PXRD, NMR and UV-VIS spectroscopy.

In **chapter 2**, literature known hybrid organic-inorganic $\{V_{10}\}$ capsules were used as a starting point to synthesize molecules which could act as "molecular flask"-like catalysts for oxidation reactions. In order to make the interior more accessible for organic molecules the bent ligand thiophene-2,5-bisphosphonate (PSP^{4-}) was used to synthesize the novel POV-based capsules **NH_4-V_{10} (1)** and **Na-V_{10} (2)**. Due to the bent in the ligand the capsule displayed flexible window sizes, which were found to be dependent on the guest-molecule inside the capsule. This behaviour could prove important for future catalytic applications, especially regarding a capture and release mechanism of guest molecules. The successful inclusion of a heteroatom into the $\{V_{10}\}$ capsule additionally exemplifies the possibility of tuning the electronic environment within the cage. These two improvements over the literature known compounds show the versatility of the $\{V_{10}\}$ system and its potential to be tailored for desired applications. The synthesis of **NH_4-V_{10}** and **Na-V_{10}** therefore represents an important step up towards POV-based capsules for oxidation catalysis.

Decreasing the pH and prolonging the reaction time in the synthesis of **Na-V_{10}** led to the torus shaped compound **Na-V_{12} (3)**, whose structure consists of three rare V^{IV} cubane units that are arranged in a triangle and bridged by six PSP^{4-} ligands. The geometrically frustrated compound was found to display an unusual spin ground state of S=1, which we hypothesize to result from unidentified magnetic pathways between the cubane units. Additionally, the compound was found to selectively bind alkali metal cations in the centre of the structure, favouring potassium over sodium in the solid state. The high magnetic anisotropy together with the unusual spin ground state, geometric frustration and crown-ether like behaviour makes this compound a highly interesting compound for further magnetic investigations as well as binding studies.

Increasing the bend in the bisphosphonate ligand in order to amplify the effect of the flexible window sizes led to the synthesis of a family of supramolecular hybrid organic-inorganic

polyoxovanadate clusters **V_{20}H-AM (**AM = Cs **(5)**, Rb **(6)**, K **(7)**). In **chapter 3** the use of benzene-1,3-bisphosphonate as a ligand together with heavier alkali metal chloride salts in the synthesis of a {V_{20}} torus, in which four pentanuclear {V_5^*} half-capsules are arranged around a cube of alkali metal cations in an inverted fashion was described. The central alkali metal cube is building out cation-π interactions with the benzene rings of the aromatic ligands. To maximise this interaction the bisphosphonate ligands changes its binding mode to the pentanuclear half-capsule from *syn-syn*, as in {V_{10}} to *anti-anti*, leading to the inverted half-capsules in the structure. Additionally, a previously unknown flexibility of the pentanuclear half-capsule is demonstrated by its isomerisation due to steric hindrance caused by this arrangement. To the best of our knowledge this is the first time that cation-π interactions are used as structure directing templating agents in POM chemistry. Given the ubiquity of aromatic ligand used in the construction of hybrid organic-inorganic POMs these finding could lead to an entirely new family of cation-templated hybrid POMs. The strength and importance of the cation-π interactions were shown by proving the stability of the {V_{20}} species in aqueous solution via ESI-MS. This stability is remarkable as the cation-π interactions are in direct competition to the sizeable hydration enthalpy of the respective alkali metal. The appearance of cation-π interactions in metalorganic species that were synthesized from aqueous solution is therefore rarely found in the literature, making the {V_{20}} system such exceptional compounds. While DOSY-NMR indicated partial degradation in solution, possibly due to cation leeching, the combined solid-state and solution studies proved that the cation-π interactions are an integral part of the molecule.

In **chapter 4** the effect of the cation-π interactions in the {V_{20}} systems as well as their adaptability to steric and electronic changes was probed. Improved cation-π interactions lead to reduced crystallisation times in **$V_{20}NH_2$-Rb (8)**, while no compound could be obtained for ligands with reduced cation-π interactions. This behaviour exemplifies the impact of the cation-π interactions on the system as well as the tolerance for electronic changes to the ligand. The ability of the system to tolerate sterically demanding groups was probed with the synthesis of **$V_{20}{}^tB$-AM** (AM = Cs (**11**), Rb (**10**), K (**12**)), in which a *tert*-butyl group was attached to the DPB-H ligand in the 5-position. Originally conceptualised as a way to prevent cation leeching and partial degradation, this series of compound was found to exhibit similar solution behaviour as the **V_{20}H-AM** compounds, indicating different pathway of degradation in solution than cation leeching. The compounds synthesized in chapter 4 exemplified the versatility of the system and its potential to be chemically modified.

The displayed adaptability in chapter 4 motivated us to expand the {V_{20}} system towards {V_{30}} compounds in which six pentanuclear half-capsules are arranged around the alkali metal cube.

This work is described in **chapter 5**. By adding an additional phosphonate group to the DPB-H ligand it was possible to synthesize four novel {V_{30}} compounds, **V_{30}-K (13)**, **V_{30}-Rb (14)**, **V_{30}-Na (15)** and **V_{30}-Cs (16)**. The {V_{30}} compounds feature varying arrangements of inward-facing and outward-facing {V_5} and {V_5^*} half-capsules, which were categorised as three out of six possible isomers. Most interestingly, the arrangement of the half-capsules was found to have a direct impact on the presence of the alkali metal cube and therefore the cation-π interactions in the structure. Cations of the alkali metal cube were found to only be positioned between two adjacent inverted half-capsules, leading to isomers with only half a cube in the centre or no cube at all. Structural analysis together with theoretical calculations highlighted the importance of assisting AM-μ_3O^{2-} bonds for the cation-π interactions. These findings also explain why the {V_{20}} system favours inverted half-capsules instead of normal oriented ones in the {V_{10}} capsules, as the latter would not be able to build out the supporting AM- μ_3O^{2-} bonds. The synthesis of **V_{30}-Na**, which did not feature cation-π interactions, additionally confirmed our hypothesis from chapter 3, that sodium would not build out cation-π interactions and therefore the {V_{20}} system due to its high hydration energy.

The insights into the effects and stabilisation of cation-π interactions, gained from the {V_{20}} and {V_{30}} structures will prove invaluable for the design and synthesis of future cation-π templated hybrid POMs. We have proven that cation-π interactions are a valuable addition to existing templating strategies, whose effects can be tuned by simple modifications to the organic ligand. Not only does our approach open up a new route to otherwise unattainable structures, it also provides insights into general cationic effects in anionic hybrid POMs. We further as demonstrated a so far unknown amount of flexibility of the pentanuclear half-capsule, whose structural adaptability might be transferable to other POVs. These compounds represent a completely novel type of supramolecular assembly in the ever-growing fields of hybrid POMs and POM based polyhedra.[1-4] In summary we have laid the foundation for the use of cation-π interactions in hybrid POMs, upon which future research into the area can expand on.

In **chapter 6** we report the structures of four novel thiomolybdate compounds based on the dimeric {$Mo^{V}_2O_2S_2$} building block. The structures demonstrate how the dimeric {$Mo^{V}_2O_2S_2$} building block, which is prone to build out planar ring structures, reacts to structural challenges posed by highly functionalised ligands. While **Mo_2 (17)** uses the oxygen donor of the tetrahydrofuran ring to build out a dimeric compound **Mo_{16} (18)** and **Mo_{12} (19)** favour the planar ring structure at the expense of twisting the carboxylate groups of the ligand into position. Only the addition of a Mo^{VI} source results in the loss of ring planarity. **Mo_{30} (20)** features a mixed-valent double-decker ring system made from two twisted {Mo_{15}} rings, which are templated by

a mellitate anion each. Interestingly, some molybdenum ions in the compound are bridged simultaneously by μ_2-S^{2-} and μ_2-O^{2-} anions. It is not unlikely that this motif is a result of aerobic oxidation of the $\{Mo_2O_2S_2\}$ dimer, which would present an insight into the oxidation behaviour of thiomolybdate ring systems. The presented thiomolybdate structures present an interesting addition to the plethora of existing thiomolybdate ring systems in the literature. The high number of carboxylic acid moieties force atypical arrangements of either the ligand or the inorganic cluster.

8.2 Outlook

The synthetic success in this thesis and the discovery of cation-π interactions as integral part of hybrid organic-inorganic polyoxovanadates in this thesis presents a promising starting point for future research.

The discovery of flexible window sizes in the $\{V_{10}\}$ compounds from their crystal structures poses the question about the mechanism and behaviour of this effect in solution. Investigations into the effect of different guests on the window sizes should be undertaken alongside catalytic studies. Especially the effect of variable window sizes caused by the products and reagents of organic reactions inside the capsule would be of interest. As the capsule and windows in **NH_4-V_{10}** and **Na-V_{10}** are still too small for most organic guests, synthetic effort should be put into elongating the ligand to increase the windows, capsule and subsequently also the extent of the flexibility. Larger aromatic systems could act as the windowpanes for larger capsules. Given the proven tolerance for heteroatoms, bond angles and ligand sizes the $\{V_{10}\}$ system serves as an easy to modify model system for POV cages, whose properties can be tuned towards the desired application.

The magnetic properties of $\{V_{12}\}$ torus have only been investigated on a preliminary level. Further magnetic measurements as well as theoretical calculations of the $\{V_{12}\}$ capsule are needed to fully understand the magnetic interactions. The unusual S=1 ground spin state was hypothesized to be caused by magnetic interactions between the cubane units at low temperature. As those units are far apart there is no clear exchange mechanism present. It would be highly interesting to see if the presence of the cation in the middle of the structure plays a role in the exchange. The theoretically simple to model d^1 ions in the structure should be of advantage. On a broader scope however it is an interesting question to ask in what way the pentanuclear half-capsule and the vanadium(IV) cubane unit are synthetically related. Both structural motifs have been synthesized alongside each other with both sulfate[5] and phosphonate ligands. Investigation

into their formation could give mechanistic insights into the formation of basic polyoxovanadate building blocks.

The $\{V_{20}\}$ system represent the first examples, in which cation-π interactions are being used as structure-directing templating agents. While much is yet to be investigated about the strength and stability of cation-π supported POM assemblies we have proven that these non-covalent interactions in combination with anionic POM fragments can overcome the high hydration enthalpies of alkali metals in aqueous solution. These results will pave the way to novel hybrid organic-inorganic polyoxometalate systems, which are designed to maximise cation-π interactions. Future routes to be explored include the extension of cation-π supported hybrid POMs to other POM building metals like tungsten and molybdenum, as well as the use of non-spherical cations such as tetraalkylammonium species to explore the templating effect. The catalytical properties are worthy of investigation, as is the general influence of the cation-π interactions on the electronic and magnetic properties of the hybrid POMs.

While the possibilities for the synthesis of novel supramolecular hybrid POMs are seemingly endless there are a few aspects of the described $\{V_{20}\}$ systems, which can be expanded upon in the future. Firstly, the effect of the cation-π interactions on the $\{V_{20}\}$ systems should be further investigated. The scope of the system could be probed with different cations such as ammonium as well as different substituents on the ligand such as –CN, -F, -Cl, which modulate the cation-π interactions. The effect of the observed cation-π-π-cation interaction is also not yet entirely clear and should be further investigated via theoretical calculations in combination with structural analysis. While X-ray crystallography is an excellent tool to characterise cation-π interactions in the solid state, solution studies would give a greater insight into their stability, possible leeching effects and general behaviour. Heteronuclear NMR techniques, such as ^{39}K, ^{87}Rb or ^{133}Cs-NMR can be used to identify cation-π interactions as the alkali metal will be affected by the magnetic properties of aromatic system.

In general, the catalytic properties of the $\{V_{20}\}$ system need to be explored. Especially the differences or potential similarities between the $\{V_{10}\}$, $\{V_{20}\}$ and $\{V_{30}\}$ systems are worthy of investigation. Due to the structural similarities they are ideal candidates to investigate the difference between the $\{V_5\}$ and $\{V_5^*\}$ half-capsule as well as the effect of turning the half-capsule inside-out. Catalytic properties could be tuned by altering the electronic structure of the system via the addition of functional groups.

The free 5-position on the DPB-H ligand also opens up the possibility for additional binding sites, such as carboxylates, sulfonates or simple hydroxy groups. This could give rise to higher nuclearity polyoxovanadate species or mixed-metal systems with added functionalities. The $\{V_{30}\}$ structures described in this thesis are an example of this approach. While POM-based metal organic polyhedra have seen a surge over the last years, examples with more than one structural motif are still rare. The occurrence of both the $\{V_5\}$ as well as the $\{V_5^*\}$ half-capsule gives rise to a number of isomers, which provided insight into the stabilisation of the cation-π interactions. Synthetic effort should therefore be undertaken to synthesise the three missing isomers of the $\{V_{30}\}$ structures that have not been synthesized yet to verify the conclusions drawn.

In case of the thiomolybdate structures reported, one of the most interesting aspects is the occurrence of a molybdenum dimer which is both sulfur and oxygen bridged. This could give an insight into the oxidation behaviour of the $\{Mo_2O_2S_2\}$ dimer within ring systems. Given the double-decker structure of **Mo_{30}** structure it should also be possible to expand this system into triple-decker $\{Mo_{45}\}$ and even higher nuclearity structures.
Unfortunately, the yields could not be optimized in time of this thesis for all of the compounds. The yields of the largely optimized reactions are satisfactory, as is the case for **NH_4-V_{10}**, **Na-V_{12}**, **V_{20}H-Cs**, and **V_{20}H-Rb**, which could be obtained as good quality batches of crystals. The low yields for the other compounds are to be understood as the pure yields, for which crystals were hand-picked and washed carefully to remove impurities. Large portions of the products, such as impure powders that precipitated during the reaction, had to be discarded to ensure the purity of the batches. The reaction yield is therefor much higher than the reported one. Through optimization of the reaction conditions the unwanted side-products of the reactions can usually be avoided. Future research will therefor focus on optimising and rationalising the reaction conditions for the $\{V_{20}\}$ and $\{V_{30}\}$ compounds.

1. J.-X. Liu, X.-B. Zhang, Y.-L. Li, S.-L. Huang and G.-Y. Yang, *Coord. Chem. Rev.*, 2020, **414**, 213260.
2. A. V. Anyushin, A. Kondinski and T. N. Parac-Vogt, *Chem. Soc. Rev.*, 2020, **49**, 382-432.
3. P. Ma, F. Hu, J. Wang and J. Niu, *Coord. Chem. Rev.*, 2019, **378**, 281-309.
4. X.-X. Li, D. Zhao and S.-T. Zheng, *Coord. Chem. Rev.*, 2019, **397**, 220-240.
5. A. Ignaszak, N. Patterson, M. Radtke, M. R. J. Elsegood, J. W. A. Frese, J. L. Z. F. Lipman, T. Yamato, S. Sanz, E. K. Brechin, T. J. Prior and C. Redshaw, *Dalton Trans.*, 2018, **47**, 15983-15993.